UNIVERSIDAD AUTÓNOMA DE BAJA CALIFORNIA

INSTITUTO DE INGENIERÍA

MAESTRÍA Y DOCTORADO EN CIENCIAS E INGENIERÍA

"SISTEMA DE VISIÓN EN 3D MEDIANTE BARRIDO LÁSER PARA NAVEGACIÓN AUTÓNOMA DE ROBOTS MÓVILES"

TESIS PARA OBTENER EL GRADO DE:
DOCTOR EN CIENCIAS

PRESENTA
LUIS CARLOS BÁSACA PRECIADO

DIRECTOR
DR. OLEG SERGIYENKO

MEXICALI, B. C. ***OCTUBRE DE 2013***

RESUMEN de la tesis de Luis Carlos Básaca Preciado, presentada como requisito parcial para la obtención del grado de DOCTOR EN CIENCIAS, EN EL AREA DE OPTOELECTRONICA. Mexicali, Baja California, México, Septiembre de 2013.

SISTEMA DE VISIÓN EN 3D MEDIANTE BARRIDO LASER PARA NAVEGACIÓN AUTÓNOMA DE ROBOTS MÓVILES

Resumen aprobado por:

____

Dr. Oleg Sergiyenko

Esta tesis doctoral es la culminación y presentación de resultados de una investigación que comenzó en agosto del 2009. Como su título indica, esta tesis describe el desarrollo y la demostración de un sistema de visión en 3D dirigido al área de aplicación de navegación autónoma de robots móviles.

En el capítulo I de esta tesis, se presenta un análisis del estado de arte, la importancia y el impacto de los sistemas de visión y la navegación autónoma en la actualidad, así como también los objetivos generales y específicos, planteamiento de problema e hipótesis de esta investigación.

El sistema de visión presentado se basa en un método llamado “Triangulación dinámica”, el cual describe el formalismo matemático que permite el cálculo de coordenadas en 3D de algún objeto (u obstáculo en el caso de un robot móvil). A lo largo de esta tesis se describe en detalle el funcionamiento de dicho método y su forma de implementación, al igual que su comprobación mediante una simulación y experimentación mediante un prototipo físico.

Para probar el método de triangulación dinámica, un prototipo físico fue diseñado y fabricado para llevar a cabo las operaciones del método con componentes optoelectrónicos y eléctricos (como lentes, espejos, aperturas, láseres, actuadores, sensores, entre otros). A este prototipo se le llamó “Sistema de Barrido por Láser Prototipo II”. Todo lo referente a este sistema, incluyendo el método en que se basa, su diseño y desarrollo (mecánico y de software de control), se encuentra descrito en el capítulo II y III de esta tesis.

El objetivo principal de esta investigación es el desarrollo e implementación del sistema de visión como parte sensorial de un sistema de navegación autónoma para robots móviles. El sistema de navegación utiliza los datos provenientes del sistema de visión para analizar su entorno y tomar decisiones que eventualmente lleven al robot móvil a alcanzar su meta de manera segura. El desarrollo de dicho sistema, cuyo diseño se basa en una plataforma de desarrollo móvil existente en la industria, se encuentra en la parte final del capítulo II.

Las simulaciones realizadas de ambos sistemas y sus resultados respectivos se presentan en el capítulo IV. Los resultados de la experimentación realizada con el prototipo II y el análisis de los datos obtenidos se encuentran en el capítulo V. El capítulo VI presenta las conclusiones generales de esta investigación, sus implicaciones y el trabajo a futuro ligado a esta investigación (el cual se encuentra fuera del alcance de esta tesis). Por último, al final de este documento se encuentran las referencias, apéndices y anexos correspondientes, incluyendo copia de las publicaciones realizadas durante mi tiempo como alumno de doctorado.

ABSTRACT of the thesis of Luis Carlos Básaca Preciado, presented as partial requirement for obtaining the degree of DOCTOR IN SCIENCES IN THE AREA OF OPTOELECTRONICS. Mexicali, Baja California, México, Septiembre de 2013.

3D VISION SYSTEM USING LASER SCANNING FOR AUTONOMOUS NAVIGATION OF MOBILE ROBOTS

Abstract approved by:

____

Dr. Oleg Sergiyenko

This thesis is the culmination and presentation of results of an investigation that began in August 2009. As its title indicates, this thesis describes the development and demonstration of a 3D vision system aimed to the application area of autonomous navigation of mobile robots.

Chapter I of this thesis provide an analysis of the state of the art, the significance and impact of vision systems and autonomous navigation today, as well as general and specific objectives, problem statement and hypothesis of this research.

The presented vision system is based on a method called "Dynamic Triangulation", which describes the mathematical formalism that allows the calculation of 3D coordinates of an object (or obstacle in the case of a mobile robot). Throughout this thesis, is described in detail the functioning of the method and its way of implementation, as well as its demonstration through software simulation and experimentation using a physical prototype.

To test the dynamic triangulation method, a physical prototype was designed and manufactured to perform the method steps by means of optoelectronic and electrical components (such as lenses, mirrors, apertures, lasers, actuators, sensors, among others). This prototype was called "Laser Scanning System Prototype II". Everything about this system, including the underlying method, design and development (mechanical and control software), is described in Chapters II and III of this thesis.

The main objective of this research is to develop and implement a vision system as a sensory part of the autonomous navigation system for mobile robots. The navigation system employs data from the vision system to analyze its surroundings and make decisions that eventually lead the mobile robot to reach its goal safely. The development of this system, whose design is based on an existing mobile development platform in the industry, is found at the end of Chapter II.

Simulations of both systems and their respective results are presented in Chapter IV. The results of experimentation with the prototype II and analysis of the obtained data is found in Chapter V. Chapter VI presents the overall conclusions of this research, its implications and future work linked to this investigation (which is outside the scope of this thesis). Finally, at the end of this document are the corresponding references, appendices and annexes, including copies of the published research papers during my time as a doctorate student.

AGRADECIMIENTOS Y DEDICATORIA

Quiero agradecer primeramente a Dios por haberme dado la sabiduría y fortaleza para realizar y concluir mis estudios de doctorado y esta tesis.

Agradezco profundamente a mi esposa Gaby por ser mi compañera en esta aventura que es la vida, por todo su amor y apoyo incondicional, por motivarme siempre a ser una mejor persona, por soportar mis desveladas, por estar siempre a mi lado cuando te necesito y por esa sonrisa que me regalas cada día, te amo.

A mis padres Luis y Cristina y a mi hermano José Eduardo por su gran apoyo, por ser mi ejemplo a seguir, por ser mis amigos, por indicarme siempre el camino correcto, por hacerme saber que siempre puedo contar con ustedes, por ser mi conciencia y mis consejeros y por enseñarme que el éxito no significa dinero sino contar con el amor y compañía de la familia, ustedes son la mejor familia que pude tener, los amo.

Gracias Gaby, Cristina, Luis y José por estar siempre a mi lado, por soportar a veces mis enojos y cansancio, por sus palabras de aliento y motivación, por todos los consejos que me han dado durante estos últimos cuatro años, por su amor y apoyo incondicional y por siempre impulsarme a seguir mis sueños. Por todo esto y más, a ustedes dedico este esfuerzo personal y este logro académico y profesional, los amo con todo mí ser.

Agradezco a mis amigos Omar, Polet, Manuel, Viri, Joaquín, Rocío y Raymundo, por todo su apoyo, interés y palabras de ánimo; gracias por ser parte de mi vida ya que sin ustedes no sería tan interesante y divertida.

A toda mi familia, a mi tata Chuy y a mi nana Chalita, a mis tíos, tías, primos, primas y a mis suegros por estar al pendiente de mi avance y por siempre preocuparse por mi bienestar, los quiero mucho.

También quiero agradecer a mi director de tesis, Dr. Oleg Sergiyenko por su apoyo y dirección de principio a fin durante mis estudios de doctorado y por sus enseñanzas que apreciaré para toda la vida.

A mi compañero de estudios y amigo Julio por su constante apoyo y dedicación al proyecto, por compartir las comidas, desveladas y sobre todo por el interés de desarrollar juntos una investigación de calidad.

Al Dr. Moisés Rivas, por su apoyo y enseñanzas durante el desarrollo de esta investigación, la redacción de esta tesis y por ser parte del comité de revisión.

Al Instituto de Ingeniería de la Universidad Autónoma de Baja California y a todo su personal, por abrirme sus puertas y ser mí casa de estudios, aprendizaje y desarrollo desde Agosto del 2009.

Y por último pero no menos importante, a todos los lectores y sinodales de esta tesis, gracias por su tiempo y dedicación, y por haber contribuido a mi formación académica.

ÍNDICE GENERAL

CAPÍTULO I. INTRODUCCIÓN

1. Antecedentes y estado del arte

La navegación autónoma de robots móviles y las tareas de prevención de colisiones son cada vez más importantes, no sólo en la industria automotriz, sino también en la investigación científica, por ejemplo, la *NASA* [1-3] ha comunicado durante conferencias de prensa que ha invertido alrededor de $1,000 millones de dólares en expediciones a Marte de sus robots móviles *Sojourner* [4], *Spirit* [5], *Opportunity* [6] *y Curiosity* [7].

Dichos *Mars Rovers* (ver figura 1), han ayudado en la búsqueda de la historia del agua en Marte [8] y de señales de condiciones atmosféricas capaces de sostener vida microbiana. DEPTHX, proyecto por la *Carnegie Mellon University* en México [9], intenta proveer la autonomía necesaria para que un robot submarino pueda realizar el mapeo de espacios tridimensionales como cavernas y minas, su objetivo es el Cenote Zacatón en México (ver figura 2). Los vehículos autónomos como *Stanley* (ver figura 3) en el *DARPA Grand Challenge* [10-14] por la Universidad de *Stanford* [15] que buscan resolver la tarea del manejo de automóviles de manera autónoma mediante la fusión de múltiples sensores y aplicando algoritmos avanzados de inteligencia artificial.

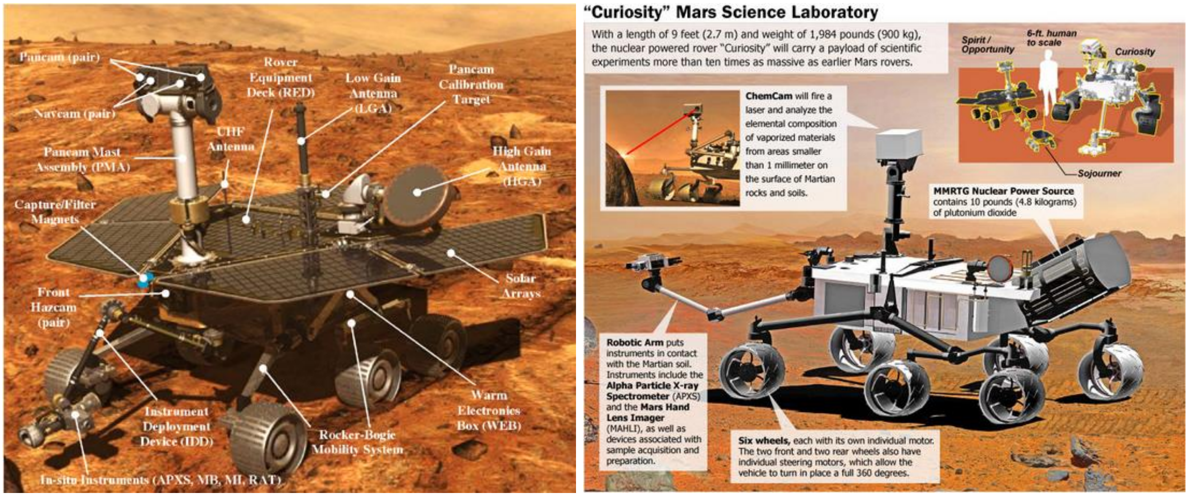

Figura 1. En la Izquierda el modelo de los Rovers Exploradores de Marte “Opportunity/Spirit”. En la derecha el Laboratorio de Ciencia de Marte “Curiosity”, el cual aterrizó en marte el pasado 26 de septiembre de 2013.

Debido a estos hechos creo que la realización de investigaciones en esta área es muy importante ya que es un área joven que posee mucho conocimiento por descubrir además de un gran potencial de aprovechamiento en muchos sectores de la industria.

Actualmente existen múltiples opciones en cuanto a sistemas de visión por computadora, como lo son los sistemas que utilizan una o más cámaras (*stereo vision*), los que utilizan láseres como RADAR óptico o *LIDAR* [16-17], *RADAR* [18], *SONAR* [19-22], sistemas basados en posicionamiento global (*GPS*) [23-25], entre otros [26] y cada uno de estos sistemas o métodos tiene sus ventajas y desventajas entre sí.

Vehículos autónomos como *Stanley* de la Universidad de *Stanford* y la mayoría de los vehículos que han participado en el DARPA Grand Challenge o en el DARPA Urban Challenge [27-30], como *Boss* de la Universidad de *Carnegie Mellon* [31], *Odin* del Tecnológico de *Virginia* [32], *Talos* del *MIT* [33], entre otros, utilizan una combinación de sensores como los mencionados anteriormente para adquirir la información necesaria para detectar obstáculos, caminos y cualquier información necesaria para una navegación segura. Esto es muy importante y les brinda una gran ventaja en comparación con los vehículos autónomos que utilizan un solo sensor para detectar obstáculos. Sin embargo, mientras más sensores son incluidos en el vehículo autónomo, se obtiene una mayor cantidad de información que tiene que ser procesada en tiempo real, lo cual aumenta considerablemente el costo dicho vehículo tanto por la cantidad de sensores como por la capacidad de procesamiento de datos que se necesita; lo que en conclusión puede ser considerado como una gran desventaja.

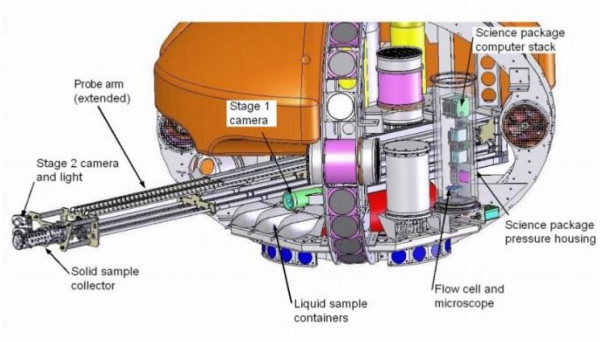

Figura 2. Robot DEPTHX, proyecto realizado por la Universidad *Carnegie Mellon,* su objetivo es generar un mapa digital de la zona del cenote Zacatón en México.

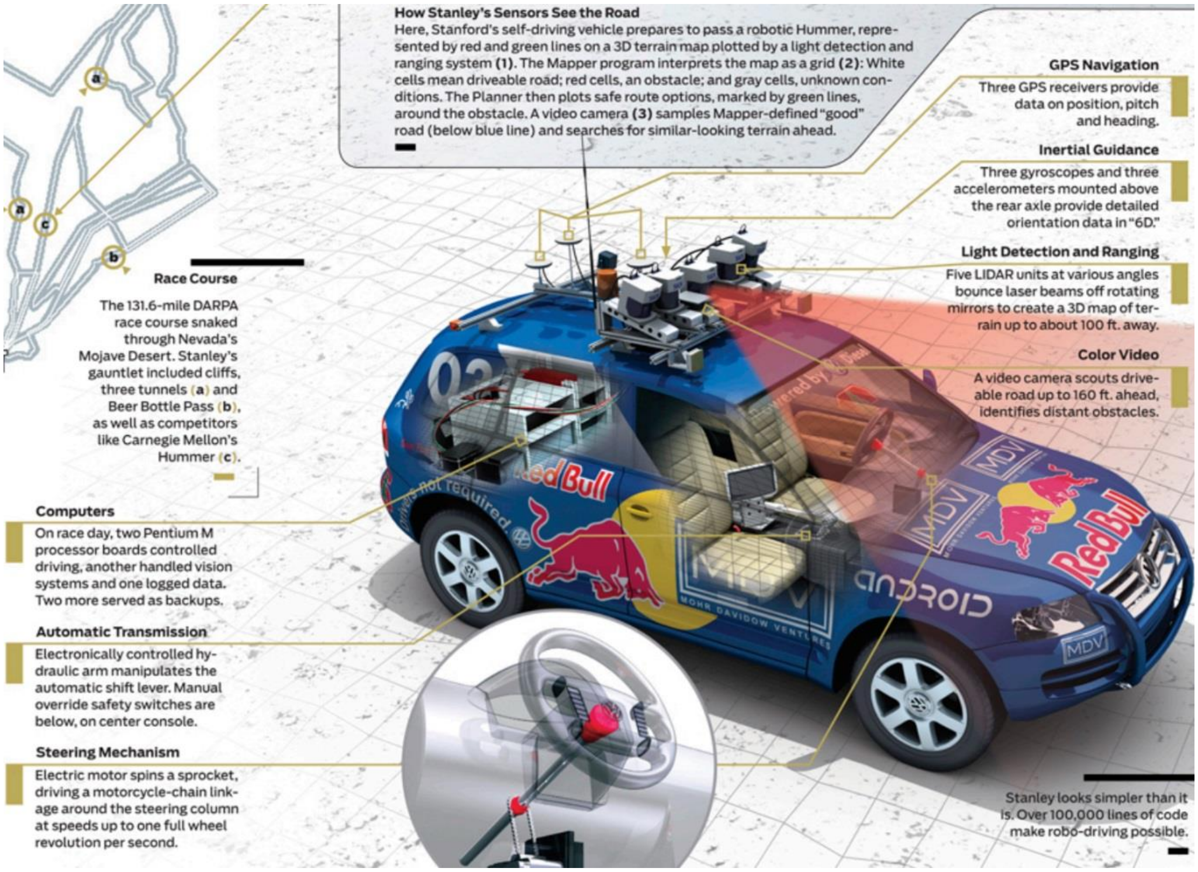

Figura 3. Stanley – El vehículo autónomo de la Universidad Stanford que ganó la competencia DARPA Grand Challenge.

Por ejemplo, el sensor LIDAR HDL-64E (ver figura 4) de la compañía Velodyne, es considerado como uno de los mejores en el mercado. Sin embargo, su elevado costo ($75,000.00 USD) lo convierte en un sensor difícil de adquirir [34]. A pesar de esto fue el sensor LIDAR más utilizado en los automóviles autónomos de las competencias DARPA Grand y Urban Challenge. Sus características principales son:

- 64 láseres/detectores
- Campo de visión de 360°
- Resolución angular de 0.09°

- Lectura de más de 1.3 M de p/s
- Actualización del FOV: 5 – 15 Hz
- Rango: 50 m
- Velocidad de barrido: 300 – 900 RPM
- Costo: $75,000.00 USD

En consecuencia, como se muestra en todas las publicaciones mencionadas sobre los vehículos autónomos que participaron en los retos de *DARPA* [31-33, 35], los robots móviles equipados con dichos sistemas multisensoriales complejos, todavía no son capaces de alcanzar altas velocidades de manejo (<40 mph), lo cual es causado principalmente por la necesidad de resolver en tiempo real la difícil tarea de búsqueda de datos óptimos entre una gran cantidad de información proveniente de múltiples sensores [36].

En la mayoría de las investigaciones actuales se presentan robots autónomos (de bajo costo) que utilizan telémetros láser 2D y servomotores para su rotación [37-42,]. Otros proponen sistemas de mono o estéreo visión [43-48], que utilizan dos cámaras para obtener dos imágenes del mismo objeto desde diferentes puntos de vista y reconstruir una escena en 3D, este enfoque no provee verdaderas coordenadas cartesianas del objeto u obstáculo, ya que sólo permite una evaluación de la forma y tamaño del obstáculo basado en complejos algoritmos probabilísticos de procesamiento de imágenes [49-53].

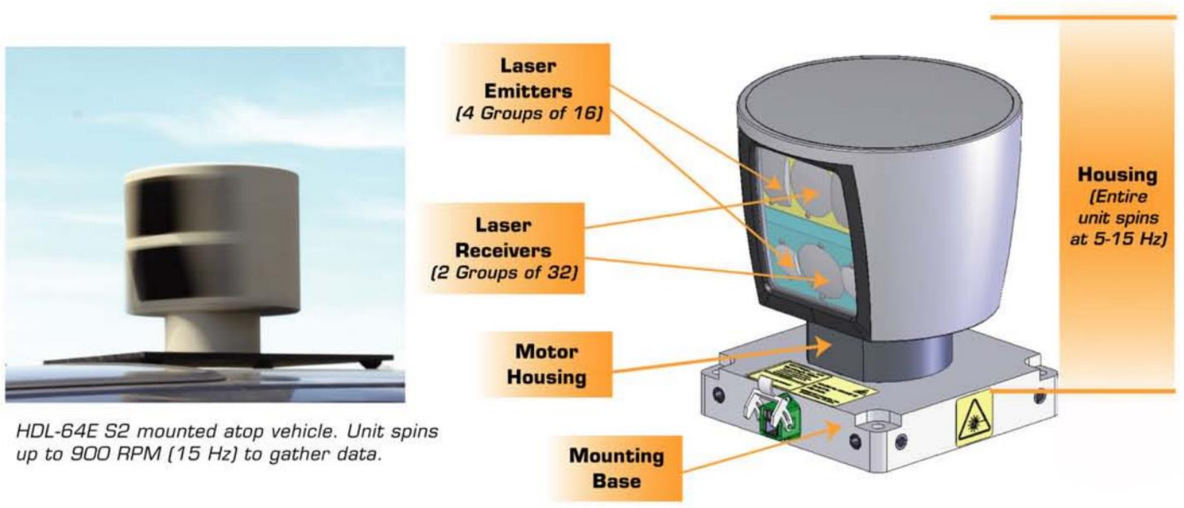

Figura 4. El sensor LIDAR HDL-64E de la compañía Velodyne, está diseñado para detección de obstáculos y navegación de vehículos autónomos y naves marinas.

Los sistemas que utilizan métodos de luz estructurada para la medición de formas en 3D [54-55], presentan grandes ventajas respecto a los sistemas de estéreo visión, por ejemplo, desempeño más rápido de las mediciones y algoritmos de procesamiento más simples, pero también presentan algunas desventajas tales como equipos de mayor costo, mayores dimensiones del sistema 3D en general y la necesidad de estar conectado a una fuente de alimentación de CA.

Estas características pueden limitar este sistema para aplicaciones estáticas (como el autor afirma en las conclusiones de [54]), tales como gráficos por computadora, diagnósticos médicos, cirugía plástica, inspección industrial e ingeniería inversa, en lugar de aplicaciones móviles como navegación de robos, exploración de minas, monitoreo de la salud estructural [56-58], operaciones de rescate, entre otros.

Si bien, cabe destacar que este tipo de sistema puede ser modificado para ser utilizado en aplicaciones móviles tomando en cuenta algunas concesiones.

Este último acercamiento puede llegar a ser muy prometedor en un futuro cercano, pero actualmente se requiere de mucho tiempo de procesamiento, genera grandes cantidades de información para analizar, carece de precisión y las soluciones actuales no permiten todavía una completa reconstrucción en 3D de la escena.

2. Objetivo general

Esta investigación propone una forma robusta y precisa de obtener un mapa digitalizado del espacio circundante al robot con calidad metrológica mediante mediciones ópticas, es decir, un sistema de visión llamado “Sistema de Barrido por Láser”, de bajo costo y alta precisión, que utiliza un láser para crear un mapa digital en 3D de su campo de visión y un sistema de navegación que utilice dicho sistema de visión para garantizar la correcta toma de decisiones en relación a la trayectoria que debe tomar el robot móvil para llegar de forma segura a su destino.

3. Objetivos específicos

- Desarrollo de un método innovador para realizar barrido espacial con láser basado en el método de triangulación dinámica.
- Desarrollo del formalismo matemático para calcular coordenadas en 3D.
- Optimización del formalismo para procesamiento de información en “tiempo real” y aumento de velocidad del sistema.
- Simulación por computadora de los diferentes modos de trabajo del sistema.
- Desarrollo del algoritmo y software de control de los elementos mecatrónicos del sistema en LabVIEW.
- Desarrollo del circuito para el acondicionamiento de la señal en el canal del fototransistor y la detección de obstáculos.
- Análisis metrológico del sistema en general y de las causas que provocan error (aumento de incertidumbre).
- Aplicación de los métodos estadísticos para disminución de la incertidumbre.
- Análisis y estudio de los diferentes tipos de motores disponibles y formas de control para incrementar la exactitud y precisión del barrido. Propuestas:
    - Servo motores
    - Motores de pasos
    - Motores de corriente directa
- Selección de una plataforma de desarrollo o robot móvil para basar el sistema de navegación.

- Implementación del sistema de barrido por láser en un robot móvil con el fin de desarrollar un sistema de navegación de alta resolución.
- Desarrollo y simulación de un sistema de navegación basado en los datos provenientes del sistema de barrido por láser.
- Desarrollo y simulación un método para calcular la trayectoria de un robot móvil.
- Desarrollo de modelo matemático para el control de la posición y orientación de un robot móvil, basado en su análisis cinemático.

4. Planteamiento del problema

El sistema de barrido por láser consiste en generar un mapa digital de su entorno el cual contiene las coordenadas 3D precisas de los objetos u obstáculos que se encuentran dentro del campo de visión, por lo tanto al poseer dichas coordenadas es posible conocer la distancia a la que se encuentran diferentes obstáculos frente a nuestro sistema.

Este sistema puede ser utilizado en un robot móvil para desarrollar e implementar un sistema de navegación que le permita al robot moverse libremente en un ambiente con obstáculos y diferentes caminos posibles; ya que utilizando el sistema de barrido por láser, el robot conocerá su posición exacta en relación a algún obstáculo que tenga que ser rodeado o un muro que le indique al robot que debe girar para continuar su camino.

El sistema de navegación presentado, consiste en un nuevo método de planeación o cálculo de trayectorias y el modelo matemático de un robot móvil de 4WD *Skid-steer* (4 llantas de tracción y dirección por deslizamiento), usado para navegar exitosamente y sin colisiones, a través de cualquier entorno desconocido y llegar de manera segura a su meta u objetivo.

5. Hipótesis

El sistema de barrido por láser es capaz de crear un mapa digital con las coordenadas en 3D de cualquier objeto u obstáculo que se encuentre dentro de su campo de visión. Dicho sistema puede ser implementado en un robot móvil para utilizar sus datos como entrada de un sistema de navegación. Mediante el análisis de estos datos, el Sistema de Navegación calculará la trayectoria óptima y le permitirá al robot móvil tomar decisiones y navegar en diferentes tipos de ambientes desconocidos sin colisionar con algún obstáculo para llegar a su objetivo por el camino más corto y seguro posible.

6. Contexto de la investigación

Esta investigación fue realizada en su totalidad en el Laboratorio de Optoelectrónica y Mediciones del Instituto de Ingeniería de la Universidad Autónoma de Baja California, Campus Mexicali, bajo la supervisión del Jefe del Laboratorio de Optoelectrónica y mi director de tesis, el Dr. Oleg Sergiyenko.

El diseño y fabricación de circuitos, el diseño de software, la experimentación, el análisis y la presentación de resultados en forma de publicaciones, fueron llevados a cabo en el laboratorio mencionado anteriormente.

El tipo de investigación que se realizó se puede definir como un proyecto de investigación aplicada, el cual promueve tanto la teoría como la aplicación práctica, ya que la metodología que se utilizó (llamada triangulación dinámica) para obtener las coordenadas en 3D de obstáculos detectados, es aplicada en un prototipo físico del sistema de visión (el cual fue diseñado por nosotros y fabricado en una empresa de maquinado externa); este sistema a su vez es implementado en el sistema de navegación en un robot móvil.

7. Limitaciones de la investigación

El prototipo II estuvo listo para pruebas a mediados del 2011, aproximadamente dos años después de haber ingresado al doctorado, lo cual apresuró la etapa de pruebas y análisis de resultados. A pesar de ello, los resultados obtenidos de las pruebas con el prototipo II fueron satisfactorios.

La adquisición o fabricación de un robot móvil para implementar físicamente la integración de los sistemas de barrido por láser y navegación presentados en esta tesis, se encuentra fuera de los límites de la investigación.

No obstante, en la sección 4 del capítulo II se presenta un robot móvil sobre el cual fue basado el diseño y desarrollo de los sistemas presentados en esta investigación; por consiguiente, la adquisición de dicho robot con el fin de implementar los sistemas aquí presentados, es un objetivo primordial de investigación a futuro, el cual será perseguido a corto plazo.

CAPÍTULO II. DESARROLLO EXPERIMENTAL

1. Sistema de barrido por láser

El sistema de barrido con láser se compone de tres subsistemas principales: El subsistema de posicionamiento de láser, el subsistema de apertura de barrido y el método que hemos llamado triangulación dinámica.

1.1 Triangulación dinámica

Como se mencionó anteriormente, el sistema de barrido con láser está fundamentado mediante la aplicación del método de triangulación dinámica. Lo hemos llamado de esta manera debido a que el subsistema de posicionamiento de láser y el subsistema de apertura de barrido cuentan con un grado de libertad en uno de sus componentes el cual les permite realizar un movimiento rotacional en su propio eje, esto le brinda al sistema de visión un campo de visión en teoría de 180°.

Esta propiedad permite que los subsistemas puedan tener ángulos variables y por consecuencia, generar triángulos de luz láser en diferentes formas y por periodos de tiempo muy cortos (milisegundos).

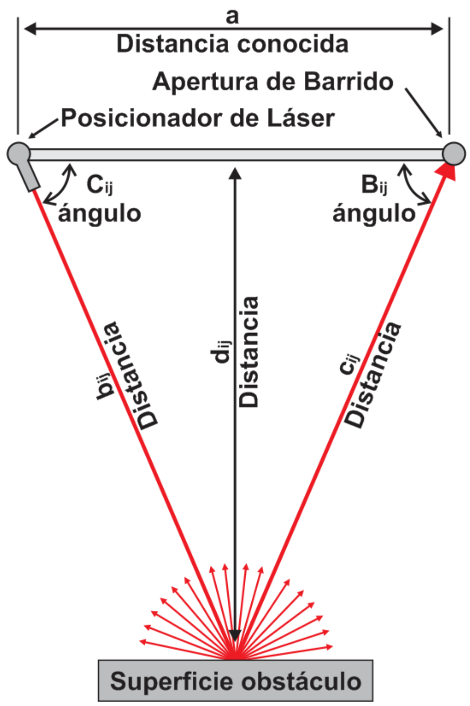

Figura 5. Descripción gráfica del método de triangulación dinámica usado en el sistema de barrido por láser para calcular las coordenadas de un obstáculo.

Cuando la luz láser es reflejada por un obstáculo y detectada en la apertura de barrido, se forma un triángulo de luz láser que nos brinda la información necesaria para calcular las coordenadas en 3D del obstáculo que se encuentra frente al sistema. Ver figura 5.

El método mostrado en la figura 5 funciona para calcular coordenadas en dos dimensiones (X, Y). Sin embargo, el propósito de este sistema es calcular coordenadas en 3 dimensiones (profundidad *"X"*, ancho *"Y"*, y alto *"Z"*) y para cumplir ese propósito, se agregó un mecanismo de rotación al sistema de barrido con láser (ver figura 6), el cual permite al sistema rotar en su propio eje para realizar barridos en diferentes valores de altura a través del eje Z, de esta manera agregando la tercer dimensión o coordenada Z.

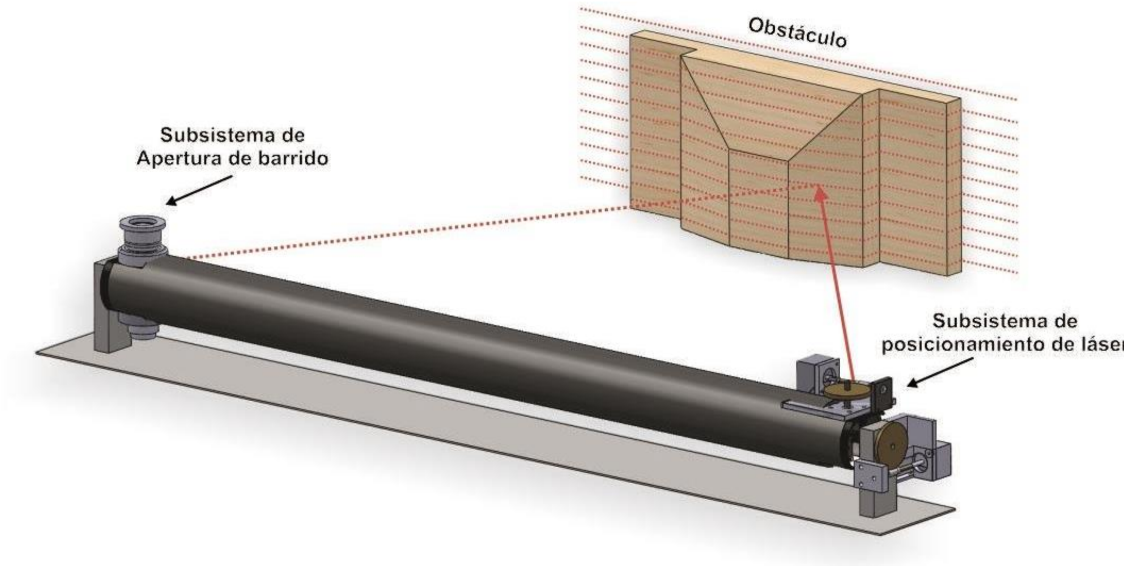

Figura 6. Modelo en 3D del Sistema de Barrido por Láser con mecanismo de rotación.

1.2 Subsistema de posicionamiento de láser

La función principal de este subsistema es la de direccionar el rayo de luz láser hacia la parte frontal del sistema. Este consiste de varios elementos los cuales interactúan de la siguiente manera.

Al energizar el láser, éste emite su haz de luz hacia un espejo fijo con un corte de 45°, este espejo refleja la luz láser ortogonalmente hacia otro espejo con corte de 45° el cual gira sobre su propio eje y es controlado por un motor de pasos. Al mover este motor controlamos la dirección y posición en la cual queremos direccionar el haz de luz láser. Al mismo tiempo que se controla la posición del láser se realiza un barrido con la apertura de barrido, lo cual permite verificar la presencia de obstáculos y calcular su posición dentro del campo de visión (ver figura 7). En la sección 1 del capítulo III se encuentra una lista detallada de los componentes de este subsistema.

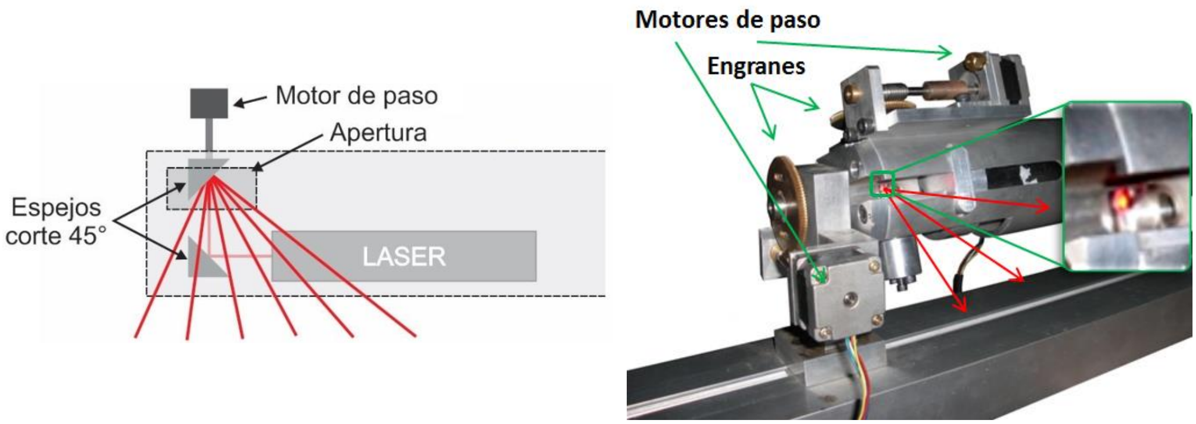

(a) (b)

Figura 7. (a) Diagrama del principio del funcionamiento del Subsistema de posicionamiento de láser. (b) Fotografía real del subsistema con acercamiento al espejo con corte de 45° y reflexión de luz láser.

1.3 Subsistema de apertura de barrido

La apertura de barrido es el componente más importante del sistema de barrido por láser y su función principal es la de detectar obstáculos. Para lograr esto la apertura recibe los rayos de luz láser reflejados a través de la apertura hacia un espejo con corte de 45° el cual gira sobre su propio eje a una velocidad constante gracias a un motor de corriente directa. Los rayos del láser reflejados hacia el espejo son ahora reflejados ortogonalmente hacia un arreglo de lentes el cual concentra todos los rayos en un punto donde es colocado un sensor de alto (fototransistor de alta velocidad y rápida recuperación), cuando este sensor es activado se considera que un obstáculo ha sido detectado por el sistema (ver figura 8). El sensor de cero, monitorea la posición del motor para poder determinar cuando el espejo ha girado 360°, esta información es indispensable para poder calcular el ángulo B_{ij} mencionado en la figura 5.

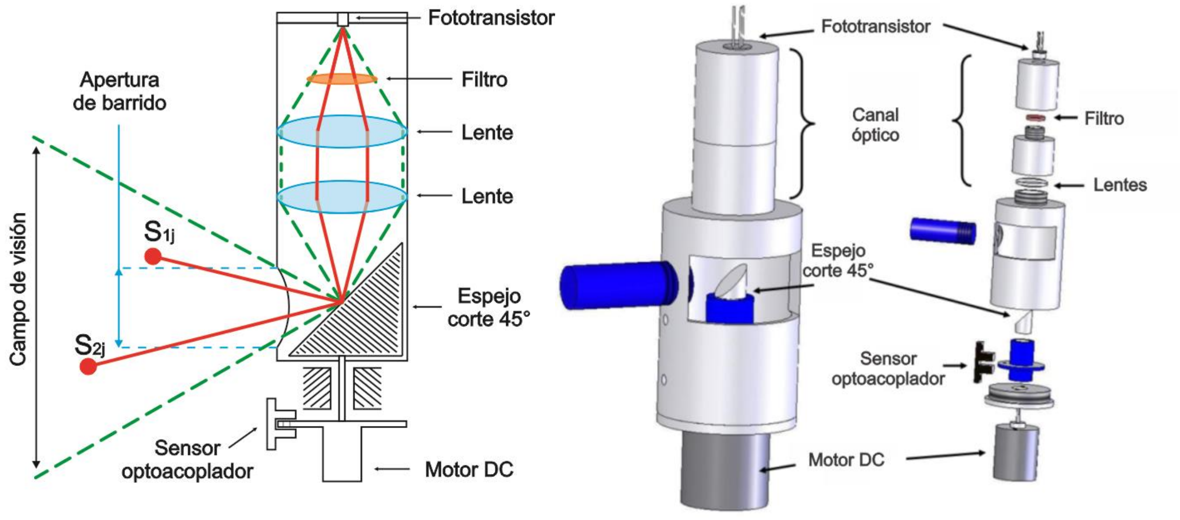

(a) (b)

Figura 8. (a) Diagrama del subsistema de apertura de barrido. (b) Modelo 3D de la apertura de barrido.

Para calcular el ángulo B_{ij}, utilizamos el sensor cero para conocer el momento en que inicia y termina una vuelta completa del espejo de la apertura, basándonos en un pulso de referencia (el cual es una señal cuadrada con frecuencia de 20 hz), contamos la cantidad de pulsos desde que inicia una vuelta hasta que se activa el sensor de alto, es decir, cuando se detecta un obstáculo. En ese momento también contamos la cantidad de pulsos de referencia que tomó dar una vuelta completa. Ver figura 9.

Utilizando los datos obtenidos mediante los sensores de alto y cero, es posible calcular el ángulo B_{ij} mediante la siguiente ecuación [59-60]:

$$B_{ij} = \frac{2\pi \cdot N_A}{N_{2\pi}} \tag{1}$$

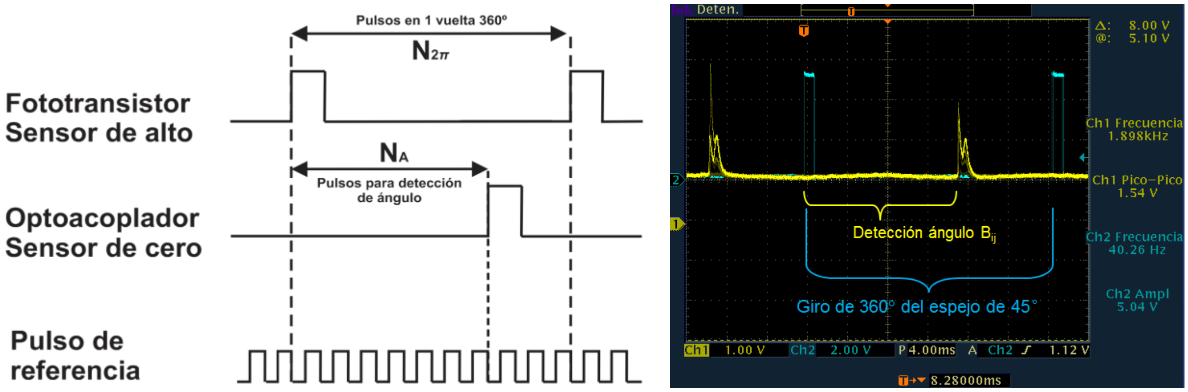

(a) (b)

Figura 9. Señales utilizadas para el cálculo del ángulo B_{ij} en la apertura de barrido. (a) Descripción de señales. (b) captura de pantalla de señales reales en el osciloscopio.

Donde N_A es la cantidad de pulsos de referencia al momento que el sensor de alto se active y $N_{2\pi}$ es la cantidad de pulsos de referencia cuando el espejo con corte de 45° realiza una vuelta completa activando el sensor de cero.

1.4 Cálculo de coordenadas en 3D

Para poder calcular las coordenadas x, y, z de cada punto reflejado de algún obstáculo, desarrollamos un conjunto de ecuaciones derivadas a partir de la ley de senos (ecuaciones 2 – 5). Estas ecuaciones requieren que los valores de los ángulos B_{ij}, C_{ij}, $\Sigma_{\beta j}$ y la base a (distancia entre el centro de cada uno de los subsistemas de posicionamiento de láser y apertura de barrido), sean conocidos para calcular las coordenadas en 3D [61-63].

$$x_{ij} = a \frac{\sin B_{ij} \cdot \sin C_{ij} \cdot \cos \sum_{j=1}^{j} \beta_j}{\sin\left[180° - \left(B_{ij} + C_{ij}\right)\right]}, \qquad (2)$$

$$y_{ij} = a\left(\frac{1}{2} - \frac{\sin B_{ij} \cdot \cos C_{ij}}{\sin\left[180^\circ - \left(B_{ij} + C_{ij}\right)\right]}\right) \text{ cuando Bij} \leq 90º, \tag{3}$$

$$y_{ij} = -a\left(\frac{1}{2} + \frac{\sin B_{ij} \cdot \cos C_{ij}}{\sin\left[180^\circ - \left(B_{ij} + C_{ij}\right)\right]}\right) \text{ cuando Bij} \geq 90º, \tag{4}$$

$$z_{ij} = a \cdot \frac{\sin B_{ij} \cdot \sin C_{ij} \cdot \sin \sum_{j=1}^{j} \beta_j}{\sin\left[180^\circ - \left(B_{ij} + C_{ij}\right)\right]} \tag{5}$$

Durante la operación del sistema de barrido por láser, las coordenadas x, y, z de todos los puntos que fueron detectados por el sistema, son calculadas y almacenadas en una matriz multidimensional de 20x20x4. La primera dimensión de esta matriz contiene un mapa digital del campo de visión del sistema o el espacio frontal del robot móvil, cada posición *ij* de la matriz (1ra dimensión) puede tener un valor de *0* ó *1*. Un valor de *0* indica que en ese punto no se detectó reflexión por lo tanto no hay obstáculo. Un valor de *1* indica que si hubo reflexión de luz láser detectada y por lo tanto hay un obstáculo en ese punto.

La segunda dimensión contiene los datos del ángulo B_{ij}. Para cada posición *ij* de la matriz de la primera dimensión donde se encuentre un valor de 1, se calcula el ángulo B_{ij} correspondiente y es almacenado en la misma posición *ij* en la matriz de la segunda dimensión.

El mismo proceso se realiza para los valores del ángulo C_{ij} en la tercera dimensión y para los valores de $\Sigma_{\beta j}$ en la cuarta dimensión. Ver figura 10.

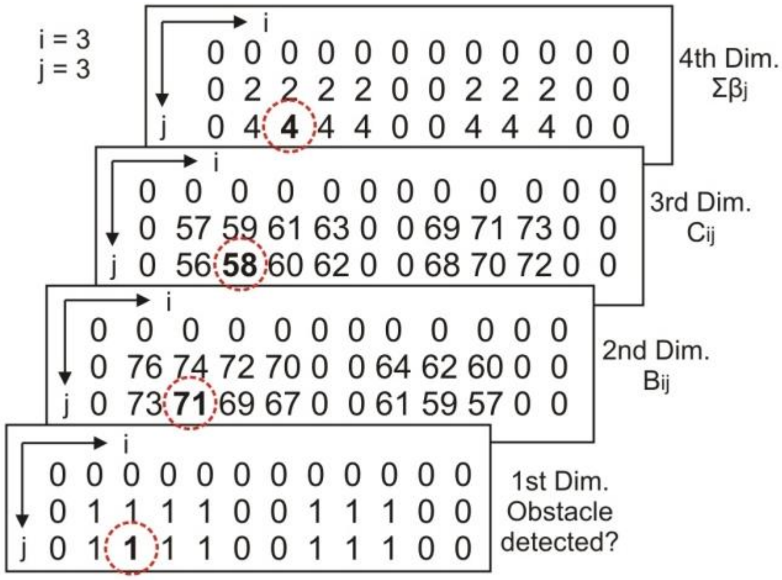

Figura 10. Matriz multidimensional de 20x20x4 para almacenamiento de resultados del sistema de medición de coordenadas mediante barrido por láser.

Los resultados de ángulos almacenados en la matriz multidimensional se utilizan para calcular las coordenadas *X*, *Y*, *Z* para cada posición *ij* de la matriz de la primera dimensión donde se encuentre un valor de *1*.

En otra matriz multidimensional de 20x20x3, se almacenan los resultados de las coordenadas calculadas, en la primera dimensión se almacenan los valores de *X*, en la segunda los valores de *Y* y en la tercera los valores de *Z*.

Esta información se utiliza en el sistema de navegación como datos de entrada, los cuales después de ser analizados proporcionan la información necesaria para tomar decisiones de navegación (evasión de obstáculos y planeo de ruta o trayectoria).

2. Diseño de hardware electrónico para el control del sistema de barrido por láser

El sistema de barrido por láser y sus subsistemas son controlados por una computadora portátil a través de diferentes interfaces digitales. A continuación se muestra en la figura 11 un diagrama de bloques general del hardware electrónico utilizado.

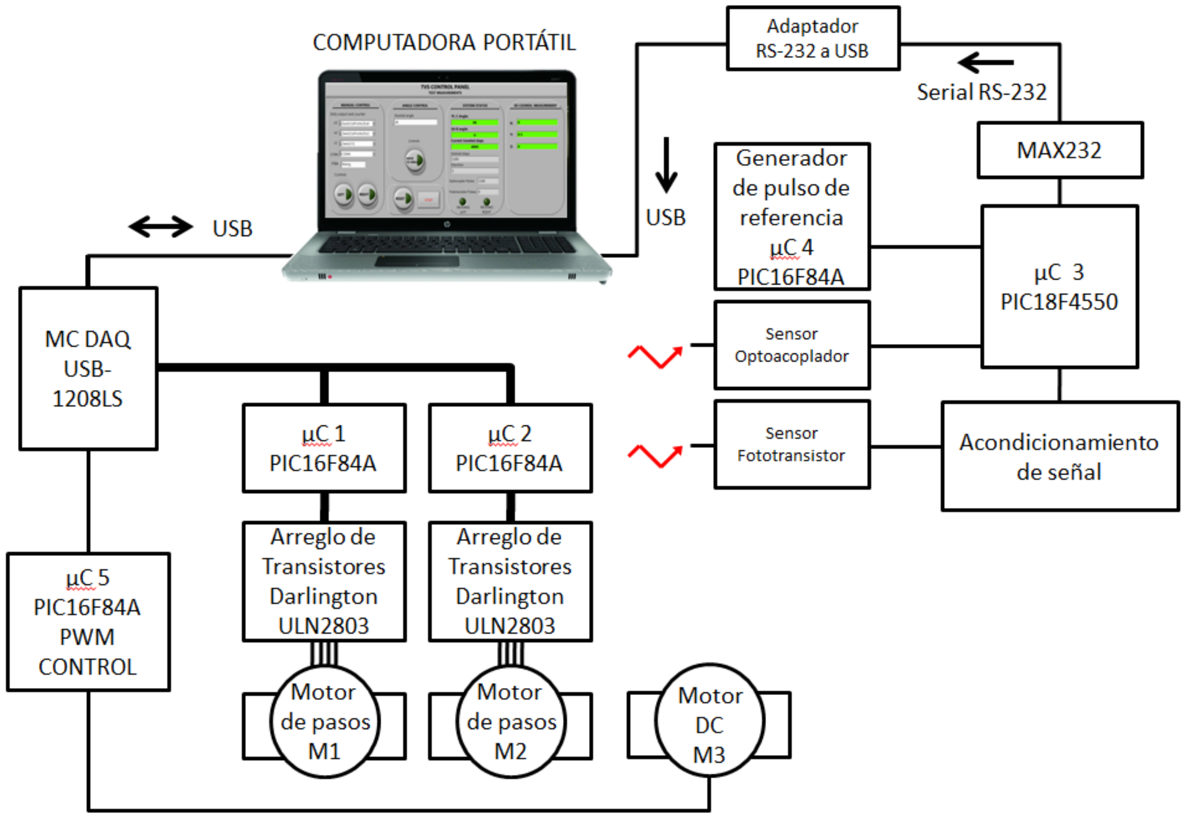

Figura 11. Diagrama de bloques del hardware electrónico del sistema de barrido por láser.

2.1 Sistema de adquisición de datos DAQ USB-1208LS

La interface principal utilizada para comunicar la computadora con los microcontroladores no. 1, 2 y 5 es el sistema de adquisición de datos del fabricante Measurement Computing MC DAQ USB-1208LS (ver figura 12).

Las características principales de este DAQ son las siguientes [64]:

- Dos salidas análogas de 10
- Un contador externo de 32 bits
- Entrada externa disparadora
- 8 entradas análogas sencillas (11 bit) o 4 diferenciales (12 bit)
- 16 entradas/salidas digital
- Compatible con NI LabVIEW

El DAQ mencionado fue seleccionado por las características anteriores, las cuales son suficientes para realizar las tareas de operación del sistema de barrido por láser y principalmente por su compatibilidad con el software LabVIEW y su bajo costo en comparación de otros sistemas de adquisición de datos de características similares.

El DAQ USB-1208LS realiza dos funciones principales en el sistema. La primera es comunicar bidireccionalmente la computadora con los microcontroladores no. 1 y 2 para controlar la dirección y el ángulo a girar de los motores de pasos del subsistema de posicionamiento de laser (M1 y M2). La segunda es enviar la señal de control necesaria al microcontrolador no. 5 para activar el control por PWM del motor de corriente directa M3 en el momento preciso.

Figura 12. Sistema de adquisición de datos MC DAQ USB-1208LS utilizado para comunicar la computadora con el resto de la circuitería del sistema de barrido.

2.2 Control de motor DC mediante PWM y microcontrolador.

Para controlar y mantener una velocidad constante en el giro del espejo de la apertura de barrido, se implementó un control mediante modulación de ancho de pulso o PWM [65] (por sus siglas en inglés que significan *Pulse Width Modulation*).

PWM es una técnica para simular una salida analógica mediante una salida digital. El control digital se usa para crear una onda cuadrada, una señal que cambia constantemente entre encendido y apagado. Este patrón de encendido-apagado puede simular voltajes entre 0 y 5v, simplemente variando la proporción de tiempo entre encendido y apagado [66]. A la duración del tiempo de encendido se le llama ciclo de trabajo (*duty cicle*). Para variar el valor analógico se modula el ancho de pulso de la señal. Si el patrón de encendido-apagado es repetido suficientemente rápido por ejemplo con un motor DC, el resultado es la variación de la señal entre 0 y 5v, controlando la velocidad del motor.

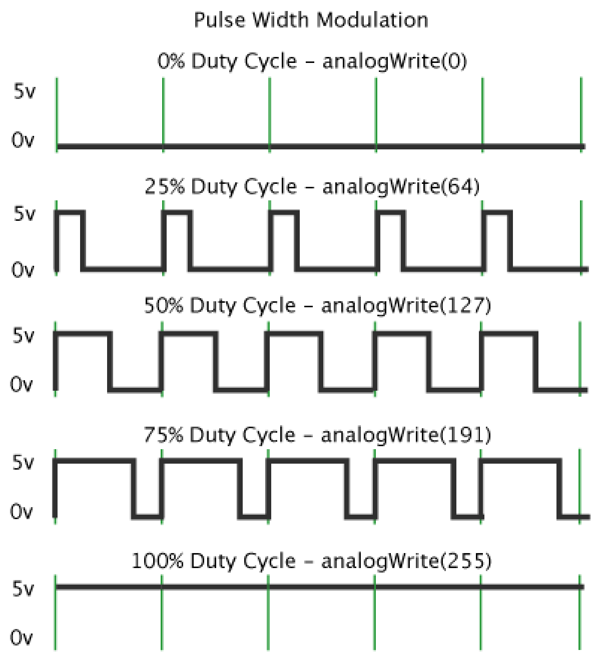

Figura 13. Diferentes ciclos de trabajo de una señal PWM.

Se utilizó un microcontrolador PIC16F84A (ver figura 14), para generar la señal PWM requerida por el motor DC de la apertura de barrido. Consultar el apéndice A para ver el código utilizado para generar dicha señal.

En la figura 13 se muestran varias gráficas con diferentes ciclos de trabajo, las líneas verdes representan un periodo. Este periodo es la inversa de la frecuencia la señal PWM, la cual se estableció en este sistema a 200 Hz, lo que equivale a periodos de 5 ms cada uno.

También se pueden observar en una escala de 0 – 100%, incrementos de 25% en el ciclo de trabajo. Esto simula una señal analógica (variable de 0 – 5v) a partir de una señal de salida digital (0v ó 5v). Por ejemplo, basándose en la figura 13; cuando el ciclo de trabajo es 0%, la salida analógica simulada es 0v, a 25% la salida es 1v, a 50% la salida es 2.5v, a 75% la salida es 3.75v y a 100% la salida es 5v.

2.3 Control de motores de pasos mediante microcontroladores

Dos microcontroladores PIC16F84A (ver figura 14) fueron seleccionados para realizar las operaciones más específicas del sistema de barrido por láser debido a su capacidad de procesamiento, bajo costo y facilidad de reposición.

Los microcontroladores no. 1 y 2 (de acuerdo al diagrama de la figura 11) fueron utilizados para generar la secuencia digital necesaria para controlar el movimiento de los motores de pasos. La secuencia convencional utilizada para motores de pasos (ver tabla 1) energiza solo una bobina por cada paso de la secuencia, debido a esto el motor no es capaz de generar el torque necesario para mover el subsistema de posicionamiento de láser.

	A	B	C	D
1	1	0	0	0
2	0	1	0	0
3	0	0	1	0
4	0	0	0	1

Tabla 1. Secuencia digital convencional para motor de pasos.

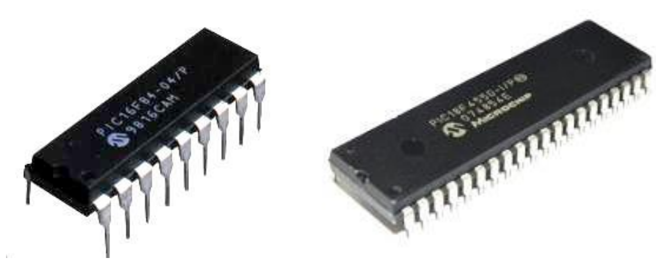

Figura 14. Microcontroladores PIC16F84A y PIC18F4550 del fabricante Microchip.

Otra secuencia conocida energiza primeramente dos bobinas, después una y después repite la secuencia sucesivamente. Esta secuencia es conocida como secuencia de medio paso (ver tabla 2). La ventaja es que provee torque y movimiento más suave del motor pero disminuye su velocidad a la mitad, lo cual sería una gran desventaja para el sistema de barrido por láser.

	A	B	C	D
1	1	1	0	0
2	0	1	0	0
3	0	1	1	0
4	0	0	1	0
5	0	0	1	1
6	0	0	0	1
7	1	0	0	1
8	1	0	0	0

Tabla 2. Secuencia digital para motor de pasos que brinda torque pero sacrifica velocidad.

La secuencia digital utilizada en el sistema de barrido demuestra varias ventajas sobre las otras secuencias mencionadas ya que al mantener energizadas dos bobinas del motor de pasos en cada momento, el motor genera un movimiento con mayor torque y permite utilizar motores más pequeños y de menor torque para mover el cilindro de aluminio del sistema de barrido por láser. La secuencia utilizada se muestra en la tabla 3.

	A	B	C	D
1	1	1	0	0
2	0	1	1	0
3	0	0	1	1
4	1	0	0	1

Tabla 3. Secuencia digital para motor de pasos que brinda mayor torque.

Como se mencionó anteriormente los microcontroladores no. 1 y 2 generan las secuencias para controlar los motores de pasos, sin embargo antes de enviar dichas señales a los motores de pasos, es necesario amplificar la corriente para poder energizar las bobinas de los motores. La forma en que esto es realizado es mediante un arreglo de transistores Darlington ULN2803 entre los microcontroladores y los motores.

El diagrama de conexión del ULN2803 se muestra en la figura 15 y el diagrama del circuito controlador completo en la figura 16.

Los transistores NPN tipo Darlington integrados en este circuito integrado, son idealmente utilizados para realizar interfaces entre circuitería digital de nivel bajo lógico (TTL, CMOS, PMOS) y los componentes que requieren de mayor corriente/voltaje como lámparas, relevadores, motores o cualquier otro componente con carga similar; por lo tanto es un componente ideal para controlar los motores de pasos utilizados en el sistema de barrido por láser.

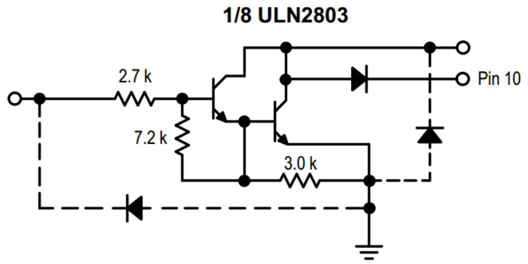

Figura 15. Diagrama interno de conexión del arreglo de transistores Darlington ULN2803.

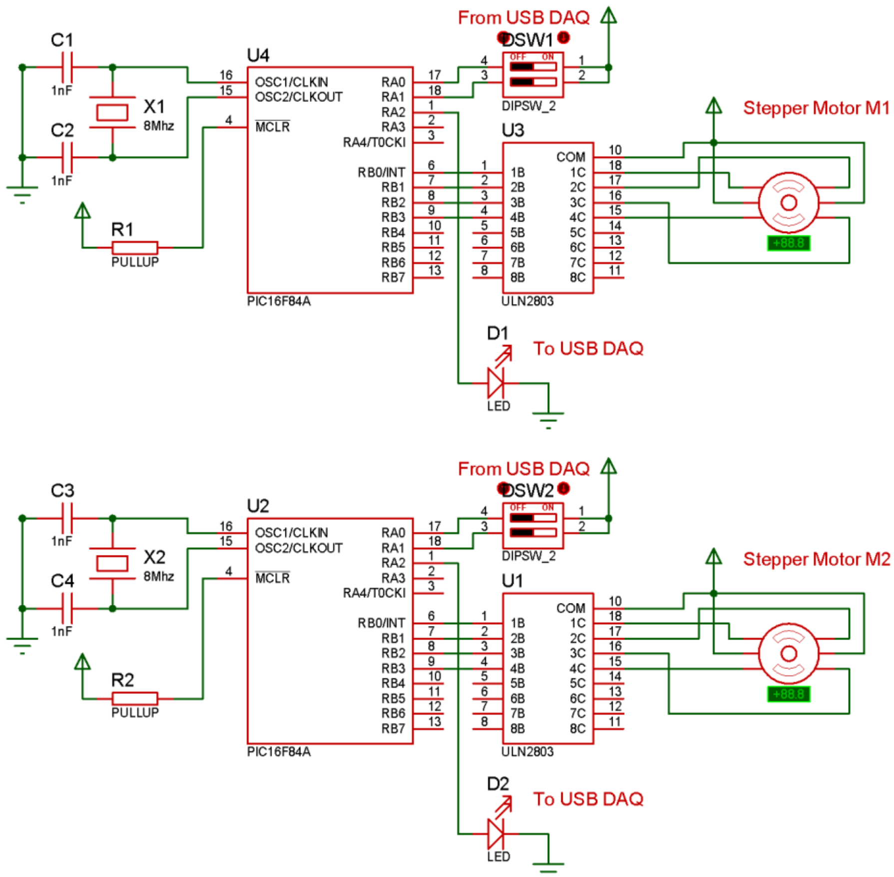

(a)

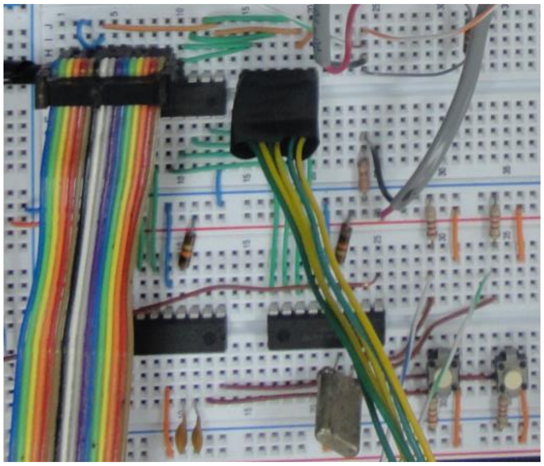

(b)

Figura 16. Circuito controlador de motores de pasos utilizando microcontroladores PIC16F84A. (a) Diagrama electrónico de la simulación del circuito. (b) Circuito alambrado.

Otra función que realizan los microcontroladores es la de enviar un pulso digital al contador del DAQ USB-1208LS (terminal RA2, figura 16) justo después de recibir la instrucción de dar un paso a cualquier motor, esto crea una retroalimentación que permite conocer la cantidad de pasos dados por cada motor y por consecuencia su posición angular, de esta manera evitando el uso de codificadores rotatorios en cada motor con el propósito de alcanzar el objetivo de construir un sistema de bajo costo. Consultar el apéndice A para ver el código de los microcontroladores mencionados en esta sección.

2.4 Sensores y acondicionamiento de señal

Como se menciona en la sección 1.3 de este capítulo, el subsistema de apertura de barrido cuenta con dos sensores, un fototransistor de alta velocidad para detectar obstáculos en el campo de visión y un optoacoplador utilizado para monitorear las revoluciones del espejo que se encuentra dentro de la apertura de barrido.

El fototransistor utilizado es el BPW77NA fabricado por VISHAY INTERTECHNOLOGY, INC. Sus principales características son su alta velocidad de recuperación después de saturación y su sensibilidad.

A pesar de esto, la señal obtenida de este sensor al detectar un obstáculo se encuentra en el rango de 50 – 200 mV (dependiendo de la distancia del obstáculo). Por lo tanto es necesario acondicionar esta señal para convertirla en una señal útil para el microcontrolador PIC18F4550.

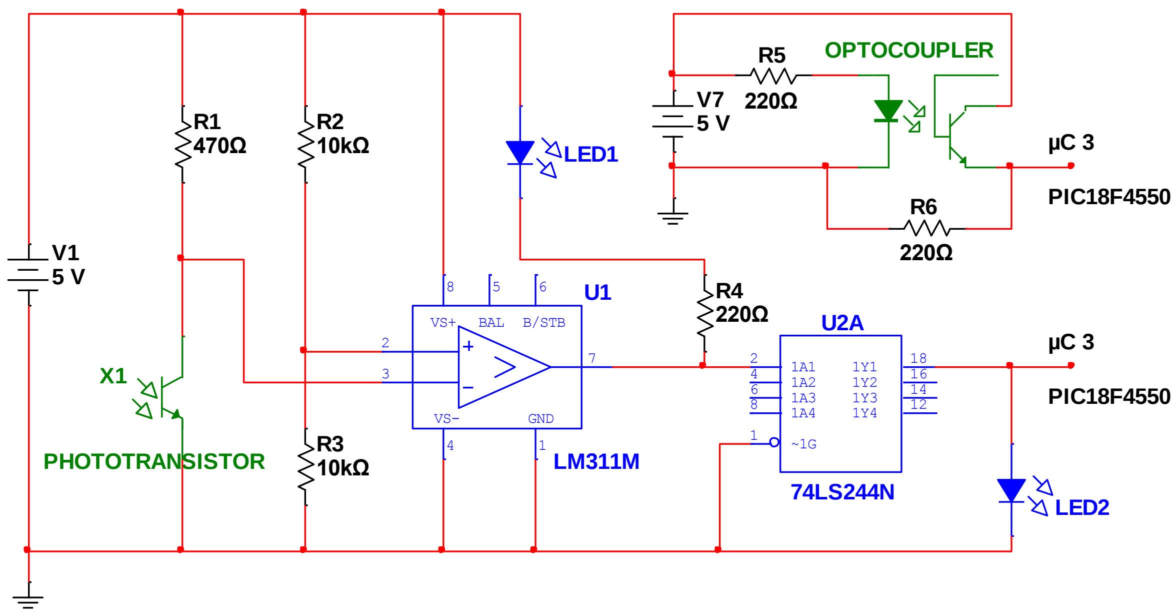

(a)

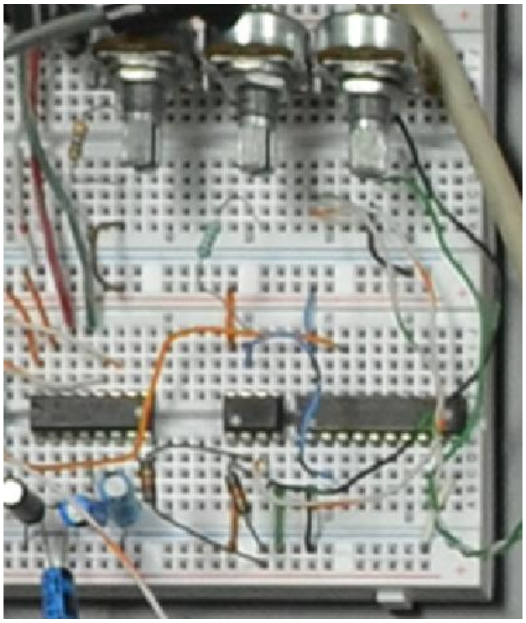

(b)

Figura 17. Circuito acondicionador de señal de entrada del fototransistor y optoacoplador. (a) Diagrama electrónico de la simulación del circuito. (b) Circuito alambrado.

El circuito de acondicionamiento de señal utilizado se muestra en la figura 17. En este circuito, el fototransistor (X1) se encuentra en configuración de emisor común; es decir que la señal entra por la base del fototransistor y sale por el colector. Cuando la luz del láser llega a la base, la corriente de base (I_B) comienza a aumentar, por consecuencia el fototransistor empieza a conducir entre sus terminales colector y emisor; y debido a que el emisor está conectado a tierra, el voltaje de salida que está conectado a la terminal no inversora (3) del comparador LM311 comienza a disminuir a razón que aumenta la incidencia de luz en el fototransistor. Al momento que el voltaje del fototransistor sea menor a la mitad del voltaje de la fuente (terminal no. 12 del LM311), la salida del comparador será positiva (+5v), esto le indica al microcontrolador no. 3 que se ha detectado un obstáculo. Cabe mencionar que modificando el valor de la resistencia R1 es posible aumentar o disminuir la sensibilidad del sensor, de acuerdo a las necesidades del sistema.

Una vez adquirida y acondicionada la señal del fototransistor, esta es enviada al microcontrolador no. 3 al igual que la señal generada por el optoacoplador y el pulso de referencia generado por el microcontrolador no. 4 (PIC16F684).

El microcontrolador no. 3 (PIC18F4550, ver figura 14) tiene la tarea de contar los pulsos de los sensores y de enviarlos a la computadora portátil para calcular el ángulo B_{ij} (mediante la ecuación 1). Para obtener estos datos necesarios, el microcontrolador cuenta la cantidad de pulsos de referencia que transcurren en el periodo de tiempo desde que se activa la señal del optoacoplador (sensor cero) hasta que se activa la señal del fototransistor (sensor de alto). Ver figura 18.

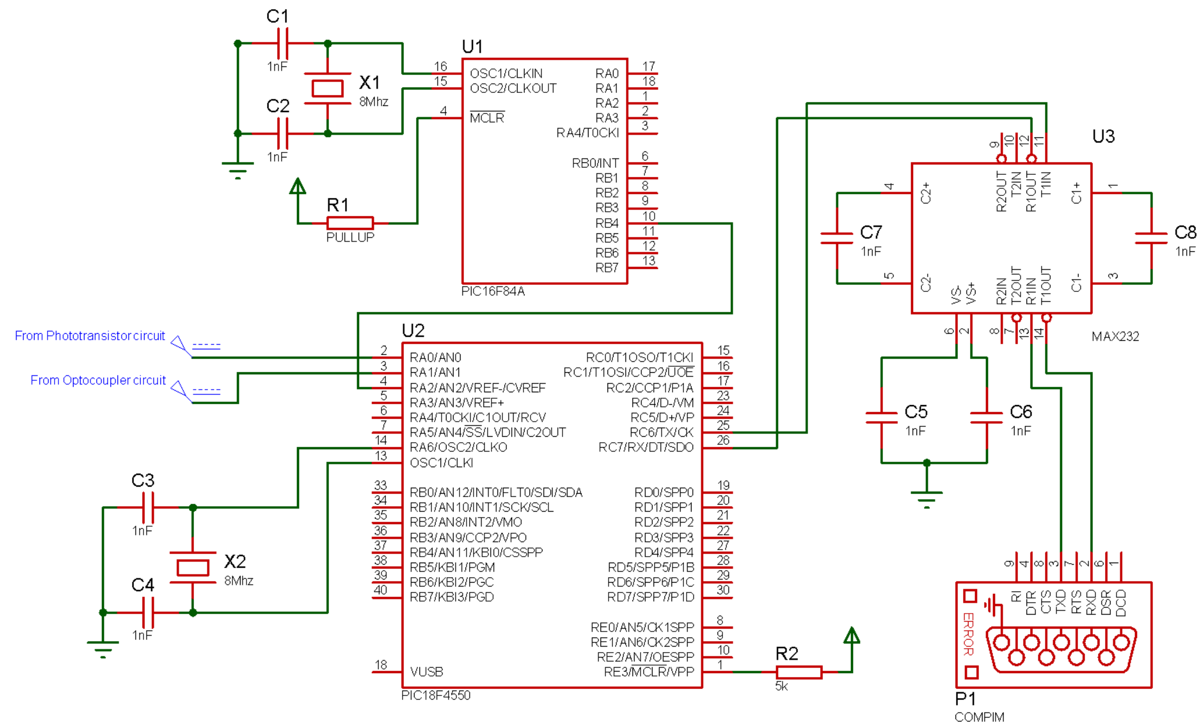

(a)

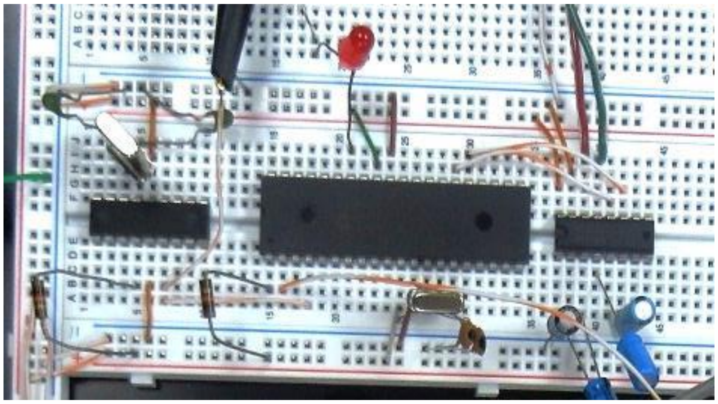

(b)

Figura 18. Contador de pulsos de señales de entrada de los sensores fototransistor y optoacoplador, para cálculo del ángulo B_{ij}. (a) Diagrama electrónico de la simulación del circuito. (b) Circuito alambrado.

Una vez que esta información es obtenida, se envía a la computadora a través del puerto serial y del circuito integrado MAX232, utilizando un adaptador serial/USB para computadora.

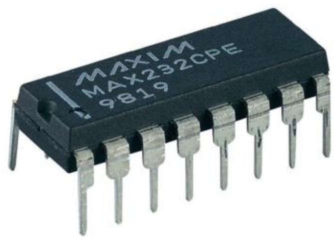

Figura 19. Circuito integrado MAX232, convertidor de señales serial RS-232 – TTL.

El MAX232 (ver figura 19) es un circuito integrado desarrollado por la empresa Maxim Integrated Products. Su función principal es la de convertir las señales de un puerto serial RS-232 a señales compatibles con circuitos lógicos TTL (0 – 5v) o viceversa.

En este caso el microcontrolador no. 3 genera las señales de comunicación serial en un rango de 0 – 5v y el MAX232 convierte estas señales al rango de -3 a +15v para hacerlas compatibles con el puerto serial de computadora. Consultar el apéndice A para ver el código de los microcontroladores mencionados en esta sección.

3. Software para el control del sistema de barrido por láser

Como se menciona en la sección anterior, el sistema de barrido por láser y sus subsistemas son controlados por una computadora portátil. La plataforma principal de desarrollo utilizada en el control del sistema es LabVIEW™ 2011 de National Instruments.

3.1 LabVIEW y diseño de instrumentos virtuales

LabVIEW (acrónimo de Laboratory Virtual Instrumentation Engineering Workbench) es una plataforma y entorno de desarrollo para diseñar sistemas con un lenguaje de programación visual gráfico llamado lenguaje G. Este software es recomendado para diferentes aplicaciones como, adquisición y procesamiento de datos, automatización de sistemas de pruebas y validación, control de instrumentos, sistemas embebidos de monitoreo y control, enseñanza académica, control y diseño simulado o real, entre otras; esto debido a que acelera la productividad por su naturaleza de programación gráfica [67].

Algunas características más específicas que LabVIEW posee son el manejo de:

- Interfaces de comunicaciones:
  - Puerto serial
  - Puerto paralelo
  - GPIB
  - PXI
  - VXI
  - TCP/IP, UDP, DataSocket
  - Irda
  - Bluetooth
  - USB
- Posee capacidad de interactuar con otros lenguajes y aplicaciones:
  - DLL: librerías de funciones
  - .NET
  - ActiveX
  - Multisim
  - Matlab/Simulink
  - AutoCAD, SolidWorks, etc.

- Herramientas gráficas y textuales para el procesado digital de señales.
- Visualización y manejo de gráficas con datos dinámicos.
- Adquisición y tratamiento de imágenes.
- Control de movimiento (combinado incluso con todo lo anterior).
- Aplicaciones en Tiempo Real.
- Programación de FPGA's para control o validación.
- Sincronización entre dispositivos.

Los programas en LabVIEW son llamados instrumentos virtuales (VI's). El instrumento virtual desarrollado en LabVIEW para el sistema de barrido por láser, permite comunicar todos los circuitos digitales, microcontroladores y sensores en un ambiente gráfico y paralelo donde es posible monitorear y controlar todas las señales del sistema y calcular las coordenadas 3D de un obstáculo detectado.

Los VI's se componen de dos partes principales. La primera es el panel frontal (ver figura 20), cuya característica principal es mostrar una interface gráfica al usuario para la utilización del programa mediante controles (entradas de datos) e indicadores (salidas de datos que pueden ser indicadores numéricos, gráficas, etc.) cuando el programa se esté ejecutando. Otra característica importante del panel frontal es la capacidad de observar cambios en los valores de variables o datos del programa en tiempo real mientras se está ejecutando el programa.

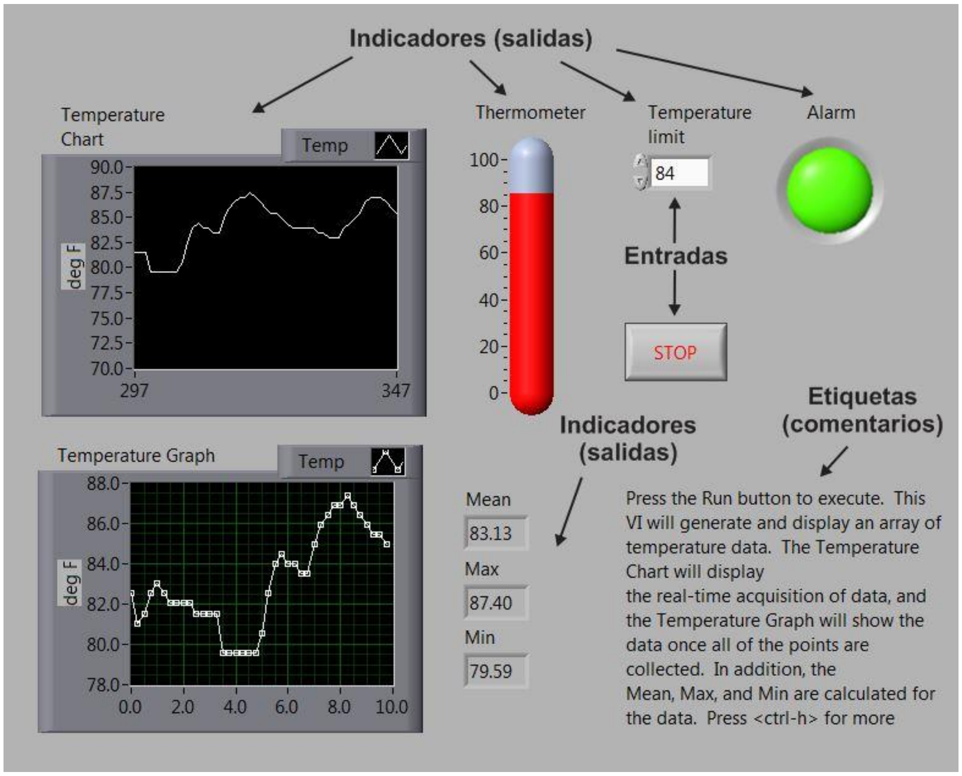

Figura 20. Ejemplo del panel frontal de un VI en LabVIEW.

El panel frontal de la figura 20 es un ejemplo de un VI simple que genera un arreglo de números aleatorios que representan lecturas de temperatura. Un indicador muestra la adquisición de datos en tiempo real y otro grafica los datos una vez que todos los puntos son recopilados. También se muestran los valores máximo, mínimo, la media y un indicador LED que muestra el estado de una alarma de temperatura.

La segunda parte de un VI es el diagrama de bloques (figura 21); en esta parte se define la funcionalidad del programa, en otras palabras, es donde las instrucciones son programadas gráficamente mediante funciones, cables de datos que las interconectan, estructuras de datos, entre otras.

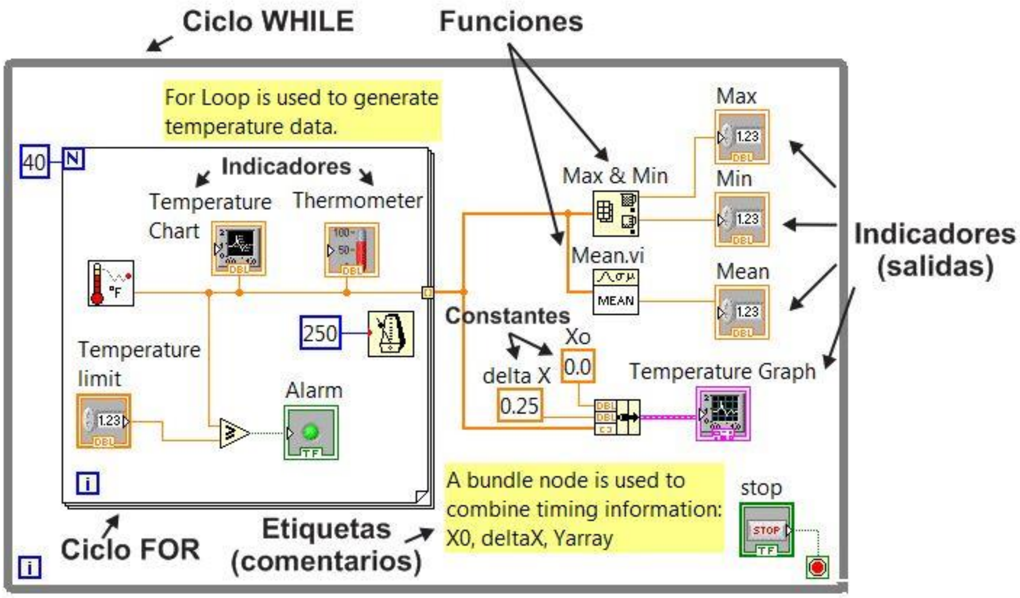

Figura 21. Ejemplo de un diagrama a bloques de un VI en LabVIEW.

El diagrama a bloques de la figura 21 utiliza funciones básicas preprogramadas como el ciclo *WHILE*, el ciclo *FOR*, comparadores, constantes, arreglos, indicadores, entre otros; interconectadas entre sí con cables virtuales, para realizar las operaciones deseadas de adquisición de datos, comparación y despliegue de datos de temperatura.

El panel frontal del VI diseñado para realizar pruebas de mediciones con el sistema de barrido por láser se muestra en la figura 22.

En la parte izquierda del panel frontal se muestra el control manual del sistema, en esta sección se utilizan controles para seleccionar diferentes opciones de puertos de entrada, puerto serial, puerto de contador, entre otras, para configurar la comunicación de la computadora con el DAQ USB-1208LS a través de una interface USB y con el microcontrolador no. 3 a través de una interface USB/RS-232. Una vez configurados los puertos, es posible utilizar los botones de control manual, izquierda y derecha, para colocar el láser en cualquier posición deseada (ángulo C_{ij}).

En la segunda sección del panel frontal se muestra el control por ángulo, en esta parte es posible indicarle al programa el ángulo C_{ij} deseado y mover el láser a ese ángulo al presionar el botón, *"move to angle"*. También se encuentra el botón *"Reset"* utilizado para la calibración inicial de la posición del sistema.

La tercera sección muestra el estado del sistema, en esta parte solo se encuentran indicadores de diferentes variables del sistema, por ejemplo, los ángulos actuales C_{ij} y B_{ij}, la cantidad de pasos dados por el motor de pasos, la dirección del motor, los pulsos contados del optoacoplador y del fototransistor. En la cuarta y última sección se muestran los resultados de las coordenadas calculadas por el VI (X, Y, Z).

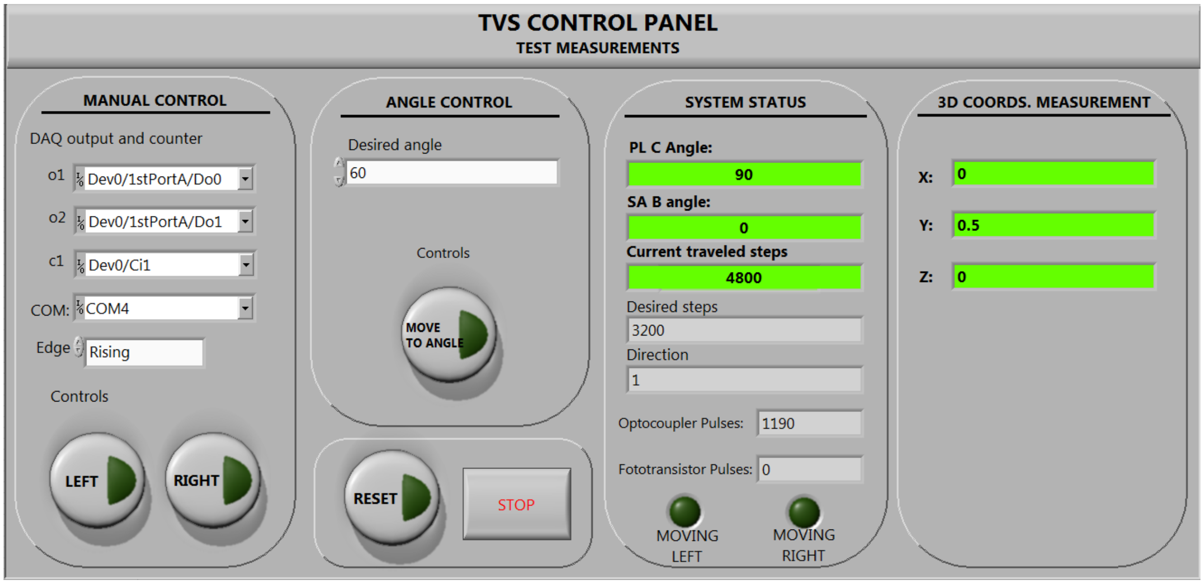

Figura 22. Panel frontal del VI para realizar mediciones de prueba.

A continuación se muestra el diagrama de bloques completo del VI desarrollado para controlar el sistema de barrido por láser y calcular las coordenadas de los obstáculos detectados (ver figura 23).

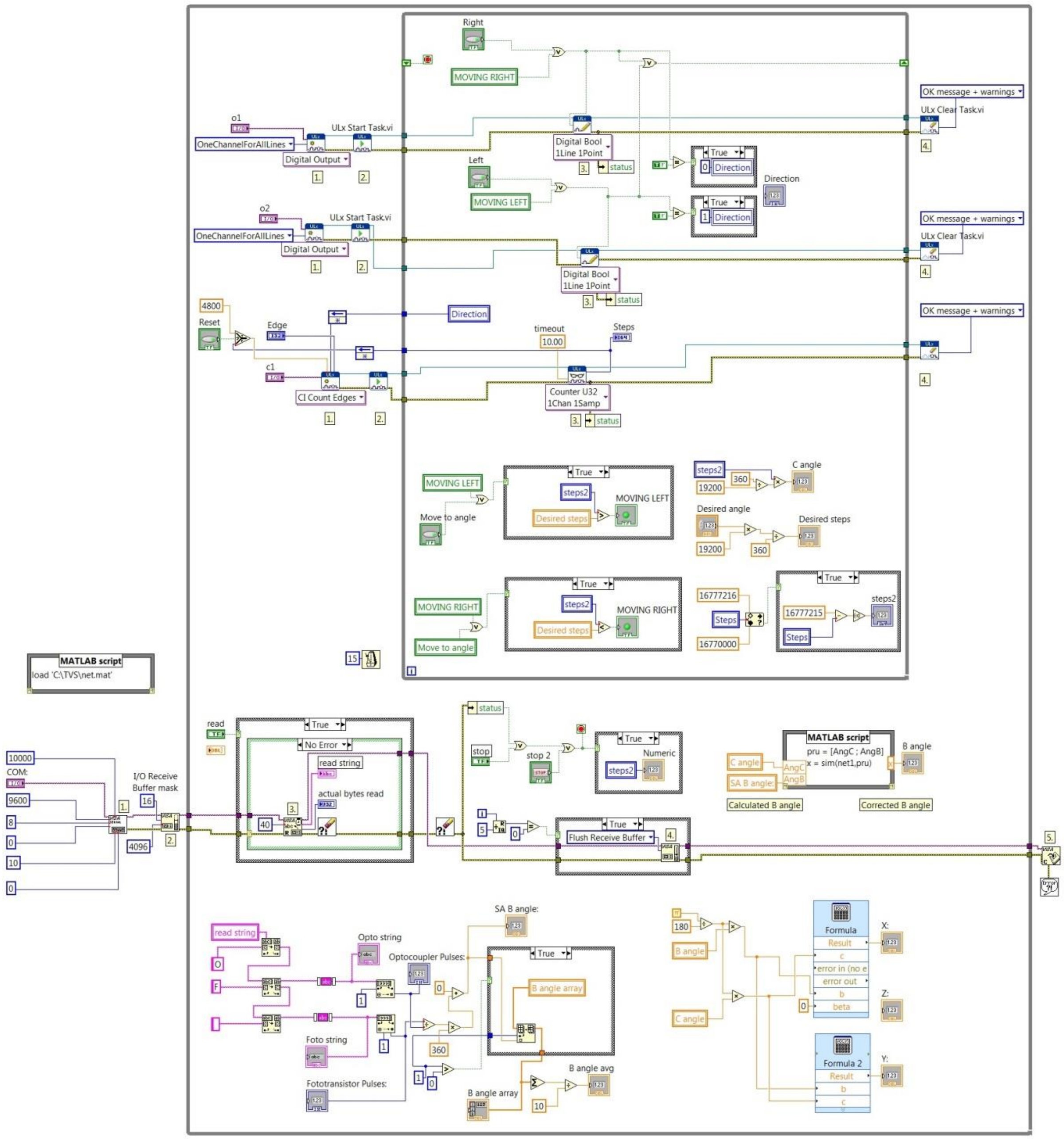

Figura 23. Diagrama de bloques del VI para pruebas de medición de coordenadas.

Las funciones principales programadas en este VI son las de controlar el giro y posición de los motores de pasos del subsistema de posicionamiento de láser, comunicarse con los microcontroladores para transmitir la información necesaria para calcular el ángulo B_{ij} y el ángulo C_{ij}, corregir el ángulo B_{ij} mediante la aplicación de una red neuronal previamente entrenada en Matlab, desplegar información del estado del sistema durante su funcionamiento y calcular las coordenadas de cualquier obstáculo detectado.

El diagrama de bloques mostrado en la figura 24 muestra la configuración básica para programar un puerto de salida digital de 1 bit utilizando el DAQ USB-1208LS de MC. En la función 1 se configura el puerto como *"Digital Output"* o salida digital y se especifica le pin físico de salida en el DAQ, la función 2 prepara el DAQ para la operación de escritura o tarea, la función 3 recibe el valor a escribir y realiza la escritura en el puerto, por último la función 4 detiene la tarea de escritura y libera los recursos reservados por la misma.

La operación de escritura de un puerto digital es utilizada dos veces para general las señales de control e indicarle a un microcontrolador la dirección en la que deben girar los motores de pasos y cuando deben activarse, utilizando dos puertos independientes de 1 bit cada uno. Ver figura 25.

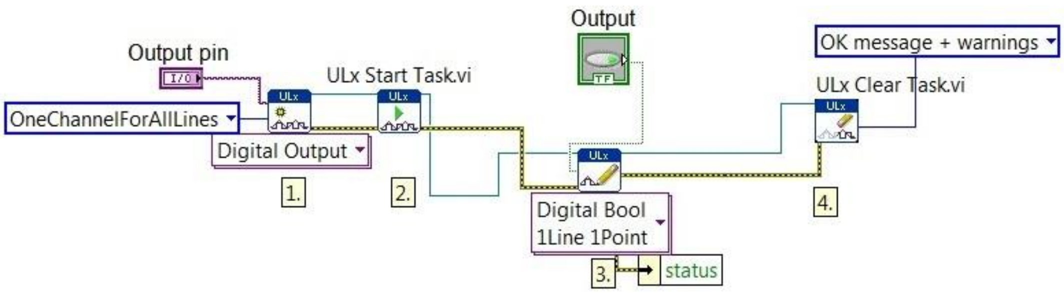

Figura 24. Programa básico para configurar un puerto como salida digital en el DAQ USB-1208LS.

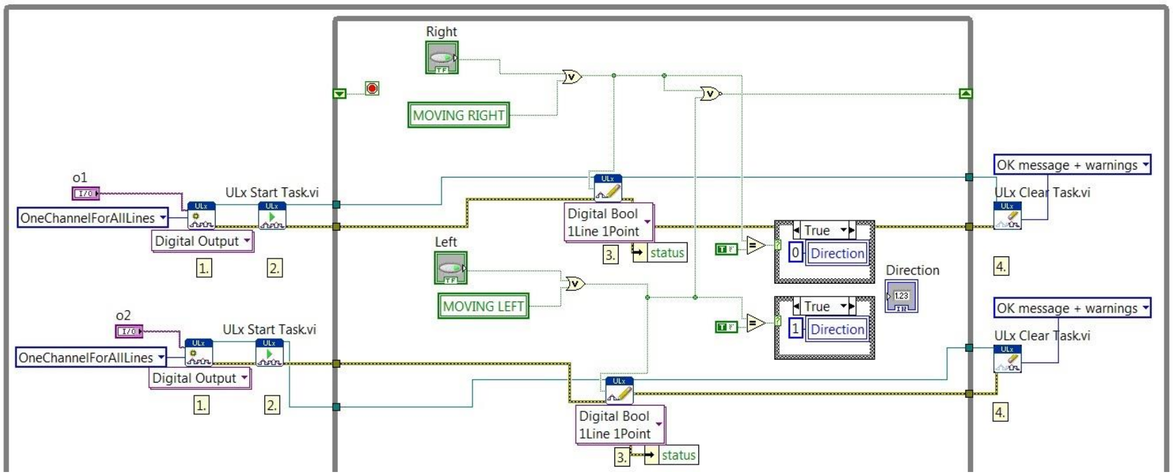

Figura 25. Escritura de dos bits de control indicadores de dirección de giro para motores de pasos.

Las estructuras “case” o de decisión (figura 25), son utilizadas para crear una variable local e indicarle a una función de entrada tipo contador, la dirección en la que debe contar; en otras palabras, indican si debe incrementar o disminuir la variable de salida del contador.

En la figura 26 se muestra la configuración de una señal de entrada del DAQ tipo contador, esta entrada es utilizada para contar la cantidad de pasos que los motores de pasos realizan y dependiendo de la dirección del giro del motor, el contador aumenta o disminuye su valor de salida.

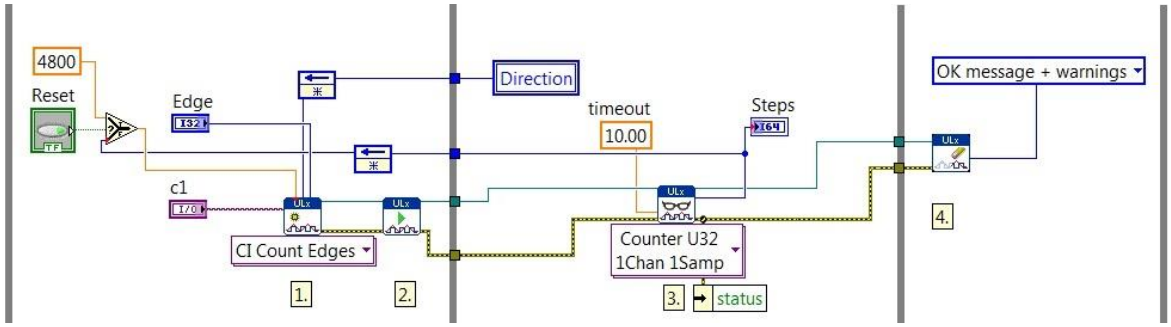

Figura 26. Configuración de una señal de entrada tipo contador en el DAQ USB-1208LS.

Los pasos contados a través del DAQ son utilizados para calcular en ángulo o posición actual de cada motor (ángulo C_{ij} y $\Sigma\theta_j$).

En la función 1 de la figura 26, se configura la tarea como tipo contador y se indica que pin de entrada se utilizará, también posee una entrada en donde se le puede indicar al contador un valor inicial para contar. Esta opción es realmente útil debido a que permite implementar un selector para utilizar dos valores iniciales distintos dependiendo de una condición de entrada; es decir, utilizando esta opción es posible agregar al sistema la capacidad de calibrar su posición inicial de barrido.

Para realizar una operación de barrido y cálculo de coordenadas con el sistema, lo primero que se debe realizar es posicionar el láser en un ángulo de 90° (ángulo C_{ij}) mediante el control manual. Una vez llegada a la posición deseada, se presiona el botón de *"Reset"* en el panel frontal (ver figura 22) y automáticamente el programa asigna un valor inicial de 4800 a la entrada del contador, indicando así que el láser del sistema se encuentra a 90°.

La función 2 prepara el DAQ para la operación de lectura tipo contador, la función 3 realiza la operación de contar los pulsos recibidos en el pin de entrada configurado en la función 1 y va almacenando el resultado o valor del contador en la variable *"steps"* o pasos; por último, la función 4 detiene la tarea de lectura y libera los recursos reservados por la misma.

Para realizar el control de la posición del láser del sistema mediante un ángulo deseado (entrada del usuario del programa), se implementó la solución mostrada en la figura 27. En la parte inferior derecha de la figura se toma el valor obtenido mediante el contador y se convierte a un valor útil para las necesidades del sistema (desplazamiento de rango). Una vez acondicionado el valor del contador ahora llamado "steps2", este es transformado a su valor angular y presentado al usuario como el ángulo C. Es importante mencionar que debido a la relación del motor de pasos (1.8° por paso) y el engrane utilizado (96 dientes), el motor realiza 19,200 pasos para dar una vuelta completa. Por lo tanto, es necesario multiplicar el ángulo deseado (indicado por el usuario), por 19,200 y dividirlo entre 360° para calcular el número de pasos necesarios para alcanzar el ángulo deseado C, es decir, la posición deseada del láser del sistema.

En la parte izquierda del diagrama (figura 27), se encuentra la función que representa el botón *"Move to angle"* (mover al ángulo) en el panel frontal y la variable local *"MOVING LEFT"* (avanzando a la izquierda). Al momento que el botón es presionado o si el sistema ya se encuentra en movimiento hacia el ángulo deseado, el programa compara la posición actual (en cantidad de pasos) con la posición deseada y continua avanzando en la dirección necesaria hasta llegar a la posición o ángulo indicado por el usuario.

De acuerdo a lo explicado en la sección 2.4 de este capítulo. El microcontrolador no. 3 (ver figura 14), recibe las señales acondicionadas de los sensores de la apertura de barrido (optoacoplador y fototransistor) y según lo explicado en la sección 1.3 de este capítulo (ver figura 9), cuenta la cantidad de pulsos de referencia al momento que el sensor de alto o fototransistor se active (N_A) y la cantidad de pulsos de referencia cuando el espejo con corte de 45° realiza una vuelta completa activando el sensor de cero u optoacoplador ($N_{2\pi}$). Una vez que el microcontrolador obtiene los valores de N_A y $N_{2\pi}$, los envía a la computadora portátil mediante comunicación serial.

En la figura 28 se muestra la configuración del puerto serial VISA en LabVIEW para recibir los datos enviados por el microcontrolador no. 5. LabVIEW ha implementado el lenguaje VISA, el cual es el lenguaje de E/S estándar para programación de instrumentación. VISA por sí mismo no provee capacidades de programación de instrumentación, sin embargo, es un API de alto nivel (Interfaz de Programación de Aplicaciones) que se comunica con controladores de bajo nivel. VISA es capaz de controlar VXI, GPIB o instrumentos seriales y realizar las llamadas apropiadas a los controladores dependiendo del tipo de instrumento utilizado [67]; por lo tanto el puerto serial VISA es la opción más adecuada para la comunicación del microcontrolador externo con la computadora portátil del sistema de barrido por láser.

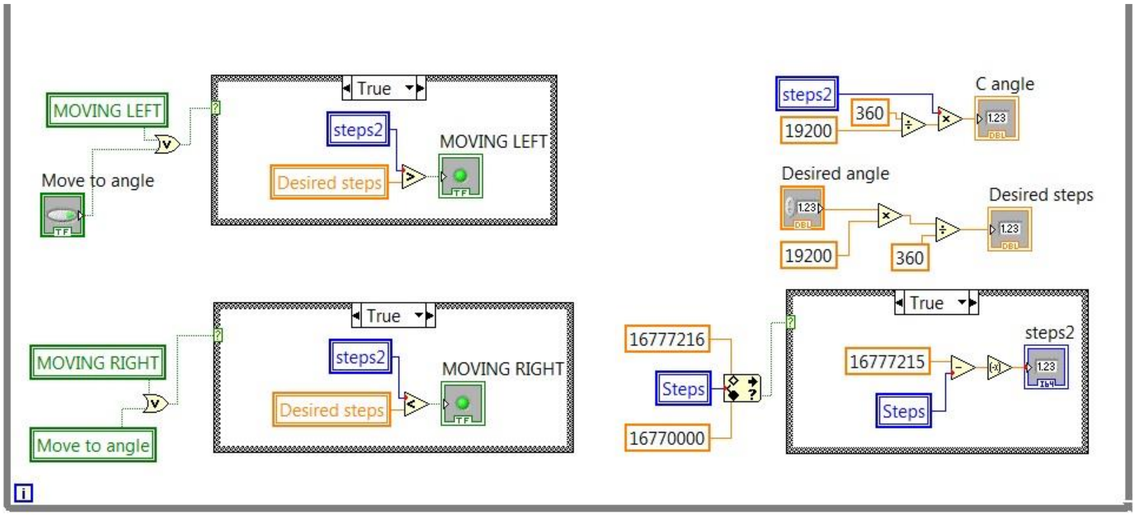

Figura 27. Operaciones lógicas y aritméticas para realizar el control por ángulo del láser del sistema.

Para implementar la comunicación serial de este sistema con el microcontrolador externo, las siguientes funciones son utilizadas:

- Función 1 - *VISA Configure Serial Port*: Inicializa el puerto serial especificado por el nombre del recurso VISA a la configuración especificada.
- Función 2 - *VISA Set I/O Buffer Size*: Establece el tamaño del búfer E/S.
- Función 3 - *VISA Read*: Lee del dispositivo conectado, el número de bytes especificados y almacena los datos leídos en el buffer de lectura.
- Función 4 - *VISA Flush I/O Buffer*: Vacía el búfer de E/S especificado por la máscara.
- Función 5 - *VISA Close*: Cierra una sesión del dispositivo especificado por el nombre del recurso VISA.

Primeramente, en la función 1 se configuran los parámetros de comunicación como, tiempo de espera, el nombre del recurso VISA, velocidad de transmisión, bits de datos, paridad, bits de parada y control de flujo. En la función 2 se establece el tamaño del búfer de E/S a 4,096 bytes y la máscara a 16, indicando que se utilizará el búfer de entrada.

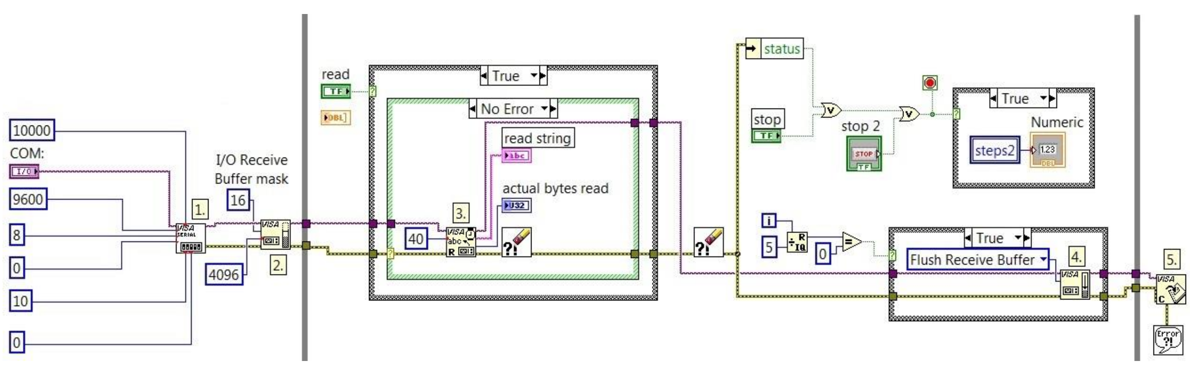

Figura 28. Configuración y lectura del puerto serial en LabVIEW para comunicación con el microcontrolador encargado de las señales de los sensores.

En la función 3, se establece el número de bytes por leer a 40 y el puerto a leer, se lee el puerto y se almacenan los datos provenientes del microcontrolador no. 5 (N_A y $N_{2\pi}$) en una variable tipo *string* (cadena de caracteres) llamada "*read string*". Es importante mencionar que esta función se encuentra dentro de una estructura *case* o de decisión para darle al programa la capacidad de leer el puerto serial solo cuando es necesario en vez de leerlo todo el tiempo. En la función 4 se especifica el búfer de entrada y este se vacía. Por último, la función 5 cierra la sesión del dispositivo especificado por el nombre del recurso VISA o número de puerto serial y libera los recursos del mismo.

Una vez obtenidos los datos del puerto serial, es necesario manipularlos e interpretarlos para obtener los valores numéricos de N_A y $N_{2\pi}$, ya que el puerto serial da como salida una variable tipo *string*.

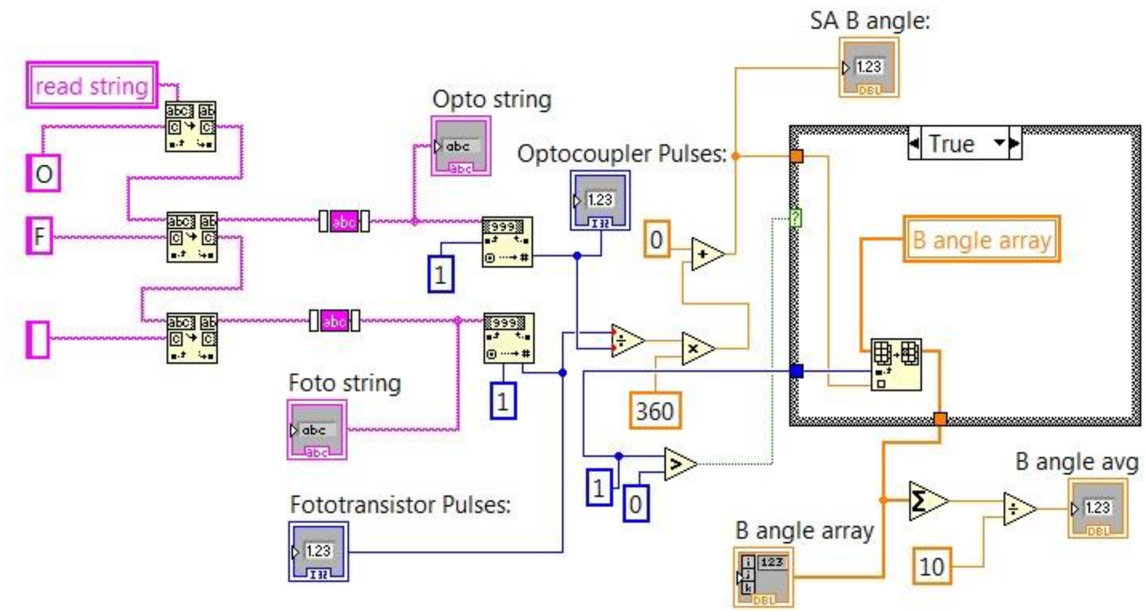

Figura 29. Manipulación de los datos obtenidos mediante el puerto serial VISA y cálculo del ángulo B.

El microcontrolador no. 5 está programado para enviar los datos en forma de paquete, es decir, envía un *string* que contiene los dos valores (N_A y $N_{2\pi}$) en el formato "O'valor_na' F'valor_n2pi' ", por ejemplo, "O1754 F323 ", donde la "O" indica que el número adyacente es el valor de pulsos del Optoacoplador (N_A) y la "F" indica que el número adyacente es el valor de pulsos del Fototransistor ($N_{2\pi}$).

La figura 29 muestra la manipulación del *string* obtenido del puerto serial VISA para adquirir de él los valores numéricos de N_A y $N_{2\pi}$. En la parte superior izquierda de esta figura se utiliza la función *"Search/Split String"* para encontrar el caracter delimitador (en este caso las letras "O", "F" y el carácter de espacio " ") y dividir el *string* en dos a partir del caracter delimitador. Sigamos el ejemplo del siguiente *string* "214 O1754 F323 O184", ya que debido a la forma de lectura del puerto serial, es posible tener un valor incompleto al inicio y al final del *string*. Primeramente se busca la letra "O" y se obtiene el resto del *string*, después se busca la letra "F" y al encontrarla se divide el *string* nuevamente, en este momento se tienen dos *strings* con el siguiente formato: "O1754 " y "F323 0184". Se busca el carácter de espacio " " y se divide el *string* para obtener "F323".

Ahora que tenemos "01754 " y "F323", enviamos los *strings* a la función "*Trim Whitespace*", esta función elimina cualquier carácter espacio que haya quedado en los extremos del *string*, dando como resultado "01754" y "F323". Por último, estas *strings* son enviadas a la función "*Decimal String To Number*", la cual a partir de un offset (en este caso "1" para evitar las letras "O" y "F" al inicio de los *strings*) convierten los números en *string* a su valor numérico decimal. Ver figura 30.

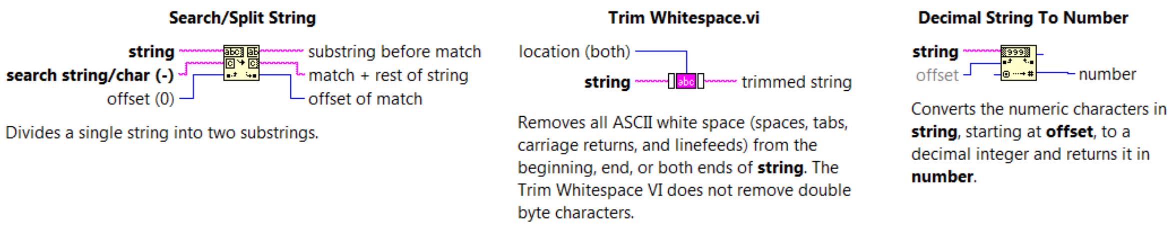

Figura 30. Funciones de LabVIEW para manipulación de variables tipo *string* utilizadas para adquirir los valores N_A y $N_{2\pi}$.

Una vez obtenidos los valores numéricos de N_A y $N_{2\pi}$, utilizamos la ecuación 1 mostrada en la sección 1.3 de este capítulo, para calcular el ángulo B_{ij} y el resultado es almacenado en la variable "*SA B Angle*". Ver figura 29.

Como se menciona en la sección 2.2 del capítulo V, se desarrolló y entrenó una red neuronal en MATLAB®, con el objetivo de corregir el error presentado en el cálculo del ángulo B y por consecuencia, mejorar la precisión de los resultados del cálculo de coordenadas. La red neuronal (previamente entrenada) se carga al programa en LabVIEW mediante una función llamada "*MATLAB Script Node*".

Esta función llama al software de MATLAB para ejecutar comandos y programas. Para utilizarla es necesario contar con una copia del software instalada en la computadora, ya que LabVIEW abre una ventana de comandos de MATLAB en el fondo para ejecutar las secuencias de comandos escritas en la sintaxis del lenguaje MATLAB. Es importante mencionar que ya que LabVIEW utiliza la tecnología ActiveX para implementar *"MATLAB Script Nodes"*, sólo están disponibles en el sistema operativo Windows.

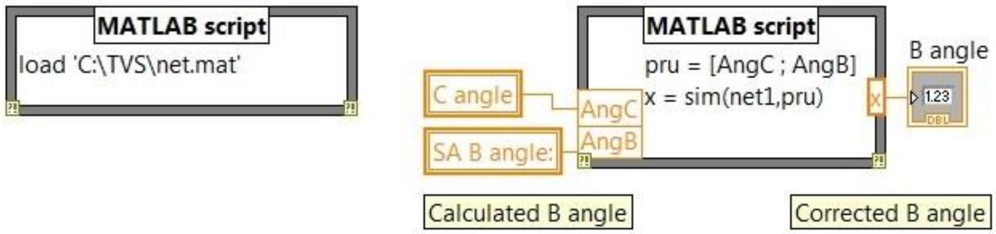

Figura 31. Nodos de secuencia de comandos de MATLAB, utilizados para ejecutar comandos y programas de MATLAB dentro de LabVIEW.

Utilizando dichos nodos de secuencia de comandos de MATLAB, se carga la red neuronal en el programa de LabVIEW y también se utiliza para aplicar la red neuronal en tiempo real, a los valores del ángulo B. Ver figura 31. En la parte derecha de la figura se muestran las variables locales "*C angle*" y "*SA B angle*" como entradas del nodo de MATLAB, el nodo cuenta con dos comandos, el primero une los valores del ángulo C y el ángulo B en una sola matriz y el segundo utiliza el comando "*sim*" para aplicar la red neuronal "*net1*" (previamente cargada en otro nodo), utilizando la matriz de ángulos B y C como entrada y almacenando los resultados en "x", que se convierte en la variable "*B angle*" del programa en LabVIEW.

Después de aplicar la red neuronal, el programa obtiene la variable "*C angle*" que almacena el valor del ángulo C respecto a una coordenada y la variable "*B angle*" que almacena el valor del ángulo B respecto a la misma coordenada pero corregido por la red neuronal. Una vez obtenidos dichos valores, se procede a calcular las coordenadas del obstáculo detectado según las ecuaciones 2 – 5, presentadas en la sección 1.4 del capítulo II. Las ecuaciones son programadas y calculadas, utilizando la función de LabVIEW llamada

"*Formula*", la cual utiliza una interface similar a una calculadora para crear fórmulas matemáticas con entradas y salidas. Ver figura 32 y figura 33. Por último, los resultados del cálculo de coordenadas son almacenados y presentados en pantalla mediante las variables X, Y, Z. Ver figura 22.

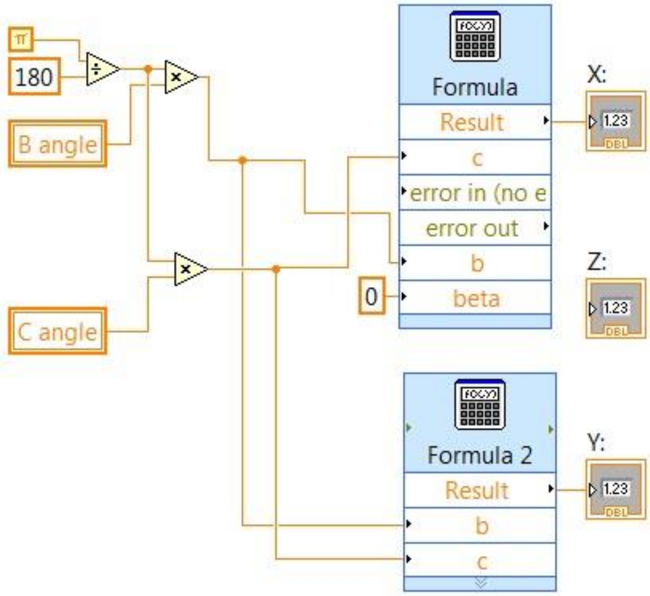

Figura 32. Cálculo de coordenadas mediante la función "*Formula*" de LabVIEW.

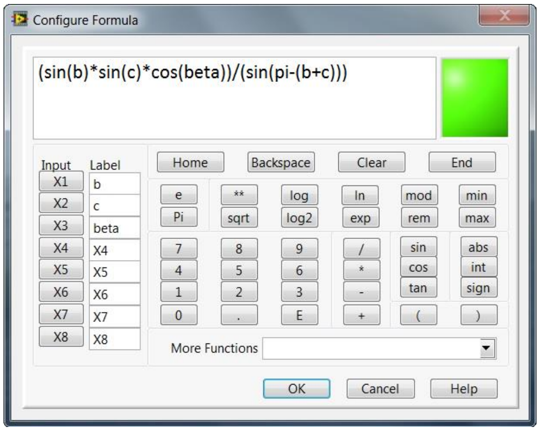

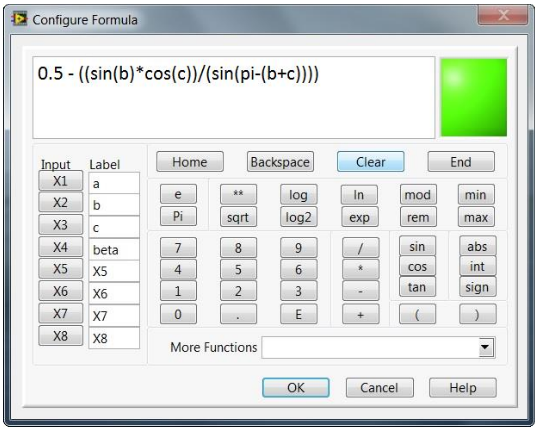

Figura 33. Pantalla de programación de las ecuaciones para el cálculo de coordenadas, mediante la función "Formula".

3.2 Programación de microcontroladores

El VI desarrollado en LabVIEW permite la comunicación entre la computadora y los microcontroladores, logrando el control efectivo y preciso del sistema de barrido por láser. Sin embargo, también es necesario programar los microcontroladores anteriormente mencionados para realizar funciones más específicas como operación de motores, generar secuencias, realizar cálculos, entre otras. El lenguaje utilizado para la programación de los microcontroladores es PIC C, el compilador es CCS C de Custom Computer Services, Inc. y se utilizó el editor PCWHD IDE.

La sección 2 de este capítulo trató sobre el diseño electrónico del TVS y las operaciones mencionadas, además de la lógica detrás de dichas operaciones.

Las funciones principales del sistema de barrido por láser que son realizadas por microcontroladores son:

- Generación de secuencias para el control de motores de pasos.
- Generación de pulsos de referencia utilizados para calcular el ángulo B_{ij}.
- Monitoreo de señales de sensores y procesamiento de información.
- Cálculo del ángulo B_{ij} y comunicación vía serial.
- Control de motor DC de la apertura de barrido mediante PWM.

El código de cada programa de microcontrolador utilizado se encuentra en el apéndice A.

4. Plataforma de desarrollo inteligente: robot móvil

La implementación física del sistema de visión en un robot móvil no es un objetivo de esta investigación; sin embargo, para desarrollar el sistema de navegación fue necesario seleccionar una plataforma de desarrollo o robot móvil existente en la industria para basarse en su diseño, dimensiones, peso, velocidad, capacidades físicas de movimiento y de procesamiento. Esto con el propósito de tener la opción de implementar el sistema de visión y navegación en dicho robot para experimentación, en caso de adquirirlo.

4.1 Robot móvil PIONEER 3-AT y sus características

Diversos modelos de robots conocidos fueron considerados preliminarmente y al final se decidió integrar el sistema de visión y navegación con la plataforma robótica de desarrollo inteligente llamada PIONEER 3-AT diseñado y fabricado por la empresa Adept MobileRobots LLC (ver figura 34).

Figura 34. Plataforma robótica de desarrollo inteligente llamada PIONEER 3-AT en cual se basa la investigación para implementar el sistema de barrido por láser y el sistema de navegación.

El PIONEER 3-AT es una plataforma robótica altamente versátil de cuatro ruedas motrices, diseñado para proyectos al aire libre, para terrenos difíciles o experimentación en laboratorio. Los robots PIONEER son reconocidos mundialmente en aplicaciones de investigación o enseñanza. Su versatilidad, fiabilidad y durabilidad, los han hecho la plataforma preferida para la robótica inteligente avanzada. [68]

Los robots PIONEERS son personalizables, actualizables y capaces de soportar cargas entre 5 y 12 kg dependiendo del tipo de terreno. Estas y otras características hacen a esta plataforma una excelente elección para integrar y basar el desarrollo de los sistemas de esta investigación.

A continuación se presentan las especificaciones técnicas del PIONEER 3-AT:

- Construcción
  - Cuerpo: aluminio de 1.6 mm
  - Llantas: neumáticos reforzados
- Operación
  - Peso del robot: 12 kg
  - Carga útil de operación:
    - Loseta/piso: 12 kg
    - Pasto/tierra: 10 kg
    - Asfalto: 5 kg
- Forma de manejo: *Skid Steering Drive* o giro por derrape

- Radio para girar: 0 cm
- Radio de giro: 34 cm
- Máxima velocidad de avance/retroceso: 0.7 m/s
- Velocidad de rotación: 140°/s
- Máximo escalón transitable: 10 cm
- Máxima brecha transitable: 15 cm
- Máxima pendiente transitable: 35%
- Terreno transitable: Asfalto, piso, arena y tierra (llantas de baja fricción disponible para alfombra/uso interior).

- Energía
    - Tiempo de funcionamiento: 2-4 horas con 3 baterías (sin accesorios)
    - Tiempo de carga: 12 horas (estándar) o 2.4 horas (con cargador de alta capacidad)
    - Fuentes de alimentación:
        - 5 V a 1.5 A conmutada
        - 12 V a 2.5 A conmutada
- Baterías
    - Soporta hasta 3 a la vez
    - Capacidad: 7.2 Ah (cada una)
    - Química: Plomo ácido
    - Baterías intercambiables durante operación: Si

- Microcontrolador E/S
    - Comunicación serial
    - 32 entradas digitales
    - 8 salidas digitales
    - 7 entradas análogas
    - 3 puertos de expansión seriales

4.2 Análisis del modelo cinemático del robot móvil

La información obtenida mediante el análisis cinemático de un robot permite controlarlo para llegar a una posición deseada y conocer su posición en cualquier instante de tiempo, debido a esto, el análisis cinemático de un robot móvil es indispensable para realizar la tarea de navegación.

Existen dos tipos de análisis, el de cinemática directa y el de cinemática inversa. Supongamos que tenemos un robot cuya configuración es conocida. Esto significa que conocemos todas las longitudes entre los marcos de referencia de los diferentes elementos del robot, por ejemplo, las llantas, sensores, cámaras, sistemas de visión, actuadores, etc. El análisis de cinemática directa es el cálculo de la posición y orientación del robot; en otras palabras, mediante el uso de ecuaciones de cinemática directa es posible calcular donde se encuentra el robot en cualquier instante de tiempo.

Cuando se desea mover el robot a una posición y orientación deseada, es necesario calcular los ángulos que las llantas deben girar y la distancia que el robot debe desplazarse.

Esto es llamado, análisis de cinemática inversa. Esto significa que en vez de sustituir las variables conocidas del robot en las ecuaciones de cinemática directa del robot, es necesario encontrar la inversa de estas ecuaciones para poder calcular los valores de ángulos y distancias necesarios para mover al robot a la posición y orientación deseada.

Esta sección presenta un análisis cinemático basado en el robot móvil PIONEER 3-AT y como se menciona anteriormente, este análisis hace posible controlar al robot de manera precisa en un espacio tridimensional.

La convención de ejes utilizada para la asignación de marcos de referencia es la siguiente; el eje Z se encuentra en dirección hacia arriba (paralelo a la gravedad), el eje Y en dirección a la derecha del robot (este) y el eje X en dirección hacia enfrente (norte). Ver figura 35.

En la figura 35 es mostrada la asignación de marcos de referencia del robot móvil incluyendo el sistema de barrido instalado en la parte superior frontal del mismo. El marco de referencia “0”, es la referencia fija para navegación, el marco “r” representa el marco del robot y se encuentra localizado en el centro de gravedad del robot móvil. Los marcos “w1”, “w2”, “w3” y “w4” representan los marcos de las llantas (estos marcos se encuentran paralelos a los ejes de rotación en el centro de cada llanta y giran con ellas). Los marcos “e” y “s” se encuentran en el sistema de barrido y representan a los subsistemas de posicionamiento de láser y apertura de barrido, respectivamente.

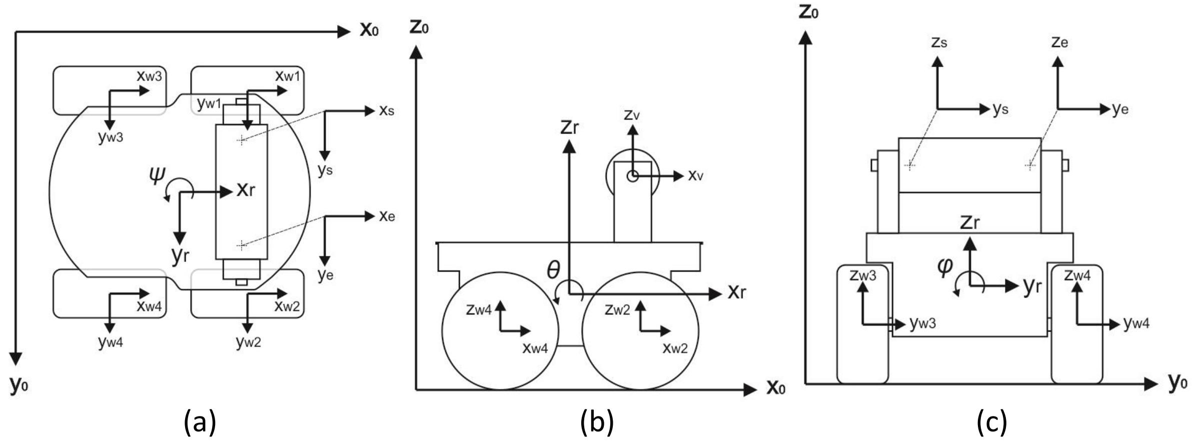

Figura 35. Asignación de marcos de referencia del robot móvil con el sistema de barrido instalado. (a) Vista superior, ejes X, Y. (b) Vista lateral, ejes X, Z. (c) Vista trasera, ejes Y, Z; [75].

De acuerdo a [69-71], para representar la posición y orientación de un objeto en el espacio, son necesarias seis piezas de información, tres para representar la posición y tres para representar la orientación. Para representar la posición se utiliza una matriz de transformación homogénea para trasladar el robot móvil a la posición deseada, después se utilizan ángulos RPY (roll, pitch, yaw) para ajustar el robot a la orientación deseada. Los ángulos RPY son una secuencia de tres rotaciones respecto a los ejes en movimiento $\vec{n}$, $\vec{o}$, $\vec{a}$ (normal, orientación y acercamiento respectivamente), del marco de referencia actual.

En otras palabras, cada rotación respecto a los ejes $\vec{n}$, $\vec{o}$, $\vec{a}$ es representada por una matriz de 4x4 (matriz de transformación homogénea) y la multiplicación de dichas matrices describe la orientación deseada de un objeto en el espacio utilizando ángulos RPY; esto es mostrado en la ecuación 8.

La secuencia de los ángulos RPY consiste en las siguientes transformaciones; rotación de ϕ respecto al eje $\vec{a}$ del robot, llamado giro (roll), rotación de θ respecto al eje $\vec{o}$ del robot, llamado inclinación (pitch) y rotación de ψ respecto al eje $\vec{n}$ del robot, llamado guiñada. Todos los ángulos son medidos y considerados positivos en el sentido de las manecillas de un reloj de acuerdo a la regla de la mano derecha. Los ejes $\vec{n}$, $\vec{o}$, $\vec{a}$ (del marco de referencia actual), son paralelos a X, Y, Z (del marco de referencia fijo) en la posición de origen [69].

4.2.1 Modelo de cinemática directa

La secuencia de transformaciones establecida en la ecuación 7, define el modelo de cinemática directa del robot PIONEER 3-AT.

Las siguientes ecuaciones fueron desarrolladas [75] para controlar la posición y orientación del robot móvil en un espacio tridimensional en relación a un marco de referencia fijo.

$$ {}^{0}T_{r} = Trans(x, y, z) \times RPY(\varphi, \theta, \psi) \tag{6} $$

$$ {}^{0}T_{r} = Trans(x, y, z) \times Rot(\vec{a}, \varphi) \times Rot(\vec{o}, \theta) \times Rot(\vec{n}, \psi) \tag{7} $$

$$ {}^{0}T_{r} = \begin{bmatrix} 1 & 0 & 0 & x \\ 0 & 1 & 0 & y \\ 0 & 0 & 1 & z \\ 0 & 0 & 0 & 1 \end{bmatrix} \times \begin{bmatrix} c\varphi & -s\varphi & 0 & 0 \\ s\varphi & c\varphi & 0 & 0 \\ 0 & 0 & 1 & 0 \\ 0 & 0 & 0 & 1 \end{bmatrix} \times \begin{bmatrix} c\theta & 0 & s\theta & 0 \\ 0 & 1 & 0 & 0 \\ -s\theta & 0 & c\theta & 0 \\ 0 & 0 & 0 & 1 \end{bmatrix} \times \begin{bmatrix} 1 & 0 & 0 & 0 \\ 0 & c\psi & -s\psi & 0 \\ 0 & s\psi & c\psi & 0 \\ 0 & 0 & 0 & 1 \end{bmatrix} \tag{8} $$

$$ {}^{0}T_{r} = \begin{bmatrix} c\phi c\theta & c\phi s\theta s\psi - s\phi c\psi & c\phi s\theta c\psi + s\phi s\psi & x \\ s\phi c\theta & s\phi s\theta s\psi + c\phi c\psi & s\phi s\theta c\psi - c\phi s\psi & y \\ -s\theta & c\theta s\psi & c\theta c\psi & z \\ 0 & 0 & 0 & 1 \end{bmatrix} \tag{9} $$

$$
{}^{0}T_{r} = \begin{bmatrix} 1 & 0 & 0 & a \\ 0 & c\psi & -s\psi & b \\ 0 & s\psi & c\psi & c \\ 0 & 0 & 0 & 1 \end{bmatrix} \tag{10}
$$

donde, las primeras tres columnas de la ecuación 9 representan los vectores unitarios para la orientación ($\vec{n}, \vec{o}, \vec{a}$) ; la última columna representa el vector de posición en coordenadas cartesianas (X, Y, Z); ${}^{0}T_{r}$ significa matriz de transformación del marco de referencia “r” respecto al marco de referencia “0” (marco de referencia fijo); “$c\phi$” es utilizado como una abreviación de “*cos* ϕ” y “$s\phi$” para “*sin* ϕ” (lo mismo aplica para los ángulos “θ” y “ψ”).

Una forma de obtener los ángulos RPY actuales es mediante el uso avanzado de acelerómetros con filtros adaptativos LMS [72-74].

Utilizando el modelo de cinemática directa (ecuación 9) es posible calcular la posición y orientación del robot en cualquier instante de tiempo y también a partir de este modelo se desarrolla el modelo o las ecuaciones de cinemática inversa que permiten mover y controlar el robot móvil hacia una posición y orientación deseada.

Es importante mencionar que los valores de rotación en la ecuación 7 (o los elementos x_{11}-x_{33} de la matriz en la ecuación 9) obtenidos de los acelerómetros y la cuarta columna en cada matriz de la ecuación 8 (o la última columna de la ecuación 9), definen la posición espacial del robot móvil en coordenadas cartesianas. Al mismo tiempo el sistema de barrido por láser obtiene y representa las coordenadas de obstáculos detectados en el mismo volumen espacial, por lo tanto las coordenadas cartesianas de cualquier obstáculo detectado son transformadas al sistema de coordenadas del robot móvil.

4.2.2 Consideraciones especiales del robot móvil

Tomando algunas consideraciones, se estableció una tabla de parámetros de marcos de referencia del robot móvil, la cual permite representar la posición y orientación entre cada marco de referencia presentado en la asignación de marcos de referencia (ver figura 35).

Transformación	x (mm)	y (mm)	z (mm)	ψ (grados)	θ (grados)	ϕ (grados)
${}^{r}T_{s}$	-111.7	120.6	264.1	0	variable	0
${}^{r}T_{w1}$	198.9	-135.8	28.5	0	variable	0
${}^{r}T_{w2}$	-198.9	-135.8	28.5	0	variable	0
${}^{r}T_{w3}$	198.9	135.8	28.5	0	variable	0
${}^{r}T_{w4}$	-198.9	135.8	28.5	0	variable	0

Tabla 4. Parámetros de marcos de referencia para el robot móvil, en condiciones ideales.

La siguiente nomenclatura es utilizada en la tabla 4; por ejemplo, ${}^{r}T_{s}$ representa la matriz de transformación del marco de referencia “s” al marco de referencia “r” y lo mismo aplica para el resto de las transformaciones.

En la tabla 4 también se muestran las seis piezas de información o seis grados de libertad que posee el robot móvil. Las primeras tres columnas X, Y, Z, muestran los tres movimientos lineales que representan las distancias entre un marco de referencia y otro; y las últimas tres representan los ángulos RPY ψ, θ, ϕ, es decir, la rotación entre un marco de referencia y otro. Estos parámetros pueden ser variables o valores conocidos.

Las consideraciones establecidas para el robot móvil son que operará en condiciones ideales de superficie en un ambiente interior (durante la primera etapa de experimentación en laboratorio), para demostrar la funcionalidad del sistema de barrido por láser en la tarea de navegación de robot.

Debido a esta suposición el robot móvil es limitado en dos de sus tres ángulos de libertad rotacionales, es otras palabras, los ángulos ϕ (roll) y θ (pitch) son establecidos como “0” (ver figura 35) en ${}^{0}T_{r}$ de la ecuación 10, debido a que se considera que el robot solo transitaría por terreno plano, sin inclinaciones de ningún tipo; de esta manera simplificando los modelos de cinemática directa e inversa y reduciendo el tiempo de cálculo en las ecuaciones.

Experimentación adicional a futuro en caso de adquirir el robot móvil, será llevada a cabo tanto en condiciones ideales como en condiciones no ideales o variación de los parámetros de rotación ϕ y θ.

4.2.3 Modelo de cinemática inversa

Asumiendo que la posición y orientación deseada, en este caso la meta o siguiente destino del robot móvil, es conocida; tres ecuaciones (12-14) son desarrolladas a partir del modelo de cinemática directa completo (ecuación 11) [75].

$$ {}^{0}T_{r} = \begin{bmatrix} r_{11} & r_{12} & r_{13} & px \\ r_{21} & r_{22} & r_{23} & py \\ r_{31} & r_{32} & r_{33} & pz \\ 0 & 0 & 0 & 1 \end{bmatrix} = \begin{bmatrix} c\phi c\theta & c\phi s\theta s\psi - s\phi c\psi & c\phi s\theta c\psi + s\phi s\psi & a \\ s\phi c\theta & s\phi s\theta s\psi + c\phi c\psi & s\phi s\theta c\psi - c\phi s\psi & b \\ -s\theta & c\theta s\psi & c\theta c\psi & c \\ 0 & 0 & 0 & 1 \end{bmatrix} \qquad (11) $$

$$\varphi = ATAN2(r_{21}, r_{11}) \tag{12}$$

$$\theta = ATAN2(-r_{31}, r_{11}c\phi + r_{21}s\phi) \tag{13}$$

$$\psi = ATAN2(-r_{23}c\phi + r_{13}s\phi, r_{22}c\phi - r_{12}s\phi) \tag{14}$$

Donde, la ecuación 11 representa el modelo de cinemática directa y los ángulos RPY (ϕ, θ, ψ) son desconocidos. Las ecuaciones 12-14 muestran los parámetros necesarios para calcular dichos ángulos desconocidos.

Estas ecuaciones forman el modelo de cinemática inversa del robot móvil y son utilizadas para controlar su localización deseada, en otras palabras, con este modelo es posible determinar el valor de cada ángulo RPY para posicionar el robot móvil en la posición y orientación deseada.

5. Sistema de navegación para un robot móvil

Parte del objetivo general de esta investigación es implementar el sistema de barrido por láser en un robot móvil y utilizar el mapa digital que genera mediante el cálculo de coordenadas en 3D, como datos de entrada para un sistema de navegación de dicho robot móvil. Este sistema de navegación garantiza la correcta toma de decisiones en relación a la trayectoria que debe tomar el robot móvil para llegar de forma segura a su destino [75].

5.1 Integración de los sistemas de barrido por láser y navegación

En la figura 36 podemos observar un modelo en 3D donde se muestra una escena de cómo se vería el sistema de barrido por láser montado en un robot móvil, el robot se observa navegando en un ambiente desconocido y encontrando obstáculos en su camino. También se indica como el haz de luz láser es direccionado hacia la parte frontal del sistema y la manera en que la apertura de barrido recibe los rayos de luz láser reflejados. Por último, se muestran los ejes X, Y, Z del sistema de coordenadas cartesianas de referencia fijo y los ejes de las coordenadas calculadas por el sistema de barrido por láser.

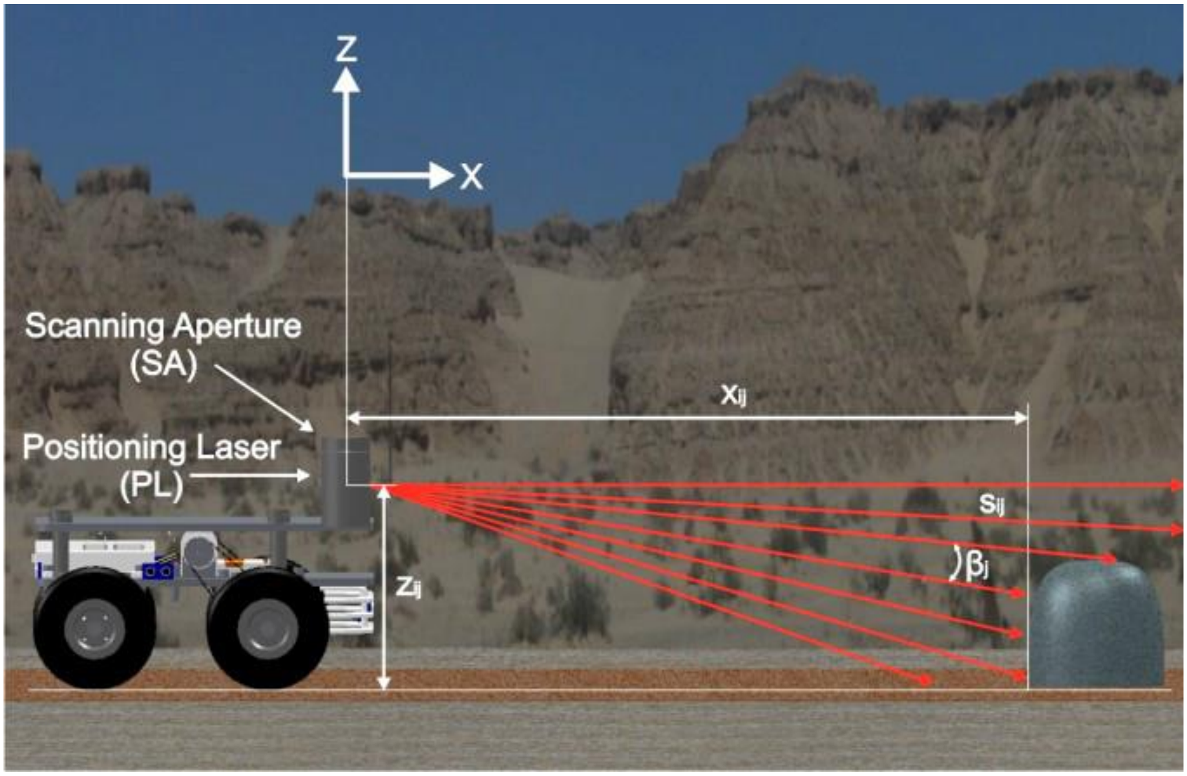

(a) Vista lateral.

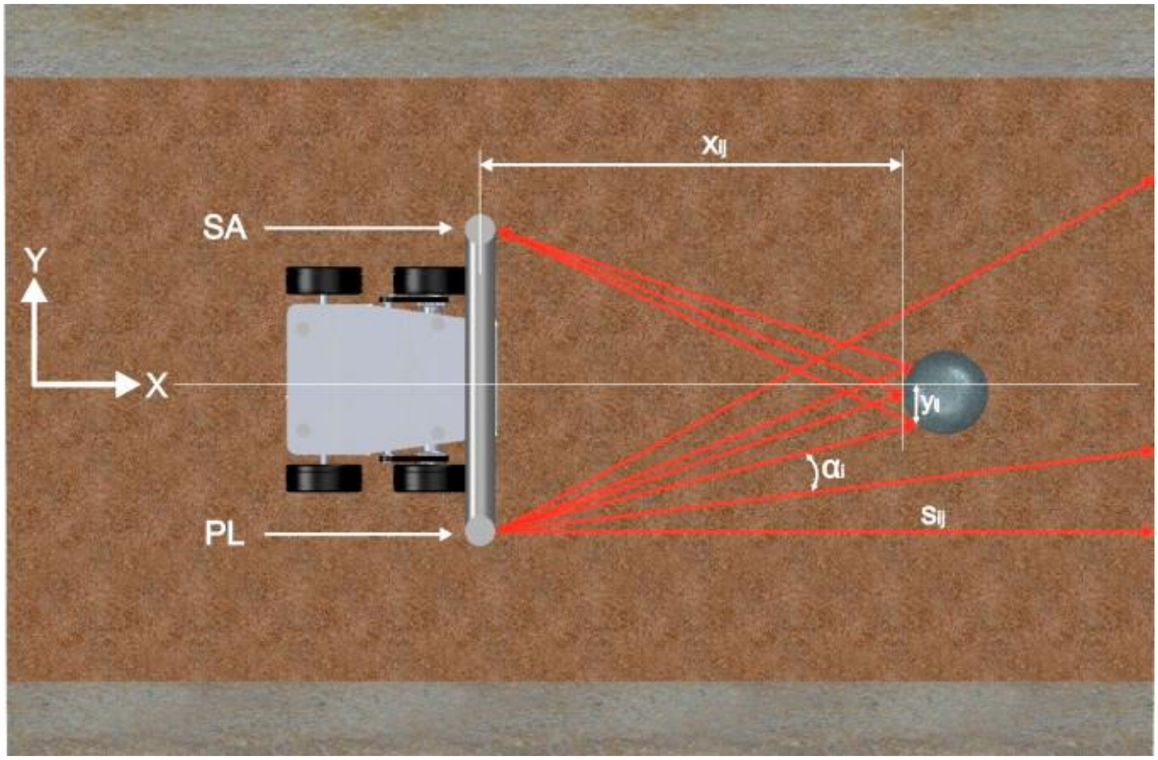

(b) Vista superior.

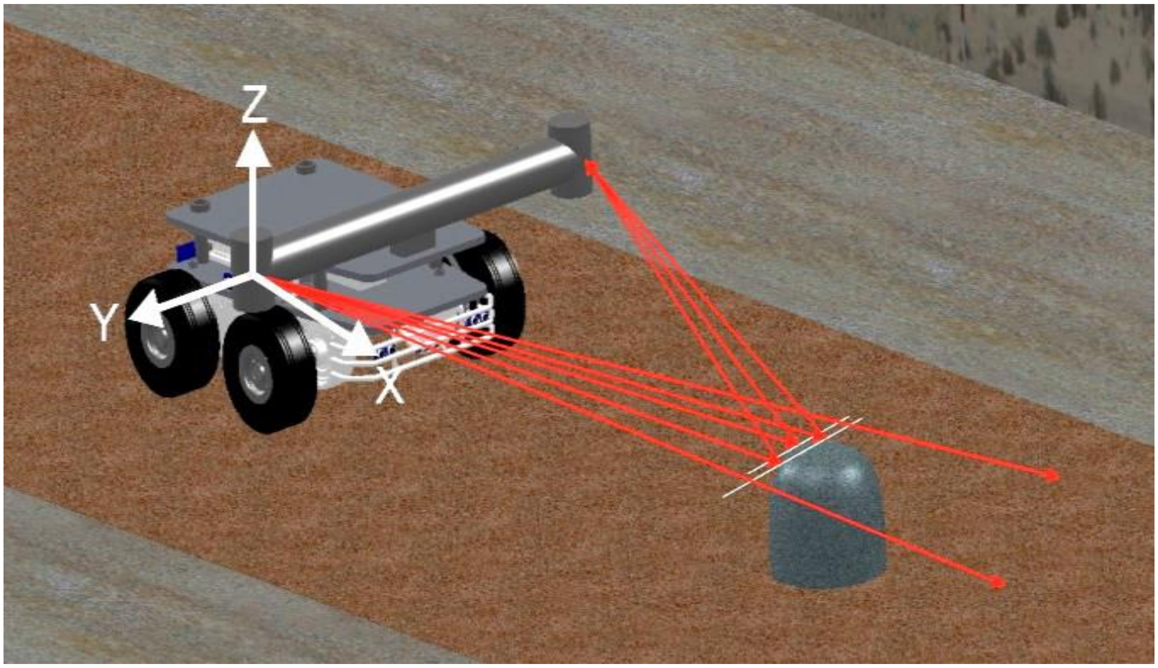

(c) Vista isométrica.

Figura 36. Modelo 3D del sistema de barrido por láser montado sobre un robot móvil.

La planeación de trayectoria y la evasión de obstáculos son las tareas más importantes del sistema de navegación, por lo tanto es igual de importante saber en qué momento calcular dicha trayectoria, cuando indicarle al sistema de barrido que debe ser activado y que hacer antes y después de estos procesos; debido a esto se elaboró un diagrama de flujo que indica el funcionamiento en conjunto de los sistemas de barrido por láser y navegación. El diagrama de flujo presentado en la figura 37 se explica por sí mismo, sin embargo algunos puntos requieren una explicación más a fondo.

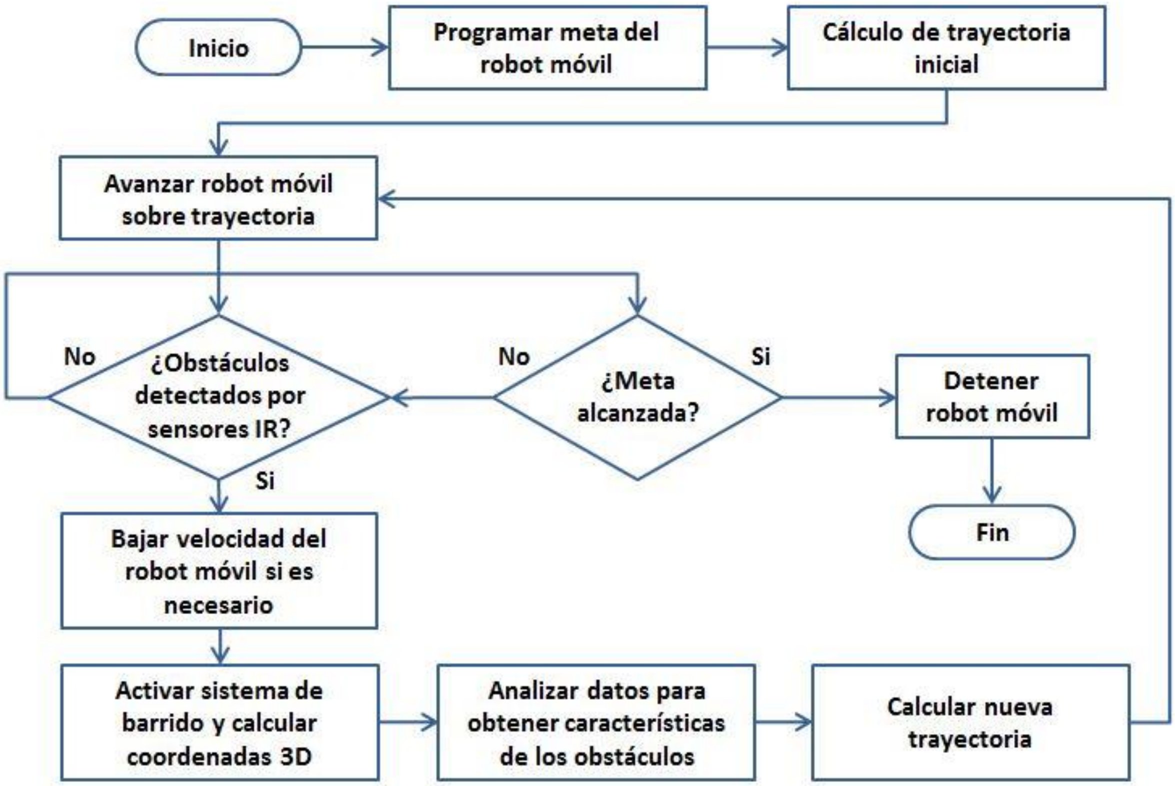

Figura 37. Este diagrama de flujo indica de manera general los pasos a seguir para la operación del robot móvil y los sistemas que lo componen.

El primer paso es programar el destino o meta final del robot móvil. Después de realizar este paso todas las acciones posteriores se ejecutan de manera autónoma. El siguiente paso calcula la trayectoria inicial, la cual será una línea recta entre la posición actual o inicial del robot y la meta.

Después, el robot móvil comenzará a avanzar siguiendo la trayectoria inicial calculada y en el momento en que los sensores IR detecten la presencia de alguno o más obstáculos, darán la señal de activación para que el sistema de barrido por láser realice un barrido del campo de visión del robot. Inmediatamente calcularán las coordenadas en 3D de cualquier obstáculo encontrado. Al finalizar estos cálculos, los resultados se analizarán para obtener las principales características y cualquier información útil sobre los obstáculos encontrados. Por ejemplo, características como: altura, ancho, profundidad, distancia entre obstáculos (si aplica), entre otras.

Esta información será utilizada por el sistema de navegación para calcular una nueva trayectoria con el fin de que el robot móvil llegue a la meta de manera segura. Después de que la nueva trayectoria sea calculada (ver sección 5.3 de este capítulo), el robot móvil seguirá esta trayectoria hasta que se encuentre algún obstáculo o llegue a la meta.

Si algún otro obstáculo es encontrado durante cualquier momento en la navegación de la trayectoria actual, el mismo proceso se repetirá hasta que el robot móvil llegue a su meta, después de eso el robot móvil se detendrá y entrará en un estado libre para esperar que una nueva meta sea programada.

5.2 Características y especificaciones básicas del sistema de navegación

Debido a la naturaleza del robot móvil seleccionado, específicamente el hecho de que las llantas del robot son fijas y no pueden girar, el método utilizado para girar y maniobrar dicho robot es llamado *skid-steer*, esto significa que el robot gira por medio de derrape. Para girar hacia la izquierda, se activa el motor de la llanta 2 hacia adelante al mismo tiempo que el motor de la llanta 3 en dirección contraria. Para girar hacia la derecha, se activa el motor de la llanta 1 hacia adelante y el motor de la llanta 4 hacia atrás. Durante un giro, los otros dos motores que no se utilizan estarán sin energía para que se encuentren libres para derrapar e ir con el movimiento del robot. El resultado es que el robot puede girar sobre su propio eje para ajustar su orientación sin cambiar su posición.

Existe la posibilidad de que girar el robot móvil con este método pueda generar un causa de incertidumbre en la posición del robot [76-78], sin embargo este problema está fuera del alcance de esta investigación, por lo tanto no será abordado y no se considerará como fuente de error.

El principal objetivo del robot móvil será llegar a su destino o meta final de manera segura, evadiendo cualquier obstáculo que encuentre en su trayectoria. La trayectoria inicial será el camino más cercano entre las coordenadas de inicio y las coordenadas de la meta y será recalculada en el momento que el robot móvil detecte un obstáculo. En dado caso que el robot móvil no detecte obstáculos, esa trayectoria llevará al robot móvil a su meta final.

El robot contará con codificadores magnéticos en las cuatro llantas para conocer la distancia recorrida y un giroscopio de 3 ejes para monitorear su orientación (ángulos RPY) en cada nueva posición y orientación. A su vez estará equipado con un conjunto de sensores IR, los cuales estarán configurados para detectar rápidamente presencia a una distancia fija y serán utilizados como medio de informar al sistema de barrido por láser que hay algún obstáculo y es tiempo de realizar un barrido de la escena para calcular las coordenadas en 3D e indicar la posición exacta y cantidad de obstáculos detectados.

Se decidió utilizar estos sensores en conjunto con el sistema de barrido debido a su velocidad de respuesta y a su bajo consumo de energía en comparación a tener los tres motores del sistema de barrido activados durante todo el tiempo de navegación.

5.3 Planeación de trayectoria

Después de que el sistema de barrido por láser ha detectado algún obstáculo en su campo de visión, el siguiente paso lógico es calcular una nueva trayectoria para que el robot móvil pueda evadir el obstáculo y llegar a la meta.

Para poder calcular una nueva trayectoria se toma en consideración las dimensiones del robot móvil y un margen de seguridad, entonces se calculan ciertos puntos clave que eviten el obstáculo tomando en cuenta lo mencionado anteriormente y que lleguen a la meta, después se calcula una función curva que pasara a través de todos los puntos previamente calculados para suavizar la trayectoria y por consiguiente el movimiento del robot móvil.

El primer acercamiento fue usar la cantidad mínima de puntos para formar una curva, lo cual es tres. El resultado es una curva que evita exitosamente el obstáculo y llega a la meta, sin embargo al tener forma de semicírculo resulta en una trayectoria más larga de lo necesario. Ver figura 38.

Por lo tanto se formuló otro acercamiento para mejorar la solución, en este caso utilizamos 10 puntos base para calcular la trayectoria y formar la curva, el resultado (mostrado en la figura 39-b) es que la curva no solo evade el obstáculo exitosamente y llega al obstáculo, sino que también reduce la distancia recorrida del robot móvil entre un 12-15% y por consiguiente reduce el consumo de energía del robot, mientras que el tiempo de cálculo –

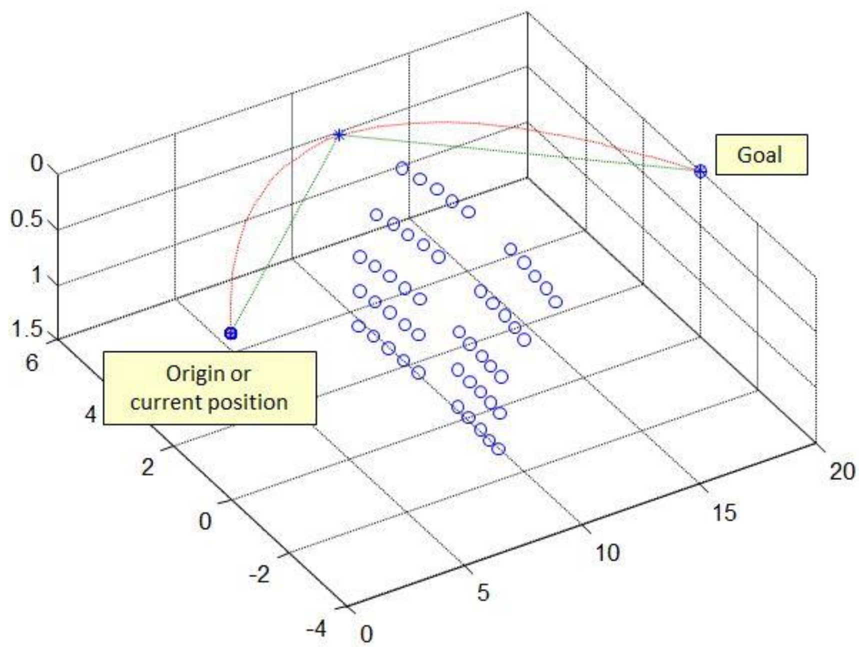

Figura 38. Trayectoria del robot móvil generada en una simulación de MATLAB utilizando una curva en base a tres puntos (escala en metros).

únicamente incrementa en 1.2 ms debido al incremento de puntos base para calcular la nueva trayectoria. Este intercambio permite ahorrar recursos del robot significativamente.

El primero de los diez puntos base utilizados para calcular la nueva trayectoria es la posición actual del robot móvil o inicio de trayectoria; el segundo punto es calculado ya sea en el lado derecho o izquierdo del obstáculo a evadir, dependiendo de qué extremo del obstáculo está más cerca al robot. De esta manera aseguramos que el obstáculo se evadirá por el lado que genere la trayectoria más corta hacia la meta. A este punto se le agrega un factor de seguridad del 50% del ancho del robot móvil para asegurar que no habrá colisión con el obstáculo a la hora de navegar alrededor de este. Finalmente, desde el tercer punto hasta el décimo (el cual es la meta final), se forma una línea recta (ver figura 39).

Para calcular la nueva trayectoria basada en los diez puntos, se utiliza el formalismo *spline*. En simulación se utilizó una función interna de MATLAB llamada *spline*, la cual dada las coordenadas de los diez puntos base, utiliza una interpolación cúbica polinomial para encontrar los nuevos valores de y, los cuales son los valores de la función Y (rango de los diez puntos) en los valores de la interpolante x (la cual tiene los valores del nuevo dominio para la curva). En otras palabras calcula todos los valores de pares de coordenadas x, y que pasen por los diez puntos en forma de curva (ver figura 39) [75].

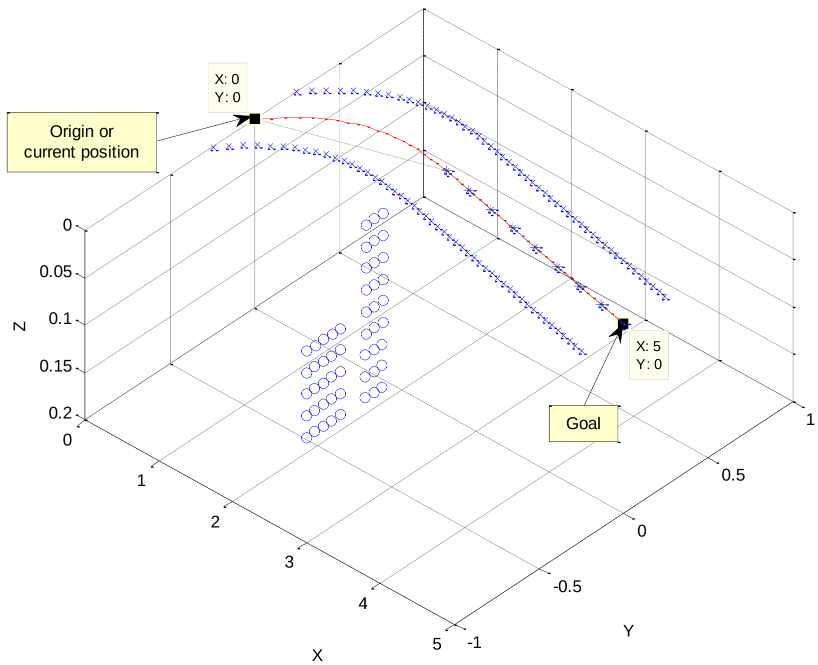

(a)

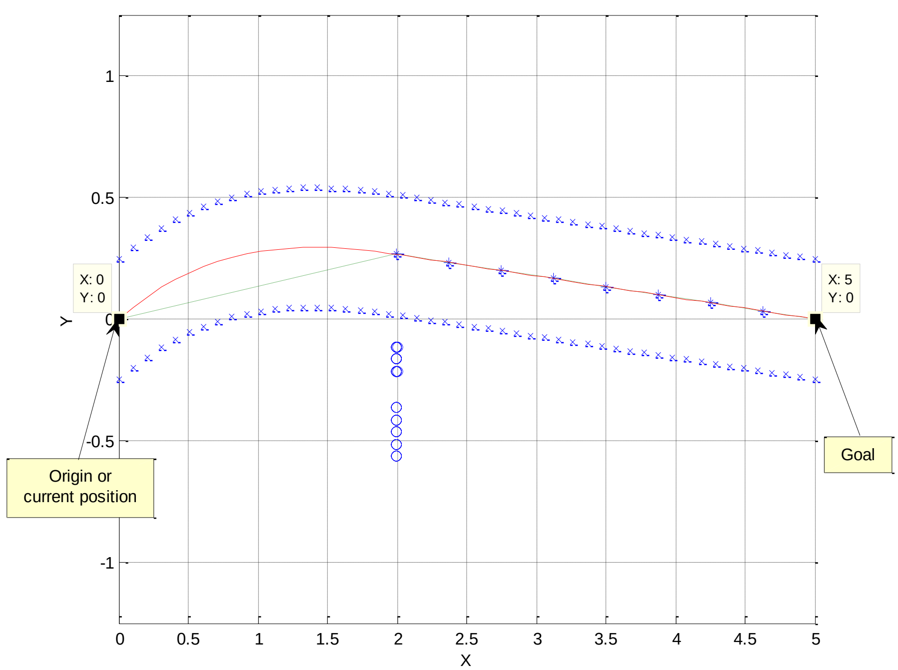

(a)

Figura 39. Trayectoria del robot móvil generada en una simulación de MATLAB® utilizando una curva en base a diez puntos (escala en metros). (a) Vista isométrica 3D. (b) Vista superior 2D.

El resultado son dos vectores (uno para valores de x, otro para valores de y) los cuales contienen los valores de la nueva trayectoria en forma de curva, desde la posición actual del robot hasta la meta, pasando por los 10 puntos base.

Actualmente la nueva trayectoria generada en forma de curva es representada por 50 pares de coordenadas, lo cual ha demostrado ser suficiente para formar una curva suave, sin embargo este parámetro puede ser ajustado de acuerdo a las necesidades del robot móvil.

En la figura 39-a, la trayectoria se representa por la línea solida color rojo, los asteriscos color azul representan los diez puntos base, las líneas color azul formadas por cruces representan los límites físicos del robot, los círculos color azul representan puntos de coordenadas 3D (x, y, z calculadas por el sistema de barrido por láser), y cada grupo de círculos azules representa un obstáculo detectado. En este caso se muestran dos grupos lo cual significa que dos obstáculos diferentes fueron detectados.

Es importante mencionar que en la figura 39-b los obstáculos son evadidos por el lado izquierdo del robot móvil. Para determinar la dirección en la cual el robot móvil evadirá un obstáculo, se desarrolló un algoritmo que determina la nueva trayectoria en base al camino más corto a la meta y selecciona la trayectoria más corta.

CAPÍTULO III. MATERIALES, EQUIPO Y DISEÑO MECÁNICO DEL PROTOTIPO II

Esta sección trata sobre los materiales y equipo necesarios para fabricar y trabajar con el prototipo II del sistema de barrido por láser.

1. Diseño mecánico del subsistema de posicionamiento de láser

Como se menciona en la sección 1.2 del capítulo II, la función principal del subsistema de posicionamiento de láser es la de direccionar el rayo de luz láser hacia el campo de visión del sistema de barrido por láser. Para lograr esta función, este subsistema utiliza los siguientes componentes:

- Un láser rojo
  - Longitud de onda: 632.8 nm
  - Diámetro del haz: 0.68 mm
  - Voltaje: 110 VAC
  - Potencia: 20 mW
  - Helio y neón (HeNe)
  - Clase: III-b
  - Modelo: 1135P
  - Fabricante: JDS UNIPHASE
- Dos motores de pasos unipolares
  - 1.8° por paso
  - 4 fases

- 12 V @ 0.4 A
- Torque: 3.4 kg.cm
- No. de parte: 42BYGH404-R
- Fabricante: JAMECO

- Dos engranes de bronce anti-juego
  - Dientes: 96
  - Diámetro: 2”
  - Ángulo de presión: 20°
  - No. de parte: S1B83A-C048B096D
  - Fabricante: SDP/SI
- Dos engranes de gusano o sinfín de acero
  - Ángulo de presión: 20°
  - Pitch: 48
  - Diámetro: 0.375”
  - No. de parte: S1D93Z-P048SD
  - Fabricante: SDP/SI
- Dos espejos con corte de 45°
  - Diámetro: 10 mm
  - Longitud: 15 mm
  - Refleja luz en un 90%
  - No. de parte: 45-944
  - Fabricante: Edmund Optics

Figura 40. Laser HeNe rojo 632.8 nm

Los motores de pasos (ver figura 41) fueron implementado para realizar dos funciones principales, la primera es el posicionamiento del haz del láser hacia el campo de visión del sistema y la segunda es la capacidad de girar el cilindro del sistema en su propio eje para modificar su inclinación y calcular coordenadas en el plano Z.

Para realizar estas funciones los motores de pasos controlan el movimiento de un engrane especial que posee la característica de ser anti-juego, es decir, al momento de que el motor cambia de dirección, el engrane compensa el juego entre dientes y el motor no pierde pasos al cambiar de dirección, evitando un error acumulativo en el conteo de pasos. El engrane es controlado gracias a otro engrane tipo gusano o sinfín, el cual se acopla directamente a la flecha del motor y sus dientes ensamblan directamente con los del engrane anti-juego (ver figura 42).

El engrane utilizado para posicionar el láser del sistema (ver figura 40) esta acoplado directamente con una flecha que a su vez esta ensamblada con un espejo con corte de 45° (ver figura 43), controlando su giro. Este espejo recibe el haz de luz láser de otro espejo con corte de 45° fijo al cilindro y lo direcciona hacia el campo de visión del sistema.

Figura 41. Motor de pasos, 12v a 0.4 A.

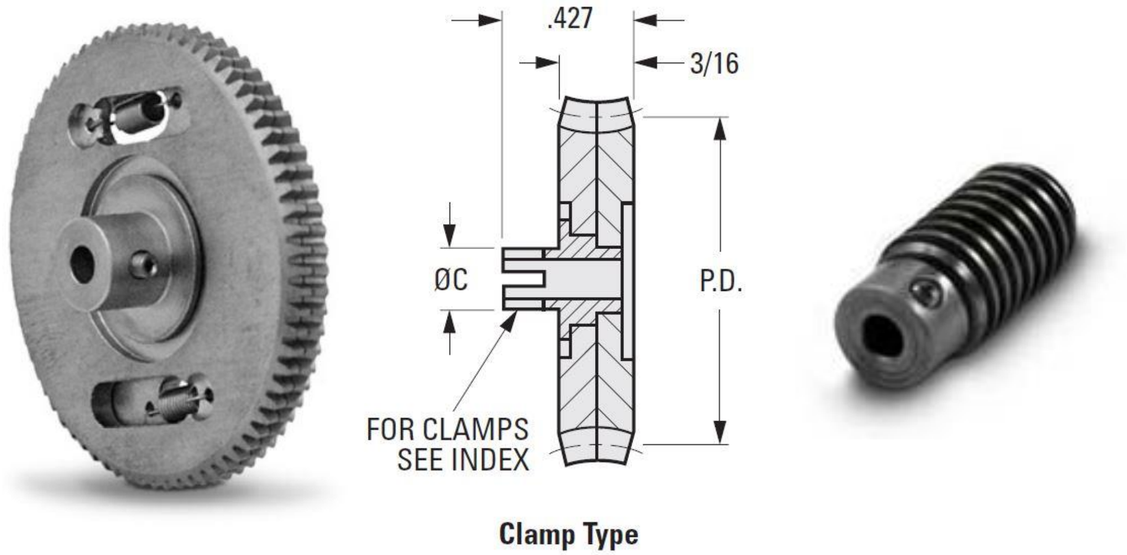

Figura 42. Engrane anti-juego y Engrane de gusano o sinfín de acero

En la figura 44 se muestra el subsistema de posicionamiento de laser completamente ensamblado y en operación. También se puede observar que debido a una buena etapa de diseño y planeación, el modelo en 3D antes de fabricar el sistema y el prototipo fabricado son prácticamente iguales. Diferentes vistas del subsistema y planos de sus partes se encuentran en el apéndice E.

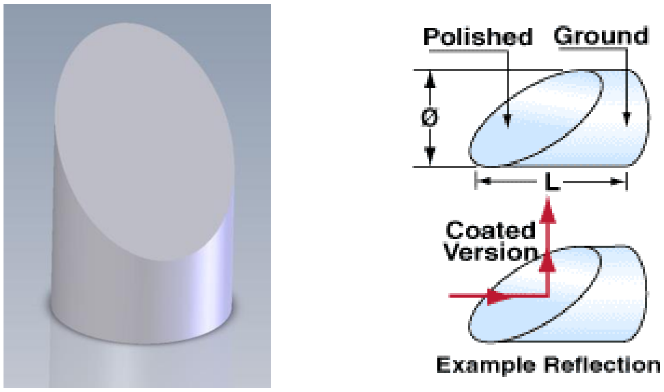

Figura 43. Espejo con corte de 45° y ejemplo de reflexión.

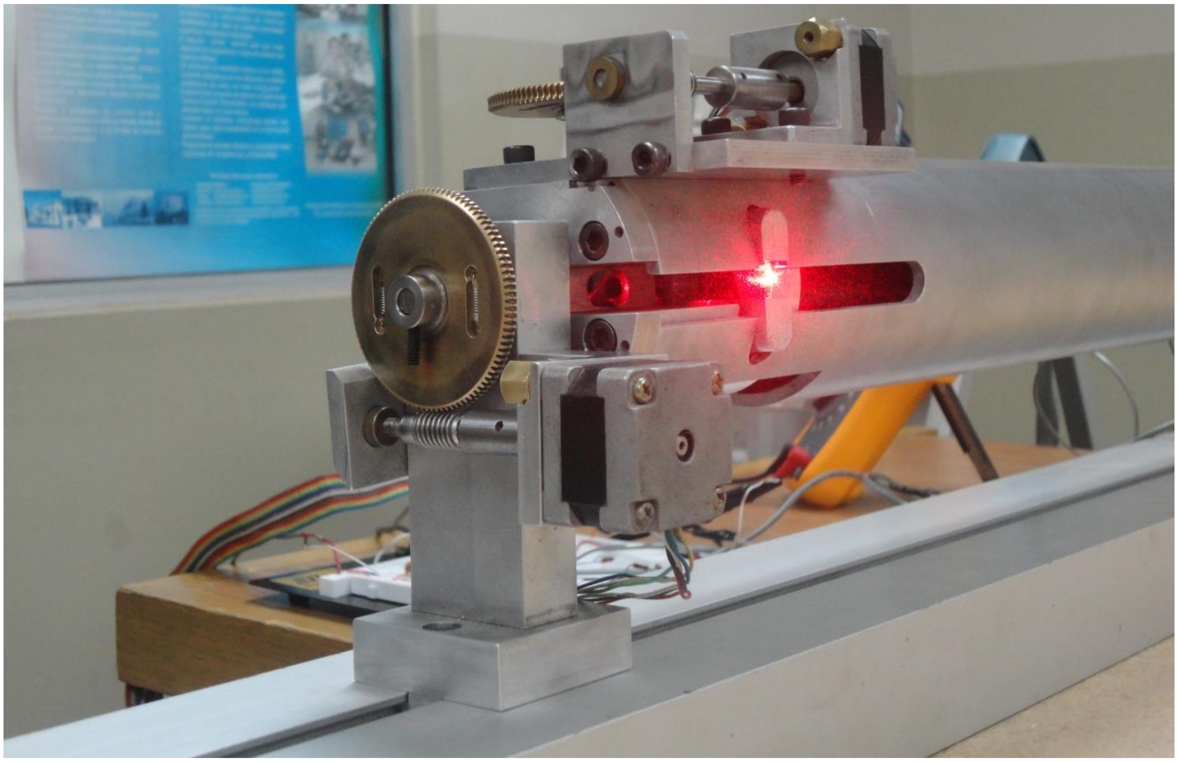

(a)

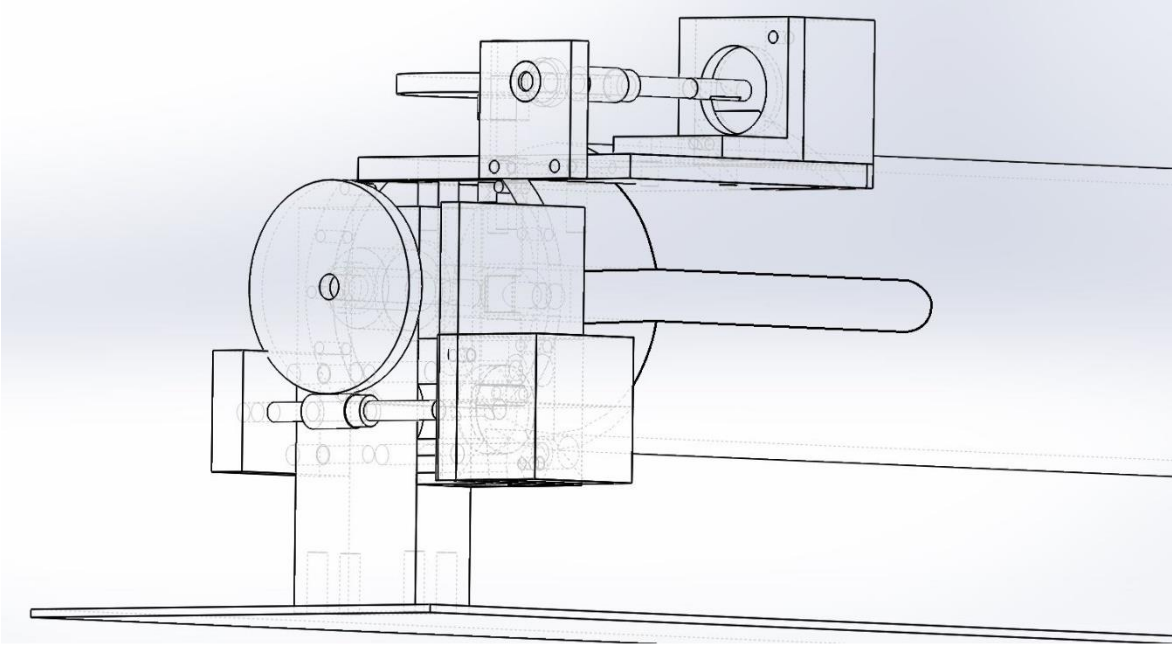

(b)

Figura 44. Subsistema de posicionamiento de láser. (a) fotografía en laboratorio de optoelectrónica. (b) modelo 3D.

2. Diseño mecánico del subsistema de apertura de barrido

Como se menciona en la sección 1.3 del capítulo II, la función principal del subsistema de apertura de barrido es la recibir o detectar la reflexión del rayo de luz láser reflejado por algún obstáculo dentro del campo de visión del sistema de barrido por láser, con el fin de calcular las coordenadas de dicho obstáculo. Este subsistema se conforma por los siguientes componentes:

- Un espejo con corte de 45°
    - Diámetro: 10 mm
    - Longitud: 15 mm
    - Refleja luz en un 90%
    - No. de parte: 45-944
- Dos lentes biconvexos
    - Diámetro: 20 mm
    - Distancia focal: 30 mm
    - Radio de curvatura: 30.08 mm
    - Espesor del centro: 5.30 mm
    - Longitud de onda de diseño: 587.6 nm
    - No. de parte: 45-294
    - Fabricante: Edmund Optics
- Un filtro de interferencia

- Diámetro: 11.8 mm
- Longitud de onda permitida: 632 nm (bloquea el resto)
- Diseñado para líneas de láseres HeNE
- No. de parte: 43-081
- Fabricante: Edmund Optics

- Un motor de corriente directa
  - Voltaje nominal: 12 VDC
  - Rango de voltaje: 6 – 12 VDC
  - Corriente (máxima eficiencia): 1.30 A
  - Velocidad (máxima eficiencia): 12586 RPM
  - Torque (máxima eficiencia): 52.0 g.cm
  - No. de parte: MD5-2070-R
  - Fabricante: JAMECO
- Un sensor fototransistor
  - Cantidad de pines: 3
  - Voltaje máximo colector-emisor: 70 VDC
  - Corriente de entrada: 50 mA
  - Máximo voltaje de salida: 70 VDC
  - Voltaje nominal: 70 VDC
  - Consumo de energía: 250 mW
  - Longitud de onda: 850 nm

- Polaridad: NPN
- No. de parte: BPW77NA
- Fabricante: VISHAY INTERTECHNOLOGY, INC.

- Un sensor optoacoplador o fotointerruptor
  - Cantidad de pines: 4
  - Altura: 11 mm
  - Grosor: 6.35 mm
  - Longitud: 24.7 mm
  - Voltaje máximo colector-emisor: 30 VDC
  - Corriente directa máxima: 50 mA
  - Corriente máxima de colector: 20 mA
  - No. de parte: H21A1
  - Fabricante: ISOCOM COMPONENTS

Figura 45. Motor de corriente directa para rotación de espejo en apertura de barrido (12 VDC, 12586 RPM).

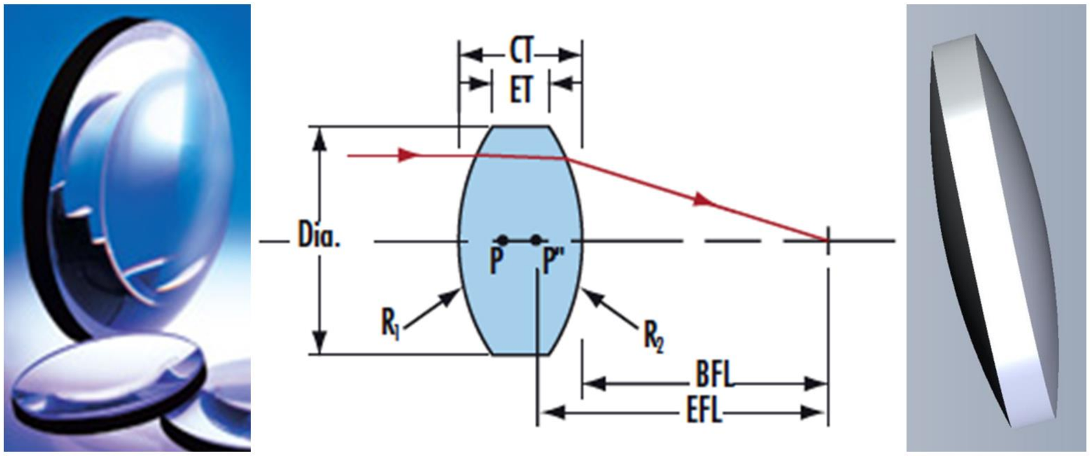

Figura 46. Lentes biconvexos de 20 mm y 587.6 nm.

De acuerdo al funcionamiento del subsistema de apertura de barrido explicado en la sección 1.3 del capítulo II; los rayos de luz láser reflejados hacia el interior de la apertura son recibidos por un espejo con corte de 45° que gira sobre su propio eje debido a que está directamente acoplado con un motor de corriente directa (ver figura 45), este espejo es igual a los espejos utilizados en el subsistema de posicionamiento de láser (ver figura 43). El espejo refleja los rayos laser ortogonalmente hacia un juego de lentes biconvexos (ver figura 46), que concentran los rayos de luz láser recibidos en un solo punto.

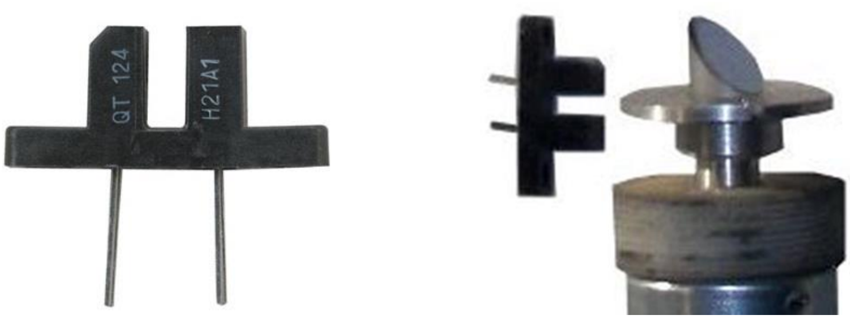

Figura 47. Sensor optoacoplador utilizado para contar las revoluciones del espejo de la apertura de barrido.

Debido a que la función principal de la apertura de barrido es obtener la información necesaria para calcular el ángulo B, fue necesario implementar un sensor optoacoplador o fotointerruptor (ver figura 47) para detectar el momento en que el espejo da una vuelta completa y contar la cantidad de vueltas que pasan hasta la detección de un obstáculo, este valor es llamado $N_{2\pi}$ y se utiliza en la ecuación 1 para calcular el ángulo B.

Finalmente los rayos de luz láser pasan por un filtro de interferencia de 632 nm (ver figura 49) para asegurar que solo la luz del láser rojo llegue al sensor fototransistor (ver figura 48), el cual al activarse envía una señal indicando que hay detección de algún obstáculo.

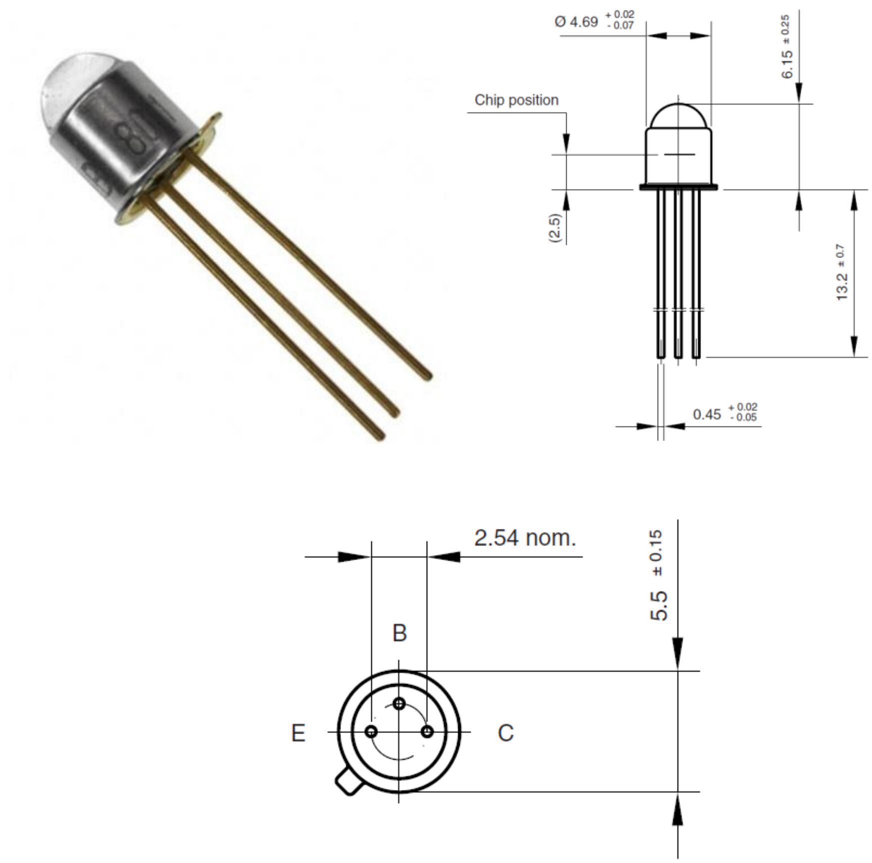

Figura 48. Sensor fototransistor de alta velocidad, utilizado para detección de obstáculos.

Figura 49. Filtro de interferencia, solo permite el paso de señales de 632 nm.

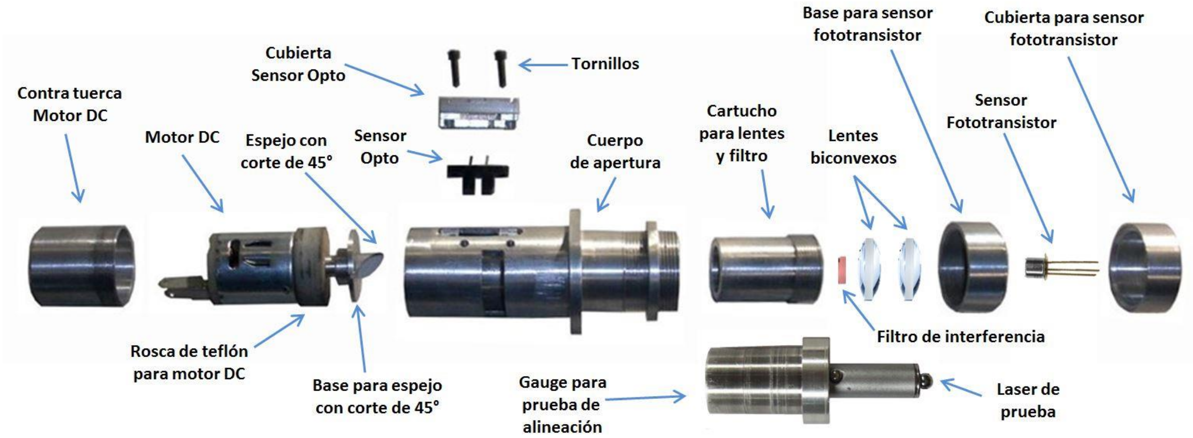

Figura 50. Vista de explosión de los componentes del subsistema de apertura de barrido.

En la figura 51 se muestra el subsistema de apertura de barrido completamente ensamblado y en la figura 50 se muestran todos sus componentes en una vista de explosión. Al igual que con el subsistema de posicionamiento de láser, también se puede observar que debido a una buena etapa de diseño y planeación, el modelo en 3D antes de fabricar el subsistema y el prototipo fabricado son prácticamente iguales. Diferentes vistas del subsistema y planos de sus partes se encuentran en el apéndice E.

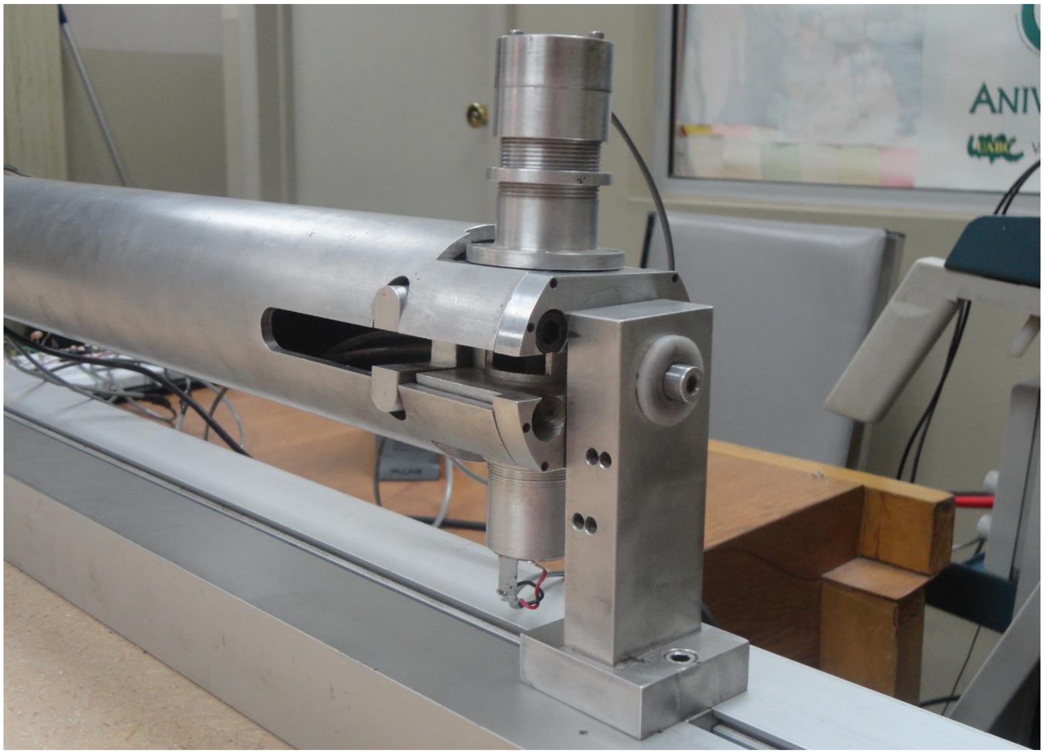

(a)

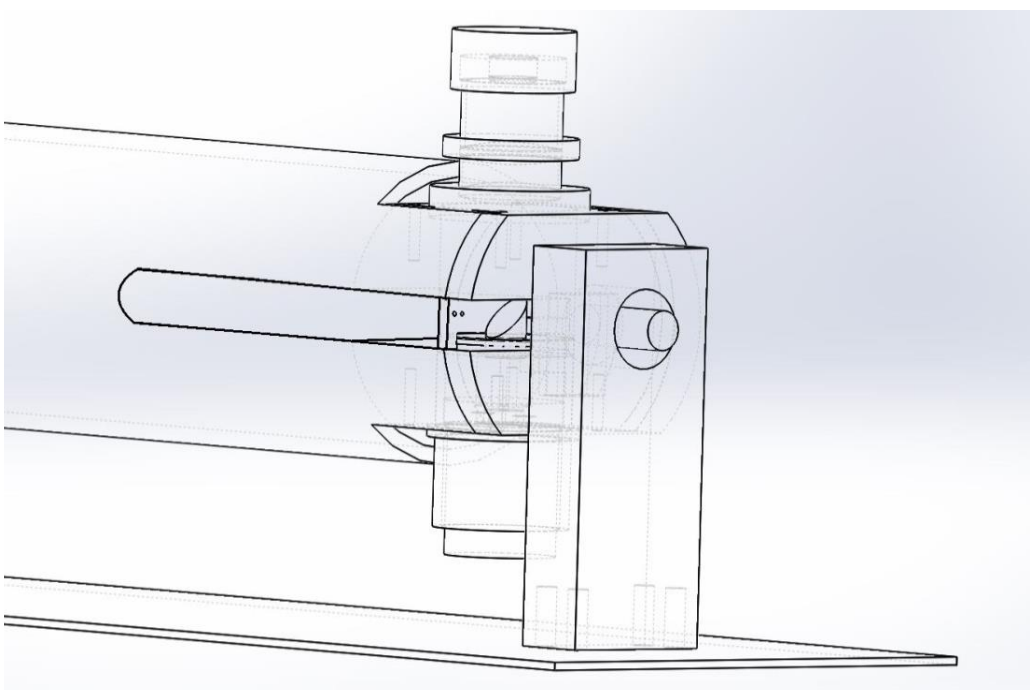

(b)

Figura 51. Subsistema de apertura de barrido. (a) fotografía en laboratorio de optoelectrónica. (b) modelo 3D.

3. Ventajas del prototipo II sobre el prototipo I

El prototipo I (ver figura 52) fue el primer prototipo del sistema de barrido por láser construido para demostrar el principio de la triangulación dinámica.

Sin embargo, a pesar de que se comprobó la teoría de la triangulación dinámica y se obtuvieron buenos resultados en las mediciones de coordenadas con este prototipo (resultados en la sección 2 del capítulo V); algunas fuentes de incertidumbre fueron detectadas, las cuales fue posible eliminar con un diseño mecánico mejorado.

3.1. Subsistemas de posicionamiento de láser y rotación del sistema

El prototipo II (ver figura 53), posee varias ventajas en comparación a su predecesor; la más importante siendo la implementación de un cilindro de aluminio el cual, a diferencia de su predecesor, contiene la mayor parte de los componentes del sistema, incluyendo el láser.

El resultado de esta acción y de la distribución especifica de los componentes, coloca el centro de gravedad del sistema dentro del cilindro de aluminio, lo cual brinda la capacidad de rotar el cilindro sobre su propio eje, utilizando un motor de pasos y un juego de engranes mostrado junto con el subsistema de posicionamiento de laser en la figura 44.

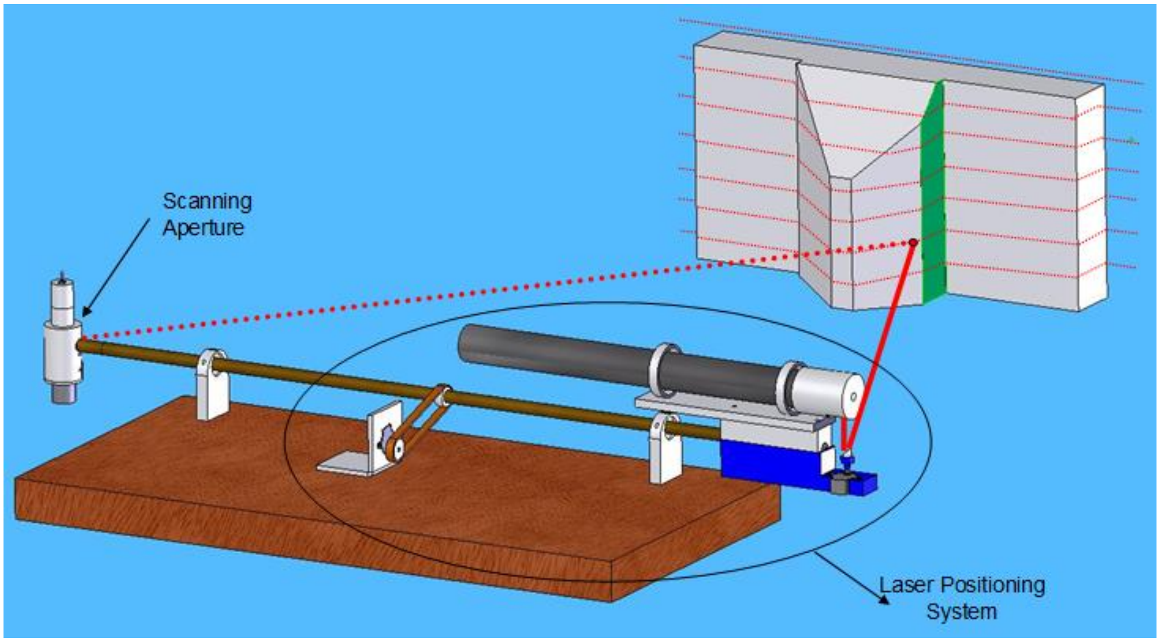

(a)

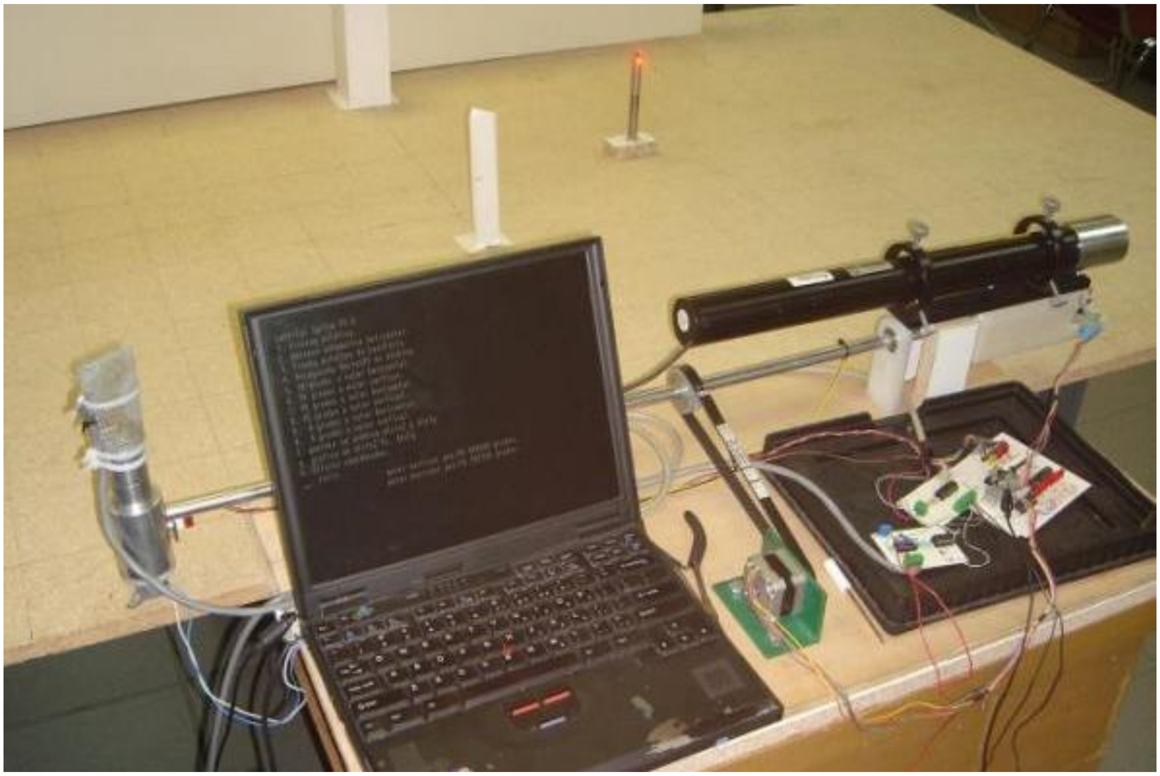

(b)

Figura 52. Prototipo I del sistema de barrido por laser. (a) Modelo 3D. (b) Fotografia en laboratorio.

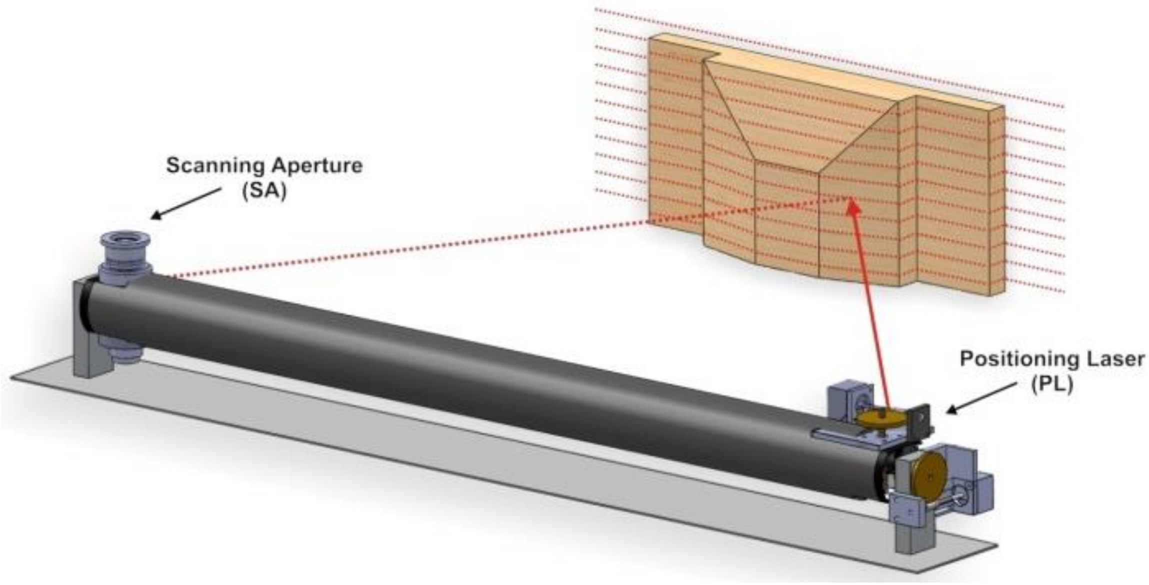

(a)

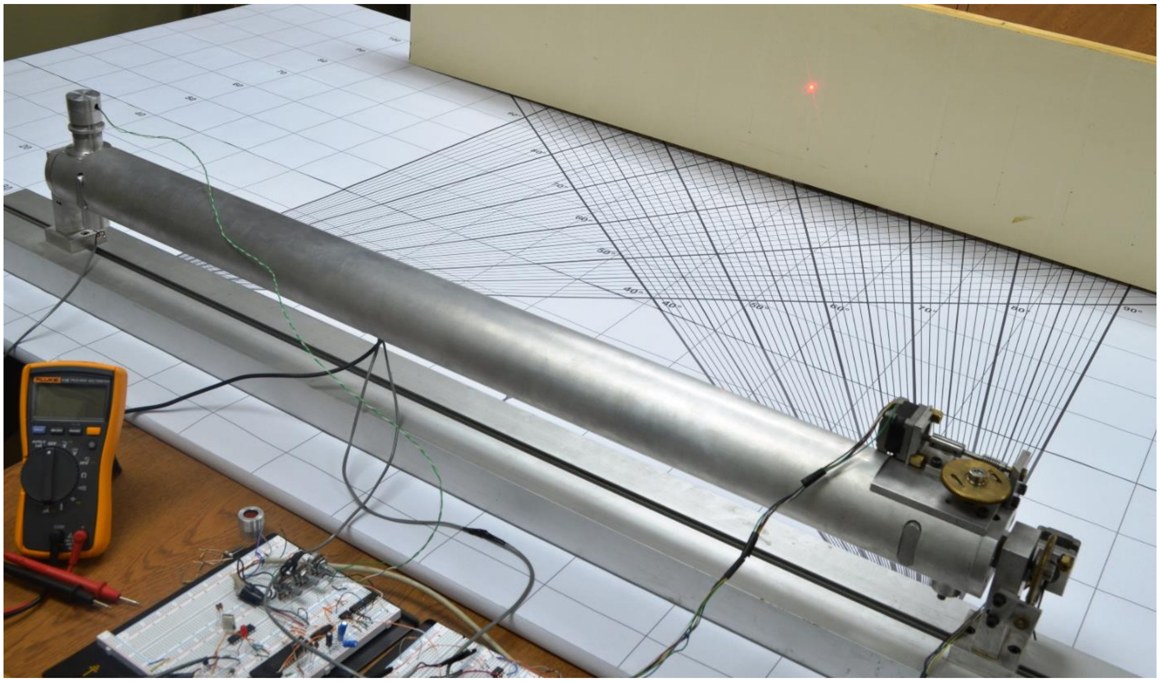

(b)

Figura 53. Prototipo II del sistema de barrido por laser. (a) Modelo 3D. (b) Fotografia en laboratorio.

Esta forma de rotación del sistema sobre su propio eje es mucho más eficiente en comparación con el sistema de motor/banda utilizado en el prototipo I (ver figura 52), debido a que permite la rotación del sistema de barrido utilizando un motor de pasos de menor torque, menor consumo de corriente y menor costo, por consecuencia reduciendo el consumo energético total del sistema. El bajo consumo de corriente es una ventaja muy importante debido a la intención de utilizar este sistema en aplicaciones móviles como la navegación de robots autónomos, donde la dependencia de la duración de la carga de baterías para energizar los sistemas es crítica.

Es importante mencionar que en el prototipo I no fue posible girar el sistema debido a que el motor de pasos ensamblado a la banda no poseía el torque necesario, ya que el centro de gravedad del sistema se encontraba fuera del mismo, mayormente debido a que el láser se encontraba instalado fuera de la barra de rotación en forma paralela a esta, provocando la necesidad de mayor o menor torque dependiendo de la inclinación del láser.

Comparando directamente los subsistemas de posicionamiento de láser, en el prototipo II únicamente se utilizó aluminio para fabricar sus componentes. Esto permitió una precisión superior en el maquinado y ensamble de los mismos, a diferencia de los componentes hechos de teflón en el prototipo I propensos al desgaste y deformación.

Por otra parte, la implementación de los engranes anti-juego aumentó la precisión del posicionamiento del láser en un 9,600%, de 200 pasos por revolución a 19,200; lo cual le dio la capacidad al sistema de medir ángulos con resolución de 0.01875°. Aunque este subsistema no posee un juego de engranes o una transmisión para variar el tamaño de cada paso o la resolución del sistema, mediante el software de control es posible doblar la resolución a 0.009375° a cambio de sacrificar velocidad en el posicionamiento del láser y por consecuencia en la velocidad de barrido del sistema.

Otras fuentes de incertidumbre detectadas en el prototipo I fueron las distancias entre los espejos y el láser, al reducir la distancia entre el láser y los dos espejos con corte de 45° en el prototipo II, se redujo el diámetro del haz de luz láser emitido por el subsistema de posicionamiento en un 50%. Esto se traduce en un incremento considerable en el rango de visión del sistema de barrido, aumentando el límite superior del rango de visión, de 1m (prototipo I) a 2.5m (prototipo II). Sin embargo por cuestiones de practicidad y dimensiones de la mesa de pruebas, en la experimentación realizada con el prototipo II, el sistema fue calibrado para detectar obstáculos en un rango de 0.4 – 1 m de distancia en el eje de coordenadas *Y*.

3.2. Subsistema de apertura de barrido

El principio físico de la apertura de barrido (presentado en la sección 1.3 del capítulo II), es mantenido del prototipo I al II, sin embargo se mejoraron algunos aspectos del diseño mecánico. La mejora o ventaja principal es el encapsulamiento de los componentes en forma de cartucho removible, instalado dentro del cilindro principal del sistema, con el fin de facilitar y agilizar la calibración de los componentes antes de realizar pruebas de medición. La forma de cartucho también permite intercambiar rápidamente entre aperturas con diferentes características como lentes más fuertes, un sensor de mayor velocidad de respuesta o un motor más estable, por mencionar algunas, con el fin de realizar experimentación en diferentes condiciones y aumentar los límites y capacidades del sistema de barrido. Cabe mencionar que este tipo de experimentación es pensada a futuro y está fuera de los límites de esta tesis, ya que al término de esta investigación, solo se ha fabricado una apertura de barrido.

Es importante mencionar que una de las características más importantes de las aperturas de barrido de ambos prototipos, es la alineación de los planos del sistema. Existen tres planos (ver figura 54), los cuales son generados de la siguiente manera:

- Plano A, generado por:
    - Vector formado por los centros de los espejos fijo y giratorio (posicionamiento de láser).
    - Punto de reflexión en el obstáculo detectado.
- Plano B, generado por:
    - Punto de reflexión en el obstáculo detectado.
    - Vector formado por el centro del espejo y el centro del fototransistor (apertura de barrido).
- Plano C, generado por:
    - Punto en el centro del espejo giratorio (posicionamiento de laser)
    - Punto de reflexión en el obstáculo detectado.

- Punto en el centro del espejo giratorio (apertura de barrido)

Para que la apertura de barrido sea capaz de ver la reflexión de los rayos del láser provenientes de la reflexión de un obstáculo, los planos A, B y C deben ser coincidentes en todo momento.

En el prototipo I la apertura de barrido se instalaba roscándola en un extremo de la barra principal del sistema (ver figura 52), lo cual cumplía la función de ensamblarla, sin embargo era complicado mantenerla en su lugar o encontrar la posición específica para alinear el plano de visión. La forma de cartucho en el prototipo II también resolvió este problema debido a que solo existe la opción de introducir la apertura en una sola posición, la cual fue previamente medida y calibrada durante la fabricación del sistema, eliminando efectivamente el problema de desalineación del plano de visión.

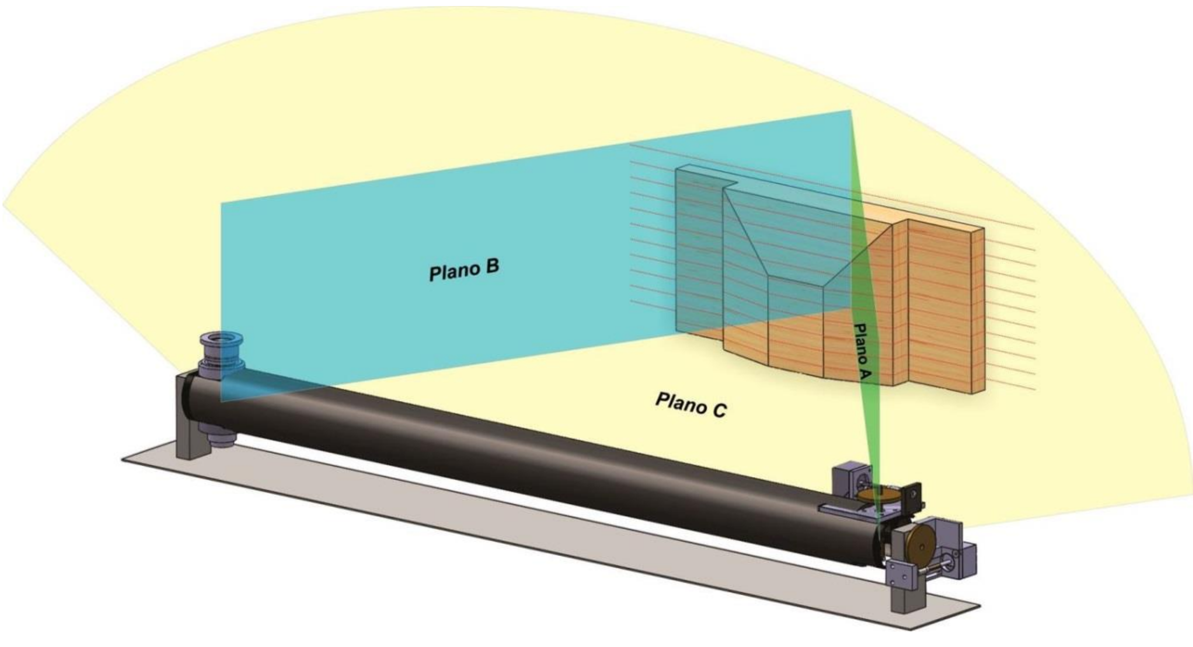

Figura 54. Planos A, B y C para alineación del sistema de barrido por láser.

CAPÍTULO IV. SIMULACIÓN DE LOS SISTEMAS DE BARRIDO POR LÁSER Y NAVEGACIÓN EN MATLAB®

En esta sección se presentan dos experimentos computacionales o simulaciones, una del sistema de navegación y otra del cálculo de coordenadas en 3D mediante triangulación dinámica, ambas con sus respectivos resultados. El software principal utilizado para las simulaciones es MATLAB® (R2012a), sin embargo también SolidWorks es utilizado.

1. MATLAB®, software para simular los sistemas de navegación y barrido por láser

Las simulaciones presentadas en esta investigación fueron realizadas con la ayuda del software MATLAB® de MathWorks®. Su nombre significa Laboratorio de Matrices (del inglés MATrix LABoratory).

MATLAB es un lenguaje de alto nivel y un ambiente interactivo para la computación numérica, visualización y programación. Utilizando MATLAB, es posible analizar datos, desarrollar algoritmos y crear modelos y aplicaciones. El lenguaje, las herramientas y las funciones matemáticas integradas, le permiten al usuario explorar múltiples acercamientos y alcanzar una solución más rápidamente que con hojas de datos o lenguajes de programación tradicional como C/C++ o Java™ [79].

Además de ser una herramienta de software matemático, también ofrece un entorno de desarrollo integrado (IDE), un lenguaje propio llamado "M", la creación de interfaces de usuario (GUI), comunicación con otros programas como C++ y LabVIEW, y comunicación con dispositivos de adquisición de datos como el NI DAQ USB y el microcontrolador Arduino.

Por último, MATLAB contiene integrada la herramienta Simulink®, la cual provee un ambiente de programación mediante diagrama de bloques para simulación multidominio y diseño en base a modelos matemáticos. Brinda soporte para simulación, generación automática de código, y pruebas y verificación continuas de sistemas embebidos.

Las características más utilizadas en las simulaciones de esta investigación fueron: la generación de funciones para facilitar la programación y la estructura de los programas principales, la capacidad de graficar conjuntos de datos provenientes del sistema de visión, herramientas estadísticas, herramientas para diseño y entrenamiento de redes neuronales, y la capacidad de interpretar código de MATLAB en programas de LabVIEW [80].

2. Simulación del cálculo de coordenadas en 3D mediante triangulación dinámica

Los objetivos principales de esta simulación son demostrar el método de triangulación dinámica y comprobar el resultado de las ecuaciones 2 – 5, presentadas en la sección 1.4 del capítulo II de esta tesis. Para lograr este objetivo, se diseñó en SolidWorks [81] un modelo en 3D del sistema de barrido por láser, incluyendo obstáculos y la meta. Ver figura 55.

En este modelo se trazaron líneas desde el subsistema de posicionamiento de láser hasta un obstáculo y de regreso a la apertura de barrido; estas líneas simulaban los rayos del láser del sistema y también la reflexión de dichos rayos hacia la apertura de barrido en un entorno ideal.

El modelo con los obstáculos y las líneas trazadas, permitió realizar mediciones precisas e ideales de los ángulos B_{ij}, C_{ij}, y $\Sigma_{\beta j}$, además de las distancias de los obstáculos hacia el sistema, distancia entre obstáculos, distancia hacia la meta, etc.

Los datos mencionados fueron almacenados en forma de matrices en un archivo de datos .mat en donde son importados por el programa en MATLAB para ser almacenados en forma de una matriz multidimensional 20x20x4, como se menciona en la sección 1.4 del capítulo II**.**

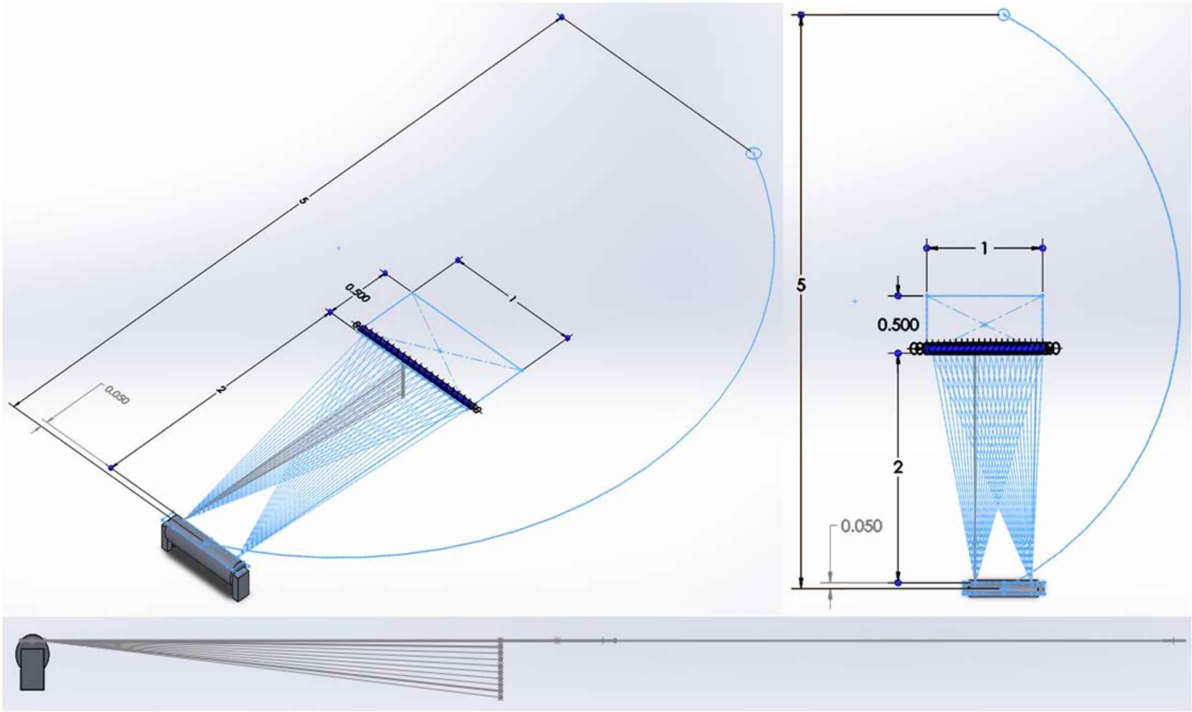

Figura 55. Vista superior, lateral e isométrica del modelo 3D del sistema de barrido por láser para simulación del cálculo de coordenadas en 3D.

Una vez almacenados los datos de esta manera, el programa crea otra matriz multidimensional de 20x20x3 llamada "res" para almacenar los resultados. En la primera dimensión se almacenan los resultados de las coordenadas X, en la segunda los resultados de Y, y en la tercera los de Z.

Después, utilizando dos ciclos FOR anidados, se recorren todas las posiciones *ij* de la primera dimensión de la matriz de 20x20 (mapa digital), después se verifica en cada posición *ij* si hubo detección de obstáculo; si la hubo, se procede a llamar a los valores C_{ij}, B_{ij}, $\Sigma_{\beta j}$, en sus correspondientes matrices para introducirlos en las ecuaciones (2 – 5) de cálculo de coordenadas X, Y, Z. Una vez calculadas, se almacenan en la matriz "res".

En la figura 56 se muestra un fragmento del código de esta simulación, el código completo se encuentra en el apéndice B.

Una vez terminado los cálculos, el programa grafica en 3D (ver figura 57) los resultados del cálculo de coordenadas. El análisis de estos resultados demuestra que las coordenadas calculadas X, Y, y Z de los obstáculos detectados, posición del sistema y meta, son correctas al compararlas con su valor real/virtual en el modelo 3D del sistema de barrido; por consiguiente validando el método de triangulación dinámica.

```matlab
clc
clear all

fprintf('\n         *** VISION SYSTEM CALCULATIONS *** \n');

load obs_input3;
fov = zeros(20,20,4);
fov(:,:,1) = digmap;
fov(:,:,2) = bangle;
fov(:,:,3) = cangle;
fov(:,:,4) = betasum;

a = .48;    % long barra
aj = 0;
res = zeros(20,20,3);

tcalc = tic;
for i = 1:size(fov,1)
    for j = 1:size(fov,2)
        if fov(i,j,1) == 1
            aj = aj + 1;
            res(i,j,1) = a*((sind(fov(i,j,2))*sind(fov(i,j,3))*cosd(fov(i,j,4)))/(sind(180-fov(i,j,2)-fov(i,j,3))));
            res(i,j,2) = a*((1/2)-((sind(fov(i,j,2))*cosd(fov(i,j,3)))/(sind(180-fov(i,j,2)-fov(i,j,3)))));
            res(i,j,3) = a*((sind(fov(i,j,2))*sind(fov(i,j,3))*sind(fov(i,j,4)))/(sind(180-fov(i,j,2)-fov(i,j,3))));
        end
    end
end
```

Figura 56. Fragmento del código de la simulación de cálculo de coordenadas 3D.

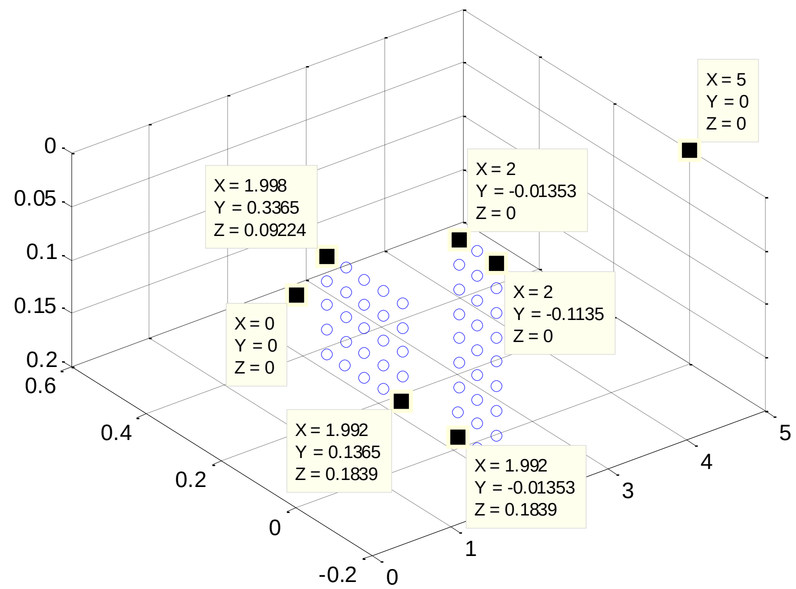

(a)

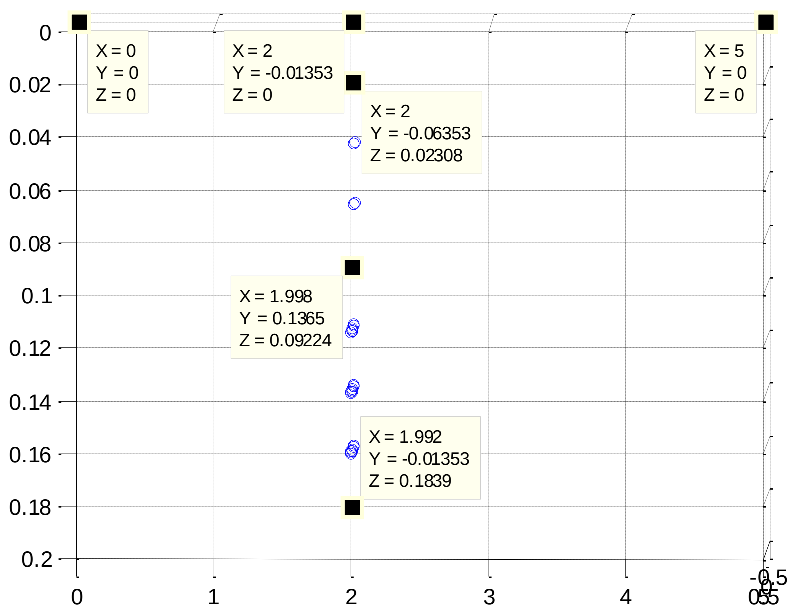

(b)

Figura 57. Gráficas de los resultados de cálculo de coordenadas 3D basadas en el modelo del sistema de barrido en SolidWorks. (a) Vista isométrica 3D. (b) Vista lateral derecha.

3. Simulación del sistema de navegación y datos de salida del sistema de barrido por láser

Esta simulación tiene como objetivos demostrar: la compatibilidad entre el sistema de navegación y el de barrido por láser, incluyendo el análisis, transformación y manipulación de datos de un sistema a otro; y la capacidad del programa para calcular una nueva trayectoria de navegación para el robot móvil en el menor tiempo y distancia posible.

3.1 Manipulación de datos, cálculo de coordenadas 3D y nueva trayectoria.

Como se menciona en la sección 1.4 del capítulo II, los datos provenientes del sistema de barrido por láser, son exportados en forma de una matriz multidimensional que se expresa de la siguiente manera: 20x20x4. El primer número indica la cantidad de renglones, el segundo la cantidad de columnas y el tercero indica el número de matrices (o dimensiones) ligadas que contiene. Cabe mencionar que los tamaños establecidos de las matrices (20x20), son solamente para pruebas en el laboratorio y es muy probable que aumenten en caso de aplicación real.

La matriz de la primera dimensión contiene un mapa digital del campo de visión del robot móvil; cada posición *ij* de la matriz puede tener un valor booleano de “0” o “1”, el “0” indica que no hubo reflexión detectada y el “1” indica que se detectó un obstáculo. La matriz de la segunda dimensión almacena los ángulos B_{ij} correspondientes a cada valor “1” que se encuentre en la matriz de la primera dimensión. El mismo comportamiento sucede con los valores almacenados en la tercera y cuarta dimensión, en la tercera se almacenan los valores del ángulo C_{ij} y en la cuarta los valores del ángulo $\Sigma_{\beta j}$. Ver figura 58.

La figura 58 muestra un ejemplo en el cual i=3 y j=3, por lo tanto, los ángulos necesarios en la triangulación dinámica para calcular las coordenadas del obstáculo son B_{ij} = 71° (ángulo de la apertura de barrido), C_{ij} = 58° (ángulo del láser) y $\Sigma_{\beta j}$ = 4° (ángulo de rotación en Z). Cabe mencionar que, como se explica en las secciones 3 y 4 del capítulo II, estos valores provienen de los sensores y son enviados a la computadora a través de los microcontroladores, interfaces de comunicación y el sistema de adquisición de datos.

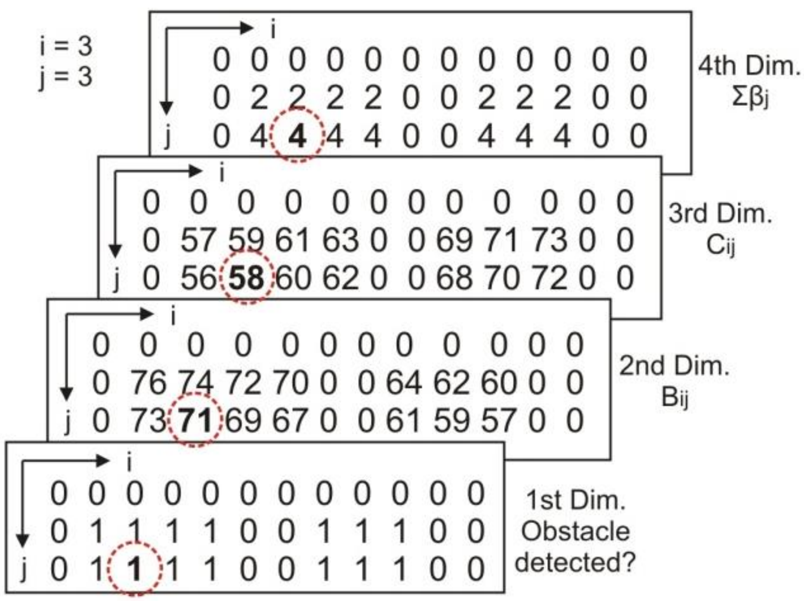

Figura 58. Matriz multidimensional de 20x20x4 para almacenamiento de resultados del sistema de medición de coordenadas mediante barrido por láser.

El programa desarrollado en MATLAB® para simular el sistema de navegación y el de barrido por láser, fue llamado BANS (Basaca Navigation System) o sistema de navegación Basaca, el cual está diseñado para calcular la trayectoria necesaria que el robot móvil debe recorrer para llegar a la meta programada; lo cual logra basándose en los datos provenientes del sistema de barrido por láser para evadir colisiones con obstáculos detectados y localizados, y al mismo tiempo evitar movimientos o giros bruscos en la dirección del robot.

El programa utilizado para calcular las coordenadas en 3D de obstáculos detectados en el campo de visión del robot móvil es el mismo que se presenta en la sección anterior. En la figura 56 se muestra un fragmento del código; para ver el programa completo consultar el apéndice B.

Este programa también calcula el tiempo transcurrido durante las diferentes etapas del sistema de navegación como lo son: el cálculo de coordenadas de los obstáculos detectados, el análisis de características de los obstáculos detectados, distancia entre obstáculos, cálculo de nueva trayectoria, entre otros. A continuación se muestra un fragmento de la salida de información desplegada en pantalla por BANS para pruebas y monitoreo del sistema de navegación; consultar el apéndice B para ver el resto.

```
              *** TVS CALCULATIONS ***

   --> Quantity of calculated distances: 156

   --> Quantity of calculated points: 52

             *** OBSTACLES CHARACTERISTICS ***

   --> Quantity of detected obstacles: 2

   --> Obstacle 1

        * Height (z): 0.2761 m

        * Wide (y): 0.2512 m

        * Depth (x): 0.0063 m

   --> Obstacle 2

        * Height (z): 0.1839 m

        * Wide (y): 0.1428 m

        * Depth (x): 0.0085 m

    *** NAVIGATION SYSTEM CALCULATION ***

--> Distance between detected obstacles (y): 0.1253 m

--> Distance between the robots reference frame and the left limit (y+): 0.3572 m

--> Distance between the robots reference frame and the right limit (y-): 0.1428 m

--> Shortest distance between the robot's reference frame and obstacle 1 (x): 1.9915 m

--> Shortest distance between the robot's reference frame and obstacle 2 (x): 1.9915 m

--> DECISION MAKING

        * What's the robots current position?

curloc =

     1     0     0     0
     0     1     0     0
     0     0     1     0
     0     0     0     1
    * How many obstacles were detected? 2

    * Does the robot fit between the obstacles? No

    * Avoid obstacle by left or right (shortest trajectory distance)?  Right

    * Therefore, the robot will avoid the obstacle by its right side.

    * Calculating new trajectory...
```

En esta simulación, después de que la nueva trayectoria es calculada, el programa utiliza las coordenadas calculadas anteriormente (X, Y, Z) para realizar una gráfica en 3D de los obstáculos detectados en el campo de visión, indicando en esta, la posición actual del robot móvil, la meta a alcanzar y la nueva trayectoria que el robot móvil debe seguir. De esta manera se puede observar en la gráfica, que la trayectoria calculada evita exitosamente los obstáculos detectados y llega a la meta.

El objetivo de estas gráficas es informativo y una ayuda visual útil para el usuario, sin embargo el robot móvil no las requiriere para la tarea de navegación y pueden ser omitidas en el programa final para ahorrar recursos y tiempo de procesamiento.

El siguiente código es parte del programa utilizado para calcular y graficar la nueva trayectoria desde la posición actual del robot hacia la meta, una vez que se ha detectado un obstáculo. Consultar apéndice B para ver el programa completo.

```
py2 = (limy + (mbwidth/2)) * 1.4;
ypr = linspace(py2,py3,9)';
y = [py' ypr']';
xpr = linspace(minx1,px3,9)';
x = [px' xpr']';
f = linspace(px, px3, 500);
g = spline(x,y,f);
g1 = (g + (mbwidth/2));
g2 = (g - (mbwidth/2));
plot(x,y,'*',x,y,':',f,g,'r-',f,g1,'bx',f,g2,'bx')
```

Para calcular la nueva trayectoria, primeramente es necesario conocer la posición actual del robot móvil y las coordenadas de la meta que se desea alcanzar. La información requerida es obtenida de la matriz de transformación homogénea; una vez obtenida, la nueva trayectoria es calculada y graficada como se explica en la sección 5.3 del capítulo II.

3.2 Resultados de la simulación del funcionamiento del sistema de navegación

El resultado de esta simulación es la obtención de una nueva trayectoria que lleva al robot móvil de manera segura desde su posición actual hasta la meta. La gráfica de este resultado se muestra en la figura 59.

Utilizando un conjunto de valores de entrada diferente (mismos obstáculos, pero en diferente posición) y realizando la simulación, se observa una diferencia en la gráfica de la nueva trayectoria calculada.

A diferencia de las gráficas en la figura 59; en la figura 60 se puede observar que los obstáculos son evadidos por el lado derecho del robot móvil. Demostrando de esta manera que el programa no solo busca una trayectoria que evite obstáculos y llegue a la meta, sino que también elige la trayectoria más corta.

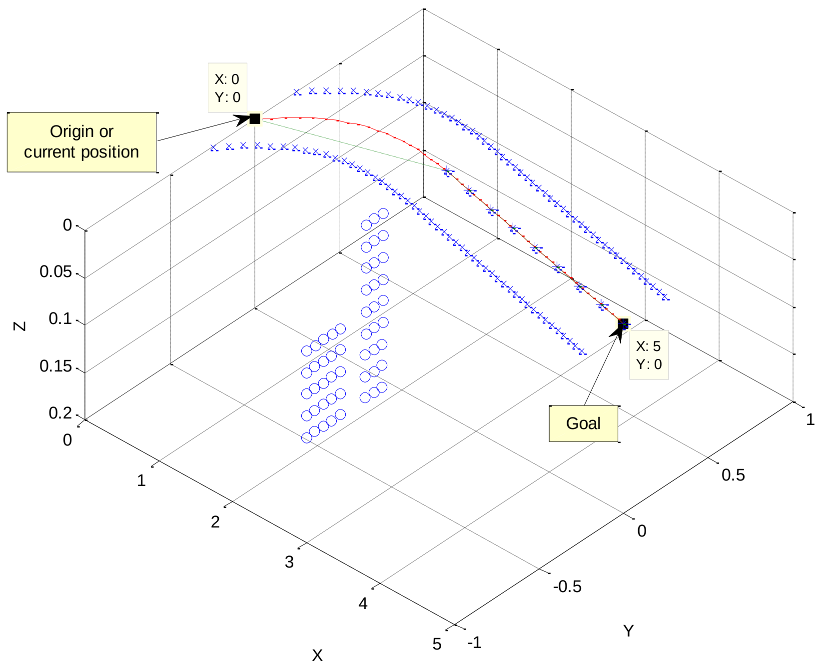

(a)

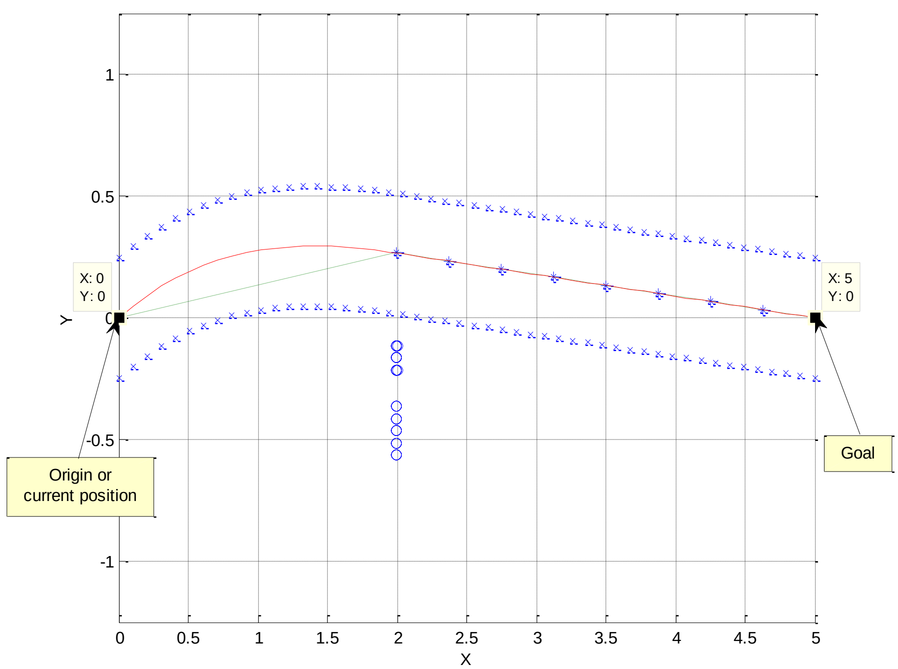

(b)

Figura 59. Trayectoria del robot móvil generada en una simulación de MATLAB® utilizando una curva en base a diez puntos (escala en metros). (a) Vista isométrica 3D. (b) Vista superior 2D.

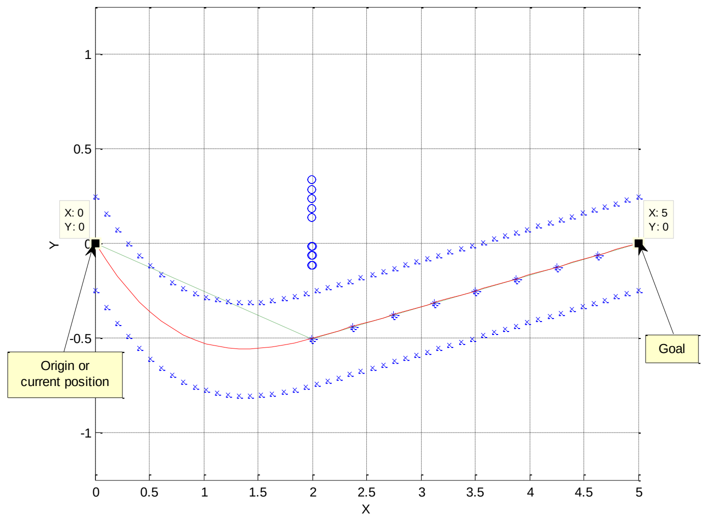

Figura 60. Vista superior (2D) de una trayectoria que evade obstáculos por el lado derecho del robot móvil.

Los diferentes algoritmos y operaciones calculadas durante la simulación fueron categorizados y monitoreados para obtener su tiempo promedio de ejecución. Para cada categoría de operaciones fueron medidas y promediadas treinta muestras de tiempo, con las cuales se generó la siguiente tabla de tiempos (tabla 5) y la figura 61.

OPERACIÓN	TIEMPO DE EJECUCIÓN (ms)	(%)
Cálculo de coordenadas en 3D	20.1590	20.5
Manipulación y acondicionamiento de datos de entrada	10.7818	10.9
Análisis de datos y obtención de características de obstáculos detectados	38.1835	38.7
Toma de decisiones (robot móvil)	10.3025	10.5
Cálculo de nueva trayectoria	6.8921	7.0
Operaciones de cinemática inversa	12.2402	12.4
Tiempo total	98.5592	100

Tabla 5. Distribución de tiempos de ejecución de las operaciones principales de los sistemas de barrido y navegación.

La tabla 5 muestra el promedio de tiempo de ejecución de las principales operaciones de los dos sistemas integrados como, el cálculo de coordenadas, el análisis de datos y obtención de características de obstáculos detectados, cálculo de nueva trayectoria, entre otras. La figura 61, refleja la relación en tiempo entre las diferentes etapas de la navegación del robot móvil. Gracias a este estudio de tiempos se detectaron las operaciones que requieren la mayor parte del tiempo de ejecución (por ejemplo, el análisis de datos y caracterización: 39%) y se calculó que el tiempo promedio de ejecución de la combinación de los dos sistemas es menor a 0.1 s.

Las características de la computadora utilizada para realizar los cálculos y simulaciones presentadas, son las siguientes:

- Procesador: Intel® Core™ i7 CPU Q720 @ 1.6 GHz
- Memoria RAM: DDR3 8 GB
- Sistema Operativo: Windows 7 64-bit

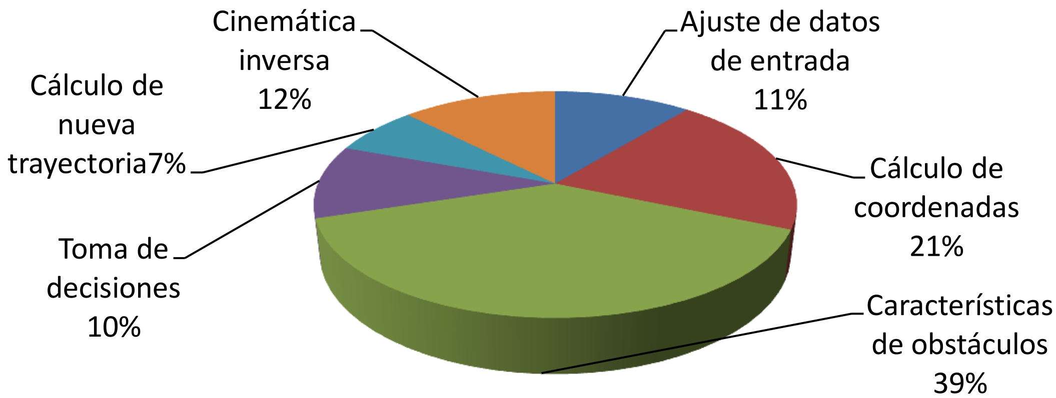

Figura 61. Gráfica de pastel de la distribución de tiempos entre las diferentes operaciones de los sistemas de barrido por láser y navegación.

CAPÍTULO V. RESULTADOS DE EXPERIMENTACIÓN Y ANÁLISIS ESTADÍSTICO DE LOS DATOS OBTENIDOS

1. Resultados experimentales del Prototipo I del Sistema de Barrido por Láser

Como es mencionado anteriormente, el prototipo I del sistema de barrido por láser fue construido y probado por colegas del mismo laboratorio de optoelectrónica. Los resultados presentados a continuación ya han sido publicados anteriormente en [82-85], y son mencionados en esta investigación únicamente como punto de referencia.

Las primeras pruebas realizadas con el prototipo I, consistieron de 16 mediciones en la mesa de pruebas. Los obstáculos utilizados fueron colocados en puntos conocidos para comparar los resultados obtenidos, los cuales se muestran en la tabla 6. Los resultados fueron en su mayor parte positivos, el error mínimo calculado fue de 0.07%; sin embargo hubo algunas excepciones en la parte más alejada del campo de visión, donde el error máximo calculado fue de 26% (ver figura 62).

En pruebas posteriores, se realizaron 50 mediciones con el prototipo I en diferentes coordenadas conocidas para verificar la precisión del sistema en 2D. Un fragmento de los resultados de las mediciones es presentado en la tabla 7. La tabla de resultados completa se encuentra en el apéndice C.

PUNTO DE PRUEBA	VALORES TEÓRICOS				VALORES MEDIDOS			
	X (m)	Y (m)	B (°)	C (°)	*x(m)*	*y(m)*	*B (°)*	*C (°)*
A	0.75	0.75	108.43	30.96	0.79	0.77	109.29	31.81
B	1	0.75	104.04	38.66	1.06	0.77	104.38	39.9
C	1	0.5	90.00	45.00	1.12	0.56	93.55	46.4
D	0.75	0.5	90.00	36.87	0.76	0.48	89.16	37.61
E	0.5	0.5	90.00	26.57	0.503	0.506	90.07	26.71
F	0.5	0.25	63.43	33.69	0.49	0.22	60.51	34.27
G	0.75	0.25	71.57	45.00	0.77	0.23	71.22	46.5
H	1	0.25	75.96	53.13	1.06	0.249	76.75	54.84
I	1	0	63.43	63.43	1.1	0.01	66.28	65.21
J	0.75	0	56.31	56.31	0.74	-0.01	55.34	56.77
K	0.5	0	45.00	45.00	0.49	-0.01	43.73	45
L	0.5	-0.25	33.69	63.43	0.52	-0.25	34.73	65.21
M	0.75	-0.25	45.00	71.57	0.81	-0.24	47.68	72.77
N	1	-0.25	53.13	75.96	1.11	-0.24	56.47	76.81
O	1	-0.5	45.00	90.00	1.26	-0.5	51.49	90.17
P	0.75	-0.5	36.87	90.00	0.8	-0.51	38.62	90.87

Tabla 6. Resultados de primeras pruebas de medición de coordenadas con el prototipo I.

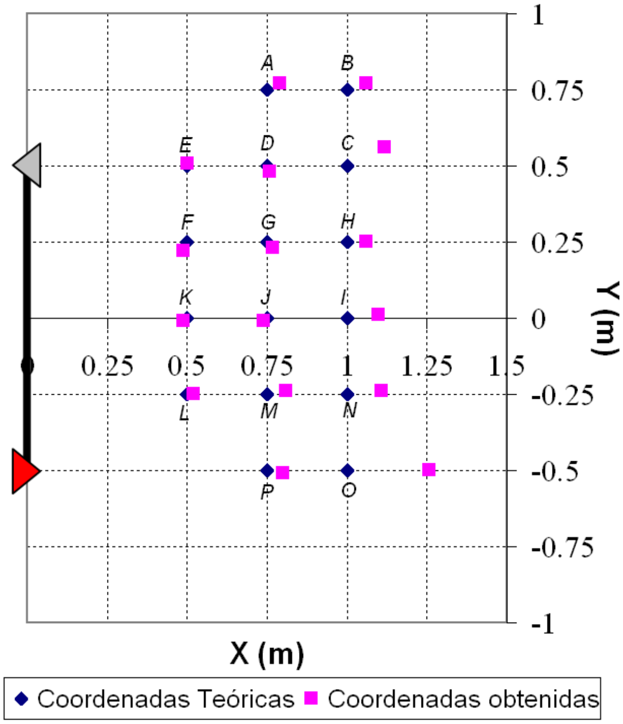

Figura 62. Gráfica de comparación de coordenadas teóricas y obtenidas con el prototipo I.

Punto de prueba	Valor teórico				Valor medido			
	X (m)	Y (m)	B (°)	C (°)	*x(m)*	*y(m)*	*B (°)*	*C (°)*
B	120	120	120,26	35,22	124,21	128,68	123,43	34,8
D	100	100	116,57	33,69	99,83	104,48	118,46	32,87
F	100	80	106,70	37,57	95,3	76,86	106,4	36,91
H	120	60	94,76	47,49	122,92	63,49	96,38	47,28
…	…	…	…	…	…	…	…	…
L1	80	-80	31,61	110,56	80,52	-80,21	31,81	110,56
N1	120	-80	42,71	104,04	121,01	-78,73	43,34	103,35
P1	100	-100	33,69	116,57	101,65	-96,18	35,06	114,43
R1	100	-120	30,47	124,99	111,73	-126,15	32,09	124,27

Tabla 7. Resultados de pruebas de medición en el campo de visión completo, prototipo I.

El análisis de los datos proporcionados por estas pruebas resultó en la división del campo de visión en tres zonas diferentes, donde cada zona indicaba un rango de precisión o nivel de confiabilidad distinto de las otras, desde 80 – 95%. Por conclusión, además de la precisión, este análisis estableció el campo de visión del prototipo I. Ver figura 63.

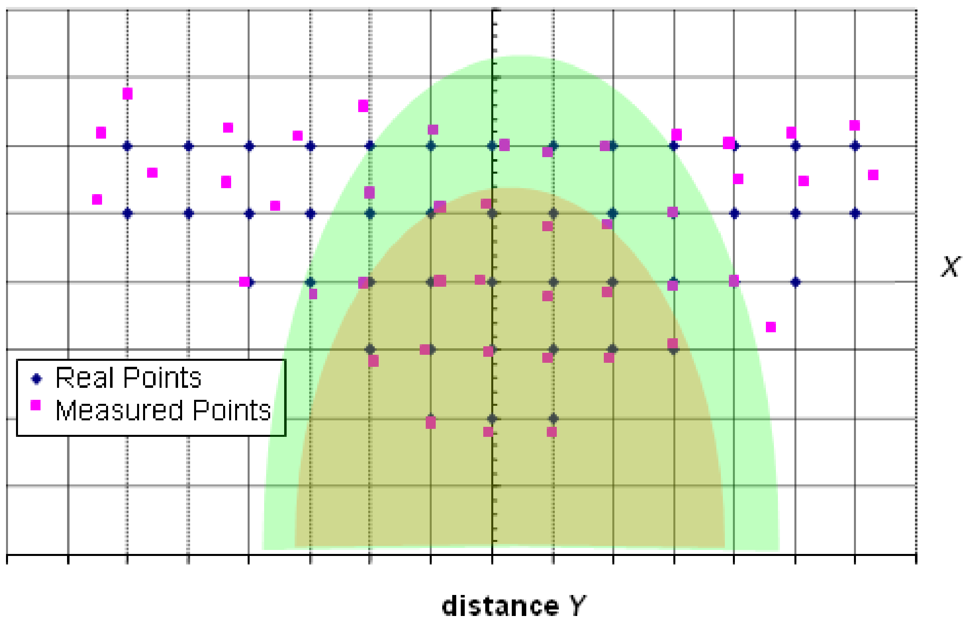

Figura 63. Gráfica de comparación de coordenadas reales, coordenadas medidas y zonas de precisión.

2. Resultados experimentales del Prototipo II del Sistema de Barrido por Láser

El objetivo principal de la experimentación realizada con el prototipo II es la comprobación de resultados de medición de coordenadas del sistema de barrido por láser. La experimentación fue realizada en el Laboratorio de Optoelectrónica y Mediciones del Instituto de Ingeniería de la UABC, donde se utilizó una mesa de pruebas plana y nivelada para soportar el sistema de barrido por láser y los obstáculos de prueba. Ver figura 65.

2.1 Lineamientos y explicación de las pruebas realizadas

Las pruebas consistieron en la colocación de diversos obstáculos estáticos en coordenadas conocidas, para posteriormente realizar barridos y calcular las coordenadas de los obstáculos detectados, el resultado es una tabla de comparaciones entre coordenadas medidas manualmente y las calculadas por el sistema de barrido. Es importante mencionar que estas pruebas se realizaron en 2D para probar el nuevo prototipo en su forma más simple y demostrar su capacidad de medición en etapas.

Para facilitar la medición de coordenadas reales de los obstáculos colocados en la mesa de pruebas y como ayuda visual; se diseñó una plantilla a escala para la mesa de pruebas (ver figura 64) que contiene una cuadricula graduada en unidades de longitud y grados, además de indicar la posición correcta del sistema de barrido sobre la mesa de pruebas.

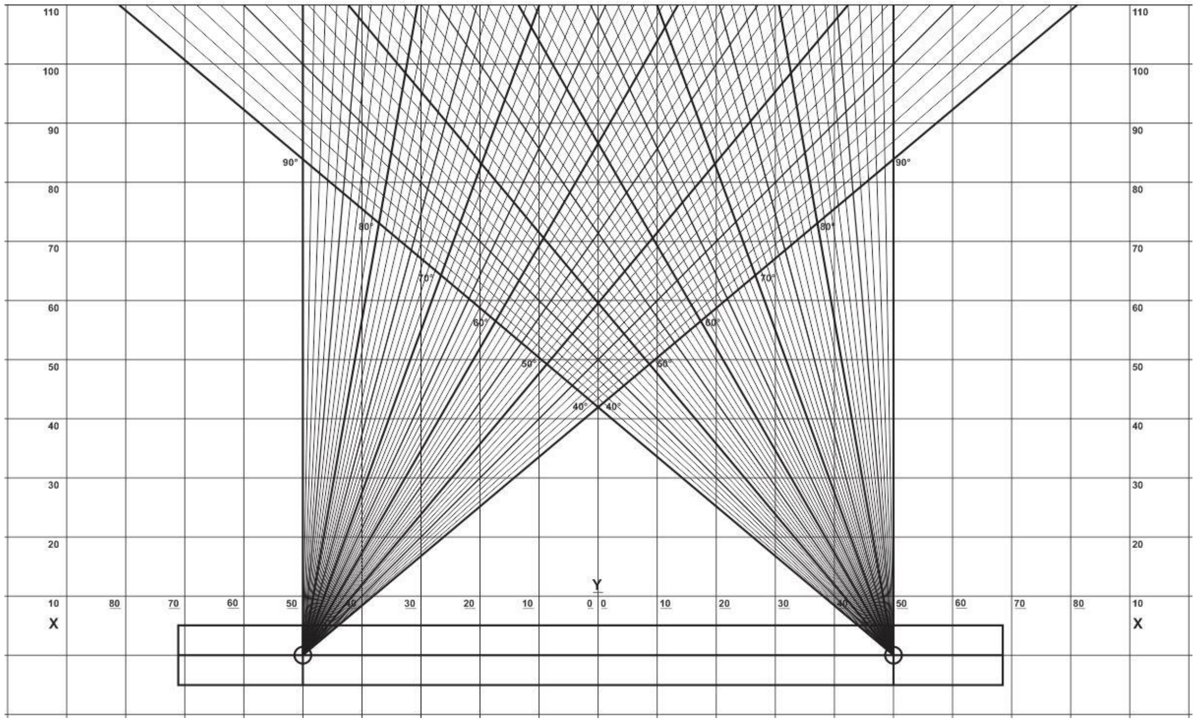

Figura 64. Plantilla de la mesa de pruebas para rápida colocación y medición de obstáculos de prueba.

Sin embargo, basándose en los resultados de las simulaciones presentados en el capítulo IV, está comprobado que el método de triangulación dinámica funciona para calcular coordenadas en 3D; no obstante, las pruebas en 3D con el prototipo II están programadas para realizarse en un futuro a corto plazo.

Las pruebas realizadas demostraron que el prototipo II posee un mayor nivel de confiabilidad en sus mediciones que su predecesor. De acuerdo a publicaciones anteriores [59, 83-84] y como se menciona en la sección 1 de este capítulo, el primer prototipo poseía un nivel de confiabilidad entre 80 – 95% (dependiendo de la zona dentro del campo de visión, ver figura 63), en el cálculo de coordenadas en 2D.

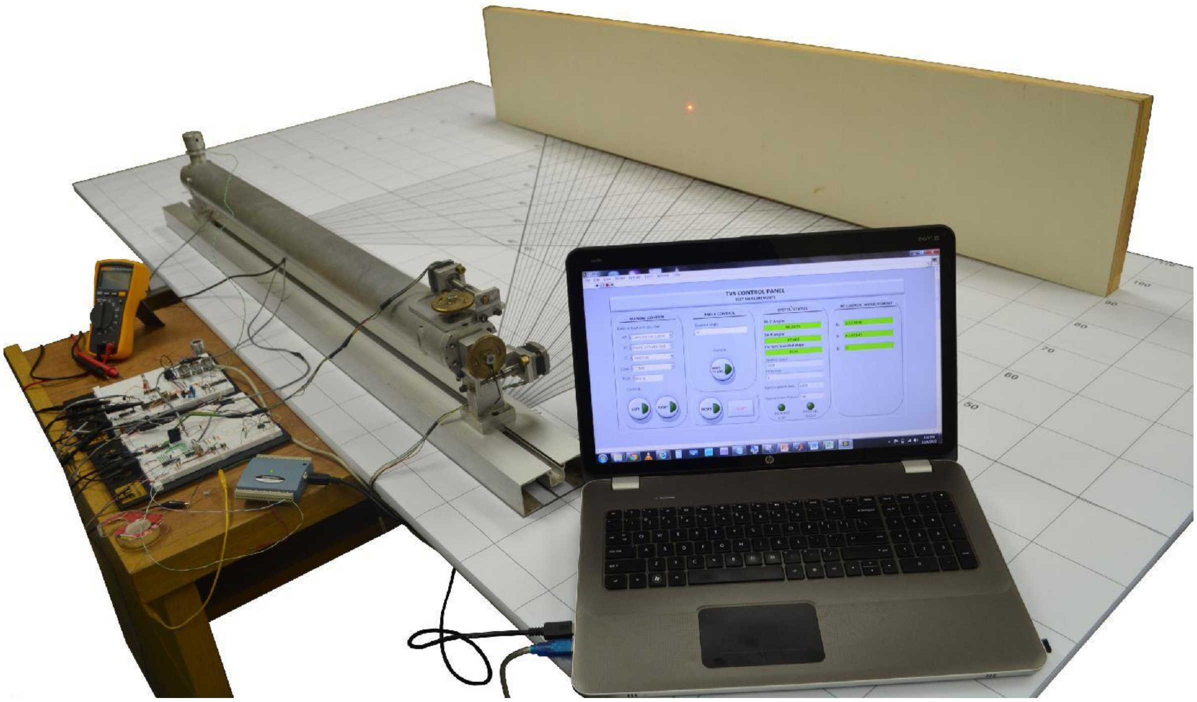

Figura 65. Sistema de Barrido por Laser en funcionamiento.

Los primeros resultados obtenidos con el prototipo II mostraron un nivel de confiabilidad muy amplio en el cálculo de coordenadas, entre 85 – 98%, sin ningún tipo de manipulación de datos. Este incremento en comparación el prototipo anterior es mayormente debido a las mejoras en el diseño mecánico explicadas en el capítulo III y en [59, 82]. En la figura 65 se muestra el sistema de barrido por láser en funcionamiento.

2.2 Aumento de nivel de confiabilidad de las coordenadas medidas mediante la aplicación de una red neuronal

Con el objetivo de mejorar y estabilizar el nivel de confiabilidad de los resultados del prototipo II, se desarrolló una red neuronal utilizando el método de Levenberg-Marquardt [86]. Este método es utilizado principalmente para resolver problemas de ajuste de curvas por mínimos cuadrados, es decir, dados un conjunto de pares de datos empíricos *m* de variables independientes y dependientes (x_i, y_i), optimiza los parámetros del modelo de curva $f(x, \beta)$ para que la suma de los cuadrados de las desviaciones sea mínima [87-88]:

$$S(\beta) = \sum_{i=1}^{m} [y_i - f(x_i, \beta)]^2 \tag{15}$$

Sin embargo, el algoritmo de Levenberg presentaba algunas desventajas [89] y Marquardt contribuyó en la solución del problema, lo cual resultó en el algoritmo conocido como Levenberg-Marquardt, el cual ha sido aplicado a la red neuronal del sistema de barrido por láser [87, 75 ,90-91].

$$\left(J^T J + \lambda diag\left(J^T J\right)\right)\delta = J^T [y - f(\beta)] \tag{16}$$

La red neuronal fue entrenada en MATLAB® [92] con los datos directos del sistema de barrido y el resultado fue un incremento en el nivel de confiabilidad promedio del 5.44% en mediciones de X y 3.61% en Y. En conclusión, la red neuronal corrigió efectivamente los errores en los cálculos de coordenadas X, Y, minimizando el error promedio a 1.94% [75].

En la figura 66 se muestra un diagrama en MATLAB® de la red neuronal diseñada y aplicada; sus principales características son: 1 entrada, 1 salida y 4 capas.

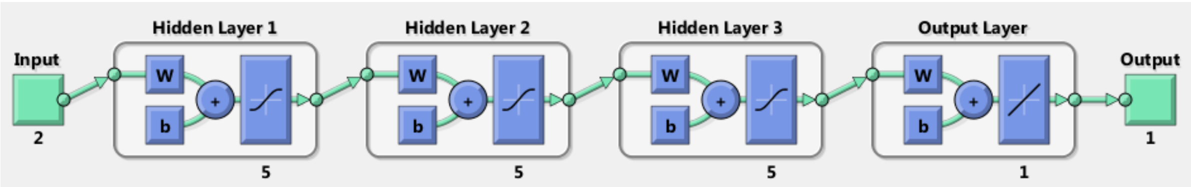

Figura 66. Diagrama en MATLAB de la red neuronal diseñada para corregir coordenadas.

Después de comprobar el incremento de precisión de los resultados a través de la red neuronal, esta fue integrada al programa desarrollado en LabVIEW que controla el sistema de barrido por láser, con el fin de corregir el error en el cálculo del ángulo B_{ij} en tiempo real, lo cual produjo el mismo resultado positivo que en la etapa de pruebas donde la red neuronal era aplicada después de obtener los resultados de medición de coordenadas.

2.3 Presentación y análisis estadístico de resultados

En la tabla 8 se muestra un resumen y comparación de los resultados de experimentación obtenidos en mediciones de coordenadas con el prototipo II antes y después de integrar la red neuronal.

Nivel de confiabilidad promedio de las coordenadas calculadas (%)	x	93.14% (sin red neuronal)	80.13% (min.) 98.74% (máx.)
	y	95.25% (sin red neuronal)	80.95% (min.) 99.58% (máx.)
Nivel de confiabilidad promedio de las coordenadas corregidas con la red neuronal (%)	x	98.58% (incremento de +5.44%)	91.31% (min.) 99.96% (máx.)
	y	98.88% (incremento de +3.63%)	89.95% (min.) 99.99% (máx.)
Error promedio calculado	ΔB (grados)	3.9466	n/a
	Δx (m)	0.0686	n/a
	Δy (m)	-0.0592	n/a
Error promedio corregido	ΔB (grados)	0.2998	≈ 3.65 error reducido
	Δx (m)	0.0095	≈ 0.059 error reducido
	Δy (m)	-0.0146	≈ 0.045 error reducido

Tabla 8. Comparación de los resultados de experimentación obtenidos en mediciones de coordenadas con el prototipo II antes y después de integrar la red neuronal.

En la tabla 9 y tabla 10, se muestran un fragmento de los resultados de experimentación obtenidos con el prototipo II utilizados para generar el resumen mostrado en la tabla 8. Los datos incluyen ángulos y coordenadas reales medidos, ángulos y coordenadas calculados y corregidos.

Valores reales (grados, m)				Ángulos medidos (grados)		Coordenadas calculadas (m)		Errores calculados		
Ángulo C	**Ángulo B**	**X**	**Y**	**Ángulo C**	**Ángulo B**	**X**	**Y**	**ΔB (grados)**	**ΔX (m)**	**ΔY (m)**
64.7	62.3	1.0	-0.027	64.9687	67.5996	1.1375	-0.0312	5.2996	0.13746	-0.0042
62.6	64.25	1.0	-0.016	62.9625	67.1964	1.0744	-0.0483	2.9464	0.0744	-0.0323
61.3	65.5	1.0	-0.046	61.9687	68.9497	1.0902	-0.0804	3.4497	0.0902	-0.0344
59.7	67.3	1.0	-0.0850	59.9625	73.4938	1.1434	-0.1612	6.1938	0.1434	-0.0762
…	…	…	…	…	…	…	…	…	…	…
50	40.8	0.5	0.078	49.9312	45.3699	0.5470	0.0399	4.5699	0.0470	-0.0381
46.8	43.6	0.5	0.026	46.9500	45.7943	0.5244	0.0101	2.1943	0.0244	-0.0159
45	45.2	0.5	-0.002	44.9438	46.4971	0.5126	-0.0136	1.2971	0.0126	-0.0116
43	47.3	0.5	-0.038	42.9562	49.0435	0.5149	-0.0531	1.7435	0.0149	-0.0151

Tabla 9. Fragmento de resultados de cálculo de ángulos y coordenadas con el prototipo II (sin red neuronal).

Después de corregir los resultados de las mediciones del prototipo II utilizando la red neuronal entrenada con el método Levenberg-Marquardt, los resultados demostraron un comportamiento diferente en comparación a los del prototipo I.

Como se menciona en la sección 1 de este capítulo, el prototipo I presentaba zonas de medición notables donde presentaba mayor o menor precisión dependiendo de la posición dentro del campo de visión donde se encontrara el obstáculo en medición.

Valores reales (grados, m)				**Ángulos medidos (grados)**		**Ángulos corregidos y nuevas coordenadas calculadas**			**Nuevo error calculado**		
Ángulo C	**Ángulo B**	**X**	**Y**	**Ángulo C**	**Ángulo B**	**Ángulo B**	**X**	**Y**	**ΔB (grados)**	**ΔX (m)**	**ΔY (m)**
64.7	62.3	1.0	-0.027	64.9687	67.5996	62.6312	1.0156	0.0257	0.3312	0.0156	0.0527
62.6	64.25	1.0	-0.016	62.9625	67.1964	64.3507	1.0096	-0.0152	0.1007	0.0096	0.0008
61.3	65.5	1.0	-0.046	61.9687	68.9497	65.4971	1.0119	-0.0388	-0.0029	0.0119	0.0072
59.7	67.3	1.0	-0.0850	59.9625	73.4938	68.5265	1.0292	-0.0951	1.2265	0.0292	-0.0101
…	…	…	…	…	…	…	…	…	…	…	…
50	40.8	0.5	0.078	49.9312	45.3699	41.8864	0.5112	0.0700	1.0864	0.0112	-0.0080
46.8	43.6	0.5	0.026	46.9500	45.7943	42.8568	0.4970	0.0357	-0.7432	-0.0030	0.0097
45	45.2	0.5	-0.002	44.9438	46.4971	43.9339	0.4902	0.0088	-1.2661	-0.0098	0.0108
43	47.3	0.5	-0.038	42.9562	49.0435	46.9810	0.4982	-0.0351	-0.3190	-0.0018	0.0029

Tabla 10. Fragmento de resultados de corrección de ángulos y coordenadas con el prototipo II (red neuronal).

Analizando los resultados del prototipo II en vez de encontrar un comportamiento similar, el sistema mostro un error sistemático en la mayor parte del campo de visión, efectivamente estableciendo una sola zona de medición con un nivel de confiabilidad o precisión del 95 – 99 % para ambas coordenadas X, Y.

Esto puede ser observado en la figura 67 y en la figura 68, mientras que el error de las coordenadas medidas varía de acuerdo a la distancia y ángulo hacia el centro del sistema de barrido (x=0, y=0), el error en las coordenadas corregidas se mantiene bajo (tiende a 0 cm) y constante.

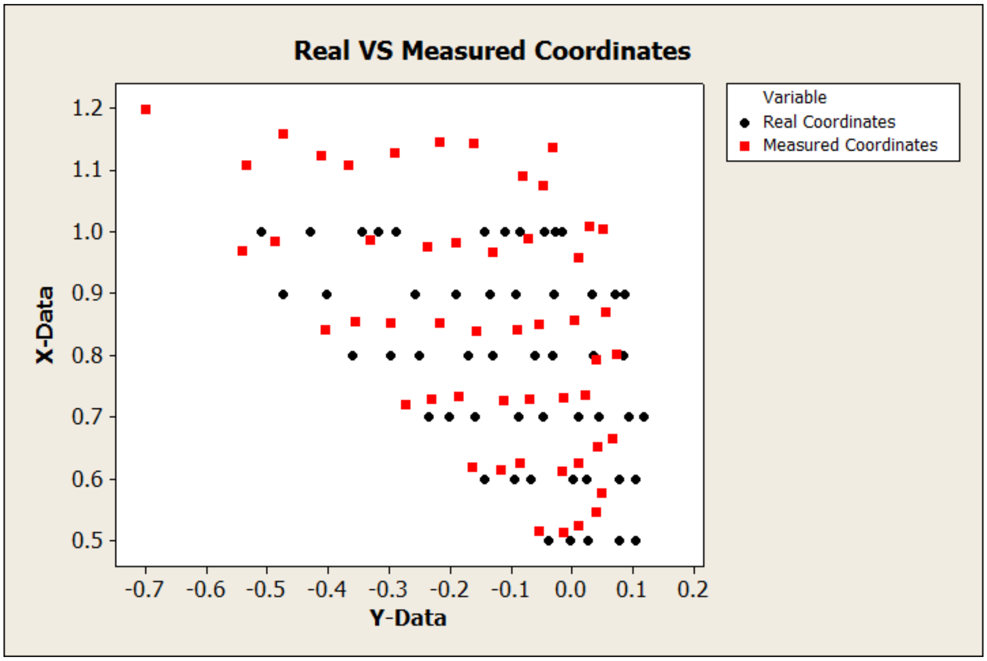

Figura 67. Gráfica de comparación entre las coordenadas reales y medidas obtenidas de pruebas con el prototipo II (escala en m). El error es mayor en cada punto medido.

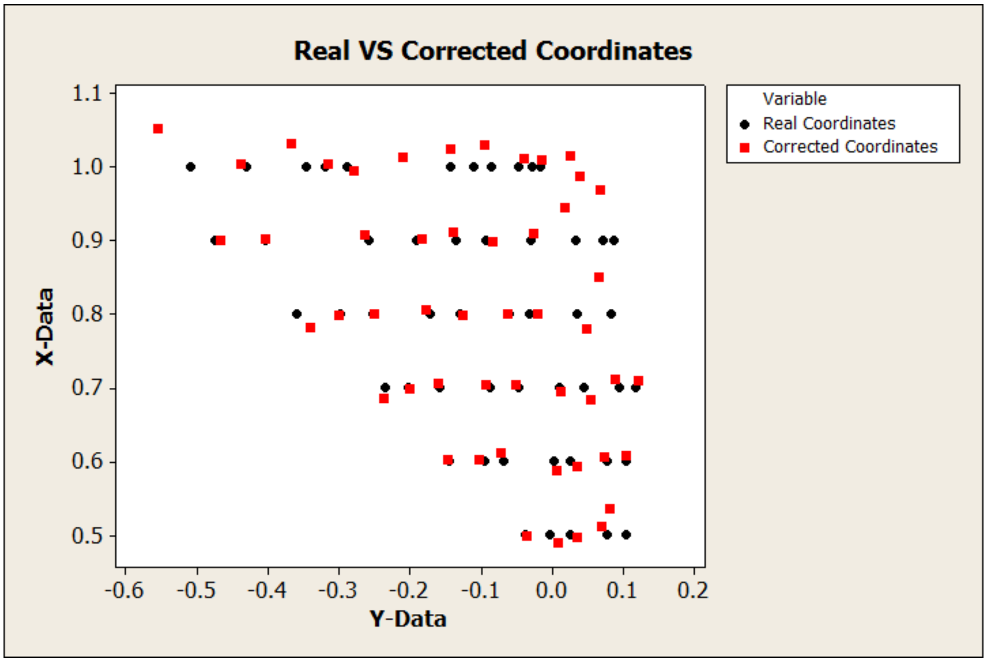

Figura 68. Gráfica de comparación entre las coordenadas reales y corregidas obtenidas de pruebas con el prototipo II (escala en m). El error es menor en cada punto corregido.

Utilizando los datos experimentales del prototipo II, fueron generadas gráficas de probabilidad de los errores de las coordenadas calculadas y corregidas. En dichas gráficas (ver figura 69) es posible observar que el error es constante o tiene a 0 cm en la mayor parte del campo de visión del sistema, sin embargo puede llegar a variar entre 1 – 1.5 cm en los extremos del campo de visión.

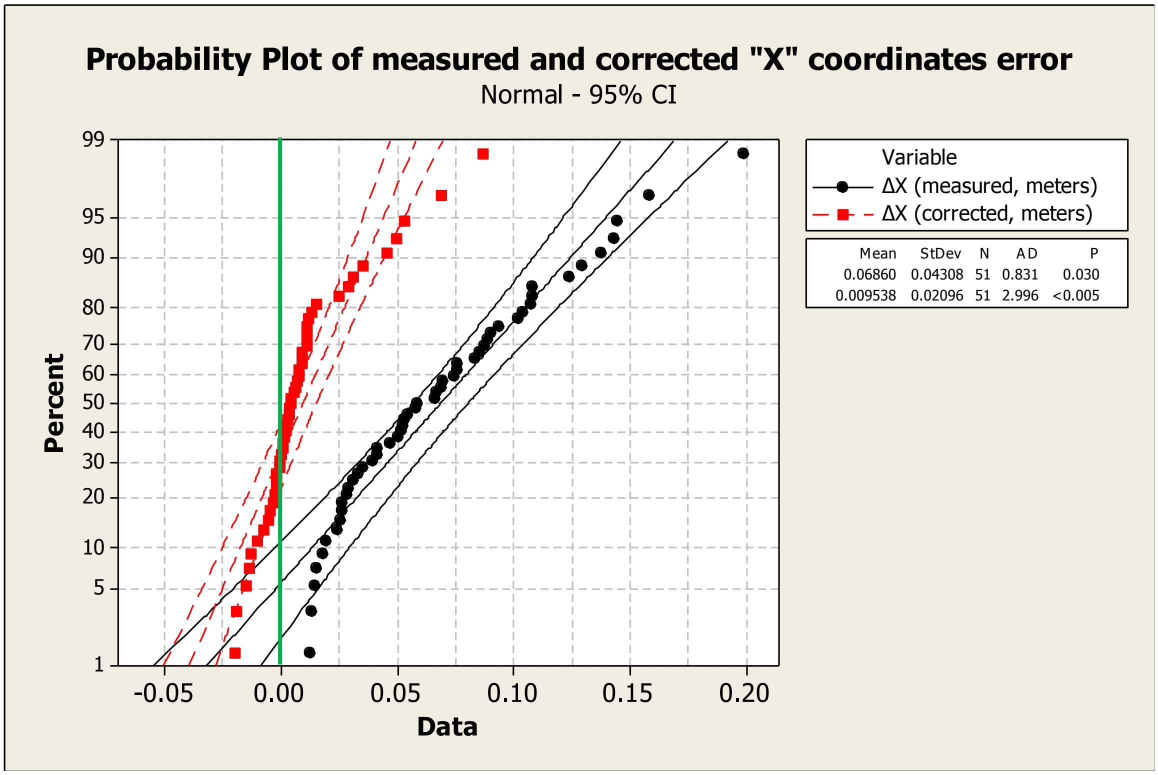

(a)

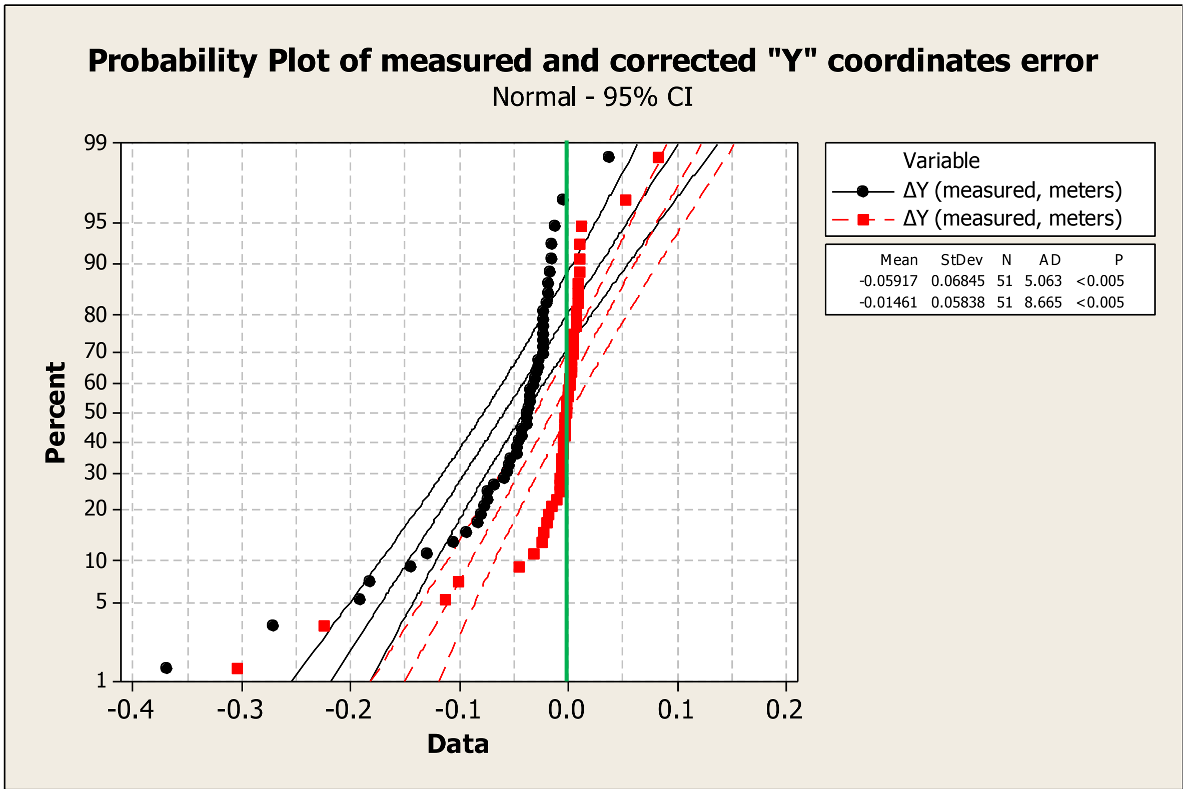

(b)

Figura 69. Comparación de gráficas de probabilidad del error de las coordenadas calculadas y corregidas. (a) El error en X tiende a 0 m. (b) El error en Y tiende a 0 m.

CAPÍTULO VI. CONCLUSIONES

1. Conclusiones

Esta investigación se enfocó en el diseño, desarrollo, construcción e integración de dos sistemas, barrido por láser y navegación. Partiendo del análisis de los resultados de simulaciones y experimentos presentados en esta tesis, se concluye lo siguiente:

- Se desarrolló un método novedoso llamado triangulación dinámica que mediante formalismo matemático basado en la ley de senos y las leyes de reflexión de la luz, permite realizar el cálculo de coordenadas en 3D de un campo de visión perteneciente al sistema de barrido por láser.
- Por primera vez el método de triangulación dinámica fue simulado en Matlab basado en una escena digital con dimensiones y coordenadas conocidas; el resultado de esta simulación fue la comprobación teórica del formalismo matemático del método.
- Una vez comprobado el método de triangulación dinámica, se diseñó y fabricó un sistema mecatrónico de alta precisión llamado sistema de barrido por láser. Este sistema conformado por una serie de sensores, actuadores eléctricos y componentes optoelectrónicos, realizan la operación de barrido y aplican el

método de triangulación dinámica para calcular coordenadas en 3D de objetos u obstáculos dentro de su campo de visión con una precisión promedio del 94%.

- Se desarrolló una interface de control y adquisición de datos en LabVIEW que permite controlar el sistema de barrido por láser.
    - Este programa controla de manera manual y automática todos los aspectos del sistema de barrido incluyendo los actuadores, lo que permite su posicionamiento en cualquier ángulo deseado o realizar una secuencia de movimientos llamado barrido por láser.
    - De igual manera, este programa monitorea las señales provenientes de los sensores del sistema para su procesamiento y posteriormente calcular las coordenadas de objetos dentro del campo de visión.
    - Todos los resultados de mediciones presentados en esta investigación fueron recopilados utilizando este programa como herramienta de medición de coordenadas y detección de obstáculos.
- Una red neuronal fue desarrollada y entrenada aplicando el método de Levenberg-Marquardt mediante Matlab; este método sobresalió entre otros como Polak-Ribière y quasi-Newton debido a que mostró mayor capacidad en la predicción de errores [87]. La aplicación de la red neuronal y Levenberg-Marquardt dentro de la interface de control de LabVIEW permitió corregir en tiempo real los resultados de las mediciones de coordenadas del sistema de barrido por láser, incrementando su nivel de confiabilidad o precisión a un total de 98.5% promedio.

- El sistema de navegación BANS es un programa novedoso diseñado para trabajar con los datos provenientes del sistema de barrido por láser y el robot móvil PIONEER 3-AT. BANS recibe y manipula dichos datos y utiliza un formalismo matemático para calcular la trayectoria óptima de la posición actual del robot móvil hacia su meta programada, evitando toda posible colisión y generando las señales de control correspondientes para los actuadores del robot móvil.
- Los resultados mencionados en los puntos anteriores (obtenidos de la experimentación con el sistema de barrido por láser y el sistema de navegación), confirman y demuestran verdadera la hipótesis planteada al inicio de la investigación.
- Dado que la hipótesis se ha comprobado verdadera, es correcto establecer lo siguiente:
  - El sistema de barrido por láser es capaz de crear un mapa digital y calcular las coordenadas 3D de obstáculos dentro de su campo de visión,
  - El sistema de navegación, mediante el análisis de los datos de salida del sistema de barrido por láser, calcula las trayectorias óptimas necesarias para que el robot móvil pueda navegar en terrenos desconocidos de manera segura hasta llegar a su objetivo.

2. Futuras líneas de investigación y oportunidades de mejora

Es posible mejorar el sistema de barrido por láser en diferentes áreas, ya sea aumentar su nivel de confiabilidad, agregándole nuevas funciones, entre otras.

A continuación se muestra una lista de acercamientos o temas de investigación a futuro relacionados directamente con el sistema de barrido por láser y el sistema de navegación presentados:

- Mejorar la alineación de los componentes mecánicos.
  - Esto se puede realizar mediante la fabricación de otro prototipo (ya sea otra copia del prototipo II o un prototipo nuevo), con un mayor estándar de calidad en la fabricación y ensamble de sus componentes.
- Utilizar otro tipo de fuente de emisión o láser.
  - Un láser de mayor potencia, con un haz de luz de menor diámetro y en modo de laser pulsado.
- Aumentar la velocidad de barrido del sistema:
  - Cambiando los motores de pasos por servo motores o motores de corriente directa de alta velocidad con codificadores para retroalimentación de su posición angular.
  - Eliminar cualquier tipo de motor o componentes móviles y explorar la opción de utilización de una cámara como un sistema de visión de alta velocidad.

    - Utilizar una proyección en forma de maya o rejilla de luz láser y múltiples sensores para detección de obstáculos de manera simultánea.
- Adquirir o fabricar un robot móvil para implementar los sistemas.
    - De preferencia el Pioneer 3-AT *mobile robot research platform,* en el cual está basado el sistema de navegación presentado en esta investigación.
- Diseño y fabricación del prototipo III cuyas características principales serían el aumento de velocidad de barrido mediante la implementación de servomotores y la disminución de sus dimensiones con el objetivo de implementarse físicamente en un robot móvil.
- Diseño del sistema de control para el robot móvil adquirido, basado en la información proveniente del sistema de barrido por láser.
    - Realizar pruebas de navegación con distintos algoritmos de cálculo de trayectoria y hacer comparaciones.

3. Reflexión personal

La realización de esta investigación durante los últimos cuatro años y la redacción de esta tesis han sido un gran desafío y un reto tanto personal como profesional. Al ver este documento terminado pienso en todos los sacrificios que he realizado durante los últimos meses y años, como el no dedicarle el tiempo habitual a mi esposa y a mis padres, no poder asistir a reuniones familiares para aprovechar los fines de semana, noches de desvelo, entre otras. El escribir esta tesis implicó cambiar mis hábitos de trabajo y por algún tiempo mi estilo de vida, acciones que para mí no fueron nada fáciles. Sin embargo en este momento, puedo decir que todo ha valido la pena y que esta experiencia me ha ayudado en mi crecimiento personal y profesional de una manera increíble y me ha dejado mucho más en comparación a lo invertido.

La presentación de esta tesis me deja muchas enseñanzas y una enorme satisfacción como persona e investigador, ya que para mí no solo demuestra el fin de una etapa que fue mi preparación predoctoral, más importante que eso, marca el inicio de mi carrera como doctor en el ámbito académico y de investigación; y puedo decir con seguridad que aún me queda un camino muy largo por delante respecto a la investigación y generación de nuevos conocimientos.

Respecto al tema de esta tesis, los sistemas de visión y navegación autónoma poseen una gran gama de aplicaciones con impacto directo en la sociedad y en la vida cotidiana, desde la exploración de otros planetas y lugares peligrosos para el hombre, hasta el poder subir a nuestro propio automóvil e indicarle que nos lleve directamente a casa, de manera segura y sin preocupaciones. Estas aplicaciones que antes se veían como temas del futuro, cada vez se encuentran más cerca de ser posibles gracias a las investigaciones realizadas en este ámbito. Por lo tanto, me brinda alegría y orgullo el poder ser parte de un grupo de investigadores mexicanos que aporta nuevo conocimiento para acercarnos más a este tipo de aplicaciones que alguna vez fueron consideradas como imposibles o extremadamente complejas.

LISTA DE ARTÍCULOS, PONENCIAS Y OTROS DOCUMENTOS CIENTÍFICOS PUBLICADOS DURANTE EL PERIODO 2009 – 2013

Revistas con factor de impacto:

- Artículo publicado en la revista “Optics and Lasers in Engineering” (factor de impacto 1.916) de la editorial internacional Elsevier. Título: “Optical 3D laser measurement system for navigation of autonomous mobile robot”. Agosto 2013. En imprenta. Publicado en línea http://dx.doi.org/10.1016/j.optlaseng.2013.08.005.
- Artículo publicado en la revista “Optics and Lasers in Engineering” (factor de impacto 1.916) de la editorial internacional Elsevier. Título: “Optical Monitoring of Scoliosis by 3D Medical Laser Scanner”. Agosto 2013. En imprenta. Publicado en línea http://dx.doi.org/10.1016/j.optlaseng.2013.07.026.
- Artículo publicado en la revista “Optics and Lasers in Engineering” (factor de impacto 1.916) de la editorial internacional Elsevier. Título: “Optimization of 3D laser scanning speed by use of combined variable step”. Agosto 2013. En imprenta. Publicado en línea http://dx.doi.org/10.1016/j.optlaseng.2013.08.011.
- Artículo publicado en la revista “Signal Processing” (factor de impacto 1.851) de la editorial internacional Elsevier. Título: “Surface recognition improvement in 3D medical laser scanner using Levenberg–Marquardt method”. Volumen 93, número 2, febrero 2013. Publicado en línea http://dx.doi.org/10.1016/j.sigpro.2012.07.001.

Capítulos de libro:

- Capítulo del libro llamado “Optoelectronic Devices and Properties”. Publicado por la editorial IN-TECH, Vienna, Austria, 2011. ISBN 978-953-307-204-3. Nombre del capítulo: “3D Body & Medical

Scanners' Technologies: Methodology and Spatial discriminations". http://dx.doi.org/10.5772/16233.

- Capítulo del libro llamado "Optoelectronic Devices and Properties". Publicado por la editorial IN-TECH, Vienna, Austria, 2011. ISBN 978-953-307-204-3. Nombre del capítulo: "Electromechanical 3D optoelectronic scanners: resolution constraints and possible ways of its improvement". http://dx.doi.org/10.5772/14263.

Congresos y ponencias internacionales:

- Artículo publicado y ponencia realizada en el Congreso Internacional "IEEE PHOTONICS CONFERENCE 2012" en Burlingame, California, Estados Unidos, 23 – 27 de noviembre del 2012. Título: "Optoelectronic 3D Laser Scanning Technical Vision System based on Dynamic Triangulation". ISBN: 978-1-4577-0731-5. http://dx.doi.org/10.1109/IPCon.2012.6358788
- Artículo publicado en el Congreso Internacional "IEEE PHOTONICS CONFERENCE 2012" en Burlingame, California, Estados Unidos, 23 – 27 de noviembre del 2012. Título: "Analysis of laser light reflectance on the human skin for optoelectronic devices". ISBN: 978-1-4577-0731-5. http://dx.doi.org/10.1109/IPCon.2012.6358498.
- Artículo publicado en el Congreso Internacional "Pan American Health Care Exchanges (PAHCE) 2011" en Rio de Janeiro, Brasil, 28 de marzo – 1 de abril del 2011. Título: "Continuous monitoring of rehabilitation in patients with scoliosis using automatic laser scanning". ISBN: 978-1-61284-915-7. http://dx.doi.org/10.1109/PAHCE.2011.5871941.
- Artículo publicado en el Congreso Internacional "ROC&C 2011 Vigesimosegunda Reunión Internacional de Otoño, Comunicaciones, Computación, Electrónica, Automatización, Robótica Y Exposición Industrial" en Acapulco, México. 27 de noviembre – 3 de diciembre 2011. Título: "Optimization of laser TVS for robot navigation using combined scanning with variable step". ISBN 978-607-95630-1-1.

- Artículo publicado en el Congreso Internacional “ROC&C 2011 Vigesimosegunda Reunión Internacional de Otoño, Comunicaciones, Computación, Electrónica, Automatización, Robótica Y Exposición Industrial” en Acapulco, México. 27 de noviembre – 3 de diciembre 2011. Título: “Improve a 3D Laser Scanner Resolution by a Feed-Forward Backpropagation Neural Network”. ISBN 978-607-95630-1-1.
- Artículo publicado y ponencia realizada en el Congreso Internacional “IECON 2010 36th Annual Conference of the IEEE Industrial Electronics Society” en Glendale, Arizona, Estados Unidos, Noviembre 2010. ISBN 978-1-4244-6390-9. Título: “Resolution improvement of Dynamic Triangulation method for 3D Vision System in Robot Navigation task”. http://dx.doi.org/10.1109/IECON.2010.5675082.
- Artículo publicado y ponencia realizada en el Congreso Internacional “ISIE 2010 IEEE International Symposium on Industrial Electronics” en Bari, Italia, Junio 2010. ISBN 978-1-4244-6390-9. Título: “3D Laser Scanning Vision System for Autonomous Robot Navigation”. http://dx.doi.org/10.1109/ISIE.2010.5637874.

Congresos y ponencias nacionales:

- Ponencia realizada en el 1er Torneo de Robótica de la Universidad Politécnica de Baja California (UPBC) llevado a cabo del 29 al 30 de marzo de 2012. Título: “Sistema de visión por barrido láser para navegación de un robot móvil”.
- Artículo publicado y ponencia realizada en el 2do Congreso Nacional de Estudiantes de Posgrado del Instituto de Ingeniería, UABC, Mexicali, B.C., Noviembre 2010. Ponencia titulada “Aumento de resolución de un sistema de visión en 3D mediante el método de triangulación dinámica para la tarea de navegación autónoma de robots móviles”, ISBN en trámite.

- Artículo publicado y ponencia realizada en el 1er Congreso Nacional de Estudiantes de Posgrado del Instituto de Ingeniería, UABC, Mexicali, B.C., Noviembre 2009. Ponencia titulada “Sistema de Visión en 3D mediante Barrido Láser para Navegación de Robots Autónomos”. ISBN 978-607-7753-33-9.
- Ponencia realizada en la Universidad del Valle de México Campus Mexicali (UVM) dirigida a estudiantes del área de Ingeniería Mecatrónica e Industrial. Diciembre de 2009. Título: “Sistema de Visión en 3D mediante Barrido Laser para Navegación de Robots Autónomos”.

Patentes:

- Título: “SISTEMA DE BARRIDO ÓPTICO PARA MEDICIÓN DE ÁNGULOS, COORDENADAS Y DESPLAZAMIENTO DE OBJETOS EN UN PLANO BIDIMENSIONAL”.
    - Presentada en mayo 2011.
    - En trámite (IMPI).
- Título: “MÉTODO DE BARRIDO ÓPTICO PARA MEDICIÓN DE ÁNGULOS, COORDENADAS Y DESPLAZAMIENTO DE UNO O VARIOS PUNTOS EN UN PLANO BIDIMENSIONAL”.
    - Presentada en mayo 2011.
    - En trámite (IMPI).

REFERENCIAS

[1] http://www.nasa.gov/mission_pages/mer/mer-20070824.html

[2] National Research Council. A Performance Assessment of NASA's Astrophysics Program. Washington, DC: The National Academies Press, 2007.

[3] Clancey, W. Working on Mars:Voyages of Scientific Discovery with the Mars Exploration Rovers. MIT Press, 2012.

[4] J. Matijevic. Autonomous Navigation and the Sojourner Microrover. Science, 17 April 1998, 454-455. [DOI:10.1126/science.280.5362.454]

[5] Richard V. Morris, Steven W. Ruff, Ralf Gellert, Douglas W. Ming, Raymond E. Arvidson, Benton C. Clark, et. al. Identification of Carbonate-Rich Outcrops on Mars by the Spirit Rover. Science, 23 July 2010, 421-424.Published online 3 June 2010 [DOI:10.1126/science.1189667]

[6] S. W. Squyres, A. H. Knoll, R. E. Arvidson, J. W. Ashley, J. F. Bell III, W. M. Calvin, P. R. Christensen, B. C. Clark, et. al. Exploration of Victoria Crater by the Mars Rover Opportunity. Science, 22 May 2009, 1058-1061. [DOI:10.1126/science.1170355]

[7] Blake, D.F., R.V. Morris, G. Kocurek, S.M. Morrison, R.T. Downs, D. Bish, D.W. Ming, K.S. Edgett, et. al, Curiosity at Gale Crater, Mars: Characterization and analysis of the Rocknest sand shadow, Science, 341(6153):1239505, doi:10.1126/science.1239505, 2013.

[8] Cheng, Y., Maimone, M. W., and Matthies, L., (2006) Visual odometry on the Mars exploration rovers - A tool to ensure accurate driving and science imaging. IEEE Robotics & Automation Magazine, 13(2), 54–62.

[9] Fairfield, N., Kantor, G., Wettergreen, D., (2010). Segmented SLAM in Three-Dimensional Environments. Journal of Field Robotics, 27(1), 85-103.

[10] Eli Kintisch. DARPA 'Bots Navigate Mojave. Science, 14 October 2005, 213. [DOI:10.1126/science.310.5746.213c]

[11] Multiple authors, "Special Issue on the DARPA Grand Challenge 2005 (Part 1)," Journal of Field Robotics 23(8), 2006.

[12] Multiple authors, "Special Issue on the DARPA Grand Challenge 2005 (Part 2)," Journal of Field Robotics 23(9), 2006.

[13] Tucker Balch, Henrik Christensen, Vince Camp, Tom Collins, Magnus Egerstedt, Robert Schafrik, Michael Hoffman, Joshua Witter, Ben Johnson, Dave Wooden, Karl Kluge, et. al. DARPA Urban Challenge – Team Sting. June 2007.

[14] Mason, R., "The Golum Group/ University of California at Los Angeles Autonomous Ground Vehicle in the DARPA Grand Challenge," Journal of Field Robotics, Vol. 23, Issue 8, Aug 2006.

[15] Thrun, S. et al. (2006). Stanley: The robot that won the DARPA Grand Challenge, Journal of Robotic Systems, 23(9).

[16] Ulrich Weiss, Peter Biber, Plant detection and mapping for agricultural robots using a 3D LIDAR sensor, Robotics and Autonomous Systems, Volume 59, Issue 5, May 2011, Pages 265-273, ISSN 0921-8890, http://dx.doi.org/10.1016/j.robot.2011.02.011.

[17] Gangqiang Zhao, Xuhong Xiao, Junsong Yuan, Gee Wah Ng, Fusion of 3D-LIDAR and camera data for scene parsing, Journal of Visual Communication and Image Representation, Available online 18 June 2013, ISSN 1047-3203, http://dx.doi.org/10.1016/j.jvcir.2013.06.008.

[18] Giulio Reina, Annalisa Milella, James Underwood, Self-learning classification of radar features for scene understanding, Robotics and Autonomous Systems, Volume 60, Issue 11, November 2012, Pages 1377-1388, ISSN 0921-8890, http://dx.doi.org/10.1016/j.robot.2012.03.002.

[19] O. Wijk, H.I. Christensen, Localization and navigation of a mobile robot using natural point landmarks extracted from sonar data, Robotics and Autonomous Systems, Volume 31, Issues 1–2, 30 April 2000, Pages 31-42, ISSN 0921-8890, http://dx.doi.org/10.1016/S0921-8890(99)00085-8.

[20] Bill Triggs, Model-based sonar localisation for mobile robots, Robotics and Autonomous Systems, Volume 12, Issues 3–4, April 1994, Pages 173-186, ISSN 0921-8890, http://dx.doi.org/10.1016/0921-8890(94)90024-8.

[21] K. Demirli, İ.B. Türkşen, Sonar based mobile robot localization by using fuzzy triangulation, Robotics and Autonomous Systems, Volume 33, Issues 2–3, 30 November 2000, Pages 109-123, ISSN 0921-8890, http://dx.doi.org/10.1016/S0921-8890(00)00082-8.

[22] A. Elfes. Sonar-based real-world mapping and navigation. IEEE Journal of Robotics and Automation RA, 3 (3) (1987), pp. 249–265.

[23] J. Lee, Global Positioning/GPS, In: Editors-in-Chief: Rob Kitchin and Nigel Thrift, Editor(s)-in-Chief, International Encyclopedia of Human Geography, Elsevier, Oxford, 2009, Pages 548-555, ISBN 9780080449104, http://dx.doi.org/10.1016/B978-008044910-4.00035-3.

[24] Kang Hou, Hanxu Sun, Qingxuan Jia, Yanheng Zhang, An Autonomous Positioning and Navigation System for Spherical Mobile Robot, Procedia Engineering, Volume 29, 2012, Pages 2556-2561, ISSN 1877-7058, http://dx.doi.org/10.1016/j.proeng.2012.01.350.

[25] David Schleicher, Luis M. Bergasa, Manuel Ocaña, Rafael Barea, Elena López, Low-cost GPS sensor improvement using stereovision fusion, Signal Processing, Volume 90, Issue 12, December 2010, Pages 3294-3300, ISSN 0165-1684, http://dx.doi.org/10.1016/j.sigpro.2010.05.017.

[26] López, Moisés R.; Sergiyenko, Oleg; & Tyrsa, Vera. Machine Vision: Approaches and Limitations, In Computer Vision, Book edited by: Xiong Zhihui, ISBN 978-953-7619-21-3, November 2008, I-Tech, Vienna, Austria

[27] Sarah Gray, Bruce Thorne, Zeke Susman, Josh Johnston, Tom Petroff, Dale Lord, et. al. DARPA Urban Challenge Technical Paper. April 13, 2007.

[28] A. Rieder, B. Southall, G. Salgian, R. Mandelbaum, H. Herman, P. Rander, T. Stentz, "Stereo perception on an off-road vehicle", in Intelligent Vehicle Symposium, 2002. IEEE.

[29] Carl Crane , David Armstrong , Antonio Arroyo , Antoin Baker , Doug Dankel , Greg Garcia , Nicholas Johnson , Jaesang Lee , Shannon Ridgeway , Eric Schwartz , Eric Thorn , Steve Velat , Ji Hyun Yoon. [30] Lessons Learned at the DARPA Urban Challenge. 2008 Florida Conference on Recent Advances in Robotics, FCRAR 2008.

[31] Urmson, C., Anhalt, J. et al. (2008), Autonomous driving in urban environments: Boss and the Urban Challenge. J. Field Robotics, 25: 425–466. doi: 10.1002/rob.20255

[32] Bacha, A., Bauman, C. et al. (2008), Odin: Team VictorTango's entry in the DARPA Urban Challenge. Journal of Field Robotics, 25(8), 467–492.

[33] Leonard, J., Barrett, D., How, J., Teller, S. et al. (2007). Team MIT Urban Challenge Technical Report. CSAIL Technical Reports. http://hdl.handle.net/1721.1/39822. MIT-CSAIL-TR-2007-058. Accessed 11 June 2011.

[34] Velodyne website. http://velodynelidar.com/lidar/lidar.aspx

[35] Buehler, M., Iagnemma, K., and Singh, S., editors (2006). The 2005 DARPA Grand Challenge: The Great Robot Race. Springer, Berlin.

[36] Lanshen Guo; Fang Wang; Minglu Zhang; Lixin Sun, "Study on robot perception system of multi-sensors information fusion based on fuzzy neural network," Intelligent Control and Automation, 2008. WCICA 2008. 7th World Congress on , vol., no., pp.5728,5732, 25-27 June 2008. doi: 10.1109/WCICA.2008.4592802

[37] Surmann, H., K. Lingemann, A. Nüchter and J. Hertzberg (2001). A 3D Laser Range Finder for Autonomous Mobile Robots. Proceedings of the 32nd International Symposium on Robotics. 153-158.

[38] Andersen, J. C., Blas, M. R., Ravn, O., et. al. (2006). Traversable terrain classification for outdoor autonomous robots using single 2D laser scans. Integrated Computer-Aided Engineering. 13(3), 223-232.

[39] Marco Baglietto, Antonio Sgorbissa, Damiano Verda, Renato Zaccaria, Human navigation and mapping with a 6DOF IMU and a laser scanner, Robotics and Autonomous Systems, Volume 59, Issue 12, December 2011, Pages 1060-1069, ISSN 0921-8890, http://dx.doi.org/10.1016/j.robot.2011.08.005.

[40] S. Berrabah, Y. Baudoin, H. Sahli, SLAM for robotic assistance to fire-fighting services, 8th World Congress on Intelligent Control and Automation, WCICA, 2010, 2010, pp. 362–367.

[41] B. Cinaz, H. Kenn, Head. SLAM – simultaneous localization and mapping with head-mounted inertial and laser range sensors, in: 12th IEEE International Symposium on Wearable Computers, 2008, ISWC 2008, 2008.

[42] Tarek Al-Hawari, Samir Khrais, Omar Al-Araidah, Abdullah F. Al-Dwairi, 2D laser scanner selection using fuzzy logic, Expert Systems with Applications, Volume 38, Issue 5, May 2011, Pages 5614-5619, ISSN 0957-4174, http://dx.doi.org/10.1016/j.eswa.2010.10.074.

[43] Du, Y., Gao, X., Liu, Z., Sun, M. (2008). The new navigation system for automatic guided vehicle. Chinese Control and Decision Conference 2008, 4653 – 4658.

[44] Byczkowski, T., Lang, J. (2009). A Stereo-Based System with Inertial Navigation for Outdoor 3D Scanning. Canadian Conference on Computer and Robot Vision 2009. CRV '09. 221 – 228.

[45] Hwang, C. L., Shih, C. Y. (2009). A Distributed Active-Vision Network-Space Approach for the Navigation of a Car-Like Wheeled Robot. IEEE Transactions on Industrial Electronics, 56(3), 846–855.

[46] James L. Crowley, Philippe Bobet, Karen Sarachik, Stephen Mely, Michel Kurek, Mobile robot perception using vertical line stereo, Robotics and Autonomous Systems, Volume 7, Issues 2–3, August 1991, Pages 125-138, ISSN 0921-8890, http://dx.doi.org/10.1016/0921-8890(91)90037-L.

[47] G. Michalos, S. Makris, A. Eytan, S. Matthaiakis, G. Chryssolouris, Robot Path Correction Using Stereo Vision System, Procedia CIRP, Volume 3, 2012, Pages 352-357, ISSN 2212-8271, http://dx.doi.org/10.1016/j.procir.2012.07.061.

[48] R. Correal, G. Pajares, J.J. Ruz, Automatic expert system for 3D terrain reconstruction based on stereo vision and histogram matching, Expert Systems with Applications, Available online 12 September 2013, ISSN 0957-4174, http://dx.doi.org/10.1016/j.eswa.2013.09.003.

[49] K. Genovesea, L. Casalettoa, J.A. Rayasb, et. al. Stereo-Digital Image Correlation (DIC) measurements with a single camera using a biprism. Optics and Lasers in Engineering, 51(3), 2013, 278–285.

[50] Yihao Zhou, Yan Qiu Chen. Feature matching for automated and reliable initialization in three-dimensional digital image correlation. Optics and Lasers in Engineering, 51(3), 2013, 213–223.

[51] Tiago Pintoa, Christian Kohlerb, Armando Albertazzi. Regular mesh measurement of large free form surfaces using stereo vision and fringe projection. Optics and Lasers in Engineering, 50(7), 2012, 910–916.

[52] Zhao Penga, Ni Guo-Qiangb. Simultaneous perimeter measurement for 3D object with a binocular stereo vision measurement system. Optics and Lasers in Engineering, 48(4), 2010, 505–511.

[53] Lipnickas, A., and Knyš A., (2009). A Stereovision System for 3-D Perception. Electronics & Electrical Engineering. 91, 99-102.

[54] Song Zhang and Peisen S. Huang. High-resolution, real-time three-dimensional shape measurement, Opt. Eng. 45(12), (Dec 13, 2006). http://dx.doi.org/10.1117/1.2402128

[55] Huang, P. & Han, X. (2006). On improving the accuracy of structured light systems", Proc. SPIE 6382, Two- and Three-Dimensional Methods for Inspection and Metrology IV, 63820H (October 12, 2006); doi:10.1117/12.692631. http://dx.doi.org/10.1117/12.692631.

[56] Rivas Lopez, M., Sergiyenko, O., et. al (2008). Spatial data acquisition by laser scanning for robot or SHM task. IEEE-IES Proceedings "International Symposium on Industrial Electronics ISIE-2008, Cambridge, United Kingdom, 1458-1463.

[57] M. Rivas Lopez, O. Yu. Sergiyenko, V.V. Tyrsa, W. Hernandez Perdomo, L.F. Devia Cruz, D. Hernandez Balbuena, L.P. Burtseva, and J.I. Nieto Hipolito. Optoelectronic Method for Structural Health Monitoring. Structural Health Monitoring, March 2010; vol. 9, 2: pp. 105-120., first published on September 24, 2009

[58] P. Frank Pai, Lu Huang, Jiazhu Hu, and Dustin R. Langewisch. Time-Frequency Method for Nonlinear System Identification and Damage Detection. Structural Health Monitoring, June 2008; vol. 7, 2: pp. 103-127.

[59] Basaca, L.C., Rodriguez, J.C., Sergiyenko, O., et. al (2010). Resolution improvement of Dynamic Triangulation method for 3D Vision System in Robot Navigation task. Proceedings of IEEE-36th Annual Conference of IEEE Industrial Electronics IECON'10, 2886 - 2891.

[60] Rivas Lopez, M., Sergiyenko, O., Tyrsa, V., (2008). Computer vision. Machine vision: approaches and limitations (pp. 395-428). Austria: I-TECH.

[61] Basaca, L.C., Rodriguez, J.C., Sergiyenko, O., (2010). 3D Laser Scanning Vision System for Autonomous Robot Navigation. Proceedings of IEEE International Symposium on Industrial Electronics ISIE-2010, Bari, Italy, 1773-1778.

[62] Sergiyenko, O., Hernandez, W., et al. (2009). Remote Sensor for Spatial Measurements by Using Optical Scanning. Sensors, 9(7), 5477-5492.

[63] Sergiyenko, O., Tyrsa, V., et. al (2009). Dynamic Laser Scanning method for Mobile Robot Navigation. Proceedings of ICCAS-SICE 2009 ICROS-SICE International Joint Conference, Japan, 4884-4889.

[64] Measurement Computing website. http://www.mccdaq.com/

[65] C-H Hsieh and J-H Chou. Analysis and optimal control of pulse width modulation feedback systems. Proceedings of the Institution of Mechanical Engineers, Part I: Journal of Systems and Control Engineering, June 1, 2004; vol. 218, 4: pp. 277-286.

[66] Arduino website. http://www.arduino.cc/

[67] National Instruments website. http://www.ni.com/

[68] Mobile Robotics website. http://www.mobilerobots.com/Mobile_Robots.aspx

[69] Niku, S.B. (2010). Introduction to Robotics: Analysis, Systems, Applications. Indianapolis, IN: Wiley.

[70] Niku, S., "Scheme for Active Positional Correction of Robot Arms". Proceedings of the 5th International Conference on CAD/CAM, Robotics and Factories of Future, Springer Verlag, pp. 590-590, 1991.

[71] Craig, John J., Introduction to Robotics: Mechanics and Control, 2nd Edition, Addison Wesley, 1989.

[72] W. Hernandez, J. de Vicente, O. Sergiyenko & E. Fernández, Improving the Response of Accelerometers for Automotive Applications by Using LMS Adaptive Filters, MDPI, Sensors, 2010, 10(1), Basel, Switzerland, 313-329; ISSN 1424-8220 / doi:10.3390/s100100313

[73] W. Hernandez, J. de Vicente, O. Sergiyenko & Eduardo Fernández, Improving the Response of Accelerometers for Automotive Applications by Using LMS Adaptive Filters: Part II, MDPI, Sensors, 2010, 10(1), Basel, Switzerland, 952-962; ISSN 1424-8220 / doi: 10.3390/s100100952

[74] Mladenov, M.; Mock, M.; Grosspietsch, K.-E., "Fault monitoring and correction in a walking robot using LMS filters," Intelligent Solutions in Embedded Systems, 2008 International Workshop on , vol., no., pp.1,10, 10-11 July 2008. doi: 10.1109/WISES.2008.4623294

[75] Luis C. Basaca-Preciado, Oleg Yu. Sergiyenko, Julio C. Rodríguez-Quinonez et. al. Optical 3D laser measurement system for navigation of autonomous mobile robot, Optics and Lasers in Engineering by Elsevier, September 2013, ISSN 0143-8166, http://dx.doi.org/10.1016/j.optlaseng.2013.08.005.

[76] Kozłowski, K. & Pazderski, D. (2004). Modeling and control of a 4-wheel skid-steering mobile robot. International Journal of Applied Mathematics and Computer Science, 14(4), 477–496.

[77] Kang, J., Kim, W., Lee, J., Yi, K., (2010). Design, implementation, and test of skid steering-based autonomous driving controller for a robotic vehicle with articulated suspension. Journal of Mechanical Science and Technology, 24(3), 793-800.

[78] J. Wang, Q. Wang, L. Jin, C. Song. Independent wheel torque control of 4WD electric vehicle for differential drive assisted steering. Mechatronics, Volume 21, Issue 1, February 2011, Pages 63-76

[79] MathWorks Matlab website. http://www.mathworks.com/products/matlab/

[80] Qiu Chengqun, "Design of Virtual Instrument Based on MATLAB and LabVIEW," Measuring Technology and Mechatronics Automation (ICMTMA), 2013 Fifth International Conference on , vol., no., pp.466,469, 16-17 Jan. 2013. doi: 10.1109/ICMTMA.2013.117

[81] SolidWorks website. http://www.solidworks.com/

[82] Sergiyenko, O., Tyrsa, V., Basaca, L.C., Rodriguez, J.C., et. al (2010). Optoelectronic Devices and Properties. Electromechanical 3D Optoelectronic Scanners: Resolution Constraints and Possible Ways of Improvement (pp. 549-582). Austria: IN-TECH.

[83] Sergiyenko, O., Tyrsa, V., Hernandez-Balbuena, D., et al. (2008). Precise Optical Scanning for practical multiapplications. Proceedings of IEEE 34th Annual IEEE Conference IECON'08, Florida, USA, 1656-1661.

[84] Sergiyenko, O. Yu. (2010). Optoelectronic System for Mobile Robot Navigation. Optoelectronics, Instrumentation and Data Processing, 46(5), October, 2010, 414-428.

[85] L.C. Basaca-Preciado, O. Sergiyenko, J.C. Rodriguez-Quinonez & M. Rivas-Lopez, Optoelectronic 3D laser scanning technical vision system based on dynamic triangulation, 2012 IEEE Photonics Conference (IPC), 2012, 648 – 649.

[86] Kenneth Levenberg (1944). "A Method for the Solution of Certain Non-Linear Problems in Least Squares". Quarterly of Applied Mathematics 2: 164–168.

[87] J.C. Rodriguez-Quiñones, O. Sergiyenko, F.F. González-Navarro, L.C. Basaca-Preciado & V. Tyrsa. Surface recognition improvement in 3D medical laser scanner using Levenberg–Marquardt method, Signal Processing by Elsevier, 93(2), February 2013, 378–386, ISSN 0165-1684.

[88] A. Abba, F. Caponio, A. Geraci & G. Ripamontii, Non-linear leastsquares in FPGA devices for digital spectroscopy, Nuclear Science Symposium Conference Record (NSS/MIC), Orlando, 2009, 563–568.

[89] D. Marquardt, An algorithm for least-squares estimation of nonlinear parameters, SIAM Journal on Applied Mathematics, 11(2), 1963, 431–441.

[90] Julio C. Rodríguez-Quinonez, Oleg Yu. Sergiyenko, Luis C. Basaca-Preciado et. al. Optical monitoring of scoliosis by 3D medical laser scanner, Optics and Lasers in Engineering by Elsevier, September 2013, ISSN 0143-8166, http://dx.doi.org/10.1016/j.optlaseng.2013.07.026.

[91] X.M. Garcia-Cruz, O. Yu. Sergiyenko, Vera Tyrsa, M. Rivas-Lopez, D. Hernandez-Balbuena, J.C. Rodriguez-Quiñonez, L.C. Basaca-Preciado, P. Mercorelli. Optimization of 3D laser scanning speed by use of combined

variable step, Optics and Lasers in Engineering by Elsevier, September 2013, ISSN 0143-8166, http://dx.doi.org/10.1016/j.optlaseng.2013.08.011

[92] Scolari, A.G.; Chaves, L.F.; Conte, R.N.; Pereira, L.F., "Strategy of localization using the neural network toolbox of the Matlab/Simulink applied to mobile robots," Industrial Electronics, 2003. ISIE '03. 2003 IEEE International Symposium on, vol.2, no., pp.1017, 1020 vol. 2, 9-11 June 2003. doi: 10.1109/ISIE.2003.1267962

APÉNDICE A.

Programas de los microcontroladores utilizados para el control del sistema de barrido por láser.

Programa que genera las secuencias digitales necesarias para el control de un motor de pasos en ambas direcciones.

```
#include <16F84A.h>
#device adc=8
#use delay(clock=4000000)
#fuses NOWDT,XT, NOPUT, NOPROTECT

//El programa genera la secuencia de control de los microcontroladores
//Al mismo tiempo genera un pulso por la salida A2 por cada paso dado
//El programa conoce en todo momento en qué estado se encuentra
//Se puede iniciar en cualquier dirección de la secuencia del motor de pasos.

void main() {

int speed;
speed = 12;

ciclo1:
   if (input(PIN_A0)==1)
   goto iniciopositivo;
   if (input(PIN_A1)==1)
   goto inicionegativo;
goto ciclo1;

iniciopositivo:
   if (input(PIN_A0)==1)
        {
         output_high(PIN_A2);    //Genera pulso de subida para labview
         primeromas:
          OUTPUT_B(0b0011);
          delay_ms(speed);
          output_low(PIN_A2);   //Genera pulso de bajada para labview
          if (input(PIN_A1)==1)
          goto primeromenos;
          if (input(PIN_A1)==0 && input(PIN_A0)==0)
          goto primeromas;
        }
```

```
    if (input(PIN_A0)==1)
         {
          output_high(PIN_A2);    //Genera pulso de subida para labview
          segundomas:
           OUTPUT_B(0b1001);
           delay_ms(speed);
           output_low(PIN_A2);   //Genera pulso de bajada para labview
           if (input(PIN_A1)==1)
           goto cuartomenos;
           if (input(PIN_A1)==0 && input(PIN_A0)==0)
           goto segundomas;
         }
    if (input(PIN_A0)==1)
         {
          output_high(PIN_A2);    //Genera pulso de subida para labview
          terceromas:
           OUTPUT_B(0b1100);
           delay_ms(speed);
           output_low(PIN_A2);   //Genera pulso de bajada para labview
           if (input(PIN_A1)==1)
           goto terceromenos;
           if (input(PIN_A1)==0 && input(PIN_A0)==0)
           goto terceromas;
         }
    if (input(PIN_A0)==1)
         {
          output_high(PIN_A2);    //Genera pulso de subida para labview
          cuartomas:
           OUTPUT_B(0b0110);
           delay_ms(speed);
           output_low(PIN_A2);   //Genera pulso de bajada para labview
           if (input(PIN_A1)==1)
           goto segundomenos;
           if (input(PIN_A1)==0 && input(PIN_A0)==0)
           goto cuartomas;
         }


inicionegativo:
    if (input(PIN_A1)==1)
         {
          output_high(PIN_A2);    //Genera pulso de subida para labview
          primeromenos:
           OUTPUT_B(0b0110);
```

```
          delay_ms(speed);
          output_low(PIN_A2);   //Genera pulso de bajada para labview
          if (input(PIN_A0)==1)
          goto primeromas;
          if (input(PIN_A1)==0 && input(PIN_A0)==0)
          goto primeromenos;
        }
   if (input(PIN_A1)==1)
        {
         output_high(PIN_A2);    //Genera pulso de subida para labview
         segundomenos:
          OUTPUT_B(0b1100);
          delay_ms(speed);
          output_low(PIN_A2);   //Genera pulso de bajada para labview
          if (input(PIN_A0)==1)
          goto cuartomas;
          if (input(PIN_A1)==0 && input(PIN_A0)==0)
          goto segundomenos;
        }
   if (input(PIN_A1)==1)
        {
         output_high(PIN_A2);    //Genera pulso de subida para labview
         terceromenos:
          OUTPUT_B(0b1001);
          delay_ms(speed);
          output_low(PIN_A2);   //Genera pulso de bajada para labview
          if (input(PIN_A0)==1)
          goto terceromas;
          if (input(PIN_A1)==0 && input(PIN_A0)==0)
          goto terceromenos;
        }
   if (input(PIN_A1)==1)
        {
         output_high(PIN_A2);    //Genera pulso de subida para labview
         cuartomenos:
          OUTPUT_B(0b0011);
          delay_ms(speed);
          output_low(PIN_A2);   //Genera pulso de bajada para labview
          if (input(PIN_A0)==1)
          goto segundomas;
          if (input(PIN_A1)==0 && input(PIN_A0)==0)
          goto cuartomenos;
        }
goto ciclo1; }
```

Programa que cuenta los pulsos de los sensores de detección de obstáculos y revoluciones de la apertura de barrido y envía la información calculada a la computadora para el cálculo del ángulo B_{ij}.

```
#include <18F4550.h>
#include <stdlib.h>

#fuses HS,NOWDT,NOPROTECT,NOLVP
#use delay(clock=20000000)
#use rs232(baud=9600, xmit=PIN_C6, rcv=PIN_C7)

//PINA0 = Entrada OptoAcoplador
//PINA1 = Entrada FotoTransistor
//PINA2 = Entrada Pulso de referencia
//cont = contador puro por ciclo
//cont1 = numero de pulsos en 1 ciclo
//cont2 = numero de pulsos hasta que se detecto el pulso fototransistor
void main() {

int16 cont, cont1,cont2, estadoA0, estadoA1, estadoA2, Cont_Env;
cont = 0;
cont1 = 0;
cont2 = 0;
estadoA0 = 0;  //Estado respecto al optoacoplador
estadoA1 = 0;  //Estado respecto al fototransistor
estadoA2 = 0;  //Estado respecto al pulso de referencia
Cont_Env = 0;  //Estado para contar o enviar, un 2 ciclos cuenta
//                y en el tercer ciclo envia

ciclo1:

if (estadoA0 == 0)
{
   if (input(PIN_A0)==1)
   {
      estadoA0 = 1;
      cont1 = cont;     //Obtenemos el numero de pulsos dentro de 1 rotacion

      if (Cont_Env == 2)
      {
         printf("O%Lu ",cont1); //La letra O se refiere a Optoacoplador
         printf("F%Lu ",cont2); //La leta F se refiere a Fototransistor
         Cont_Env = 0;
      }

      if (Cont_Env < 2)
      {
        Cont_Env = Cont_Env + 1;
      }

      cont = 0;
      cont1 = 0;
      cont2 = 0;

```

```
    }
}

if (estadoA1 == 0)
{
    if (input(PIN_A1)==1)
    {
        estadoA1 = 1;
        if (cont2 == 0)        //Solamente cuando cont2 valga 0 para
        {                      //asegurarnos que es el primer pico de subida
            cont2 = cont;      //Obtenemos el numero de pulsos hasta detectar
        }                      // fototransistor
    }
}

if (estadoA2 == 0)      //Cuenta los pulsos que se generan
{
    if (input(PIN_A2)==1)
    {
        estadoA2 = 1;
        cont = cont + 1;
    }
}

if (estadoA0 == 1)
{
    if (input(PIN_A0)==0)
    {
        estadoA0 = 0;
    }
}

if (estadoA1 == 1)
{
    if (input(PIN_A1)==0)
    {
        estadoA1 = 0;
    }
}

if (estadoA2 == 1)
{
    if (input(PIN_A2)==0)
    {
        estadoA2 = 0;
    }
}
goto ciclo1;
}
```

Programa que genera un pulso digital que es utilizado como referencia para calcular el ángulo B_{ij}.

```
#include <16F84A.h>
#device adc=8
#use delay(clock=8000000)
#fuses NOWDT,XT, NOPUT, NOPROTECT



void main() {

int speed;
speed = 25;

ciclo1:
   output_high(PIN_B0);
   delay_us(speed);
   output_low(PIN_B0);
   delay_us(speed);

goto ciclo1;

}

```

Programa utilizado para controlar el motor de corriente directa de la apertura de barrido mediante una señal PWM.

```
#include <16F84A.h>
#device adc=8
#use delay(clock=8000000)
#fuses NOWDT,XT, NOPUT, NOPROTECT

void main() {

   loop:
      if (input(PIN_A0)==1)
         goto ciclo1;
   goto loop;

   ciclo1:
      output_high(PIN_B0);
      delay_ms(4);
      output_low(PIN_B0);
      delay_ms(1);
   goto loop;
}
```

APÉNDICE B.

Código de las simulaciones realizadas en MATLAB de los sistemas de barrido y navegación

Programa que calcula las coordenadas en 3D basando sus datos de entrada en un modelo de SolidWorks del sistema de barrido por láser, cuyos ángulos y distancias fueron previamente medidos para comprobar el resultado de las ecuaciones 2 – 5 presentadas en el capítulo II y el método de triangulación dinámica.

```
clc
clear all

fprintf('\n         *** VISION SYSTEM CALCULATIONS *** \n');

load obs_input3;
fov = zeros(20,20,4);
fov(:,:,1) = digmap;
fov(:,:,2) = bangle;
fov(:,:,3) = cangle;
fov(:,:,4) = betasum;

a = .48;   % long barra
aj = 0;
res = zeros(20,20,3);

tcalc = tic;
for i = 1:size(fov,1)
    for j = 1:size(fov,2)
        if fov(i,j,1) == 1
            aj = aj + 1;
            res(i,j,1) = a*((sind(fov(i,j,2))*sind(fov(i,j,3))*cosd(fov(i,j,4)))/(sind(180-fov(i,j,2)-fov(i,j,3))));
            res(i,j,2) = a*((1/2)-((sind(fov(i,j,2))*cosd(fov(i,j,3)))/(sind(180-fov(i,j,2)-fov(i,j,3)))));
            res(i,j,3) = a*((sind(fov(i,j,2))*sind(fov(i,j,3))*sind(fov(i,j,4)))/(sind(180-fov(i,j,2)-fov(i,j,3))));
        end
    end
end
tiempo = toc(tcalc)*1000;
fprintf('\n   --> Calculation time: %.4f ms ',tiempo);
fprintf('\n   --> Quantity of calculated distances: %d ',aj*3);
fprintf('\n   --> Quantity of calculated points: %d ',aj);

x = reshape(res(:,:,1),1,[])'; % reacomodo los valores en una sola fila
y = reshape(res(:,:,2),1,[])'; % igual
z = reshape(res(:,:,3),1,[])'; % igual

x = vertcat(x,5); % agrego origen x
y = vertcat(y,0); % agrego origen y
z = vertcat(z,0); % agrego origen z

figure; scatter3(x,y,z)
set(gca,'ZDir','reverse')
figure; scatter(x,y)
tiempo2 = toc(tcalc)*1000;
fprintf('\n   --> Plot time: %.4f ms \n\n',tiempo2-tiempo);
```

Información útil desplegada por BANS respecto al sistema de barrido y de navegación. Cálculo de coordenadas 3D y nueva trayectoria utilizando datos reales entrada.

```
        *** VISION SYSTEM CALCULATIONS ***

   --> Calculation time: 13.5726 ms
   --> Quantity of calculated distances: 156
   --> Quantity of calculated points: 52
   --> Plot time: 9.1365 ms


       *** OBSTACLES CHARACTERISTICS ***

   --> Quantity of detected obstacles: 2

   --> Obstacle 1
        * Height (z): 0.2761 m
        * Wide (y): -0.2000 m
        * Depth (x): 0.0063 m

   --> Obstacle 2
        * Height (z): 0.1839 m
        * Wide (y): -0.1000 m
        * Depth (x): 0.0085 m

       *** NAVIGATION SYSTEM CALCULATION ***

   --> Distance between detected obstacles (y): 0.4500 m
   --> Distance between the robots reference frame
         and the left limit (y+): 0.0135 m
   --> Distance between the robots reference frame
         and the right limit (y-): 0.1365 m
   --> Shortest distance between the robot's reference frame
         and obstacle 1: 1.9915 m
   --> Shortest distance between the robot's reference frame
         and obstacle 2: 1.9915 m

   --> DECISION MAKING

        * What's the robots current position?

curloc =

     1     0     0     0
     0     1     0     0
     0     0     1     0
     0     0     0     1


        * How many obstacles were detected? 2
```

```
        * Does the robot fit between the obstacles? No

        * Avoid obstacle by left or right?
            (shortest trajectory distance)  (y)? Right

        * Therefore, the robot will turn towards
            the Right side to avoid obstacles

        * Calculating new trajectory...
           - The following points will be used to
             generate the curve:
                + P1 (0.0000,0.0000)
                + P2 (1.9915,-0.5040)
                + P3 (2.3676,-0.4410)

         X            Y          Yaw       Dist. between points
         0            0            0            0
   -0.0911       0.1020     131.7446       0.1368
   -0.1724       0.2041      -1.5499       0.1305
   -0.2446       0.3061      -1.5725       0.1250
   -0.3079       0.4082      -1.5906       0.1201
   -0.3630       0.5102      -1.6039       0.1159
   -0.4101       0.6122      -1.6119       0.1124
   -0.4498       0.7143      -1.6144       0.1095
   -0.4826       0.8163      -1.6111       0.1072
   -0.5088       0.9184      -1.6017       0.1054
   -0.5290       1.0204      -1.5861       0.1040
   -0.5435       1.1224      -1.5644       0.1031
   -0.5529       1.2245      -1.5366       0.1025
   -0.5576       1.3265      -1.5027       0.1021
   -0.5580       1.4286      -1.4632       0.1020
   -0.5546       1.5306      -1.4181       0.1021
   -0.5478       1.6327      -1.3679       0.1023
   -0.5382       1.7347      -1.3130       0.1025
   -0.5261       1.8367      -1.2537       0.1028
   -0.5120       1.9388      -1.1905       0.1030
   -0.4963       2.0408      -1.1238       0.1032
   -0.4796       2.1429      -1.0540       0.1034
   -0.4622       2.2449      -0.9815       0.1035
   -0.4446       2.3469      -0.9068       0.1035
   -0.4272       2.4490      -0.8312       0.1035
   -0.4101       2.5510      -0.7629       0.1035
   -0.3931       2.6531      -0.7043       0.1034
   -0.3761       2.7551      -0.6541       0.1034
   -0.3591       2.8571      -0.6107       0.1035
   -0.3420       2.9592      -0.5712       0.1035
   -0.3248       3.0612      -0.5348       0.1035
   -0.3077       3.1633      -0.5011       0.1035
   -0.2906       3.2653      -0.4702       0.1035
   -0.2735       3.3673      -0.4421       0.1035
   -0.2564       3.4694      -0.4166       0.1035
   -0.2393       3.5714      -0.3932       0.1035
   -0.2223       3.6735      -0.3718       0.1035
   -0.2052       3.7755      -0.3520       0.1035
   -0.1881       3.8776      -0.3337       0.1035
   -0.1710       3.9796      -0.3167       0.1035
   -0.1539       4.0816      -0.3010       0.1035
```

```
   -0.1539    4.0816   -0.3010    0.1035
   -0.1368    4.1837   -0.2864    0.1035
   -0.1197    4.2857   -0.2729    0.1035
   -0.1026    4.3878   -0.2603    0.1035
   -0.0855    4.4898   -0.2485    0.1035
   -0.0684    4.5918   -0.2375    0.1035
   -0.0513    4.6939   -0.2272    0.1035
   -0.0342    4.7959   -0.2175    0.1035
   -0.0171    4.8980   -0.2085    0.1035
         0    5.0000   -0.2000    0.1035


        * Proving position and orientation with the
          direct and inverse kinematics equations...

         X            Y               Z            Roll         Pitch      Yaw
         0         0         0         0         0         0
   -0.0911    0.1020         0         0         0  131.7446
   -0.1724    0.2041         0         0         0   -1.5499
   -0.2446    0.3061         0         0         0   -1.5725
   -0.3079    0.4082         0         0         0   -1.5906
   -0.3630    0.5102         0         0         0   -1.6039
   -0.4101    0.6122         0         0         0   -1.6119
   -0.4498    0.7143         0         0         0   -1.6144
   -0.4826    0.8163         0         0         0   -1.6111
   -0.5088    0.9184         0         0         0   -1.6017
   -0.5290    1.0204         0         0         0   -1.5861
   -0.5435    1.1224         0         0         0   -1.5644
   -0.5529    1.2245         0         0         0   -1.5366
   -0.5576    1.3265         0         0         0   -1.5027
   -0.5580    1.4286         0         0         0   -1.4632
   -0.5546    1.5306         0         0         0   -1.4181
   -0.5478    1.6327         0         0         0   -1.3679
   -0.5382    1.7347         0         0         0   -1.3130
   -0.5261    1.8367         0         0         0   -1.2537
   -0.5120    1.9388         0         0         0   -1.1905
   -0.4963    2.0408         0         0         0   -1.1238
   -0.4796    2.1429         0         0         0   -1.0540
   -0.4622    2.2449         0         0         0   -0.9815
   -0.4446    2.3469         0         0         0   -0.9068
   -0.4272    2.4490         0         0         0   -0.8312
   -0.4101    2.5510         0         0         0   -0.7629
   -0.3931    2.6531         0         0         0   -0.7043
   -0.3761    2.7551         0         0         0   -0.6541
   -0.3591    2.8571         0         0         0   -0.6107
   -0.3420    2.9592         0         0         0   -0.5712
   -0.3248    3.0612         0         0         0   -0.5348
   -0.3077    3.1633         0         0         0   -0.5011
   -0.2906    3.2653         0         0         0   -0.4702
```

```
   -0.2906    3.2653         0         0         0   -0.4702
   -0.2735    3.3673         0         0         0   -0.4421
   -0.2564    3.4694         0         0         0   -0.4166
   -0.2393    3.5714         0         0         0   -0.3932
   -0.2223    3.6735         0         0         0   -0.3718
   -0.2052    3.7755         0         0         0   -0.3520
   -0.1881    3.8776         0         0         0   -0.3337
   -0.1710    3.9796         0         0         0   -0.3167
   -0.1539    4.0816         0         0         0   -0.3010
   -0.1368    4.1837         0         0         0   -0.2864
   -0.1197    4.2857         0         0         0   -0.2729
   -0.1026    4.3878         0         0         0   -0.2603
   -0.0855    4.4898         0         0         0   -0.2485
   -0.0684    4.5918         0         0         0   -0.2375
   -0.0513    4.6939         0         0         0   -0.2272
   -0.0342    4.7959         0         0         0   -0.2175
   -0.0171    4.8980         0         0         0   -0.2085
         0    5.0000         0         0         0   -0.2000


        *** THE ROBOT HAS REACHED ITS GOAL ***
fx >> 
```

Código utilizado para calcular una nueva trayectoria del robot móvil (desde su posición actual hacia la meta programada), después de haber detectado algún obstáculo.

```
function [x,y,f,g,tiempo] = newtraj(curloc,goal,limy,minx1)
%UNTITLED4 Summary of this function goes here
%   Detailed explanation goes here
tic
px = curloc(1,4);
py = curloc(2,4);
% pz = curloc(3,4)

goalT = fwdkin2(goal(1), goal(2), goal(3), goal(4), goal(5), goal(6)) ;
px3 = goalT(1,4);
py3 = goalT(2,4);
% pz3 = goalT(3,4)

avgx = (px+px3)/2;
px2 = avgx;
% if limy > 0
%     py2 = (limy + 0.2465) * 1.4;
% end
% if limy < 0
%     py2 = (limy - 0.2465) * 1.4;
% end

py2 = (limy - 0.2465) * 1.4; % falta arreglar esta parte del codigo py2 neg o pos??

ypr = linspace(py2,py3,9)';
y = [py' ypr']';
xpr = linspace(minx1, px3, 9)';
x = [px' xpr']';

% y = [py py2 py3 ]';     % x
% x = [px px2 px3 ]';     % y

f = linspace(0, px3, 50); %500 en articulo
g = spline(x,y,f);
g1 = (g + 0.2465);
g2 = (g - 0.2465);

tiempo = toc*1000;
plot(x,y,'*',x,y,':',f,g,'r-',f,g1,'bx',f,g2,'bx') % este es el bueno
end
```

APÉNDICE C.

Tablas de resultados de pruebas realizadas con el prototipo I

Resultados experimentales de medición de coordenadas.

Punto de prueba	Valor teórico				Valor medido			
	X (m)	Y (m)	B (°)	C (°)	*x(m)*	*y(m)*	*B (°)*	*C (°)*
B	120	120	120,26	35,22	124,21	128,68	123,43	34,8
D	100	100	116,57	33,69	99,83	104,48	118,46	32,87
F	100	80	106,70	37,57	95,3	76,86	106,4	36,91
H	120	60	94,76	47,49	122,92	63,49	96,38	47,28
J	80	60	97,13	36,03	77	58,62	96,57	35,33
L	80	40	82,87	41,63	79,99	42,15	84	40,95
N	120	40	85,24	53,13	119,86	40,04	84,48	53,08
O	120	20	75,96	59,74	119,22	19,48	76,01	59,76
P	100	20	73,30	55,01	97,6	19,15	72,94	54,67
Q	80	20	69,44	48,81	79,11	18,7	68,39	49,04
R	60	20	63,43	40,60	60,33	21,7	64,3	40,07
S	40	20	53,13	29,74	39,14	19,59	52,07	29,35
T	40	0	38,66	38,66	36,52	1,06	36,52	36,73
U	60	0	50,19	50,19	59,8	0,9	49,39	50,625
V	80	0	57,99	57,99	80,93	3,49	56,7	60,11
W	100	0	63,43	63,43	103,58	1,51	63,45	64,68
X	120	0	67,38	67,38	120,72	-4,7	66,23	69,43
Y	120	-20	59,74	75,96	118,54	-18,36	59,95	75,05
Z	100	-20	55,01	73,30	96,72	-18,37	54,7	71,9
A1	80	-20	48,81	69,44	75,79	-18,33	48,03	67,32
B1	60	-20	40,60	63,43	58	-18,53	39,5	61,52
C1	40	-20	29,74	53,13	36,17	-20,31	27,3	50,62
D1	60	-40	33,69	80,54	58,05	-38,63	33,6	78,92
E1	80	-40	41,63	82,87	77,46	-38,26	40,46	81,38
F1	100	-40	48,01	84,29	97,1	-38,02	46,94	82,96
H1	120	-60	47,49	94,76	123,68	-61,03	48,21	95,09
J1	80	-60	36,03	97,13	78,9	-59,73	35,37	97,03
L1	80	-80	31,61	110,56	80,52	-80,21	31,81	110,56
N1	120	-80	42,71	104,04	121,01	-78,73	43,34	103,35
P1	100	-100	33,69	116,57	101,65	-96,18	35,06	114,43
R1	100	-120	30,47	124,99	111,73	-126,15	32,09	124,27

APÉNDICE D.

Tablas de resultados de pruebas realizadas con el prototipo II

Resultados de cálculo de ángulos y coordenadas con el prototipo II (sin red neuronal).

Real Values (degrees, m)				Measured angles (degrees)		Calculated coordinates (m)		Calculated errors		
C angle	B angle	X	Y	C angle	B angle	X	Y	ΔB (degrees)	ΔX (m)	ΔY (m)
64.7	62.3	1.0	-0.027	64.9687	67.5996	1.1375	-0.0312	5.2996	0.13746	-0.0042
62.6	64.25	1.0	-0.016	62.9625	67.1964	1.0744	-0.0483	2.9464	0.0744	-0.0323
61.3	65.5	1.0	-0.046	61.9687	68.9497	1.0902	-0.0804	3.4497	0.0902	-0.0344
59.7	67.3	1.0	-0.0850	59.9625	73.4938	1.1434	-0.1612	6.1938	0.1434	-0.0762
57.2	70.2	1.0	-0.143	57.9375	76.117	1.1448	-0.2171	5.917	0.1448	-0.0741
54.6	74.3	1.0	-0.11	54.9750	79.5349	1.1292	-0.2914	5.2349	0.1292	-0.1814
51.7	78	1.0	-0.2875	51.9750	83.1396	1.1083	-0.3667	5.1396	0.1083	-0.0792
50.5	79.9	1.0	-0.318	50.9812	85.4484	1.1237	-0.4105	5.5484	0.1237	-0.0925
49.8	81.2	1.0	-0.345	49.9312	88.7413	1.1586	-0.4745	7.5413	0.1586	-0.1295
46.8	86.3	1.0	-0.43	46.9500	91.7871	1.1075	-0.5346	5.4871	0.1075	-0.1046
44.7	90.5	1.0	-0.509	44.9812	99.4492	1.1987	-0.6995	8.9492	0.1987	-0.1905
65.25	56.75	0.9	0.087	65.9437	61.2048	1.0040	0.0518	4.4548	0.1040	-0.0352
64.5	57.7	0.9	0.071	64.9500	62.3292	1.0083	0.0287	4.6292	0.1083	-0.0423
62.5	59.4	0.9	0.033	62.9812	61.9322	0.9586	0.0112	2.5322	0.0586	-0.0218
59.5	62.5	0.9	-0.03	59.9437	66.6218	0.9892	-0.0724	4.1218	0.0892	-0.0424
56.4	65.8	0.9	-0.093	56.9625	69.0069	0.9671	-0.1289	3.2069	0.0671	-0.0359
54.9	68	0.9	-0.135	54.9562	72.4962	0.9836	-0.1898	4.4962	0.0836	-0.0548
52.5	71	0.9	-0.19	52.9312	74.8963	0.9758	-0.2366	3.8963	0.0758	-0.0466
50	75	0.9	-0.257	49.9500	80.2548	0.9878	-0.3303	5.2548	0.0878	-0.0733
45	83.7	0.9	-0.403	44.9812	89.2128	0.9858	-0.4865	5.5128	0.0858	-0.0835
42.27	88.27	0.9	-0.474	42.9375	92.4444	0.9690	-0.5414	4.1744	0.0690	-0.0674
62.5	53.8	0.8	0.084	62.9625	57.3998	0.8697	0.0562	3.5998	0.0697	-0.0278
59.8	56.2	0.8	-0.034	59.9812	59.5533	0.8579	0.0043	3.3533	0.0579	0.0383
56.5	59.6	0.8	-0.031	56.9625	62.2866	0.8506	-0.0532	2.6866	0.0506	-0.0222
54.9	61.3	0.8	-0.06	54.9532	64.0569	0.8419	-0.0904	2.7569	0.0419	-0.0304
51.8	65.15	0.8	-0.013	51.9375	67.7942	0.8395	-0.1573	2.6442	0.0395	-0.1443
50	67.8	0.8	-0.171	49.9500	71.6571	0.8531	-0.2171	3.8571	0.0531	-0.0461
46.8	72.7	0.8	-0.025	46.9312	76.5534	0.8519	-0.2963	3.8534	0.0519	-0.2713
45.2	75.9	0.8	-0.297	44.9438	80.4557	0.8546	-0.3563	4.5557	0.0546	-0.0593

43	80	0.8	-0.0359	42.9375	83.5093	0.8414	-0.4043	3.5093	0.0414	-0.3684
61.4	48.5	0.7	0.118	61.9687	54.4377	0.8017	0.0732	5.9377	0.1017	-0.0448
59.9	49.8	0.7	0.094	59.9625	55.7399	0.7941	0.0409	5.9399	0.0941	-0.0531
57	52.1	0.7	0.045	56.9812	54.6148	0.7352	0.0222	2.5148	0.0352	-0.0228
55	54	0.7	0.01	54.9750	56.3265	0.7315	-0.0127	2.3265	0.0315	-0.0227
52	57.1	0.7	-0.047	51.9750	59.493	0.7293	-0.0703	2.393	0.0293	-0.0233
50	59.8	0.7	-0.088	49.9312	61.8445	0.7266	-0.1111	2.0445	0.0266	-0.0231
46.7	63.9	0.7	-0.158	46.9687	66.7397	0.7335	-0.1847	2.8397	0.0335	-0.0267
44.9	67	0.7	-0.202	44.9438	69.6663	0.7286	-0.2300	2.6663	0.0286	-0.0280
43.6	69.2	0.7	-0.235	42.9562	72.4924	0.7197	-0.2730	3.2924	0.0197	-0.0380
56.5	44.8	0.6	0.104	56.9438	49.6188	0.6661	0.0665	4.8188	0.0661	-0.0375
55	46	0.6	0.078	54.9750	50.2468	0.6525	0.0427	4.2468	0.0525	-0.0353
51.6	48.6	0.6	0.025	51.9562	50.7757	0.6255	0.0106	2.1757	0.0255	-0.0144
50	50.2	0.6	0.002	49.9500	51.6904	0.6133	-0.0155	1.4904	0.0133	-0.0175
46.6	54.2	0.6	-0.067	46.9312	56.5217	0.6265	-0.0857	2.3217	0.0265	-0.0187
45.2	56	0.6	-0.094	44.9812	58.0337	0.6155	-0.1159	2.0337	0.0155	-0.0219
43	59.2	0.6	-0.144	42.9562	61.4634	0.6181	-0.1639	2.2634	0.0181	-0.0199
51.7	39	0.5	0.105	51.9750	46.3636	0.5762	0.0494	7.3636	0.0762	-0.0556
50	40.8	0.5	0.078	49.9312	45.3699	0.5470	0.0399	4.5699	0.0470	-0.0381
46.8	43.6	0.5	0.026	46.9500	45.7943	0.5244	0.0101	2.1943	0.0244	-0.0159
45	45.2	0.5	-0.002	44.9438	46.4971	0.5126	-0.0136	1.2971	0.0126	-0.0116
43	47.3	0.5	-0.038	42.9562	49.0435	0.5149	-0.0531	1.7435	0.0149	-0.0151

Resultados de corrección de ángulos y coordenadas con el prototipo II (con red neuronal).

Real Values (degrees, m)				**Measured angles (degrees)**		**Corrected angles and new calculated coordinates**			**New calculated error**		
C angle	**B angle**	**X**	**Y**	**C angle**	**B angle**	**B angle**	**X**	**Y**	**ΔB (degrees)**	**ΔX (m)**	**ΔY (m)**
64.7	62.3	1.0	-0.027	64.9687	67.5996	62.6312	1.0156	0.0257	0.3312	0.0156	0.0527
62.6	64.25	1.0	-0.016	62.9625	67.1964	64.3507	1.0096	-0.0152	0.1007	0.0096	0.0008
61.3	65.5	1.0	-0.046	61.9687	68.9497	65.4971	1.0119	-0.0388	-0.0029	0.0119	0.0072
59.7	67.3	1.0	-0.0850	59.9625	73.4938	68.5265	1.0292	-0.0951	1.2265	0.0292	-0.0101
57.2	70.2	1.0	-0.143	57.9375	76.117	70.7391	1.0248	-0.1419	0.5391	0.0248	0.0011
54.6	74.3	1.0	-0.11	54.9750	79.5349	74.0587	1.0137	-0.2105	-0.2413	0.0137	-0.1005
51.7	78	1.0	-0.2875	51.9750	83.1396	77.4557	0.9955	-0.2785	-0.5443	-0.0045	0.0090
50.5	79.9	1.0	-0.318	50.9812	85.4484	79.5244	1.0048	-0.3142	-0.3756	0.0048	0.0038
49.8	81.2	1.0	-0.345	49.9312	88.7413	82.6647	1.0311	-0.3673	1.4647	0.0311	-0.0223
46.8	86.3	1.0	-0.43	46.9500	91.7871	86.4637	1.0041	-0.4380	0.1637	0.0041	-0.0080

44.7	90.5	1.0	-0.509	44.9812	99.4492	92.9181	1.0530	-0.5537	2.4181	0.0530	-0.0447
65.25	56.75	0.9	0.087	65.9437	61.2048	59.6463	0.9690	0.0674	2.8963	0.0690	-0.0196
64.5	57.7	0.9	0.071	64.9500	62.3292	61.3678	0.9869	0.0388	3.6678	0.0869	-0.0322
62.5	59.4	0.9	0.033	62.9812	61.9322	61.2830	0.9453	0.0179	1.8830	0.0453	-0.0151
59.5	62.5	0.9	-0.03	59.9437	66.6218	62.4770	0.9093	-0.0262	-0.0230	0.0093	0.0038
56.4	65.8	0.9	-0.093	56.9625	69.0069	65.1377	0.8979	-0.0839	-0.6623	-0.0021	0.0091
54.9	68	0.9	-0.135	54.9562	72.4962	68.3947	0.9113	-0.1391	0.3947	0.0113	-0.0041
52.5	71	0.9	-0.19	52.9312	74.8963	70.5935	0.9027	-0.1820	-0.4065	0.0027	0.0080
50	75	0.9	-0.257	49.9500	80.2548	75.3960	0.9081	-0.2634	0.3960	0.0081	-0.0064
45	83.7	0.9	-0.403	44.9812	89.2128	83.8731	0.9025	-0.4031	0.1731	0.0025	-0.0001
42.27	88.27	0.9	-0.474	42.9375	92.4444	87.8892	0.8996	-0.4668	-0.3808	-0.0004	0.0072
62.5	53.8	0.8	0.084	62.9625	57.3998	56.3338	0.8500	0.0662	2.5338	0.0500	-0.0178
59.8	56.2	0.8	-0.034	59.9812	59.5533	54.8774	0.7805	0.0490	-1.3226	-0.0195	0.0830
56.5	59.6	0.8	-0.031	56.9625	62.2866	59.1127	0.8010	-0.0209	-0.4873	0.0010	0.0101
54.9	61.3	0.8	-0.06	54.9532	64.0569	61.2879	0.8005	-0.0615	-0.0121	0.0005	-0.0015
51.8	65.15	0.8	-0.013	51.9375	67.7942	64.9321	0.7995	-0.1260	-0.2179	-0.0005	-0.1130
50	67.8	0.8	-0.171	49.9500	71.6571	68.1909	0.8060	-0.1775	0.3909	0.0060	-0.0065
46.8	72.7	0.8	-0.025	46.9312	76.5534	72.5919	0.8011	-0.2488	-0.1081	0.0011	-0.2238
45.2	75.9	0.8	-0.297	44.9438	80.4557	75.9260	0.7983	-0.2999	0.0260	-0.0017	-0.0029
43	80	0.8	-0.0359	42.9375	83.5093	78.3853	0.7811	-0.3395	-1.6147	-0.0189	-0.3036
61.4	48.5	0.7	0.118	61.9687	54.4377	48.7337	0.7093	0.1224	0.2337	0.0093	0.0044
59.9	49.8	0.7	0.094	59.9625	55.7399	50.3907	0.7114	0.0887	0.5907	0.0114	-0.0053
57	52.1	0.7	0.045	56.9812	54.6148	50.9854	0.6849	0.0549	-1.1146	-0.0151	0.0099
55	54	0.7	0.01	54.9750	56.3265	53.5431	0.6946	0.0132	-0.4569	-0.0054	0.0032
52	57.1	0.7	-0.047	51.9750	59.493	57.4400	0.7040	-0.0505	0.3400	0.0040	-0.0035
50	59.8	0.7	-0.088	49.9312	61.8445	59.9479	0.7044	-0.0925	0.1479	0.0044	-0.0045
46.7	63.9	0.7	-0.158	46.9687	66.7397	64.2564	0.7063	-0.1594	0.3564	0.0063	-0.0014
44.9	67	0.7	-0.202	44.9438	69.6663	66.7265	0.6983	-0.1997	-0.2735	-0.0017	0.0023
43.6	69.2	0.7	-0.235	42.9562	72.4924	69.0430	0.6863	-0.2371	-0.1570	-0.0137	-0.0021
56.5	44.8	0.6	0.104	56.9438	49.6188	45.1885	0.6082	0.1042	0.3885	0.0082	0.0002
55	46	0.6	0.078	54.9750	50.2468	46.5689	0.6070	0.0746	0.5689	0.0070	-0.0034
51.6	48.6	0.6	0.025	51.9562	50.7757	47.8437	0.5925	0.0364	-0.7563	-0.0075	0.0114
50	50.2	0.6	0.002	49.9500	51.6904	49.2631	0.5876	0.0061	-0.9369	-0.0124	0.0041
46.6	54.2	0.6	-0.067	46.9312	56.5217	54.9791	0.6114	-0.0715	0.7791	0.0114	-0.0045
45.2	56	0.6	-0.094	44.9812	58.0337	56.5456	0.6019	-0.1023	0.5456	0.0019	-0.0083
43	59.2	0.6	-0.144	42.9562	61.4634	59.6011	0.6022	-0.1467	0.4011	0.0022	-0.0027
51.7	39	0.5	0.105	51.9750	46.3636	42.6663	0.5356	0.0811	3.6663	0.0356	-0.0239
50	40.8	0.5	0.078	49.9312	45.3699	41.8864	0.5112	0.0700	1.0864	0.0112	-0.0080
46.8	43.6	0.5	0.026	46.9500	45.7943	42.8568	0.4970	0.0357	-0.7432	-0.0030	0.0097
45	45.2	0.5	-0.002	44.9438	46.4971	43.9339	0.4902	0.0088	-1.2661	-0.0098	0.0108
43	47.3	0.5	-0.038	42.9562	49.0435	46.9810	0.4982	-0.0351	-0.3190	-0.0018	0.0029

APÉNDICE E.

Imágenes y planos del modelado y fabricación del prototipo II

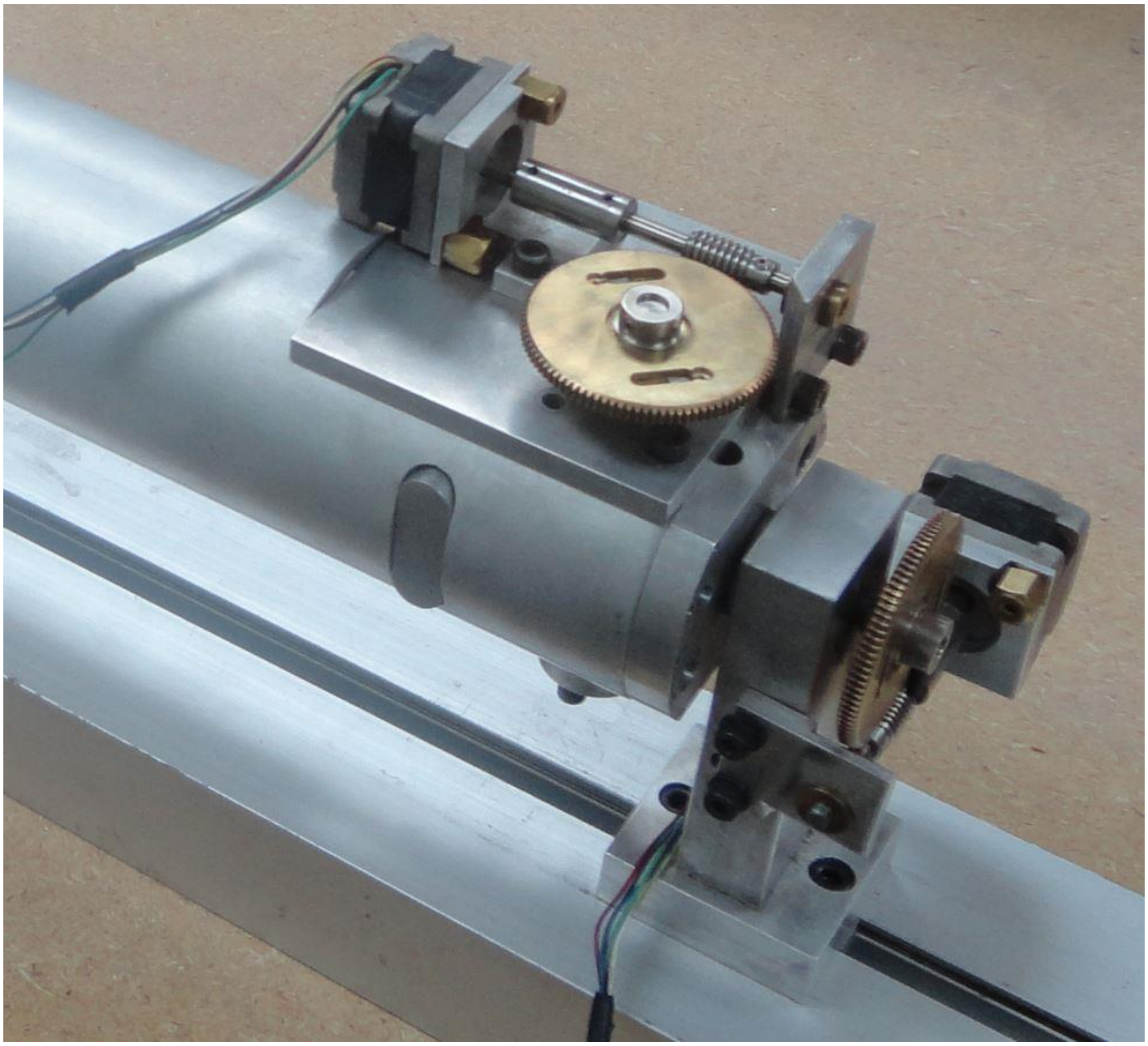

Vista angular superior del subsistema de posicionamiento de láser en el prototipo II.

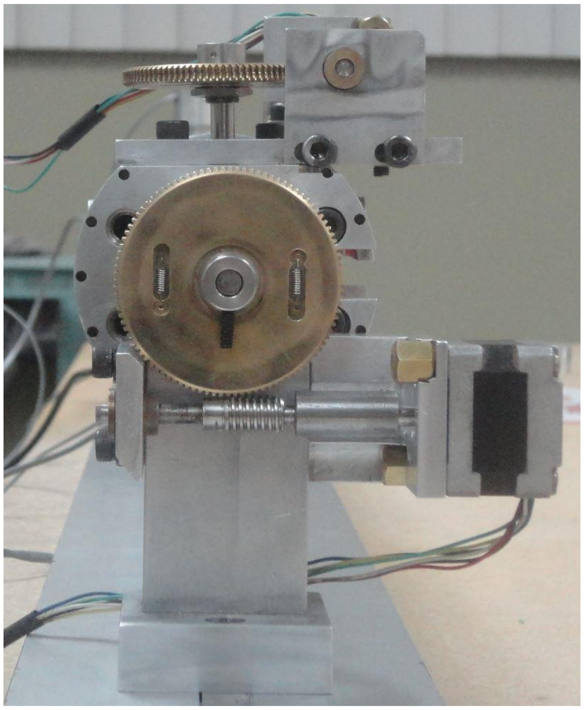

Vista lateral del subsistema de posicionamiento de láser en el prototipo II.

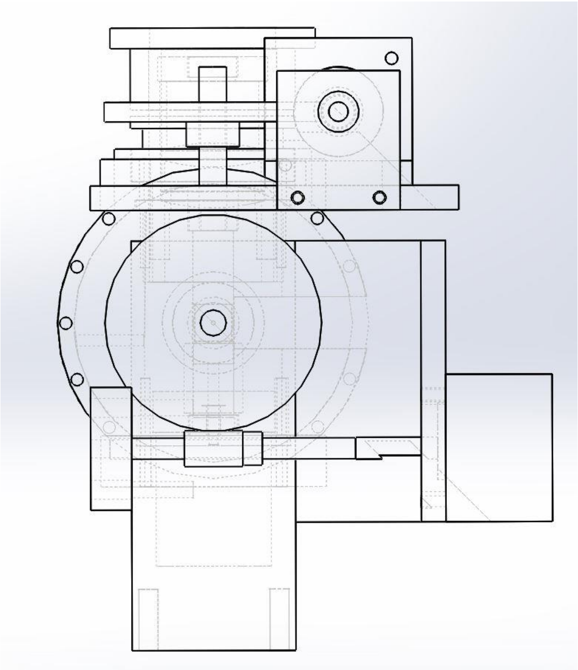

Vista lateral del modelo 3D del subsistema de posicionamiento de láser, prototipo II.

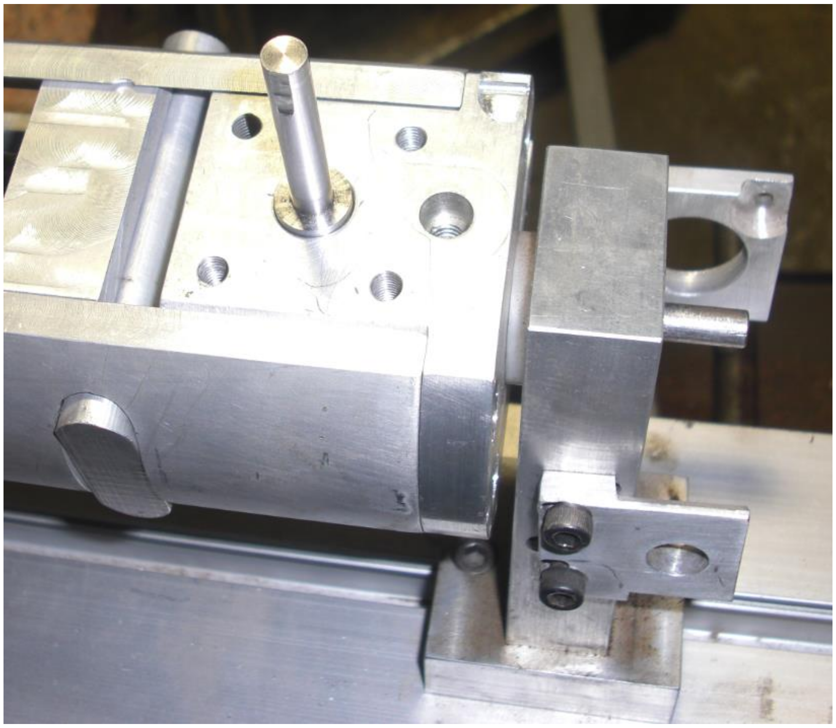

Subsistema de posicionamiento de láser durante su fabricación

Engrane anti-juego, flecha con espejo corte 45° y guía de la flecha

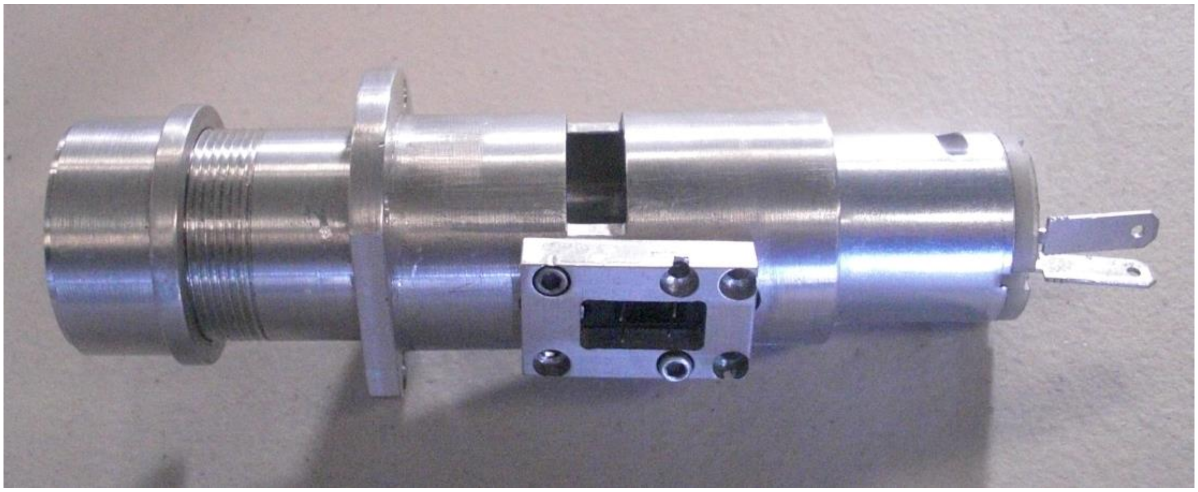

Subsistema de apertura de barrido, cartucho ensamblado.

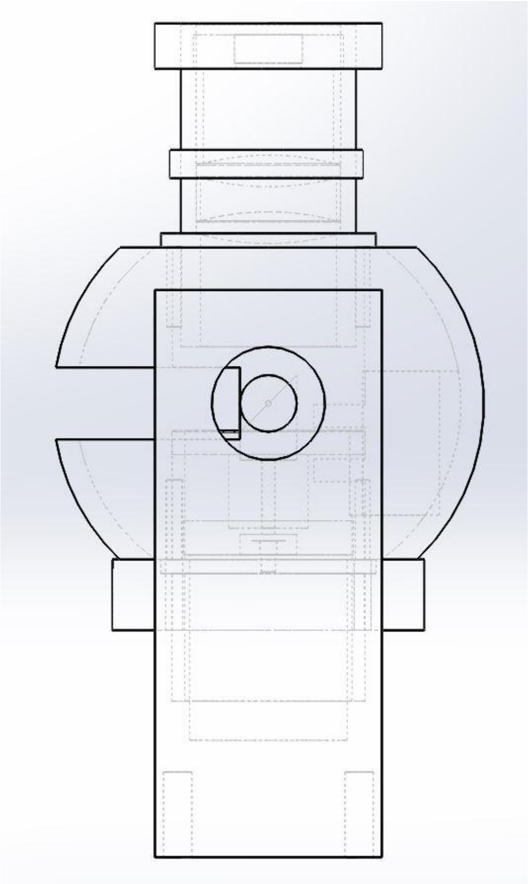

Vista lateral del modelo 3D del subsistema de apertura de barrido, prototipo II.

ANEXOS

Optics and Lasers in Engineering ∎ (∎∎∎∎) ∎∎∎–∎∎∎

Contents lists available at ScienceDirect

Optics and Lasers in Engineering

journal homepage: www.elsevier.com/locate/optlaseng

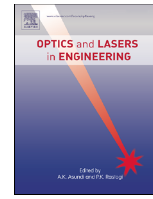

Optical 3D laser measurement system for navigation of autonomous mobile robot

Luis C. Básaca-Preciado [a], Oleg Yu. Sergiyenko [a,*], Julio C. Rodríguez-Quinonez [a], Xochitl García [a], Vera V. Tyrsa [d], Moises Rivas-Lopez [a], Daniel Hernandez-Balbuena [b], Paolo Mercorelli [c], Mikhail Podrygalo [d], Alexander Gurko [d], Irina Tabakova [e], Oleg Starostenko [f]

[a] Optoelectronics and Automated Measurement Laboratory, Engineering Institute of the Autonomous University of Baja California (UABC), Mexicali, B.C., Mexico
[b] Engineering Faculty of the Autonomous University of Baja California (UABC), Mexicali, B.C., Mexico
[c] Institute of Product and Process Innovation, Leuphana University of Lueneburg, Germany
[d] Kharkov National Highway and Automobile University, Ukraine
[e] Kharkov National University of Radioelectronics, Kharkov, Ukraine
[f] Kharkov Universidad de Las Americas, Puebla, Mexico

ARTICLE INFO

Article history:
Received 9 February 2013
Received in revised form
5 August 2013
Accepted 7 August 2013

Keywords:
Autonomous navigation
Vision system
Mobile robot
3D laser scanner
Trajectory planning

ABSTRACT

In our current research, we are developing a practical autonomous mobile robot navigation system which is capable of performing obstacle avoiding task on an unknown environment. Therefore, in this paper, we propose a robot navigation system which works using a high accuracy localization scheme by dynamic triangulation. Our two main ideas are (1) integration of two principal systems, 3D laser scanning technical vision system (TVS) and mobile robot (MR) navigation system. (2) Novel MR navigation scheme, which allows benefiting from all advantages of precise triangulation localization of the obstacles, mostly over known camera oriented vision systems. For practical use, mobile robots are required to continue their tasks with safety and high accuracy on temporary occlusion condition. Presented in this work, prototype II of TVS is significantly improved over prototype I of our previous publications in the aspects of laser rays alignment, parasitic torque decrease and friction reduction of moving parts. The kinematic model of the MR used in this work is designed considering the optimal data acquisition from the TVS with the main goal of obtaining in real time, the necessary values for the kinematic model of the MR immediately during the calculation of obstacles based on the TVS data.

1. Introduction

Autonomous robot navigation and collision prevention tasks are becoming very important not only in the automotive industry but also in scientific research such as planet exploration e.g., the Mars Rover by NASA [1], exploration of unknown or dangerous terrain such as DEPTHX project by Carnegie Mellon University in Mexico [2], autonomous vehicles like Stanley in the DARPA Grand Challenge by Stanford University [3], among others.

Optical methods seem to be a very attractive option for such solution. However, its application is still of great demand due to its main weak point, which supposes that most of optical methods are for probabilistic estimation, not for measurement of real obstacle spatial position. Or those methods that can measure, they are still very sensitive to vibrations or any other kinds of mechanical noise. This paper is aiming to propose a robust and precise way to obtain a digitized map of robot's surrounding with metrological quality by means of optical measurements.

Autonomous vehicles such as Stanley from Stanford University (see Fig. 1) and most of the vehicles that have participated in the DARPA Grand or Urban Challenge [4] like Boss by Carnegie Mellon University [5], Odin by Virginia Tech [6], Talos from MIT [7], among others, use a combination or fusion of sensors to acquire the necessary information to detect obstacles and roads, required for safe traveling such as Light Detection and Raging (LIDAR), RADAR, Stereo Vision, GPS, Inertial navigation system. This is very important and a great advantage in comparison with autonomous

* Corresponding author. Tel.: +52 6861687170.
E-mail addresses: luis.basaca@uabc.edu.mx (L.C. Básaca-Preciado), srgnk@iing.mxl.uabc.mx, srgnk@mail.ru (O.Yu. Sergiyenko), julio.rodriguez37@uabc.edu.mx (J.C. Rodríguez-Quinonez), xomagac@hotmail.com (X. García), vera-tyrsa@mail.ru (V.V. Tyrsa), mrivas@uabc.edu.mx (M. Rivas-Lopez), mercorelli@uni.leuphana.de (P. Mercorelli), pmikh@rambler.ru (M. Podrygalo), agrk@mail.ru (A. Gurko).

0143-8166/$ - see front matter © 2013 Published by Elsevier Ltd.
http://dx.doi.org/10.1016/j.optlaseng.2013.08.005

Fig. 1. Stanley—the Stanford Autonomous Vehicle that won the DARPA Grand Challenge.

vehicles using a single sensor to detect obstacles. However, the more sensors are included the higher the cost of the autonomous vehicle, this can be considered a great disadvantage if the available processing resources are not enough for full sensor fusion.

Nonetheless, the evident high cost of such systems is not its worst disadvantage; it still undermines another one. Such a versatility of the devices in use remains due to an uncertain situation in regards to which one of the multiple sensory system provides in a present moment the most proper information about the surrounding of the mobile robot.

In other words, such complex multisensory system always provides redundant information about the current situation on the robot's trajectory, and the most important task in this case is to properly filter this information and to correctly detect which one of the multisensory components is the most correct (less error) in a current moment. Such task is the main problem in dead reckoning and it consumes a huge capacity of computational resource.

Accordingly, as it is shown in all the mentioned publications about the autonomous vehicles that participated in the DARPA challenges [4], mobile robots equipped with such complex multi-sensory system still cannot achieve sufficient velocity, which is caused, first of all, by the necessity to solve in real time the difficult task of optimal data search.

Most of the relevant research, present autonomous robots using 2D laser range finders and servo motors for rotation [8,9]. Others propose stereo vision systems that utilizes two cameras to obtain two images of the same object from different points of view and reconstruct a 3D scene, such approach does not give true Cartesian coordinates of the object or obstacle, it just permits an evaluation of the shape and size of the obstacle, based on complex probabilistic algorithms of image processing [10–14]. Finally, it is very time consuming for a processor, it lacks precision, present solutions does not yet allow for a full 3D-reconstruction of the scene and it does not guarantee for errors or image misunderstanding.

Systems that use structured light methods for 3D shape measurement such as [37] present great advantages over stereo vision systems e.g., faster measurement performance and simpler processing algorithms but they also present a few disadvantages such as higher cost equipment, greater dimensions of the overall 3D system and the need of being connected to an AC power supply; these characteristics may limit this system to static applications as the author states in the conclusions of [37], such as computer graphics, medical diagnostics, plastic surgery, industrial inspection and reverse engineering instead of mobile applications such as robot navigation, mine exploration, rescue operations, among others. Although it is worth mentioning that this type of system may be modified to be applied in mobile applications but with some trade-offs.

Therefore, in this paper we present an autonomous mobile robot navigation system that utilizes a low cost high precision vision system with sufficient reliability of information about the surrounding of the mobile robot to allow the mobile robot's navigation system to make decisions regarding the path or trajectory it should follow to achieve its goal.

Our navigation system consists of a new method of motion planning and the mathematical model of a four wheel, four motor skid-steer mobile robot used to successfully navigate without collisions in an (indoor and outdoor) environment with obstacles.

This navigation system obtains the surrounding environment information by means of a 3D laser scanning vision system which is briefly explained in Section 2. The mechanical characteristics and specifications of the mobile robot are explained in Section 3. The mobile robot kinematics model is found in Section 4. In Section 5 our navigation system is presented. Section 6 presents the simulation results of our work with the TVS and the navigation system; followed by the statistical analysis of the data obtained through experimentation in Section 7; and at the end, the conclusions of this work are presented.

2. Technical vision system (TVS)

As mentioned before, the presented navigation system will obtain the environment information from our TVS. This system has been partially presented before in [15,16,35]; therefore the explanation will only contain the most important aspects of the TVS.

2.1. Dynamic triangulation method

The TVS is based on a method we developed which is called dynamic triangulation, it is called dynamic due to the rotation ability of the positioning laser and the scanning aperture, allowing us to have moving angles that can form laser light triangles with different shapes for a very short period of time and when a triangle is formed thanks to the reflected light of an obstacle surface, we obtain all the necessary information to calculate the 3D coordinates.

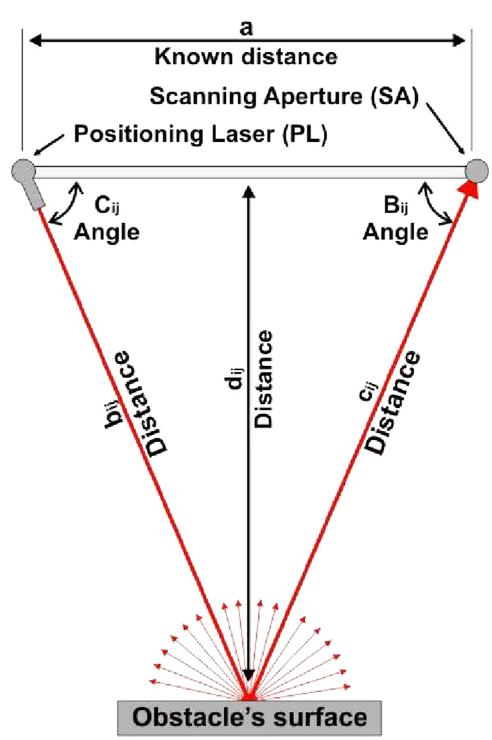

Fig. 2. Dynamic triangulation method.

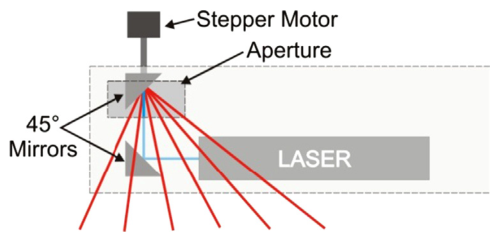

Fig. 3. Positioning laser principle.

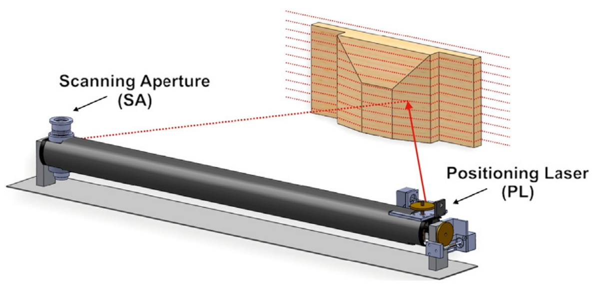

Fig. 4. TVS with tilt mechanism 3D model.

Fig. 2 shows the dynamic triangulation method used by the TVS. The main components of the TVS are the positioning laser (PL) and the scanning aperture (SA).

2.2. Positioning laser (PL)

The PL contains the next main elements which interact in the following way: a laser that emits its beam toward a fixed 45° mirror; this mirror redirects the beam orthogonally into a rotating 45° mirror which rotation is driven by a stepper motor. By controlling this motor we control the direction at which we want to direct the laser to verify the presence of obstacles; PL is driven by a stepper motor to control the laser direction. See Fig. 3.

The SA principle is more complex than the PL and it will be explained later, however the purpose of the SA is to receive the reflected laser rays indicating that an obstacle has been detected and to calculate the B_{ij} angle which is needed for the 3D coordinates calculation.

The method shown in Fig. 2 functions for 2D coordinates measurement x and y. However, we desire to measure 3D coordinates and in order to do that, we added to the TVS a tilt mechanism (see Fig. 4) which allows us to rotate the device in order to perform additional scans at different heights along z axis, thus adding the third dimension coordinate z.

2.3. Scanning aperture (SA)

The SA is the most important component of the TVS (see Fig. 5) and is in charge of receiving the reflected laser rays through the aperture into a 45° rotating mirror which is rotated with constant speed by a DC motor. Then the captured laser rays are redirected orthogonally to a lens array to finally be received by the stop sensor (high speed photo-transistor) and when is activated we know an obstacle has been detected. The Zero sensor monitors the motor's position so we can know the precise time the mirror rotates 360°; this information will be used later to calculate the B_{ij} angle.

The following equation is used to calculate angle B_{ij}:

$$B_{ij} = \frac{2\pi N_A}{N_{2\pi}} \tag{1}$$

where N_A is the number of reference pulses when laser rays are detected by the stop sensor and $N_{2\pi}$ is the number of reference pulses when the 45° mirror completes a 360° turn detected by the zero sensor. See Fig. 5. For a more detailed explanation and figures see [16,18].

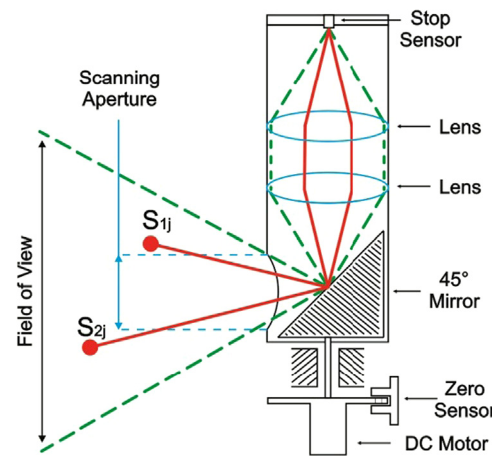

Fig. 5. Scanning aperture (SA).

2.4. 3D coordinates calculation

In order to calculate the x, y and z coordinates of any reflected point from an obstacle surface, we developed a set of equations derived from the law of sines (Eqs. (2)–(5)). These equations require the angles B_{ij}, C_{ij}, $\Sigma_{\beta j}$ and a (fixed distance between the center of PL and the center of SA) to calculate the 3D coordinates [15].

$$x_{ij} = a \frac{\sin B_{ij} \cdot \sin C_{ij} \cdot \cos \sum_{j=1}^{j} \beta_j}{\sin[180° - (B_{ij} + C_{ij})]}, \tag{2}$$

$$y_{ij} = a\left(\frac{1}{2} - \frac{\sin B_{ij} \cdot \cos C_{ij}}{\sin[180° - (B_{ij} + C_{ij})]}\right) \quad \text{at} \quad B_{ij} \le 90°, \tag{3}$$

$$y_{ij} = -a\left(\frac{1}{2} + \frac{\sin B_{ij} \cdot \cos C_{ij}}{\sin[180° - (B_{ij} + C_{ij})]}\right) \quad \text{at} \quad B_{ij} \ge 90°, \tag{4}$$

$$z_{ij} = a \cdot \frac{\sin B_{ij} \cdot \sin C_{ij} \cdot \sin \sum_{j=1}^{j} \beta_j}{\sin[180° - (B_{ij} + C_{ij})]} \tag{5}$$

During the TVS operation, the x, y, z coordinates are calculated and stored in a multidimensional $20 \times 20 \times 4$ matrix. The first dimension contains a digital map of the field of view of the mobile robot; each matrix ij position can have a value of 0 or 1. A 0 means no obstacle is found and a 1 means reflection was detected and an obstacle is found at that point.

The second dimension contains the B_{ij} angle information, for each ij position of the 1st dimension; a corresponding and calculated B_{ij} angle is stored at the same position on the 2nd dimension. This also occurs for C_{ij} angle on the 3rd dimension and the $\Sigma_{\beta j}$ on the 4th dimension. This information is then sent to the mobile robot navigation system to analyze and take navigation decisions e.g., obstacle avoidance and trajectory planning.

Experimental results have been obtained from TVS prototype I and some are published on [18–21]. However, we can assure that the TVS prototype I has a 95% confidence level on its coordinates measurements [15]. A prototype II has been fabricated with several mechanical improvements over prototype I [16,17], new experimental results are presented in Section 7.

Please cite this article as: Básaca-Preciado LC, et al. Optical 3D laser measurement system for navigation of autonomous mobile robot. Opt Laser Eng (2013), http://dx.doi.org/10.1016/j.optlaseng.2013.08.005

3. Mobile robot specifications

As shown in our previous publications in this scope, until now we have been considering the proposed TVS as a pure theoretical task to resolve. However, on the present stage of research it is desirable connect our TVS with a certain industrially fabricated mobile robot in order to fully integrate them to each other by their working parameters (weight, size, operation speed, mobility skills, etc.)

Several known robot models were considered preliminary but we decided to base our work in the Pioneer 3-AT (Fig. 6) which is a small, four-wheel, four-motor skid-steer intelligent robotics platform, which in our opinion is well matched with our offered TVS. The Pioneer 3-AT can fulfill our needs of a mobile robot platform to implement our navigation and 3D vision systems due to its powerful microcontroller (44.2368 MHz Renesas SH2 32-bit RISC µC with 32KRAM and 128K FLASH; ARCOS firmware), the four wide pneumatic tires which in conjunction with the four DC motors equipped with encoders (135,465 ticks per revolution), provide high traversability and maneuverability, three long duration batteries (12 VDC at 7.2 Ah each) that last 4–6 continuous hours and the option to have an onboard laptop computer.

All of these characteristics make the Pioneer 3-AT a very suitable research development platform to implement our navigation and 3D vision system for autonomous mobile robots. On the next section the kinematics analysis for the mobile robot is presented.

4. Mobile robot kinematics

This section presents a kinematic analysis and the necessary transforms to control our mobile robot in a three dimensional space.

Fig. 6. Pioneer 3-AT mobile robotic platform.

The axis convention used for the frame assignment is that the z axis points up (aligned with local gravity), the y axis points to the right of the mobile robot (east) and the x axis points forward (north).

The frame assignment is shown in Fig. 7a–c. Frame 0 is the reference frame for navigation, the frame r stands for robot frame and is located at the center of gravity of the mobile robot, w1–w4 is for wheels 1 to 4 (these frames are located in the rotation axis at the center of the wheels and they rotate with the wheels), frames e and s are located in the vision system (mounted on a tilt mechanism that rotates around the x axis) and they belong to the emitter and sensor respectively.

In order to represent the position and orientation in space we need six pieces of information, three for position and three for orientation. For position we use a homogeneous transform matrix to translate the mobile robot to the desired position and then we use RPY angles (roll, pitch, yaw) to adjust the robot to the desired orientation, RPY angles are a sequence of three rotations about the current frame $\vec{a}$, $\vec{o}$, $\vec{n}$ moving axes (approach, orientation and normal) respectively, i.e., each rotation about $\vec{a}$, $\vec{o}$, $\vec{n}$ axes is represented with a 4×4 matrix and the multiplication of these three matrices describes the desired orientation of an object in space using RPY angles, this is shown in Eq. (8). The $\vec{a}$, $\vec{o}$, $\vec{n}$ axes (from the current frame) are parallel to x, y, z (reference frame) at the origin position (before any movement) [22]. The sequence of transformations stated on Eq. (7), defines the forward kinematics model for this robot which represents the current position and orientation of the robot relative to a fixed reference frame.

The following equations were defined to control the position and orientation of the mobile robot in a tridimensional space relative to a fixed reference frame:

$$^{0}T_{r} = Trans(x,y,z) \times RPY(\varphi,\theta,\psi) \tag{6}$$

$$^{0}T_{r} = Trans(x,y,z) \times Rot(\vec{a},\varphi) \times Rot(\vec{o},\theta) \times Rot(\vec{n},\psi) \tag{7}$$

$$\begin{aligned} ^{0}T_{r} = &\begin{bmatrix} 1 & 0 & 0 & x \\ 0 & 1 & 0 & y \\ 0 & 0 & 1 & z \\ 0 & 0 & 0 & 1 \end{bmatrix} \times \begin{bmatrix} c\varphi & -s\varphi & 0 & 0 \\ s\varphi & c\varphi & 0 & 0 \\ 0 & 0 & 1 & 0 \\ 0 & 0 & 0 & 1 \end{bmatrix} \\ &\times \begin{bmatrix} c\theta & 0 & s\theta & 0 \\ 0 & 1 & 0 & 0 \\ -s\theta & 0 & c\theta & 0 \\ 0 & 0 & 0 & 1 \end{bmatrix} \times \begin{bmatrix} 1 & 0 & 0 & 0 \\ 0 & c\psi & -s\psi & 0 \\ 0 & s\psi & c\psi & 0 \\ 0 & 0 & 0 & 1 \end{bmatrix} \end{aligned} \tag{8}$$

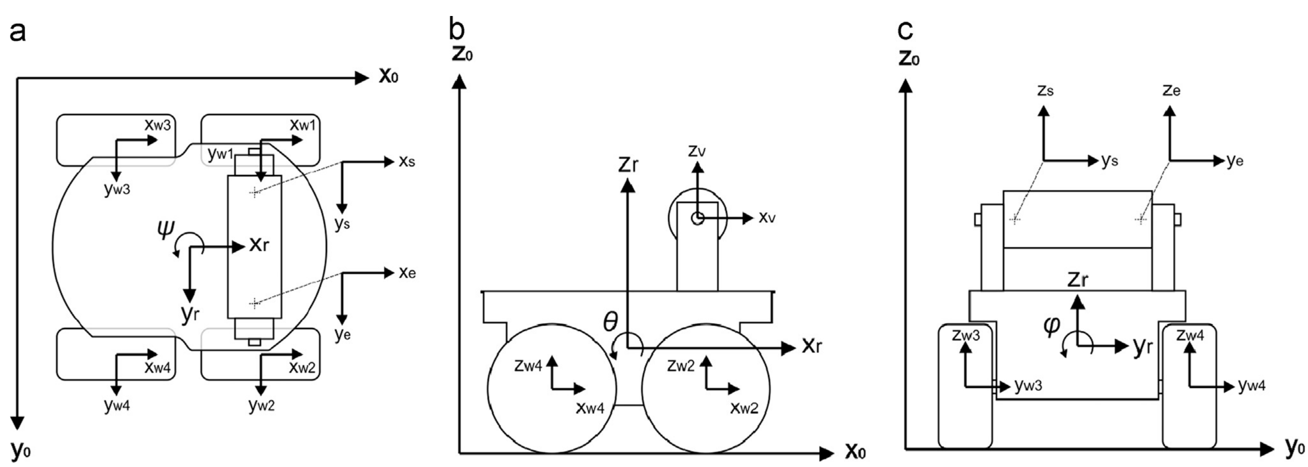

Fig. 7. Frames assignment: (a) top view; (b) side view; and (c) back view.

Please cite this article as: Básaca-Preciado LC, et al. Optical 3D laser measurement system for navigation of autonomous mobile robot. Opt Laser Eng (2013), http://dx.doi.org/10.1016/j.optlaseng.2013.08.005

$$^{0}T_r=\begin{bmatrix} c\varphi c\theta & c\varphi s\theta s\psi - s\varphi c\psi & c\varphi s\theta c\psi + s\varphi s\psi & x \\ s\varphi c\theta & s\varphi s\theta s\psi + c\varphi c\psi & s\varphi s\theta c\psi - c\varphi s\psi & y \\ -s\theta & c\theta s\psi & c\theta c\psi & z \\ 0 & 0 & 0 & 1 \end{bmatrix} \tag{9}$$

$$^{0}T_r=\begin{bmatrix} 1 & 0 & 0 & a \\ 0 & c\psi & -s\psi & b \\ 0 & s\psi & c\psi & c \\ 0 & 0 & 0 & 1 \end{bmatrix} \tag{10}$$

where the first three columns of Eq. (9) represents the unit vectors for orientation ($\vec{n}, \vec{o}, \vec{a}$), the last column represents the position vector in Cartesian coordinates (x, y, z), $^{0}T_r$ stands for transformation matrix of frame r relative to frame 0 (or reference frame), $c\varphi$ is used as an abbreviation of $\cos\varphi$ and $s\varphi$ for $\sin\varphi$ (the same for angles θ and ψ).

The RPY angles (roll, pitch, yaw) sequence consist of the following transformations: a rotation of φ about the robot's $\vec{a}$ axis, called roll; a rotation of θ about the robot's $\vec{o}$ axis, called pitch; and a rotation of ψ about the robot's $\vec{n}$ axis, called yaw. Angles are measured counterclockwise positive according to the right hand rule. By doing this forward kinematics analysis (Eq. (9)); We can calculate the position and orientation of the robot at any instant and we can use this equation to find the inverse kinematics equations that will enable us to calculate the variables needed to control and move the mobile robot to a desired position and orientation. RPY angles we can get using the advanced accelerometers interrogation system with LMS adaptive filter already presented in [32,33]

It is important to state that rotations values in Eq. (7) (or elements x_{11}–x_{33} of matrix in Eq. (9)) coming from accelerometers using formalism of [32,33] and fourth column in all matrixes of Eq. (8) (or last column in general matrix of Eq. (9)) are defining the spatial position of our robot in Cartesian coordinates fixed to robot body; at the same time our TVS System (Section 2, Figs. 3–5) represent the Cartesian coordinates of the obstacles located in the same spatial volume. The Cartesian coordinates of obstacles robot can be easily transformed into the robot Cartesian system.

Our kinematic model does not have such a general nature as Dynamic Bayesian Network in due to simplification of our task conditions, but taking into account specific conditions of our robot operation it is sufficient for our practical application, and can be even more simplified for selected pair "TVS–navigation system". Taking into consideration some assumptions we can write a frame parameters table for the mobile robot, that will allow us to represent the position and orientation between every frame presented in the frame assignment (Fig. 7).

Table 1 specifies six degrees of freedom x, y, z which are three linear movements for position and ψ, θ, φ which are the RPY angles for orientation. These parameters can be variables or known values. The assumptions we made are that our mobile robot will operate in ideal floor conditions and in an indoor environment on the first stage of laboratory experimentation (in order to prove TVS functionality for this task), therefore φ and θ are set to 0 in $^{0}T_r$, leaving less variables to work with, simplifying the forward and inverse kinematics model (see Eq. (10)) and reducing the calculation time for the equations. Further experimentation will be carried out in a condition of non-zero state of φ and θ parameters.

Table 1
Frame parameter table for mobile robot at ideal conditions.

Transform	x (mm)	y (mm)	z (mm)	ψ (deg)	θ (deg)	ϕ (deg)
$^{r}T_s$	−111.7	120.6	264.1	0	var	0
$^{r}T_{w1}$	198.9	−135.8	28.5	0	var	0
$^{r}T_{w2}$	−198.9	−135.8	28.5	0	var	0
$^{r}T_{w3}$	198.9	135.8	28.5	0	var	0
$^{r}T_{w4}$	−198.9	135.8	28.5	0	var	0

The following nomenclature is used in Table 1, $^{0}T_r$ represents the transformation matrix from the frame r to the frame 0 and the same applies for the rest of the transforms; The values on the first three columns are distances in x, y, z coordinates from one frame to another and the last three columns show the angle values or rotation from one frame to another.

Assuming that the desired position and orientation achieved by Cartesian coordinates and RPY angles are known, three equations can be found from the forward kinematics model (Eqs. (12)–(14)).

$$^{0}T_r=\begin{bmatrix} r_{11} & r_{12} & r_{13} & px \\ r_{21} & r_{22} & r_{23} & py \\ r_{31} & r_{32} & r_{33} & pz \\ 0 & 0 & 0 & 1 \end{bmatrix}=\begin{bmatrix} c\varphi c\theta & c\varphi s\theta s\psi - s\varphi c\psi & c\varphi s\theta c\psi + s\varphi s\psi & a \\ s\varphi c\theta & s\varphi s\theta s\psi + c\varphi c\psi & s\varphi s\theta c\psi - c\varphi s\psi & b \\ -s\theta & c\theta s\psi & c\theta c\psi & c \\ 0 & 0 & 0 & 1 \end{bmatrix} \tag{11}$$

$$\varphi = ATAN2(r_{21}, r_{11}) \tag{12}$$

$$\theta = ATAN2(-r_{31}, r_{11}c\varphi + r_{21}s\varphi) \tag{13}$$

$$\psi = ATAN2(-r_{23}c\varphi + r_{13}s\varphi, r_{22}c\varphi - r_{12}s\varphi) \tag{14}$$

where Eq. (11) represents the known forward kinematic model and φ, θ, ψ are the unknown RPY angles. These equations form the inverse kinematic model of the mobile robot and are used to control the location of the mobile robot i.e., with this model we will be able to determine the value of each angle in order to place the mobile robot at a desired position and orientation.

5. Navigation system

As it was mentioned before, we are implementing our navigation system on the Pioneer 3-AT Robotics Platform which is a four-wheel, four-motor skid-steer mobile robot. Therefore some basic standards for mobility and operation have to be defined in order to implement the proposed TVS and navigation system in this platform.

5.1. Navigation system basic standards

The first is that due to the skid-steer characteristic of the mobile robot, the method used to steer the mobile robot to the left will be to activate the motor of wheel 2 in forward direction along with the motor of wheel 3 in reverse direction. To steer the mobile robot to the right, we will activate the motor of wheel 1 in forward direction and the motor of wheel 4 in reverse direction. During the steer operation the other two motors of the wheels that are not being used (motors 1 and 4 for left and 2 and 3 for right) will be left de-energized and free to skid in order to go along the motion. It is well known and noted that using a skid-steer method [23,24] may produce a source for uncertainty; therefore we will return to this topic in future research and compare it to other types of steering such as differential drive assisted steering [25], but for the time being we will focus on the TVS and navigation system integration.

Secondly, the main objective of our mobile robot will be to reach a final goal by avoiding any obstacles found in its trajectory. The initial trajectory will be set to the shortest secure path between the starting point and the final goal and it will be adjusted as the mobile robot detects and avoids obstacles. In the case that the mobile robot (while following a plotted trajectory) does not detect any obstacle, that trajectory will lead the mobile robot to the goal.

Please cite this article as: Básaca-Preciado LC, et al. Optical 3D laser measurement system for navigation of autonomous mobile robot. Opt Laser Eng (2013), http://dx.doi.org/10.1016/j.optlaseng.2013.08.005

The mobile robot will be using optical encoders on the four wheels to keep track of the traveled distance and a 3-axis accelerometer to monitor the orientation (RPY angles) in every new current position. It will also be equipped with a set of IR sensors. These sensors will be set to detect in a fixed distance and they will be used as a means to inform the TVS that an obstacle is inbound and a scan needs to be performed.

In other words we will be using the IR sensors to perform fast obstacle detection (presence/absence) and then the TVS will scan the field of view to calculate the 3D coordinates of the obstacle (s) visible surface to establish the exact position of the detected obstacle.

5.2. Trajectory planning

After the mobile robot detects an obstacle in its field of view, the next logical step is to plot a new trajectory for the mobile robot to reach its goal.

In order to plot a new trajectory we first take into consideration the mobile robot size and safe margins, then we calculate a certain quantity of points in space that evade the obstacle and which will lead the mobile robot to the goal by following linear movements, then we calculate a curve that will pass through those points in order to smooth the trajectory and hence the mobile robot movement.

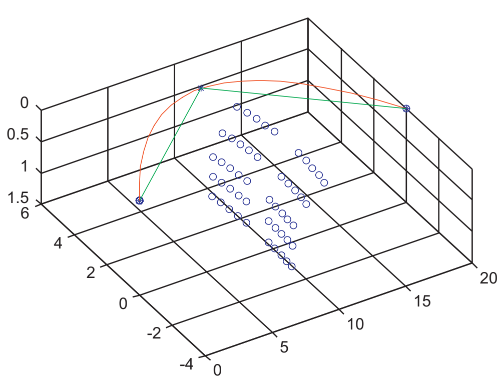

Fig. 8. Mobile robot trajectory from a Matlab simulation (scale in m), using a 3 points curve.

Our first approach was to use the minimum quantity of points needed to form a curve which is three, the result is a curve that successfully evades the obstacles and reaches the goal but in the other hand the traveled distance in form of a semi-circle results more than what is necessary (see Fig. 8).

Therefore we simulated another approach which uses 10 points instead of three to plot the trajectory and form the curve, the result (shown in Fig. 9b) is that the curve not only evades the obstacles and reaches the goal but it also reduces the traveled distance of the trajectory by 12–15% while the calculation time with more discrete points grows up only 1.2 ms. This trade-off permits us save robot resources significantly, meanwhile the operating time of control system increases insignificantly.

The first of the 10 points is the current location of the mobile robot, the second point is calculated to be on the left or right of the obstacle (depending on which end is closer to the mobile robot frame) and it is added a 50% safe margin and the robot's width to allow the mobile robot to go around the obstacle without colliding. Finally, from the third to the last one, which is the goal, a straight line is formed (this line is also smoothened as part of the curve, see Fig. 9).

To calculate the points of the curve, the robot can use the spline formalism. To simulate these we use an internal Matlab function called "spline", this function given the coordinates of the 10 point mentioned before, uses a cubic spline interpolation to find the new y, which is the values of the underlying function Y (range of the 10 points) at the values of the interpolant x (which has the new domain values for the curve).

The results are two vectors (x, y) with the values for the new trajectory from the current location of the mobile robot to the goal (solid red line on Fig. 9). Currently the new trajectory consists of 50 calculated points, this has proven to be enough for curve smoothness but this parameter can be adjusted as needed.

On Fig. 9a, a plotted view of a new trajectory is shown. The red solid line is the calculated trajectory for the mobile robot, the lines made of blue x's indicate the physical limits of the mobile robot (width); the blue circles are the detected points of an obstacle (each point contains x, y, z coordinates calculated with the TVS). Each group of blue circles represent a detected obstacle (two groups in this figure meaning two obstacles were found on this simulation), and the blue asterisks are the points used to form the trajectory curve; this is clearly seen in Fig. 9b. It is also important to note in this figure that the obstacles are being avoided by

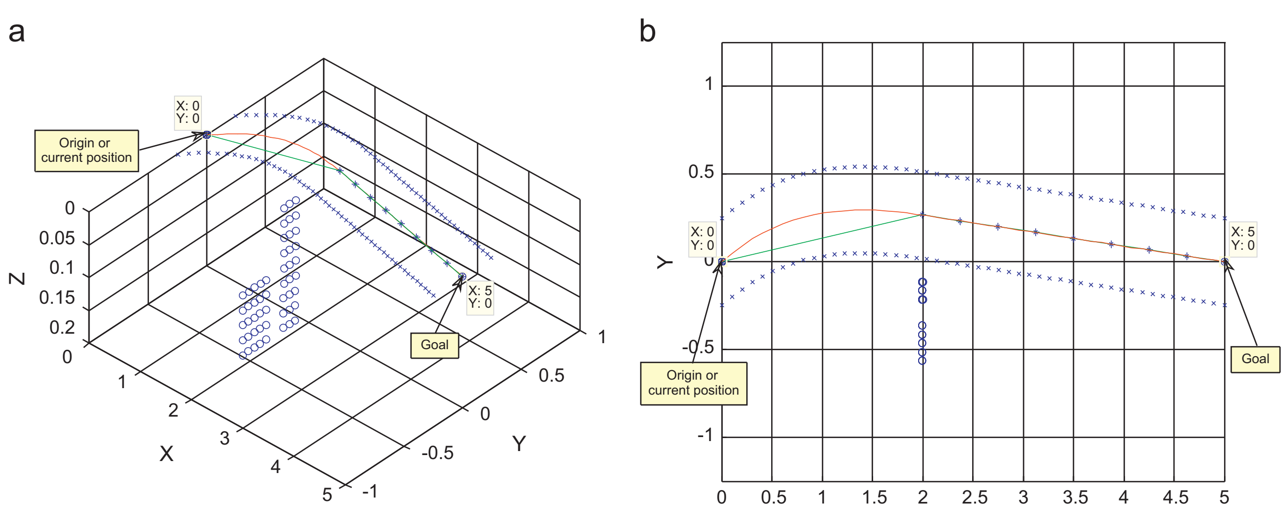

Fig. 9. Mobile robot trajectory from a Matlab simulation (scale in m), using a 10 points curve: (a) isometric view and (b) top view. (For interpretation of the references to color in this figure, the reader is referred to the web version of this article.)

Please cite this article as: Básaca-Preciado LC, et al. Optical 3D laser measurement system for navigation of autonomous mobile robot. Opt Laser Eng (2013), http://dx.doi.org/10.1016/j.optlaseng.2013.08.005

the left side of the mobile robot because our algorithm estimates the preliminary level of curvature of both possible trajectories (to the left and to the right) and selects the lower curvature i.e., the shorter trajectory.

5.3. Navigation system operation and TVS integration

Trajectory planning is a very important element of the navigation system, but it is more important to know when to calculate it or when to call the TVS to perform a scan, and what to do before and after these processes, therefore a general operations flow chart is presented. The flowchart in Fig. 10 is for the most part self-explanatory; nevertheless a few things require further explanation.

After programming the goal of the mobile robot, all following tasks are performed autonomously. The first step is to calculate and initial trajectory, this will be a straight path between the initial position (mobile robot frame origin) and the goal. After that, the mobile robot will move forward, following the calculated trajectory and it will stop as soon as an obstacle is detected by the IR sensors or if the goal has been reached.

If an obstacle has been detected, the mobile robot will stop and will call the TVS to perform a scan of the mobile robot field of view and then it will continue to calculate the 3D coordinates of any obstacle found. After calculations are done, the data will be analyzed to obtain the main characteristics and useful information of the obstacle(s), e.g., height, width, depth, distance between obstacles (if applicable), distance from the mobile robot to the obstacle (x) and to the left or right limits (y), etc.

This information will be used to calculate a new trajectory for the mobile robot to reach its goal. After the new trajectory is calculated as explained in Section 5.2, the mobile robot will follow this trajectory until either an obstacle is found or the goal is reached.

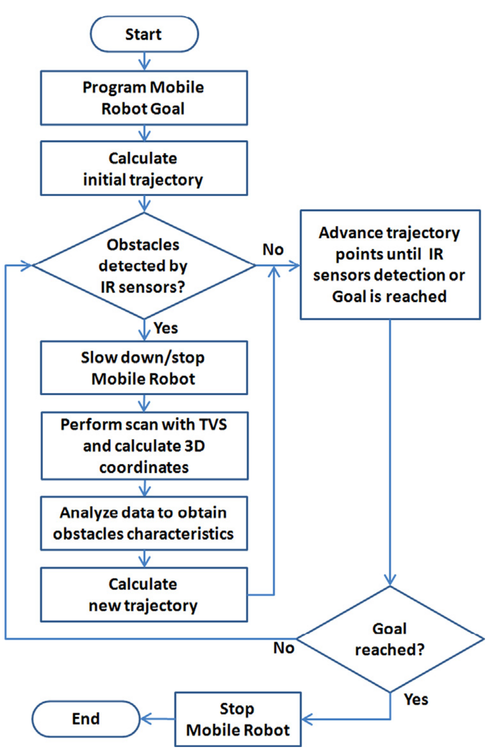

Fig. 10. Navigation system general operations flowchart.

If another obstacle is found, the same process will be repeated until the mobile robot reaches its goal, after that, the mobile robot will stop and enter a "waiting for new goal" mode.

6. Navigation system and technical vision system (TVS) simulation results

The computational experiments presented in this paper have many purposes. One of the most important is to prove the compatibility between the navigation system and TVS, in order to use the data provided by the TVS in the navigation system, this data has to be transformed and analyzed, e.g., axes rotation and adjustment, manipulation of data stored in arrays, data filtering, etc. [29,30].

As mentioned in Section 2, the data provided by the TVS comes in the form of a multidimensional $20 \times 20 \times 4$ matrix. The 1st dimension contains a digital map of the field of view of the mobile robot; each matrix ij position can have a value of 0 or 1. The 2nd dimension has the B_{ij} angles, the 3rd has the C_{ij} angles and the $\Sigma_{\beta j}$ are on the 4th dimension.

Fig. 11 shows an example in which $i=3$ and $j=3$ therefore $B_{ij}=71^\circ$ (laser angle), $C_{ij}=58^\circ$ (aperture angle) and $\Sigma_{\beta j}=4^\circ$ (vertical tilt angle).

MATLAB® (R2012a) was used to perform the simulations. The program named BASACA NAVIGATION SYSTEM (BANS) is designed to calculate robot's desired trajectory basing on 3D data from TVS to avoid collision with detected and located obstacles and at the same time avoiding sharp movements of robot's steering. Part of the code (see Appendix A) was written to calculate the 3D coordinates of detected obstacles on a scanned field of view of the mobile robot, using Eqs. (2)–(5), presented in Section 2.

The code mentioned before is just a fragment of the main Matlab program, what it does is that using two nested FOR cycles, the program runs through every position of the $20 \times 20 \times 1$ matrix and (the digital map) and if the contents of an ij position is 1, it calls for the B_{ij}, C_{ij}, and $\Sigma_{\beta j}$ values of that specific position (on the other dimensions). While it calculates the 3D coordinates, the program creates a $20 \times 20 \times 3$ matrix to store the results, the 1st dimension stores x values, the 2nd y values and the 3rd, z values.

This program also calculates the elapsed time on the coordinate's calculation, the obstacles characteristics and important distances to name a few; a fragment of the output information of BANS used for tests monitoring is shown in Appendix A.

On this simulation, after the new trajectory is calculated, the program uses x, y, z (3D coordinates calculated before) to form a 3D plot of the obstacle(s), then the origin or the mobile robot current location and the goal are added to the graph and after that, it plots in that same graph the x and y values of the new trajectory to demonstrate that the path evades the obstacle and reaches the goal. For proper autonomous robot operation, graphs will not be

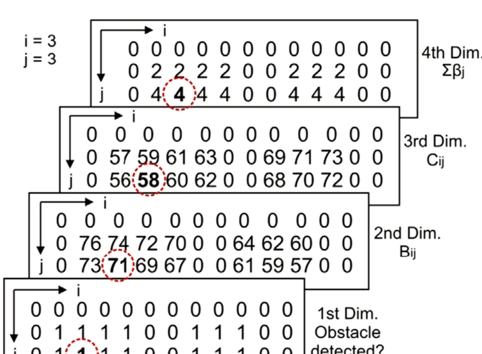

Fig. 11. Multidimensional matrix for TVS data storage and manipulation.

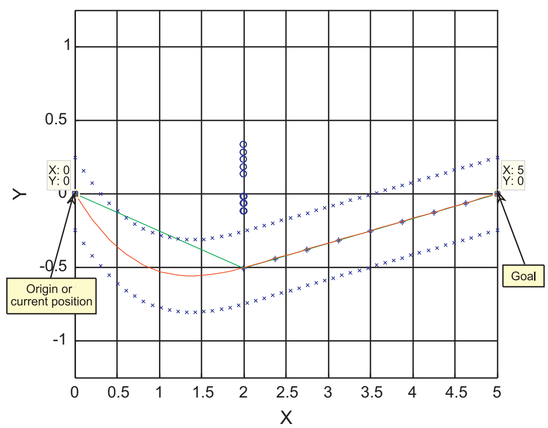

Fig. 12. Top view of the trajectory plotted to avoid obstacle by the right side of the mobile robot.

Table 2
TVS and navigation system calculation time distribution.

Operation	Calculation time (ms)	(%).
Obstacle's 3D coordinates	20.1590	20.5
Obstacle's characteristics	38.1835	38.7
Decision making	10.3025	10.5
New trajectory	6.8921	7.0
Inverse kinematics	12.2402	12.4
Total time	98.5592	100

processed or displayed to save processing time. Part of the code used to calculate the new trajectory is shown in Appendix A.

To calculate the new trajectory, first we need to know the current location of the mobile robot and the goal coordinates, the information needed is obtained from the homogeneous transform matrix and then as explained in Section 5.2, the trajectory is calculated and plotted. Fig. 9a and b shows the result of the obstacle(s) 3D coordinates and new trajectory calculation obtained with the MATLAB® code presented in this section.

In Fig. 12, a different set of inputs is being used in the simulation; therefore we have different obstacle locations and obstacle avoidance by the right side of the mobile robot.

The different algorithms and operations calculated during simulations were categorized and monitored to obtain their average duration time. For every category, 30 time samples were measured and averaged to obtain Table 2 and Fig. 13, this figure reflects the relations in time between different stages in robot's navigation, such as: data adjustment from TVS to the navigation system, obstacle's detection, location and characteristics, decision making, new trajectory planning and inverse kinematics.

The characteristics of the computer used to perform the calculations and simulations are

- Intel® Core™ i7 CPU Q720@1.6 GHz
- DDR3 8 GB RAM
- Windows 7 64-bit Operating System

7. Experimentation results and statistical analysis of the obtained data

Experimentation was performed in a controlled laboratory environment. A calibrated optical table was used to support the TVS and run 2D measurement tests with static obstacles at known locations, the third coordinate was not considered because of the

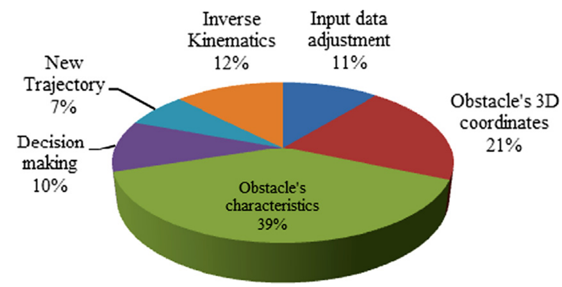

Fig. 13. Pie chart of time distribution in different stages of calculations in TVS and navigation system.

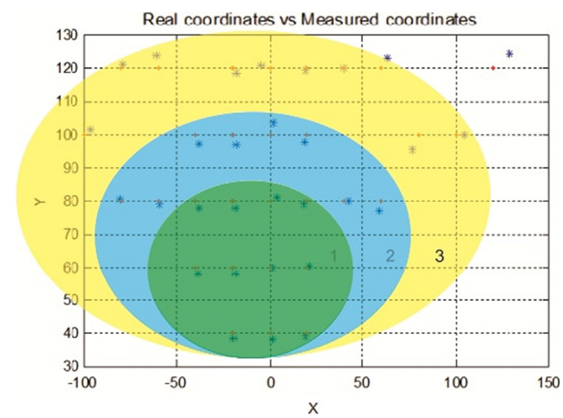

Fig. 14. Comparison graph of obstacle's real coordinates and measured coordinates with the TVS prototype I (scale in cm). (For interpretation of the references to color in this figure, the reader is referred to the web version of this article.)

same electric motor and other similar conditions of measurement, but it will be included in near future tests.

The tests performed proved that the second TVS prototype has a higher confidence level than its predecessor. According to our previous publications [15,16,35]; the first TVS prototype demonstrated 95% confidence level for coordinates measurements at the center of its field of view and it decreased for the angles at the ends. We identified three different regions inside the field of view of the TVS prototype I and each one presented different accuracy or confidence level.

The three regions are shown in Fig. 14; the first and smaller region (green) proves to be the best measurement space of the TVS with 95% average confidence level. The second (blue) and third (yellow) regions, demonstrated lower measurement confidence level. The finding of these areas allowed us to establish the working space of the TVS which is a very important piece of information to the navigation system of the mobile robot platform.

However, the first tests with TVS prototype II showed a wide range of confidence level, from 85% to 98% without any kind of data manipulation; this increase is mostly due to the mechanical improvements explained in [16]. In order to increase and stabilize the measurements confidence level a neural network was developed using the Levenberg–Marquardt method. This method is used primarily in the least square curve fitting problem: given a set of m empirical datum pairs of independent and dependent variables, (x_i, y_i) optimize the parameters b of the model curve $f(x, \beta)$ so that the sum of the squares of the deviations becomes minimal [31,34]

$$S(\beta)=\sum_{i=1}^{m}[y_i-f(x_i,\beta)]^2 \qquad (15)$$

Table 3
Average confidence level and error of TVS prototype II coordinates measurements.

Average confidence level of calculated coordinates (%)	x	93.14%
	y	93.93%
Average confidence level of corrected coordinates (%)	x	98.58% (+5.44% increase)
	y	97.54% (+3.61% increase)
Average calculated error	ΔB (deg)	3.9466
	Δx (m)	0.0686
	Δy (m)	−0.0592
Average corrected error	ΔB (deg)	0.2998
	Δx (m)	0.0095
	Δy (m)	−0.0146

Table 4
TVS prototype II angle measurements and coordinates calculation (simplified table).

Real values (deg, m)				**Measured angles (deg)**		**Calculated coordinates (m)**		**Calculated errors**		
***C* angle**	***B* angle**	***X***	***Y***	***C* angle**	***B* angle**	***X***	***Y***	**Δ*B* (degrees)**	**Δ*X* (m)**	**Δ*Y* (m)**
64.7	62.3	1.0	−0.027	64.9687	67.5996	1.1375	−0.0312	5.2996	0.13746	−0.0042
62.6	64.25	1.0	−0.016	62.9625	67.1964	1.0744	−0.0483	2.9464	0.0744	−0.0323
61.3	65.5	1.0	−0.046	61.9687	68.9497	1.0902	−0.0804	3.4497	0.0902	−0.0344
59.7	67.3	1.0	−0.0850	59.9625	73.4938	1.1434	−0.1612	6.1938	0.1434	−0.0762
…	…	…	…	…	…	…	…	…	…	…
50	40.8	0.5	0.078	49.9312	45.3699	0.5470	0.0399	4.5699	0.0470	−0.0381
46.8	43.6	0.5	0.026	46.9500	45.7943	0.5244	0.0101	2.1943	0.0244	−0.0159
45	45.2	0.5	−0.002	44.9438	46.4971	0.5126	−0.0136	1.2971	0.0126	−0.0116
43	47.3	0.5	−0.038	42.9562	49.0435	0.5149	−0.0531	1.7435	0.0149	−0.0151

Table 5
TVS corrected angle measurements, coordinates and error calculation (simplified table).

Real values (deg, m)				**Measured angles (deg)**		**Corrected angles and new calculated coordinates**			**New calculated error**		
***C* angle**	***B* angle**	***X***	***Y***	***C* angle**	***B* angle**	***B* angle**	***X***	***Y***	**Δ*B* (deg)**	**Δ*X* (m)**	**Δ*Y* (m)**
64.7	62.3	1.0	−0.027	64.9687	67.5996	62.6312	1.0156	0.0257	0.3312	0.0156	0.0527
62.6	64.25	1.0	−0.016	62.9625	67.1964	64.3507	1.0096	−0.0152	0.1007	0.0096	0.0008
61.3	65.5	1.0	−0.046	61.9687	68.9497	65.4971	1.0119	−0.0388	−0.0029	0.0119	0.0072
59.7	67.3	1.0	−0.0850	59.9625	73.4938	68.5265	1.0292	−0.0951	1.2265	0.0292	−0.0101
…	…	…	…	…	…	…	…	…	…	…	…
50	40.8	0.5	0.078	49.9312	45.3699	41.8864	0.5112	0.0700	1.0864	0.0112	−0.0080
46.8	43.6	0.5	0.026	46.9500	45.7943	42.8568	0.4970	0.0357	−0.7432	−0.0030	0.0097
45	45.2	0.5	−0.002	44.9438	46.4971	43.9339	0.4902	0.0088	−1.2661	−0.0098	0.0108
43	47.3	0.5	−0.038	42.9562	49.0435	46.9810	0.4982	−0.0351	−0.3190	−0.0018	0.0029

Levenberg algorithm had some disadvantages [36] and Marquardt contributed to the problem which resulted in the Levenberg–Marquardt algorithm, which is the one we applied to our neural network [31]

$$(J^TJ+\lambda diag(J^TJ))\delta = J^T[y-f(\beta)] \tag{16}$$

The neural network was trained with the raw data from the TVS and the result was a 5.44% confidence level increase on x coordinate measurements and 3.61% increase on y, i.e., the neural network effectively corrected the x and y coordinates measurements, minimizing the average error in x to less than 1 cm and in y to 1.5 cm.

The neural network was integrated in the TVS test measurements software to correct the error in the B_{ij} angle measurement in real time, this resulted in the before mentioned accuracy increase. See Table 3 for the summary of the analysis of the experimentation data and Tables 4 and 5 for a sample of angle measurements and coordinate calculations and errors.

After correcting the TVS prototype II measurements, the results demonstrated a different behavior in comparison to its

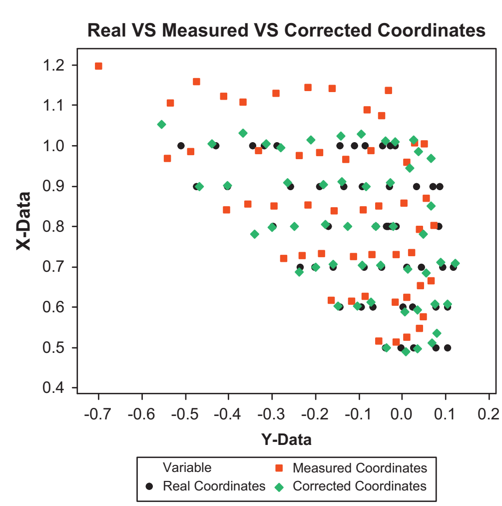

Fig. 15. Comparison graph of obstacle's real, measured and corrected coordinates with the TVS prototype II (scale in m).

Please cite this article as: Básaca-Preciado LC, et al. Optical 3D laser measurement system for navigation of autonomous mobile robot. Opt Laser Eng (2013), http://dx.doi.org/10.1016/j.optlaseng.2013.08.005

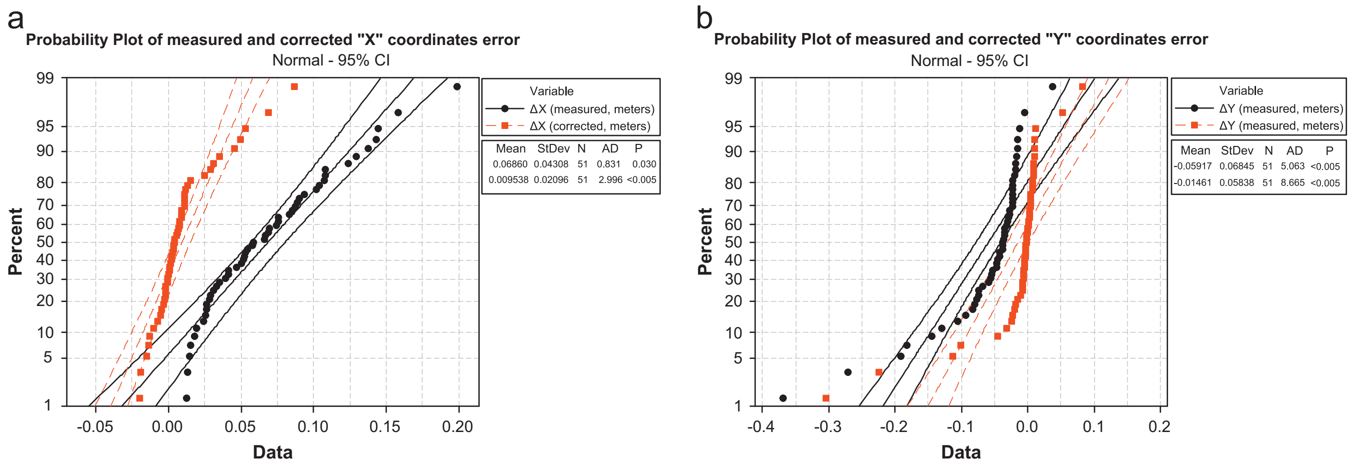

Fig. 16. Probability plots of x and y measured and corrected coordinates errors: (a) x error tends to 0 m; and (b) y error tends to 0 m.

predecessor, instead of having a divided field of view with different accuracy regions, we observed that the error was behaving in the same way for the most part of the field of view, effectively leaving only one region with a stable confidence level range which is 95–99% for both x and y coordinates. This can be observed in Fig. 15, while the measured coordinates error changes according to the distance and angle to the center of the TVS ($x=0$, $y=0$), the error in the corrected coordinates remains low and stable.

Using the experimentation data from the TVS prototype II we generated probability plots with the errors from the measured and corrected coordinates (x and y). In these plots, Fig. 16a and b, it can be observed that the error is consistent at 0 cm for the most part of the field of view, but it can vary by 1–1.5 cm in the ends.

8. Conclusions

In the present paper we introduced the use of our novel original TVS based on dynamic triangulation [15,16,26,27] for practical navigation of a mobile robot. The data obtained by TVS was used for the control of the robot under simulation (Pioneer 3-AT, as most popular among low-cost robots in applied laboratory tasks) considering robot's kinematics under mathematical model as Eqs. (6)–(14)).

BANS was firstly designed to permit calculations of the mobile robot's desired trajectory as a continuous line built on n discrete points (where n is a real number reasonably constrained by 500 in real time for the considered TVS and mobile robot), basing on 3D data from TVS to avoid collision with detected and located obstacles and at the same time avoiding sharp movements of robot's steering. Thus, two principal advantages are assumed over other known robot navigators [26–28] (1) smoother trajectory to facilitate the work of the mechanical part of robot's steering, and (2) significantly shorter trajectory (optimized by variation of n) up to 12–16% length of the robot's path on each obstacle, which is a crucial point for any navigation principle from the point of view of resources saving (fuel and electric energy).

One of the most attractive impacts of BANS is that it gives in real time (exactly during the calculations) the values of variables in Eqs. (11)–(14), in each of n points, which are necessary to perform robot's kinematic control.

Also it is notable that the use of 3D laser TVS as sensory part of robot's navigation is a unique system among known, which gives a metrological quality of the obstacle location and shape. It permits to consider the robot and the obstacle as parts of the same notation system, e.g., Cartesian coordinates, without post-processing or probabilistic solutions.

It is important to note that our system in comparison to others has significantly wide opening angle of field of view (theoretically up to $\approx 160^{\circ}$), while omnidirectional vision (fish-eye like) claim to provide 180°, actually due to image curvature and excessive postprocessing time, those systems are still at a disadvantage; and our system is a perfect match for operation in completely dark environment (e.g., mines, caves exploration, rescue operations, etc.), which is completely impossible for camera systems.

Although 3D scene reconstruction is not a requirement for mobile robot navigation, short term future investigation includes tests and detailed 3D measurements data for surface reconstruction, obtained with the presented TVS to experiment in different applications such as computer graphics, medical diagnostics [31] and structural health monitoring [19], which we will demonstrate that are within our TVS capabilities.

Finally, the use of the chosen among three others method of Levenberg–Marquardt [31] helps us to increase the metrological accuracy of 3D points coordinates up to 5%, comparing to our own previous results.

Appendix A. Supporting information

Supplementary data associated with this article can be found in the online version at http://dx.doi.org/10.1016/j.optlaseng.2013.08.005.

References

[1] Cheng Y, Maimone MW, Matthies L. Visual odometry on the Mars exploration rovers—a tool to ensure accurate driving and science imaging. IEEE Robotics Autom Mag 2006;13(2):54–62.
[2] Fairfield N, Kantor G, Wettergreen D. Segmented SLAM in three-dimensional environments. J Field Robotics 2010;27(1):85–103.
[3] Thrun Sebastian, Montemerlo Mike, Dahlkamp Hendrik, Stavens David, Aron Andrei, Diebel James, et al. Stanley: the robot that won the DARPA Grand Challenge.
J Robotic Syst 2006;23:9.
[4] Buehler M, Iagnemma K, Singh S, editors. The 2005 DARPA Grand Challenge: the great robot race. Berlin: Springer; 2006.
[5] Urmson C, Anhalt J, Bagnell Drew, Baker Christopher, Bittner Robert, Clark MN, et al. Autonomous driving in urban environments: Boss and the Urban Challenge. J Field Robotics 2008;25:425–66, http://dx.doi.org/10.1002/rob.20255.
[6] Bacha A, Bauman R, Faruque A, Fleming M, Terwelp C, et al. Odin: Team ictorTango's entry in the DARPA Urban Challenge. J Field Robotics, 25; 467–92.
[7] Leonard J, Barrett D, How J, Teller S, et al. Team MIT Urban Challenge Technical Report. CSAIL Technical Reports. Available from: 〈http://hdl.handle.net/1721.1/39822. MIT-CSAIL-TR-2007-058〉; 2007 [accessed 11.06.11].

Please cite this article as: Básaca-Preciado LC, et al. Optical 3D laser measurement system for navigation of autonomous mobile robot. Opt Laser Eng (2013), http://dx.doi.org/10.1016/j.optlaseng.2013.08.005

[8] Surmann H, Lingemann K, Nüchter A, Hertzberg J. A 3D laser range finder for autonomous mobile robots. In: Proceedings of the 32nd international symposium on robotics; 2001: p. 153–8.
[9] Andersen JC, Blas MR, Ravn O, Andersen NA, Blanke M. Traversable terrain classification for outdoor autonomous robots using single 2D laser scans. Integrated Comput-Aided Eng 2006;13(3):223–32.
[10] Genovesea K, Casalettoa L, Rayasb JA, Floresb V, Martinez Amalia. Stereo-Digital Image Correlation (DIC) measurements with a single camera using a biprism. Opt Lasers Eng 2013;51(3):278–85.
[11] Zhou Yihao, Chen Yan Qiu. Feature matching for automated and reliable initialization in three-dimensional digital image correlation. Opt Lasers Eng 2013;51(3):213–23.
[12] Pintoa Tiago, Kohlerb Christian, Albertazzi Armando. Regular mesh measurement of large free form surfaces using stereo vision and fringe projection. Opt Lasers Eng 2012;50(7):910–6.
[13] Penga Zhao, Guo-Qiangb Ni. Simultaneous perimeter measurement for 3D object with a binocular stereo vision measurement system. Opt Lasers Eng 2010;48(4):505–11.
[14] Lipnickas A, Knyš A. A stereovision system for 3-D perception. Electron Electr Eng 2009;91:99–102.
[15] Basaca LC, Rodriguez JC, Sergiyenko O. 3D laser scanning vision system for autonomous robot navigation. In: Proceedings of IEEE international symposium on industrial electronics ISIE-2010, Bari, Italy; 2010: p. 1773–8.
[16] Luis C. Básaca, Julio C. Rodríguez, Oleg Sergiyenko, Vera V. Tyrsa, Wilmar Hernández, Juan I. Nieto Hipólito, et al., Resolution improvement of dynamic triangulation method for 3D vision system in robot navigation task. In: Proceedings of IEEE—36th annual conference of IEEE industrial electronics IECON'10; 2010: p. 2886–91.
[17] Oleg Sergiyenko, Vira Tyrsa, Luis Carlos Basaca Preciado, Julio Cesar Rodriguez Quinonez, Wilmar Hernandez, Juan Ivan Nieto Hipolito, et al., Optoelectronic devices and properties. Electromechanical 3D optoelectronic scanners: resolution constraints and possible ways of improvement. Austria: IN-TECH; 2010 (p. 549–82).
[18] Rivas Lopez M, Sergiyenko O, Tyrsa V. Computer vision. Machine vision: approaches and limitations. Austria: I-TECH; 2008 (p. 395–428).
[19] Moisés Rivas, Oleg Sergiyenko, Mario Aguirre, Luis Devia, Vera Tyrsa, Ismael Rendón, Spatial data acquisition by laser scanning for robot or SHM task. In: IEEE–IES Proceedings of the international symposium on industrial electronics ISIE-2008, Cambridge, United Kingdom; 2008: p. 1458–63.
[20] Sergiyenko O, Tyrsa V, Hernandez-Balbuena D, Rivas López M, Rendón López I, Devia Cruz L. Precise optical scanning for practical multiapplications. In: Proceedings of the IEEE 34th Annual IEEE Conference IECON'08, Florida, USA; 2008: p. 1656–61.
[21] Sergiyenko OYu. Optoelectronic system for mobile robot navigation. Optoelectron, Instrum Data Process 2010;46(5):414–28.
[22] Niku SB. Introduction to robotics: analysis, systems, applications. Indianapolis, IN: Wiley; 2010.
[23] Kozłowski K, Pazderski D. Modeling and control of a 4-wheel skid-steering mobile robot. Int J Appl Math Comput Sci 2004;14(4):477–96.
[24] Kang J, Kim W, Lee J, Yi K. Design, implementation, and test of skid steering-based autonomous driving controller for a robotic vehicle with articulated suspension. J Mech Sci Technol 2010;24(3):793–800.
[25] Wang J, Wang Q, Jin L, Song C. Independent wheel torque control of 4WD electric vehicle for differential drive assisted steering. Mechatronics 2011;21(1):63–76.
[26] Sergiyenko O, Hernandez W, Tyrsa V, Devia Cruz L, Starostenko O, Pena-Cabrera M. Remote sensor for spatial measurements by using optical scanning. Sensors 2009;9(7):5477–92.
[27] Oleg Y. Sergiyenko, Vera V. Tyrsa, Luis F. Devia, Wilmar Hernandez, Oleg Starostenko, Moisés Rivas Lopez, Dynamic laser scanning method for mobile robot navigation. In: Proceedings of the ICCAS–SICE 2009 ICROS–SICE international joint conference, Japan; 2009: p. 4884–9.
[28] Du Y, Gao X, Liu Z, Sun M. The new navigation system for automatic guided vehicle. In: Proceedings of the Chinese control and decision conference; 2008: p. 4653–8.
[29] Byczkowski T, Lang J. A stereo-based system with inertial navigation for outdoor 3D scanning. In: Proceedings of the Canadian conference on computer and robot vision, CRV'09; 2009: p. 221–8.
[30] Hwang CL, Shih CY. A distributed active-vision network-space approach for the navigation of a car-like wheeled robot. IEEE Trans Ind Electron 2009;56(3):846–55.
[31] Rodriguez-Quiñones JC, Sergiyenko O, González-Navarro FF, Basaca-Preciado LC, Tyrsa V. Surface recognition improvement in 3D medical laser scanner using Levenberg–Marquardt method. Signal Process (Elsevier) February 2013;93(2):378–86 (ISSN 0165-1684).
[32] Hernandez W, de Vicente J, Sergiyenko O, Fernández E. Improving the response of accelerometers for automotive applications by using LMS adaptive filters, MDPI, sensors1424-8220. Switzerland: Basel; http://dx.doi.org/10.3390/s100100313 (p. 313–29).
[33] Hernandez W, de Vicente J, Sergiyenko O, Fernández Eduardo. Improving the response of accelerometers for automotive applications by using LMS adaptive filters: Part II, MDPI, sensors1424-8220. Switzerland: Basel; http://dx.doi.org/10.3390/s100100952 (p. 952–62).
[34] Abba A, Caponio F, Geraci A, Ripamontii G. Non-linear leastsquares in FPGA devices for digital spectroscopy. Nuclear Science Symposium Conference Record (NSS/MIC), Orlando; 2009: p. 563–8.
[35] Basaca-Preciado LC, Sergiyenko O, Rodriguez-Quinonez JC, Rivas-Lopez M. Optoelectronic 3D laser scanning technical vision system based on dynamic triangulation. In: Proceedings of the 2012 IEEE photonics conference (IPC); 2012: p. 648–9.
[36] Marquardt D. An algorithm for least-squares estimation of nonlinear parameters. SIAM J Appl Math 1963;11(2):431–41.
[37] Zhang Song, Huang Peisen S. High-resolution, real-time three-dimensional shape measurement. Opt Eng 2006;45(12).

Optoelectronic 3D Laser Scanning Technical Vision System based on Dynamic Triangulation

Luis C. Basaca-Preciado*; Oleg Yu. Sergiyenko; Julio C. Rodriguez-Quinonez; Moises Rivas-Lopez
Optoelectronics and Automated Measurement Laboratory
Engineering Institute of the Autonomous University of Baja California, Mexicali, B.C., México.
luis.basaca@uabc.edu.mx

***Abstract*—Using a laser as emitter and a scanning aperture as sensor we developed a vision system capable of measuring the 3D coordinates of detected objects. This system is intended for autonomous robot navigation task.**

Keywords; 3D laser scanner; vision system; scanning aperture; autonomous mobile robot.

I. INTRODUCTION

Autonomous navigation and obstacle avoidance tasks are becoming very important not only in the automotive industry but also in scientific research such as rover planet exploration [1]. To accomplish these tasks, several approaches and sensor technologies are being used in autonomous vehicles [2, 3, 4], such as the combination or fusion of sensors used to acquire the necessary information to detect obstacles and roads, sensors required for safe traveling such as LIDAR, RADAR, Stereo Vision, GPS, among others. Although sensor integration is an approach that successfully provides the necessary information to perform the obstacle avoidance task, it also provides an increased overall cost of the autonomous vehicle.

Hence, in this paper we present a low cost high precision Technical Vision System (TVS) which is based in our Dynamic Triangulation principle that utilizes a positioning laser and a rotating scanning aperture to measure the *x*, *y* and *z* coordinates of detected objects with metrological precision.

Although the TVS was developed to provide information to an autonomous mobile robot navigation system, it is fully capable of performing other tasks such as, structural health monitoring, biometric parameters measurements and 3D modeling.

II. TECHNICAL VISION SYSTEM (TVS)

As mentioned before; the TVS is composed of two main parts (positioning laser and scanning aperture) and a principle called Dynamic Triangulation.

A. Dynamic Triangulation principle

The TVS is based on a principle we developed which is called Dynamic Triangulation, it is called dynamic due to the rotation ability of the positioning laser and the scanning aperture, allowing us to have moving angles that can form laser light triangles with different shapes for a very short period of time; when a triangle is formed, thanks to the detection of the reflected light of an obstacle surface, we obtain all the necessary information to calculate its 3D coordinates.

Fig. 1 shows the dynamic triangulation principle used by the TVS. The main components of the TVS are the Positioning Laser (PL) and the Scanning Aperture (SA).

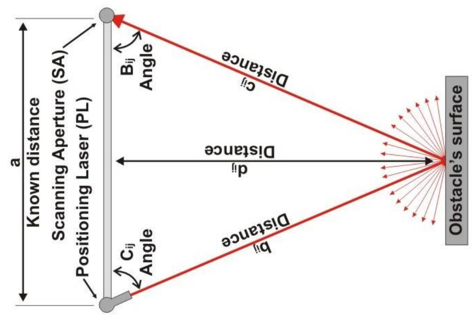

Figure 1. Dynamic Triangulation principle.

B. Positioning Laser (PL)

The PL is composed by a set of two 45° mirrors, a red laser (635nm, 20mW) and a stepper motor; these elements are assembled as shown in Fig. 2. By controlling the stepper motor rotation we control the direction at which we want to direct the laser to verify the presence of obstacles with the SA.

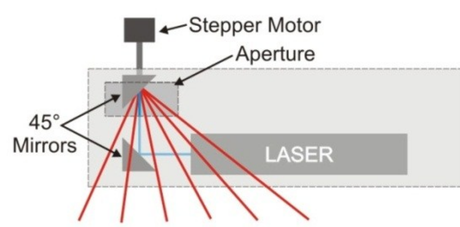

Figure 2. Positioning Laser.

The principle shown in Fig. 1 allows us to measure *x* and *y* coordinates and in order to measure *z* (for 3D coordinates) we added to the TVS a tilt mechanism (see Fig. 3) which allows us to rotate the device in order to perform scans at different heights along the *z* axis.

C. Scanning Aperture (SA)

The SA is the most important component of the TVS (see Fig. 4) and its purpose is to receive the reflected laser rays through the aperture into a 45° mirror which is rotated at constant speed by a DC motor; then these laser rays are redirected orthogonally to a lens array to finally be received by the stop sensor (high speed photo-transistor), when this sensor

978-1-4577-0733-9/12/$26.00 ©2012 IEEE

is activated we know an obstacle has been detected. The Zero sensor monitors the mirror's revolutions; this information is used to calculate the angle at which the reflected laser light enters the aperture (B_{ij} angle, equation 1), which is needed for the 3D coordinates calculation.

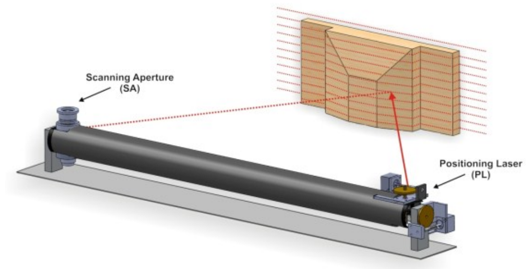

Figure 3. TVS with tilt mechanism 3D model.

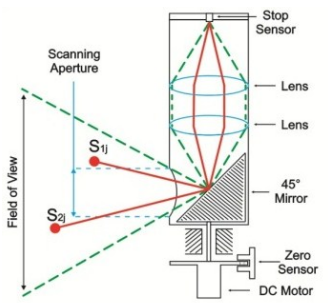

Figure 4. Scanning Aperture (SA).

The following equation is used to calculate angle Bij:

$$B_{ij} = \frac{2\pi \cdot N_A}{N_{2\pi}} \tag{1}$$

where, N_A is the number of reference pulses when laser rays are detected by the stop sensor and $N_{2\pi}$ is the number of reference pulses per revolution detected by the zero sensor. See Fig. 4. For a more detailed explanation; see [5, 6].

D. 3D Coordinates calculation

In order to calculate the x, y and z coordinates of any reflected point from an obstacle surface, we developed a set of equations derived from the law of sines (equations 2 - 5). These equations require the angles B_{ij}, C_{ij}, $\Sigma\beta_j$ and a (fixed distance between the center of PL and the center of SA) to calculate the 3D coordinates [6].

$$x_{ij} = a \frac{\sin B_{ij} \cdot \sin C_{ij} \cdot \cos \sum_{j=1}^{j} \beta_j}{\sin\left[180° - \left(B_{ij} + C_{ij}\right)\right]}, \tag{2}$$

$$y_{ij} = a\left(\frac{1}{2} - \frac{\sin B_{ij} \cdot \cos C_{ij}}{\sin\left[180° - \left(B_{ij} + C_{ij}\right)\right]}\right) \text{ at } B_{ij} \leq 90°, \tag{3}$$

$$y_{ij} = -a\left(\frac{1}{2} + \frac{\sin B_{ij} \cdot \cos C_{ij}}{\sin\left[180° - \left(B_{ij} + C_{ij}\right)\right]}\right) \text{ at } B_{ij} \geq 90°, \tag{4}$$

$$z_{ij} = a \cdot \frac{\sin B_{ij} \cdot \sin C_{ij} \cdot \sin \sum_{j=1}^{j} \beta_j}{\sin\left[180° - \left(B_{ij} + C_{ij}\right)\right]} \tag{5}$$

When the TVS performs a scan, the x, y and z coordinates are calculated and stored in a matrix. This information is then sent to the mobile robot navigation system to analyze and take navigation decisions e.g. obstacle avoidance and trajectory planning. See Fig. 5.

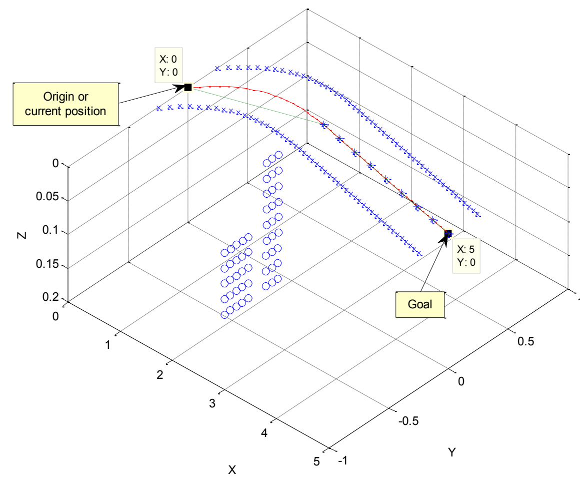

Figure 5. Mobile robot trajectory (solid red line) from a Matlab® simulation (scale in meters). Blue circles are a plot of the measured coordinates with the TVS, of the detected obstacle(s), each circle has x, y and z value.

III. Conclusions

In this paper we presented the use of our novel original TVS based on the dynamic triangulation principle for practical navigation of an autonomous mobile robot. TVS experimental results and tests conditions are published on [5, 6, 7]. However, we can assure that the TVS prototype I has a 95% confidence level on its coordinates measurements. A prototype II with several mechanical improvements is going through test stage, new experimental results will be published in the near future.

It is notable that the use of our TVS (as a robot's vision system for navigation), which gives a metrological quality of the obstacle location and shape without post-processing or probabilistic solutions is a unique system among known.

References

[1] Cheng, Y. et al. (2006) Visual odometry on the Mars exploration rovers - A tool to ensure accurate driving and science imaging. IEEE Robotics & Automation Magazine, 13(2), 54–62.

[2] Fairfield, N. et al. (2010). Segmented SLAM in Three-Dimensional Environments. Journal of Field Robotics, 27(1), 85-103.

[3] Thrun, S. et al. (2006). Stanley: The robot that won the DARPA Grand Challenge, Journal of Robotic Systems, 23(9).

[4] Bacha, A., Bauman, C., Faruque, R., Fleming, M., Terwelp, C., Reinholtz, C., Hong, D., Wicks, A. et al. (2008), Odin: Team VictorTango's entry in the DARPA Urban Challenge. Journal of Field Robotics, 25(8), 467–492.

[5] Rivas Lopez, M. et al. (2008). Computer vision. Machine vision: approaches and limitations (pp. 395-428). Austria: I-TECH.

[6] Basaca, L.C. et al (2010). Resolution improvement of Dynamic Triangulation method for 3D Vision System in Robot Navigation task. Proceedings of IEEE-36th Annual Conference of IEEE Industrial Electronics IECON'10, 2886 - 2891.

[7] Sergiyenko, O. Yu. (2010). Optoelectronic System for Mobile Robot Navigation. Optoelectronics, Instrumentation and Data Processing, 46(5), October, 2010, 414-428.

Resolution improvement of Dynamic Triangulation method for 3D Vision System in Robot Navigation task

Luis C. Básaca[1], Julio Rodríguez[1], Oleg Yu. Sergiyenko[1], Vira V. Tyrsa[2], W. Hernandez[3], Juan Ivan Nieto Hipólito[4], Oleg Starostenko[5]

[1]Engineering Institute of Autonomous University of Baja California

[2]Polytechnic University of Baja California

[3]Polytechnic University of Madrid

[4]Autonomous University of Baja California, Campus Ensenada

[5]Universidad de Las Américas, Puebla, México

lubakun@gmail.com, julio_qas@hotmail.com, srgnk@iing.mxl.uabc.mx, vera-tyrsa@yandex.ru, whernan@ics.upm.es, jnieto@uabc.mx, oleg.starostenko@udlap.mx

***Abstract*-This paper presents a technical vision system designed to resolve multiple tasks which are fundamental for autonomous navigation. These tasks include detecting the presence of a significant obstacle for a mobile robot, locate its position in the mobile robot's field of view and create a digital map of the obstacle's visible surface with metrological accuracy. This technical vision system has been introduced and explained in other publications; therefore this paper focuses mostly on signal conditioning, processing and resolution increase for mobile robot navigation.**

I. INTRODUCTION

Through the years autonomous navigation has proved to be a very interesting and challenging field involving multiple tasks in order to achieve autonomous behavior on a mobile robot. Among those tasks exists the particular problem of detecting surrounding obstacles to avoid collisions, many different approaches have been presented to resolve this problem such as, stereo vision, global positioning systems, radar, IR sensor, ultrasonic sensors, laser, a combination of any of these, among others.

Currently GPS devices are able to fix positions with errors of the order of 1 cm to 100 m in real time; however there are certain areas where satellites cannot provide full nor partial coverage and the accuracy cannot be guaranteed [1].

Other systems use monocular vision which process single 2D images obtained from a camera to represent the real 3D world, due to the single 2D image nature, depth cannot be obtained from these images; therefore additional sensors are require to obtain that information.

Also, image processing is time consuming due to the great amount of information an image provides and for navigation systems where fast decisions have to be made, is not the best option [2].

The presented Technical Vision System (TVS) utilizes laser scanning and a method called dynamic triangulation, which allows the system to generate a digital map of the mobile robot field of view with adjustable resolution, and for every point of the digital map it calculates its 3D coordinates (X, Y, Z) and stores them in memory. Theoretically the TVS posses a <180° field of view, but in practice it can be limited due to the TVS's components own size.

The generated data can be used by a mobile robot navigation system to resolve tasks such as obstacle avoidance and path planning.

II. TVS AND DYNAMIC TRIANGULATION

As stated before the TVS provides 3D coordinates, (position X, Y and depth Z) of an obstacle or object found in the field of view in front of a mobile robot.

The TVS consists of two devices, each one installed on the opposite ends of a horizontal bar, the devices are called Positioning Laser (PL) and Scanning Aperture (SA) (See Fig.1) [3].

We called our method Dynamic Triangulation due to the fact that the Positioning Laser has the ability to rotate and redirect the laser beam in 180° theoretically and the Scanning Aperture rotates 360° at a constant speed, meaning the TVS has two dynamic angles.

These angles exist for a very short period of time when scanning plane hits the projected laser spot. This provides the mobile robot with the advantage of having a field of view of greater size than traditional static triangulation systems that strongly limit the robot's field of view by optical sensor size [4, 5].

The Positioning Laser, controlled by a stepper motor, utilizes a 45° mirror to reflect and redirect the laser beam through the field of view towards any obstacle found. After reaching an obstacle the laser rays are reflected from the surface, part of them specularly (according to the reflection law) and some diffusely (in every direction), [6], depending on the surface material, this is called mixed reflection (See Fig. 2).

The rays that are reflected to the Scanning Aperture reach a 45 mirror that redirects the rays to a photo receiver sensor. At this moment a laser triangle is formed for an instant and the *Bij* angle is calculated (See Fig. 1) [7].

978-1-4244-5226-2/10/$26.00 ©2010 IEEE

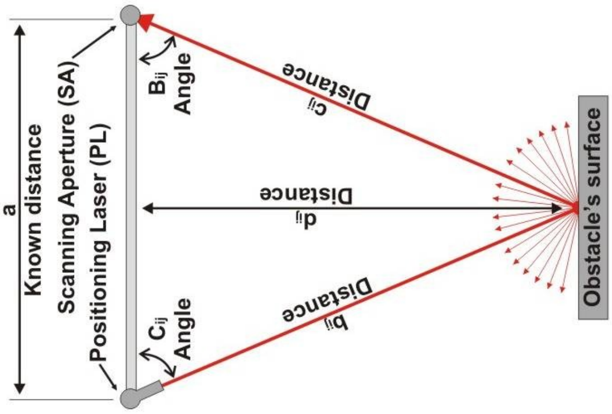

Fig. 1. Dynamic Triangulation.

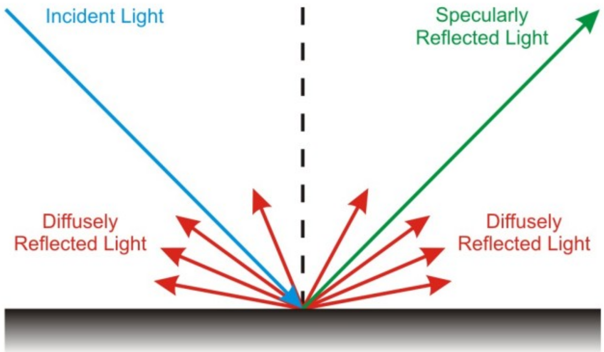

Fig. 2. Mixed Reflection.

Based on the law of sines as well as correlation between the sides and the height in a triangle represented on Fig. 1, we found the formulas to calculate distance d from base a up to the point highlighted by the laser beam (See Fig. 1). Using the angles Bij, Cij, $\sum_{j=1}^{n}\beta_j$ and base a, we calculate the 3D coordinates for each highlighted point with the following formulas:

$$x_{ij} = a\frac{\sin B_{ij}\cdot\sin C_{ij}\cdot\cos\sum_{j=1}^{j}\beta_j}{\sin\left[180^\circ-\left(B_{ij}+C_{ij}\right)\right]}, \tag{1}$$

$$y_{ij} = a\left(\frac{1}{2}-\frac{\sin B_{ij}\cdot\cos C_{ij}}{\sin\left[180^\circ-\left(B_{ij}+C_{ij}\right)\right]}\right) \text{ at } B_{ij}\le 90^\circ, \tag{2}$$

$$y_{ij} = -a\left(\frac{1}{2}+\frac{\sin B_{ij}\cdot\cos C_{ij}}{\sin\left[180^\circ-\left(B_{ij}+C_{ij}\right)\right]}\right) \text{ at } B_{ij}\ge 90^\circ, \tag{3}$$

$$z_{ij} = a\cdot\frac{\sin B_{ij}\cdot\sin C_{ij}\cdot\sin\sum_{j=1}^{j}\beta_j}{\sin\left[180^\circ-\left(B_{ij}+C_{ij}\right)\right]} \tag{4}$$

Fig. 3 shows the TVS mounted on a mobile robot and its operation in an outdoor environment. The laser beam, the X_{ij}, Y_{ij} and Z_{ij} distances and other angles are marked up to represent the TVS operation.

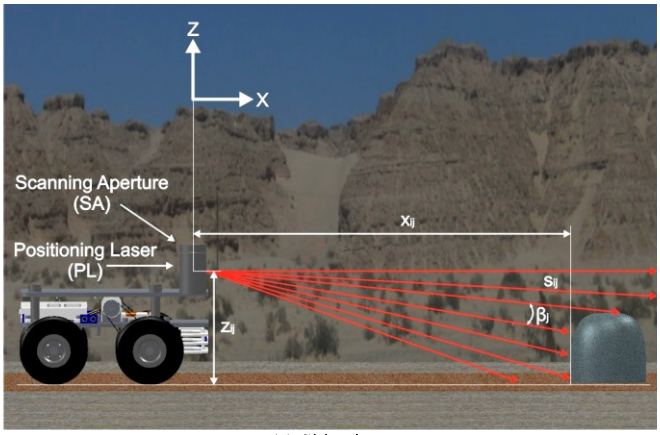

(a) Side view.

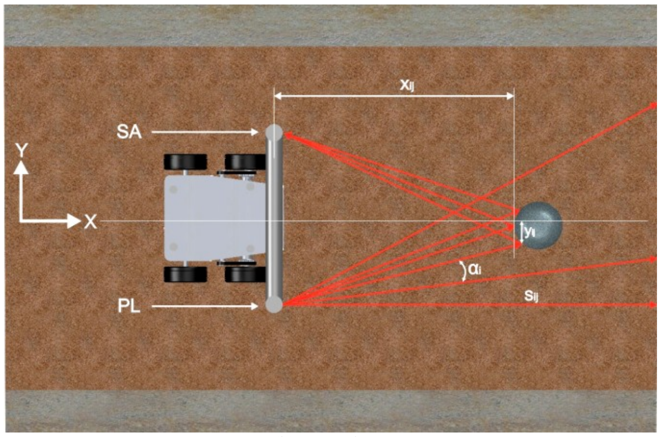

(b) Top view.

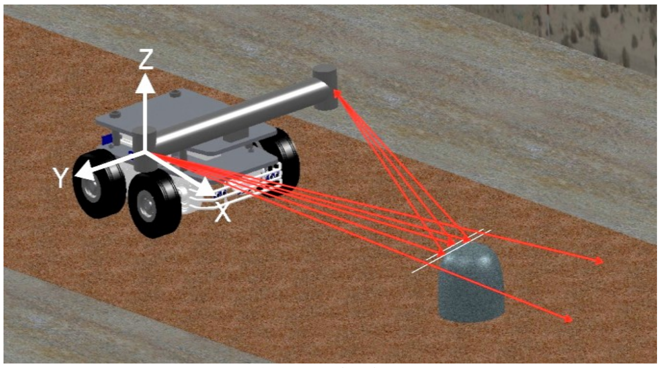

c) Isometric view.
Fig. 3. TVS mounted on a mobile robot and operation.

Each point that is highlighted on the obstacle surface (Fig. 3, *a-c*) by a beam of laser is called Sij. For each Sij, Cartesian coordinates X, Y, and Z (set by formulas 1-4) are obtained. The accuracy of coordinates measurement is not uniform (see Fig. 4) in all TVS field-of-view, but in the olive and green zone correspondingly it is not more than 1% and 4% out of level of confidence [7, 8]. Usually, modern regular step drives are operated with average velocity of 1 KHz. It means that we can obtain coordinates at least of 1000 points per second, each X, Y, and Z with metrological accuracy and defined uncertainties.

Analysis of spatial distribution of the measurement's uncertainty permits us two conclusions: 1. The TVS must be implemented with maximal attention to the center of the real field-of-view of the final designed system, and its practical coincidence with the TVS uncertainty diagram on Fig. 4. Such variation of relative error is a sign for new prototype design with improved mechanical alignment.

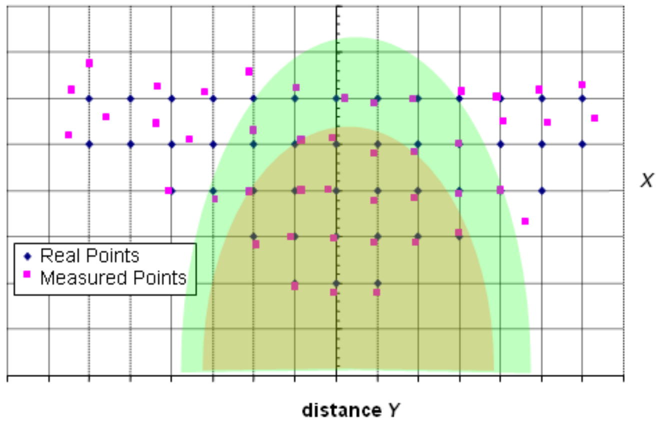

Fig. 4. TVS field-of-view and "accuracy zones" (according to [7]).

III. Noise Filtering for Guaranteed Localization

One of the most challenging points of normal TVS functioning is the presence of typical input noise mixed with the "stop-signal" train in the form of the screenshot on Fig. 6. This noise can be filtered by specially designed circuit (Fig. 7) with the aim of guaranteed detection of true position of the scanning ray reflected points, in other words the guaranteed localization of the real "stop-pulses".

The preliminary analysis of this noise sources leads us to the conclusion that is a complex combination of mechanical noise in electric drive and sinusoidal noise of power supply, arbitrary distributed along the TVS base-bar. Therefore, the best solution in this case is a special filter design (Fig. 7) for the experimentally defined noise bandwidth.

As stated before the TVS has two devices, the Positioning Laser and the Scanning Aperture, inside the last one, there is a 45° mirror, a lens, and a photo receiver sensor. (See Fig. 5)

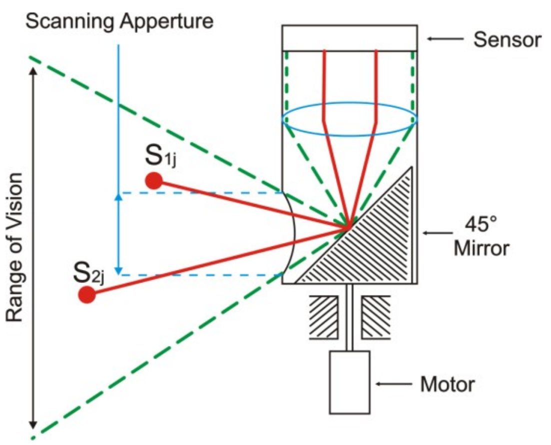

Fig. 5. Scanning Aperture.

The laser rays that reflect diffusely from the obstacle's surface are directed in every direction and only a few rays reach the photo receiver sensor, from the total energy of the laser beam that is directed to the obstacle only 2% - 5% (as indicate our quantitative simulation in MathCAD) is reflected and sensed by our photo receiver, therefore the signal provided by the sensor is in the range of millivolts and it requires a signal conditioning stage before interpreting.

As in every system, noise is present here too in the signal acquired from the photo receiver, after studying the signal we observed that the noise reaches maximum amplitude of 120 mV (see Fig. 6) with frequencies that vary between 400 Hz and 20 KHz. To eliminate this noise a Butterworth third order low pass filter (-60 dB per decade) was designed and implemented, see Fig. 7. The filter's output connects to a voltage level detector with a reference voltage of 120mV to reject the noise amplitude, whenever an obstacle is detected by the photo receiver a spike in the signal is detected, the voltage of this spike varies depending on the distance of the detected obstacle but is always greater than 120mV from the noise amplitude. The output of the voltage level detector is a signal of 5Vdc when an obstacle is detected and remains at 0Vdc when there is no obstacle, in other words providing us with a 0-5Vdc square signal which indicate us whether an object is present or not.

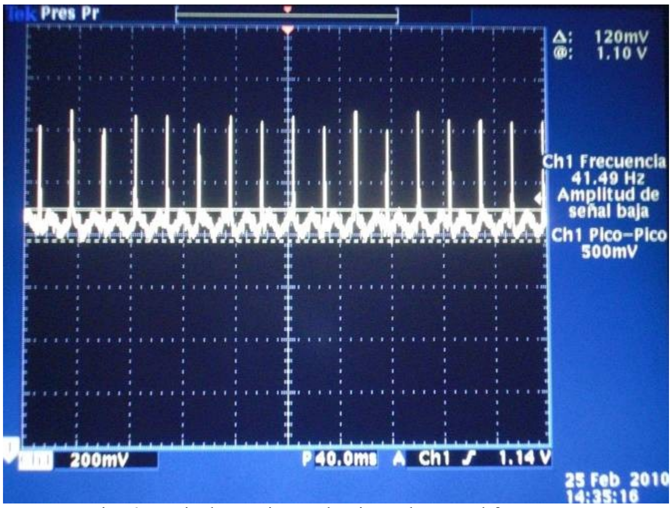

Fig. 6. Typical experimental noise voltage and frequency.

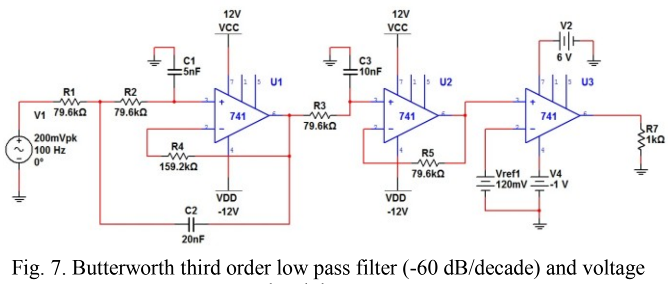

Fig. 7. Butterworth third order low pass filter (-60 dB/decade) and voltage level detector.

The Butterworth type filter was chosen over other types such as Chebyshev filters due to Butterworth's more linear phase response and flat frequency response in our passband according to [8]. Our filter was designed as follows:

$$\omega_c = 200;\ C_3 = 10nF \quad (5)$$

where ω_c is the cutoff frequency, the value assigned is 200 Hz in order to let pass the frequency band between 0 and 200 Hz, letting pass the signal of a detected obstacle and attenuating all the frequencies higher than 200 Hz.

$$C_1 = \frac{1}{2}C_3 = 5nF \quad (6)$$

$$C_2 = 2C_3 = 20nF \quad (7)$$

$$R = \frac{1}{\omega_c C_3} = \frac{1}{(6.25)(200)(5x10^{-9})} = 79.617k\Omega \quad (8)$$

$$R_1 = R_2 = R_3 = R = 79.617k\Omega \quad (9)$$

$$R_{f1} = 2R = 159.235k\Omega \quad (10)$$

$$R_{f2} = R = 79.617k\Omega \quad (11)$$

The filter with -60 dB/decade attenuation is achieved by cascading a -40 dB/decade filter and a -20 dB/decade filter. The total closed loop gain is the multiplication of each filter's gain. See Fig. 8 for the frequency response of the circuit shown on Fig. 7, [8].

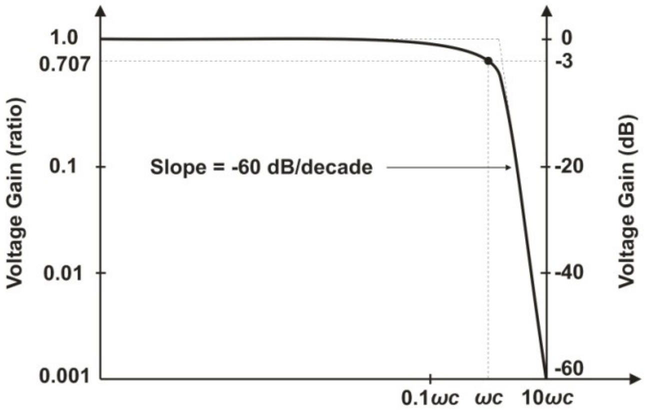

Fig. 8. Frequency response for Butterworth third order low pass filter (-60 dB/decade).

IV. SIMULATIONS

The circuit presented on Fig. 7 was simulated with software from National Instruments, NI Multisim 10. Fig. 9, a shows a caption of a Simulated Tektronix Oscilloscope with three signals, trace 1 is the circuit input signal that simulates the photo receiver output, this is the signal that is filtered and amplified, for this simulation the input signal is 200mV at 100 Hz. Trace 2 is the filter output, as shown below, the signal has the same amplitude as the original as long as its frequency is in the passband region (below 200 Hz), therefore it's not attenuated, it also has a delay of 8ms which is acceptable. And the last, trace 3, is the voltage level detector output, this signal will be 5Vdc if the signal voltage coming from the filter is greater than Vref (120mVdc), meaning an obstacle has been detected, and it remains 0Vdc if there is no obstacle in sight.

Fig. 9, b shows the case when the input signal is 200mV at 400 Hz, this frequency is in the stopband region (higher than 200 Hz), for this reason the trace 2 signal which is the filter output is attenuated to 35mV that for this purpose equals 0V. Therefore trace 3 remains at 0Vdc.

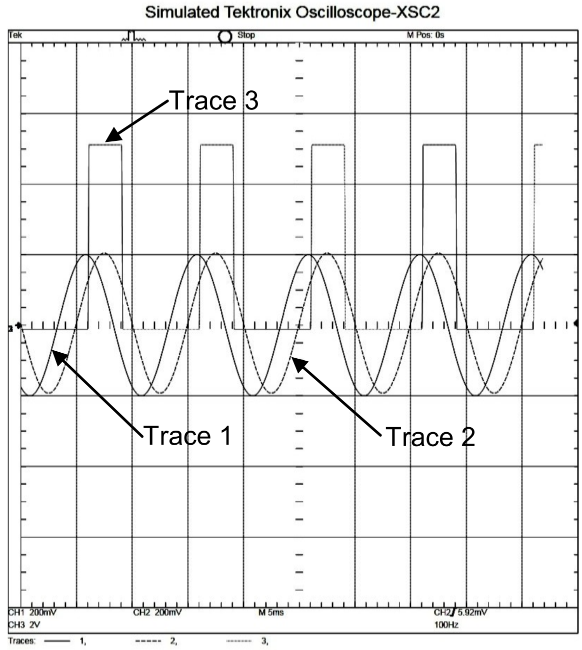

(a) Input signal is 200mV at 100 Hz; output is a 0-5Vdc square signal.

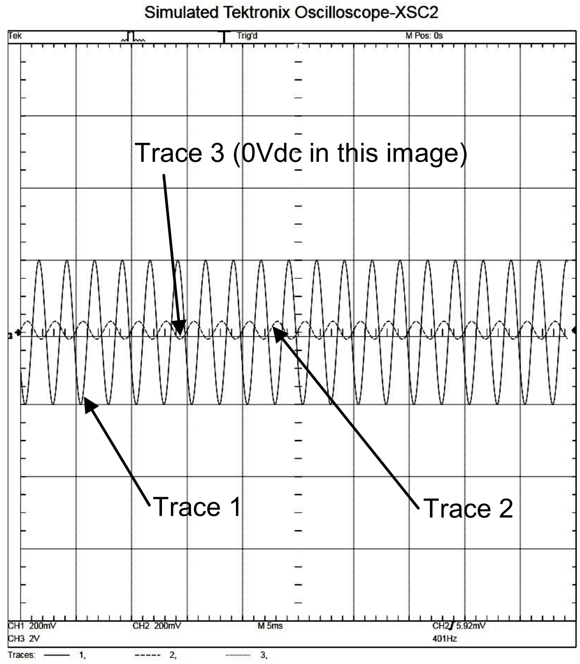

(b) Input is 200mV at 400 Hz; output is attenuated due to input frequency being higher than cutoff frequency (200 Hz), regardless of the input voltage.
Fig. 9. Low pass filter and voltage level detector output (circuit on Fig. 7).

Thus, our simulation demonstrates that the designed filter can attenuate the experimentally detected undesired noise in TVS prototype above 400Hz.

V. EXPERIMENTATION

A series of tests have been conducted with a functioning Prototype I, resulting in 95% accuracy on 2D coordinate's measurement. Uncertainty measurement does not overcome a 5% threshold in any point. Experimental results can be found in [3, 4, 7]. Currently, Prototype II is being fabricated (80% complete) and a new series of tests including 3D coordinate's measurement will be conducted as soon as it's completed.

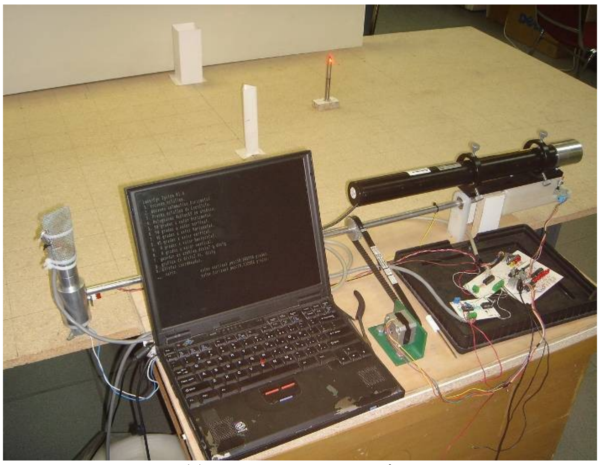

(a) Prototype I system view

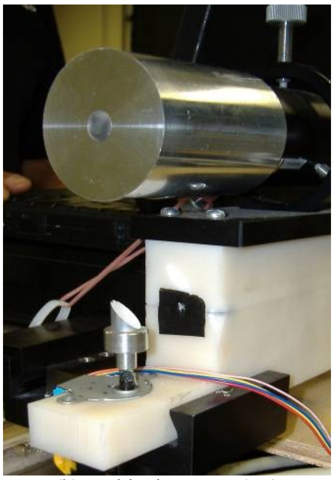

(b) Positioning Laser (PL)

(c) Scanning Aperture (SA)
Fig. 10. Prototype I.

Figure 10 shows Prototype I, this system was the first we built to demonstrate our method and although testing and experimentation were successful, we detected uncertainty points (See Fig. 4) that could be eliminated with an improved mechanical design.

Prototype II shown in Fig. 11, a, has several advantages in comparison to its predecessor; the most important is that in the new design most of the components, including the Laser are installed inside a cylindrical tube, thus placing the center of gravity in the center of the tube and providing an easier and more precise way of rotating the tube than the band used in Prototype I (see Fig. 10, a).

In other words this improvement decreases the TVS own torque which provide us with several advantages over Prototype I such as:

- The possibility of using an electric motor rated with lower torque, voltage and current per phase consumption.
- As a result, full system power consumption is reduced.
- Extended battery life which is essential for mobile applications.

(a) Full Size Prototype II system view.

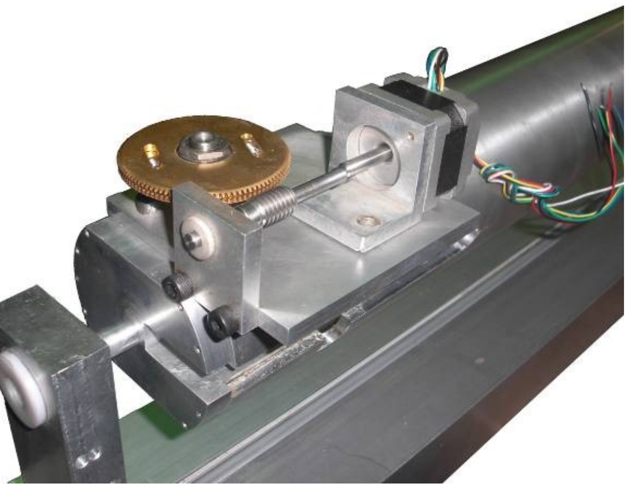

(b) Positioning Laser (PL).

(c) Scanning Aperture (SA).
Fig. 11. Prototype II.

Moreover, cross-comparing Fig. 10, b and Fig. 11, b and the pair Fig. 10, c - Fig. 11, c, in the constructions of PL and SA, the following improvements are presented.

The older Positioning Laser design used a fixture with a 45° mirror attached to the laser to redirect the laser beam in a 90° angle to a second 45° mirror which is attached directly to a stepper motor (Fig. 10, b). This motor is controlled to redirect the laser beam orthogonally to scan the area in front of the mobile robot.

On the other hand, the new PL design (Fig. 11, b) is based on the same general principle but has mechanical differences. E.g. the new PL has no fixture attached directly to the laser; instead of attaching the 45° mirror, part of the inside surface of the cylindrical tube is machined with mirror finish, with this, the possibility of uncertainty due to mirror displacement or improperly installed fixture is eliminated. It is the way to decrease the uncertainty deviation on Fig.4.

Another uncertainty source is that the more far away the surface marked by the laser, the greater the laser beam or spot diameter becomes. Fig 10, b shows that the laser beam travels a certain distance and is redirected by a mirror on two occasions, due to this travel, at the PL output the laser beam diameter is already greater than the originally emitted laser beam diameter.

Hence, another improvement is that the distances between the laser and the mirrors, i.e. the laser beam travel was reduced from centimeters to millimeters, by doing this the laser beam diameter in the PL output equals to the beam diameter emitted from the laser output, maintaining the lowest beam diameter possible within the TVS, therefore theoretically increasing the TVS range. Analysis of laser spot diameter variation is given in [9], it shows that this circumstance plays a significant role in total uncertainty distribution, and this part of general design is critical for total uncertainty decrease.

The Scanning Aperture design is maintained from Prototype I to II (Fig 10, c and Fig 11, c), the only difference is that the new SA is smaller in size and is installed within the cylindrical tube, however it's important to mention that the most critical point with the SA is to maintain it aligned in the same plane as PL in order to be able to create the dynamic triangle more solid or fixed in mechanical meaning, i.e. only this design guarantee that scanning ray and scanning plane are meeting exactly in the same plane triangle.

VI. CONCLUSIONS

- The presented TVS is fully capable of solving the obstacle detection task in autonomous navigation for mobile robots field, by detecting any number of obstacles in the mobile robot's field of view, locating their positions and creating a digital map of the obstacle visible surface in a short time with metrological accuracy.
- Appropriate Signal conditioning is essential to the process in order to prevent additional uncertainty sources to affect the coordinate's measurement, therefore keeping the confidence level at the 95% demonstrated during experimentation.
- Faster system response time can be achieved by replacing conventional operational amplifiers used in the filter and amplification stages with fast response operational amplifiers; thus reducing the time to calculate obstacle's coordinates and giving more time for the mobile robot's navigation tasks such as path planning or goal seeking.
- Currently the low pass filters used in the signal conditioning stage were designed with a cutoff frequency of 200Hz, since our system frequency is lower than that and the noise present in our signal is higher, it's an advantage for the TVS, but if at some point we increase the TVS frequency and becomes overlapped with the noise frequencies, another approach of signal conditioning would be required.
- This 3D resolution improvement is useful for robot navigation task as well as for another practical application of this method [10, 11].

ACKNOWLEDGEMENT

This work has been partially supported by the Ministry of Science and Innovation (MICINN) of Spain under the research project TEC2007-63121, and the Universidad Politecnica de Madrid.

REFERENCES

[1] Jose Guivant, Eduardo Nebot, Stephan Baiker. "Autonomous Navigation and Map building Using Laser Range Sensors in Outdoor Applications", Journal of Robotic Systems, Vol, 17 No 10, October 2000, pp 565-583.

[2] Quoc V. Do1, Peter Lozo2 and Lakhmi C. Jain. "Vision-Based Autonomous Robot Navigation", Studies in Computational Intelligence (SCI) 8, 2005, pp. 65–103.

[3] Oleg Sergiyenko, et al. Precise Optical Scanning for practical multiapplications. Proceedings of IEEE 34th Annual IEEE Conference IECON'08, Florida, USA, 2008, p. 1656-1661.

[4] M. Rivas Lopez, Oleg Sergiyenko, Vera Tyrsa. "Computer vision" book. Edited by Xiong Zhihui, Chapter 22 "Machine vision: approaches and limitations", pp. 395-428. Editorial I-TECH, Vienna, Austria 2008, 538p.

[5] M. Petrov et al. Optical 3D Digitizers: Bringing Life to the Virtual World. IEEE Computer Graphics and Applications, Vol. 18, Issue 3, May/June 1998, pp 28-37.

[6] Raymond A. Serway, "Physics: for Scientists and Engineers with Modern Physics" 3rd Edition, Updated Printing, Philadelphia: Saunders, 1990, 1253p.

[7] Moisés Rivas, Oleg Sergiyenko, Mario Aguirre, Luis Devia, Vera Tyrsa, and Ismael Rendón (2008) Spatial data acquisition by laser scanning for robot or SHM task. IEEE-IES Proceedings "International Symposium on Industrial Electronics"(ISIE-2008), Cambridge, United Kingdom, 30 of June -2 of July, 2008, pp.1458-1463.

[8] Robert Coughlin and F Driscoll, Operational Amplifiers and Linear Integrated circuits, sixth edition, Pearson Education, 2001, ISBN-10: 0130149918.

[9] Luis C. Básaca, Julio C. Rodríguez, Oleg Sergiyenko 3D Laser Scanning Vision System for Autonomous Robot Navigation, IEEE International Symposium on Industrial Electronics (ISIE-2010), Bari, Italy, July 4-7, 2010, in press.

[10] O. Yu. Sergiyenko, W. Hernandez, V. V. Tyrsa, D. Hernández-Balbuena. Precise Optical Scanning for multiuse. Proceedings of IEEE-35th Annual Conference of IEEE Industrial Electronics (IECON'09), 3-5 November, 2009, Porto, Portugal, pp.3399-3404.

[11] Moisés Rivas López, Oleg Sergiyenko, Vera Tyrsa, Wilmar Hernandez Perdomo, Daniel Hernández Balbuena, Luis Devia Cruz, Larisa Burtseva, Juan Iván Nieto Hipólito. Optoelectronic method for structural health monitoring. SAGE Publications, "International Journal of Structural Health Monitoring", Vol.9, No.2, March, 2010, pp.105-120.

3D Laser Scanning Vision System for Autonomous Robot Navigation

Luis C. Básaca[1], Julio Rodríguez[1], Oleg Yu. Sergiyenko[1], Vera V. Tyrsa[2], Wilmar Hernández[3], Juan I. Nieto Hipólito[4], Oleg Starostenko[5]

[1]*Engineering Institute of Autonomous University of Baja California;* [2]*Polytechnic University of Baja California;* [3]*Polytechnic University of Madrid;* [4]*Autonomous University of Baja California, Campus Ensenada;* [5]*Universidad de Las Americas, Puebla*

lubakun@gmail.com[1], julio_qas@hotmail.com[1], srgnk@iing.mxl.uabc.mx[1], vera-tyrsa@yandex.ru[2], whernan@ics.upm.es[3], jnieto@uabc.mx[4], oleg.starostenko@udlap.mx[5]

Abstract- **The presented Technical Vision System realizes the principle of dynamic triangulation. This technique is able to resolve in real time a triple task: to detect a presence of significant obstacle in a robot's neighborhood; locate its position in a robot's field-of-view; obtain in a short time a digital map of the obstacle visible surface with metrological accuracy of coordinates and adjustable step of discretization. Some aspects of theoretical backgrounds, technical design, optical principle, mathematical framework, signal processing, prototype design and experimentation are presented in this paper.**

I. Introduction

One of the main issues and challenges of a navigation system is to detect the presence of static and dynamic obstacles and the distance from a mobile robot to those obstacles. There are several ways of performing this operation; Lipnickas and Knyš [1] propose a system that utilizes two cameras to obtain two images of the same object from different points of view and reconstruct a 3D scene.

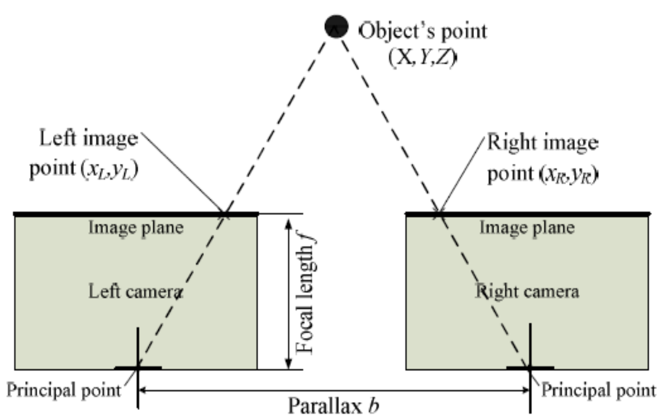

Fig. 1. Illustration of the stereo geometry. [1]

The accuracy of 3D data reconstruction depends on the accuracy of the disparities, system calibration, images rectification and overall stereo system construction [1]. The algorithms used for the mentioned operations do not provide high accuracy, making this method not the best option for obstacle detection.

Other systems (see Fig. 2. [2]) propose solutions based on fixed 2D laser scanners. Mobile robot with a 2D laser scanner would only be able to see or detect obstacles in a horizontal line in front of itself with a fixed angle and limited distance, not true 3D information.

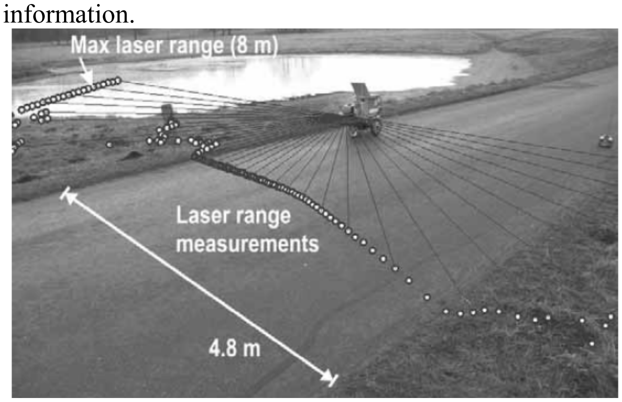

(a) Isometric View

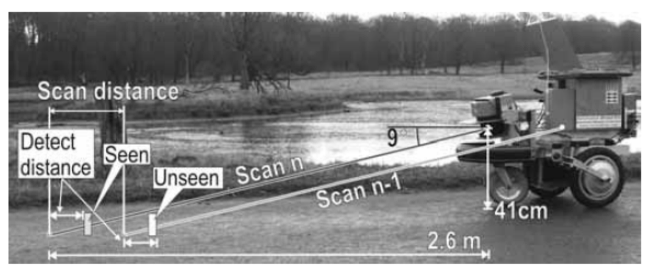

(b) Side view

Fig. 2. Mobile Robot with fixed 2D Laser Scanner. [2]

Our system uses 3D laser scanning dynamic triangulation to obtain the distance from the mobile robot to an obstacle with very high accuracy, this information is used to pinpoint the exact 3D coordinates of an obstacle, providing the mobile robot with the ability to detect the presence of obstacles theoretically in a 180° area. In reality the field-of-view of our proposed system can be limited in the less spatial angle due to own sizes of controlled

978-1-4244-6392-3/10/$26.00 ©2010 IEEE

robot and its task duty. It permits to filter the unnecessary information and increase functioning speed of robot's control system.

II. Technical Vision System (TVS)

The mobile robot's navigation techniques must have a reliable accuracy in wide ranges. This is the reason we are developing new ways to recognize the obstacles that are in front of the mobile robot, we call this a Technical Vision System or TVS. This new vision system provides information on depth and position, 3D coordinates (X, Y, Z) of objects found in the field of vision in front of mobile robot.

The TVS basically consists of a bar with very accurate dimensions in which two devices are installed, one on each side of the bar, a Positioning Laser (PL) and a Scanning Aperture (SA) that contains a revolving sensor, Fig. 3.

As stated before this system utilizes a Dynamic Triangulation method to obtain the exact coordinates of an object, following is the explanation of this method and after that we'll focus on the TVS operation. The Dynamic Triangulation method differs from other known triangulations [6, 7] first of all because two dynamic angles measurement permit increase significantly the system operating range, comparing to systems with only one angle and reflected spot positioning on the fixed optical matrix.

III. Dynamic Triangulation

Dynamic Triangulation is the base of our system; we use it to obtain 3D coordinates of objects or obstacles that are in the field of vision in front of mobile robot.

As shown in Fig. 3, a laser beam is projected from the Positioning Laser (PL) onto the surface of an obstacle, illuminating it and reflecting back rays onto the revolving sensor inside the Scanning Aperture (SA) [3, 8].

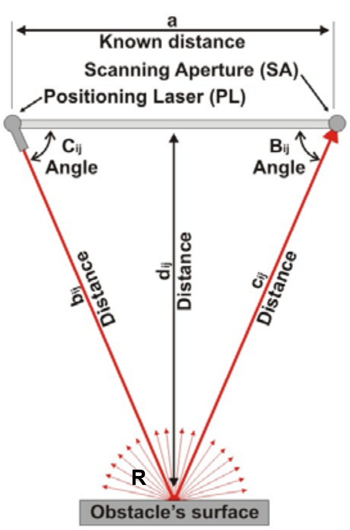

Fig. 3. Dynamic triangulation.

There are two types of light reflection, specular and diffuse. When a beam of light encounters a smooth mirror-like reflecting surface, the reflected rays will be parallel to each other and according to the Law of Reflection, the angle of reflection will be equal to the angle of incidence; this is called Specular Reflection. On the contrary, if the beam of light encounters a rough reflecting surface, the rays will reflect in every direction, this is called Diffuse Reflection (see Fig. 4 [4 (p. 989), 5 (p. 870-871)]).

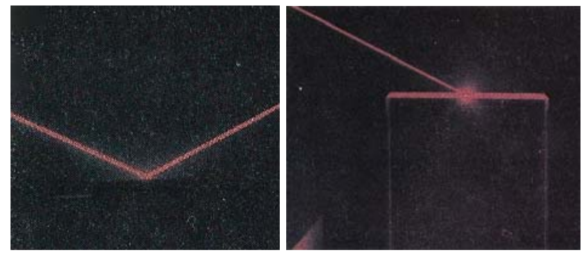
a) Specular reflection b) Diffuse reflection
Fig. 4. Types of light reflection. [4]

Although light can be reflected specularly (i.e. a mirror) or diffusely (i.e. a piece of wood), many materials present mixed reflection, meaning that some light rays are reflected specularly and some diffusely, this is shown in figure 5.

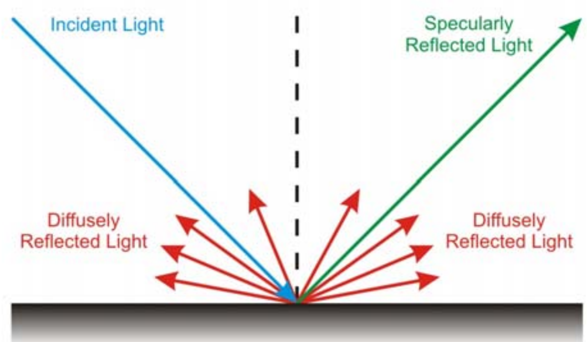

Fig. 5. Mixed Reflection is a combination of Specular and Diffuse Reflection.

Due to the mentioned above, the most probable reflection type in a robot navigation task is the last one (Fig. 5). It is clear that a portion of emitted energy in a photoreceiver is strongly dependant on mutual positioning of reflection point R and SA on Fig. 3 in the geometry of Fig 5. However as shown in experimentation with prototype (Figs. 12-14), in the worst case of reflection, when the reflected signal is converted to an electrical signal by the photoreceiver sensor, it has an acceptable voltage level on reasonable striking distances.

Then using the theorem of sines as well as correlation between the sides and the height in a triangle represented on Fig. 3, it is possible to find the formula to calculate distance d from base a up to points highlighted by the laser beam.

$$d_{ij} = a \frac{\sin B_{ij} \cdot \sin C_{ij}}{\sin\left[180^\circ - \left(B_{ij} + C_{ij}\right)\right]}, \tag{1}$$

Where, indexes i and j represents the step number in horizontal (i) and vertical (j) directions during general 3D scanning.

Using value of angles B_{ij}, C_{ij}, $\sum_{j=1}^{n}\beta_j$ and base a, it is possible to calculate the cartesian coordinates of the each laser highlighted points on each ij-step of 3D scanning process, by the following formulas:

$$x_{ij} = a\frac{\sin B_{ij}\cdot\sin C_{ij}\cdot\cos\sum_{j=1}^{j}\beta_j}{\sin\left[180^\circ-\left(B_{ij}+C_{ij}\right)\right]}, \qquad (2)$$

$$y_{ij} = a\left(\frac{1}{2}-\frac{\sin B_{ij}\cdot\cos C_{ij}}{\sin\left[180^\circ-\left(B_{ij}+C_{ij}\right)\right]}\right) \text{ at } B_{ij}\le 90^\circ, \qquad (3)$$

$$y_{ij} = -a\left(\frac{1}{2}+\frac{\sin B_{ij}\cdot\cos C_{ij}}{\sin\left[180^\circ-\left(B_{ij}+C_{ij}\right)\right]}\right) \text{ at } B_{ij}\ge 90^\circ, \qquad (4)$$

$$z_{ij} = a\cdot\frac{\sin B_{ij}\cdot\sin C_{ij}\cdot\sin\sum_{j=1}^{j}\beta_j}{\sin\left[180^\circ-\left(B_{ij}+C_{ij}\right)\right]} \qquad (5)$$

IV. TVS OPERATION

The TVS is designed to detect objects that are in its range of vision. This system contains a high-power laser with a collimator where a beam of laser light is generated and redirected from PL, the beam reaches the surface of an object or obstacle in sight and is reflected from it. The reflected light reaches a photo receiver sensor inside the SA which measures the angle of light incidence, this angle is called B_{ij}. As stated before B_{ij}, C_{ij} and $\sum_{j=1}^{n}\beta_j$ are needed to calculate the obstacle's 3D coordinates.

PL and SA are both installed on each end of a horizontal bar as shown in Fig. 6, b.

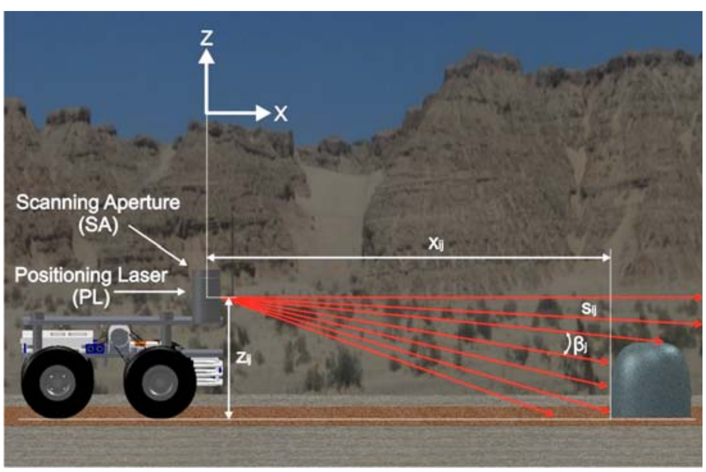

(a) Side View

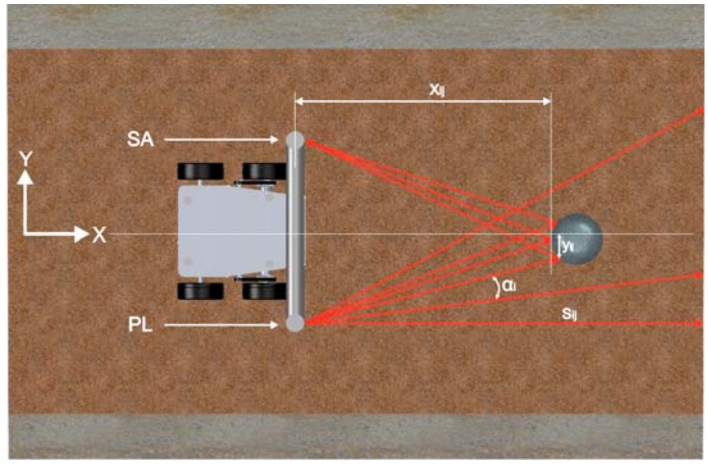

(b) Top View

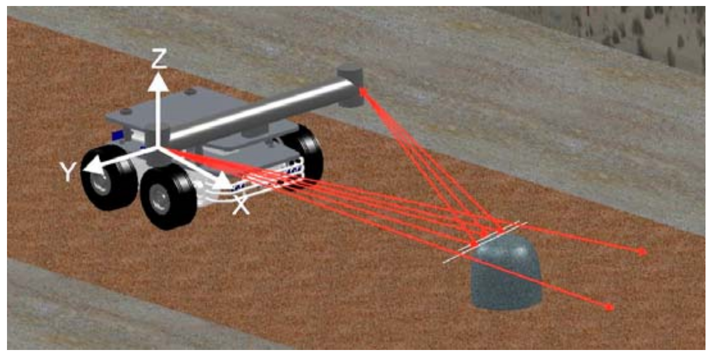

(c) Isometric View

Fig. 6. Operation principle of a TVS.

Each point that is highlighted on the obstacle surface by a beam of laser light emitted from PL is called S_{ij}. The laser is redirected in PL by using a 45° mirror attached to a stepper motor with an encoder, allowing us to obtain the angle C_{ij} at any time, which is the angle between each S_{ij} and the horizontal bar. The angle between each S_{ij} is called α_i.

The following formula is used to calculate the angle C_{ij}:

$$C_{ij} = C_{\max} - \sum_{i=1}^{n}\alpha \qquad (5)$$

Where, C_{max} is an initial angle of the Positioning Laser (PL) position.

The SA is the part that receives the reflected rays to calculate the angle B_{ij} and it consists of a revolving 45° mirror that is inside an aperture, a sensor which marks a zero point when it detects the mirror has completed a 360° turn and a photo receiver sensor to detect instance of time when a ray reflected in S_{ij} reaches it (Fig. 7).

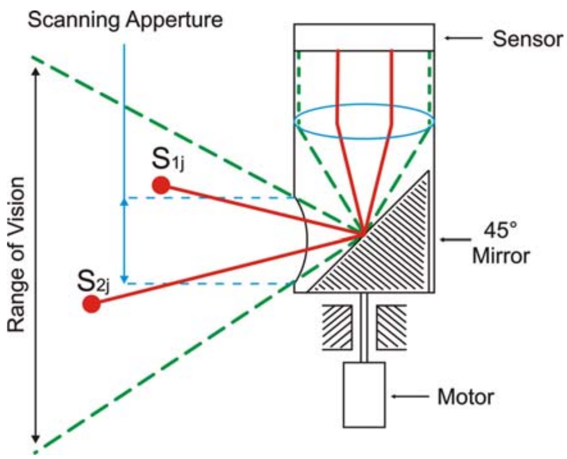

(a) Principle

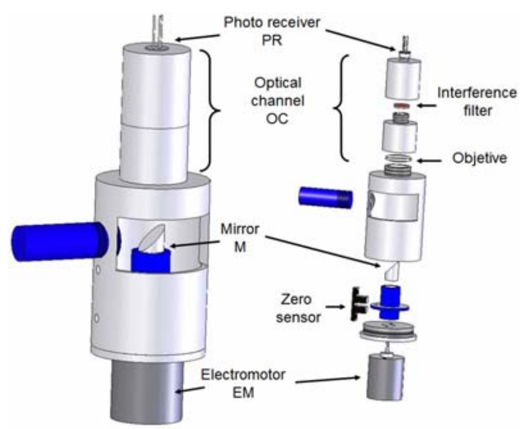

(b) General Design [6]

Fig. 7. Scanning aperture.

If the photo receiver sensor (PR) (Fig. 7) detects a ray of light we take the number of pulses between the zero sensor pulse and the PR sensor pulse and calculate the angle B_{ij}. (Fig. 3) The SA is continuously rotated by the DC motor EM with precise constant velocity to obtain the ratio between a 360° turn and its time.

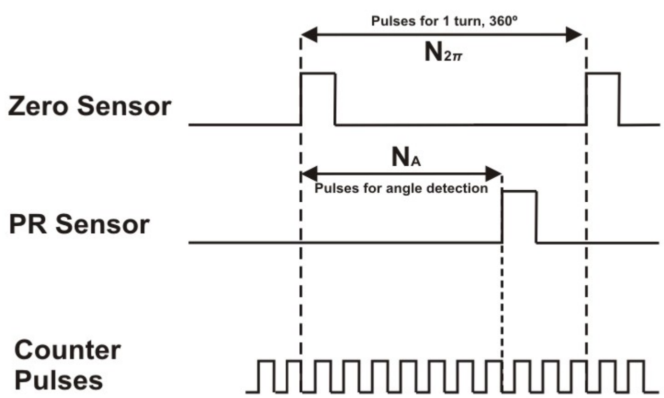

Fig. 8. Photoelectric signals and angle detection.

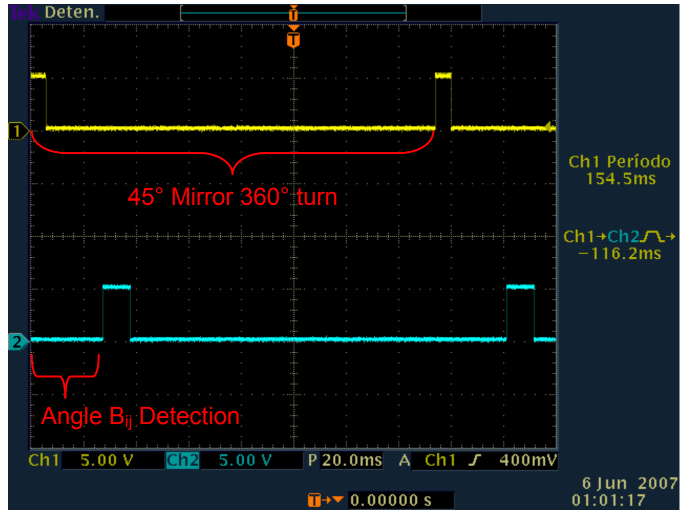

Fig. 9. Angle Detection, signal from PR and Zero sensors obtained during experimentation with prototype explained in section IV. [6]

The following formula is used to calculate the angle B_{ij}:

$$B_{ij} = \frac{2\pi \cdot N_A}{N_{2\pi}} \tag{5}$$

Where, N_A is the number of counter pulses when light is detected and $N_{2\pi}$ is the number of counter pulses when the 45° mirror completes a 360° turn [6] Figs. 8 and 9.

After the calculation of the angles and the 3D coordinates and taking into consideration the known size of the mobile robot, we can design a navigation system about how to avoid collisions, determine if a small object can or cannot be evaded and warn false alarms.

V. SPATIAL RESOLUTION

After some experimentation with the 3D laser scanner vision system, the width of the laser point was determined, see Table I.

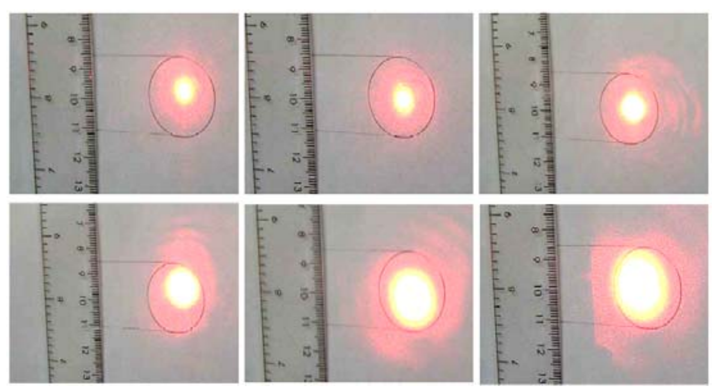

Fig. 10. Laser highlighted spot diameter vs operating distance.

TABLE I. [3]
LASER POINT WIDTH

d, m	1	2	3	4	5
σd, mm	0,10	0,41	0,93	1,65	2,57
d, m	10	20	30	50	100
σd, mm	10,28	41,14	92,55	257,11	1028,43

Based on this data we can obtain reliable results with point sizes of only 1 cm for distances of 10 m (Fig. 10). The scanning method takes constant readings at different points and you get a general map of the surrounding objects. Even small objects can be easily detected so the mobile robot's onboard computer can make decisions about whether there are risks of collision or not and which is the best possible path to travel.

VI. INCREASE OF THE ACCURACY OF COORDINATES MEASUREMENT BY SPOT CENTER SEARCH

A noisy pulse of the real electric signal is one of the principal causes of coordinate's measurement uncertainty. To decrease it we implement an innovating method of signal energy center search (similar to the geometric center of a theoretical pulse).

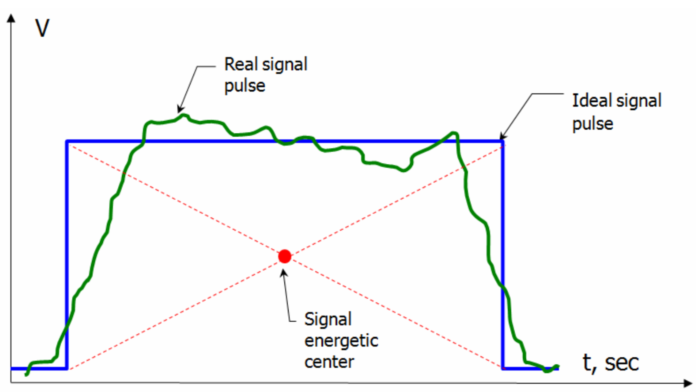

Fig. 11. Signal energetic center search. [8]

Fig. 11 shows the real signal pulse vs the ideal signal pulse and it also shows that the energetic center of the signal is in the same location for both signals.

VII. PROTOTYPE CONSTRUCTION AND EXPERIMENTATION

An experimental prototype of the mentioned TVS was constructed to prove the introduced method. A prototype was built with the follows components:

- Aluminum base bar with 1m of length.
- Stepper motors for vertical and horizontal scanning.
- 20mW laser (JDS Uniphase, model 1136P).
- Two mirrors with 45° cut.
- DC motor (MD5-2554AS-AA, Jameco).
- High-speed photo receiver (15.0mm2 TO-2 Silicon Detector).
- A lens in the aperture part to get a fine convergence of light in photo receiver.
- Start-sensor (OT124 H21A, Jameco).
- Interference filter to get only the selected source of light.
- IBM Pentium II Laptop using a "Turbo C" program in MS-DOS, parallel port interface.

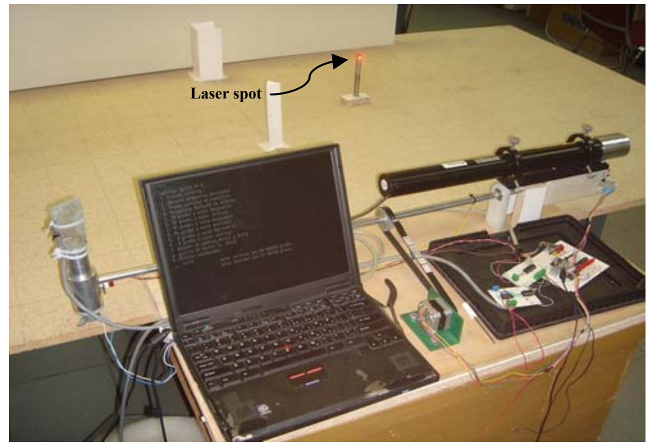

Fig. 12. Complete prototype system view. [8]


Fig. 13. Scanning aperture (locations in TVS) [8]

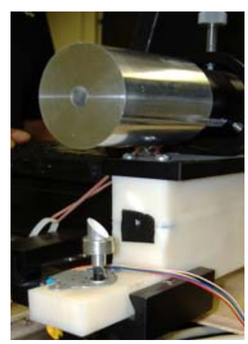
Fig. 14. Emisor part (Positioning Laser, PL) [8]

The complete prototype is 1m long and is shown in Fig. 12 during operation. The PL and SA parts of the prototype are shown in Figs. 13 and 14. This prototype was tested 50 times in different locations in grid nodes to verify accuracy on vision by different angles in 2D, in Table II are partially shown the measured values by the prototype.

TABLE II [8]
EXPERIMENTAL RESULTS OF COORDINATES MEASUREMENTS

Test Point	Theoric Value				Measured Value			
	X (m)	Y (m)	B (°)	C (°)	*x(m)*	*y(m)*	*B (°)*	*C (°)*
B	120	120	120,26	35,22	124,21	128,68	123,43	34,8
D	100	100	116,57	33,69	99,83	104,48	118,46	32,87
F	100	80	106,70	37,57	95,3	76,86	106,4	36,91
H	120	60	94,76	47,49	122,92	63,49	96,38	47,28
J	80	60	97,13	36,03	77	58,62	96,57	35,33
L	80	40	82,87	41,63	79,99	42,15	84	40,95
N	120	40	85,24	53,13	119,86	40,04	84,48	53,08
O	120	20	75,96	59,74	119,22	19,48	76,01	59,76
P	100	20	73,30	55,01	97,6	19,15	72,94	54,67
Q	80	20	69,44	48,81	79,11	18,7	68,39	49,04
R	60	20	63,43	40,60	60,33	21,7	64,3	40,07
S	40	20	53,13	29,74	39,14	19,59	52,07	29,35
T	40	0	38,66	38,66	36,52	1,06	36,52	36,73
U	60	0	50,19	50,19	59,8	0,9	49,39	50,625
V	80	0	57,99	57,99	80,93	3,49	56,7	60,11
W	100	0	63,43	63,43	103,58	1,51	63,45	64,68
X	120	0	67,38	67,38	120,72	-4,7	66,23	69,43
Y	120	-20	59,74	75,96	118,54	-18,36	59,95	75,05
Z	100	-20	55,01	73,30	96,72	-18,37	54,7	71,9
A1	80	-20	48,81	69,44	75,79	-18,33	48,03	67,32
B1	60	-20	40,60	63,43	58	-18,53	39,5	61,52
C1	40	-20	29,74	53,13	36,17	-20,31	27,3	50,62
D1	60	-40	33,69	80,54	58,05	-38,63	33,6	78,92
E1	80	-40	41,63	82,87	77,46	-38,26	40,46	81,38
F1	100	-40	48,01	84,29	97,1	-38,02	46,94	82,96
H1	120	-60	47,49	94,76	123,68	-61,03	48,21	95,09
J1	80	-60	36,03	97,13	78,9	-59,73	35,37	97,03
L1	80	-80	31,61	110,56	80,52	-80,21	31,81	110,56
N1	120	-80	42,71	104,04	121,01	-78,73	43,34	103,35
P1	100	-100	33,69	116,57	101,65	-96,18	35,06	114,43
R1	100	-120	30,47	124,99	111,73	-126,15	32,09	124,27

Analyzing the measurement numerical results, it is possible to say that all the experiments were carried out at 95% confidence level. Uncertainty measurement (especially its offset error) does not overcome a 5% threshold in any point. In static mode TVS can perform significant accuracy increase that is suitable for robot “vision with attention”, or for another TVS practical applications [8, 11].

VIII. CONCLUSIONS

Assuming mentioned above it is possible to say that:

- Presented TVS is able to solve in real time a triple task: to detect a presence of significant obstacle in a robot’s neighborhood; locate its position in a robot’s field-of-view; obtain in a short time digital map of the obstacle visible surface with metrological accuracy of coordinates and adjustable step of discretization. This is achieved by proper stepper-motor use and software control of the scanning speed.
- This kind of technical vision realization is unique over others [1, 7, 9, 10], it can represent information about objects inside robot’s field-of-view as the coordinates matrix of n points on the obstacle visible surface. Uncertainty of these automated measurements is fixed, and can be evaluated easily by well known mathematical formalism [6].
- TVS is not antagonistic towards CCD-means of the environmental information perception. On the contrary, TVS and CCD can mutually complement each other in many real cases.
- TVS represents the realization of an idea of a computer vision in the form of an analogue-digital model of space in front of the robot. This model can be easily transformed by computer means into an image, suitable for a human-operator to percept.

REFERENCES

[1] A. Lipnickas, and A. Knyš. 2009. "A Stereovision System for 3-D Perception." Electronics & Electrical Engineering, no. 91: 99-102. ISSN: 1392-1215.

[2] Andersen, Jens Christian, Morten Rufus Blas, Ole Ravn, Nils A. Andersen, and Mogens Blanke. 2006. "Traversable terrain classification for outdoor autonomous robots using single 2D laser scans." Integrated Computer-Aided Engineering 13, no. 3: 223-232. ISSN: 10692509.

[3] Oleg Sergiyenko, et al. Precise Optical Scanning for practical multiapplications. Proceedings of IEEE 34th Annual IEEE Conference IECON’08, Florida, USA, 2008, p. 1656-1661.

[4] Raymond A. Serway, “Physics: for Scientists and Engineers with Modern Physics” 3rd Edition, Updated Printing, Philadelphia: Saunders, 1990, 1253p.

[5] Eugene Hecht,”Physics”, Pacific Grove, California: Brooks/Cole, 1994. 1128p.

[6] M. Rivas Lopez, Oleg Sergiyenko, Vera Tyrsa. “Computer vision” book. Edited by Xiong Zhihui, Chapter 22 “Machine vision: approaches and limitations”, pp. 395-428. Editorial: I-TECH, Vienna, Austria, 2008, 538 p.

[7] M. Petrov et al. Optical 3D Digitizers: Bringing Life to the Virtual World. IEEE Computer Graphics and Applications, Vol. 18, Issue 3, May/June 1998, pp 28-37.

[8] Moisés Rivas, Oleg Sergiyenko, Mario Aguirre, Luis Devia, Vera Tyrsa, and Ismael Rendón. Spatial data acquisition by laser scanning for robot or SHM task. IEEE-IES Proceedings “International Symposium on Industrial Electronics”(ISIE-2008), Cambridge, United Kingdom, June - July, 2008, pp.1458-1463

[9] Lei Wang. Takashi Emura. and Takashi Ushiwata October 1-3, 2000. Automatic Guidance of a Vehicle Based on DGPS and a 3D Map. 2000 IEEE Intelligent Transportation Systems Conference Proceedings, Dearborn (MI), USA, p.131-136.

[10] Jose Guivant, Eduardo Nebot, Stefan Baiker. April 2000. High Accuracy Navigation Using Laser Range Sensors in Outdoor Applications. Proceedings of the 2000 IEEE International Conference on Robotics & Automation,V.4 San Francisco, CA, p. 3817-3822.

[11] Moisés Rivas López, Oleg Sergiyenko, Vera Tyrsa, Wilmar Hernandez Perdomo, Daniel Hernández Balbuena, Luis Devia Cruz, Larisa Burtseva, Juan Iván Nieto Hipólito. Optoelectronic method for structural health monitoring. SAGE, “Structural Health Monitoring”, Vol.9, No.2, 2010, pp.105-120.

2do Congreso Nacional de Estudiantes de Posgrado del Instituto de Ingeniería,
Instituto de Ingeniería – UABC, Maestría y Doctorado en Ciencias e Ingeniería
ISBN:

Aumento de resolución de un sistema de visión en 3D mediante el método de triangulación dinámica para la tarea de navegación autónoma de robots móviles

Luis C. Básaca, Oleg Yu. Sergiyenko, Julio Rodríguez
*E-mail: lubakun@gmail.com, srgnk@iing.mxl.uabc.mx, julio_qas@hotmail.com

Abstract

This paper presents a technical vision system designed to resolve multiple tasks which are fundamental for mobile robots autonomous navigation. These tasks include detecting the presence of a significant obstacle for a mobile robot, finding the position of the obstacle in the field of view of the mobile robot and the creation of a digital map containing the 3D coordinates of the obstacle's visible surface with metrological accuracy. This paper focuses mostly on signal conditioning and processing of the input signals from our sensors in order to eliminate possible noise signals, increase the resolution of the vision system and guarantee the detection and position of an obstacle for the mobile robot.

Keywords: 3D Vision System, Dynamic Triangulation, mobile robot, autonomous navigation, noise filtering.

Resumen

En este artículo se presenta un sistema de visión técnica diseñado para resolver múltiples tareas las cuales son fundamentales para la navegación autónoma de robots móviles. Estas tareas incluyen la detección de la presencia de un obstáculo significativo para un robot móvil, la localización del obstáculo dentro del campo de visión del robot móvil y la creación de un mapa digital que contiene las coordenadas en 3D de la superficie visible del obstáculo con una precisión metrológica. Este documento se centra principalmente en el acondicionamiento y procesamiento de señales de entrada de nuestros sensores con el objetivo de eliminar posibles señales de ruido, aumentar la resolución del sistema de visión y garantizar la detección y posición de un obstáculo para el robot móvil.

Palabras clave: Sistema de Visión en 3D, Triangulación Dinámica, robot móvil, navegación autónoma, filtrado de ruido.

1. Introducción

A través de los años la navegación autónoma ha probado ser un campo muy interesante y desafiante el cual envuelve múltiples tareas con el fin de lograr un comportamiento autónomo en un robot móvil. Entre esas tareas existe el problema particular de la detección de obstáculos que rodean al robot móvil para evitar colisiones durante la navegación.

Distintos enfoques han sido presentados para resolver este problema como lo son, estéreo visión, sistemas de posicionamiento global, radar, sensores infrarrojos, sensores ultrasónicos, láser, combinaciones de sensores, entre otros.

Actualmente los dispositivos GPS son capaces de fijar posiciones con errores del orden de 1cm hasta 100m en tiempo real; sin embargo existen ciertas áreas del planeta donde los satélites no pueden proporcionar una cobertura total o parcial, por lo tanto la precisión no puede ser garantizada [1].

Otros sistemas utilizan visión monocular la cual procesa imágenes individuales en 2D, obtenidas de una cámara para representar el mundo real en 3D, pero debido a la naturaleza particular de las imágenes en 2D, la profundidad no puede ser obtenida de estas imágenes; por consiguiente sensores adicionales son requeridos para obtener esa información.

Además, el procesamiento de imágenes requiere una gran cantidad de tiempo debido a la vasta cantidad de información que una imagen de una cámara digital proporciona; lo cual es no es la mejor opción para sistemas de navegación donde la rápida toma de decisiones es crucial [2].

El Sistema de Visión Técnica o TVS (*Technical Vision System*) utiliza el barrido por láser y un método al cual llamamos triangulación dinámica, lo que le permite al sistema generar un mapa digital del campo de visión del robot móvil además de calcular y almacenar en memoria las coordenadas en 3D (X, Y, Z) para cada punto o coordenada del mapa digital. Teóricamente el TVS posee un campo de visión de aproximadamente 180°, lo cual en la práctica puede ser limitado debido al tamaño de las partes mecánicas del TVS. Los datos generados por el TVS pueden ser utilizados por el sistema de navegación de un robot móvil para resolver tareas como la evitación de obstáculos o planeación de ruta.

2. EL TVS y la triangulación dinámica

Como se mencionó anteriormente, el TVS proporciona las coordenadas en 3D de un obstáculo u objeto posicionado dentro del campo de visión del robot móvil. El TVS consiste de dos dispositivos instalados uno en cada extremo de un cilindro horizontal, los dispositivos son llamados Posicionador de Láser y Apertura de Barrido (ver figura 1) [3].

Llamamos a nuestro método Triangulación Dinámica debido a que el posicionador de láser posee la capacidad de girar y dirigir el rayo láser en 180° teóricamente y la apertura de barrido posee componentes internos los cuales giran con una velocidad constante, por lo tanto el TVS posee dos ángulos dinámicos. Estos ángulos que forman el triángulo, existen solamente por un corto periodo de tiempo cuando el plano de barrido coincide con el punto del láser proyectado en un obstáculo. Esto le proporciona al robot móvil la ventaja de tener un campo de visión de mayor tamaño comparado con los sistemas de triangulación estáticos, los cuales limitan el campo de visión del robot móvil estrictamente al tamaño del sensor óptico [4].

El posicionador de láser es controlado por un motor de pasos y utiliza dos espejos de 45° para reflejar y dirigir el haz de láser a través del campo de visión hacia cualquier obstáculo encontrado. Después de alcanzar un obstáculo el haz de láser es reflejado de la superficie en forma de rayos, algunos de ellos especulares (según la ley de reflexión) y otros de manera difusa (en todas direcciones) dependiendo del material de la superficie [3], a esto se le llama reflexión mixta (ver figura 2).

Los rayos que son reflejados hacia la apertura de barrido llegan a un espejo de 45° dentro de la apertura, el cual dirige los rayos ortogonalmente hacia un sensor fototransistor. En este instante de tiempo un triangulo (de base conocida) es formado por el láser y el ángulo B_{ij} es calculado (ver figura 1) [5].

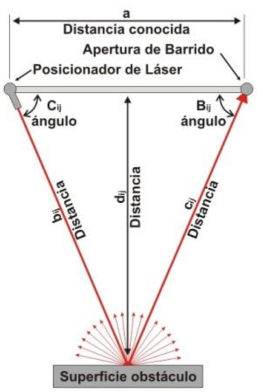

Figura 1. Triangulación Dinámica.

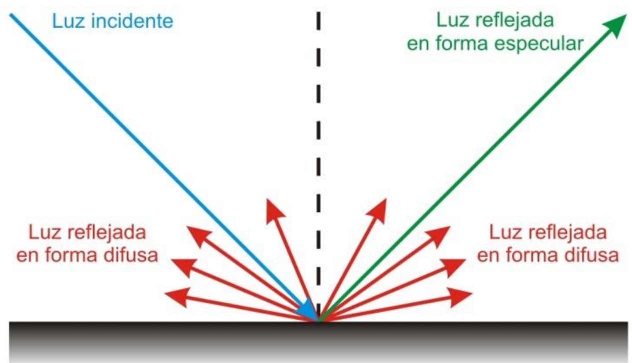

Figura 2. Reflexión Mixta.

Basándonos en la ley de senos al igual que en la correlación entre los lados y la altura de un triangulo, hemos desarrollado las formulas para calcular la distancia *d* de la base *a* hasta el punto marcado por el láser (ver figura 1). Utilizando los ángulos B_{ij}, C_{ij}, $\sum_{j=1}^{n}\beta_j$ y la base *a*, calculamos las coordenadas en 3D de cada punto que es marcado por el láser en un obstáculo y reflejado hacia el sensor con las siguientes formulas:

$$x_{ij} = a\frac{\sin B_{ij}\cdot\sin C_{ij}\cdot\cos\sum_{j=1}^{j}\beta_j}{\sin\left[180°-\left(B_{ij}+C_{ij}\right)\right]}, \tag{1}$$

$$y_{ij} = a\left(\frac{1}{2}-\frac{\sin B_{ij}\cdot\cos C_{ij}}{\sin\left[180°-\left(B_{ij}+C_{ij}\right)\right]}\right) \text{ at } \mathrm{B_{ij}} \leq 90°, \tag{2}$$

$$y_{ij} = -a\left(\frac{1}{2}+\frac{\sin B_{ij}\cdot\cos C_{ij}}{\sin\left[180°-\left(B_{ij}+C_{ij}\right)\right]}\right) \text{ at } \mathrm{B_{ij}} \geq 90°, \tag{3}$$

$$z_{ij} = a\cdot\frac{\sin B_{ij}\cdot\sin C_{ij}\cdot\sin\sum_{j=1}^{j}\beta_j}{\sin\left[180°-\left(B_{ij}+C_{ij}\right)\right]}, \tag{4}$$

La figura 3 muestra el TVS montado sobre un robot móvil y su operación en un ambiente al aire libre. El haz de láser, las distancias X_{ij}, Y_{ij}, Z_{ij} y otros ángulos se muestran en la figura 3 para representar la operación del TVS.

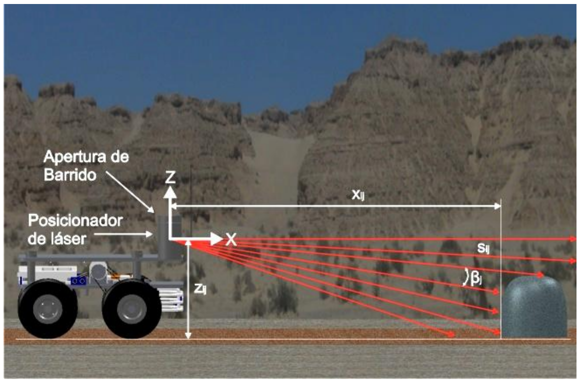

(a) Vista lateral.

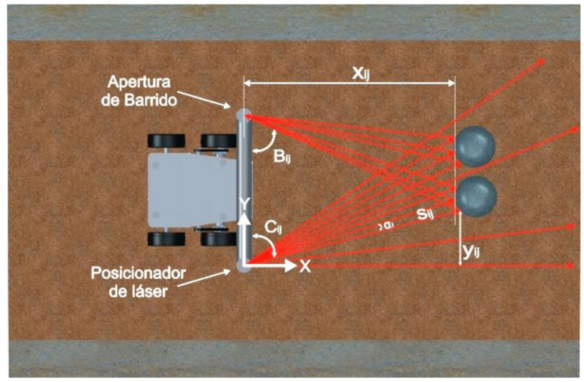

(b) Vista superior.

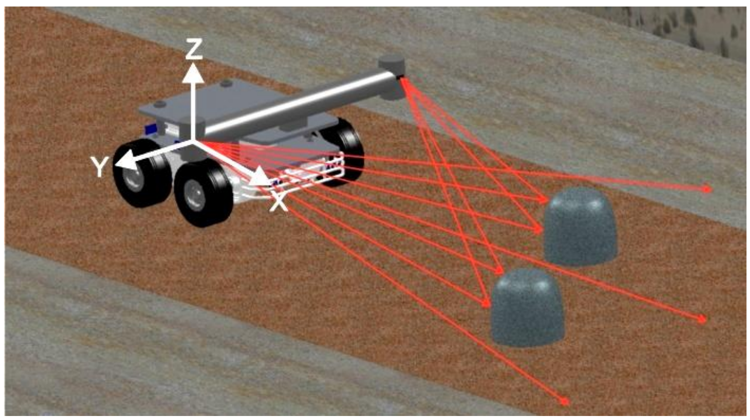

c) Vista isométrica.

Figura 3. Operación del TVS montado sobre un robot móvil.

Cada punto que es marcado en la superficie del obstáculo (ver figura 3, a-c) por un haz de láser se le llama S_{ij}. Para cada S_{ij} son calculadas las coordenadas cartesianas X_{ij}, Y_{ij} y Z_{ij} mediante las fórmulas 1-4. A través de experimentación, analizando mediciones dentro y fuera del campo de visión, encontramos que la precisión de la medición de coordenadas no es uniforme en todo el campo, sin embargo, (ver figura 4), la parte amarilla oscura de la imagen muestra una incertidumbre del 1% y la parte verde muestra un 4%, lo que significa que contamos un nivel de confiabilidad del 99% y 96% respectivamente para esas zonas de nuestro campo de visión [5, 6]. Por lo general, los controladores estándar de motores de pasos son operados con una frecuencia promedio de 1KHz, lo cual significa que podemos obtener por lo menos 1000 puntos por segundo, cada valor de X, Y y Z con precisión metrológica e incertidumbres definidas.

El análisis de la distribución espacial de la incertidumbre de las mediciones nos llevó a la conclusión que el TVS debe ser implementado con máxima atención al centro del campo de visión real del diseño final del sistema general[1]. Dicha variación del error relativo es una señal y oportunidad de mejora para diseñar un nuevo prototipo con mejor alineamiento mecánico.

[1]El sistema general se refiere al sistema final donde se utilizará el TVS, puede ser un robot móvil, un sistema de monitoreo de estructuras u otro.

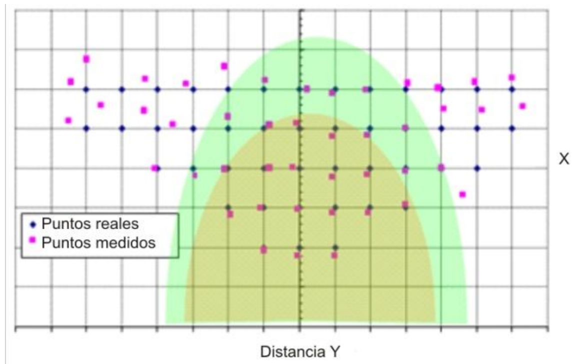

Figura 4. Campo de visión del TVS y zonas de precisión[2].

3. Filtrado de ruido y acondicionamiento de señal para la localización garantizada del obstáculo

Uno de los puntos más desafiantes del funcionamiento normal del TVS es la presencia de ruido típico en la señal de entrada mezclado con la señal proveniente de nuestro sensor fototransistor como se muestra en la figura 5. Este ruido puede ser filtrado por un circuito diseñado específicamente (ver figura 6), con el fin de garantizar la detección de la posición real de los rayos reflejados de la superficie del obstáculo.

El análisis preliminar de las fuentes de ruido nos llevó a la conclusión de que tenemos una combinación compleja de ruido mecánico en los motores de pasos y corriente directa y ruido senoidal de nuestra fuente de alimentación, que se encuentra distribuido arbitrariamente a lo largo de la base del TVS. Por lo tanto, la mejor solución en este caso es el diseño de un filtro especial (ver figura 6) para el ancho de banda del ruido encontrado experimentalmente.

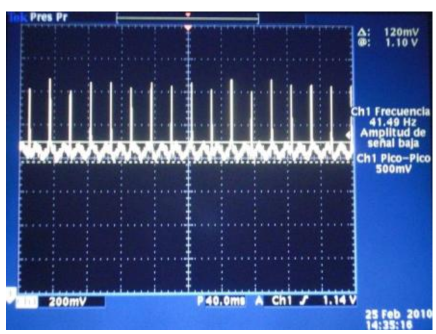

Figura 5. Mezcla de ruido típico y señal útil en la señal de entrada proveniente de nuestro sensor.

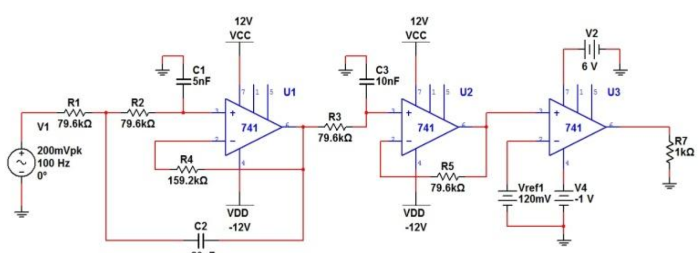

Figura 6. Filtro pasabajas Butterworth de tercer orden (-60 dB/década) y detector de nivel de voltaje.

[2] La tabla con los valores resultantes de la experimentación pueden ser consultados en [3].

Como se menciona anteriormente, el TVS contiene dos dispositivos, el posicionador de láser y la apertura de barrido, dentro de la apertura se encuentra un espejo de 45°, un lente y un sensor fototransistor (ver figura 7).

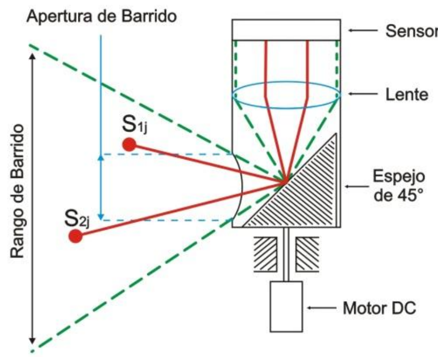

Figura 7. Apertura de Barrido.

Los rayos del láser que son reflejados difusamente de la superficie del obstáculo son reorientados en todas direcciones y solo algunos rayos alcanzan el fototransistor, de la energía total del láser que es emitida hacia el obstáculo por el posicionador de láser, solo del 2% - 5% (como lo indica nuestra simulación cuantitativa en MathCAD) es reflejado y detectado por nuestro fototransistor, por consiguiente la señal proporcionada por el sensor se encuentra en el rango de milivolts y requiere de una etapa de acondicionamiento antes de ser interpretada como una señal útil.

Como en todo sistema, en el nuestro también tenemos la presencia de ruido, mezclado en la señal que leemos de nuestro sensor fototransistor, después de estudiar la señal podemos observar que el ruido alcanza una amplitud máxima de 120 mV (ver figura 5) y su frecuencia varía desde 400Hz hasta 20KHz. Para eliminar este ruido se diseñó e implementó un filtro pasabajas Butterworth de 3er orden (ver figura 6). La salida del filtro entra a un detector de nivel de voltaje con un voltaje de referencia de 120mV para eliminar la amplitud del ruido, en cualquier momento que un obstáculo sea detectado por el sensor obtenemos un pulso en la señal, el tiempo y amplitud de este pulso varían dependiendo de la distancia del obstáculo detectado pero siempre es mayor a la amplitud del ruido (120mV) por lo tanto es posible filtrar el ruido. Al final del filtrado y acondicionamiento la señal proporcionada por el sensor se convierte en un pulso cuadrado que va de 0-5Vdc cuando no se detecta o cuando se detecta un obstáculo, respectivamente.

Seleccionamos el tipo de filtro Butterworth en vez de otros como Chebyshev, debido a que los filtros Butterworth poseen una respuesta de fase más lineal y una respuesta en frecuencia plana en nuestro ancho de banda de acuerdo a [6]. Nuestro filtro fue diseñado como se indica a continuación:

$$\omega_c = 200;\ C_3 = 10nF \tag{5}$$

donde, ω_c es la frecuencia de corte con un valor de 200Hz para dejar pasar señales con frecuencia de 0-200Hz, atenuando así todas las señales con frecuencia mayor a 200Hz.

$$C_1 = \frac{1}{2} C_3 = 5nF \tag{6}$$

$$C_2 = 2C_3 = 20nF \tag{7}$$

$$R = \frac{1}{\omega_c C_3} = \frac{1}{(6.25)(200)(5x10^{-9})} = 79.617k\Omega \tag{8}$$

$$R_1 = R_2 = R_3 = R = 79.617k\Omega \tag{9}$$

$$R_{f1} = 2R = 159.235k\Omega \tag{10}$$

$$R_{f2} = R = 79.617k\Omega \tag{11}$$

El filtro de 3er orden con atenuación de -60dB/década se consigue conectando en cascada un filtro de -40 dB/década y uno de -20dB/década. La ganancia total de lazo cerrado es la multiplicación de la ganancia de cada filtro [6].

4. Simulaciones

El circuito presentado en la figura 6 fue simulado con NI Multisim 10. La figura 8 muestra una captura de pantalla de un osciloscopio Tektronix simulado con tres señales, señal 1 es la de entrada al circuito que simula la señal del sensor fototransistor (la cual es filtrada y amplificada). La señal 2 es la salida del filtro la cual puede ser atenuada (ver figura 8, b) o puede pasar tal cual (ver figura 8, a) dependiendo de la frecuencia de esta (menor a 200Hz). La señal 3 es la salida del detector de nivel de voltaje, la cual será de 5Vdc si la señal que proviene del filtro es más positiva que el voltaje de referencia de 120mV (indicando que un obstáculo fue detectado) o será de 0Vdc si no se detectó algún obstáculo.

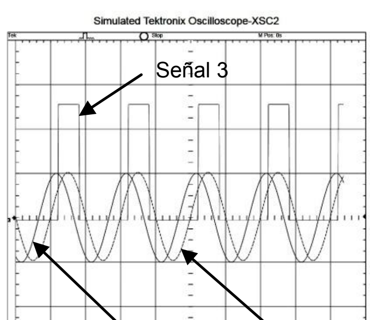

(a)

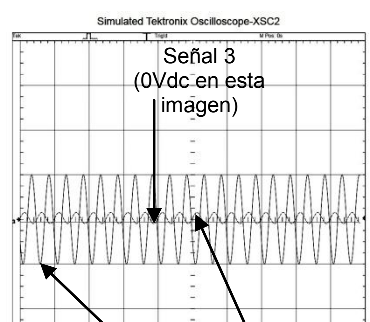

(b)

Figura 8. Señales de entrada y salida del filtro pasabajas y detector de nivel de voltaje (circuito en figura 7). (a) La señal de entrada es de 200mV at 100Hz; la salida es una señal cuadrada de 0-5Vdc. (b) La señal de entrada es de 200mV at 400Hz; la salida es atenuada debido a que su frecuencia es mayor a la de corte (200Hz), independientemente del voltaje de entrada.

En consecuencia, nuestra simulación demuestra que el filtro diseñado puede atenuar el ruido mayor a 400Hz detectado experimentalmente en el TVS.

Conclusiones

El TVS presentado en este artículo es capaz de resolver el problema de la detección de obstáculos en el campo de visión de un robot móvil autónomo, indicar la posición de dichos obstáculos y de crear un mapa digital de la superficie del obstáculo con las coordenadas en 3d en un corto periodo de tiempo y con precisión metrológica.

El acondicionamiento y tratamiento de señal realizado es esencial para el proceso de medición con el fin de prevenir fuentes de incertidumbre adicionales que puedan afectar la medición de coordenadas; debido a este tratamiento es posible mantener el nivel de confiabilidad de las mediciones en un mínimo de 96% en la zona mencionada (demostrado durante la experimentación).

El TVS es capaz de alcanzar un tiempo se respuesta de mayor velocidad mediante la actualización de sus componentes amplificadores operacionales tradicionales, utilizados en el acondicionamiento de señal (amplificación y filtrado) con amplificadores operacionales de alta velocidad; por consiguiente, reduciendo el tiempo necesario para calcular las coordenadas de un obstáculo detectado y proporcionando más tiempo para otras tareas de navegación del robot móvil como la planeación de una ruta.

La mejora de resolución en las mediciones del TVS le permite ser una opción viable para la tarea de navegación autónoma de robots móviles así como para otras aplicaciones como la medición de parámetros biométricos [7] o el monitoreo de estructuras [8].

Referencias

[1] Jose Guivant et al., "Autonomous Navigation and Map building Using Laser Range Sensors in Outdoor Applications", *Journal of Robotic Systems*, Vol, 17 No 10, October 2000, pp 565-583.
[2] Quoc V. Do1 et al., "Vision-Based Autonomous Robot Navigation", *Studies in Computational Intelligence (SCI)* 8, 2005, pp. 65–103.
[3] Luis C. Básaca et al., "3D Laser Scanning Vision System for Autonomous Robot Navigation", *Proceedings of IEEE International Symposium on Industrial Electronics (ISIE-2010), Bari (Italy)*, July 4-7 2010, pp. 1773-1778, ISBN 978-1-4244-6391-6, 2010.
[4] M. Rivas Lopez et al., *"Computer vision" book*. Edited by Xiong Zhihui, Chapter 22 "Machine vision: approaches and limitations", pp. 395-428. Editorial I-TECH, Vienna, Austria 2008, 538p.
[5] Luis C. Básaca et al., "Resolution improvement of Dynamic Triangulation method for 3D Vision System in Robot Navigation task", *Proceedings of IEEE-36th Annual Conference of IEEE Industrial Electronics (IECON'10)*, 7-10 November 2010, [IN PRESS].
[6] Robert Coughlin and F. Driscoll, "*Operational Amplifiers and Linear Integrated circuits*", sixth edition, Pearson Education, 2001, ISBN-10: 0130149918.
[7] Julio Rodríguez et al., "3D Body & Medical Scanners' Technologies: Methodology and Spatial discriminations", *Optoelectronic Devices and Properties*, IN-TECH, Vienna, Austria, 2011, [ACCEPTED]
[8] Moisés Rivas López et al., "Optoelectronic method for structural health monitoring", SAGE Publications, *International Journal of Structural Health Monitoring*, Vol.9, No.2, March, 2010, pp.105-120.

Sistema de Visión en 3D mediante Barrido Láser para Navegación de Robots Autónomos

Luis C. Básaca[1], Oleg Yu. Sergiyenko[2], Julio Rodríguez[3]
[1, 2, 3] Instituto de Ingeniería de la Universidad Autónoma de Baja California, Mexicali, B.C., México
[1] lubakun@gmail.com; [2] srgnk@iing.mxl.uabc.mx; [3] julio_qas@hotmail.com

RESUMEN

El sistema de visión técnica que aquí se presenta se basa en el principio de la triangulación dinámica. Esta técnica es capaz de resolver en tiempo real una triple tarea: detectar la presencia de un obstáculo significativo en el entorno de un robot, localizar su posición en el campo de visión del mismo y obtener en poco tiempo un mapa digital de la superficie visible del obstáculo con coordenadas precisas y exactas. Algunos aspectos de antecedentes teóricos, el diseño técnico, el principio óptico, la estructura matemática, procesamiento de señales, diseño de prototipos y experimentación se presentan en este documento.

Palabras clave: Sistema de visión, triangulación dinámica, robot móvil, barrido por láser.

1. INTRODUCCIÓN

Uno de los principales problemas del sistema de navegación es detectar la presencia de obstáculos estáticos y dinámicos y la distancia de un robot móvil a estos obstáculos. Existen varias maneras de realizar esta operación; Lipnickas and Knyš [1] proponen un sistema que utiliza dos cámaras para obtener dos imágenes del mismo objeto de diferentes puntos de vista y reconstruir una imagen en 3D. La exactitud de la reconstrucción de los datos en 3D depende de la precisión de las disparidades, calibración del sistema, rectificación de las imágenes y en general de la construcción del sistema. Los complejos algoritmos usados para las operaciones mencionadas carecen de alta precisión, dejando a este método como una opción no viable para detección de obstáculos con alta precisión y exactitud.

Otros sistemas (ver Fig. 1. [2]) proponen soluciones basadas en sistemas de barrido de láser fijos en 2D, nuestra ventaja es debido al hecho de que nuestro sistema es tridimensional, nuestro robot móvil tendrá una imagen frontal completa de su entorno a diferentes distancias; y un robot móvil con un sistema de barrido de láser en 2D solo sería capaz de ver o detectar obstáculos en una línea horizontal frente a él con un ángulo fijo y una distancia limitada.

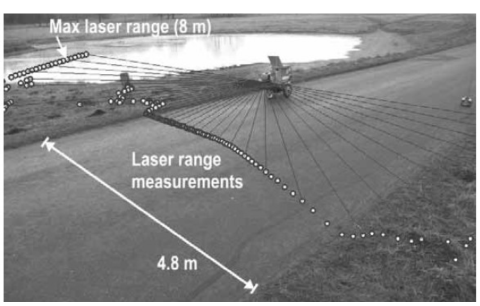

(a) Vista isométrica

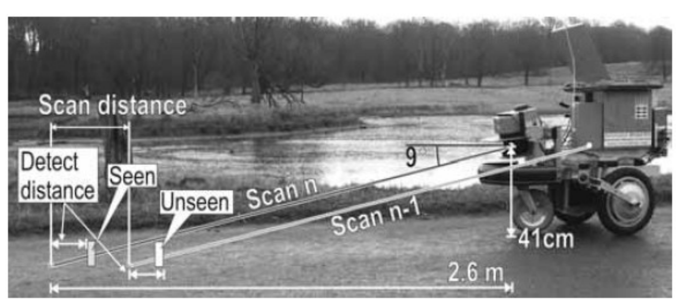

b) Vista lateral

Figura 1. Robot móvil con sistema de barrido de láser fijo en 2D [2]

Nuestro sistema usa barrido de láser y triangulación dinámica para obtener la distancia de un robot móvil a un obstáculo con gran precisión, esta información es usada para localizar las coordenadas 3D exactas de un obstáculo, proporcionando al robot móvil la habilidad de detectar la presencia de obstáculos teóricamente en un área de 180°, a diferencia del sistema introducido en Fig. 1 y [2], que tiene barrido en un solo plano. En realidad el campo de visión de nuestro sistema propuesto puede ser limitado en ángulo espacial debido a las propias dimensiones del robot controlado y a su tarea asignada; de la misma manera, el sistema permite filtrar la información innecesaria e incrementar la velocidad de funcionamiento del sistema de control del robot.

2. SISTEMA DE VISIÓN TÉCNICA (TVS)

Las técnicas de navegación de un robot móvil deben poseer exactitud confiable en amplios rangos. Esta es la razón por la cual nos encontramos desarrollando nuevos métodos de identificación de obstáculos que pueda encontrar en su camino un robot móvil, a esto le llamamos "Sistema de Visión Técnica" o "TVS" por sus siglas en inglés que significan *"Technical Vision System"*. Este nuevo sistema de visión provee información en cuanto a posición incluyendo profundidad, es decir coordenadas en 3D (X, Y, Z) de los objetos encontrados en el campo de visión frente al robot móvil.

El TVS básicamente consiste en una barra horizontal de dimensiones altamente precisas en la cual dos dispositivos se encuentran instalados, uno en cada extremo de la barra, un Posicionador de Láser (PL) y una Apertura de Escaneo (SA) que contiene un foto sensor, (Fig. 3) ambos por sus siglas en ingles *"Positioning Laser"* y *"Scanning Aperture"* respectivamente.

Como se mencionó anteriormente, este sistema utiliza un método de Triangulación Dinámica para obtener las coordenadas exactas de un objeto, a continuación se encuentra la explicación de este método y posteriormente nos enfocaremos en la operación del TVS. El método de Triangulación Dinámica difiere de otros métodos [6, 7] primeramente porque maneja la medición de dos ángulos dinámicos, permitiendo de esta manera, incrementar significativamente el rango operativo del sistema, en comparación con sistemas tradicionales de un solo ángulo.

3. TRIANGULACIÓN DINÁMICA

La triangulación dinámica es la base de nuestro sistema; la usamos para obtener coordenadas en 3D de objetos u obstáculos que están en el campo de visión frente a un robot móvil. Como se muestra en la Fig. 2, un haz de luz láser se proyecta desde PL hasta la superficie de un obstáculo, iluminándola y reflejando de regreso rayos de luz hacia el foto sensor dentro del SA [3].

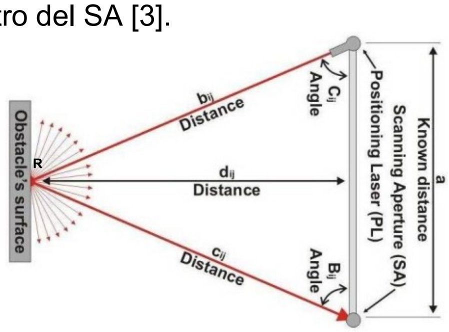

Figura 2. Triangulación Dinámica

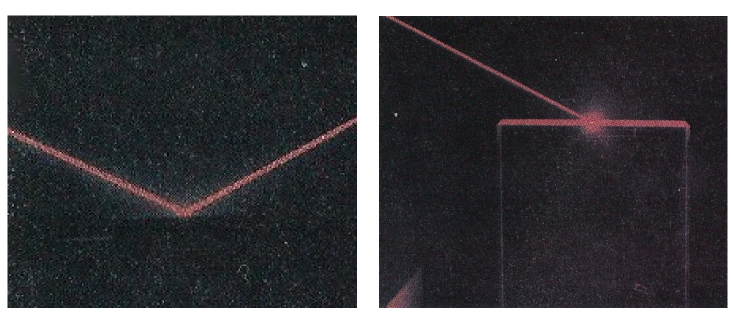

a) Reflexión Especular b) Reflexión Difusa

Figura 3. Tipos de reflexión de luz [4]

Existen dos tipos de reflexión de luz, especular y difusa. Cuando un haz de luz llega a una superficie suave reflectora como espejo, los rayos de luz reflejados serán paralelos entre si y de acuerdo a la Ley de Reflexión, el ángulo de reflexión será igual al ángulo de incidencia; esto es llamado Reflexión Especular. Por el contrario, si el haz de luz encuentra una superficie reflectora áspera, los rayos de luz serán reflejados en todas direcciones, esto es llamado Reflexión Difusa (ver Fig. 3 [4(p. 989), 5(p. 870-871)]).

A pesar de que la luz puede ser reflejada especularmente (P. ej. un espejo) o difusamente (P. ej. un pedazo de madera), muchos materiales presentan reflexión mixta, esto significa que algunos rayos de luz son reflejados especularmente y otros difusamente. Ver Fig. 4.

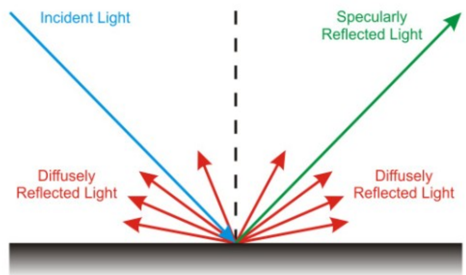

Figura 4. La reflexión mixta es una combinación de Reflexión Especular y Difusa

Debido a lo mencionado anteriormente, el tipo de reflexión más probable en una tarea de navegación de un robot es la última (Fig. 4). Está claro que una porción de la energía emitida en el foto sensor es fuertemente dependiente de un posicionamiento mutuo entre el punto de reflexión R y SA (Fig. 2), como se observa en la geometría de la Fig. 4. Sin embargo, como se muestra en los resultados de experimentación con el prototipo (Figs. 11-13), en el peor caso de reflexión, cuando la señal reflejada es convertida en una señal eléctrica por el foto sensor, ésta tiene un nivel de voltaje aceptable para distancias de alcance de visión razonables.

Partiendo del teorema de senos y de la relación entre los lados y la altura en un triángulo representados en la Fig. 2, es posible encontrar una fórmula para calcular la distancia *d* desde la barra horizontal *a* hasta los puntos marcados por el haz de luz láser.

$$d_{ij} = a \frac{\sin B_{ij} \cdot \sin C_{ij}}{\sin\left[180° - \left(B_{ij} + C_{ij}\right)\right]}, \tag{1}$$

Donde, los índices *i* y *j* representan el número de pasos en direcciones horizontal (i) y vertical (j) durante un barrido general en 3D.

Usando el valor de los ángulos B_{ij}, C_{ij}, $\sum_{j=1}^{n} \beta_j$ y la base *a*, es posible calcular las coordenadas cartesianas de cada punto marcado por el láser en cada paso *ij* del proceso de barrido en 3D, mediante las siguientes formulas:

$$x_{ij} = a \frac{\sin B_{ij} \cdot \sin C_{ij} \cdot \cos \sum_{j=1}^{j} \beta_j}{\sin\left[180° - \left(B_{ij} + C_{ij}\right)\right]}, \tag{2}$$

$$y_{ij} = a\left(\frac{1}{2} - \frac{\sin B_{ij} \cdot \cos C_{ij}}{\sin\left[180° - \left(B_{ij} + C_{ij}\right)\right]}\right) \quad \text{cuando } B_{ij} \leq 90°, \tag{3}$$

$$y_{ij} = -a\left(\frac{1}{2} + \frac{\sin B_{ij} \cdot \cos C_{ij}}{\sin\left[180° - \left(B_{ij} + C_{ij}\right)\right]}\right) \quad \text{cuando } B_{ij} \geq 90°, \tag{4}$$

$$z_{ij} = a \cdot \frac{\sin B_{ij} \cdot \sin C_{ij} \cdot \sin \sum_{j=1}^{j} \beta_j}{\sin\left[180^\circ - \left(B_{ij} + C_{ij}\right)\right]} \tag{5}$$

4. OPERACIÓN DEL TVS

El TVS está diseñado para detectar objetos que se encuentran en su rango de visión. Este sistema contiene un láser de alta potencia con un colimador donde un haz de luz láser es generado y redireccionado desde PL, el haz alcanza la superficie de un objeto u obstáculo a la vista y es reflejado por éste. La luz reflejada llega a un foto sensor dentro de SA, donde el ángulo de incidencia de la luz es medido, este ángulo es llamado B_{ij}. Como se mencionó anteriormente B_{ij}, C_{ij} and $\sum_{j=1}^{n} \beta_j$ son necesarios para calcular las coordenadas en 3D del obstáculo. PL y SA se encuentran instalados en cada extremo de la barra horizontal como se muestra en la Fig. 5, b.

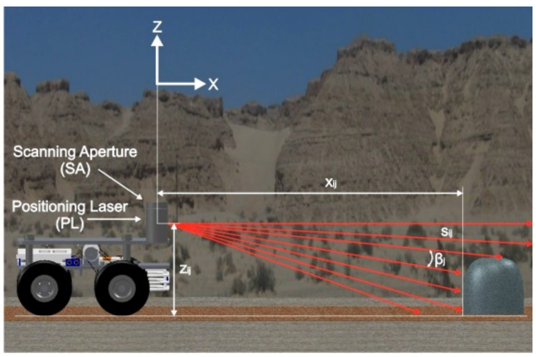

(a) Vista Lateral

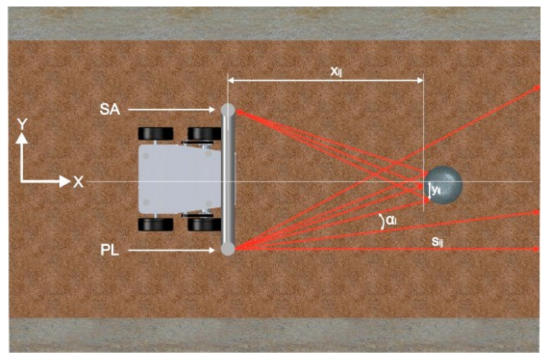

(b) Vista Superior

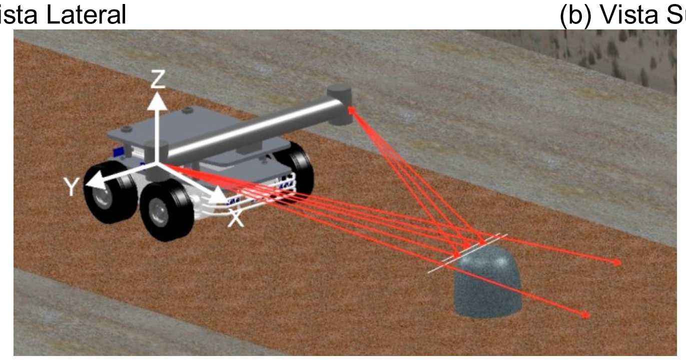

(c) Vista Isométrica

Figura 5. Principio de Operación de un TVS

Cada punto que es marcado en la superficie del obstáculo por un haz de luz láser emitido por PL es llamado S_{ij} (Fig. 5, a). El láser se redirecciona en PL mediante un espejo de 45° que se encuentra fijo a un motor de pasos, permitiéndonos obtener el ángulo C_{ij} en cualquier instante de tiempo, este ángulo se forma desde cada S_{ij} hasta la barra horizontal. El ángulo entre cada S_{ij} es llamado α_i. La siguiente fórmula es usada para calcular el ángulo C_{ij}:

$$C_{ij} = C_{\max} - \sum_{i=1}^{n} \alpha \tag{5}$$

Donde, C_{max} es el ángulo inicial del Posicionador de Láser (PL).

El dispositivo SA recibe los rayos de luz láser que son reflejados por la superficie del obstáculo para calcular el ángulo B_{ij} y se conforma de un espejo rotatorio de 45° que se encuentra dentro de la apertura, un sensor de presencia llamado sensor cero que detecta el instante de tiempo en el cual el espejo ha completado una vuelta de 360° y un foto sensor (PR) que detecta el instante de tiempo en el cual un rayo reflejado desde un punto de la superficie de un obstáculo (S_{ij}) llega a este (Fig. 6).

(a) Principio (b) Diseño General

Figura 6. Apertura de Escaneo, SA.

Si el foto sensor (PR) (Fig. 6, b) detecta un rayo de luz, tomamos la cantidad de pulsos entre el pulso del sensor cero y el pulso de PR para el cálculo del ángulo B_{ij} (Fig. 2). Dentro del dispositivo SA el espejo de 45° se encuentra rotando mediante un motor DC con una velocidad constante y precisa para poder calcular correctamente el valor del ángulo B_{ij}.

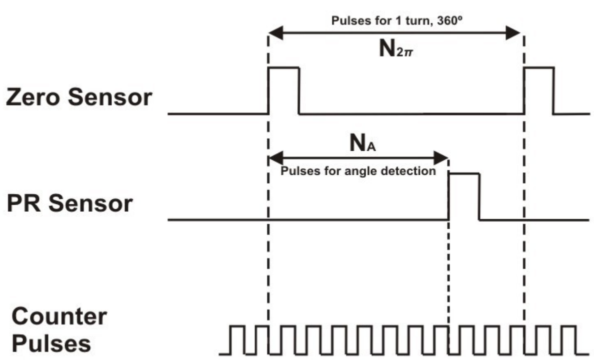

Figura 7. Señales fotoeléctricas y detección de ángulo

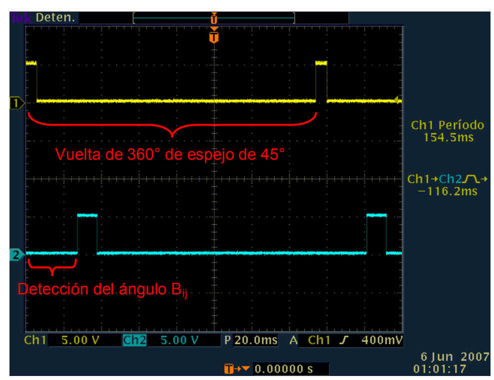

Figura 8. Detección de ángulo, señal de PR y sensor cero obtenido durante experimentación con el prototipo explicado en la sección IV

La siguiente formula es usada para calcular el ángulo B_{ij}:

$$B_{ij} = \frac{2\pi \cdot N_A}{N_{2\pi}} \tag{5}$$

Donde, N_A es la cantidad de pulsos del contador cuando PR detecta luz y $N_{2\pi}$ es el número de pulsos del contador cuando el espejo de 45° da una vuelta de 360° [6] Figs. 7 y 8.

Después de calcular los ángulos, las coordenadas en 3D y tomando en consideración las dimensiones conocidas de un robot móvil, es posible desarrollar un sistema de navegación que tome en cuenta las coordenadas en 3D espaciales para evitar colisiones y analizar diferentes trayectorias para llegar a un objetivo.

5. RESOLUCIÓN ESPACIAL

Después de haber realizado varios experimentos con el sistema de visión de barrido láser, el ancho de la punta del láser fue determinado, ver Tabla I.

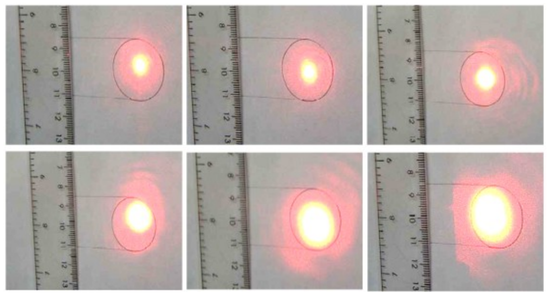

Figura 9. Diámetro del punto marcado por el láser vs distancia de operación

Tabla I. Ancho De Punto Del Láser [3]

d, m	1	2	3	4	5
σd, mm	0,10	0,41	0,93	1,65	2,57
d, m	10	20	30	50	100
σd, mm	10,28	41,14	92,55	257,11	1028,43

Basados en esta información podemos obtener resultados confiables con puntos de solo 10 cm de diámetro para distancias de 10 m (Fig. 9). El método de barrido toma lecturas constantes en diferentes puntos y se obtiene un mapa general de los objetos en el entorno. Las distancias entre los puntos son muy pequeñas; esto elimina errores como áreas que no son cubiertas por el láser. Hasta objetos pequeños pueden ser detectados fácilmente para que la computadora de un robot móvil pueda tomar decisiones acerca de si existe un riesgo de colisión o no y que trayectoria es la mejor para tomar.

6. INCREMENTO DE LA PRECISIÓN DE MEDICIÓN DE COORDENADAS MEDIANTE LA BÚSQUEDA DEL CENTRO DE EMISIÓN DE LUZ

Una de las principales causas de incertidumbre en la medición de coordenadas es tener un pulso con ruido de la señal eléctrica real proveniente del sensor PR. Para disminuir la incertidumbre, implementamos un método innovador de búsqueda del centro energético de la señal (similar al centro geométrico de un pulso teórico).

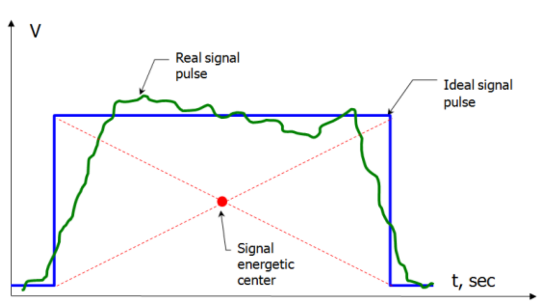

Figura 10. Búsqueda del centro energético de la señal

La Fig. 10 muestra un pulso de la señal real contra uno de la señal ideal; de igual manera muestra que el centro energético de la señal se encuentra en el mismo lugar en ambas señales.

7. CONSTRUCCIÓN DE PROTOTIPO Y EXPERIMENTACIÓN

- Un prototipo experimental del TVS fue construido para demostrar la funcionalidad del nuestros métodos.

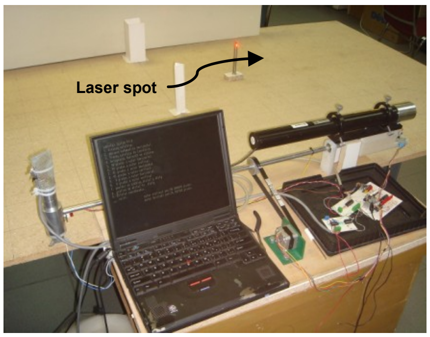

Figura 11. Vista del Prototipo del Sistema Completo

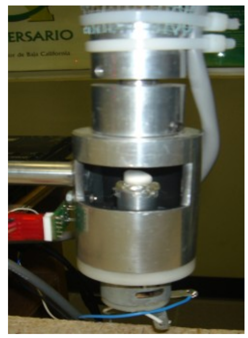

Figura 12. Apertura de Escaneo, SA en el TVS

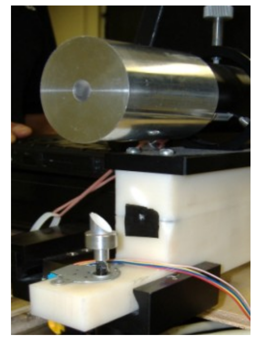

Figura 13. Posicionador de Láser, PL en el TVS

El prototipo completo mide 1m de longitud y es mostrado en la Fig. 11 durante operación. Los dispositivos PL y SA del prototipo son mostrados en la Fig. 12 y Fig. 13. Este prototipo fue probado 50 veces en diferentes posiciones en una mesa de prueba cuadriculada con gran exactitud para verificar la precisión del sistema de visión en diferentes ángulos en 2D, en la Tabla II se muestran parcialmente los valores medidos por el prototipo.

Tabla II. Resultados experimentales de medición de coordenadas

Punto de prueba	Valor Teórico				Valor Medido			
	X (m)	Y (m)	B (°)	C (°)	*x(m)*	*y(m)*	*B (°)*	*C (°)*
B	120	120	120,26	35,22	124,21	128,68	123,43	34,8
D	100	100	116,57	33,69	99,83	104,48	118,46	32,87
F	100	80	106,70	37,57	95,3	76,86	106,4	36,91
H	120	60	94,76	47,49	122,92	63,49	96,38	47,28
J	80	60	97,13	36,03	77	58,62	96,57	35,33
L	80	40	82,87	41,63	79,99	42,15	84	40,95
N	120	40	85,24	53,13	119,86	40,04	84,48	53,08
O	120	20	75,96	59,74	119,22	19,48	76,01	59,76
P	100	20	73,30	55,01	97,6	19,15	72,94	54,67
Q	80	20	69,44	48,81	79,11	18,7	68,39	49,04
R	60	20	63,43	40,60	60,33	21,7	64,3	40,07
S	40	20	53,13	29,74	39,14	19,59	52,07	29,35
T	40	0	38,66	38,66	36,52	1,06	36,52	36,73
U	60	0	50,19	50,19	59,8	0,9	49,39	50,625
V	80	0	57,99	57,99	80,93	3,49	56,7	60,11
W	100	0	63,43	63,43	103,58	1,51	63,45	64,68
X	120	0	67,38	67,38	120,72	-4,7	66,23	69,43
Y	120	-20	59,74	75,96	118,54	-18,36	59,95	75,05
Z	100	-20	55,01	73,30	96,72	-18,37	54,7	71,9
A1	80	-20	48,81	69,44	75,79	-18,33	48,03	67,32
B1	60	-20	40,60	63,43	58	-18,53	39,5	61,52
C1	40	-20	29,74	53,13	36,17	-20,31	27,3	50,62
D1	60	-40	33,69	80,54	58,05	-38,63	33,6	78,92
E1	80	-40	41,63	82,87	77,46	-38,26	40,46	81,38
F1	100	-40	48,01	84,29	97,1	-38,02	46,94	82,96
H1	120	-60	47,49	94,76	123,68	-61,03	48,21	95,09
J1	80	-60	36,03	97,13	78,9	-59,73	35,37	97,03
L1	80	-80	31,61	110,56	80,52	-80,21	31,81	110,56
N1	120	-80	42,71	104,04	121,01	-78,73	43,34	103,35
P1	100	-100	33,69	116,57	101,65	-96,18	35,06	114,43
R1	100	-120	30,47	124,99	111,73	-126,15	32,09	124,27

Analizando los resultados numéricos de las mediciones de coordenadas, es posible afirmar que todos los experimentos fueron llevados a cabo con un nivel de confianza del 95%. La incertidumbre en las mediciones no es mayor a 5% en ningún punto.

8. CONCLUSIONES

De acuerdo con todo lo mencionado anteriormente es posible afirmar que:

- El TVS es capaz de resolver en tiempo real una tarea triple: la detección de una presencia u obstáculo significativo en el entorno de un robot, localizar su posición dentro del campo de visión del mismo y crear rápidamente un mapa digital de la superficie visible de un obstáculo con precisión metrológica de coordenadas.
- Estas características son logradas gracias al uso correcto y óptimo de los motores de pasos, de la actualización y mejora del software y de la implementación de la técnica *"Microstepping"* que nos permite duplicar la resolución de barrido de nuestro sistema.
- Esta clase de realización de visión técnica es única respecto a otras [1, 7, 9], puede representar información acerca de objetos dentro del campo de visión de un robot como una matriz de coordenadas de n puntos, en la superficie visible del obstáculo.
- El TVS no es antagónico hacia la utilización de cámaras CCD para la percepción de información del entorno. Por el contrario, TVS y CCD pueden complementarse mutuamente cuando la participación de un operador humano es necesaria durante la percepción aparte de la realizada por la computadora integrada.
- TVS representa la realización de una idea de visión por computadora en la forma de un modelo análogo-digital del espacio frente a un robot. Este modelo puede ser transformado fácilmente mediante una computadora en una imagen adecuada para que un operador humano la perciba y entienda.

9. REFERENCIAS

[1] A. Lipnickas, and A. Knyš. 2009. *A Stereovision System for 3-D Perception.* Electronics & Electrical Engineering, no. 91: 99-102. ISSN: 1392-1215.

[2] Andersen, Jens Christian, Morten Rufus Blas, Ole Ravn, Nils A. Andersen, and Mogens Blanke. 2006. *Traversable terrain classification for outdoor autonomous robots using single 2D laser scans.* Integrated Computer-Aided Engineering 13, no. 3: 223-232. ISSN: 10692509.

[3] Oleg Sergiyenko, et al. *Precise Optical Scanning for practical multiapplications*. Proceedings of IEEE 34th Annual IEEE Conference IECON'08, Florida, USA, 2008, p. 1656-1661.

[4] Raymond A. Serway. *Physics: for Scientists and Engineers with Modern Physics.* Philadelphia: Saunders, 3rd Edition, Updated Printing, 1990.

[5] Eugene Hecht. *Physics*. Pacific Grove, California: Brooks/Cole, 1994.

[6] M. Rivas Lopez, Oleg Sergiyenko, Vera Tyrsa. *Computer vision* book. Edited by Xiong Zhihui, Chapter 22 *Machine vision: approaches and limitations*, pp. 395-428. Editorial: I-TECH, Vienna, Austria, 2008, 538 p.

[7] M. Petrov et al. *Optical 3D Digitizers: Bringing Life to the Virtual World*. IEEE Computer Graphics and Applications, Vol. 18, Issue 3, May/June 1998, pp 28-37.

[9] Lei Wang. Takashi Emura. and Takashi Ushiwata October 1-3, 2000. *Automatic Guidance of a Vehicle Based on DGPS and a 3D Map*. 2000 IEEE Intelligent Transportation Systems Conference Proceedings, Dearborn (MI), USA, p.131-136.

Signal Processing 93 (2013) 378–386

Contents lists available at SciVerse ScienceDirect

Signal Processing

journal homepage: www.elsevier.com/locate/sigpro

Surface recognition improvement in 3D medical laser scanner using Levenberg–Marquardt method

Julio C Rodriguez-Quinonez*, Oleg Sergiyenko, Felix F. Gonzalez-Navarro, Luis Basaca-Preciado, Vera Tyrsa

Engineering Institute of Autonomous University of Baja California, Mexicali, Baja California, Mexico

ARTICLE INFO

Article history:
Received 23 November 2011
Received in revised form
28 June 2012
Accepted 1 July 2012
Available online 10 August 2012

Keywords:
Levenberg–Marquardt method
Laser
Scanner
Triangulation

ABSTRACT

The 3D measurements of the human body surface or anatomical areas have gained importance in many medical applications. Three dimensional laser scanning systems can provide these measurements; however usually these scanners have non-linear variations in their measurement, and typically these variations depend on the position of the scanner with respect to the person. In this paper, the Levenberg–Marquardt method is used as a digital rectifier to adjust this non-linear variation and increases the measurement accuracy of our 3D Rotational Body Scanner. A comparative analysis with other methods such as Polak–Ribire and quasi-Newton method, and the overall system functioning is presented. Finally, computational experiments are conducted to verify the performance of the proposed system and its method uncertainty.

1. Introduction

Medical professionals traditionally prefers manual measurement of the body size and shape to assess health status and guide treatment. External measurements of the body just undermines useful. Medical professionals widely use size and shape to assess nutritional status and developmental normality and to calculate the requirements of drug, radiotherapy, and chemotherapy dosages, as well as the production of prostheses [1]. In earlier work [2,3], we developed a system with the capability to realize precise measurements by 3D point clouds [4] sampled from the surface of human body, however to increase even more the precision, we develop a digital rectifier to approach the measurements to their real value. A simple approximation method based on Gauss–Markov can find the lowest possible mean squared [5] and approximate the measurements to their real value; however requires identically distributed data. Also, experimental results of [6] clearly show that uncertainty of our system is distributed non-uniformly, with quantized centered error distribution.

Application of neural network methods and algorithms may be a solution to this problem which cannot be easily solved by traditional methods. The history of neural networks started in mid twentieth century when simple neural network with limited capabilities were conceived. They never got into the main stream applications at that time due to poor generalization capabilities and lack of specificity with high memory loads. After two decades, the whole concept of neural networks changed when the multi-layer neural networks with backpropagation learning algorithm was presented [7]. From that time, many different researchers studied the area of artificial neural networks, which led to a vast range of different neural architectures applied to a plethora of different problems. At present, neural networks are used as principal solutions for various problems like grouping and classification, pattern recognition, approximation, prediction, clusterization and

* Corresponding author.
E-mail address: julio.rodriguez37@uabc.edu.mx (J.C. Rodriguez-Quinonez).

0165-1684/$ - see front matter © 2012 Published by Elsevier B.V.
http://dx.doi.org/10.1016/j.sigpro.2012.07.001

memory simulation. Neural networks may initially seem complex and computer intensive, but actually may integrate well with a Medical environment in various distinct applications [7–9].

Properly trained backpropagation networks tend to give reasonable answers when presented with inputs that they have never seen. Typically, a new input leads to an output similar to the correct output for input vectors used in training that are similar to the new input being presented. This generalization property makes it possible to train a network on a representative set of input/target pairs and get good results without training the network on all possible input/output pairs. Feedforward networks often have one or more hidden layers of sigmoid neurons followed by an output layer of linear neurons. Multiple layers of neurons with nonlinear transfer functions allow the network to learn nonlinear [10] and linear relationships between input and output vectors [7]. This general property is very useful in our case because between input and output vectors, which are vectors of true and measured values of 3D scanner, the relation has complex stochastic character.

Three popular artificial neural network feedforward backpropagation training methods namely; quasi-Newton, Polak–Rebiere and Levenberg–Marquardt methods are compared in the present study to assess accuracy for surface recognition improvement in the 3D Medical Laser Scanner developed and mentioned a continuation.

2. Overall system function

Dynamic triangulation (Fig. 1) is the method and theoretical base of our system; we use it to obtain the 3D coordinates of the body that are in the field of view (FOV) in front of the system. We call it dynamic triangulation because of the fact that triangle in Fig. 1 in real time exists at very short interval, when projected laser ray, changing its spatial position each 0.001 s, reaches a unique condition to be able to enter into rotating

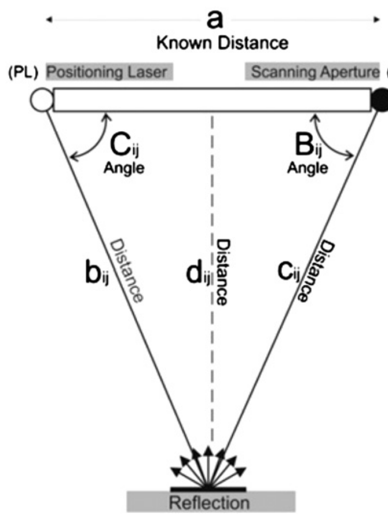

Fig. 1. Dynamic triangulation principle, spatial position of scanning aperture and positioning laser.

photoreceiver through mixed (diffuse+specular) reflection on the human body surface. The time of existence of the spatial figure presented in Fig. 1 is variable and dependent on the rotational velocities of the laser positioning system and scanning aperture.

As shown in Fig. 2 a laser beam is projected from the positioning laser (PL) onto the body, and reflecting it back onto the revolving sensor inside the scanning aperture (SA) [6,11]. Then, using the theorem of sinus, the correlation between the triangle sides and the width and height in the triangle of Fig. 1, it is possible to develop a formula to calculate distance d from base a up to points highlighted by the laser beam on to the body:

$$d_{ij} = a\frac{\sin B_{ij} * \sin C_{ij}}{\sin[180-(B_{ij}+C_{ij})]} \tag{1}$$

where indexes i and j represent respectively the step number in horizontal and vertical directions during the 3D Body Scanning. To perform the vertical scanning the system rotates to get the angle β_j as show in Fig. 3.

Using angles B_{ij}, C_{ij}, $\sum_{j=1}^{n}\beta_j$ and the known distance of the base a, it is possible to calculate the Cartesian coordinates of each laser highlighted points on each ij step of 3D Body scanning process, based on the following formulas:

$$x_{ij} = a\frac{\sin B_{ij} * \sin C_{ij} * \cos \sum_{j=1}^{n}\beta_j}{\sin[180-(B_{ij}+C_{ij})]} \tag{2}$$

$$y_{ij} = a\left(\frac{1}{2} - \frac{\sin B_{ij} * \cos C_{ij}}{\sin[180-(B_{ij}+C_{ij})]}\right) \quad \text{at } B_{ij} \le 90^\circ \tag{3}$$

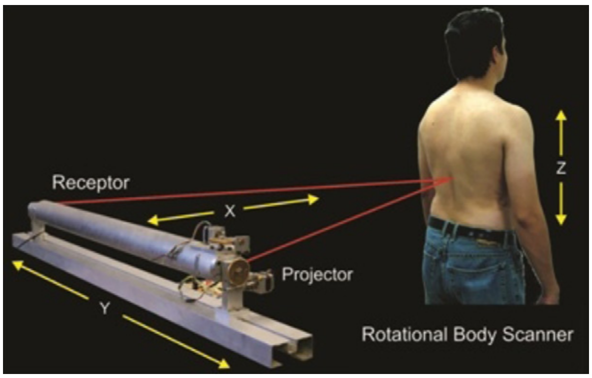

Fig. 2. 3D Rotational Body Scanner. Experimental application for body/column scanning.

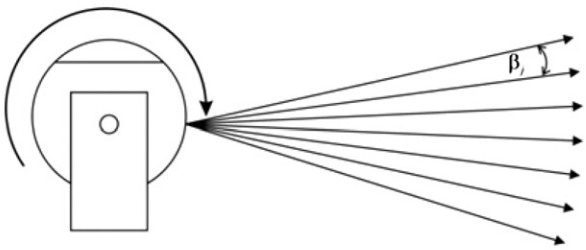

Fig. 3. Rotation of the dynamic triangulation principle and the angle β_j.

$$y_{ij} = a\left(\frac{1}{2} + \frac{\sin B_{ij} * \cos C_{ij}}{\sin[180 - (B_{ij} + C_{ij})]}\right) \quad \text{at } B_{ij} \geq 90^\circ \tag{4}$$

$$z_{ij} = a\frac{\sin B_{ij} * \sin C_{ij} * \sin \sum_{j=1}^{n} \beta_j}{\sin[180 - (B_{ij} + C_{ij})]} \tag{5}$$

The Rotational Body Scanner uses the principle of Dynamic Triangulation Scanner [3,12]. The rotation of the system is given by a shaft–gear mechanism. The horizontal scanning is performed by a step motor which rotates a mirror which reflects the laser beam generated by the laser which is inside of the system bar as shown in Fig. 1. As the Dynamic triangulation, our system has a receptor SA (Fig. 4) and consist of five main components: (A) 45° rotational mirror, whose principal function is to direct the laser light beam towards the lenses (targets). (B) Targets, whose function is to concentrate the light beam onto photodetector. (C) DC Motor, which rotates the mirror. (D) Photodetector, it captures the light beam located within the frequency range of the laser. (E) Flat Bearing, allows the rotation in the angular axis of the system β_j.

In addition, like Dynamic triangulation, our system has a PL which is in-built system of the projector. The system projector has 5 main components (Fig. 5), which are the

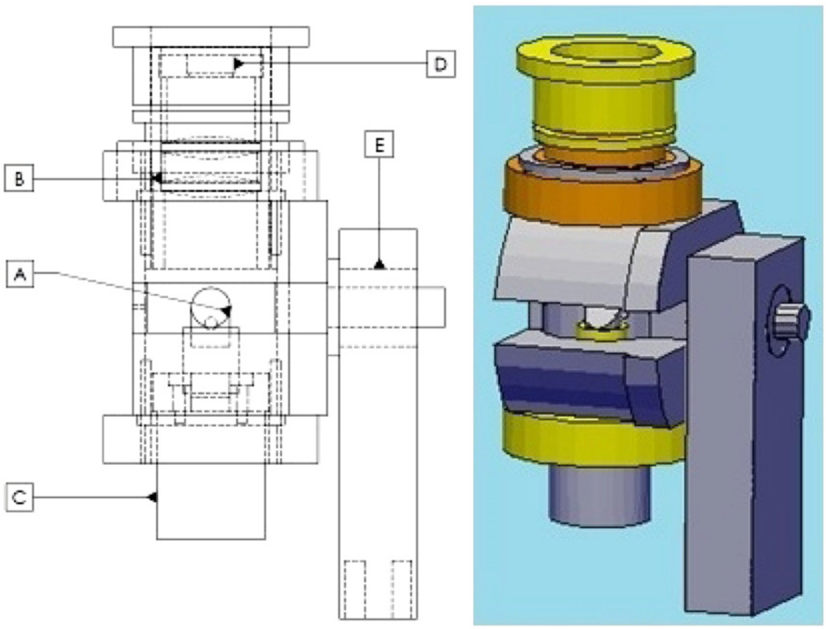

Fig. 4. Front view of the receptor and components. (A) 45° rotational mirror, (B) targets, (C) DC motor, (D) photodetector, (E) flat bearing.

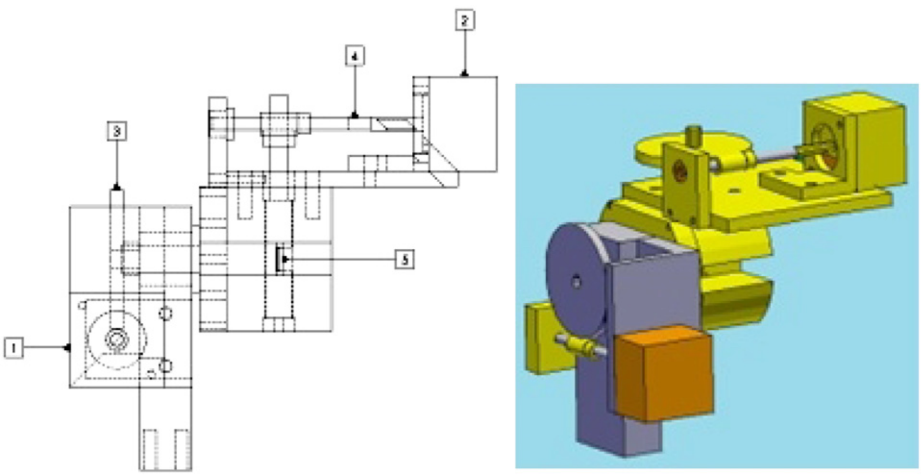

Fig. 5. Front view of the system projector. (1) Step motor of angular rotation, (2) step motor for the mirror rotation, (3) system rotation gear, (4) mirror rotation gear, (5) mirror.

following: (1) Step Motor of angular rotation, whose main function is to control the rotation of the entire system. (2) Step motor for the mirror rotation, which controls the mirror rotation. (3) System rotation gear increases the precision of the system since it gives a 10:1 ratio gear-motor. (4) Mirror rotation gear increases the precision of the system giving a 10:1 ratio gear. (5) Mirror, reflects the laser light beam towards the scanning body.

The laser light projector emits the light at different angles towards the body. And at the same time, the receptor rotates until it detects the light deflected by the body. When the mirror of the receptor deflects the scattered light towards the target and concentrates the light towards the photodetector, an electronic pulse is emitted which indicates that the point has been detected. A relationship between the rotation time and detection time shows the angle in which the receptor detects the point. Since the projector rotation is controlled by the user, the angle of the projector is known at all times. The relationship between the two angles and the known distance between the projector and receptor gives each of the captured coordinates. As shown in Fig. 1, the projector and receptor are separated by a bar that gives the exact distance of 1 m between their centers, and located in the bar is the laser light source.

Within the bar the laser also gets aligned and locked avoiding measurement errors. The triangulation principle used is well known [2,3,11,13] and some of the advantages given by this system are the angular rotational mechanism, which allows the rotation with no chains [6], an increment in resolution by 10 times by using gears that gives one rotation, for each 10 rotations that gives the step motor, inaccuracy caused by friction is decreased by using polytetrafluortethylene flat bearings which has the lowest friction coefficient of all materials [14], and the economic fabrication cost. While pure optoelectronic system has the capability to generate a 3D point cloud of the measured surface, the average system performance is 95% [3,6], making it necessary to develop a tool that allows us to correct the measurement uncertainty. For this reason the digital rectifier has been developed

3. Digital rectifier method

To obtain accurate measurements we use different mathematical algorithms and recognized methodology [15–18] to train a neural network, by which the regression method can make an adjustment of our measurements and theoretically approximated to the real value. To make the adjustment we train the network with different algorithms, and then we make a comparison between them and select the best training method for our case.

3.1. Nonlinear conjugate gradient methods

The basis for a nonlinear conjugate gradient method is too effectively applying the linear conjugate gradient method, where the residual is replaced by the gradient. A model quadratic function is never explicitly formed, so it is always combined with a "line search" method [19]. The first nonlinear conjugate gradient method was proposed by Fletcher and Reeves [15] as follows. Given a step direction p_K, use the line search to find the step length a_K such that $x_{K+1}=x_k+a_kp_k$. Then compute

$$\beta_{K+1}=\frac{\nabla f^T(x_{k+1})\cdot\nabla f(x_{k+1})}{\nabla f^T(x_k)\cdot\nabla f(x_k)} \tag{6}$$

$$\beta_{K+1}=\beta_{K+1}p_k\nabla f(x_{k+1}) \tag{7}$$

where β_{k+1} is the correction factor and is minimal in some cases. It is essential that the line search for choosing a_K satisfies the strong Wolfe conditions; this is necessary to ensure that the directions p_K are descent directions [15]. An alternate method, which generally (but not always) works better in practice, is that of Polak and Ribiere [15], where Eq. (6) is replaced with

$$\beta_{K+1}=\frac{\nabla f^T(x_{k+1})\cdot(\nabla f(x_{k+1})-\nabla f(x_k))}{\|\nabla f(x_k)\|^2} \tag{8}$$

In formula (8), it is possible that $\beta(K+1)$ can become negative, in which case it can be used as the algorithm modified by using

$$p_{K+1}=\max(\beta_{K-1},0)p_k-\nabla f(x_{k+1}) \tag{9}$$

The advantage of conjugate gradient methods is that they need relatively little memory space for large-scale problems and requires no numerical linear algebra, so each step is quite fast. The disadvantage is that they typically converge much more slowly than "Newton" or "quasi-Newton" methods [15,17]. Also, steps are typically poorly scaled for length, so the "line search" algorithm may require more iterations each time to find an acceptable step.

3.2. Quasi-Newton method

In optimization, quasi-Newton methods [17] (also known as variable metric methods) are algorithms for finding local minima of functions. Quasi-Newton methods are based on Newton's method to find the stationary point of a function, where the gradient is 0. Newton's method assumes that the function can be locally approximated as a quadratic in the region around the optimum, and use the first and second derivatives (gradient and Hessian) to find the stationary point. In quasi-Newton methods the Hessian matrix of second derivatives of the function to be minimized does not need to be computed. The Hessian is updated by analyzing successive gradient vectors instead. Quasi-Newton methods are a generalization of the secant method [20] to find the root of the first derivative for multi-dimensional problems. In multi-dimensions the secant equation is under-determined, and quasi-Newton methods differ in how they constrain the solution, typically by adding a simple low-rank update to the current estimate of the Hessian. The model to find the local minima in the quasi-Newton method is

$$m_k(x_k+p)=f_k+p^Tf_k+\tfrac{1}{2}p^T\beta_kp \tag{10}$$

where f_k, ∇f_k and β_k are a scalar, vector, and matrix, respectively. As the notation indicates, f_k and ∇f_k are chosen to be the function and gradient values at the point

x_k, so that m_k and f are in agreement to first order at the current iterate x_k [15]. The matrix β_k is a correction factor and is used in place of the Hessian matrix. The most common quasi-Newton methods to update the β_k matrix are currently the symmetric rank one SR1 (11) formula and the Broyden, Fletcher, Goldfarb, and Shanno widespread BFGS (12) method:

$$\beta_{k+1} = \beta_k + \frac{(y_k - \beta_k \Delta x_k)(y_k - \beta_k \Delta x_k)^T}{(y_k - \beta_k \Delta x_k)^T \Delta x_k} \tag{11}$$

$$\beta_{k+1} = \beta_k + \frac{y_k y_k^T}{y_k^T \Delta x_k} - \frac{\beta_k \Delta x_k (\beta_k \Delta x_k)^T}{\Delta x_k^T \beta_k \Delta x_k} \tag{12}$$

However, Newton based methods – quasi-Newton methods (e.g., BFGS method) – tend to converge in fewer iterations, although each iteration typically requires more computation than a conjugate gradient iteration as Newton-like methods require computing the Hessian (matrix of second derivatives) in addition to the gradient. Quasi-Newton methods also require more memory to operate.

3.3. Levenberg–Marquardt method

The primary application of the Levenberg–Marquardt algorithm is in the least squares curve fitting problem: given a set of m empirical datum pairs of independent and dependent variables, (x_i, y_i) optimize the parameters $\boldsymbol{\beta}$ of the model curve $f(x, \boldsymbol{\beta})$ so that the sum of the squares of the deviations becomes minimal [21]:

$$S(\beta) = \sum_{i=1}^{m} [y_i - f(x_i, \beta)]^2 \tag{13}$$

Like other numeric minimization algorithms, the Levenberg–Marquardt algorithm is an iterative procedure. To start a minimization, we provide an initial guess for the parameter vector, $\boldsymbol{\beta}$. In each iteration step, the parameter vector, $\boldsymbol{\beta}$, is replaced by a new estimate, $\boldsymbol{\beta} + \boldsymbol{\delta}$. To determine $\boldsymbol{\delta}$, the functions $f(x_i, \beta + \delta)$ are approximated by their linearizations

$$f(x_i, \beta + \delta) \approx f(x_i, \beta) + J_i \delta \tag{14}$$

where

$$J_i = \frac{\partial f(x_i, \beta)}{\partial \beta} \tag{15}$$

is the gradient (row-vector in this case) of f with respect to $\boldsymbol{\beta}$. At its minimum, the sum of the squares, $S(\beta)$, the gradient of S with respect to $\boldsymbol{\delta}$ will be zero. The above first-order approximation of $f(x_i, \beta + \delta)$ gives

$$S(\beta + \delta) \approx \sum_{i=1}^{m} (y_i - f(x_i, \beta) - J_i \delta)^2 \tag{16}$$

or in vector notation,

$$S(\beta + \delta) \approx \| \boldsymbol{y} - \boldsymbol{f}(\beta) - \boldsymbol{J}\delta \|^2 \tag{17}$$

Taking the derivative with respect to $\boldsymbol{J}$ and setting the result to zero gives

$$(\boldsymbol{J}^{\boldsymbol{T}} \boldsymbol{J})\delta = \boldsymbol{J}^{\boldsymbol{T}} [\boldsymbol{y} - \boldsymbol{f}(\beta)] \tag{18}$$

where $\boldsymbol{J}$ is the Jacobian matrix [18] whose ith row equals J_i, and where $\boldsymbol{f}$ and $\boldsymbol{y}$ are vectors with ith component $f(x_i, \beta)$ and y_i, respectively. This is a set of linear equations which can be solved for $\boldsymbol{\delta}$.

Marquardt's contribution [16] is to replace this equation by a "damped version",

$$(\boldsymbol{J}^{\boldsymbol{T}} \boldsymbol{J} + \lambda \boldsymbol{I})\delta = \boldsymbol{J}^{\boldsymbol{T}} [\boldsymbol{y} - \boldsymbol{f}(\beta)] \tag{19}$$

where $\boldsymbol{I}$ is the identity matrix, giving as the increment, $\boldsymbol{\delta}$, to the estimated parameter vector, $\boldsymbol{\beta}$. The (non-negative) damping factor, λ, is adjusted at each iteration. If reduction of S is rapid, a smaller value can be used, bringing the algorithm closer to the Gauss–Newton algorithm, whereas if an iteration gives insufficient reduction in the residual, λ can be increased, giving a step closer to the gradient descent direction. Note that the gradient of S with respect to $\boldsymbol{\beta}$ equals $-2(\boldsymbol{J}^T [\boldsymbol{y} - \boldsymbol{f}(\beta)])^T$. Therefore, for large values of λ, the step will be taken approximately in the direction of the gradient. If either the length of the calculated step, $\boldsymbol{\delta}$, or the reduction of the sum of the squares from the latest parameter vector, $\boldsymbol{\beta} + \boldsymbol{\delta}$, fall below predefined limits, iteration stops and the last parameter vector, $\boldsymbol{\beta}$, is considered to be the solution. Levenberg's algorithm has the disadvantage that if the value of damping factor, λ, is large, inverting $\boldsymbol{J}^{\boldsymbol{T}} \boldsymbol{J} + \lambda \boldsymbol{I}$ is not used at all. Marquardt provided the insight that we can scale each component of the gradient according to the curvature so that there is larger movement along the directions where the gradient is smaller. This avoids slow convergence in the direction of small gradient. Therefore, Marquardt [16] replaced the identity matrix, $\boldsymbol{I}$, with the diagonal of $\boldsymbol{J}^{\boldsymbol{T}} \boldsymbol{J}$, resulting in the Levenberg–Marquardt algorithm:

$$(\boldsymbol{J}^{\boldsymbol{T}} \boldsymbol{J} + \lambda\, diag(\boldsymbol{J}^{\boldsymbol{T}} \boldsymbol{J}))\delta = \boldsymbol{J}^{\boldsymbol{T}} [\boldsymbol{y} - \boldsymbol{f}(\beta)] \tag{20}$$

4. Digital rectifier analysis

We use the methods mentioned above to train a neural network. The trained neural network is feedforward backpropagation type. A feedforward backpropagation neural network consists of two layers. The first layer, or hidden layer, has a tansigmoid (tan-sig) activation function, and the second layer, or output layer, has a linear activation function. Thus, the first layer limits the output to a narrow range, from which the linear layer can produce all values. The output of each layer can be represented by [22]

$$\boldsymbol{Y}_{Nx1} = f(\boldsymbol{W}_{NxM} \boldsymbol{X}_{M,1} + \boldsymbol{b}_{N,1}) \tag{21}$$

where $\boldsymbol{Y}$ is a vector containing the output from each of the N neurons in a given layer, $\boldsymbol{W}$ is a matrix containing the weights for each of the M inputs for all N neurons, $\boldsymbol{X}$ is a vector containing the inputs, $\boldsymbol{b}$ is a vector containing the biases and $f(\cdot)$ is the activation function [23,22]. The network was created using the neural network toolbox from Matlab 7.12.0 (The MathWorks, Natick, MA, USA). In a backpropagation network, there are two steps during training that are used alternately. The backpropagation step calculates the error in the gradient descent and propagates it backwards to each neuron in the output layer, then hidden layer. In the second step, the weights and biases are then recomputed, and the output from the

Table 1
Polak–Ribiere performance analysis, from 0.2 of learning rate to 0.9, running four tests for each learning rate.

Learning rate	Obtained performances				Avg. error performance
	Take 1	Take 2	Take 3	Take 4	
Polak-Ribiere					
0.2	0.00199	0.001113	0.000555	0.001938	0.001400162
0.4	0.00054	0.000190	0.001006	0.000586	0.000465549
0.6	0.00032	0.000334	0.003047	0.002702	0.001281126
0.8	0.00132	0.001306	0.007933	0.002532	0.002617578
0.9	0.00046	0.000280	0.001181	0.001657	0.000715481

Table 2
Quasi-Newton performance analysis, from 0.2 of learning rate to 0.9, running four tests for each learning rate.

Learning rate	Obtained performances				Avg. error performance
	Take 1	Take 2	Take 3	Take 4	
Quasi Newton					
0.2	0.004958	0.000943	0.001563	0.028447	0.0071826
0.4	0.000682	0.000241	0.043977	0.001240	0.0092285
0.6	0.000736	0.000224	0.004156	0.002144	0.0014526
0.8	0.002366	0.001082	0.000430	0.003766	0.0015293
0.9	0.000519	0.001008	0.004237	0.001444	0.0014421

activated neurons is then propagated forward from the hidden layer to the output layer. The network is initialized with random weights and biases, and was then trained using the Levenberg–Marquardt Algorithm mentioned before [22]. The training data consists of 60 samples from 80 measurements; each sample is taken in cross validation form [24]. I.e. the network was trained to predict the absolute error of x, y, z measurement, for all conditions at once. The length of the training data was 60 points. The network contained five neurons, three layers and was trained until an acceptable percentage error was achieved. The test data consisted of the remaining 20 samples from each trial. The training is performed with Polak–Ribiere, quasi-Newton and Levenberg–Marquardt methods to compare their performance.

5. Experimentation

To perform the experimentation we use the same 80 measurement samples from the surface of human body as input and reference points for quasi-Newton, Polak–Rebiere and Levenberg–Marquardt methods; we use 60 measurement samples as training data of the neural network, and 20 measurement samples as test data. Since it is difficult to calculate analytically the learning rate to which a neural network will have a better performance, we decided to test each method in a five different learning

Table 3
Levenberg–Marquardt performance analysis, from 0.2 of learning rate to 0.9, running four tests for each learning rate.

Learning rate	Obtained performances				Avg. error performance
	Take 1	Take 2	Take 3	Take 4	
Levenberg–Marquardt					
0.2	7.70E−05	0.000250	0.000166	0.000225	0.0001440
0.4	1.83E−05	0.000842	0.000163	0.002995	0.0008039
0.6	6.61E−05	2.35E−05	0.000304	0.001943	0.0004675
0.8	0.000916	0.000134	0.000443	0.000165	0.0003320
0.9	5.47E−05	5.25E−05	0.000213	0.000498	0.0001636

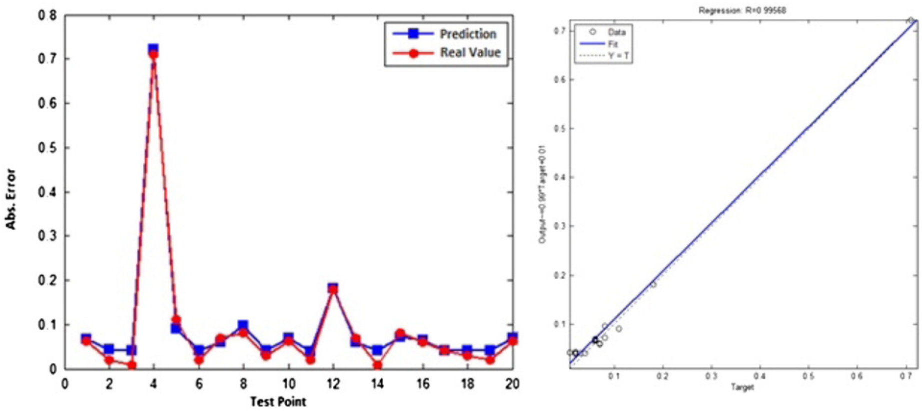

Fig. 6. Predicted error for each sample test point is compared with its real error (left), the error was predicted using a neural network and a regression plot fit (right), trained with the Polak–Ribiere method. (For interpretation of the references to color in this figure caption, the reader is referred to the web version of this article.)

rates in a range from 0.2 to 0.9. In each learning rate we calculate the performance 4 times and the average performance is obtained (Table 1, 2 and 3). The graphic (Figs. 6, 7 and 8) shows in red the actual absolute error of the scanner measurements and in blue the absolute error of the scanner measurement, predicted by the respective mathematical method used to train the neural network (Levenberg–Marquardt, Polak–Rebiere, quasi-Newton). The aim is that the predicted errors (blue squares of the graphs) are as close as possible to the actual values of error (red circle graphs).

We note that the use of a neural network provides an acceptable approximation of the measurement error (up to 99.98%), and therefore be able to correct this error, the most significant difference is presented by modifying the method of training, where the method of Levenberg–Marquardt showed a higher capability in the error prediction task than Polak–Ribiere and quasi-Newton methods (Fig. 9). Additionally the Wilcoxon signed rank test shows that even when the performances of the Levenberg–Marquardt, Polak-Ribiere and quasi-Newton methods are almost the same, the test indicates a clear statistically significant difference between the methods (Table 4). This error approximation method has been tested in our developed medical scanner, however, do not depend on any physical variable of our scanner, the methods have the capability to be used in any other laser scanner.

6. Conclusion

The precision of the scanners, specially the medical scanners, is a highly important task; therefore having the capability to adjust the scanner measurements by a mathematical algorithm gives us a simple solution to the complex problem of the precision. A Levenberg–Marquardt method was used to train a neural network and adjust the scanner measurements; this method shows a reliability of 99.98% in the measurement adjustment, meanwhile Polak–Rebiere and quasi-Newton methods show a reliability of 99.56% and 99.53% respectively. In addition the Levenberg–Marquardt method shows more stability in the error performance at different

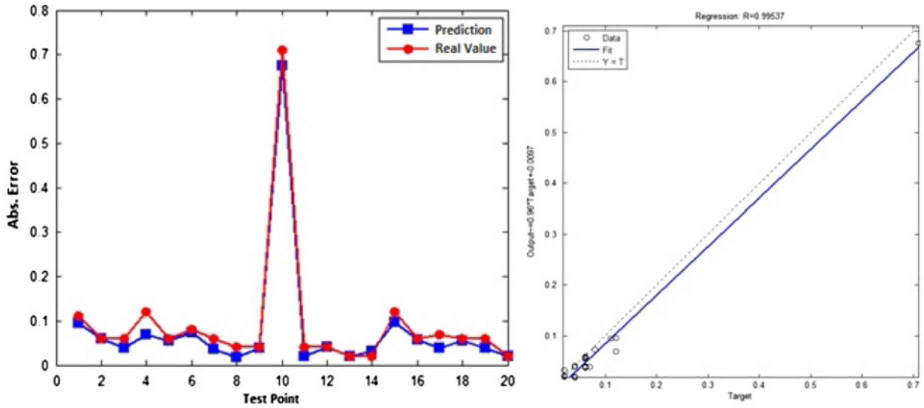

Fig. 7. Predicted error for each sample test point is compared with its real error (left), the error was predicted using a neural network and a regression plot fit (right), trained with the quasi-Newton method. (For interpretation of the references to color in this figure caption, the reader is referred to the web version of this article.)

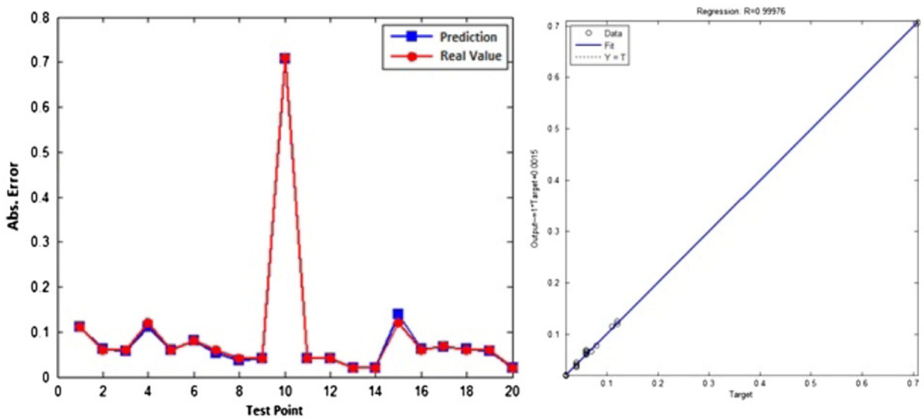

Fig. 8. Predicted error for each sample test point is compared with its real error (left), the error was predicted using a neural network and a regression plot fit (right), trained with the Levenberg–Marquardt method. (For interpretation of the references to color in this figure caption, the reader is referred to the web version of this article.)

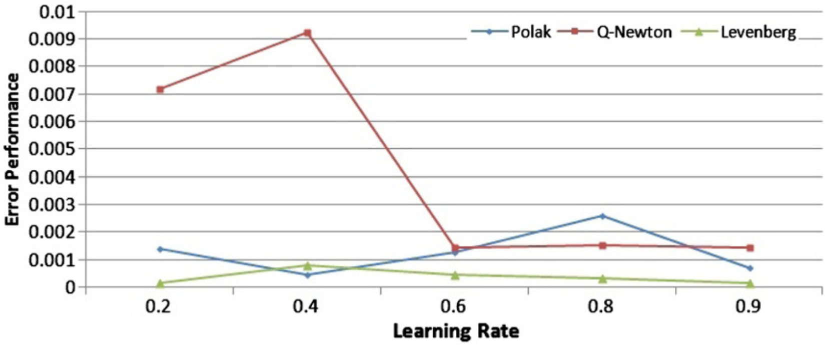

Fig. 9. Comparing the error performance of the three methods at different learning rates.

Table 4
Statistical difference between the error predictions made by the Levenberg–Marquardt method, Polak–Ribire and quasi-Newton methods determinate by the Wilcoxon signed rank test.

Compared sample	Levenberg–Marquardt p value $<$ 0.05
Quasi Newton	0.0187
Polak–Ribiere	0.0366

Table 5
Average performance and standard deviation with/without digital rectifier.

Methodology	Average performance (%)	Standard deviation (%)
With digital rectifier	99.98	0.007
Without digital rectifier	95	1.75

learning rates (Fig. 9). The experimentation shows that the Levenberg–Marquardt method has a better performance over the Polak–Rebiere and quasi-Newton methods in the measurement adjustment task for this particular medical laser scanner, and it can be used as a solution to improve the performance of our system (Table 5). Another advantage of the proposed system is that it can be used in conjunction with localization error methodologies [25] even for more dimensional tasks; or with mathematical improvements to the Levenberg–Marquardt method, as in Ref. [26] to improve the convergence speed. However the identification of the components that cause the uncertainty of the measurements and the correction of this problem are the task for future research.

References

[1] P. Treleaven, J. Wells, 3d body scanning and healthcare applications, Computer 40 (7) (2007) 28–34.
[2] J. Rodriguez-Quinonez, O. Sergiyenko, V. Tyrsa, L. Basaca, M. Rivas, 3D body & medical scanners' technologies: methodology and spatial discriminations, in: Optoelectronic Devices and Properties, Intech, 2011, pp. 307–322.
[3] J. Rodriguez-Quinonez, O. Sergiyenko, V. Tyrsa, L. Basaca, J. Hipolito, Continuous monitoring of rehabilitation in patients with scoliosis using automatic laser, in: Pan American Health Care Exchanges—PAHCE, Rio de Janeiro, Brazil, 2011, pp. 410–414.
[4] J. Cheng, M. Qiao, W. Bian, D. Tao, 3d human posture segmentation by spectral clustering with surface normal constraint, Signal Processing 91 (9) (2011) 2204–2212.
[5] N. Kong, J. Shin, P. Park, A two-stage affine projection algorithm with mean-square-error-matching step-sizes, Signal Processing 91 (11) (2011) 2639–2646.
[6] M. Rivas, O. Sergiyenko, V. Tyrsa, Machine vision: approaches and limitations, in: Computer Vision, Intech, 2008, pp. 395–428.
[7] R. Shankarapillai, M. Ananthakrishnan, N. Rai, A. Mathur, L. Mathur, Periodontitis risk assessment using two artificial neural networks—a pilot study, International Journal of Dental Clinics 2 (4) (2010) 36–40.
[8] F.F. Gonzalez-Navarro, et al., Feature and model selection with discriminatory visualization for diagnostic classification of brain tumors, Neurocomputing 73 (4–6) (2010) 622–632.
[9] A. Vellido, Outlier exploration and diagnostic classification of a multi-centre h-mrs brain tumour database, Neurocomputing 72 (13–15) (2009) 3085–3097.
[10] E. Florian, A. Chevreuilc, P. Loubaton, Blind source separation of convolutive mixtures of non-circular linearly modulated signals with unknown baud rates, Signal Processing 92 (3) (2012) 715–726.
[11] O. Sergiyenko, et. al, Precise optical scanning for practical multi-applications, in: IEEE-34th Annual Conference of IEEE Industrial Electronics (IECON' 08), Orlando, 2008, pp. 1656–1661.
[12] L. Basaca, et al., 3d laser scanning vision system for autonomous robot navigation, in: ISIE 2010, Bari, Italy, 2010, pp. 1773–1779.
[13] M. Rivas, et al., Spatial data acquisition by laser scanning for robot shm task, in: ISIE 2008, Cambridge, 2008, pp. 1458–1463.
[14] R.L. Mottl, Machine Elements in Mechanical Design, Pearson Prentice Hall, 2003.
[15] J. Nocedal, S.J. Wright, Numerical Optimization, Springer, 1999.
[16] D. Marquardt, An algorithm for least-squares estimation of non-linear parameters, SIAM Journal on Applied Mathematics 11 (2) (1963) 431–441.
[17] J.F. Bonnans, J.C. Gilbert, C. Lamarechal, C.A. Sagastizabal, Numerical Optimization, Springer, 2006.
[18] B.M. Wilamowski, H. Yu, Improved computation for Levenberg–Marquardt training, IEEE Transactions on Neural Networks 21 (6) (2010) 930–937.
[19] B.M. Wilamowski, H. Yu, 〈http://reference.wolfram.com/mathematica/tutorial/unconstrainedoptimizationconjugategradientmethods.html〉, 2011.
[20] S. Bolognani, S. Zampieri, Distributed quasi-Newton method and its application to the optimal reactive powerflow problem, in: IFAC Workshop on Distributed Estimation and Control in Networked Systems, Annecy, 2010, pp. 305–310.
[21] A. Abba, F. Caponio, A. Geraci, G. Ripamontii, Non-linear least-squares in fpga devices for digital spectroscopy, in: Nuclear Science Symposium Conference Record (NSS/MIC), Orlando, 2009, pp. 563–568.
[22] T. Mathworks, Neural Networks Toolbox Users Guide, The Mathworks, 2000.

[23] A.L. Betker, T. Szturm, Z. Moussavii, Application of feedforward backpropagation neural network to center of mass estimation for use in a clinical environment, in: Engineering in Medicine and Biology Society, Man, 2003, p. 2714.
[24] M. Sugiyama, M. Krauledat, K.R. Muller, Covariate shift adaptation by importance weighted cross validation, Journal of Machine Learning Research (2007) 985–1005.
[25] B. Huang, C. Yu, B.D. Anderson, Analyzing localization errors in one-dimensional sensor networks, Signal Processing 92 (2) (2012) 427–438.
[26] M.K. Transtruma, J.P. Sethnaa, Improvements to the Levenberg–Marquardt algorithm for nonlinear least-squares minimization, Computational Physics submitted for publication, http://arxiv.org/abs/1201.5885.

Optics and Lasers in Engineering ∎ (∎∎∎∎) ∎∎∎–∎∎∎

Contents lists available at ScienceDirect

Optics and Lasers in Engineering

journal homepage: www.elsevier.com/locate/optlaseng

Optical monitoring of scoliosis by 3D medical laser scanner

Julio C. Rodríguez-Quiñonez [c], Oleg Yu. Sergiyenko [a,*], Luis C. Basaca Preciado [a], Vera V. Tyrsa [b], Alexander G. Gurko [b], Mikhail A. Podrygalo [b], Moises Rivas Lopez [a], Daniel Hernandez Balbuena [c]

[a] *Engineering Institute of Autonomous University of Baja California, Mexicali, Mexico*
[b] *Kharkov National Highway and Automobile University, Kharkov, Ukraine*
[c] *Engineering Faculty of Autonomous University of Baja California, Mexicali, Mexico*

A R T I C L E I N F O

Article history:
Received 6 March 2013
Received in revised form
6 July 2013
Accepted 31 July 2013

Keywords:
Laser
Scanner
Triangulation
Scoliosis

A B S T R A C T

Three dimensional recording of the human body surface or anatomical areas have gained importance in many medical applications. In this paper, our 3D Medical Laser Scanner is presented. It is based on the novel principle of dynamic triangulation. We analyze the method of operation, medical applications, orthopedically diseases as Scoliosis and the most common types of skin to employ the system the most proper way. It is analyzed a group of medical problems related to the application of optical scanning in optimal way. Finally, experiments are conducted to verify the performance of the proposed system and its method uncertainty.

1. Introduction

Medical professionals have traditionally measured the body's size and shape by hand to assess health status and guide treatment. Now, 3D body-surface scanners are transforming the ability to accurately measure a person's body size, shape, and skin-surface area [1]. Advances in technology have enabled to perform more efficiently diagnosis and studies of the internal structure of the human body. MRI, VATS, CT, ultrasound and X-rays [2] have revolutionized the capability to study physiology and anatomy in vivo and to assist in the diagnosis and monitoring of a multitude of disease phases. Different technologies to develop the human body scanning have been developed, however, these technologies fall in measurement error when the phase unwrapping will fall into an error, for example when an improper value of Gray coding is caused by mistake at the partial boundary of two adjacent binary words [3]. Moreover several scanner technologies have critical limitation on their field-of-view due to pixel camera limitations [4,5].

With the capability to visualize significant structures in great detail, 3D image methods are a valuable resource for the analysis and surgical treatment of many pathologies.

While clinicians use measurements of body properties to assess risk and guide health management, patients use the same information in the context of other aspects of their lives, in particular their body image and sense of self-esteem [1]. 3D scanners also provide visualization, which is important for clinician–patient interaction in cosmetic surgery. In addition to providing simulation models to use in illustrating potential effects of treatment, visualization lets medical professionals demonstrate changes to the patient. Such models can potentially greatly improve the patient's understanding of treatment [1].

Recently, vision sensors have received more and more attention due to their high precision and rich information [6,7] and used in high technology applications such as robotic surgery [8] as is the case of laser scanners.

Nowadays, there are two mainstream non-contact optical measurement techniques that are well established with high technical and economic performance, based upon projected fringe and laser scanning methods [9].

The first one, methods based on structured light, creates correspondences and gives specific codewords to every unitary position in the image. In this approach one of the cameras is substituted by an active device (a projector), which projects a structured light pattern onto the scene. This active device is modeled as an inverse camera, being the calibration step a similar procedure to the one used in a classical stereo vision system [10]. The projected pattern imposes the illusion of texture onto an object, increasing the number of correspondences. Therefore,

* Corresponding author. Tel.: +52 686 168 7170.
E-mail addresses: srgnk@iing.mxl.uabc.com, srgnk@uabc.edu.mx, srgnk@hotmail.com (O.Yu. Sergiyenko).

0143-8166/$ - see front matter © 2013 Elsevier Ltd. All rights reserved.
http://dx.doi.org/10.1016/j.optlaseng.2013.07.026

surface reconstruction is possible when looking for differences between projected and recorded patterns [11]. From the captured structured patterns, the codewords can be decoded. If the codewords are unique, the correspondence between the projector sensor and the camera sensor is uniquely identified, and 3D information can be calculated through triangulation [12]. There are a several structured light scanners based on 2-D fringe projected, including moire technique, phase measuring profilometry, Fourier transformation profilometry, modulation measurement profilometry, spatial phase detection, color-coded fringe projection, gray- coded binary fringe sequences, etc [13]. These measurement methods are not based on ionizing radiation, and the measurement process may be repeated frequently without any harm to the patient′s health [14].

Looking from the point of view of acquired data and user, measurement objects by structured light generates a huge amount of redundant data, which requires extra time for measurement, big storage space and is computationally costly during cloud alignment, registration and refinement procedures as well as during the post processing feature extraction [9].

The second technology is the laser scanners; there are several ways to perform a laser scanning operation; Lerch [15] describe the Vitus Smart 3D Laser Scanning. The scanning assembly is 4′ wide by 4′ deep by 10′ height with a structural frame to keep the device stationary; curtains are hung from the frame to minimize outside light. Located in each of the four corners is a vertical column containing the essential scanning equipment: a low energy laser, and two charge coupled device (CCD) cameras, all of which ride together in an elevator assembly that travels up and down in the vertical column.

When the system is calibrated correctly, the four elevator assemblies travel down the columns in unison, sweeping the scanning zone with a horizontal plane of laser light [15]. The laser light illuminates the contours of an object standing within the scanning zone and the CCD cameras record discrete points on these contours at each horizontal plane. The entire scan takes approximately 12 s [15].

However the elevated production costs of hardware components for the Vitus 3D Laser Scanning could be considered as a disadvantage. Moreover, such four—towers system occupies a fixed considerably big indoor volume space and cannot be relocated in a short time notice nor replaced. So for a better understanding of the exact general requirements of the scanners is to match them with medical specifications, lets overview some crucial points of the medical part of the problem.

2. Medical scope of the problem

Some medical applications need the exact superficial geometry. Such type of input excludes the use of camera methods as an option, which only provides a probabilistic estimation of the image

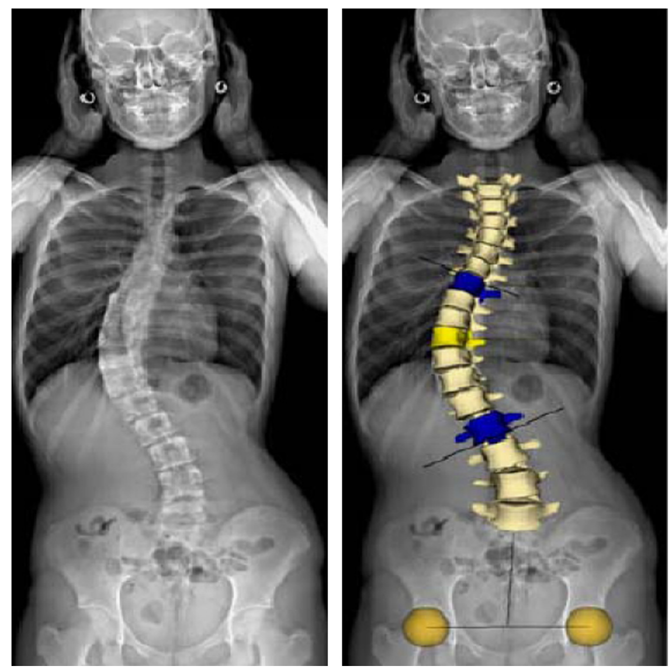

Fig. 1. Column Distortion caused by scoliosis (X-ray) [14].

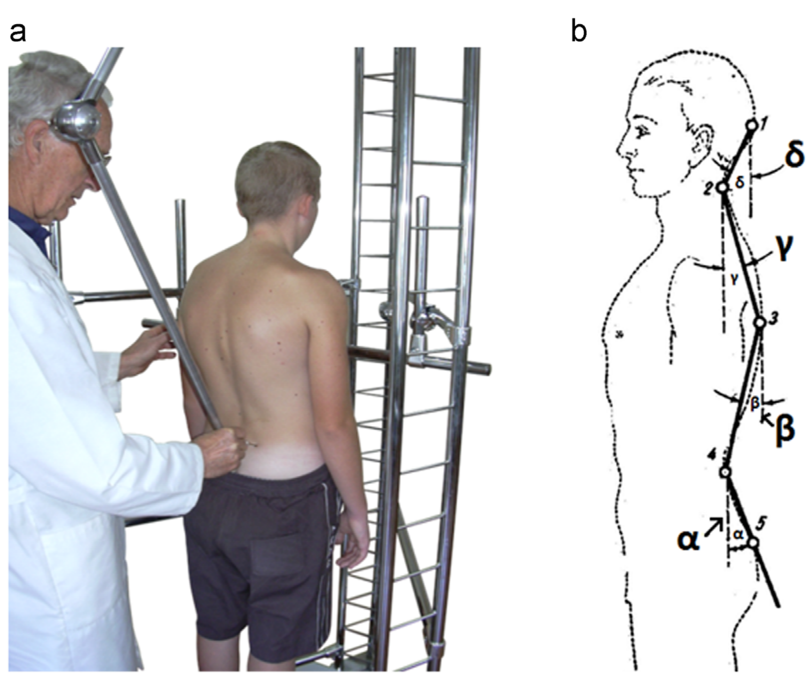

Fig. 2. Anthropometer (a) used for control and diagnoses of scoliosis (b) [16].

Please cite this article as: Rodríguez-Quiñonez JC, et al. Optical monitoring of scoliosis by 3D medical laser scanner. Opt Laser Eng (2013), http://dx.doi.org/10.1016/j.optlaseng.2013.07.026

[16]. For these critical applications, there is a need to apply a group of methods which permits to obtain the coordinate grid of the surface under inspection and define coordinate uncertainty.

We can consider plastic surgery and some orthopedic diseases treatments as those kinds of medical applications. The last one in our opinion is the most crucial 3D metrological task in modern medicine, according to the example [17,18]. One of the most known orthopedic diseases is Scoliosis see Fig. 1. Scoliosis is a multifactorial three-dimensional (3D) spinal deformity that always involves elemental deformities in the three main planes: lateral curvature in frontal, anteroposterior (mainly lordotic) deviation in sagittal, and (very characteristically) vertebral axial rotation in the horizontal plane [17]. Studies of vertebral rotation, translation and angulation have revealed that a direct nonlinear relationship may exist between these elemental components of spinal deformities, but details of this relationship remain unclear [19].

Vertebral rotation has been demonstrated to play a fundamental role in the pathomechanism of the onset of scoliosis [17]. The current techniques in scoliosis surgery are not based on its accurate measurement and evaluation [20].

The demand for an accurate evaluation of the vertebral rotation detectable in scoliosis is hardly new. All measurement methods are based on assessments of the relative positions of various posterior elements of the vertebrae. Despite use of the torsiometer, currently being the most accepted measurement method in clinical practice, its reproducibility is very limited to be quantified precisely [21,22].

Other system for the diagnosis of the disease, such is Anthropometer presented by [18] (see Fig. 2) is a healthy choice because it does not emit any harmful radiation to the body as X-rays. It operates through a pointer that scans the subject back and takes measurements as the pointer moves, interpreting by 3 disc-optical-encoders, and generates an image with traveled distances and angles measured. The measure information is: α: sacrum slope, β: spine thoracic-lumbar part slope, γ: spine upper-thoracic part slope, δ: spine cervical part slope.

In addition to obtaining the angles, the system provides the perpendicular deviation from point 1 to point 5 (see Fig. 2b), the tilt of the shoulders (G–B) and the angle of curvature of the lumbar spine. All these elements are important parameters for the diagnosis. However, this system is invasive and can cause discomfort to the patient. Also the measurement accuracy is affected by the ability of the person who makes the scan i.e. if the professional applies too much pressure with the pointer on the patient; in result the measurement will not be accurate. Another tool commonly used for the identification of the curvature in the scoliosis is the Scoliometer. An scoliometer, also known as a inclinometer, measures distortions of the torso. Some experts believe the scoliometer would make a useful device for widespread screening. Scoliometers, however, indicate rib cage distortions in more than half of children who turn out to have very minor or no sideways curves. They are therefore not accurate enough to guide treatment [22]. That is why we developed the 3D Rotational Body Scanner, a system that automatically and accurately can be used for body measurements, and thanks to the nature of light does not distort the scanned surface nor emits any harmful radiation for the human being. In the same manner, our scanner works in the most similar way, repeating the action sequence of the last presented system, which is the most widely recognized by experienced medical community.

3. Dynamic triangulation principle

There are 2 types of laser triangulation: static laser triangulation and dynamic laser triangulation. For the distance to the

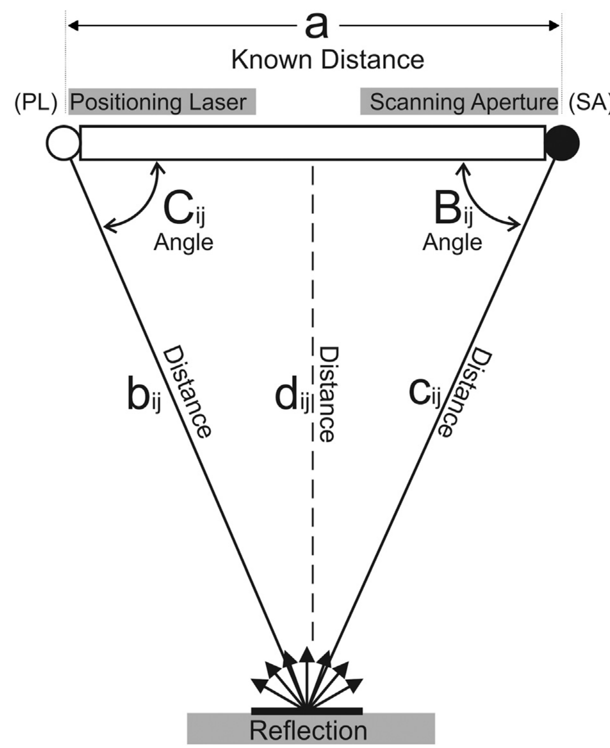

Fig. 3. Dynamic triangulation principle, spatial position of Scanning Aperture and Positioning Laser.

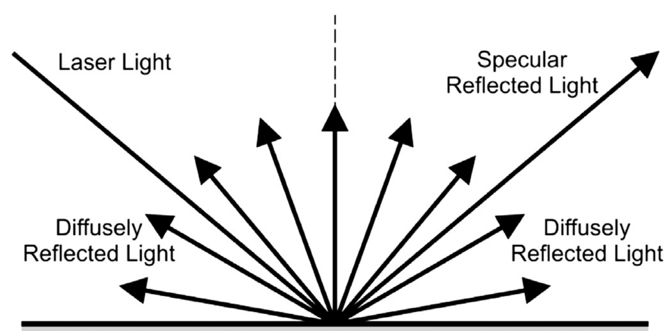

Fig. 4. The model of Mixed Reflection on smooth surface.

incident surface to be calculated in the static laser triangulation, there are three variables to be known, which are the emission angle, the angle detected by a photodetector sensor array, usually a camera, and the distance between the laser emitter and the camera. The static laser triangulation is performed by a laser light emitter which is adjusted to a known angle, and the light that is reflected by the incident surface is detected by the camera [23,24]. The main disadvantage of this procedure is the limited field-of-view (FOV) it has.

The difference with the traditional laser triangulation scheme, is that in dynamic triangulation both the laser emitter (Positioning laser) and the sensor (Scanning aperture) are movable parts that always are projecting (Positioning laser) and scanning (Scanning aperture) in different planes, that is why the triangle just exist a few milliseconds until a new revolution of the Scanning aperture is completed, this method is defined by our group as dynamic triangulation [25,26]. Not to be confused with dynamic skin triangulation in [27]. The detailed description of our scanning aperture is given in [28, p. 109] and [28, p. 1459]. This opening (SA) have a 45° mirror that reflects the entire scanning plane to a photodetector which is sensitive only to the spectrum of laser

Please cite this article as: Rodríguez-Quiñonez JC, et al. Optical monitoring of scoliosis by 3D medical laser scanner. Opt Laser Eng (2013), http://dx.doi.org/10.1016/j.optlaseng.2013.07.026

light, and the mirror is constantly rotating. Therefore, the triangle is only generated when the scanning plane detects the laser light which occurs over a period of time from 4.04 ms to 8.34 ms, according to rpm on mirror motor [30]. Dynamic triangulation is the base of our system to obtain the 3D coordinates of the body inside of FOV.

As shown in Fig. 3 laser beam is projected from the Positioning Laser (PL) onto the body, and reflecting it back onto the revolving sensor inside the Scanning Aperture (SA) [29,31].

However, in order to detect this reflection is necessary to know that there are 2 types of light reflection, specular and diffuse [32]. When a beam of light encounters a smooth mirror-like reflecting surface, the reflected light will be parallel to each other and according to the Law of Reflection, the angle of reflection will be equal to the angle of incidence; this is called Specular Reflection. On the contrary, if the beam of light encounters a rough reflecting surface as the human skin, the light beams will be reflected in every direction, this is called Diffuse Reflection. Although, light can be reflected specularly or diffusely, many materials present mixed

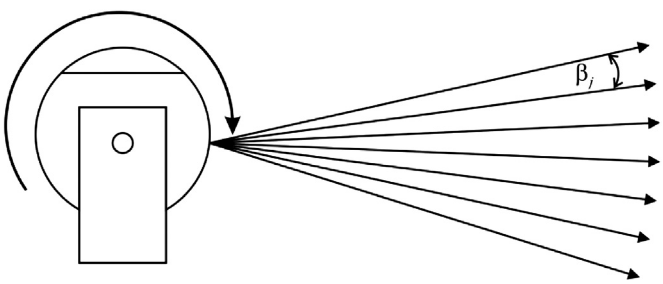

Fig. 5. Right side view representation of the scanner and the vertical angle β_j.

reflection such as the one shown in Fig. 4 which is a combination of specular and diffuse reflection.

Based on the mentioned above, the reflection type in body scanning is diffuse reflection. The model of Fig. 4 is mostly close to our case, except the surficial absorptance of the light wave by human skin, but this difference is the point of detailed analysis below in Section 5. Our system has a lenses' mechanism that allows us to detect the low signal produced by the diffusely reflected light.

Then, using the theorem of sines, the correlation between the triangle sides and the width and height in the triangle of Fig. 3, it is possible to develop a formula to calculate distance "d" from base "a" up to points highlighted by the laser beam on to the body.

$$d_{ij} = a\frac{\sin B_{ij} \times \sin C_{ij}}{\sin\,[180^\circ-(B_{ij}+C_{ij})]} \tag{1}$$

where indexes i and j represent respectively the step number in horizontal and vertical directions during the 3D Body Scanning. To perform the vertical scanning the system rotates to get the angle β_j as show in Fig. 5.

Using angles B_{ij}, C_{ij}, $\Sigma_{j=1}^{n}\beta_j$ and the known distance of the base a, it is possible to calculate the Cartesian coordinates of each laser highlighted points on each ij step of 3D Body scanning process, based on the following trigonometric formulas:

$$x_{ij} = a\frac{\sin B_{ij} \times \sin C_{ij} \times \cos \sum_{j=i}^{n}\beta_j}{\sin\,[180^\circ-(B_{ij}+C_{ij})]} \tag{2}$$

$$y_{ij} = a\left(\frac{1}{2}-\frac{\sin B_{ij} \times \cos C_{ij}}{\sin\,[180^\circ-(B_{ij}+C_{ij})]}\right) \text{ at } B_{ij} \leq 90^\circ \tag{3}$$

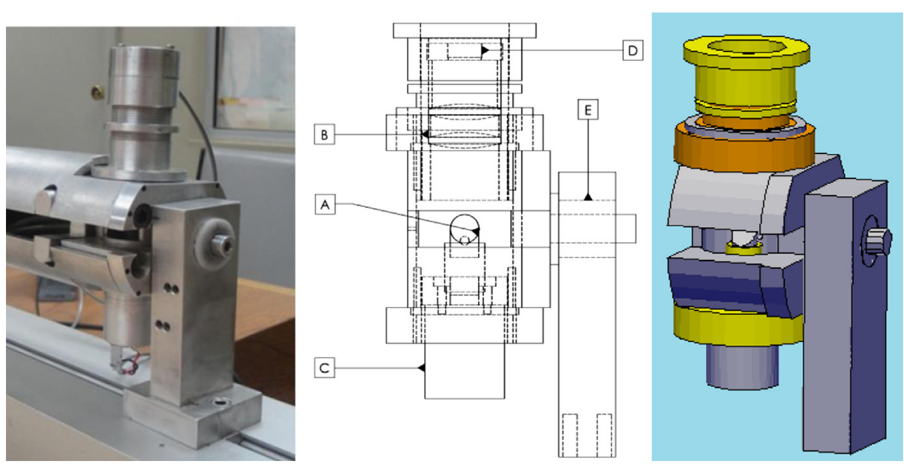

Fig. 6. View of the receiver and its components. (A) 45 degree rotational mirror, (B) Targets, (C) DC Motor, (D) Photodetector, (E) Flat Bearing.

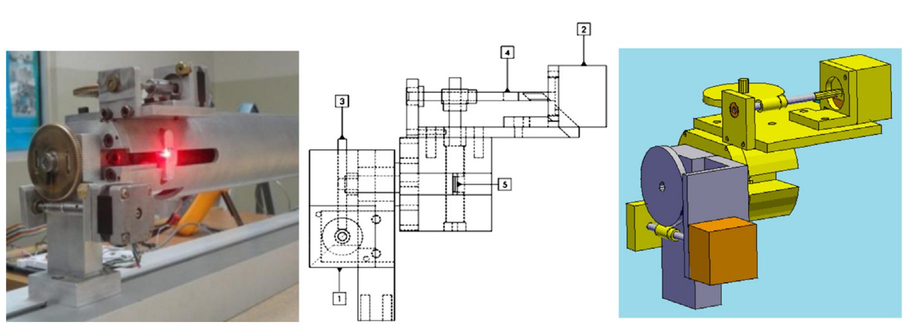

Fig. 7. View of the System projector and its components. (1) Step Motor of angular rotation, (2) Step motor for the mirror rotation, (3) System's rotation gear, (4) Mirror's rotation gear, (5) Mirror.

Please cite this article as: Rodríguez-Quiñonez JC, et al. Optical monitoring of scoliosis by 3D medical laser scanner. Opt Laser Eng (2013), http://dx.doi.org/10.1016/j.optlaseng.2013.07.026

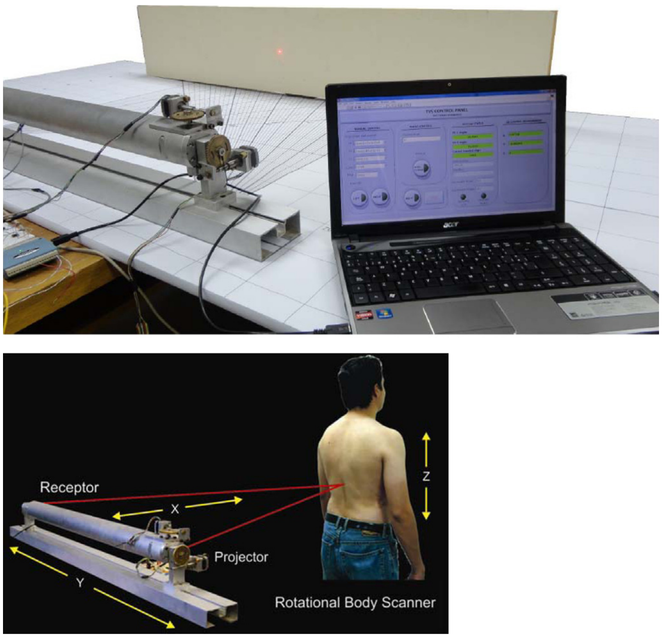

Fig. 8. 3D Medical Laser Scanner: General view and Experimental application on body/column scanning.

$$y_{ij} = a\left(\frac{1}{2}+\frac{\sin B_{ij} \times \cos C_{ij}}{\sin\,[180^\circ - (B_{ij}+C_{ij})]}\right) \text{ at } B_{ij} \geq 90^\circ \tag{4}$$

$$z_{ij} = a\frac{\sin B_{ij} \times \sin C_{ij} \times \sin \sum_{j=i}^{n} \beta_j}{\sin\,[180^\circ - (B_{ij}+C_{ij})]} \tag{5}$$

4. 3D Medical laser scanner in compact rotational design

The 3D Medical Laser Scanner uses the principle of Dynamic Triangulation Scanner mentioned above. The rotation of the system is given by a shaft-gear mechanism. The horizontal scanning is performed by a step motor which rotates a mirror who reflects the laser beam generated by the laser which is inside of the system bar "a" shown in Fig. 3. As the Dynamic triangulation, our system have a receiver SA (Fig. 6) and consist of 5 main components (A) 45 degree cut rotational mirror, whose principal function is to direct the laser light beam towards the lenses (targets). (B) Targets, whose function is to concentrate the light beam onto photodetector. (C) DC Motor, which rotates the mirror. (D) Photodetector, it captures the light beam located within the frequency range of the laser. (E) Flat Bearing, allows the rotation around the horizontal axis of the system changing angular value of "β_j".

In addition, as Dynamic triangulation, our system has a PL which is in-built system of the projector. The system projector has 5 main components (Fig. 7), which are the following: (1) Step Motor of angular rotation, whose main function is to control the rotation of the entire system. (2) Step motor for the mirror rotation, which controls the mirror rotation. (3) System's rotation gear increases the precision of the system since it gives a 10:1 ratio gear-motor. (4) Mirror's rotation gear increases the precision of the system giving a 10:1 ratio gear. (5) Mirror, reflects the laser light beam towards the scanning body.

The laser light projector emits the light at different angles towards the body. And at the same time, the receptor rotates until it detects the light deflected by the body. When the mirror of the receptor deflects the scattered light towards the target and concentrates the light towards the photodetector, an electronic pulse is emitted which indicates the point has been detected. A relationship between the rotation time and detection time shows the angle in which the receptor detects the point. Since the projector rotation is controlled by the user, the angle of the projector is known at all times. The relationship between the 2 angles and the known distance between the projector and receptor gives each of the captured coordinates. As shown in Fig. 8, the projector and receptor are separated by a bar that gives the exact distance of 1 m between their centers, and located in the bar is the laser light source.

Within the bar the laser also gets aligned and locked avoiding measurement errors. The triangulation principle used is well known, and some of the advantages given by this system are the angular rotational mechanism, which allows the rotation with no chains [33], an increment in resolution by 10 times by using gears that gives 1 rotation for each 10 rotations that gives the step motor.

5. Skin reflectance

Our system proper functioning depends significantly on accurate knowledge about reflectivity parameters of the skin surface which we are working on. It is of great importance to know that for this selected task the laser's wavelength and modulation type is no way physiologically dangerous for any kind of skin tissues, considering that inspection time length is of 0.4–4.5 min, and in each point the laser does not stops more than 4.04–8.34 ms.

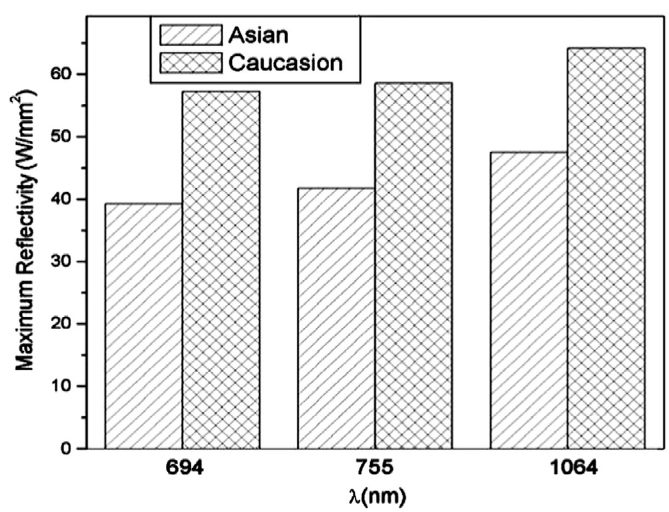

Fig. 9. Comparison of maximum reflectivity of backscattered light for Asian and Caucasian for different wavelengths.

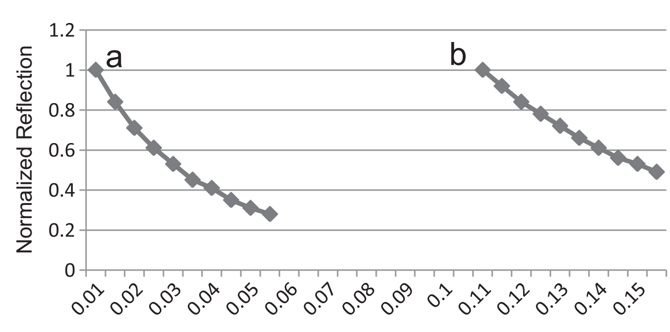

Fig. 10. Variation of normalized reflectance vs volume fraction of melanosome from skin with hemoglobin volume fraction of 5% (a) and 2% (b).

Please cite this article as: Rodríguez-Quiñonez JC, et al. Optical monitoring of scoliosis by 3D medical laser scanner. Opt Laser Eng (2013), http://dx.doi.org/10.1016/j.optlaseng.2013.07.026

Table 1
3D Laser scanning medical applications.

Measurement	Application
Shape	Screening, Abdominal Shape, Prosthetics and Obesity
Size	Anthropometric Surveys, Growth Defects, Scoliosis, Fitness and Diet
Surface Area	Lung Volume, Drug Dosage, and Diabetes
Volume	Eczema and Burns
Visualization	Application
Head	Melanomas and Eating disorders
Chest	Superficial Reconstruction
Whole body	Cosmetic Surgery

Table 2
Optical properties of Asian and Caucasian skins.

Type	Cauc. at 694 λ(nm)	Asian at 694 λ(nm)
Absorption. of Epi.(mm^{-1})	0.063	2.29
Absorption. of Derm.(mm^{-1})	0.028	.033
Scatt. of Epi.(mm^{-1})	40	28
Scatt. of Derm.(mm^{-1})	20	19

As a relatively homogenously histological structure for each definite depth, skin can be assumed to consist of three different layers, epidermis, dermis, and subcutaneous fat, where each layer propagates and absorbs light [34]. Absorption and propagation of light in epidermis depend on natural pigments called melanin [35]. Melanin is produced by cells called melanocyte that is formed in the membrane of melanosome particles, which in epidermis typically varies from 1.3% to 6.3% for lightly pigmented and from 18% to 43% for darkly pigmented specimen [36]. The dermis, with thickness varying from 1 mm to 4 mm, is composed of dense tissue with blood vessels and nerves [34]. Volume fraction of blood in the dermis layer varies from 2% to 7% [30,31]. There is absorbing natural chromophor in the blood cell, called hemoglobin, with concentrations varying from 143 g/L to 173 g/L [37,38]. The color of skin is mainly determined by level of melanin, in other words, by level of melanosome cells, and hemoglobin [39]. Subcutaneous fat can often be ignored because the amount of chromophor, that is the main parameter to absorb light, is very low in that layer [40].

We consider the Boundary Element Method (BEM) [39] as a good method to determinate the reflectance of the human Skin. Precision of the method is compared with the Monte Carlo Method (MC) and the Finite Difference Method (FDM); and it is observed that BEM offers more precise results [39]. In Fig. 9 [39], is shown the maximum reflectivity of an Asian and Caucasian Skin. The surface of skin is assumed to be uniform and roughness effects are neglected. Normalized reflectivity variation of Caucasian and Asian skins vs. volume fraction of melanosome for a wavelength of 694 nm is illustrated in Fig. 10 "a" and "b" [39].

The level of melanosome is assumed to vary from 1.3% to 5.5% and from 10% to 15.5% for Caucasian and Asian skins, respectively [41]. The concentration of hemoglobin in Caucasian and Asian skins is assumed to be 5% and 2%, respectively. The figures illustrate that reflectivity of both types of skins decreases for a larger volume fraction of melanosomes. But, for Caucasian skin, normalized reflection reduces down to 51% by increasing the volume fraction of melanosome, while for Asian skin this reduction is more pronounced and is about 71.8% [39].

Maximum reflectivity of Caucasian and Asian skins for three different wavelengths, which are often used in dermatology, 694 nm, 775 nm, and 1064 nm, is illustrated in Fig. 9. The volume fractions of hemoglobin and melanosome of Caucasian and Asian skins are assumed 1%, 2%, and 16%, 5%, respectively. For longer wavelengths the reflectance from surface of both types of skins increases Table 1.

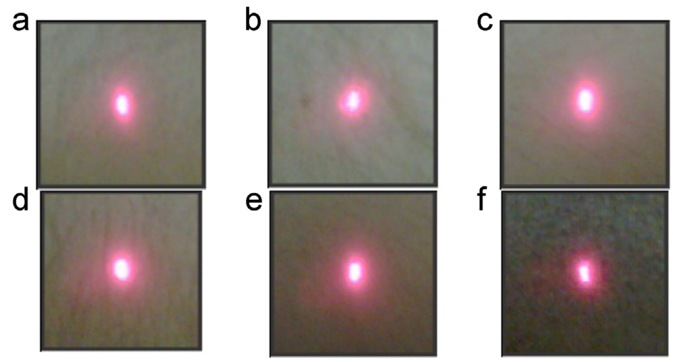

Fig. 11. Reflectance sample measurements of human skin with different pigmentation.

That is because absorption of light in those wavelengths is smaller and, therefore, a larger number of photons return back to the surface [39]. The studied propagation of laser light in two different types of skins, Caucasian and Asian types. Optical properties of skins are presented in Table 2 [41].

6. Experimentation with skin reflectivity

The experimentation described below, will be used to analyze how measurements performed can be affected by the laser beam reflectance on diverse types of skins. In Fig. 11, it can be observed the reflectance intensity measurements in human subjects which pigmentations are distinct between them. To take the skin pigmentation samples have been used people from different nationalities and ethnical origins. The figures "*a*" to "*f*" have been ordered ascending from a lightly pigmentation to a darkly pigmentation. The skin sample of figure "*a*" belongs to a Caucasian person, the skin sample of figure "*b*" belongs to a slightly tanned Caucasian person, the skin sample of figure "*c*" belongs to a Asian person, the skin sample of figure "*d*" belongs to a Latin-American person, the skin sample of figure "*e*" belongs to a Hindu person and at last one the skin sample of figure "*f*" belongs to a Afro-American person.

The experimental measurements were performed under the same conditions, such as, same illumination, ambient temperature, same camera, fixed distance "source-tissue-photodetector" and same body area.

Utilizing Matlab, the luminosity intensity of all the sampling performed was obtained. The intensity was plotted in Fig. 12, where 0 is a value assigned to a void reflectance, and 1 corresponds to maximum reflectance intensity.

For example, in Fig. 11a), the lightly pigmented skin has a natural reflectance to the ambient illumination. Therefore, in Fig. 12a) we can clearly notice this skin reflectance as a suspended amorphous plane above the reflectance axis. While is shown how the darkly pigmented skin does not have the reflectance capability as high towards the ambient illumination as the lightly pigmented skin. Hence, in Fig. 12"*f*" this reflection representation is absent due to the darkly pigmentation skin tone.

At the middle of each plot we can find the laser reflectance, which is a type of light more intense. The laser reflectance, shown in each plot as a protrusion in a cone shape, reaches maximum luminosity levels at the top of the protrusion, which is the center of the laser beam reflectance.

Analyzing the plots we can determine that the laser beam reflectance in humans with darkly pigmented skin is 5–40% better

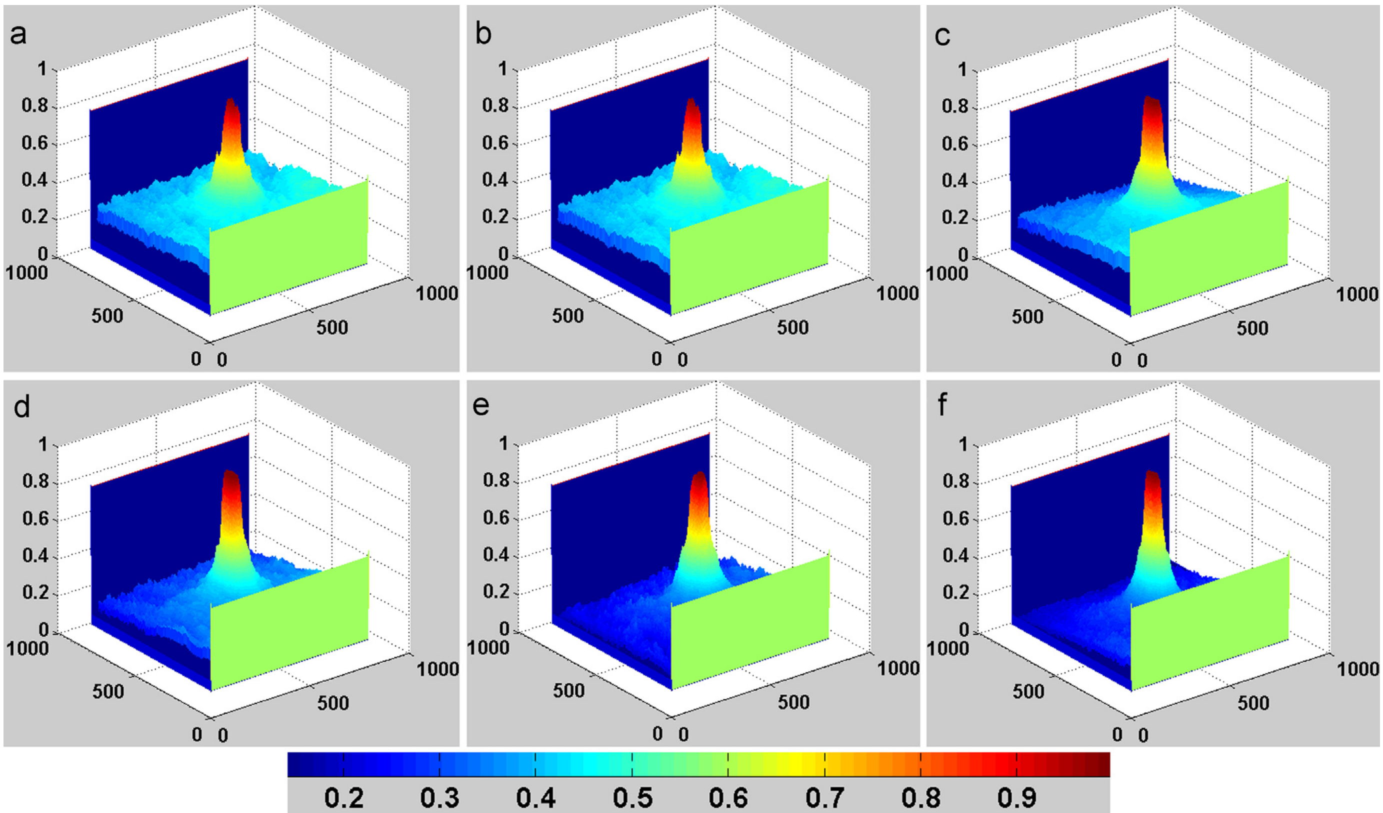

Fig. 12. Relative scale of Reflectance of laser intensity on human skin with different pigmentation.

Table 3
Measurement accuracy.

Test	X(mm)	Y(mm)	x(mm)	y(mm)	Variation X	Variation Y
A	500	250	498	247	–002	–003
B	500	188	498	186	–002	–002
C	500	125	498	123	–002	–002
D	500	063	499	062	–001	–001
E	500	000	499	–010	–001	–010
F	500	–063	500	–062	000	001
G	500	–125	501	–124	001	001
H	500	–188	502	–188	002	–001
I	500	–250	502	–250	002	000
J	750	250	751	–247	001	–003
K	750	188	751	184	001	–004
L	750	125	750	121	000	–004
M	750	063	750	060	000	–003
N	750	000	748	–004	–002	–004
O	750	–063	749	–067	–001	–005
P	750	–125	753	–128	003	–003
Q	750	–188	754	–192	004	–005
R	750	–250	754	–254	004	–004

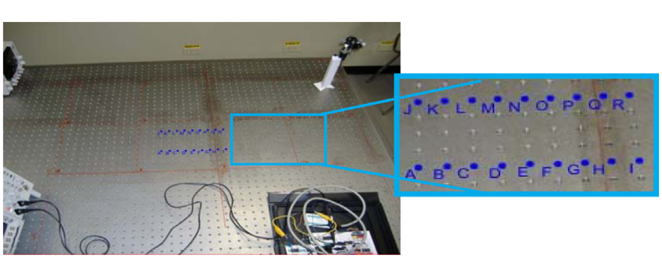

Fig. 13. Points where the test measurements are located in the precision table.

defined than of those with lightly pigmented skin as Fig. 12"*a*". Even though, for our system, is not a factor that prevents the detection of the laser beam reflectance. In addition, we can also obtain experimentally that the ambient illumination is more reflective on subjects with lightly pigmented skin, although, this characteristic does not affect the reflectance area of the laser beam. The next step to verify the pure technical precision of our system we performed experimental measurements in static 2D *(just one row of full 3D scan) comparing "$x(m)$,$y(m)$" measurements (see Table 3, Fig. 13) with the "$X(m)$,$Y(m)$" real value. The experimentation was performed under controlled conditions, over an optic precision table with Cartesian values previously defined On Fig. 13, in the marked area with *A–R* letters, is shown the physical model of the volumetric human body space available for medical scanning, but with metrological quality of the coordinates *A–R* defined by optic table holes. Afterwards, we calculated the variations between the values, shown in Fig. 14.

Since the reflectance intensity does not affect significantly our measurements, the experimentation on human subjects was performed the as shown on Fig. 8, with the following results:

The precision of the measurements obtained in Table 4 and plotted in Fig. 15 using option "point cloud" of Matlab 7.12.

This stage we can consider as Body Shape Imaging: the system represents in graphical way recently inspected vertebral column in very common and ussual form. Using the same Matlab 7.12 option we can present on the same screen two consecutive measurement results (yesterday and today, for example) in order to easy the cross-comparing, and facilitate the analysis of desease treatment progress. We provide this visualization in order to make analysis of disease treatment more natural and convenient for medical specialist. Monitoring based on this image analysis is determinate comparing the measuring data obtained by the system in the back of a person in the area where is the spine, with a manual

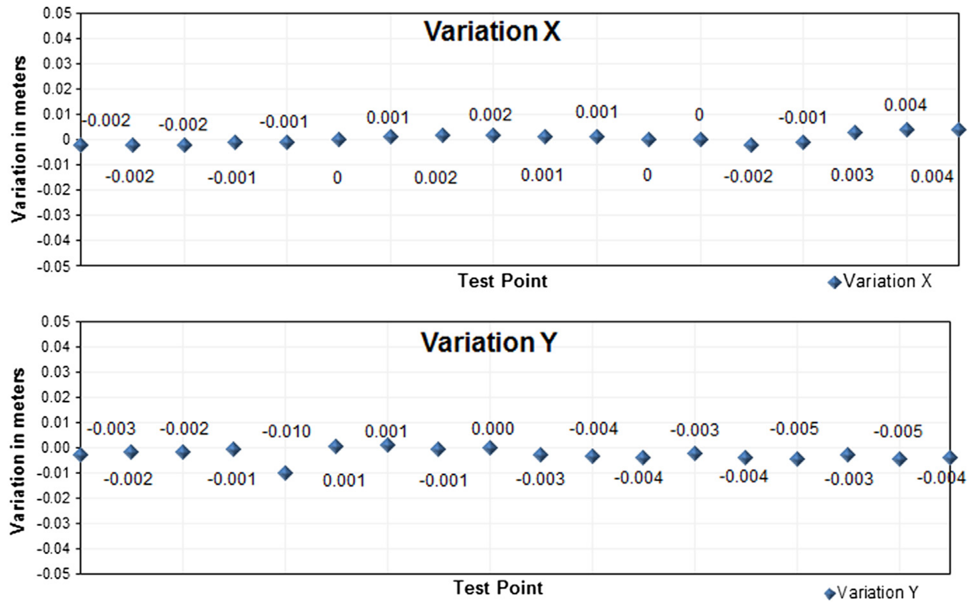

Fig. 14. Dispersion Chart of the measured values vs. real values.

Table 4
Measurement accuracy on human experimentation.

Test	X(mm)	Y(mm)	Z(mm)	% Accuracy
1	516	250	342	99.6
2	515	252	354	99.6
3	514	250	358	99.6
4	513	250	383	99.6
5	514	252	406	99.6
6	515	250	429	99.6
7	516	251	440	99.6
8	517	251	462	99.6
9	519	252	479	99.3
10	517	250	491	99.3
11	516	250	511	99.3
12	515	252	526	99.3
13	514	251	547	99.3
14	513	251	565	99.3
15	513	251	583	99.3
16	514	252	601	99.3
17	515	250	614	99.3
18	516	252	628	99.3
19	517	252	646	99.3
20	519	251	675	99.3

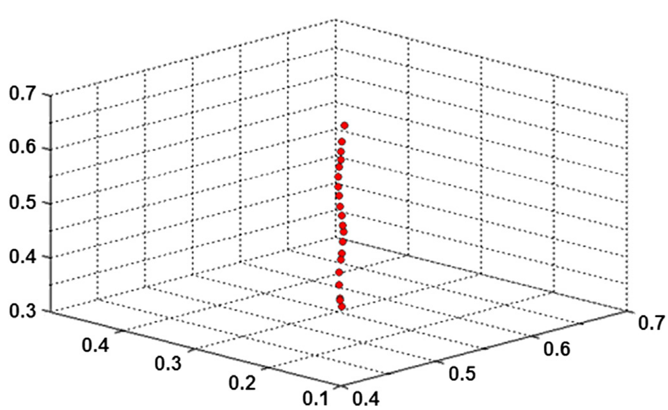

Fig. 15. Spatial distribution of the measurements in Table 4 experimentation.

measurement over the optical table, the results shows no more than 3.6–7.3 mm of absolute error (0.36–0.73% of relative uncertainty (offset)), this allows us to apply our system in the greater

Table 5
Polak–Ribiere performance analysis, from .2 of learning rate to .9, running 4 tests for each learning rate.

Learning rate	Polak–Ribiere				Average error performance
	Obtained performances				
	Take 1	Take 2	Take 3	Take 4	
0.2	0.00199	0.001113	0.000555	0.001938	0.001400162
0.4	0.00054	0.000190	0.001006	0.000586	0.000465549
0.6	0.00032	0.000334	0.003047	0.002702	0.001281126
0.8	0.00132	0.001306	0.007933	0.002532	0.002617578
0.9	0.00046	0.000280	0.001181	0.001657	0.000715481

Table 6
Quasi Newton performance analysis, from .2 of learning rate to .9, running 4 tests for each learning rate.

Learning rate	Quasi Newton				Average error performance
	Obtained performances				
	Take 1	Take 2	Take 3	Take 4	
0.2	0.004958	0.000943	0.001563	0.028447	0.0071826
0.4	0.000682	0.000241	0.043977	0.001240	0.0092285
0.6	0.000736	0.000224	0.004156	0.002144	0.0014526
0.8	0.002366	0.001082	0.000430	0.003766	0.0015293
0.9	0.000519	0.001008	0.004237	0.001444	0.0014421

part of the monitoring tasks of orthopedics diseases, such as scoliosis.

It is evident that in a case of true biometric measurements the result is affected by more additional factors, and mostly among of them own patient body movements during measurement act.

So, this unpleasant fact shows that some kinds of methodological errors are inevitable for biomedical scanning, and it cause the necessity to provide the special mathematical post processing with the main goal to decrease, or completely filter, the most rough errors in the measurement data set. Such mathematical formalism is the topic under special considering in Section 7.

Table 7
Levenberg–Marquardt performance analysis, from .2 of learning rate to .9, running 4 tests for each learning rate.

Learning rate	Levenberg–Marquardt				Average error performance
	Obtained performances				
	Take 1	Take 2	Take 3	Take 4	
0.2	7.70E−05	0.000250	0.000166	0.000225	0.0001440
0.4	1.83E−05	0.000842	0.000163	0.002995	0.0008039
0.6	6.61E−05	2.35E−05	0.000304	0.001943	0.0004675
0.8	0.000916	0.000134	0.000443	0.000165	0.0003320
0.9	5.47E−05	5.25E−05	0.000213	0.000498	0.0001636

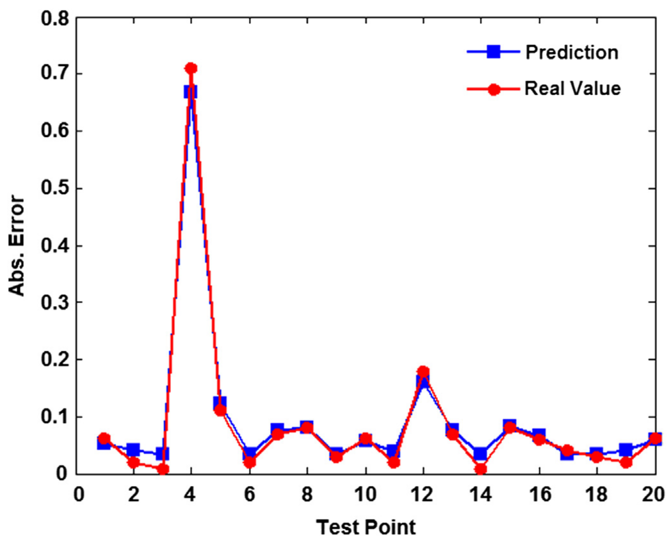

Fig. 16. Our predicted error for each sample test point is compared with its real error, the error was predicted using a neural network trained with the Polak–Ribiere method.

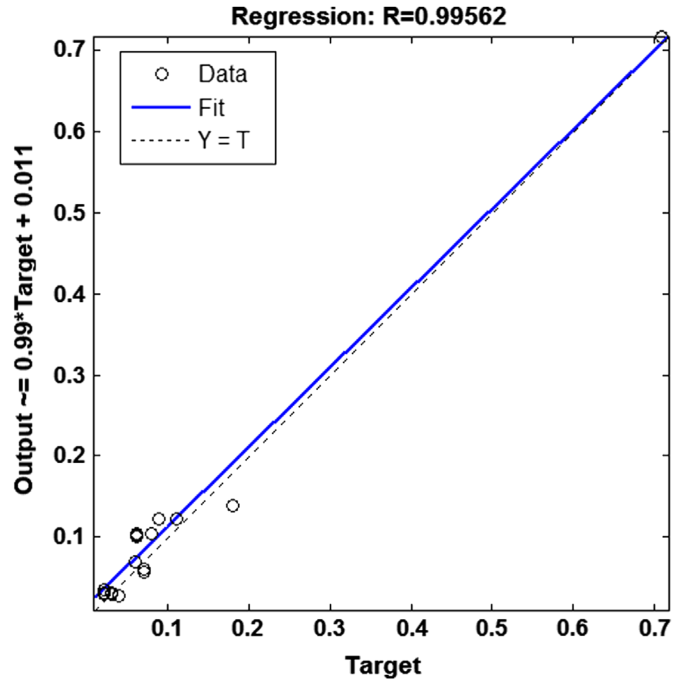

Fig. 17. Regression Plot Fit using Polak Ribiere Method.

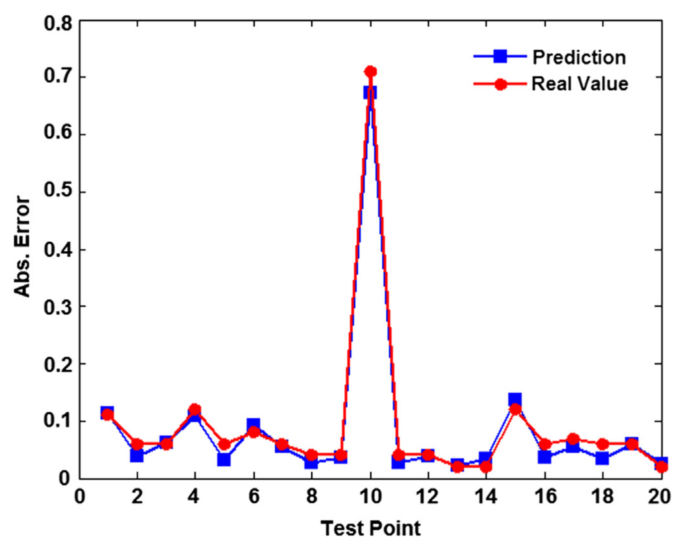

Fig. 18. our predicted error for each sample test point is compared with its real error, the error was predicted using a neural network trained with the Quasi-Newton method.

The average uncertainty of static measurements on precise optic table is 0.23–0.35% better than the results of real human measurements. In our opinion it can be explained by different mechanical influences in the measurement act, mostly the human body movements. We consider that it′s possible improve by further adjustment of the scanning velocity to the condition of real human body measurements. However it′s still clear that even the preliminary uncertainty of measurements in humans is already enough for clinical requirements, especially taking in account the uncertainty of recently used system [15,19].

As mentioned in our previous experiments reflected in [28–30,42,43] the entire FOV of our scanner has three zones of uncertainty, and central zone has exceptional accuracy less than 1% in worst point. This was the main reason to design this medical scanner application, because to measure the average human body at a distance less than 1 m we can have it exactly on the zone with the highest accuracy. This fact is considered as one of the strongest and novel contributions of our application.

7. Levenberg–Marququrdt algorithm use for rough errors filtering

In the modern technical literature exists around 20–30 efficient mathematical methods to eliminate errors in natural experimental data sets for different practical applications. For our special case constrains, as mentioned before in [44], the most proper matching shows three of them: Polak–Ribiere, Quasi-Newton, and Levenberg–Marquardt methods. They are used widely in neuronal networks for strong errors prediction and elimination. We did think that they can be useful in our case for filtering of strong errors in the results of 3D-coordinates measurement. The corresponding simulations in Matlab were carried out, and they shown the preliminary results [44]. We decided to test each method in a 5 different learning rates in a range from 0.2 to 0.9. In each learning rate we calculate the performance 4 times and the average performance is obtained (Tables 5–7). The graphic (Figs. 16, 18 and 20) shows in red the actual absolute error of the scanner measurements and in blue the absolute error of the scanner measurement, predicted by the respective mathematical method used to train the neural network (Levenberg–Marquardt, Polak–Rebiere, Quasi-Newton). The aim is that the predicted errors (blue squares of the graphs) are as close as possible to the actual values of error (red circle graphs).

Please cite this article as: Rodríguez-Quiñonez JC, et al. Optical monitoring of scoliosis by 3D medical laser scanner. Opt Laser Eng (2013), http://dx.doi.org/10.1016/j.optlaseng.2013.07.026

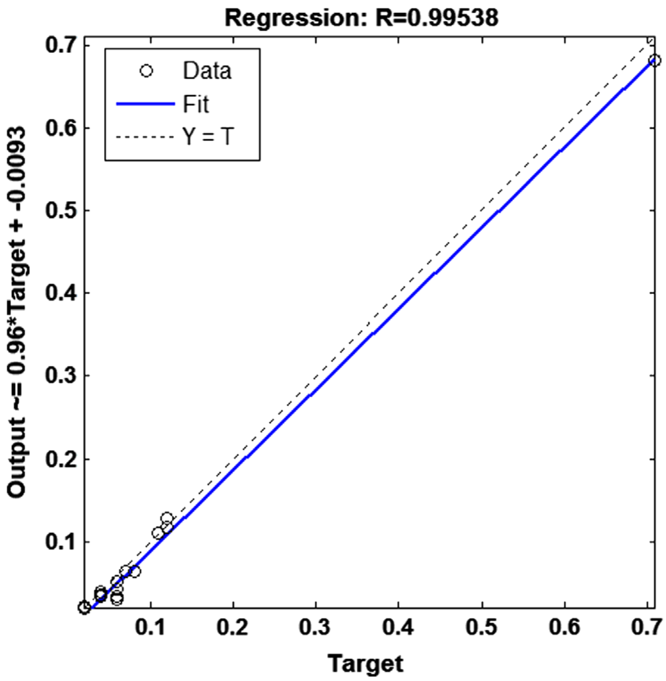

Fig. 19. Regression Plot Fit using Quasi-Newton Method.

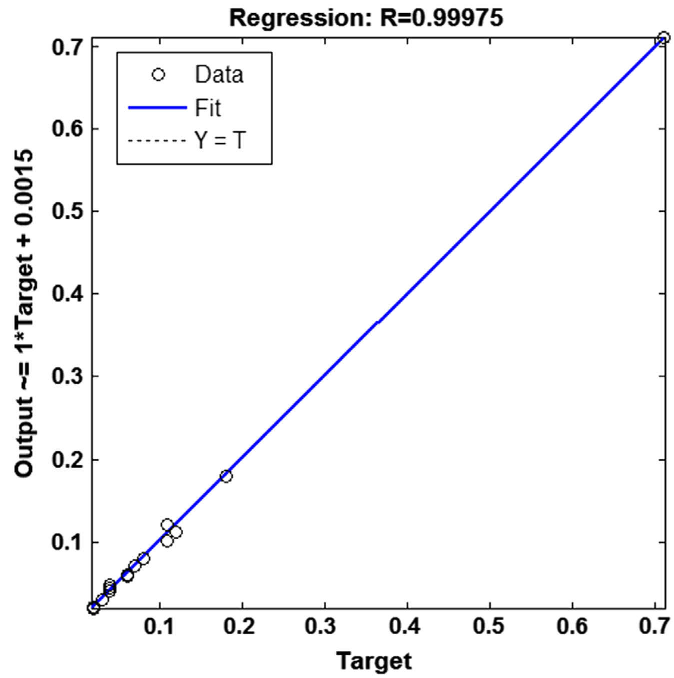

Fig. 21. Regression Plot Fit using Levenberg–Marquardt method.

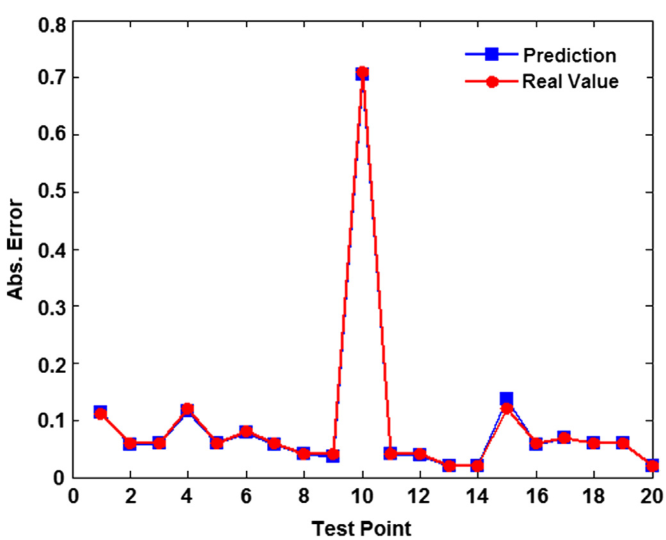

Fig. 20. our predicted error for each sample test point is compared with its real error, the error was predicted using a neural network trained with the Levenberg–Marquardt method.

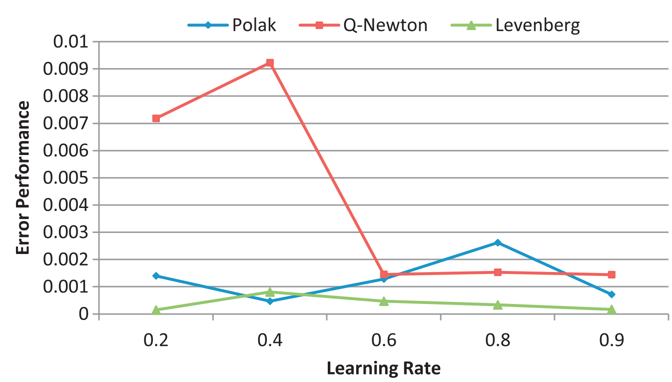

Fig. 22. Comparing the error performance of the 3 methods at different learning rates.

The precision of the scanners, specially the medical scanners is a highly important task; therefore having the capability to adjust the scanner measurements by a mathematical algorithm gives us a simple solution to the complex problem of the precision. A Levenberg–Marquardt in conditions of our practical task shows the better performance over other testes methods, as it evident from Figs. 16–22. It was applied to resolution improvement in our rotational 3D body shape scanner.

8. Energetic center search on the reflected laser spot

The next serious option to improve our scanner resolution is the use of next concept. The problem has been combated raises from the fact, that the reflected spot presented on Fig. 11 is not of regular circle shape. It represents a strictly irregular shape approximately close to circle, what in its turn causes the registered electric stop-signal of irregular form also. The typical stop-signal are shown on Fig. 23, is a Gaussian shaped signal with some noise and deformations.

This circumstance is an inevitable source of methodical uncertainty for most of known laser scanners, except ours. In our experimental prototype is applied special theoretical method, first introduced in [28]. It consider that we are operating not with real signal spot, but with its geometrical shape center. As in our theoretical method is in use the transform of lignt signals into proportional electric signals, so, for the proportional electric signals (of Fig. 23) the geometrical area below the signal curve will have the meaning of the electrical energy of this signal. Hence, this method get the name of Energetic center search.

Its geometrical representation is shown on Fig. 24.

This search can be performed by simple application of the differentiator circuit (Fig. 24b), and after differentiation we are practically working with really point, – not spatially distributed, – source of light signal. The detailed construction of this circuit is given in our group previous publication [28, p. 117].

In this case the important note is that in our medical scanning application the use of the Energetic center search method still permits up to 12–35% resolution increase, depending on the

Please cite this article as: Rodríguez-Quiñonez JC, et al. Optical monitoring of scoliosis by 3D medical laser scanner. Opt Laser Eng (2013), http://dx.doi.org/10.1016/j.optlaseng.2013.07.026

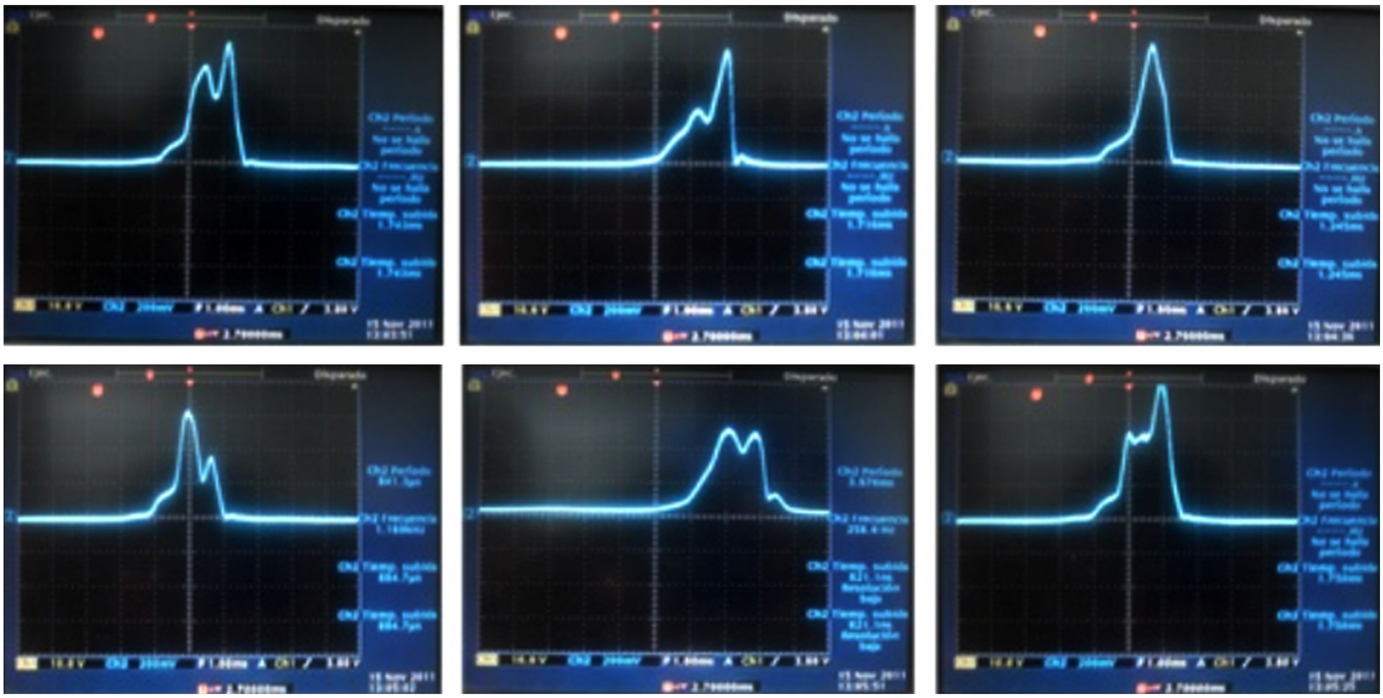

Fig. 23. Gaussian shaped stop-signal with some noise and deformations.

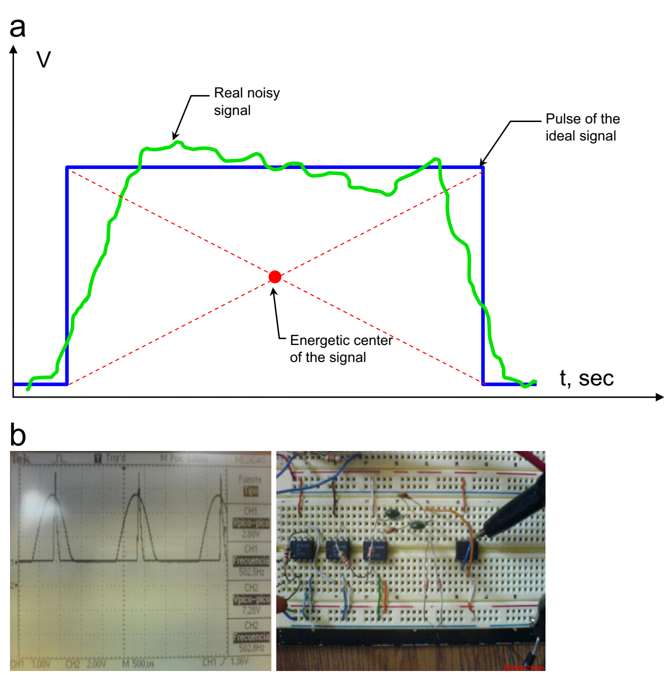

Fig. 24. Method of the signal energetic center search: (a) general purpose; (b) differentiator circuit functioning screenshot and protoboard general view.

particular shape of laser spot deformation (of Fig. 23), which is difficult to analyze or predict in any deterministic model.

9. Conclusion

In this paper, we have pointed out the advantages of 3D Rotational Body Scanner over other recently known problem solutions. It is shown that our system offers the most direct problem solution in the shape of a coordinate's measurements matrix, providing the metrological quality digital mapping of the unknown biological surface with beforehand set uncertainty. This scanner gives an additional option of adjustable resolution for any specific area/location of interest. It is shown that the matters of interaction laser-human skin are dealt with special requirements on this application. We also demonstrate the robustness of our system via experimentation, by performing accurate measurements independent of tone or pigmentation of the skin. Since the laser reflectance area measurements are well defined by overshadowing the effect of the ambient illumination which the subject may be exposed at the time of laser scanning. Coordinates measurement uncertainty satisfies the medical requirements in this case also. Some of the main advantages of our scanner over others are due to its novel construction, original dynamic triangulation scheme, it is very compact with dimensions of $3.5'\mathrm{L} \times 0.4'\mathrm{W} \times 0.8'\mathrm{H}$ compared with Vitus smart [8], ($4' \times 4' \times 10'$). Our system requires around 140 times less volume than system mentioned in [8], and does not need many indoor space for its proper functioning. One of our scanner advantages is the following. It is able to change its rotation velocity in a certain range, and as shown in our previous experimentations [30], p. 4887; [36], p. 5486–5490; [43], p. 424–425, as various scanning velocities some characteristic parameters of the scanner functioning are changing. However, it does not affect measuring uncertainty in experimentation with static objects, and in general behavior it is congruent with the data of our Table 4. In other words, our scanner shows the same uncertainty rate at different scanning velocities. This fact allow us to conclude that our scanner velocity can be adjusted carefully to the medical scanning task requirements in order to optimize the reliability of the system to patient's body own movements; and it can be considered like additional physical method for internal noise filtration. This system is a good example of modern mechatronic design, due to the fact that new advantages in 3D coordinates measurement are reached due to well balanced control of DC and stepper motors, as well as experimentally optimized functioning parameters of the system elements in interaction with practical application of dynamic triangulation theoretical method. Our 3D Rotational Body & Medical Laser Scanner is non antagonistic to other traditional

Please cite this article as: Rodríguez-Quiñonez JC, et al. Optical monitoring of scoliosis by 3D medical laser scanner. Opt Laser Eng (2013), http://dx.doi.org/10.1016/j.optlaseng.2013.07.026

tools in orthopedic treatment. Plain X-rays are cheap, easy to use and available quite easily everywhere. But it is not possible to use X-rays every day, so our offered system can be a good complement for the medical practitioner in a long-term frequent observation of the treatment development. Inquiries on the interaction of laser beams with the different types of human skin in a wider group of aspects (age variations, gender influence and presence of skin diseases) and the optimal scanning velocity selection (aiming the natural filtration of the spontaneous body movements) are the aim for future work.

Finally, we can mention that as the medical scanning [22] is not so time-restricted task, as the robot vision application for example [29–31], so our scanner prototype can operate on reduced velocities, and it provide available the application of the original theoretical method of the search of perfect coincidences between two arbitrary trains of electrical pulses, presented in our group previous publications [45–47]. The practical application of this method in the task of medical scanning is under consideration for our future work.

References

[1] Treleaven B, Wells J. 3D Body scanning and healthcare applications. Computer 2007;40(7):28–34.
[2] Kołodziej A, Baranowski W, Kusior E, Kanak J. X-ray, AFM, UV–VIS–IR analysis of a-Si:H/μc-Si:H supperlattice structure. Opt Appl 2011;XLI(2):449–54.
[3] Zhang Qican, Su Xianyu, Xiang Liqun, Sun Xuezhen. 3-D Shape measurement based on complementary Gray-code light. Opt Lasers Eng 2012;50(4):574–9.
[4] Masaya Akihiro, Fujigaki Motoharu, Matsumoto Shingo, Morimoto Yoshiharu. Shape measurement for BGA using whole-space tabulation method with FPGA memory board. Opt Lasers Eng 2012;50(4):580–5.
[5] Pan Bing, Dafang Wu, Yong Xia. Incremental calculation for large deformation measurement using reliability-guided digital image correlation. Opt Lasers Eng 2012;50(4):586–92.
[6] Fennander H, Kyrki V, Fellman A, Salminen A, Kalviainen H. Visual measurement and tracking in laser hybrid welding. Mach Vis Appl 2009;20:103–18.
[7] Mao J, Hu L, Hua D, Gao F, Wu M. Pure rotational Raman lidar with fiber Bragg grating for temperature profiling of the atmospheric boundary layer. Opt Appl 2008;XXXVIII(4):715–26.
[8] Dai, JS., Editorial: surgical robotics and its development and progress, Special issue on surgical robotics, System development, application study and performance analysis, Robotica, 28 Special Issue (2): 1-1, 2010.
[9] Stjepan, Jecić; Nenad, Drvar. The assessment of structured light and laser scanning methods in 3D shape measurement. In: Fourth international congress of Croatian society of mechanics, September, 18–20; 2003. Bizovac, Croatia.
[10] Zhang S, Peisen SH. Novel method for structured light system calibration,. Opt Eng 2006;45(8).
[11] Salvi J, Fernandez S, Pribanic T, Llado X. A state of the art in structured light patterns for surface profilometry. Pattern Recognit. 2010;43(8):2666–80.
[12] Zhang S. Recent progresses on real-time 3D shape measurement using digital fringe projection techniques. Opt Lasers Eng 2010;48(2):149–58.
[13] Xianyu S, Zhang Qican. Dynamic 3-D shape measurement method: a review,. Opt Lasers Eng 2010;48(2):191–204.
[14] Glinkowski W, Sitnik R, Witkowski M, Kocoń H, Bolewicki P, Górecki A. The method of pectus excavatum measurement based on structured light technique. J Biomed Opt 2009;14(4):044041-1–8.
[15] Lerch T, MacGillivary M, Domina T. 3D Laser Scanning: a Model of multidisciplinary research. J Text Apparel, Technol Manage1533-0915 2007;5 (4):1–21.
[16] Di W, Naiguang L. A pre-processing method for the fringe image in phase measuring profilometry. Proc SPIE0277-786X 2008;6623(66231A):1–8.
[17] Illés Tamás, Tunyogi-Csapó Miklós, Somoskeöy Szabolcs. Breakthrough in three-dimensional scoliosis diagnosis: significance of horizontal plane view and vertebra vectors. Eur Spine J1432-0932 2010.
[18] A Saleeva, S Serikov, V Kacher, O Sergiyenko, MA.Reyna Carranza Experimental research with electronic tools used for an estimation of prosthetics results – report of the international conference "PAHCE2006 – Pan American Health Care Engineering, 30 January to 3 February 2006, PAHO-IEEE, Long-Beach – Los-Angeles, California, USA, 1P. ISBN: 970-94677-0-0.
[19] Dubousset J. Three-dimensional analysis of the scoliotic deformity. In: Weinstein SL, editor. The pediatric spine: principles and practice. New York: Raven Press Ltd.; 1994. p. 479–96.
[20] Vrtovec T, Pernus F, Likar B. A review of methods for quantitative evaluation of axial vertebral rotation. Eur Spine J 2009;18:1079–90.
[21] Omeroglu H, Ozekin O, Bicimoglu A. Measurement of vertebral rotation in idiopathic scoliosis using the Perdriolle torsiometer: a clinical study on intraobserver and interobserver error. Eur Spine J 1996;5:167–71.
[22] 〈http:/health.nytimes.com/health/guides/disease/scoliosis/diagnosis.html〉.
[23] Li Zhizhong, Chang Chien-Chi, Dempsey Patrick G, Cai Xiuwen. Refraction effect analysis of using a hand-held laser scanner with glass support for 3D anthropometric measurement of the hand: a theoretical study. Measurement 2008;41(8):842–50.
[24] Fu Guoqiang, Corradi P, Menciassi A, Dario P. An integrated triangulation laser scanner for obstacle detection of miniature mobile robots in indoor environment. IEEE/ASME Trans Mechatron 2010;16(4):778–83.
[25] LC Basaca, JC Rodriguez, O Sergiyenko, V Tyrsa, W Hernandez, JI Hipolito Nieto et al., 3D Laser scanning vision system for autonomous robot navigation. In: Proceedings of IEEE (ISIE 2010), Bari, Italy; 2010.
[26] LC Basaca, J Rodriguez, OY Sergiyenko, VV Tyrsa, W Hernandez, JI Nieto Hipolito et al., Resolution improvement of dynamic triangulation method for 3D vision system in robot navigation task. In: IECON, Glendale; 2010.
[27] Edelsbrunner H, Cheng Ho-Lun, Dey TK, Sullivan J. Dynamic skin triangulation numerical mathematics, discrete & computational geometry, 25. Springer Verlag New York Inc.; 528–68.
[28] López Moisés Rivas, Sergiyenko Oleg, Tyrsa Vera, Perdomo Wilmar Hernandez, Balbuena Daniel Hernández, Cruz Luis Devia, et al. Optoelectronic method for structural health monitoring. International Journal of Structural Health Monitoring 2010;9(2):105–20.
[29] Moisés Rivas, Oleg Sergiyenko, Mario Aguirre, Luis Devia, Vera Tyrsa Ismael Rendón.. Spatial data acquisition by laser scanning for robot or SHM task. In: IEEE-IES Proceedings international symposium on industrial electronics (ISIE 2008), Cambridge, UK, June–July; 2008. p. 1458–1463.
[30] Oleg Y Sergiyenko, Vera V Tyrsa, et al. Dynamic laser scanning method for mobile robot navigation. In: Proceedings of ICCAS-SICE 2009, ICROS-SICE international joint conference, Fukuoka, Japan, August 18–21; 2009. p. 4884–4889, ISBN: 978-4-907764-33-3.
[31] Sergiyenko Oleg, et al. Precise Optical Scanning for special multiplications. In: Proceedings of IEEE 34th annual IEEE conference IECON 08, Florida, USA; 2008. p. 1656–1661.
[32] Serway Raymond A. Physics for scientists and engineers with modern physics, 2. Saunders College; 9780030226571.
[33] Rivas Lopez M, Sergiyenko O, Tyrsa V. Machine vision: approaches and limitations. In: Zhihui Xiong, editor. Computer vision. Vienna, Austria: Editorial: IN-TECH; 2008. p. 395–428.
[34] Bashkatov AN, Genina EA, Kochubey VI, Tuchin VV. Optical properties of human skin, subcutaneous and mucous tissues in the wavelength range from 400 to 2000 nm. J Phys D: Appl Phys 2005;38:2543–55.
[35] Young AR. Chromophores in human skin. Phys Med Biol 1997;42:789–802.
[36] Jacques SL, McAuliffe DJ. The melanosome: threshold temperature for explosive vaporization and internal absorption coefficient during pulsed laser irradiation. Photochem Photobiol 1991;53:769–75.
[37] Claridge E, Hidovic- Rowe D, Taniere P, Ismail T. Quantifying mucosal blood volume fraction from multispectral images of the colon. Proc SPIE 2007;6511:17–22.
[38] Yip R. Significance of an abnormally low or high hemoglobin concentration during pregnancy: special consideration of iron nutrition. Am J Clin Nutr 2000;72:272S–79SS.
[39] Ansari MA, Massudi. R. Study of light propagation in Asian and Caucasian skins by means of the Boundary Element Method. Opt Lasers Eng 2009;47 (9):965–70.
[40] Shimada M, Yamada Y, Itoh M, Yatagai T. Melanin and blood concentration in a human skin model studied by multiple regression analysis: assessment by Monte Carlo simulation. Phys Med Biol 2001;46:2397–406.
[41] 〈http:/omlc.ogi.edu/news/jan98/skinoptics.html〉.
[42] Sergiyenko O, Hernandez W, Tyrsa V, Devia Cruz L, Starostenko O, Pena-Cabrera M. Remote sensor for spatial measurements by using optical scanning. Sensors 2009;9(7):5477–92.
[43] OYu Sergiyenko. Optoelectronic system for mobile robot navigation. Springer/ Allerton Press, Inc., Optoelectronics, instrumentation and data processing, 46, 5, October, 2010, 414-428–8756428–8756-6990.
[44] Rodriguez-Quinonez Julio C, Sergiyenko Oleg, González-Navarro Felix F, Basaca-Preciado Luis, Tyrsa Vera. Surface recognition improvement in 3D medical laser scanner using Levenberg–Marquardt method. Signal Process0165-1684 2013;93(2):378–86.
[45] Balbuena Daniel Hernández, Sergiyenko Oleg, Tyrsa Vera, Burtseva Larysa, López Moisés Rivas. Signal frequency measurement by rational approximations. Measurement0263-2241 2009;42(1):136–44, http://dx.doi.org/10.1016/j.measurement.2008.04.009.
[46] Sergiyenko O, Hernandez Balbuena D, Tyrsa V, Rosas Méndez PLA, Rivas Lopez M, Hernandez W, et al. Analysis of jitter influence in fast frequency measurements. Measurement0263-2241 2011;44(7):1229–42, http://dx.doi.org/10.1016/j.measurement.2011.04.001.
[47] Sergiyenko OY, Hernandez Balbuena D, Tyrsa VV, Rosas Mendez PLA, Hernandez W, Nieto Hipolito JI, et al. Automotive FDS resolution improvement by using the principle of rational approximation. IEEE Sens J1530-437X 2012;12 (5):1112–21 (May).

Please cite this article as: Rodríguez-Quiñonez JC, et al. Optical monitoring of scoliosis by 3D medical laser scanner. Opt Laser Eng (2013), http://dx.doi.org/10.1016/j.optlaseng.2013.07.026

Optics and Lasers in Engineering ∎ (∎∎∎∎) ∎∎∎–∎∎∎

Contents lists available at ScienceDirect

Optics and Lasers in Engineering

journal homepage: www.elsevier.com/locate/optlaseng

Optimization of 3D laser scanning speed by use of combined variable step

X.M. Garcia-Cruz [a,c], O.Yu. Sergiyenko [a,*], Vera Tyrsa [b], M. Rivas-Lopez [a], D. Hernandez-Balbuena [a], J.C. Rodriguez-Quiñonez [a], L.C. Basaca-Preciado [a], P. Mercorelli [d]

[a] Laboratory of Optoelectronics and Automatic Measurements, Engineering Institute and Faculty of Universidad Autónoma de Baja California, Blvd. Benito Juárez y Calle de la Normal S/N, Col. Insurgentes Este, 21280 Mexicali, Baja California, Mexico

[b] Automation Department of Kharkov National Automobile and Highway University, Petrovskiy-street 25, Kharkov, Ukraine

[c] Mechanical Laboratory, Instituto Tecnológico de Mexicali, Tecnológico Ave., S/N, Col. Elias Calles, 21396 Mexicali, Baja California, Mexico

[d] Institute of Product and Process Innovation, Leuphana University of Lueneburg, Germany

ARTICLE INFO

Article history:
Received 14 April 2013
Received in revised form
1 August 2013
Accepted 12 August 2013

Keywords:
Technical vision system
Dynamic Triangulation
Scene
Scanning step
Neural Network

ABSTRACT

The problem of 3D TVS slow functioning caused by constant small scanning step becomes its solution in the presented research. It can be achieved by combined scanning step application for the fast search of n obstacles in unknown surroundings. Such a problem is of keynote importance in automatic robot navigation. To maintain a reasonable speed robots must detect dangerous obstacles as soon as possible, but all known scanners able to measure distances with sufficient accuracy are unable to do it in real time. So, the related technical task of the scanning with variable speed and precise digital mapping only for selected spatial sectors is under consideration. A wide range of simulations in MATLAB 7.12.0 of several variants of hypothetic scenes with variable n obstacles in each scene (including variation of shapes and sizes) and scanning with incremented angle value (0.6° up to 15°) is provided. The aim of such simulation was to detect which angular values of interval still permit getting the maximal information about obstacles without undesired time losses. Three of such local maximums were obtained in simulations and then rectified by application of neuronal network formalism (Levenberg–Marquradt Algorithm). The obtained results in its turn were applied to MET (Micro-Electro-mechanical Transmission) design for practical realization of variable combined step scanning on an experimental prototype of our previously known laser scanner.

1. Introduction

The task of 3D-coordinates spatial data acquisition is an important task for many practical applications, such as structural health and integrity monitoring, robot vision, micro-relief inspection, biometrics, shape recognition in security applications, physical monitoring of internal structures in complete darkness (mines, caves, underground pipelines), etc. Optical scanning, especially laser based scanning, is a very attractive approach to this solution due to its advantages over other recognized solutions. Laser scanning has direct information acquisition, relatively small quantity of data to be processed, high coherence of laser bandwidth to help noise filtering in optic channel, predictable accuracy with well-studied uncertainty distribution laws, ability to work in complete darkness (even works better this way), etc. But the most attractive advantage is fast growth in the last decade of optical sensors reliability and data stability. Nowadays, there has been a clear trend for the contactless sensors based on optical technologies [1]. Contactless can quickly acquire a large number of points (about 10,000 points per second). However, laser sensors currently on the market do not have the accuracy of the classical dynamic contact sensors. In general, the accuracy provided by the manufacturer of these devices presents a factor of 10 compared to the contact sensors. For example, with the sensor METRIS LC50 used in [1], the expanded measurement uncertainty of a sphere with 15 mm diameter is in the order of 50 μm$+/-3\sigma$. Furthermore, this accuracy depends on different parameters such as materials properties, surface texture, product color, etc. Therefore, in order to use this technique in the context, it is necessary to have a good control of their metrological properties. In recent years various optical methodologies [2] have been implemented in tracking general-purpose systems. Although, optical tracking systems have been used in several contexts, its application to align 3D point clouds generated by full field techniques has been poorly evidenced in technical literature. Moreover, some commercial solutions have been proposed (naviSCAN^{3D}, Leica T-Scan, MetraSCAN [2], and Vitus Smart 3D Laser Scanning [22]). Neither technical literature nor commercial

* Corresponding author. Tel.: +52 6861687170.
E-mail address: srgnk@mail.ru (O.Yu. Sergiyenko).

0143-8166/$ - see front matter © 2013 Elsevier Ltd. All rights reserved.
http://dx.doi.org/10.1016/j.optlaseng.2013.08.011

solutions fully provide scientific and technical evidences about performances, reliability and applicative fields of the optical tracking approaches. For example, industrial applications may involve the reconstruction of complex shapes by aligning several 3D views captured on the basis of a scanning strategy that should be settled during the measurement process [20]. In these cases, robustness and flexibility are the fundamental attributes of a multi-view methodology, but for example in robot navigation or any other dynamic application there is no way for its practical use. In [3] two-dimensional x–y laser scanning was demonstrated using a computer controlled and rotating reflective cube. This particular application was the digitizing of transparent foils and they achieved milliradian resolutions. This concept may be easily adapted to other industrial vision applications such as scanning products on an assembly line or two-dimensional extensions of bar codes. The reflective cube method described in [3] is less expensive, simpler and more durable than other techniques such as use of planar mirrors mounted on galvanometer rotors, as shown in [3] in 1992. Due to the same reason now we will not explain the lack of galvanometer rotors, but will advance the simple/durable optic scanning method (more or less based on the same idea as in [3]) which is able to give still more open angle-of-view than those of any other known techniques, except the omnidirectional vision (fish-eye lens) [16]. However, fish-eye lens gives very curvy and distorted image, which needs a time consuming post-processing. Application depth map by an efficient epipolar plane analysis method [17,18] was analyzed in [19] for omnidirectional stereo vision [15]; meanwhile our solution is able to find and digitize objects in real time, without any post-processing. Why it is important?

For robot application in an environment where many obstacles exist [4], it needs to avoid obstacles and detect gateways in order to select a valid pathway to traverse in the shortest time possible. Avoiding obstacles according to their shape will demand a lot of environment knowledge, so this method will demand high computational power. The laser scanner developed in [4] does not provide 3D shape information of the detected obstacles because of the absence of enough computational power for 3D shape reconstruction. The avoidance strategy proposed in [4] is to avoid obstacles regardless of their shape; in other words, the height information of the obstacle and the width information of the gateway are key parameters for making a judgment. For a single image, it takes 0.2 s to detect the obstacles in front of the scanner. Therefore, as the scanner scans obstacles at 10 different bending angles, it takes 2 s to scan fully. Because the scanning speed is not fast enough to deal with moving objects, currently the developed laser scanner cannot work in a changing environment; in other words, the detected obstacles must be stationary. A good review of 3D model acquisition techniques can be found in [13,14]. The main features of the proposed 3D laser scanning system in this paper compared with other kinds of 3D sensing systems for mobile robots are as follows:

compared with passive binocular or trinocular vision sensors, the proposed laser scanner can maintain more robust 3D sensing under illumination variations;

compared with time-of-flight or phase shifting laser scanners, the proposed laser scanner has less power consumption, and is cheaper;

compared with the multi-line pattern projector in a structured-lighting scanner, the proposed laser scanner has a more simple and robust mechanical construction, and reduced power consumption.

This paper addresses the design and implementation of an active 3D triangulation laser scanner. The contribution of this paper and the scientific field of the proposed system are in using a low-cost and simple method to construct a laser and wide-angle sensor system which is used for navigation of mobile robots in unknown environments [5]. The most crucial point in this case is time of scanning. In other words, the obstacle must be detected in the shortest possible time interval, but precise coordinate measurements are not necessary for all obstacle shapes, but only for its edge nearest to the robot's desired safe trajectory (see [5,7,10]). It is evident that this is possible only under the condition that the laser can scan robot's field-of-view with variable speed. In this study, we concentrate on modeling several scenes with regular obstacles, establishing a simulation tool for the analysis to find the best angles (optimal angles) for combined-step scanning, and designing stepper-motors in laser positioning system, as well as development and demonstration of an automated micro-gearbox for such tasks.

This paper is organized as follows. In Section 2 the problem formulation of slow functioning of 3D TVS caused by constant small scanning step is presented. The solution by application of combined scanning step consisting of several specific values is introduced in Section 3. The simulation of variable scanning step and data post-processing techniques are presented in Section 4. Design of Micro-Electro-mechanical Transmission for steps combination performance is proposed in Section 5. Finally, conclusions and prospects for future work are reported in Section 6.

2. Problem formulation

According to our previous research [5–12], the TVS allows us an insight into spatial coordinates measurements, with sufficient accuracy in the field of view; it also has the ability to detect obstacles inside any given scene during navigation of the autonomous robot. It can make a digital map of the obstacles within the field of view in high resolution. The current TVS uses constant scanning pitch which is not optimally efficient for robot navigation. The goal of a reliable navigation in exploration of unknown scenes is the scanning variable (combined) scanning step, which will minimize scanning time, with guaranteed detection of critical obstacles within the field of view. It must detect any obstacle as soon as possible, but having a high resolution only of the most critical obstacles (dangerous for the robot safety). It is intended that the simulations performed in the present work must answer this question by our simulation results. Based on these results, we can provide a tentative construction of electromechanical transmission. Its application can optimize the TVS function by the minimum time criterion under the condition of maintaining the maximal resolution on the nearest edge of scanned objects.

For a better understanding of the problem we have to present here the basic principle of Dynamic Triangulation and corresponding laser scanning system forming jointly with passive aperture the completed 3D Technical Vision System (TVS), firstly introduced in our previous publications [5–12], and which is the object of further development and complication in the present paper. TVS works on Dynamic Triangulation theory in order to obtain 3D coordinates of objects or obstacles on mobile robot vision; as shown in Fig. 1 [7], a laser beam is projected by a mechanism transmitter (which will be called Positioning Laser (PL)) onto the obstacle surface, reflecting back the laser beam into a revolving sensor inside, which will be called Scanning Aperture (SA) [21].

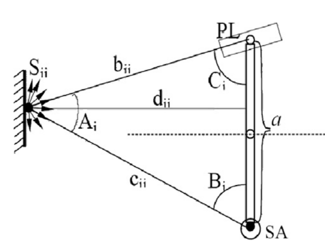

Fig. 1. Dynamic Triangulation [7].

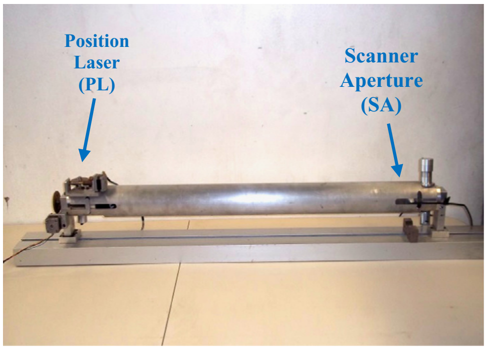

Fig. 2. Side view prototype.

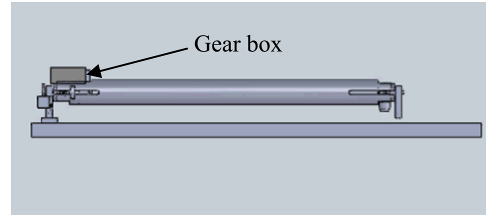

Fig. 3. TVS with the gear box proposal.

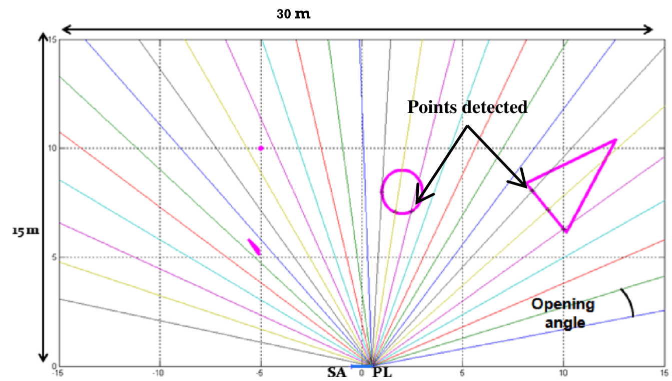

Fig. 4. Scene.

Velocity has been optimized in comparison to [7,10], where the scanner velocity is lower.

The system has Positioning Laser (PL) and Scanning Aperture (SA), and the method is Dynamic Triangulation due to the fact that the Positioning Laser has the ability to rotate and redirect the laser beam by 180° theoretically and (SA) rotates 360° at a constant speed, meaning that the TVS has two dynamic angles [10]; with this system it is possible to obtain any point in front of the mobile robot as seen in Fig. 2. PL and SA are communicated for a hollow shaft; PL has a mechanism to control the laser.

In order to calculate any coordinate in Cartesian plane, sine laws on Dynamic Triangulation was used and the obtained results are the following equations [9]:

$$x_{ij} = a\frac{\sin B_{ij}\,\sin C_{ij}\,\cos\sum_{j=1}^{j}\beta_j}{\sin\,[180^\circ - (B_{ij}+C_{ij})]} \tag{1}$$

$$y_{ij} = a\left(\frac{1}{2} - \frac{\sin B_{ij}\,\cos C_{ij}}{\sin\,[180^\circ - (B_{ij}+C_{ij})]}\right), \quad \text{for } B_{ij} \le 90^\circ \tag{2}$$

$$y_{ij} = -a\left(\frac{1}{2} + \frac{\sin B_{ij}\,\cos C_{ij}}{\sin\left[180^\circ - (B_{ij}+C_{ij})\right]}\right), \quad \text{for } B_{ij} \ge 90^\circ \tag{3}$$

$$z_{ij} = a\frac{\sin B_{ij}\,\sin C_{ij}\,\sin\sum_{j=1}^{j}\beta_j}{\sin\left[180^\circ - (B_{ij}+C_{ij})\right]} \tag{4}$$

3. Problem solution

For the above stated problem a good solution can be the application of Micro-Electromechanical Transmission combined with scanning step and the Laser Ray Positioning System of TVS on the example of robot navigation task. The multicriteria verification of such hypothesis is the main goal of the present research; the problems mentioned in Section 2 can be solved with a MET (Micro-Electromechanical Transmission). This is the most feasible of possible ways in resolution constraints improvement in electromechanical 3D optoelectronic scanners [13]. In our opinion, not all sectors of full field-of-view are of the same importance for detailed analysis. Some of them can be ignored under the simple criterion that robot cannot traverse there. So, it yields the conclusion that these sectors can be scanned roughly in minor time without loss of information for uninterrupted navigation. At the same time those sectors where the edges of the obstacles are located are critically important for the robot as those paths must be scanned with more attention. Our proposition is based on the hypothesis that variation of fixed scanning angle does not give the same losses of information; in other words certain angles exist which permit increasing the scanning velocity (bigger step) but still permitting the same quantity of information about obstacles inside the defined field-of-view. With certain assumptions we decide that the quality of information about obstacles can be reflected by the number of detected 3D points on the obstacle surface. Therefore, simulating the scanning process with different values of fixed scanning step, varying the step value with constant small increments, we can get full information about the relation between resolution and time of scanning. Such a simulation for a statistically representative set on several variants of scenes with variable number, density, size and shape of obstacles was made and firstly introduced in [21] Initial simulation was on an ideal transmission with 31 experiments; those data could not give enough information to design MET; next simulation was 101 experiments to find optimal scanning angles. The TVS uses MET with the purpose of combining different scanning angles to find obstacles during scanning in unknown environments in the fastest possible way and making digital maps of obstacles surface which are inside of field-of-view without losses of resolution and scanning time. Fig. 3 shows the proposed MET (gear box).

In Section 6 discusses the gear box of Fig. 3, based on the recommendation for best gear ratio derived from the results of simulation presented in that section.

3.1. Simulation of variable scanning step

In Fig. 4 we can see the frame which further will be called the scene, and shows the opening angle (angle between two consecutive positions of laser ray during one scanning step). Detected points are the locations where laser ray is reflected to scanning aperture (intersection point of simulated laser ray line with the figure of obstacle), and some figures within the scene are simulations of the possible obstacle shapes and locations (triangles and circles). Assumptions for TVS field-of-view in this simulation: beginning at 10 deg and finish at 170 deg. In Fig. 4 we have PL and SA to relate prototype (see Fig. 2) with the present scene. Linear sizes of scene were simulated: 30 m width and 15 m depth.

For simulated laser ray, which unfortunately due to MATLAB'S nature must have discretization for finite time of calculations, the

Please cite this article as: Garcia-Cruz XM, et al. Optimization of 3D laser scanning speed by use of combined variable step. Opt Laser Eng (2013), http://dx.doi.org/10.1016/j.optlaseng.2013.08.011

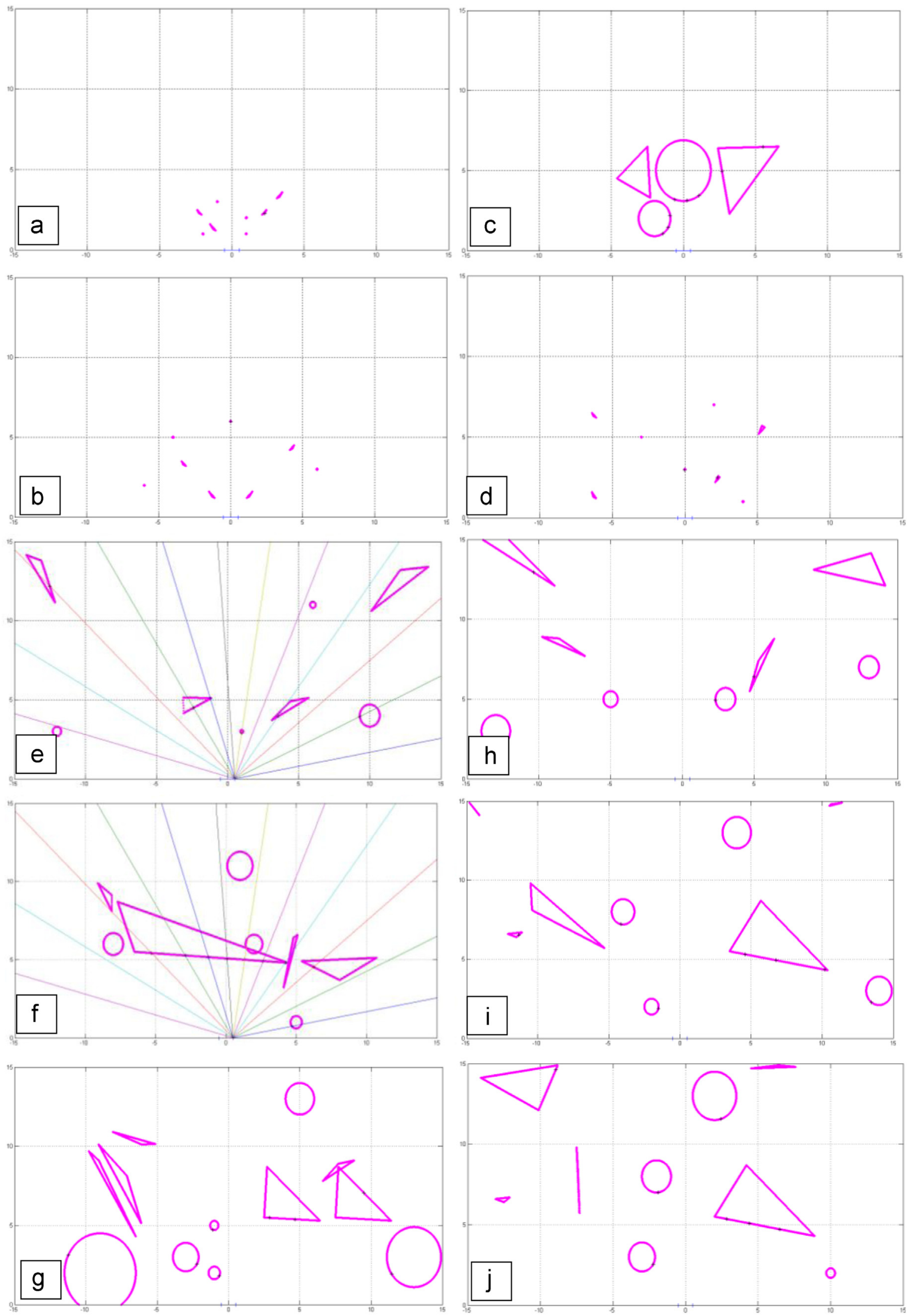

Fig. 5. Frames from simulation on MATLAB.

following model based on Euler's identity was used:

$$Ae^{i\theta}=A\cos\theta+iA\sin\theta \tag{5}$$

where θ is instant value of the opening angle, and A is the simulated length of laser ray (discretized with a radial resolution each 0.002 m up to 10 m).

For simulated obstacles the following equations were used in order to draw a triangle (with consequence: from the shortest side to the second shortest and finally the longest last side):

$$Y_{r1}=\frac{(y_1-y_2)}{(x_1-x_2)}(x-x_1)+y_1 \tag{6}$$

$$Y_{r2}=\frac{(y_2-y_3)}{(x_2-x_3)}(x_2-x_1)+y_2 \tag{7}$$

$$Y_{r3}=\frac{(y_1-y_3)}{(x_1-x_3)}(x_3-x_1)+y_3 \tag{8}$$

where Y_{r1} Y_{r2}, and Y_{r3}, are equations of the lines of triangle, and x_1, x_2, x_3, y_1, y_2, and y_3 are Cartesian coordinates of the triangle vertexes.

For simulated circles arbitrary ratios (r) and center (C), and discretization of the circle (DC) in grades (three times less than discretization of laser ray) were used, using the equations

$$\Delta\alpha=\frac{(DC\pi)}{180^\circ} \tag{9}$$

where $\alpha$are increments of $\Delta\alpha$, $\Delta\alpha$is the increment in the discretization circle obstacle and

$$\text{circle}_n=C+re^{j\alpha} \tag{10}$$

where circle_n is the obstacle drawn for n circles.

3.2. Simulation parameters

Basing on the mathematical formalism introduced above, 101 different scenes were simulated, with the following parameters:

- opening angle (0.6 deg to 15 deg with $\Delta\Theta=0.1455^\circ$ for each step);
- number of obstacles (1–13);
- obstacle position (random);
- obstacle dimensions (random)

In Fig. 5 we can see some scenes that were used in simulation; each scene was scanned with 100 different opening angles and

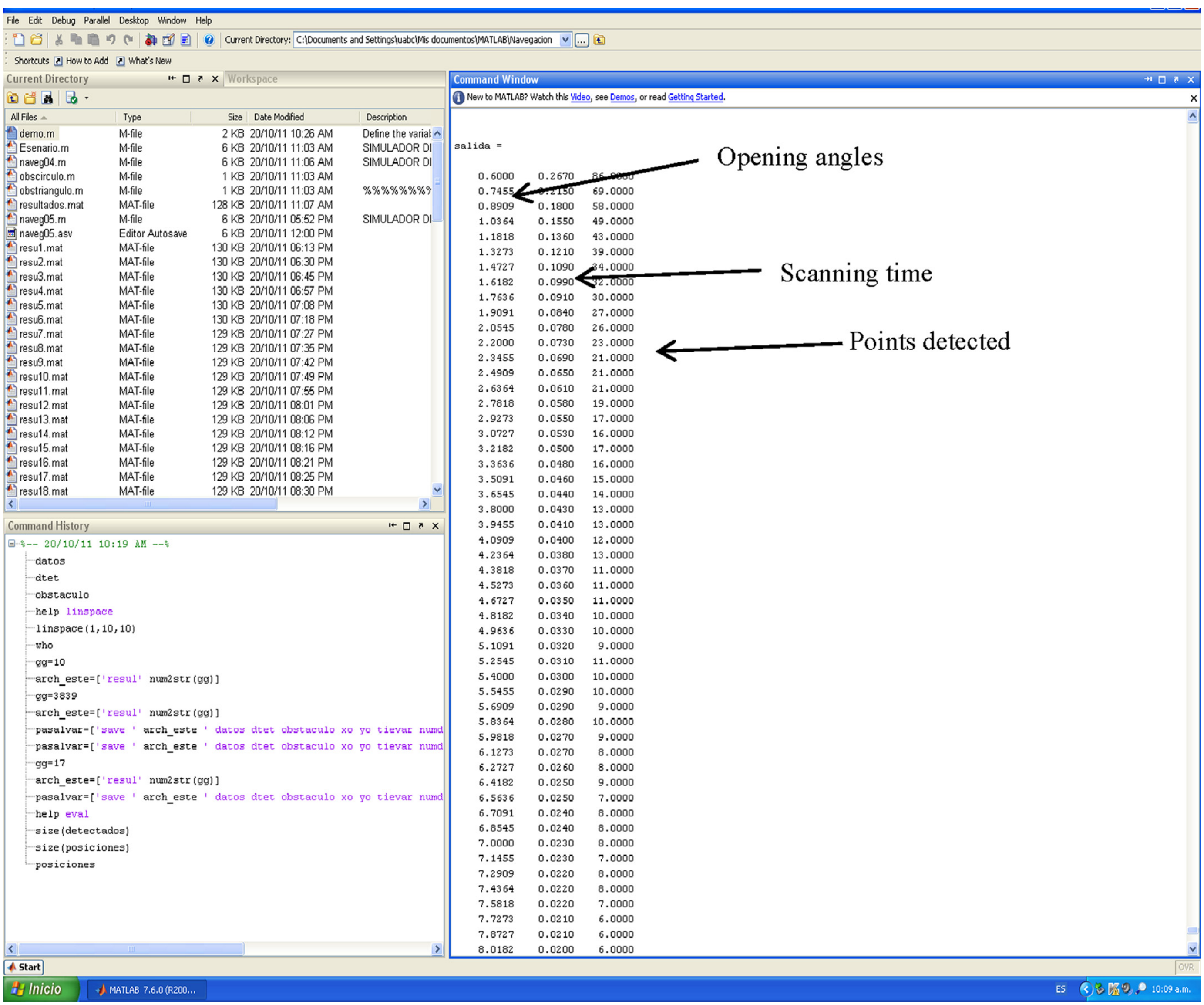

Fig. 6. Frame from simulation out in MATLAB.

varying parameters, thus yielding 10,100 frames to be analyzed; the notes were as follows:

- smaller obstacles and near positioned ones were difficult to detect, needing opening angle around 0.6 to 0.7455, and more points were detected in obstacle contour in a larger time.
- Fig. 5f has a triangle with a wall behavior; in this phenomenon all the angles take more time vs. other frames.
- Fig. 5g uses 12 obstacles; scanning time was long for most of the angles.
- Fig. 5b with 8 obstacles and opening angles 15° and 14.8545° detected one obstacle in a small time.
- If the obstacles are bigger and close together, scanning time is longer for most of the angles.
- High resolution is easier with circles than triangles. This means in practice that sharp-edged obstacles are more dangerous for robots than the smooth ones. But the presented simulation permits us to search for a simple numerical condition to classify the real scene by the number of smooth/sharp obstacles inside. This is one of the most useful advantages of our scanning method.

4. Propose for optimal angles search

A frame of the obstacle search simulation is provided in Fig. 6; the instant value of scanning step angle (see 1st column of the table in Fig. 6) is varied with increment of $\Delta\Theta = 0.1455°$ according to conditions of Section 4.1. For each value of scanning step the following were recorded: (1) the full time necessary for complete scanning of the defined frame (scene—see 2nd column of the table in Fig. 6) and (2) the number of points detected on arbitrarily located obstacle surfaces during one complete cycle of scene scanning (see 3rd column of the table in Fig. 6). Simulation brings statistical information from two different computational experiments with 30 and 101 different step values. The frame from MATLAB in Fig. 6 (first column is opening angle, second column is scanning time and third column is detected points) shows the results of the second one. The first simulation from 30 experiments presented in [21] (see Fig. 7) shows a graph of detected points vs. opening angle. It gives us the generalized behavior of three angles which have local maximums of information about obstacles (detected points) with constantly increasing scanning sped, but this information is not enough to make a final statistically backgrounded decision for design of MET. Hence we provide a second experiment on extended set of data in order to improve statistically significant representative samples for rigorous and safer MET design.

However, the results presented in [21] and in Fig. 7 help us to get a first view of the quantity and tentative values of such step angles for preliminary transmission design.

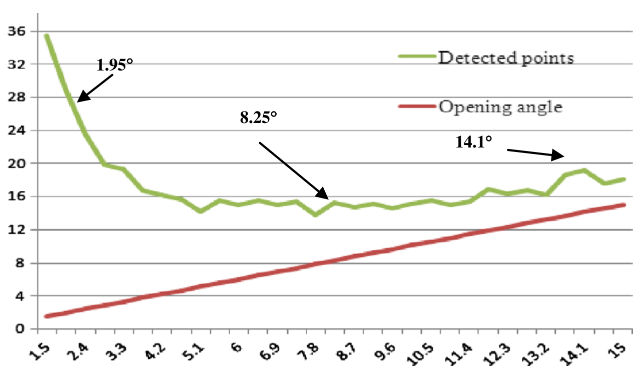

Fig. 7. Detected points vs. opening angles [21].

In the second simulation data were enough to apply some statistical methods (simulation graphic shows detected point vs. opening angles) for comparison having 30 experiments and 101 experiment (Figs. 7 and 8, respectively) and comparison between differences and made decisions. Fig. 8 shows the updated values of optimized scanning angles; with smaller angular increment of scanning step during simulation the number of simulated obstacles in scene increases from 5–9 (Fig. 7) up to 1–13 (Fig. 8) and laser length was 15 m (Fig. 7) up to 25–30 m (Fig. 8); the simulated obstacles have fixed positions in Fig. 7 vs. floated position of obstacles in simulation results of Fig. 8.

We analyzed every scene using a parameter Z that is called advance (the joint quantity of all detected points on surfaces of all

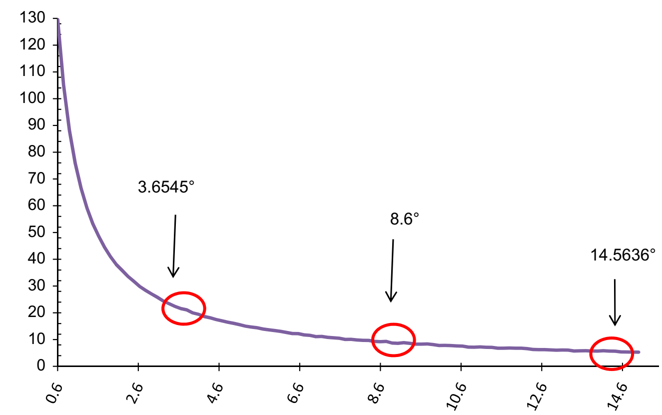

Fig. 8. Detected points vs. opening angles from 101 simulation scenes.

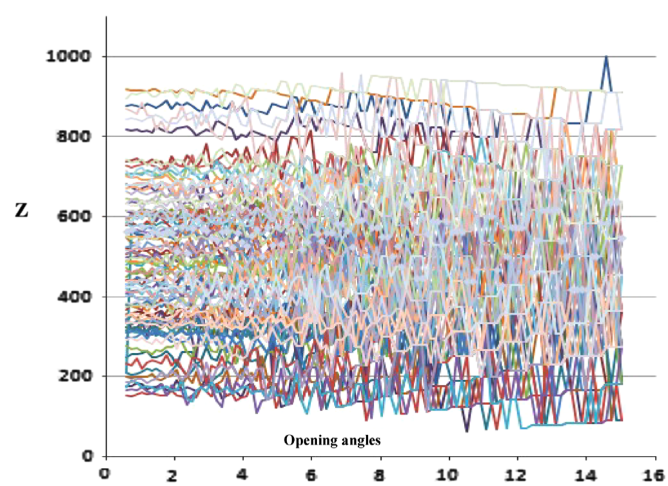

Fig. 9. Z vs. opening angles.

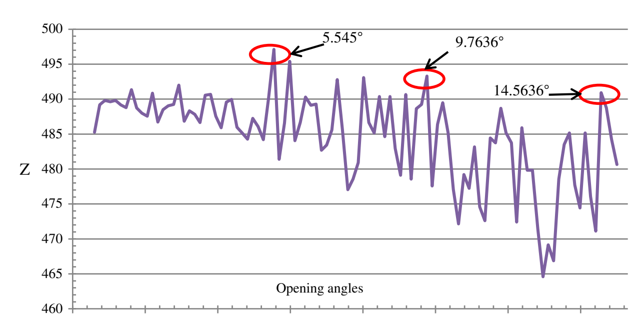

Fig. 10. Z vs. opening angles.

Please cite this article as: Garcia-Cruz XM, et al. Optimization of 3D laser scanning speed by use of combined variable step. Opt Laser Eng (2013), http://dx.doi.org/10.1016/j.optlaseng.2013.08.011

obstacles inside the scene) was and calculated as

$$Z \equiv P/t \qquad (11)$$

where P is the number of points detected on obstacles and t is the scanning time in seconds.

In Fig. 9 we can see "Z" for each scene of all simulations. This cannot be analyzed easily; this is the reason for using a statistical method to analyze all scenes by one graphic.

In Fig. 10 we can find the next optimal angles for maximum and minimum methods; this graph used the "Z" parameter and the hypothesis "Find three optimum aperture angles based on the data obtained from 101 scenes using the method connection means and the detected points vs. time", and the optimum angles are shown in Fig. 10. All obtained information for analyzed graphics is structured in Table 1.

In Table 1, the first row was analyzed with 30 simulations of [21], and in 2–5 the second simulation with 101 frames was used; the information was analyzed basing on different criteria of estimation.

Therefore, from the above considerations and the point of view of scanning velocity optimization we can conclude the following: for all possible values of scanning step there are three values of angle where the scanning velocity grows continuously but the quantity of information about obstacle changes with discrete level. Such angles are angles around 1.8–4° (blue rows of Table 2), 8.2–8.7°and 14–14.6° (green row of Table 2). Such a situation is very convenient for us in this particular task. Practically, it means the following.

The biggest angle (around 14°) permits us to scan the scene the fastest possible way. This is the biggest angle at which according to all provided 10,100 simulations no simulated obstacle was missed. At angles of bigger value already some obstacles were not detected. The next selected angle of 8.6° is appropriated for fastest rough scanning and Table 2 shows analyzed data. Angle around 8.6° seems to be the best candidates for optimal scanning; 8.6° gives 4.42 times faster than 1.9091° but still 1.72 times worse than 14.5636°. But at the same time it is still 2.32 times faster than 3.65454°, but slower 1.11 times that 9.7636°; see Table 2 for comparing angles. So, the scanning with such values of step must be conditionally optimal under constrains "velocity vs. resolution" (see details in Table 2).

The last extreme experimentally obtained value of step angle around 1.8–4° provides the slowest scanning; practically it is applicable only for precise coordinate measurement on the edge of obstacle under highest interest for collision prevention in the task of robot trajectory planning.

However, such a variation of optimal angles value caused by manual data analyses is not acceptable for final MET design. So, the next step is to apply the special mathematical formalism to rectify these angle values. The proper tool in this case in our opinion is the use of digital rectifying analyzers, nonlinear gradient methods for example.

5. Levenberg–Marquardt method

According to the experience of our previous application of this kind of scanner in static biometric monitoring, the use of neuronal network mathematics can be useful for rectifying experimentally obtained data. According to [12] it is not necessary to apply the wide variety of existing methods, because in [12] it is clearly shown that the most proper tool in this case is the Levenberg–Marquardt Algorithm. The primary application of the Levenberg–Marquardt Algorithm (LMA) is in the least squares curve fitting problem: given a set of "m" empirical datum pairs of independent and dependent variables, (x_i, y_i), optimize the parameters β of the model curve $f(x,\beta)$ so that the sum of the squares of the deviations becomes minimal [12,22]:

$$S(\beta) = \sum_{i=1}^{m} [y_i - f(x_i, \beta)]^2 \qquad (12)$$

Like other numeric minimization algorithms, the Levenberg–Marquardt is an iterative procedure. To start a minimization, we provide an initial guess for the parameter vector, β. In each iteration step, the parameter vector, β, is replaced by a new estimate, $\beta+\delta$. To determine δ, the functions $f(x_i, \beta+\delta)$ are approximated by their linearization:

$$f(x_i, \beta+\delta) \approx f(x_i, \beta) + J_{i\delta} \qquad (13)$$

where

$$J_i = \frac{\partial f(x_i, \beta)}{\partial \beta} \qquad (14)$$

is the gradient (row-vector in this case) of "f" with respect to β. At its minimum, the sum of squares, $S(\beta)$, the gradient of S with respect to δ will be zero. The above first-order approximation of $f(x_i, \beta+\delta)$ gives

$$S(\beta+\delta) \approx \sum_{i=1}^{m} [y_i - f(x_i, \beta) - J_i \delta]^2 \qquad (15)$$

Table 1
Obtained angles comparison.

	Review	Opening angle 1 (deg)	Opening angle 2 (deg)	Opening angle 3 (deg)
1	30 (1.5° to 15°, $\Delta\theta$=0.45°), Fig. 7 [21]	1.95	8.25	14.1
2	101 (0.6° to 15°, $\Delta\theta$=0.1455°), detected points vs. opening angles, (Fig. 8)	3.6545	8.6	14.5636
3	101(0.6° to 15°, $\Delta\theta$=0.1455°), Z vs. opening angles (Fig. 10)	5.5455	9.7636	14.5636
4	101 (0.6° to 15°, $\Delta\theta$=0.1455°), analysis according to the largest angle, and shorter time to scan	–	–	14.5636
5	101 (0.6° to 15°, $\Delta\theta$=0.1455°), Analysis according to the highest number of points detected	0.6	–	–

Table 2
Comparison with scanning step angle of 8.6°.

Opening angles (deg)	Detected points	Scanning time (s)	Resolution	Conclusions comparing with 8.6°
1.9091	41	0.084	High	8.6° detecting 32 points less than 1.9091° but was 4.42 times faster
3.6545	21	0.044	High	8.6° detecting 12 points less than 3.65451° but was 2.32 times faster
5.5455	14	0.029	Medium	8.6° detecting 5 points less than 5.5455° but was 1.53 times faster
9.7636	8	0.017	Low	8.6° detecting 1 point more than 9.7636° but was 1.11 times more slow
14.5636	5	0.019	Low	8.6° detecting 4 points more than 14.5636° but was 1.72 times more slow

or in vector notation

$$S(\beta+\delta) \approx ||\boldsymbol{y}-f(\beta)-\boldsymbol{J}\delta||_2 \quad (16)$$

Taking the derivative and setting the result to zero gives

$$(\boldsymbol{J}^T\boldsymbol{J})\delta = \boldsymbol{J}^T[\boldsymbol{y}-\boldsymbol{f}(\beta)] \quad (17)$$

where $\boldsymbol{J}$ is the Jacobian matrix [12,23] whose ith row equals J_i, and where $\boldsymbol{f}$ and $\boldsymbol{y}$ are vectors with ith component $f(x_i,\beta)$ and y_i, respectively. This is a set of linear equations which can be solved for δ.

Marquardt′s contribution [12,24] is to replace this equation by a "damped version"

$$(\boldsymbol{J}^T\boldsymbol{J}+\lambda\boldsymbol{I})\delta = \boldsymbol{J}^T[\boldsymbol{y}-\boldsymbol{f}(\beta)] \quad (18)$$

where $\boldsymbol{I}$ is the identity matrix, giving us the increment, δ, to the estimated parameter vector, $\boldsymbol{\beta}$. The (non-negative) damping factor, λ, is adjusted at each iteration. If reduction of S is rapid, a smaller value can be used, bringing the algorithm closer to the Gauss–Newton algorithm, whereas if iteration gives insufficient reduction in the residual, λ can be increased, giving a step closer to the gradient descent direction. Note that the gradient of S with respect to β is -2 $(\boldsymbol{J}^T[\boldsymbol{y}-\boldsymbol{f}(\beta)]^{\mathbf{T}}$. Therefore, for large values of λ, the step will be taken approximately in the direction of the gradient. If either the length of the calculated step, $\boldsymbol{\delta}$, or the reduction of sum of squares from the latest parameter vector, $\boldsymbol{\beta}+\boldsymbol{\delta}$, falls below predefined limits, iteration stops and the last parameter vector, $\boldsymbol{\beta}$, is considered to be the solution. Levenberg's algorithm has the disadvantage that if the value of damping factor, λ, is large, inverting $\boldsymbol{J}^{\boldsymbol{T}}\boldsymbol{J}+\lambda\boldsymbol{I}$ is not used at all. Marquardt provided the insight that we can scale each component of the gradient according to the curvature so that there is larger movement along the directions where the gradient is smaller. This avoids slow convergence in the direction of small gradient. Therefore, Marquardt [12,24] replaced the identity matrix, $\boldsymbol{I}$, with the diagonal of $\boldsymbol{J}^{\boldsymbol{T}}\boldsymbol{J}$, resulting in the Levenberg–Marquardt algorithm

$$(\boldsymbol{J}^T\boldsymbol{J}+\lambda diag(\boldsymbol{J}^T\boldsymbol{J}))\delta = \boldsymbol{J}^T[\boldsymbol{y}-\boldsymbol{f}(\beta)] \quad (19)$$

5.1. Applications LMA on system results

All information from the simulation was concentrated in a $[3 \times 10{,}100]$ matrix; the data was used for preparing a Neural Network (NN) with the LMA, using the following percentages: the training was 50/100, validation 25/100 (these are used to measure network generalization), and testing 25/100 (when generalization stops improving). NN regression algorithm is effective for next angle prediction; it can verify which predicted values adjust to real values with 2% error (see Fig. 11). The network is adjusted according to the error; this smart software tool already trained is capable of acquiring the constants of the scene components; based on the training it will decide which angle is the best for the next scanning.

When NNs were trained we introduced the information from Table 3 and its predicted angles:The angles predicted by NN (underlined in yellow) can be used in the intelligent control for PL speed change applying proposed design of MET, to aim scanning unknown scenes when the control system knows primarily according to real scene scans the tentative locations of obstacles, and choose the optimal angle from NN training results to get the maximum resolution scans only in small sectors of interest inside all frames of scenes. The proposed MET will be explained below.

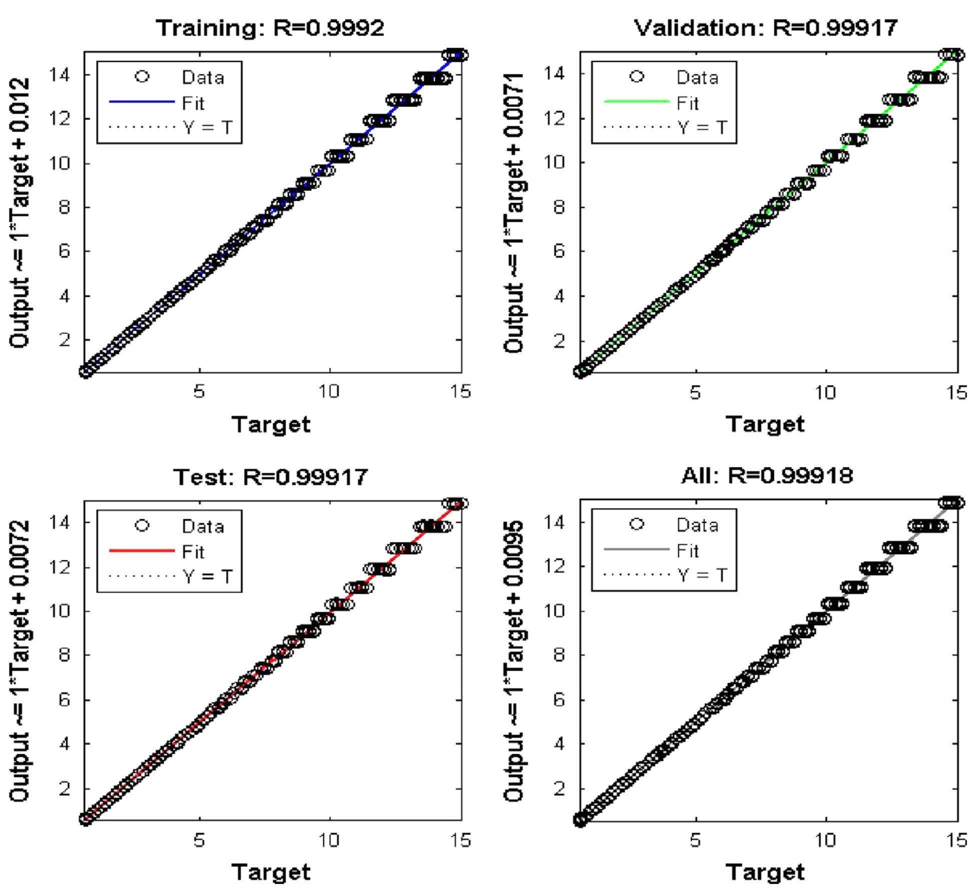

Fig. 11. Training regressions.

6. Micro-Electro-mechanical Transmission (MET)

The proposed MET is aimed to change adequately and in the shortest possible time the value of scanning step angle according to recommendations of Section 4.2. Actually system [10,21] has an anti-backlash gear 48 pitch 0.104̈ face with 20° pressure angle, 96 teeth, P.D 2.0000, gears 303 stainless steel, 2024-T4 Aluminum, and hubs 303 stainless steel; the worm wheel has 48 pitch 20° pressure angle and right hand double thread, and is it made of bronze ASTM B21 alloy 464 material; the gear and worm wheel were manufactured by PIC DESIGN. In Fig. 5 we can see a top view of the system and a 12 VDC bipolar stepper motor with step angle 1.8°, holding torque 2100 g cm, and 200 steps per revolution that is manufactured by JRP [10,21]. The current design of laser positioning system of TVS is presented in Fig. 12.

Table 3
Information to predict and results.

Variables	1	2	3	4
Number of obstacles	24	25	26	27
Scanning time	0.02	0.02	0.02	0.02
Number of points detected	18	19	20	22
Number of scene	106	106	106	106
Predicted data	**8.2269°**	**8.2101°**	**8.1851°**	**8.1046°**

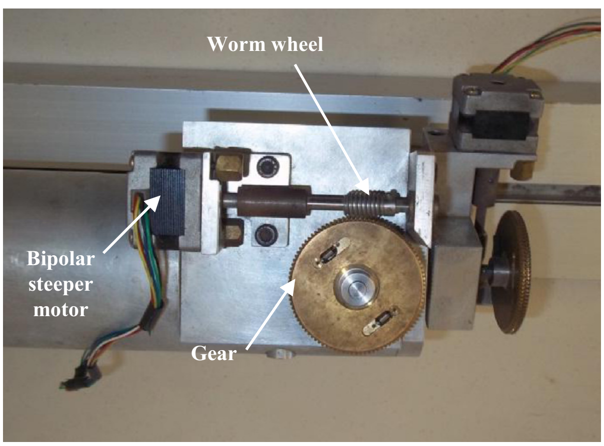

Fig. 12. Laser positioning system of TVS [21].

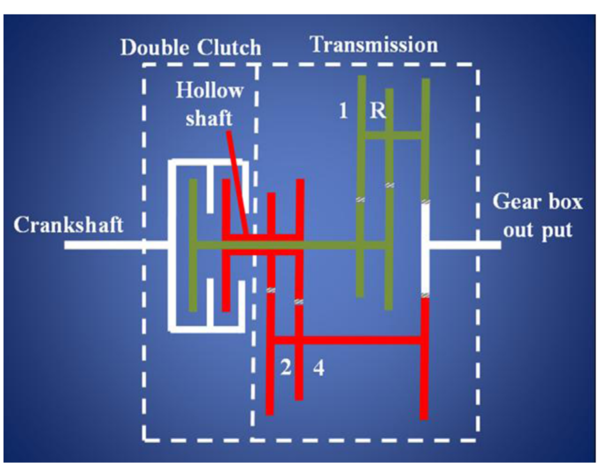

Fig. 13. DCT proposed [21].

In [21] an ideal electro-mechanical system with variable opening angle as a Dual Clutch Transmission (DCT) was proposed. Since it allows obtaining torque transfer from one clutch to another without interrupting traction, thanks to the controlled slippage of the clutches, for a primary clutch odd relationships and a secondary clutch peer relation, an electric drive can save energy [25–28]. These parameters are applicable to vehicles, but the same idea can be applied to PL [21].

However, as the present advanced research shows in a difference to [21] that optimal scanning angles are not so fixed, and varies a little according to required criterion, but the DCT permits due to its design only fixed transmission ratio, so we must to apply another principle than recommended in [21].

Comparing to our first micro-electromechanical design [21] we did observe that the design needs especially three fixed scan angles for three different transmissions ratios supposedly to be that angles simulation bring us, that was not the case. For the proposed DCT introduced in Fig. 13 [21], the available space for piece together from micro-transmission in TVS is around 0.115 m width and 0.03 m high; this space is not enough for the proposed design; maintenance of this kind of proposed transmission needs lubricant to decrease friction; DCT needs to vary velocity in three rigorously fixed speed changes and reverse; see Fig. 13.

Analyzing Continuously Variable Transmission (CVT) vs. DCT (refer Table 4), for TVS application CVT is a better option; such a transmission design is better in optimized time; it has minor energy use, low maintenance, less weight, and it avoids jumps during shift. For reduced friction CVT is better than DCT; the DCT design for actual TVS will be explained below.

The CVT uses two slots or pulleys that fit their axial widths simultaneously in opposite directions to change the transmission ratio of band that runs through the slots. To change the transmission ratio of the width to be opened and close a pulley the other so that the effective way ratios generate the desired ratio also has an infinity of possible relations, continuously varying between two limits. This design has been used for more than a century and was used in the first automobiles; other functional applications are snow blowers and lawn mowers [29]. This long experience of use in different applications with significantly distinct conditions of use shows us that CVT in practice has another advantage: it is strongly reliable and has low dependence on surrounding constrains. This is a good property for novel design with unknown practical restrictions. In Table 4 we analyze conditions and parameters for CVT vs. DCT.

Based on our data, previous design in research [21], and all information presented in Section 4, we can decide the next step. CVT has various sub-designs. We need to choose a proper principle of CVT operation mostly matched to our case conditions, for example twin cone mesh type CVT. Usually CVT cone mesh type design [29] works with chain links and pulleys, and the principle of CVT is the kind of two cones with the same dimensions,

Table 4
Comparison CVT vs. DCT.

	Optimize time	**Using energy**	**Mechanical maintenance**	**Weight**	**Jumps during shifts.**	**Friction**
CVT	More	Less	Less	Less	Lees	Influence of contact-zone between chain links on the torque capacity and dynamic performance [30]
DCT	Less	More	More	More	More	To avoid friction in this type of transmission it needs hydraulic pressure [28]

Please cite this article as: Garcia-Cruz XM, et al. Optimization of 3D laser scanning speed by use of combined variable step. Opt Laser Eng (2013), http://dx.doi.org/10.1016/j.optlaseng.2013.08.011

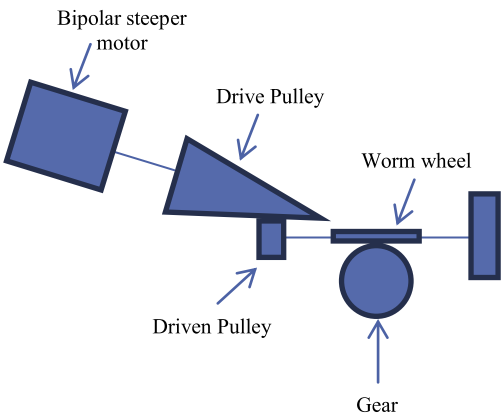

Fig. 14. MET proposed.

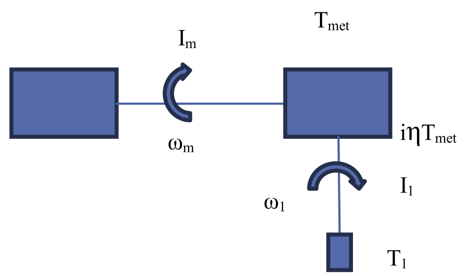

Fig. 15. Simplified model of MET proposed.

conversely placed each other. The proposed principle has infinity of possible relations, between two limits. For an economical solution we propose the design without one cone and clutch. The design will put on novel MET type “Cone mesh CVT”; this design uses one cone (which is called Drive Pulley) and one shaft (which is called Driven Pulley); for reference see Fig. 14.

Fig. 14 introduces MET components and Fig. 13 shows a simplified model of proposed MET.

From Fig. 15 we can obtain the dynamic equations of MET as follows [31]:

$$I_m \omega_m + B_m \omega_m = T_m \tag{20}$$

$$I_1 \omega_1 + B_1 \omega_1 = i\eta T_{met} - T_1 \tag{21}$$

where I_m is the equivalent rotary inertia of motor, I_1 is the equivalent rotary inertia of the active pulley of MET, ω_m is the angular velocity of motor, ω_1 is the angular velocity of the active pulley of MET, B_m, B_1, represent the equivalent damping coefficient of each axis respectively; i is the speed ratio of MET and η is the transmission efficiency. T_m is the output torque of motor; T_1 is the output torque of laser ray drive (equivalent torque of all units sum of laser positioning system).

$$T_1 = F_1 r = r\left[G + \left(m + \frac{\Sigma I_2}{r_2} + \frac{I_f i^2 \eta}{r^2}\right)\right] \tag{22}$$

In this equation, r is the radius of laser ray drive; G is the weight of all units sum of MET; I_f is the rotary inertia of laser ray drive; and m is the mass of rotary parts [31].

According to our design presented in Figs. 2 and 12, and recommendations finally derived in Section 4.2, the MET must o provide the scanning step angle value changes as soon as possible, and as evident from Eqs. (20) and (21) not too many options are there to provide it. The majority of parameters in Eqs. (20) and (21) are physical constants; even ω_m is a constant in our proposal because of the simplest and reliable design of TVS, and so, only ω_1 is the unique candidate under consideration for variable control function programming. In our opinion, this is another small advantage of our proposition: the simplest controls always are more robust. In fact, we propose to program the changes by a system processor of the position of active pulley (see Fig. 12) to satisfy the condition that the number value of ratio of controlled ω_1 and constant ω_m will deal exactly with values of one angle of 3.65°, 8.6° and 14.6°, as necessary at the moment to provide scan.

Additionally is important to note that practically received fuzzy edges of intervals of these three angles (1.8–4°, 8.2–8.7° and 14–14.6°) in the simplest way can be processed only by offered CVT due to its nature of continuous value of its gear ratio.

7. Conclusions

The present article offers the original solution able to increase the velocity of the obstacle detection and digital mapping in application to mobile robot navigation. It is possible to provide by implementation of the combined variable scanning step. During the computational experiment in the present research are obtained and rectified for application requirements the values of three particular angles which permit among others the minimal losses of information about scanned objects. Such application permit accelerate the process of automatic search of the obstacles within the scene under interest, with posterior precise measurements only those edges of obstacles which are the most close to the desired future trajectory of the robot. Such approach releases the possibility to “sectorize” the robot′s operating space in practice. The multivariable simulation of scenes in MATLAB warranties the high reliability of such empirically optimized scanning angles and the enhanced resolution of fast scanning.

The distribution and variation of these three angles due to possible versatility of the scene views is still the goal for future research.

During the simulation also are obtained the important practical recommendations about the natural constrains of dynamic scanning resolution which can be useful on the next stage of the algorithm design for robot navigation.

Comparing two kinds of micro transmission design, dual transmission clutch and the conic one, in a difference to our previous solution in [21], it is clear shown by several simulation results that conic transmission in a most quantity of practical constrains is in a better way matching to our practical application requirements.

In the scope of mentioned above, the future work must to consider the wide range simulations in MATLAB of the optimal combination of three detected angle values in the meaning to reach the desired point of scene in the shortest time but precisely in this point, with the smallest possible error of laser ray positioning.

Acknowledgments

This work was supported by the Graduate and Research Coordination of UABC, Project Program Code 2422. The authors gratefully acknowledge the grant devoted to this research.

References

[1] Isheil A, Gonnet J-P, Joannic D, Fontaine J-F. Systematic error correction of a 3D laser scanning measurement device. Opt Lasers Eng 2011;49(1):16–24.
[2] Sandro Barone, Paoli Alessandro, Razionale Armando Viviano. Shape measurement by a multi-view methodology based on the remote tracking of a 3D optical scanner. Opt Lasers Eng 2012;50(3):380–90.
[3] MacFarlane DL, Kim WY, Nilvi JS, Nuth T, Tan V. Novel two-dimensional laser scanning technique. Opt Lasers Eng 1992;17(1):1–8.
[4] Fu Guoqiang, Menciassi Arianna, Paolo Dario. Development of a low-cost active 3D triangulation laser scanner for indoor navigation of miniature mobile robots. Robotics Autonomous Syst 2012;60(10):1317–26.

[5] Sergiyenko OYu. Optoelectronic system for mobile robot navigation. Optoelectron, Instrum Data Process8756-6990 2010;46(5):414–28 (Springer/Allerton Press).
[6] Lopez MRivas, Sergiyenko Oleg, Tyrsa Vera. Computer vision. In: Zhihui Xiong, editor. Machine vision: approaches and limitations. Vienna, Austria. ISBN: 978-953-7619-21-3. p. 395–428 ([chapter 22]).
[7] Básaca Luis C,Rodríguez Julio C , Sergiyenko Oleg,Tyrsa Vera V, et al. 3D laser scanning vision system for autonomous robot navigation. In: Proceedings of IEEE international symposium on industrial electronics (ISIE-2010). Bari, Italy; July 4–7, 2010. p. 1773–79. ISBN 978-1-4244-6391-6/10.
[8] Oleg Sergiyenko, et al. Precise optical scanning for practical multiapplications. In: Proceedings of IEEE 34th annual IEEE conference IECON′08, Florida, USA; 2008, p. 1656–61.
[9] Rodríguez JC, Sergiyenko OY, Tyrsa VV, Basaca LC, Hipólito JIN. Continuous monitoring of rehabilitation in patients with scoliosis using automatic laser scanning. In: Proceedings of Pan American Health Care Exchanges – PAHCE2011 Conference, Rio de Janeiro, Brazil; 2011. p. 410–4. ISBN: 978-1-61284-918-8.
[10] Basaca, C, Rodríguez J, Yu Sergiyenko O, Tyrsa VV, Hernandez W, Hipólito JIN, et al. Resolution improvement of dynamic triangulation method for 3D vision system in robot navigation task. In: Procedings of the IECON 2010—36th annual conference on IEEE industrial electronics 10.1109/IECON.20105675082; 2010. p. 2886–91.
[11] Rivas Moisés, Sergiyenko Oleg, Aguirre Mario, Devia Luis, Tyrsa Vera, Rendón Ismael. Spatial data acquisition by laser scanning for robot or SHM task. IEEE-IES Proceedings International Symposium on Industrial Electronics (ISIE-2008). Cambridge, United Kingdom; 30 of June–2 of July, 2008. pp. 1458–63.
[12] Rodriguez-Quinonez Julio C, Sergiyenko Oleg, Gonzalez-Navarro Fernando, Basaca-Preciado Luis, Tyrsa Vera. Surface recognition improvement in 3D medical laser scanner using Levenberg–Marquardt method. Signal Process 2013;93(2):378–86 (Elsevier).
[13] Sergiyenko Oleg, Tyrsa Vira, Carlos Luis, Preciado Basaca, Rodriguez Quinonez Julio Cesar, Hernandez Wilmar, Nieto Hipolito Juan Ivan, Starostenko Oleg. Optoelectronic devices and properties. In: Sergiyenko Oleg, editor. Electromechanical 3D optoelectronic scanners: resolution constraints and possible ways of its improvement. Vienna, Austria. ISBN: 978-953-307-204-3. p. 660 ([chapter XX]).
[14] Xiong Zhihui, Chen Wang, Zhang Maojun. Computer vision. In: Zhihui Xiong, editor. Catadioptric omni-directional stereo vision and its applications in moving objects detection. INTECH; 2008; p. 493–518 [chapter26]. ISBN: 978-953-7619-21-3493–518.
[15] Christiano Couto Gava1, Raquel Frizera Vassallo, Flavio Roberti, Ricardo Carelli. Catadioptric omni-directional stereo vision and its applications in moving objects detection, 2008. [chapter5]. ISBN: 978-953-7619-21-371–98.
[16] Basu Anup, Licardie Sergio. Modeling fish-eye lenses—Intelligent robots and systems′93, IROS′93. In: Proceedings of the 1993 IEEE/RSJ international conference, vol. 3, IEEE; 1993.
[17] Zhu Z. Enviroment modeling for visual navigation. Tsinghua University; 1997 (Ph.D. Dissertation, A revised version with title“ Full view spatio-temporal visual navigation-imaging, modeling and representation of real scenes” will be published by China Higher Education Press, 2001).
[18] Zhu Z, Xu G, Lin X. Panoramic EPI generation and analysis of video from moving plataform with vibration, In: Proceedings of the IEEE CVPR; 1999. p. 531–537.
[19] Zhu Zhigang. Omnidirectional stereo vision. In: Anup Basu, Sergio Licardie. Proceedings of the workshop on Omnidirectional Vision, Modeling fish-eye lense. Intelligent Robots and Systems, IROS′93. Budapest, Hungary; 2001.
[20] Lerch T, MacGillivary M, Domina T. 3D laser scanning: a model of multidisciplinary research. J Text Apparel Technol Manage1533-0915 2007;5 (4):1–21.
[21] García-Cruz XM, Sergiyenko O.Yu, Hernández-Balbuena D, Rivas López M, Basaca Luis C, Julio Rodriguez, et al. Optimization of laser TVS for robot navigation using combined scanning with variable step. In: Proceedings of ROC&C′2011, Acapulco, Guerrero, Mexico, 6 p. CP-34, PON 57.
[22] Abba A, Caponio F., Geraci A., Ripamontii G. Non-linear least-squares in fpga devices for digital spectroscopy, In: Proceedings of the nuclear science symposium conference record (NSS/MIC), Orlando; 2009. pp. 563–68.
[23] Wilamowski BM, Yu H. Improved computation for Levenberg–Marquardt training. IEEE Trans Neural Networks 2010;21(6):930–7.
[24] Marquardt D. An algorithm for least-squares estimation of nonlinear parameters. SIAM J Appl Math 1963;11(2):431–41.
[25] Kulkarni Manish, Shim Taehyun, Zhang Yi. Shift dynamics and control of dual-clutch transmissions. Mech Mach Theory 2007;42(2):168–82.
[26] Chien Huai-Ching, Tseng Ching-Huan. An automatic transmission for bicycles: a simulation. Int J Ind Ergon 2004;33(2):123–32.
[27] Galvagno E, Velardocchia M, Vigliani A. Dynamic and kinematic model of a dual clutch transmission. Mech Mach Theory 2011;46(6):794–805.
[28] Kulkarni M, Shim T, Zhang Y. Shift dynamics and control of dual-clutch transmissions. Mech Mach Theory 2007;42:168–82.
[29] Norton Robert L. Design of machinery: an introduction to the synthesis and analysis of mechanisms and machines. McGraw-Hill Higher Education; 2004.
[30] Srivastava Nilabh, Haque Imtiaz. Clearance and friction-induced dynamics of chain CVT drives. Multibody Syst Dyn 2008;19.3:255–80.
[31] Meilan Zhou, Jiabin Wen, Xudong Wang, Yongqin Zhou, Modeling and performance simulation of transmission system for car equipped with metal pushingV-belt type CVT. In: Proceedings of the vehicle power and propulsion conference, VPPC′08, IEEE; 2008.

Analysis of Laser Light Reflectance on the Human Skin for Optoelectronic devices

Julio C. Rodriguez-Quinonez*, Oleg Sergiyenko, Luis C. Basaca-Preciado, Moises Rivas-Lopez
Optoelectronics and Automated Measurement Laboratory
Engineering Institute of Autonomous University of Baja California (UABC)
Mexicali, Baja California, Mexico

Abstract— **The laser light reflection intensity on human skin varies depending the ethnicity of each person, in this paper we present an analysis of reflection intensity and how affects the measurement of some optoelectronic devices.**

Keywords-component; Laser; Reflection; Skin, Optoelectronic

I. Introduction

The understanding of human skin reflectance is motivated by a number of compelling applications. First is the automated location and identification of humans from color images. There is a substantial body of work in this area which relies on conventional tri-color RGB sensor data and on chroma-model based approaches. Skin reflectance is also an important aspect of photo-realistic rendering of humans. This is clearly a problem of great theoretical, if not to say commercial, interest. Accurate data will lead to improved rendering and possibly display technologies [1]. Also in medicine, the increment of the precision in the new medical laser scanners is a constantly evolving task; several scanners are being developed to assist in monitoring and treatment of diverse chronic degenerative and orthopedic diseases.

As a relatively homogenously histological structure for each definite depth, skin can be assumed to consist of three different layers, epidermis, dermis, and subcutaneous fat, where each layer propagates and absorbs light [1]. Absorption and propagation of light in epidermis depend on natural pigments called melanin [2]. Melanin is produced by cells called melanocyte that is formed in the membrane of melanosome particles. Volume fraction of melanosome in epidermis typically varies from 1.3% to 6.3% for lightly pigmented and from 18% to 43% for darkly pigmented specimen [3]. The dermis, with thickness varying from 1 to 4mm, is composed of dense tissue with blood vessels and nerves [1]. Volume fraction of blood in the dermis layer varies from 2% to 7% [3] [4].There is absorbing natural chromophor in the blood cell, called hemoglobin, with concentrations varying from 143 to 173 g/L [5].The color of skin is mainly determined by level of melanin, in other words, by level of melanosome cells, and hemoglobin [6]. Subcutaneous fat can often be ignored because the amount of chromophor, that is the main parameter to absorb light, is very low in that layer [7]. However, most of the light reflection occurs on the outermost layer of the skin, the epidermis, see Fig 1.

This work was supported in part by the Engineering Institute of Baja California, UABC, Mexicali campus.

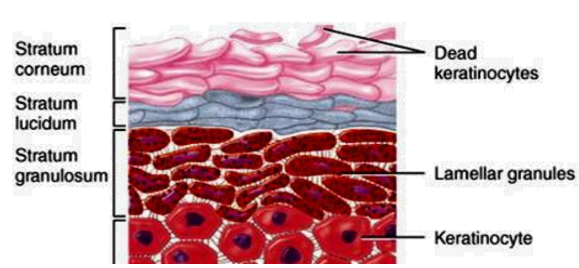

Figure 1. First four sub-layers of the epidermis showing the stratum corneum which is the layer that reflects most of the laser light and it's located on top of the stratum lucidum [8].

II. Methodology and Purpose

As discussed, there are several factors that affect the reflectivity of the skin, however, although the principle of operation of many optoelectronic devices used for human measuring are based in lasers, there only exist a few studies about the reflection of laser light over the human skin; We perform the research in this sense, looking to establish which skin color is susceptible to have more measurement uncertainty when a optoelectronic system based on laser is used.

There are several methods to determine the reflectance (Elementh Boundary Method, Monte Carlo, Finite Difference, among others) [7] [9]. However we consider that the parameters of the Bidirectional Reflection Distribution Function (reflectance angle, angle of incidence, Wavelength) [1] are the most objective to establish a correct scale of Reflectance of laser intensity on human skin with different pigmentation, and these are the parameters that we use for the experimentation explained below.

III. Experimentation

The experimentation described in this section, will be used to analyze how measurements performed can be affected by the laser beam reflectance on diverse types of skins. In Fig. 2, it can be observed the reflectance intensity measurements in human subjects which pigmentations are distinct between them. To take the skin pigmentation samples, people from different nationalities and ethnical origins have been used. The figures "a" to "f" have been ordered ascending from a light pigmentation to a darker pigmentation. The skin sample of figure "a" belongs to a Caucasian person, the skin sample of figure "b" belongs to a slightly tanned Caucasian person, the skin sample of figure "c" belongs to an Asian person, the skin

978-1-4577-0733-9/12/$26.00 ©2012 IEEE

sample of figure “d” belongs to a Latin-American person, the skin sample of figure “e” belongs to a Hindu person and at last, the skin sample of figure “f” belongs to an African-American person.

The experimental measurements were performed under the same conditions, i.e. same illumination, ambient temperature, camera, same laser at 630nm wavelength, same fixed distance “source-tissue-photodetector” and same body area.

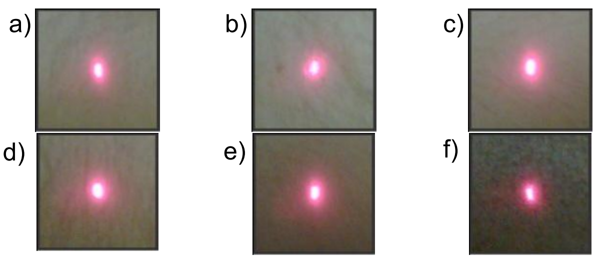

Figure 2. Reflectance sample measurements of human skin with different pigmentation.

Utilizing Matlab®, the luminosity intensity of all the sampling performed was obtained. The intensity was plotted in Fig. 3, where 0 is a value assigned to a void reflectance, and 1 corresponds to the maximum reflectance intensity.

For example, in Fig. 2 a), the light pigmented skin has a natural reflectance to the ambient illumination. Therefore, in Fig. 3 a) we can clearly notice this skin reflectance as a suspended amorphous plane above the reflectance axis. On the other hand, it is notable that the dark pigmented skin does not have the reflectance capability as high as the lightly pigmented skin, towards the ambient illumination. Hence, in Fig. 3 “f” this reflection representation is absent due to the darker pigmentation skin tone.

At the middle of each plot we can find the laser reflectance, which is a type of light with higher intensity. The laser reflectance is shown in each plot as a protrusion in a cone shape; it reaches maximum luminosity levels at the top of the protrusion, which is the center of the laser beam reflectance.

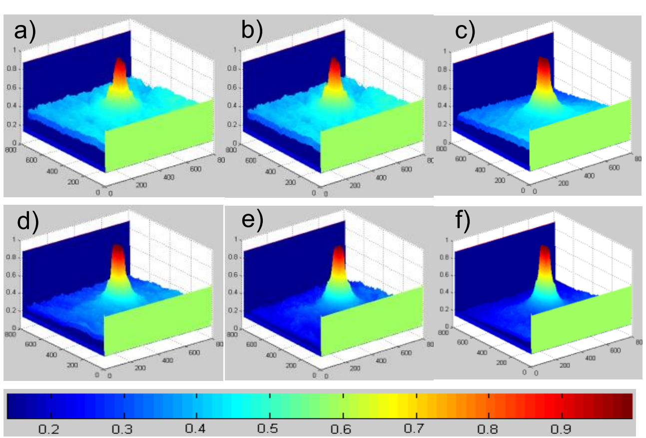

Figure 3. Relative scale of laser intensity reflection intensity on human skin with different pigmentation.

Analyzing the data and plots we can determine that the laser beam reflectance in persons with dark pigmented skin is 5% – 40% better defined than in those with lightly pigmented skin as Fig. 3 “a”. In addition, we can also obtain experimentally, that the ambient illumination is more reflective on subjects with lighter pigmented skin [10], although, this characteristic does not affect the reflectance area of the laser beam.

IV. CONCLUSION

As analyzed, the reflection of the laser light over a person’s skin is 5% - 40% better defined in persons with darker pigmentation, however performing an analysis by the Bidirectional Reflection Distribution Function, the persons with darker pigmentation have 1% of reflectance to the 630nm laser beam while the persons with lighter pigmented skin have 1.15% of reflectance to the 630nm laser beam [1], this entails that the persons with lighter pigmentation are prone to reflect the ambient light noise. However by the analysis we can note that this should not be an impediment to detect the reflection over the skin with an optoelectronic sensor, since the lighter pigmentation skin reflects up to 60% of the laser light over the ambient light noise.

REFERENCES

[1] Angelopoulou Elli, "The Reflectance Spectrum of Human Skin," GRASP Laboratory, Department of Computer and Information Science, University of Pennsylvania, Pennsylvania, Technical Report MS-CIS-99-29 1999.

[2] AN Bashkatov, EA Genina, VI Kochubey, and VV Tuchin, "Optical properties of human skin, subcutaneous and mucous tissues in the wavelength range from 400 to 2000 nm," *J Phys D: Appl Phys*, vol. 38, pp. 2543–55, 2005.

[3] AR Young, "Chromophores in human skin," *Phys Med Biol*, vol. 42, pp. 789-802, 1997.

[4] SL Jacques and DJ McAuliffe, "The melanosome: threshold temperature for explosive vaporization and internal absorption coefficient during pulsed laser irradiation," *Photochem Photobiol*, vol. 53, pp. 769–75, 1991.

[5] E Claridge, D Hidovic- Rowe, P Taniere, and T Ismail, "Quantifying mucosal blood volume fraction from multispectral images of the colon," in *Proc SPIE* , 2007, pp. 17-22.

[6] R Yip, "Significance of an abnormally low or high hemoglobin concentration during pregnancy: special consideration of iron nutrition," *Am J Clin Nutr*, vol. 72, 2000.

[7] M.A. Ansari and R Massuditi, "Study of light propagation in Asian and Caucasian skins by means of the Boundary Element Method.," *Optics and Lasers in Engineering*, vol. 47, no. 9, pp. 965-970, 2009.

[8] (2011) Dental Mnemonics. [Online]. http://dmnemonics.blogspot.com/2011/12/epidermal-layer.html

[9] M Shimada, Y Yamada, M Itoh, and T Yatagai, "Melanin and blood concentration in a human skin model studied by multiple regression analysis: assessment by Monte Carlo simulation," *Med Biol*, vol. 46, pp. 2397–406, 2001.

[10] Julio C. Rodriguez, Oleg Yu. Sergiyenko, Vera V. Tyrsa, Luis C. Basaca, and Juan Ivan Hipolito Nieto, "Continuous monitoring of rehabilitation in patients with scoliosis using automatic laser," in *Pan American Health Care Exchanges – PAHCE. Conference*, Rio de Janeiro, 2011, pp. 410-414.

Monitoreo continuo de rehabilitación en pacientes con escoliosis utilizando barrido Laser automático

Continuous monitoring of rehabilitation in patients with scoliosis using automatic laser scanning

Julio C. Rodríguez[1], Oleg Yu. Sergiyenko[1], Vera V. Tyrsa[2], Luis C. Basaca[1], Juan Iván Nieto Hipólito[1]
[1]Universidad Autónoma de Baja California UABC, Baja California, México
[2]Universidad Politécnica de Baja California, Baja California, México

Abstract — **Medical practitioners have traditionally used manual anthropometric meters and X-Ray to monitor the development and treatment of orthopedic diseases as scoliosis. With the disadvantage of generating uncertainty results in the manual methods, also X-Ray radiation can be the cause of several diseases after a long exposure. This is the reason why we developed a new method, noninvasive, without harmful radiation to human beings, assisting in monitoring the treatment of orthopedic diseases such as scoliosis. The following article presents the theoretical performance and experimental results of measurements already made with the new proposed system.**

Keywords — **Scoliosis, Triangulation, Laser.**

Resumen — **Los practicantes de la medicina tradicionalmente han utilizado medidores antropométricos manuales y Rayos-X para monitorear el desarrollo y tratamiento de enfermedades ortopédicas como la escoliosis. Generando incertidumbre en los métodos manuales y pudiendo provocar enfermedades tras una larga prolongación a la radiación de los Rayos-X. Es por esta razón que hemos desarrollado un método innovador, no invasivo y que no genera ningún tipo de radiación dañina en el ser humano, auxiliar en el monitoreo de tratamiento de enfermedades ortopédicas como la escoliosis. En el siguiente artículo presentamos el funcionamiento teórico así como resultados experimentales de las mediciones ya realizadas con este Nuevo sistema propuesto.**

Palabras Clave — **Escoliosis, Triangulación, Laser.**

I. INTRODUCCION

La escoliosis es una desviación de la columna vertebral que ocasiona una curva vista desde frente que se acompaña de la rotación de los cuerpos vertebrales y la aparición de una giba, afecta en mayor o menor medida a entre el 1.5% y 3% de la población[1]. Las causas de la escoliosis son extremadamente variadas sin embargo se pueden identificar 5 orígenes principales: *Escoliosis por adaptación*, una rotación de la pelvis, tortícolis, una pierna corta, etc., obligaran a la columna a colocarse en una posición de compensación. *Escoliosis por malformación*, Tiene origen congénito; una vértebra cuneiforme, una artrodesis vertebral, etc., fuerzan el raquis a adaptarse. *Escoliosis neurológicas y distroficas*. *Escoliosis antiálgicas*, a menudo denominada falsa escoliosis. Se debe a mecanismos justificados de defensa donde el objetivo es evitar el dolor. *Las escoliosis esenciales o Idiopáticas* [2]. Sin embargo se ha comprobado que el origen hereditario multifactorial (las formas familiares) pueden alcanzar el 43% de los orígenes de la escoliosis [2].

En la actualidad existen diversas tecnologías para realizar las mediciones utilizadas rutinariamente en el tratamiento de esta enfermedad, como son los rayos X pero cuya desventaja son las enfermedades causadas por una exposición continua a su radiación ó medidores antropométricos los cuales presentan una opción saludable sin embargo estos medidores son controlados manualmente y tienen la desventaja de depender de la habilidad del médico para utilizar estos aparatos; a la vez que las mediciones no muestran una repetitividad confiable. Es por esta razón que hemos desarrollado un método no invasivo que utiliza un sistema de visión por laser basándonos en el principio de triangulación dinámica [3] para obtener las coordenadas espaciales y realizar un mapa digital del cuerpo medido. El sistema desarrollado cuenta con un laser de 20 mw con una divergencia de 1 mrad; este haz de luz es proyectado a un espejo cortado a 45° de 10mm (+0.0mm / -0.03mm) de diámetro el cual refleja perpendicularmente la luz hacia el cuerpo. El espejo es controlado por un motor de pasos acoplado a una pequeña transmisión que permite obtener una resolución de hasta 0.004° por paso del motor. La luz proyectada es reflejada por el cuerpo sobre el cual se realizan las mediciones, este reflejo es captado por un photoreceptor de silicón de respuesta rápida (2ns). Para realizar el escaneo vertical todo el sistema tiene la capacidad de rotar sobre su mismo eje, para realizar esta tarea el sistema cuenta con otra pequeña transmisión, que al igual que el espejo del emisor puede obtener una resolución de hasta 0.004° por paso del motor, esta transmisión proporciona el torque necesario para realizar la rotación de nuestro sistema.

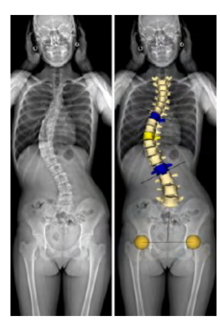

Fig. 1 Torsión de la columna causada por la escoliosis (Rayos-X) [4].

ISBN: 978-1-61284-918-8
IEEE Catalog Number: CFP1118G-ART

II PRINCIPIOS TEORICOS

Existen 2 tipos de triangulación por laser; triangulación estática y triangulación dinámica. Para realizar el cálculo de alguna coordenada espacial por medio de la triangulación estática existen 3 variables que deben ser conocidas: El ángulo de emisión del laser, el ángulo detectado por el arreglo de fotodetectores (usualmente una cámara) y la distancia entre el emisor de luz láser y la cámara.

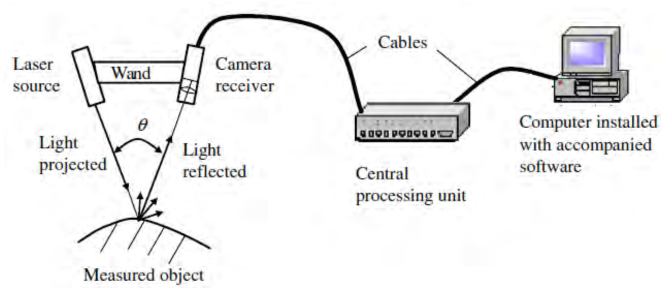

Fig. 2 Sistema típico de triangulación estática [5].

La desventaja es que la mayoría de estos sistemas realizan el escaneo en 1 solo plano dimensional y aquellos que no cuentan con un limitado campo de visión (FOV por sus siglas en ingles). Es por esta razón que desarrollamos y trabajamos con triangulación dinámica.

La diferencia entre los sistemas de triangulación estática y de triangulación dinámica es que en esta ultima el triangulo creado dura solamente algunos milisegundos. Este periodo de tiempo es resultado de nuestra apertura de escaneo (SA, por sus siglas en ingles) Fig. 3. La apertura (SA) como ya mencionamos anteriormente cuenta con un espejo en 45° que refleja todo el plano de escaneo hacia el fotodetector el cual es sensible al espectro de luz de la luz laser [3].

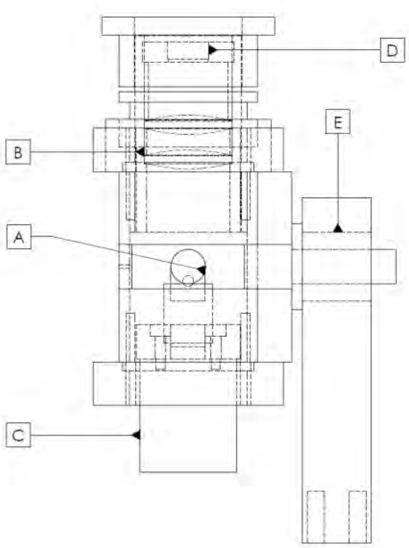

Fig. 3. Vista Frontal de la apertura de escaneo (SA).

Entonces, el triangulo solamente es generado cuando el plano de escaneo detecta el reflejo de la luz laser, esto ocurre en un periodo que va de los 4.04ms hasta los 8.34ms, dependiendo de las rpm en el motor del espejo. Este efecto es mostrado en la fig. 4 donde el canal 1 es la señal detectada y el canal 2 es la señal acondicionada.

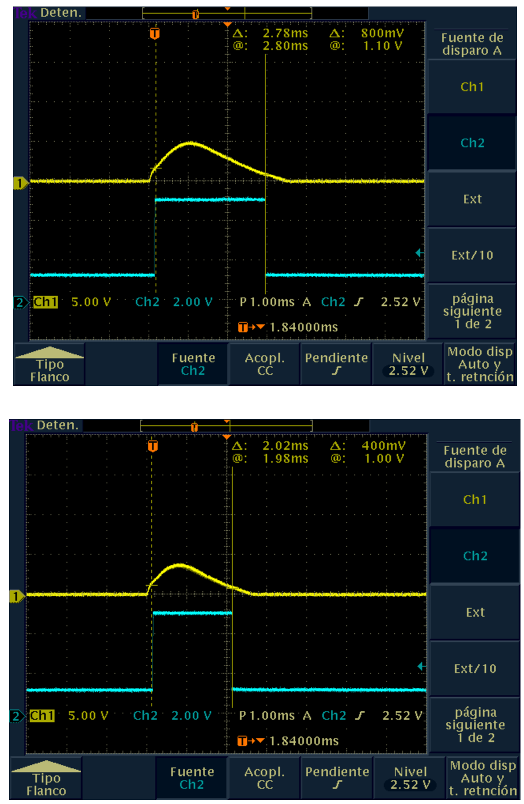

Fig. 4. Escaneos experimentales a diferentes velocidades, se puede observar que inclusive aumentando las rpm aun se puede tener una excelente señal acondicionada. (Escaneos realizados por nuestro prototipo experimental [6], [7]).

Como ya mencionamos la triangulación dinámica es el principio teórico de nuestro sistema. Como se muestra en la Fig. 5 un haz de luz laser es proyectado desde el sistema posicionador del laser (PL) sobre el cuerpo, este es reflejado de vuelta y detectado por nuestra apertura de escaneo. El sistema está diseñado para que adicionalmente rote y pueda realizar el escaneo vertical.

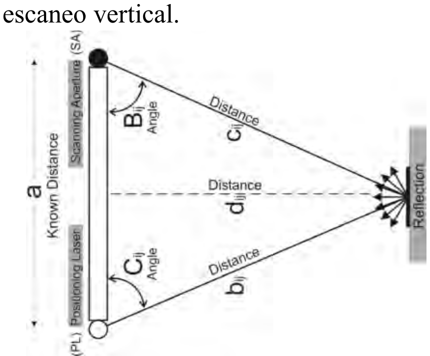

Fig.5 Principio de triangulación dinámica con PL y SA

ISBN: 978-1-61284-918-8
IEEE Catalog Number: CFP1118G-ART

Para realizar el cálculo de las coordenadas utilizamos el teorema de senos y lo adaptamos al sistema dando como resultado las siguientes formulas tanto para el cálculo de distancias como el de coordenadas.

$$d_{ij} = a\frac{\sin B_{ij} \cdot \sin C_{ij}}{\sin[180° - (B_{ij}+C_{ij})]} \quad (1)$$

$$x_{ij} = a\frac{\sin B_{ij} \cdot \sin C_{ij} \cdot \cos \sum_{j=i}^{n} \beta_j}{\sin[180° - (B_{ij}+C_{ij})]} \quad (2)$$

$$y_{ij} = a\left(\frac{1}{2} - \frac{\sin B_{ij} \cdot \cos C_{ij}}{\sin[180° - (B_{ij}+C_{ij})]}\right) \; at \; B_{ij} \leq 90° \quad (3)$$

$$y_{ij} = a\left(\frac{1}{2} + \frac{\sin B_{ij} \cdot \cos C_{ij}}{\sin[180° - (B_{ij}+C_{ij})]}\right) \; at \; B_{ij} \geq 90° \quad (4)$$

$$z_{ij} = a\frac{\sin B_{ij} \cdot \sin C_{ij} \cdot \sin \sum_{j=i}^{n} \beta_j}{\sin[180° - (B_{ij}+C_{ij})]} \quad (5)$$

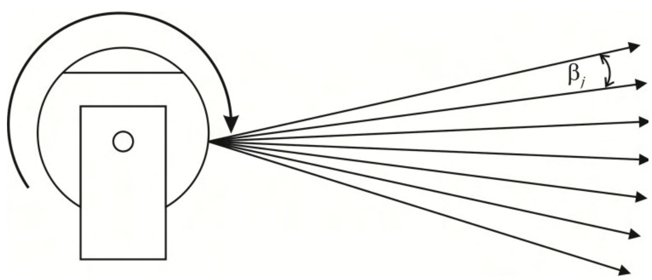

Fig. 6. Angulo β_j en base a la rotacion de nuestro sistema

III SISTEMA 3D ROTACIONAL DE ESCANEO DE CUERPOS

El sistema desarrollado es capaz de obtener las coordenadas espaciales de un cuerpo. Como ya mencionamos anteriormente el sistema cuenta con 3 elementos principales: Sistema posicionador del Laser, Apertura de escaneo y sistema de Rotación. Estos 3 elementos son tanto los actuadores como sensores del sistema. El funcionamiento de la apertura de escaneo (ver Fig. 3) fue descrito en la Sección II; mientras que el sistema posicionador del laser realiza la tarea de proyectar el haz de luz en las diferentes posiciones del barrido que se realiza. El ángulo de emisión se conoce ya que se realiza por medio de un motor de pasos, mientras que el ángulo de recepción de la apertura de escaneo se obtiene mediante una relación lineal del tiempo que tarda SA en realizar una rotación y el momento en que se detecta el haz de luz reflejado sobre el cuerpo Fig. 7.

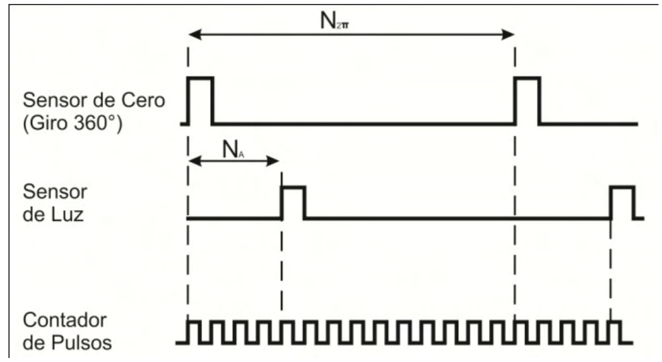

Fig. 7. Análisis para la obtención del ángulo de SA

$$B_{ij} = \frac{2\pi \cdot N_A}{N_{2\pi}} \quad (6)$$

Como se muestra en la Fig. 8. el emisor y receptor se encuentran separados a la distancia exacta de 1 metro, dentro de la barra que contiene al emisor y receptor también se encuentra el laser. Las principales ventajas de este prototipo son: Permitir la rotación sin necesidad de cadenas manteniendo el centro de gravedad dentro de nuestro sistema. Incremento en la resolución en 10 veces por medio de una pequeña transmisión que nos proporciona 1 barrido completo por cada 10 rotaciones del motor de pasos del emisor, disminución de fricción al utilizar baleros planos de politetrafluoretileno (Teflón) que proporciona el coeficiente de fricción mas bajo conocido.

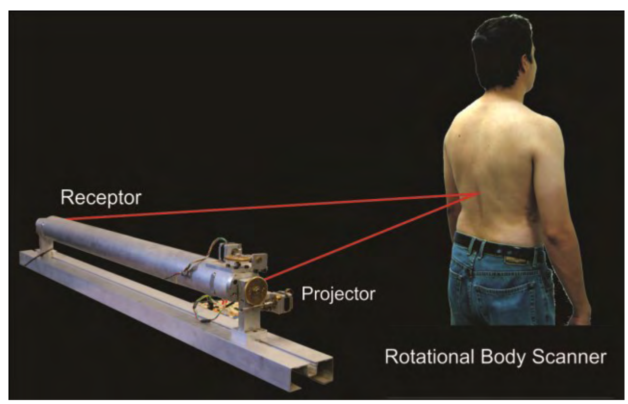

Fig. 8 Imagen del sistema Rotacional para escaneo de cuerpos en 3D

IV EXPERIMENTACION

Para verificar la precisión de nuestro sistema realizamos mediciones experimentales en 2D (una línea de medición del escaneo en 3D) comprando las mediciones (m),y(m)" (ver Tabla I), con los valores reales "X(m),Y(m)". Posteriormente calculamos la variación entre los valores reales contra los medidos. La variación existente nos permite concluir que el sistema es lo suficiente robusto para realizar la tarea de escaneo corporal.

ISBN: 978-1-61284-918-8
IEEE Catalog Number: CFP1118G-ART

TABLA I
PRECISIÓN DE LAS MEDICIONES

Prueba	X(m)	Y(m)	x(m)	y(m)	VariaciónX	VariaciónY
A	0.5	0.250	0.498	0.247	-0.002	-0.003
B	0.5	0.188	0.498	0.186	-0.002	-0.002
C	0.5	0.125	0.498	0.123	-0.002	-0.002
D	0.5	0.063	0.499	0.062	-0.001	-0.001
E	0.5	0.000	0.499	-0.010	-0.001	-0.010
F	0.5	-0.063	0.5	-0.062	0	0.001
G	0.5	-0.125	0.501	-0.124	0.001	0.001
H	0.5	-0.188	0.502	-0.188	0.002	-0.001
I	0.5	-0.250	0.502	-0.250	0.002	0.000
J	0.75	0.250	0.751	-0.247	0.001	-0.003
K	0.75	0.188	0.751	0.184	0.001	-0.004
L	0.75	0.125	0.75	0.121	0	-0.004
M	0.75	0.063	0.75	0.060	0	-0.003
N	0.75	0.000	0.748	-0.004	-0.002	-0.004
O	0.75	-0.063	0.749	-0.067	-0.001	-0.005
P	0.75	-0.125	0.753	-0.128	0.003	-0.003
Q	0.75	-0.188	0.754	-.0.192	0.004	-0.005
R	0.75	-0.250	0.754	-0.254	0.004	-0.004

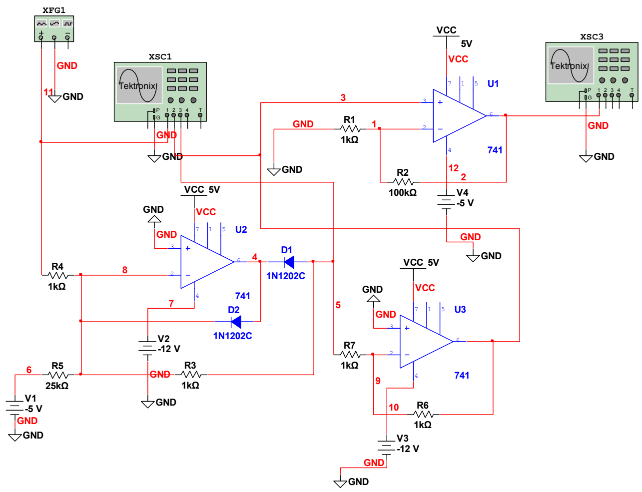

Fig. 10 Circuito de zona muerta con amplificadores de saturación.

V ELIMINACION DE RUIDO

Dado que solamente el 2-7% de la señal generada por la reflexión del laser es detectada es necesario realizar una amplificación y por medio de un circuito de zona muerta eliminar el ruido producido que genera muy pequeñas distorsiones de voltaje.

El circuito de zona muerta Fig. 10 que desarrollamos elimina cualquier señal menor a 200mV; esto elimina cualquier tipo de ruido como pequeños movimientos involuntarios del paciente o ruido ambiental que pudiese quedar después de aplicar el filtro Butterworth. La señal correspondiente al laser es mayor a 400mV lo que nos permite realizar este procedimiento. En práctica durante los experimentos realizados nuestra señal útil se encuentra sobre una señal con ruido como se presenta en la Fig. 9.

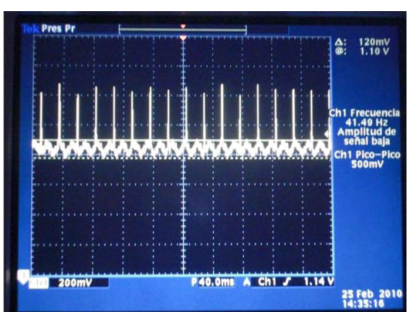

Fig 9. Señal de 200mv; las espigas muestran la señal útil.

Es esencial eliminar los posibles tipos de ruido como los observados en Fig. 9, presentes en objetos biológicos y fuentes de incertidumbre presentadas en [8-10], con este planteamiento hemos desarrollado un filtro Butterworth a 90Hz (cuya frecuencia de corte debe ser expresada en rad./seg., ver formula 7) con una atenuación a -40db detectando solamente la información que nos es útil.

$$\omega_c = (2\pi)(90) \tag{7}$$

En el circuito de zona muerta regulamos nuestro Vref a 200mV por medio de la fuente V1 y la Resistencia mR (R5), esta es calculada por medio de la formula de ganancias para los circuitos de zona muerta. El dido D2 conduce los valores de XFG1 y establece el valor del nodo 5 =-XFG1 – Vref. Cuando XFG1 excede el valor de –Vref = 200mV la salida del nodo 3 nos permite conocer las señales que exceden el valor de referencia. Existe la zona muerta cuando los valores XFG1 son inferiores a –Vref [11].

a)

b)

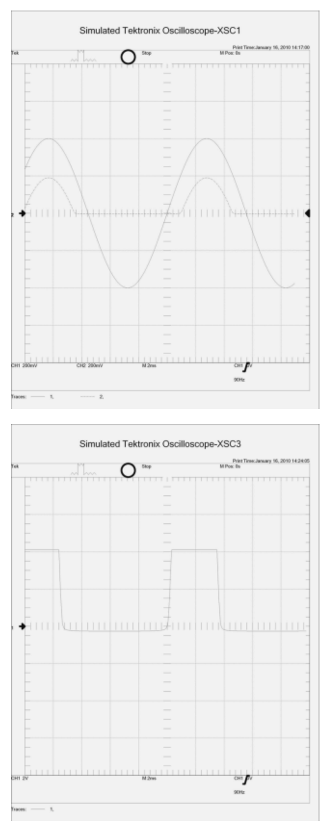

Fig. 10 a) Señal a 90 Hz después del circuito de zona muerta, b) Señal util amplificada.

ISBN: 978-1-61284-918-8
IEEE Catalog Number: CFP1118G-ART

VI CONCLUSIONES

En este artículo hemos señalado las ventajas del sistema rotacional de escaneo en 3D sobre otros métodos conocidos. Se muestra que nuestro sistema ofrece la solución más directa al problema de medición de coordenadas espaciales, proveyendo con la menor incertidumbre la calidad metrológica en mapeos digitales sobre una superficie biológica desconocida. Este escáner proporciona la opción adicional de ajustar la resolución para cualquier área ó locación de interés. La incertidumbre de las coordenadas medidas satisface las aplicaciones médicas. Algunas de las fortalezas y ventajas de nuestro sistema sobre otros existentes es su novedosa construcción y diseño, el original esquema de triangulación dinámica, es muy compacto y no requiere de grandes instalaciones para su instalación.

Adicionalmente factibilidad del método ya era comprobada en otras aplicaciones prácticas de triangulación dinámica tales como: monitoreo de construcciones y navegación de robots móviles [12].

El estudio sobre la interacción del laser con diferentes tipos de piel humana en un amplio grupo de aspectos (diferencias étnicas, nacionalidades, edad, género y enfermedades y enfermedades en la piel) y la selección de la velocidad óptima de barrido (disminuyendo la filtración natural de movimientos espontáneos del cuerpo) es tema para el trabajo futuro.

VII. REFERENCIAS

[1] John A. Herring, Mihran O. Tachdjian (2002). Tachdjian's pediatric orthopaedics. Editorial: Saunders ISBN 0721656846, Philadelphia PA.

[2]Philippe Souchard, Marc Ollier. Escoliosis su tratamiento en fisioterapia y ortopedia. Médica Panamericana, 2002 ISBN: 8479036923.

[3] Rivas López, M.; Sergiyenko, O. & Tyrsa, V. (2008). Machine vision: approaches and limitations, In: Computer vision, Xiong Zhihui, (Ed.), pp. 395-428. Editorial: IN-TECH, ISBN 978-953-7619-21-3, Vienna, Austria.

[4] Illés, Tamás; Tunyogi-Csapó, Miklós; Somoskeöy, Szabolcs (2010). Breakthrough in three-dimensional scoliosis diagnosis: significance of horizontal plane view and vertebra vectors. *European Spine Journal*, (September 2010) ISSN: 1432-0932.

[5] Zhizhong Li, Chien-Chi Chang, Patrick G. Dempsey, Xiuwen Cai. Refraction effect analysis of using a hand-held laser scanner with glass support for 3D anthropometric measurement of the hand: A theoretical study. Measurement, ELSEVIER, Vol. 41, No 8, (October 2008) pp. 842-850.

[6] Moisés Rivas López, Oleg Sergiyenko, Vera Tyrsa, Wilmar Hernandez Perdomo, Daniel Hernández Balbuena, Luis Devia Cruz, Larisa Burtseva, Juan Iván Nieto Hipólito. Optoelectronic method for structural health monitoring. *International Journal of Structural Health Monitoring*, SAGE Publications, Vol.9, No.2, March, 2010, pp.105-120

[7] O. Sergiyenko, W. Hernandez, V. Tyrsa, L. Devia Cruz, O.Starostenko, M.Pena-Cabrera. Remote Sensor for Spatial Measurements by Using Optical Scanning. MDPI, *Sensors*, 9(7), 2009, Basel, Switzerland, pp. 5477-5492.

[8] Moisés Rivas, Oleg Sergiyenko, Mario Aguirre, Luis Devia, Vera Tyrsa, and Ismael Rendón Spatial data acquisition by laser scanning for robot or SHM task. IEEE-IES Proceedings "International Symposium on Industrial Electronics"(ISIE-2008), Cambridge, UK, 2008, p.1458-1463.

[9] O. Sergiyenko, V. Tyrsa, D. Hernandez-Balbuena, M. Rivas López, I. Rendón López, L. Devia Cruz. Precise Optical Scanning for practical multiapplications. Proceedings of IEEE-34th Annual Conference of IEEE Industrial Electronics (IECON'08), Florida, USA, 10-13 November, 2008. pp.1656-1661.

[10] Oleg Y. Sergiyenko, Vera V. Tyrsa, Luis F. Devia, Wilmar Hernandez, Oleg Starostenko, Moisés Rivas Lopez. Dynamic Laser Scanning method for Mobile Robot Navigation. Proceedings of ICCAS-SICE 2009, ICROS-SICE International Joint Conference, Fukuoka, JAPAN, August 18-21, 2009, pp. 4884-4889.

[11] Robert F Coughlin, Frederick F. Driscoll. "Operational Amplifier with diodes", Operational Amplifier and lineal integrate circuits, Prentice Hall ISBN 970-17-0297-0, Mexico DF, 1999, pp 200 – 204

[12] M. Rivas López, O.Sergiyenko, V. Tyrsa, et al. Optoelectronic method for structural health monitoring. SAGE Publications, "International Journal of Structural Health Monitoring", Vol.9, No.2, March, 2010, pp.105-120. Issue Online, September, 24, 2009, ISSN 1475-9217 / doi: 10.1177/1475921709340975

ISBN: 978-1-61284-918-8
IEEE Catalog Number: CFP1118G-ART

Improve a 3D Laser Scanner Resolution by a Feed-Forward Backpropagation Neural Network

Julio C. Rodríguez[1], Oleg Yu. Sergiyenko[1], Luis C. Basaca[1] Vera V. Tyrsa[2]

[1]Engineering Institute of Autonomous University of Baja California, Polytechnic University[2]
julio_qas@hotmail.com, 1, lubakun@hotmail.com, vera@upbc.edu.mx

Abstract— **Many Laser Scanners depend of their mechanical construction to guarantee their measurements precision, however the current computational technologies allow us to improve this measurements by mathematical methods implemented in Neural Networks. In this article we're going to introduce the current laser scanner technologies, give a description of our 3D Laser Scanner and calculate their measurement error by a previously trained Neural Network. Finally, computational simulations are conducted to verify the performance of the proposed system and its method uncertainty under the use of Levenverg-Marquardt training method of a Neural Network.**

***Index Terms* - Laser, Scanner, Neural Network.**

I. Introduction

Laser scanning is an active remote sensing technique which is capable of direct range measurements between the laser scanner and the reflecting target. The results are highly accurate 3D point clouds. [HYPERLINK \l "Hof11" 1]. 3D point clouds are used for various applications, for example for 3D modelling of buildings and cities, as-built documentation, cultural heritage documentation, forensics or forest inventories 1]. One common laser scanning is the Time of flight laser scanner, which works when a 3D laser scanner is targeted to the physical objects to be scanned and the laser beam is directed over the object in a closely spaced grid of points. By measuring the time of laser flight, which is the time of travel of the laser from the scanner to the physical objects and back to the scanner, the position in three-dimensional space of each scanned point on the object is established. The result is a "cloud of points" which consists in thousands of points in 3-dimensional space that are a dimensionally accuraterepresentation of the existing object This information can then be converted into a 3D CAD model that can be manipulated using CAD software, and to which the design of the new equipment can be added [HYPERLINK \l "Ara07" 2]

ROC&C'2011 – CP-44 PONENCIA RECOMENDADA POR EL COMITÉ DE COMPUTACIÓN DEL IEEE SECCIÓN MÉXICO Y PRESENTADA EN LA REUNIÓN DE OTOÑO, ROC&C'2011, ACAPULCO, GRO., DEL 27 DE NOVIEMBRE AL 3 DE DICIEMBRE DEL 2011.

Another Scanner method is the Laser triangulation; in general can be based on two schemes. The first one uses a fixed angle of emission and variable distance; the second one, on the contrary, fixed triangulation base and variable scanning angle 3]. The first one works as follows; A laser beam is projected onto the measurement surface, where it is scattered from the surface and its image is detected by an optical detector, usually a CCD camera. By using a suitable angular arrangement between the laser and sensor positions, the detected location of the laser spot on the image plane produces an accurate measurement of the distance between the sensor and the surface [HYPERLINK \l "4" 3]. Therefore, the profile of a surface can be measured by using laser triangulation. The laser beam is made to scan across the surface of the object. The range data at each location is calculated according to its position within the image plane so that the whole 3-dimensional profile of the surface can be obtained. The positioning of the laser beam is normally controlled by an adjustable mirror system, which is able to change the angular direction of the laser beam over a 2-dimensional plane3]. A second one basic triangulation scheme is an active optical triangulation 3D digitizing systems, which visualize real-life objects. These active optical systems provide photorealistic representations of shapes and textures with reasonable speed. The laser beam reflected from a mirror is projected on the object. The diffusely reflected light is collected by the sensor, which is a linear array if a laser dot is projected or a 2D matrix (typically a charge coupled device camera) if laser stripes are projected.

However, all these scanners have accuracy limitations when taking into account the mechanical factors of the system, for example, these limitations can be laser positioner angles, pixels of the camera or rotating mechanical systems.

Application of Neural networks methods and algorithms may be solution of this problem which cannot be easily solved by traditional methods. The history of neural networks started in mid twentieth century when simple neural network with limited capabilities were conceived. They never got into the main stream applications at that time due to poor generalization capabilities and lack of specificity with high memory loads. After two decades, the whole concept of neural networks changed when the multi-layer neural networks with back propagation learning algorithm was presented [HYPERLINK \l "12" 4].

From that time, many different researchers studied the area of artificial neural networks, which led to a vast range of different neural architectures applied to a plethora of different problems. At present; neural networks are used as principal solutions for various problems like grouping and classification, pattern recognition, approximation, prediction, clusterization and memory simulation. Neural networks may initially seem complex and computer intensive, but actually may integrate well with a Medical environment in various distinct applications 4], [HYPERLINK \l "Gon10" 5], 6].

Properly trained backpropagation networks tend to give reasonable answers when presented with inputs that they have never seen. Typically, a new input leads to an output similar to the correct output for input vectors used in training that are similar to the new input being presented. This generalization property makes it possible to train a network on a representative set of input/target pairs and get good results without training the network on all possible input/output pairs. Feedforward networks often have one or more hidden layers of sigmoid neurons followed by an output layer of linear neurons. Multiple layers of neurons with nonlinear transfer functions allow the network to learn nonlinear and linear relationships between input and output vectors [HYPERLINK \l "12" 4]. This general property is very useful in our case because between input and output vectors, which are vectors of true and measured values of 3D scanner, the relation has complex stochastic character.

We develop a 3D Laser scanner based in our original principle of dynamic triangulation described below. The training method; Levenberg Marquardt, is used in a feed forward back propagation neural network is presented in the currently study to assess accuracy for surface recognition improvement in the 3D Laser Scanner.

II. System Function

Dynamic triangulation (Fig.1) is the method and theoretical base of our system; we use it to obtain the 3D coordinates of the body that are in the field of view (FOV) in front of the system. We call it dynamic triangulation because of that fact that triangle on Fig. 1 in real time exists very short interval, when projected laser ray, changing its spatial position each 0.001s, reaches an unique condition to be able to enter into rotating photoreceiver through mixed (diffuse+specular) reflection on the human body surface. The time of existence of the spatial figure presented on Fig.1 is variable and dependent on the rotational velocities of the laser positioning system and scanning aperture.

As shown in Fig. 5 a laser beam is projected from the Positioning Laser (PL) onto the body, and reflecting it back onto the revolving sensor inside the Scanning Aperture (SA) 7], [HYPERLINK \l "4" 3].

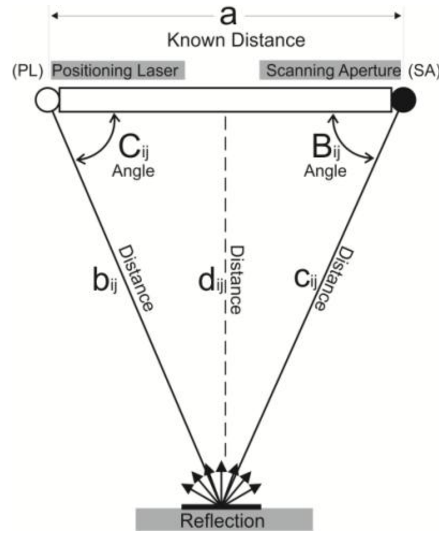

Fig. 1. Dynamic triangulation principle, spatial position of Scanning Aperture and Positioning Laser.

Then, using the theorem of sinus, the correlation between the triangle sides and the width and height in the triangle of Fig. 1, it is possible to develop a formula to calculate distance "d" from base "a" up to points highlighted by the laser beam on to the body.

$$d_{ij} = a\frac{\sin B_{ij} \cdot \sin C_{ij}}{\sin\left[180° - \left(B_{ij}+C_{ij}\right)\right]} \tag{1}$$

Where indexes i and j represent respectively the step number in horizontal and vertical directions during the 3D Body Scanning.

To perform the vertical scanning the system rotates to get the angle as show in Fig. 2.

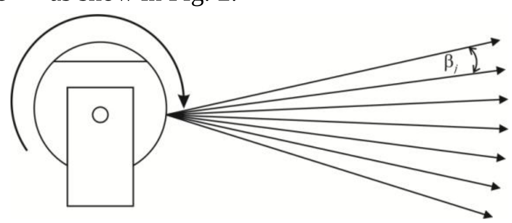

Fig. 2. Rotation of the Dynamic triangulation principle and the angle

Using angles ł, ‘, $\sum_{j=1}^{n}$ and the known distance of the base *a*, it is possible to calculate the Cartesian coordinates of each laser highlighted points on each *ij* step of 3D Body scanning process, based on the following formulas:

$$x_{ij} = a\frac{\sin B_{ij} \cdot \sin C_{ij} \cdot \cos \sum_{j=i}^{n}\beta_j}{\sin\left[180° - \left(B_{ij}+C_{ij}\right)\right]} \tag{2}$$

$$y_{ij} = a\left(\frac{1}{2} - \frac{\sin B_{ij} \cdot \cos C_{ij}}{\sin\left[180° - \left(B_{ij}+C_{ij}\right)\right]}\right) \; at\ B_{ij} \leq 90° \tag{3}$$

$$y_{ij} = a\left(\frac{1}{2} + \frac{\sin B_{ij} \cdot \cos C_{ij}}{\sin\left[180° - \left(B_{ij}+C_{ij}\right)\right]}\right) \; at\ B_{ij} \geq 90° \tag{4}$$

$$z_{ij} = a\frac{\sin B_{ij} \cdot \sin C_{ij} \cdot \sin \sum_{j=i}^{n} \beta_j}{\sin[180° - (B_{ij}+C_{ij})]} \quad (5)$$

The Rotational Body Scanner uses the principle of Dynamic Triangulation Scanner [HYPERLINK \l "16" 8], 9]}. The rotation of the system is given by a shaft-gear mechanism. The horizontal scanning is performed by a step motor which rotates a mirror who reflects the laser beam generated by the laser which is inside of the system bar "a" shown in Fig. 1. As the Dynamic triangulation, our system have a receptor SA (Fig. 3) and consist of 5 main components: A) 45 degree rotational mirror, whose principal function is to direct the laser light beam towards the lenses (targets). B) Targets, whose function is to concentrate the light beam onto photodetector. C) DC Motor, which rotates the mirror. D) Photodetector, it captures the light beam located within the frequency range of the laser. E) Flat Bearing, allows the rotation in the angular axis of the system "   ".

III NEURAL NETWORK TRAINING

To obtain accurate measurements we use the Levenberg-Marquardt algorithm and methodology recognized [HYPERLINK \l "6" 13],14]}, [HYPERLINK \l "7" 15], 16]} to train a neural network, which by the regression method can make an adjustment of our measurements and theoretically approximated to the real value.

The primary application of the Levenberg–Marquardt algorithm is in the least squares curve fitting problem: given a set of m empirical datum pairs of independent and dependent variables, (x_i, y_i), optimize the parameters $\boldsymbol{\beta}$ of the model curve $f(x,\boldsymbol{\beta})$ so that the sum of the squares of the deviations becomes minimal [HYPERLINK \l "11" 17].

$$S(\beta) = \sum_{i=1}^{m} [y_i - f(x_i,\beta)]^2 \quad (6)$$

Like other numeric minimization algorithms, the Levenberg–Marquardt algorithm is an iterative procedure. To start a minimization, we provide an initial guess for the parameter vector, $\boldsymbol{\beta}$.

In each iteration step, the parameter vector, $\boldsymbol{\beta}$, is replaced by a new estimate, $\boldsymbol{\beta} + \boldsymbol{\delta}$. To determine $\boldsymbol{\delta}$, the functions $f(x_i,\beta + \delta)$} are approximated by their linearizations

$$f(x_i,\beta + \delta) \approx f(x_i,\beta) + J_i\delta \quad (7)$$

Where,

$$J_i = \frac{\partial f(x_i,\beta)}{\partial \beta} \quad (8)$$

is the gradient (row-vector in this case) of f with respect to $\boldsymbol{\beta}$.

At its minimum, the sum of squares, $S(\beta)$, the gradient of S with respect to $\boldsymbol{\delta}$ will be zero. The above first-order approximation of $f(x_i,\beta + \delta)$ gives:

$$S(\beta + \delta) \approx \sum_{i=1}^{m} (y_i - f(x_i,\beta) - J_i\delta)^2 \quad (9)$$

Or in vector notation,

$$S(\beta + \delta) \approx ||\mathbf{y} - \mathbf{f}(\beta) - \mathbf{J}\delta||^2 \quad (10)$$

Taking the derivative with respect to $\boldsymbol{\delta}$ and setting the result to zero gives:

$$(\mathbf{J}^\mathbf{T}\mathbf{J})\delta = \mathbf{J}^\mathbf{T}[\mathbf{y} - \mathbf{f}(\beta)] \quad (11)$$

where $\mathbf{J}$ is the Jacobian matrix [16] whose i^{th} row equals J_i, and where $\mathbf{f}$ and $\mathbf{y}$ are vectors with i^{th} component $f(x_i,\beta)$ and y_i, respectively. This is a set of linear equations which can be solved for $\boldsymbol{\delta}$.

Marquardt's contribution [14] is to replace this equation by a "damped version",

$$(\mathbf{J}^\mathbf{T}\mathbf{J} + \lambda\mathbf{I})\delta = \mathbf{J}^\mathbf{T}[\mathbf{y} - \mathbf{f}(\beta)] \quad (12)$$

where $\mathbf{I}$ is the identity matrix, giving as the increment, $\boldsymbol{\delta}$, to the estimated parameter vector, $\boldsymbol{\beta}$.

The (non-negative) damping factor, λ, is adjusted at each iteration. If reduction of S is rapid, a smaller value can be used, bringing the algorithm closer to the Gauss–Newton algorithm, whereas if an iteration gives insufficient reduction in the residual, λ can be increased, giving a step closer to the gradient descent direction. Note that the gradient of S with respect to $\boldsymbol{\beta}$ equals $-2(\mathbf{J}^T[\mathbf{y} - \mathbf{f}(\beta)])^T$. Therefore, for large values of λ, the step will be taken approximately in the direction of the gradient. If either the length of the calculated step, $\boldsymbol{\delta}$, or the reduction of sum of squares from the latest parameter vector, $\boldsymbol{\beta} + \boldsymbol{\delta}$, fall below predefined limits, iteration stops and the last parameter vector, $\boldsymbol{\beta}$, is considered to be the solution.

Levenberg's algorithm has the disadvantage that if the value of damping factor, λ, is large, inverting $\mathbf{J}^T\mathbf{J} + \lambda\mathbf{I}$ is not used at all. Marquardt provided the insight that we can scale each component of the gradient according to the curvature so that there is larger movement along the directions where the gradient is smaller. This avoids slow convergence in the direction of small gradient. Therefore, Marquardt [14] replaced the identity matrix, $\mathbf{I}$, with the diagonal of $\mathbf{J}^T\mathbf{J}$, resulting in the Levenberg–Marquardt algorithm:

$$\mathbf{J}^\mathbf{T}\mathbf{J} + \lambda \mathrm{diag}(\mathbf{J}^\mathbf{T}\mathbf{J}))\delta = \mathbf{J}^\mathbf{T}[\mathbf{y} - \mathbf{f}(\beta)]. \quad (13)$$

IV NEURAL NETWORK SETUP

We use the method mentioned above to train a Neural Network. The trained Neural Network is feedfoward backpropagation type. A feedforward backpropagation neural network consists of two layers. The first layer, or hidden layer, has a *tansigmoid* (tan-sig) activation function, and the second layer, or output layer, has a linear activation function. Thus, the first layer limits the output to a narrow range, from which the linear layer can produce all values. The output of each layer can be represented by [18]:

$$Y_{Nx1} = f(W_{NxM} X_{M,1} + b_{N,1}) \tag{14}$$

Where $\boldsymbol{Y}$ is a vector containing the output from each of the N neurons in a given layer, $\boldsymbol{W}$ is a matrix containing the weights for each of the M inputs for all N neurons, $\boldsymbol{X}$ is a vector containing the inputs, $\boldsymbol{b}$ is a vector containing the biases and $f(\cdot)$ is the activation function [18], [19] . The network was created using the neural network toolbox from Matlab 7.12.0 (The MathWorks, Natick, Mass., USA).

In a backpropagation network, there are two steps during training that are used alternately. The backpropagation step calculates the error in the gradient descent and propagates it backwards to each neuron in the output layer, then hidden layer. In the second step, the weights and biases are then recomputed, and the output from the activated neurons is then propagated forward from the hidden layer to the output layer. The network is initialized with random weights and biases, and was then trained using the Levenberg-Marquardt Algorithm mentioned before [18]**.**

The training data consists of 60 samples from 80 measurements; each sample is taken in cross validation form [20]. I.e. the network was trained to predict the absolute error of x,y,z measurement, for all conditions at once. The length of the training data was 60 points. The network contained 5 neurons, 3 layers and was trained until an acceptable percentage error was achieved. The test data consisted of the remaining 20 samples from each trial. The training is performed with Polak-Ribiére, Quasi-Newton and Levenberg-Marquardt method to compare their performance.

V EXPERIMEANTATION

We decided to test the Levenberg Marquardt method in a 5 different learning rates in a range from 0.2 to 0.9. In each learning rate we calculate the performance 4 times and the average performance is obtained (Table 1). The graphic (Fig. 6) shows in red the actual absolute error of the scanner measurements and in blue the absolute error of the scanner measurement, predicted by the Levenber-Marquardt method used to train the neural network. The aim is that the predicted errors (blue squares of the graphs) are as close as possible to the actual values of error (red circle graphs). Finally the graphic on Fig.7shows the regression plot.

Levenberg-Marquardt					
Learning Rate	Obtained Performances				Average Error Performance
	Take 1	Take 2	Take 3	Take 4	
0.2	7.70E-05	0.000250	0.000166	0.000225	0.0001440
0.4	1.83E-05	0.000842	0.000163	0.002995	0.0008039
0.6	6.61E-05	2.35E-05	0.000304	0.001943	0.0004675
0.8	0.000916	0.000134	0.000443	0.000165	0.0003320
0.9	5.47E-05	5.25E-05	0.000213	0.000498	0.0001636

Table 1. Levenberg-Marquardt Performance Analysis, from .2 of learning rate to .9, running 4 tests for each learning rate.

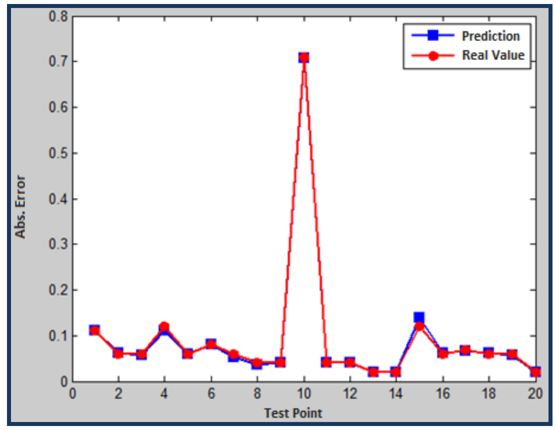

Fig. 6 our predicted error for each sample test point is compared with its real error, the error was predicted using a neural network trained with the Levenberg-Marquardt method.

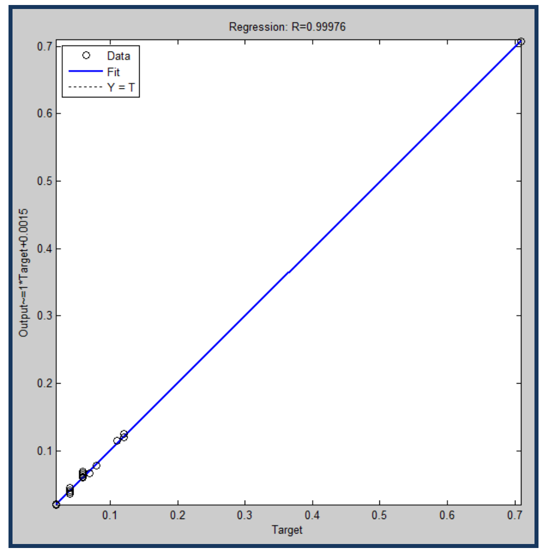

Fig. 7 Regression Plot Fit using Levenberg-Marquardt Method

VI CONCLUSION

The precision of a 3D Laser scanner is a highly important task; therefore having the capability to adjust the scanner measurements by a mathematical algorithm gives us a simple solution to the complex problem of the precision. A Levenberg-Marquardt method was used to train a neural network and adjust the scanner measurements; this method shows a reliability of 99.98% in the measurement adjustment. In addition the Neural Network trained by the Levenberg-Marquardt method shows stability in the error performance at different learning rates. The experimentation shows that our trained Neural Network has a good performance in the measurement adjustment task for this particular laser scanner. However, the testing of the performance of neural networks with different types of laser scanners and the identification of the components that cause the uncertainty of the measurements and the correction of this problem are the task for future research.

VII REFERENCES

[1] D. Hoffmeister, C. Curdt, N. Tilly, and J. Bendig, "3D Terrestrial Laser Scanning for field crop modelling," *Workshop on Remote Sensing*

Methods for Change Detection and Process Modelling, 2011.

[2] Yusuf Arayici, "An approach for real world data modelling with the 3D terrestrial laser scanner for built environment," *Automation in Construction*, vol. 16, no. 6, pp. 816-829, September 2007.

[3] Moises Rivas Lopez, Oleg Sergiyenko, and Vera Tyrsa, "Machine Vision: approaches and limitations," in *Computer Vision*, Xiong Zhihui, Ed. Vienna, Austria: INTECH, 2008, pp. 395-428.

[4] Rajesh Shankarapillai, Manju Ananthakrishnan Nair, Neema Rai, Aditi Mathur, and L.K. Mathur, "Periodontitis Risk Assessment using two artificial Neural Networks-A Pilot Study," *INTERNATIONAL JOURNAL OF DENTAL CLINICS*, vol. 2, no. 4, pp. 36-40, October 2010.

[5] Félix Fernando González-Navarro et al., "Feature and model selection with discriminatory visualization for diagnostic classification of brain tumors," *Neurocomputing*, vol. 73, no. 4-6, pp. 622-632, January 2010.

[6] Alfredo Vellido et al., "Outlier exploration and diagnostic classification of a multi-centre H-MRS brain tumour database," *Neurocomputing*, vol. 72, no. 13-15, pp. 3085-3097, August 2009.

[7] Oleg Sergiyenko et al., "Precise optical scanning for practical multiapplications," in *Proceedings of IEEE-34th Annual Conference of IEEE Industrial Electronics (IECON' 08)*, Orlando, 2008, pp. 1656-1661.

[8] Julio C. Rodriguez, Oleg Yu. Sergiyenko, Vera V. Tyrsa, Luis C. Basaca, and Juan Ivan Hipolito Nieto, "Continuous monitoring of rehabilitation in patients with scoliosis using automatic laser," in *Pan American Health Care Exchanges – PAHCE. Conference*, Rio de Janeiro, 2011, pp. 410-414.

[9] Luis C. Basaca et al., "3D Laser Scanning Vision System for Autonomous Robot Navigation," in *Proceedings of IEEE (ISIE 2010)*, Bari, Italy, 2010, pp. 1773-1779.

[10] Moises Rivas Lopez et al., "Spatial data acquisition by laser scanning for robot SHM task," in *IEEE-IES Proceedings "International Symposium on industrial Electronics" (ISIE 2008)*, Cambridge, 2008, pp. 1458-1463.

[11] Julio C. Rodriguez, Oleg Sergiyenko, Vera Tyrsa, Luis C. Basaca Preciado, and Lopez Moises Rivas, "3D Body & Medical Scanners' Technologies: Methodology and Spatial Discriminations," in *Optoelectronic Devices and Properties*, Oleg Sergiyenko, Ed. Janeza Trdine, Croatia: Intech, 2011, ch. 15, pp. 307-322.

[12] Robert L. Mott, *Machine elements in mechanical design*, 4th ed. California, USA: Pearson Prentice Hall, 2003.

[13] Jorge Nocedal and Stephen J. Wright, *Numerical Optimization*, Peter Glynn and Stephen M. Robinson, Eds. New York, USA: Springer, 1999.

[14] Donald Marquardt, "An Algorithm for Least-Squares Estimation of Nonlinear Parameters," *SIAM Journal on Applied Mathematics*, vol. 11, no. 2, pp. 431-441, 1963.

[15] J. Frederic Bonnans, J. Charles Gilbert, Claude Lamarechal, and Claudia A. Sagastizabal, *Numerical Optimization*, Second Edition ed. Berlin, Germany: Springer, 2006.

[16] Bogdan M. Wilamowski and Hao Yu, "Improved Computation for Levenberg–Marquardt Training," *IEEE Transactions On Neural Networks*, vol. 21, no. 6, pp. 930-937, June 2010.

[17] A. Abba, F. Caponio, A. Geraci, and G Ripamonti, "Non-Linear Least-Squares in FPGA Devices for Digita Spectroscopy," in *Nuclear Science Symposium Conference Record (NSS/MIC)*, Orlando, 2009, pp. 563-568.

[18] *Neural Networks Toolbox Users Guide, The Math Works*. USA, 2000.

[19] A. L. Betker, T. Szturm, and Z. Moussavi, "Application of feedforward backpropagation neural network to center of mass estimation for use in a clinical environment," in *Engineering in Medicine and Biology Society, 2003. Proceedings of the 25th Annual International Conference of the IEEE* , Man., 2003, p. 2714.

[20] Masashi Sugiyama, Matthias Krauledat, and Klaus Robert Muller, "Covariate Shift Adaptation by ImportanceWeighted Cross Validation," *Journal of Machine Learning Research*, pp. 985-1005, May 2007.

Julio C. Rodriguez Quiñonez was born in October, 22, 1985, He received the B.S.. degree in CETYS university, Mexicali, Baja California, Mexico, in 2007. Currently he studies a Ph.D. in Optoelectronics at the Engineering Institute of the Baja California Autonomous University and also teaches the courses Analog Control at UVM University.

He has written 2 book chapters and 6 Journal and Proceedings Conference papers including International Congresses like ISIE and IECON in Italy, USA, Brazil and Mexico and holds 2 Patents in Mexico. Since 2010 to date collaborated as a reviewer of the journal transaction on mechatronics.

Oleg Yu. Sergiyenko (M'09-09) was born in February, 9, 1969. He received the B.S., and M.S., degrees in Kharkiv National University of Automobiles and Highways, Kharkiv, Ukraine, in 1991, 1993, respectively. He received the Ph.D. degree in Kharkiv National Polytechnic University on specialty "Tools and methods of non-destructive control" in 1997.

He has editor of 1 book, written 4 book chapters, 57 papers and holds 1 patent of Ukraine. Since 1994 till the present time he was represented by his research works in several International Congresses of IEEE, ICROS, SICE, IMEKO in USA, England, Japan, Italy, Ukraine, and Mexico.

Dr.Sergiyenko in December 2004 was invited by Engineering Institute of Baja California Autonomous University for researcher position. He is currently Head of Applied Physics Department of Engineering Institute of Baja California Autonomous University, Mexico, director of several Masters and Doctorate thesis. He was a member of Program Committees of various international and local conferences. He is member of Scientific Council on Electric specialties in Engineering Faculty of Autonomous University of Baja California. Included in the 2010-2012 Edition of Marquis' Who's Who in the World.

Luis Carlos Básaca Preciado was born October 25, 1985. He received a B.S. degree in Cybernetics and Electronics Engineering from CETYS University, Mexicali, Baja California, Mexico in 2007. Currently he studies a Ph.D. in Optoelectronics at the Engineering Institute of the Baja California Autonomous University and also teaches the courses of Robotics and Sensors & Actuators at CETYS University.

He has written 2 book chapters and 6 Journal and Proceedings Conference papers including International Congresses like ISIE and IECON in Italy, USA, Brazil and Mexico and holds 2 Patents in Mexico.

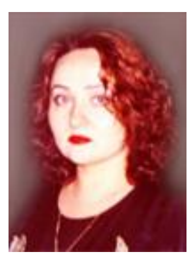

Vera V. Tyrsa was born on July, 26, 1971. She received the B.S., and M.S., degrees in Kharkiv National University of Automobiles and Highways, Kharkiv, Ukraine, in 1991, 1993, respectively. She received the Ph.D. degree in Kharkiv National Polytechnic University on specialty "Electric machines, systems and networks, elements and devices of computer technics" in 1996.

In April 1996, she joined the Kharkiv National University of Automobiles and Highways, where she holds position of associated-professor of Electrical Engineering Department (1998-2006).

She has written 3 book chapters, more than 20 papers and holds 1 patent of Ukraine. From 1994 till the present time she was represented by her research works in several International Congresses in USA, England, Italy, Japan, Ukraine, and Mexico.

In November 2006 was invited by Polytechnic University of Baja California for professor and researcher position.

Optimization of laser TVS for robot navigation using combined scanning with variable step

X.M. García-Cruz, O. Yu. Sergiyenko, D. Hernández-Balbuena
M. Rivas López, Luis C. Basaca, Julio Rodriguez, V. V. Tyrsa, P. L.A. Rosas-Méndez

***Abstract*— Many approaches to 3D object recognition have been proposed in a robot navigation task; but often they still use complex and time consuming techniques. We propose a low-cost technical vision system (TVS) for 3D data acquisition and fast surface detection by digitized points keeping Cartesian coordinates matrix. There are presented computer simulation of the laser scanning process using various scenes of scanning with different values of angular pitch, but with constant step in each scanning cycle. Analysis of simulation results shows the most critical (singular) angles, in order to reach different desired properties of each scan of FOV. Basing on this simulation results the construction of small-scale electro-mechanic transmission for TVS have been proposed.**

***Index Terms*—Dynamic triangulation, simulation, electromechanically design.**

I. Introduction

The robotic navigation task actually is an important field research around the word that is the reason of this article, focus on robotic navigation to unknown surfaces, and the simulation will be done on a rough terrain with obstacles presents. A good example is the navigation of mobile robot (MR) on another planet. However, by now such systems are in the design widely in terrestrial (indoor and outdoor) applications. Actuality the wireless location systems based on GSM and CDMA2000 communication systems, including Cell Identity (Cell-ID), Angle of Arrival (AOA) and Time-Difference of Arrival (TDOA) can provide good signal availability. But they fail to provide satisfactory high-accuracy positioning services since these communication systems are not designed for navigation [1].

As we see on [2-4], there are now some systems based on surface reconstruction and navigation using GPS. In these kind of systems good records and a high precision readings doing a static resolution can find but dynamic error for a GPS system results are unpredictable, those systems give us least information compared with radars, scanners and some sensors. As is mention on [5] GPS system needs a satellite constellation for its function, hence cannot be useful for mobile robot navigation on an unknown planet terrain [6].

Generalization of a planar camera image to a three-dimensional (3D) format is straightforward [7], since salient groupings in 3D can be detected by the human sight system based on the same principles.

This is the basis of the approach to stereo vision, where the main premise is that correct pixel correspondences are reconstructed in the form of 3D salient surfaces, while wrong correspondences are not well aligned and do not form any coherent structures.

The term “saliency” is used in papers dealing with “pattern recognition by cameras” to indicate the quality of features to be important, stand out conspicuously, be prominent, and attract our attention. The definition of saliency is that of structural saliency, which is a product of proximity and good continuation [7] or the property to attract attention due to reasons that include novelty and disagreement with surrounding elements [8]. For good saliency, however, these systems must be preliminary calibrated, i.e., self-located properly, positioned in a defined coordinates system, preliminary related to a certain scale, etc. Therefore, this group of technical devices is unacceptable for using in an unknown terrain with arbitrary initial positioning.

We can see on [11] the existence of systems using two cameras to detecting obstacles in a specific area as Lipnickas and Knyš[12] proposed. For reconstruct a 3D scene from navigation robots, but the algorithms used for the mentioned operations do not provide high accuracy. This method is not de best option for obstacle detection [12], other systems for detection obstacles can find on [13].

II. Technical Vision System

Our work is based on a dynamic triangulation in order to obtain 3D coordinates of objects or obstacles based on mobile robot vision, as shown in Figure 1. [11], a laser beam is projected by a mechanism transmitter (which be called Positioning Laser (PL)) onto obstacle surface reflecting back laser beam into revolving sensor inside witch be called Scanning Aperture (SA) [10, 14-17].

ROC&C’2011 – CP-34 PONENCIA RECOMENDADA
POR EL COMITÉ DE COMPUTACIÓN DEL
IEEE SECCIÓN MÉXICO Y PRESENTADA EN LA
REUNIÓN DE OTOÑO, ROC&C’2011, ACAPULCO, GRO.,
DEL 27 DE NOVIEMBRE AL 3 DE DICIEMBRE DEL 2011.

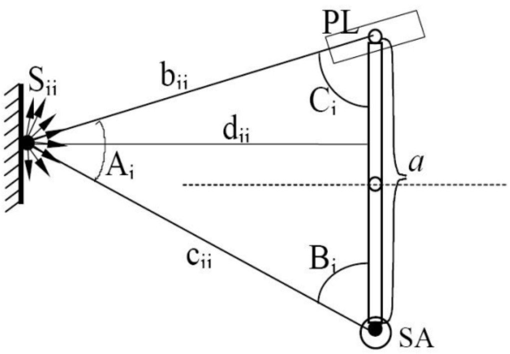

Figure 1 Dynamic Triangulation [6]

In this project simulation the velocity have been optimized in comparison on [11, 18] were the scanner velocity is lower. The current simulation project was done on MATLAB for a scene considering different steps angles that with the objective to find the optimal array system. If we see in the area of navigation the decisions upcoming from the time of landing up to the Moon of the mobile robot, then the principal beginnings of similar systems construction are established [6].

III. Description the Effect of Recent System

Our recent system runs on a computer whit an Intel Pentium three hundred MHz using a program developed in turbo C + +, which uses the interface parallel port that has the ability to transfer data at two Mb/s for communication an control governing the motors speed and the scanning to the system[6].

As mentioned in [5, 6] the system in application to mobile robot navigation has a disadvantage: loss of time in a high resolution scanning which represents the best opportunity of improvement; optimizing the scanning ride to detect on obstacle detection.

The system has Positioning Laser (PL) and Scanning Aperture (SA), that method Dynamic Triangulation due the fact that the position laser has the ability to rotate and redirect the laser beam in 180° theoretically and (SA) rotates 360° at a constant speed, meaning the TVS has two dynamic angles [18], with this system is possible to obtain any point in front of the mobile robot as seen on Figure 2.

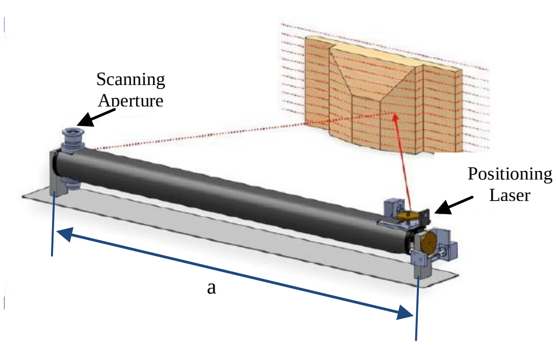

Figure 2 Prototype II

The next equations represent the triangulation on 3D scanning process, showing the angles values of B_{ij}, C_{ij} (Fig.1), $\sum_{j=1}^{j} \beta_j$ (Figure 3) and the value of constant ¨a¨ (Figure 2), is possible to calculate the Cartesian coordinates for each of the points scored by the laser, Figure 3 shows application of these formulas (1), (2), (3), (4).

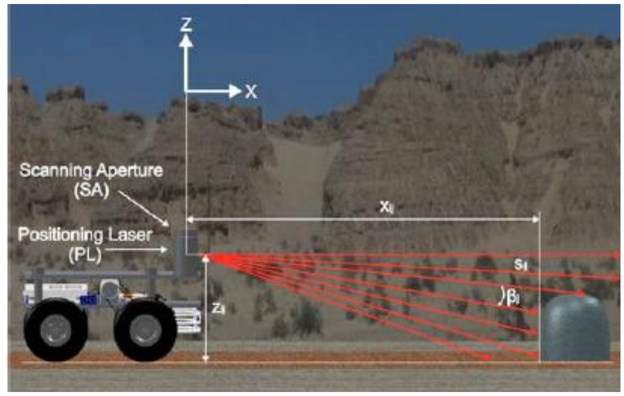

Figure 3 Prototype II, side view [18].

We calculate the 3D coordinates for each highlighted point with the following formulas:

$$x_{ij} = a\frac{Sin\ B_{ij} * Sin\ C_{ij} * Cos\ \sum_{j=1}^{j}\beta_j}{Sin\left[180° - \left(B_{ij} + C_{ij}\right)\right]} \tag{1}$$

$$y_{ij} = a\left(\frac{1}{2} - \frac{Sin\ B_{ij} * Cos\ C_{ij}}{Sin\left[180° - \left(B_{ij} + C_{ij}\right)\right]}\right)\ at\ B_{ij} \le 90° \tag{2}$$

$$y_{ij} = -a\left(\frac{1}{2} + \frac{Sin\ B_{ij} * Cos\ C_{ij}}{Sin\left[180° - \left(B_{ij} + C_{ij}\right)\right]}\right)\ at\ B_{ij} \ge 90° \tag{3}$$

$$z_{ij} = a\left(\frac{Sin\ B_{ij} * Sin\ C_{ij} * Sin\ \sum_{j=1}^{j}\beta_j}{Sin\left[180° - \left(B_{ij} + C_{ij}\right)\right]}\right) \tag{4}$$

IV. Mechanical Load of the System

In this part mechanical constitution system, parameters and operation will be explained. PL and SA are communicated for a hollow shaft, on PL has a mechanism to control the laser (as seen on Figure 4 and 5); the time optimization of this operation is the main task of the project.

The system has a anti-backlash gear 48 pitch 0.104¨ face width 20° pressure angle, 96 teeth, P.D 2.0000, gears 303 stainless steel, 2024-T4 Aluminum, hubs 303 stainless steel, the worm wheel has 48 pitch 20° pressure angle, right hand double thread, the material it makes bronze ASTM B21 alloy 464, the gear and worm wheel were manufactured by PIC DESIGN. In the Figure 5 we can see a top view for the system and a 12 VDC bipolar stepper motor with steep angle 1.8°, holding torque 2100 g-cm, 200 steps per revolution and is manufactured by JRP.

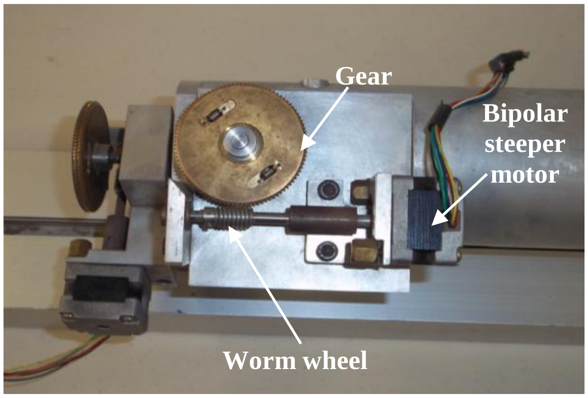

Figure 4 Position Laser (PL), side view.

The worm wheel friction consumes a significant portion of the power because the principal application is to transmit large efforts [9].

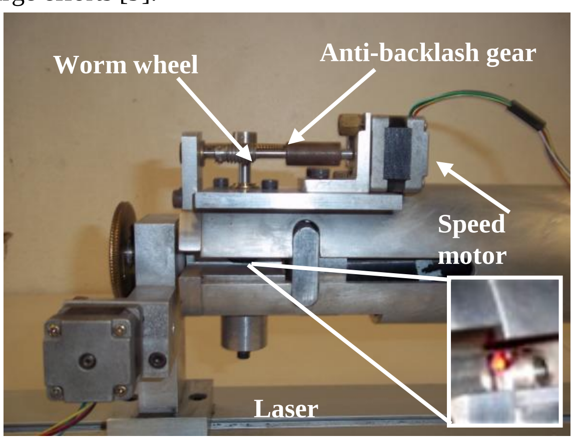

Figure 5 Position Laser (PL), top view.

The system has only one speed. On Figure we show de speed flow and how it works.

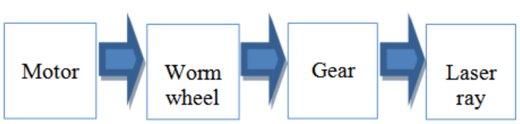

Figure 6 Speed flow in the (PL).

V. 5. Virtual Analysis of Parameters for Optimizing Scanning Time

The simulation in MATLAB was mainly for description and characterization of the proposed averaged scenario with 4 obstacles and the length of the scanner´s ray of 15m varying the scanning angle value ΔΘ=0.45°and the length robot bar system have 1m. The prototype II using a stepper motor with the steep angle 1.8° that is the reason the simulation begin on 1.5° (due to worm wheel step reduction) and finish at 15° because at this angle don't obtain important information of the points in obstacles (see Table 1) and the Figures 7a-c shows the ray detected a dangerous obstacle.

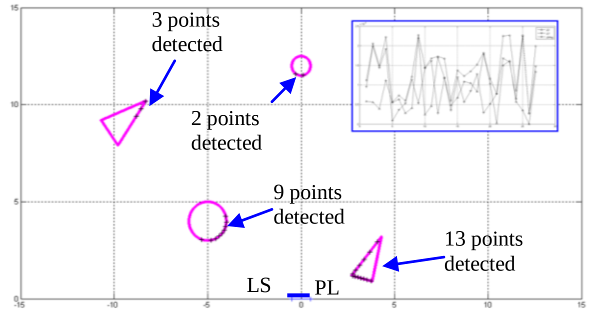

Figure 7a Simulation #2 with 1.95° 0.083 s scanning time and detected 27 points.

We can observe figure 7a, b, c, at the top right corner of the graphic the error between the natural laser trace discretization and the obstacle contour discretization during MATLAB simulation. Maximum error detect was $2.5X10^{-3}$ in the intersection of points between obstacles contour and the laser beam. In conclusion the error is minimizing with a larger angle step than a smaller angle step.

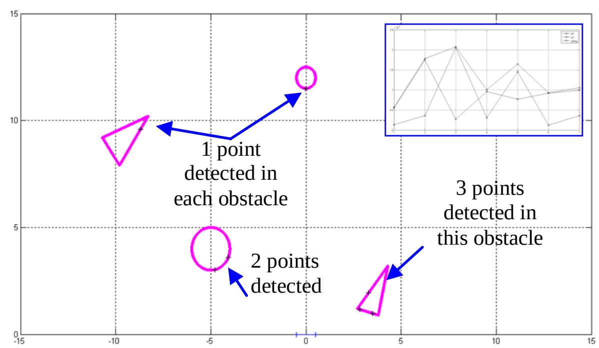

Figure 7b Simulation #16 with 8.25° 0.02 s scanning time and detected 7 points.

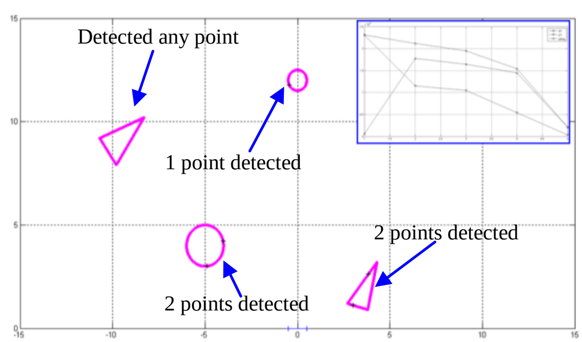

Figure 7c Simulation #29 with 14.1°, 0.012 s scanning time and detected 5 points, but not detecting the obstacle located at the dead zone.

The follow results were obtained:

Table 1 SIMULATION RESULTS

No. of runs	Opening angle, degrees	Scannin g time, s	Detecte d points
1	1.5	0.107	34
2	1.95	0.083	27
3	2.4	0.067	21
4	2.85	0.057	17
5	3.3	0.049	16
6	3.75	0.043	13
7	4.2	0.039	12
8	4.65	0.035	11
9	5.1	0.032	9
10	5.55	0.029	10
11	6	0.027	9
12	6.45	0.025	9
13	6.9	0.024	8
14	7.35	0.022	8
15	7.8	0.021	6
16	8.25	0.02	7
17	8.7	0.019	6
18	9.15	0.018	6
19	9.6	0.017	5
20	10.05	0.016	5
21	10.5	0.016	5
22	10.95	0.015	4
23	11.4	0.015	4
24	11.85	0.014	5
25	12.3	0.014	4
26	12.75	0.013	4
27	13.2	0.013	3
28	13.65	0.012	5
29	14.1	0.012	5
30	14.55	0.011	3
31	15	0.011	3

The table 1 shows on simulations numbers 22, 25, 26, 27, 30 and 31, no detected a dangerous obstacle for the robot.

Analyzing Figures 7a, b, c and the table 1 it is possible to say that at lower step-angle are obtained more points on the contour of the each obstacle and more time for full scenario scanning consumed, versus higher angle gives fewer points and less time for complete scanning.

Observing the graphics results it is possible to conclude that three angles among others are singular in meaning to optimize time (minimize it with guaranteed accuracy of dangerous obstacle detection) of our scanner functioning.

Using only one angle steep the time optimization couldn´t be done based on actually prototype II operation. The maximum time optimizations were show at runs 2, 16, 29 were the scanning systems detecting a major number of obstacles in a lower time rate. You can see the performance of this runs at figure 8b and how they presents shorter time with a more obstacles readings.

Figure 8a displays scanning time versus detected points. With a large scanning time more points were detected.

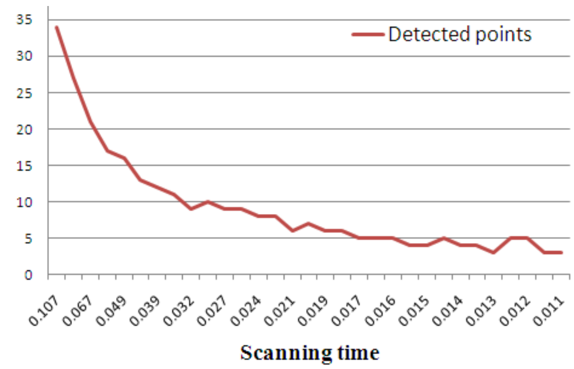

Figure 8a Scanning time vs. detected points.

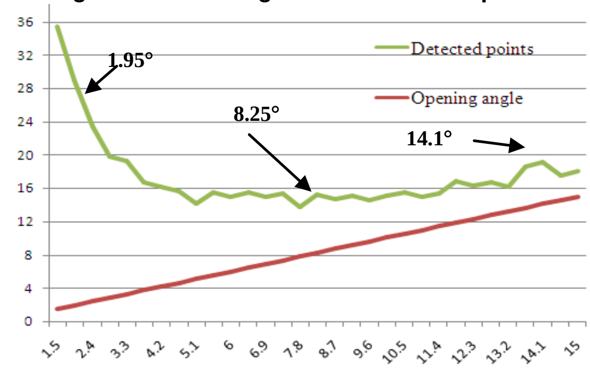

Figure 8b Detected points vs. opening angles.

In Figure 8b the results shows that a higher angle less points were detected; three of the optimized angles listed in the Figure (8b).

For the discretization of laser ray at MATLAB program the following model based on Euler´s identity was used:

$$A\ e^{i\Theta} = A\cos\Theta + i\ \mathrm{sen}\ \Theta \tag{5}$$

The line equations were used in order to draw a triangle and using the next three equations:

$$y_{r1} = \frac{(y_1 - y_2)}{(x_1 - x_2)}(x - x_1) + y_1 \tag{6}$$

$$y_{r2} = \frac{(y_2 - y_3)}{(x_2 - x_3)}(x_2 - x_1) + y_2 \tag{7}$$

$$y_{r3} = \frac{(y_1 - y_3)}{(x_1 - x_3)}(x_3 - x_1) + y_3 \tag{8}$$

Where x1, x2, x3 and y1, y2, y3 are Cartesian coordinates of the triangle vertexes. And yr1, yr2, yr3 are equations of the lines of triangle.

For modeling the circle we proposed a radio (r) center (C), and discretization of the circle (DC) in grades, and using the next equations:

$$\Delta\alpha = \left(\frac{DC \times \Pi}{180^\circ}\right) \tag{9}$$

The angle α beginning at $\Delta\alpha$ with increments of $\Delta\alpha$ to 2Π:

$$Circle_n = C + re^{j*\alpha} \tag{10}$$

VI. TRANSMISSION DESIGN TO PROVIDE A COMBINED STEP ANGLE OF THE SCANNING

Nowadays, one of the most crucial constrain of any autonomous system is energy save, especially like as in our system (Figure 9) for example: where it is possible save time and electrical resource making variable combined step, minimizing electricity consuming cycle in total. On Figure 9 we will see the diagram beginning with the dynamic triangulation, witch its connected to subsystem automatic sweep control witch feedback In Figure 8b the results shows that a higher angle less dynamic triangulation, also (DT) or (TVS) is connected electro-mechanical variable pitch sweep, feeding information to the subsystem next we proposed:

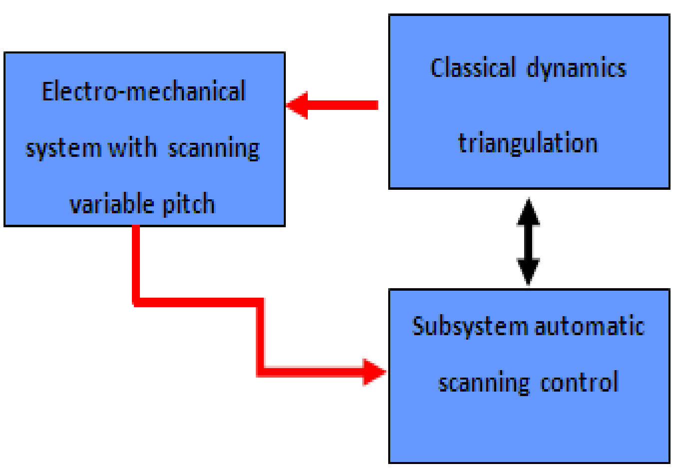

Figure 9 Core of the proposed on Position Laser (PL).

For the electro-mechanical system with scanning variable pitches the technologies existing. One of them we can utilize in order to provide a variable pitch of scanning in our system with the aim to combine a scanning pitch according to simulation results, using a certain mix of three previously mentioned angles values. We are proposed an ideal transmission as dual clutch transmissions (DCT) represent an example of these efforts, since they allow obtaining torque transfer from one clutch to another without interrupting traction, thanks to the controlled slippage of the clutches.

The two clutches are engaged alternatively in different gears and power transmission continues during a shift through the control of clutches torques.

A shift process involves the engagement of the oncoming clutch and the disengagement of the off-going clutch.

From a kinematic point of view, gear shifting of a dual clutch transmission is similar to that of a clutch-to-clutch shift in a conventional automatic transmission (AT) are equipped with torque converters that dampen shift transients the precise torque control is required to achieve launch and shift smoothness of DCT applying in to PL due to the absence of both torque converter and one-way clutches [10].

The ideal transmission proposes an automated DCT, and a primary clutch for odd relationships and a secondary clutch peer relation, an electric start saving energy, those parameters are applying to vehicles but the same idea it will be apply to PL. The scheme of such device is presented on Figure10.

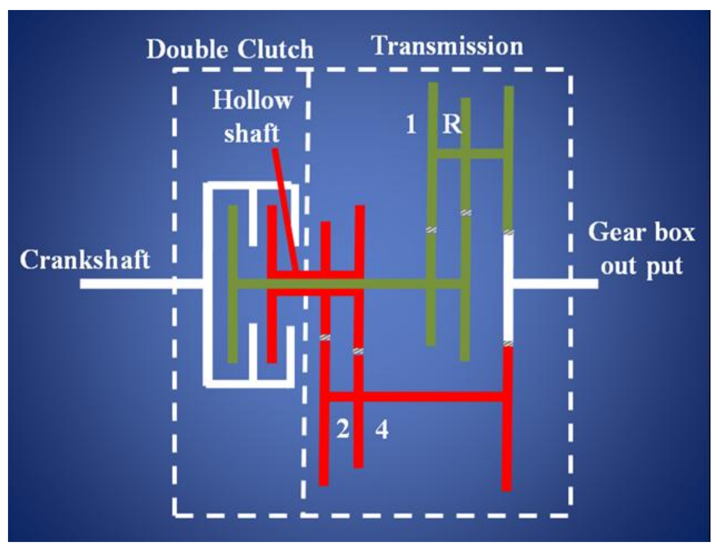

Figure 10 Dual clutch transmissions (DCT).

This proposed ideal transmission will be guaranteed the optimize time, energy and mechanical maintenance; however their efficiency is still greater than that automatic transmissions with torque converter and continuously variable transmissions [10].

The proposal transmissions have three forward speeds and a reverse speed. The transmissions input shafts will be designed as “quill-shafts”, with one solid shaft positioned inside another hollow shaft. The solid shaft carries on it the first and the reverse gear, while the hollow shaft carries the second, fourth gear [19].

We proposed the gear box will be located as a Figure 11.

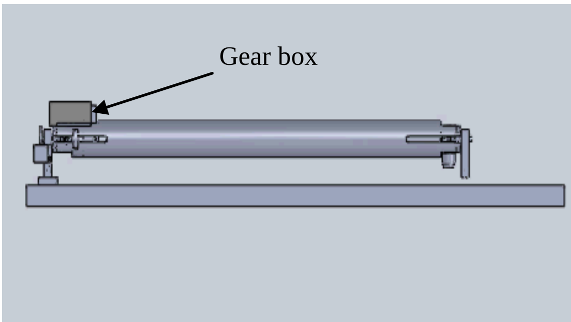

Figure 11 Prototype II with the gear box proposal.

VII. Conclusion

Assuming all mentioned we can state the next. All known laser scanning systems [2, 5, 6, 7, 11, 13, 14, 17and 18] using the constant scanning step is not efficient to robot navigation task. The most proper way to provide scanning for robot application is the combined scanning pitch. It permits optimize (minimize) scanning time with guaranteed detection of the critical obstacles inside the defined robot’s field of view. Also it permits to detect such obstacles as soon as possible, at the same time detecting with higher accuracy only (!) the most close to robot’s planned trajectory border of obstacle. For this technical task the most important question is the value of such typical angles which are permitting to combine (mix) search in a shortest time without required accuracy loss.

Present work is answering this question by our simulation results. Basing on such results, we are offer the tentative construction of such electromechanical transmission. It can permit to optimize TVS functioning by minimal time criteria.

VIII. References

[1] A. H. Sayed, A. Tarighat, and N. Khajehnouri, 2005*, ″Network-Based Wireless Location: Challenges Faced in Developing Techniques for Accurate Wirelees Location information,″* IEEE Signal Process. Mag. 22 (4), 24-40.

[2] Y. Hada. and K. Takase, “Multiple Mobile Robot Navigation Using the Indoor Global Positioning System (iGPS),” in *Proc. of the IEEE/RSJ Int. Conf. on Intelligent Robots and Systems* (Maui, USA, 2001), Vol. 2, pp. 1005–1010

[3] M. Petrov, A. Talapov, T. Robertson, et al., “Optical 3D Digitizers] M P: Bringing Life to the Virtual World,” IEEE Comput. Graph. Appl. **18** (3), 28–37 (1998).

[4] C. Kee, B. Park, J. Kim, et al., “A Guideline to Establish DGPS Reference Station Requirements,” J. Navigation **61** (1), 99–114 (2008).

[5] M. Rivas Lopez, Oleg Sergiyenko, Vera Tyrsa. “Computer vision” book. Edited by Xiong Zhihui, Chapter 22 “Machine vision: approaches and limitations”, pp. 395-428. Editorial: I-TECH, Vienna, Austria, 2008, 538 p.

[6] O. Yu. Sergiyenko 2010 *Optoelectronic System for Mobile Robot Navigation* Automatic Control Systems in Scientific Research and Industry. Optoelectronics, Instrumentation and Data Processing, Vol.46. No. 5, pp. 414-428 ISSN 8756-6990

[7] Philippos Mordohai and Gerard Medioni. Tensor Voting: A Perceptual Organization Approach to Computer Vision and Machine Learning, Morgan & Claypool Publishers, 2006 - 136p.

[8] L. Itti and P. Baldi (2005). A principled approach to detecting surprising events in video. Proceedings of IEEE CVPR2005 *International Conference on Computer Vision and Pattern Recognition* vol. 1, 20-25 June 2005 pp631-637.

[9] Robert L. Norton Design of machinery: an introduction to the synthesis of mechanisms and machines McGraw-Hill series in mechanical engineering 3 edition, 2005 ISBN 970-10-465-0.

[10**]** E. Galvagn, M. Velardocchia and A. Vigliani**,** *Dynamic kinematic model of a dual clutch transmission.* Mechanism and Machine Theory 46 2011) 794–805 Elsevier, C.so Duca degli Abruzzi, 24-10129 Torino, Italy

[11] Basaca L.C.; Rodriguez, J.; Sergiyenko, O.Yu.; Tyrsa, V.V.; Hernández, W.; Hipólito, J.I.N.; Starostenko, O.; *3D Laser Scanning Vision System for Autonomous Robot Navigation* , IEEE International Symposium on Industrial electronics (ISIE-2010), Bari Italy, July 4-7 p. 1773

[12] A. Lipnickas, and A. Knyš. 2009. “A Stereovision System for 3-D, Perception." Electronics & Electrical Engineering, no. 91: 99-102. 1392-1215.

[13] Andersen, Jens Christian Morten Rufus Blas, Ole Ravn, Nils A. Andersen, and Mogens Blanke. 2006. "Traversable terrain classification for outdoor autonomous robots using single 2D laser scans." Integrated Computer- Aided Engineering 13, no. 3: 223-232. ISSN: 10692509

[14] Oleg Sergiyenko, et al. Precise Optical Scanning for practical multiapplications. Proceedings of IEEE 34th Annual IEEE Conference IECON’08, Florida, USA, 2008, p. 1656-1661

[15] Raymond A. Serway, “Physics: for Scientists and Engineers with Modern Physics” 3rd Edition, Updated Printing, Philadelphia: Saunders, 1990, 1253p

[16] Eugene Hecht,”Physics”, Pacific Grove, California: Brooks/Cole, 1994:1128p.

[17] Moisés Rivas, Oleg Sergiyenko, Mario Aguirre, Luis Devia, Vera Tyrsa and Ismael Rendón. Spatial data acquisition by laser scanning for robot or SHM task. IEEE-IES Proceedings “International Symposium on Industria Electronics”(ISIE-2008), Cambridge, United Kingdom, June - July, 2008, pp.1458-1463.

[18] Basaca, L.C.; Rodriguez, J.; Sergiyenko, O.Yu.; Tyrsa, V.V.; Hernandez, W.; Hipólito, J.I.N.; Starostenko, O.; *Resolution improvement of Dynamic Triangulation method for ·D Vision System in Robot Navigation task* IECON 2010 - 36th Annual Conference on IEEE Industrial Electronics Society 7-10 Nov. 2010 Glendale, AZ, p2884

[19] **Manish Kulkarni, Taehyun Shim and Yi Zhang** “*Shift dynamics and control of dual-clutch transmissions”* Elsevier Mechanism and Machine Theory Volume 42, Issue 2, February 2007, Pages 168-182

IX. Resume

Xóchitl Maria García Cruz was born in October 19, 1978. She received the B.S. and M.S. degrees in Mexicali Institute Technologic, México in 2001, 2009 respectively.

M.I. Xóchitl García since 1997 has been working at Metal-Mechanical Industry. In August 2008 was invited by Polytechnic University of Baja California, Mexico and Mexicali Institute Technologic, México, for professor researcher position.

Now she works toward her PhD thesis. Her research interests are in the areas of mechanical, aerospace, robotic, electronics.

3D Body & Medical Scanners' Technologies: Methodology and Spatial Discriminations

Julio C. Rodríguez-Quiñonez[1], Oleg Sergiyenko[1], Vera Tyrsa[2], Luís C. Básaca-Preciado[1], Moisés Rivas-Lopez[1], Daniel Hernández-Balbuena[1] and Mario Peña-Cabrera[3]
[1]*Autonomous University of Baja California, Mexicali-Ensenada,*
[2]*Polytechnic University of Baja California, Mexicali,*
[3]*Research Institute of Applied Mathematics and Systems (IIMAS – UNAM)*
Mexico

1. Introduction

Medical practitioners have traditionally measured the body's size and shape by hand to assess health status and guide treatment. Now, 3D body-surface scanners are transforming the ability to accurately measure a person's body size, shape, and skin-surface area (Treleaven & Wells, 2007) (Boehnen & Flynn, 2005). In recent years, technological advances have enabled diagnostic studies to expose more detailed information about the body's internal constitution. MRI, CT, ultrasound and X-rays have revolutionized the capability to study physiology and anatomy in vivo and to assist in the diagnosis and monitoring of a multitude of disease states. External measurements of the body are more than necessary. Medical professionals commonly use size and shape to production of prostheses, assess nutritional condition, developmental normality, to analyze the requirements of drug, radiotherapy, and chemotherapy dosages. With the capability to visualize significant structures in great detail, 3D image methods are a valuable resource for the analysis and surgical treatment of many pathologies.

Taxonomy of Healthcare 3D Scanning applications				
Application	**Epidemiology**	**Diagnosis**	**Treatment**	**Monitoring**
Size	Anthropometric surveys	Growth defects	Scoliosis	Fitness and diet
Shape	Screening	Abdominal shape	Prosthetics	Obesity
Surface area		Lung volume	Drug dosage	Diabetes
Volume	Eczema		Burns	
Head Visualization		Melanomas	Eating disorders	
Chest Visualization			Facial reconstruction	
Hole Body Visualization			Cosmetic surgery	

Table 1. Taxonomy of Healthcare 3D Scanning applications

1.1 Scanning technologies

Three-dimensional body scanners employ several technologies including 2D video silhouette images white light phase measurement, laser-based scanning, and radio-wave linear arrays. Researchers typically developed 3D scanners for measurement (geometry) or visualization (texture), using photogrammetry, lasers, or millimeter wave (Treleaven & Wells, 2007).

Taxonomy of 3D Body Scanners		
Technique	**Measurement**	**Visualization**
Millimeter Wave	Radio Waves	
Photogrammetry	Structured light Moire fringe contouring Phase – measuring profilometry	Close-range photogrammetry Digital surface photogrammetry
Laser	Laser Scanners Laser range Scanners	

Table 2. Taxonomy of 3D Body Scanners

In the following section it will be described the diverse measurement techniques (see table 2) used in medical and body scanners. Listing applications, scanners types and common application areas, as well of how they operate.

2. Millimeter wave

Millimeter wave based scanners, send a safe, lower radio wave toward a person's fully clothed body; most of the systems irradiate the body with extremely low-powered millimeter waves a class of non-ionizing radiation (see Figure 1) not harmful to humans. The amount of radiation emitted in the millimeter-wave range is 10^8 times smaller than the amount emitted in the infrared range. However, current millimeter-wave receivers have at least 10^5 times better noise performance than infrared detectors and the temperature contrast recovers the remaining 10^3. This makes millimeter-wave imagine comparable in performance with current infrared systems.

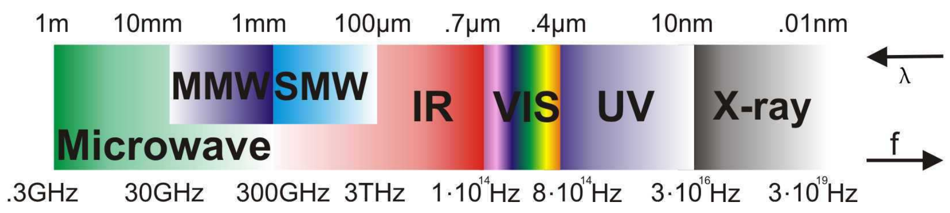

Fig. 1. Electromagnetic spectrum showing the different spectral bands between the microwaves and the X-rays

Millimeter (MMW) and Submillimeter (SMW) waves fill the gap between the IR and the microwaves (see Figure 1). Specifically, millimeter waves lie in the band of 30-300 GHz (10-1 mm) and the SMW regime lies in the range of 0.3-3 THz (1-0.1 mm). MMW and SMW radiation can penetrate through many commonly used nonpolar dielectric materials such as paper, plastics, wood, leather, hair and even dry walls with little attenuation (Howald et al., 2007) (Liu et al., 2007). Clothing is highly transparent to the MMW radiation and partially transparent to the SMW radiation (Bjarnason et al., 2004). Consequently, natural applications of MMW and SMW imaging include security screening, nondestructive inspection, and medical and biometrics imaging. Low visibility navigation is another application of MMW imaging

Is also true that MMW and SMW open the possibility to locate threats on the body and analyze their shape, which is far beyond the reach of conventional metal detection portals. A recently demonstrated proof-of-concept sensor developed by QinetiQ provides video-frame sequences with near-CIF resolution (320 x 240 pixels) and can image through clothing, plastics and fabrics. The combination of image data and through-clothes imaging offers potential for automatic covert detection of weapons concealed on human bodies via image processing techniques (Haworth et al., 2006). Other potential areas of application are mentioned below.

Medical: provide measurements of individuals who are not mobile and may be difficult to measure for prosthetic devices.

Ergonomic: provide measurements and images for manufacturing better office chairs, form-fitting car and aviation seats, cockpits, and custom sports equipment.

Fitness: provide personal measurements and weight scale for health and fitness monitoring.

2.1 3D Body millimeter wave scanner: Intellifit system

The vertical wand in the Intellifit system (see Figure 2) contains 196 small antennas that send and receive low-power radio waves. In the 10 seconds it takes for the wand to rotate around a clothed person, the radio waves send and receive low-power signals. The signals don't "see" the person's clothing, but reflect off the skin, which is basically water (Treleaven & Wells, 2007). The technology used with the Intellifit System is safer than using a cell phone. The millimeter waves are a form of non-ionizing radiation, which are similar to cell phone signals but less than 1/350th of the power of those signals, and they do not penetrate the skin. When the wand's rotation is complete, Intellifit has recorded over 200,000 points in space, basically x, y, and z coordinates. Intellifit software then electronically measures the "point-cloud", producing a file of dozens of body measurements; the raw data is then discarded.

Fig. 2. Intellifit System, cloth industry application and point cloud representation of the system

Although the system is functional to obtain a silhouette of the body, object detection as a security system and as a tool in the cloth design industry, the problem of this system is the inaccurate measurements that are closed to 1cm, which makes the system not appropriate for medical applications.

3. Photogrammetry

Photogrammetry is the process of obtaining quantitative three-dimensional information about the geometry of an object or surface through the use of photographs (Leifer, 2003). Photogrammetric theories have on a long history of developments for over a century. Intensive research has been conducted for the last 20 years for the automation of information extraction from digital images, based on image analysis methods (Emmanuel, 1999). In order for a successful three-dimensional measurement to be made, targeting points, each of which is visible in two or more photographs, are required. These targets can be unique, well-defined features that already exist on the surface of the object, artificial marks or features attached to the object, or a combination of both types. The accuracy of the reconstruction is directly linked to the number and location of the targets, as well as number of photographs and camera positions chosen. Intricate objects generally require more targets and photographs for a successful reconstruction than do flat or near-flat surfaces. (Leifer, 2003). The latest shift in photogrammetry has been the passage to fully digital technologies. In particular, low cost digital cameras with high pixel counts (> 6 mega-pixels image sensors), powerful personal computers and photogrammetric software are driving a lot of new applications for this technology. (Beraldin, 2004). As shown in Table 2, the measurement photogrammetry techniques can by refer as show below.

3.1 Structured-light systems

One of the simplest systems consists of a projector that emits a stripe (plane) of light and a camera placed at an angle with respect to the projector as shown in Figure 3. At each point

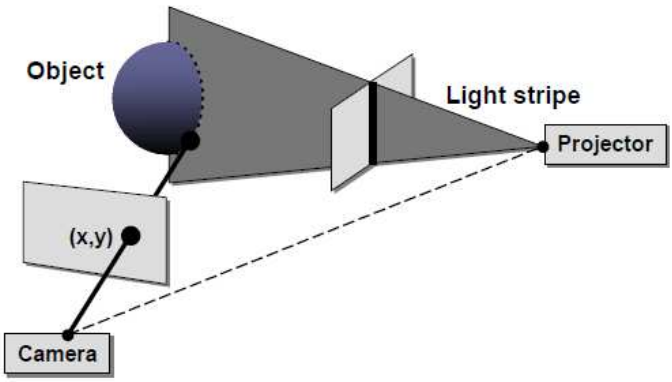

Fig. 3. Schematic layout of a single-camera, single-stripe-source triangulation system

in time, the camera obtains 3D positions for points along a 2D contour traced out on the object by the plane of light. In order to obtain a full range image, it is necessary either to sweep the stripe along the surface (as is done by many commercial single-stripe laser range scanners) or to project multiple stripes. Although projecting multiple stripes leads to faster data acquisition, such a system must have some method of determining which stripe is which (Rusinkiewicz et al., 2002). There are three major ways of doing this: assuming surface continuity so that adjacent projected stripes are adjacent in the camera image, differentiating the stripes based on color, and coding the stripes by varying their illumination over time. The first approach (assuming continuity) allows depth to be determined from a single frame but fails if the surface contains discontinuities. Using color allows more complicated surfaces but fails if the surface is textured. Temporal stripe coding is robust to moderate surface texture but takes several frames to compute depth and, depending on the design, may fail if the object moves (Rusinkiewicz et al., 2002).

3.1.1 Body and medical 3D structured light scanner: Formetric 3D/4D

The system Formetric 3D/4D is based on structured light projection. The scanning system consists of four main components: electro-mechanical elevating column for height adjustment, projector, camera and software. The projection unit emits a white light grid onto the dorsal surface of the patient standing in a defined way toward the projection device, which then obtains measuring data on the dorsal profile by means of a video-optic device from another direction (Hierholzer & Drerup, 1995). Rasterstereography excels by its precision (methodic error < 0.1 mm) and allows a radiation-free representation of the profile. For angular data, the reproducibility of an individual rasterstereographic shot is indicated with 2.8º. The measuring speed of 0.04 seconds can be considered as quick, and the total dorsal surface is registered simultaneously (Lippold et al., 2007). An automatic recognition of anatomical structures by means of the connected software provides the basis for a reconstruction of the three-dimensional profile of the dorsal surface. Figure 4 shows the Formetric 3D/4D Scanning System. By means of mathematical algorithms, a two-dimensional median sagittal or frontal-posterior dorsal profile is generated (Lippold et al., 2007). The gained information is of use for analysis and diagnosis.

Fig. 4. Formetric 3D/4D Scanning System

However, one of the disadvantages of this procedure is when a 360° view of an object is required; it is unable to use simultaneously multiple systems around the object because of interference between multiple light projections. It can give inaccurate data. Although, multiple systems use in sequence will increment the scanning time.

3.2 Moiré fringe countering

In optics moiré refers to a beat pattern produced between two gratings of approximately equal spacing. It can be seen in everyday things such as the overlapping of two window screens, the rescreening of a half-tone picture, or with a striped shirt seen on television (Creath & Wyant, 1992). The moiré effect is obtained as a pattern of clearly visible fringes when two or more structures (for example grids or diffraction gratings) with periodic geometry are superimposed. It has also been verified that the obtained fringes are a measure of the correlation between both structures. Additionally, it has been shown that the moiré effect can be obtained when other types of structures are superimposed, such as random and quasi-periodic ones or fractals. Fringe projection entails projecting a fringe pattern or grating over an object and viewing it from a different direction. It is a convenient technique for contouring objects that are too coarse to be measured with standard interferometry. A simple approach for contouring is to project interference fringes or a grating onto an object and then view it from a different direction (Calva et al., 2009). The first use of fringe projection for determining surface topography was presented by Rowe and Welford in 1967. Fringe projection is related to optical triangulation using a single point of light and light sectioning where a single line is projected onto an object and viewed in a different direction to determine the surface contour Moiré and fringe projection interferometry complement conventional holographic interferometry, especially for testing optics to be used at long wavelengths. Although two-wavelength holography (TWH) can be used to contour surfaces at any longer-than-visible wavelength, visible interferometry environmental conditions are required. Moiré and fringe projection interferometry can contour surfaces at any wavelength longer than 10-100 μm with reduced environmental requirements and no intermediate photographic recording setup (Creath & Wyant, 1992). However doesn't exist commercial scanners who take advantage of the combine technique of moiré fringe.

3.3 Phase Measuring Profilometry (PMP)

A well-known non-contact 3D measurement technique has been extensively developed to meet the demands of various applications. In such system (see Figure 5), generally, periodic

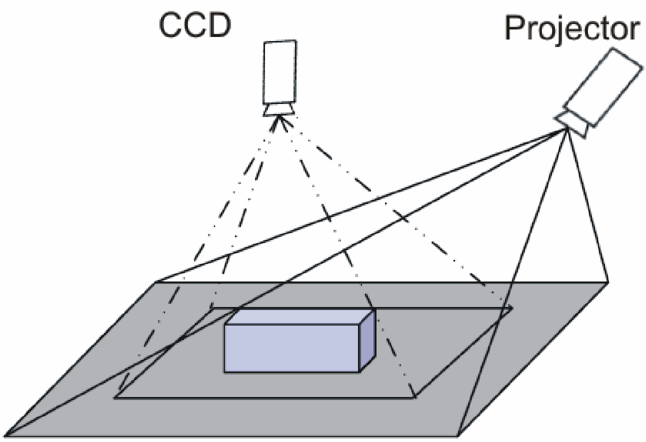

Fig. 5. The Phase Measuring Profilometry system

fringe patterns are projected on the objects surface, and the distorted patterns caused by the depth variation of the surface are recorded. The phase distributions of the distorted fringe patterns are recovered by phase-shifting technique or the method based on Fourier transformation analysis and then the depth map of the object surface is further reconstructed. Currently, light pattern is designed and generated by computer and Digital Light Projector (DLP) is popularly used to project the periodic sinusoidal fringe patterns on object surfaces. It is more flexible and accurate than conventional approaches in which grating is used for generating the sinusoidal fringe images. However, some problems still exist in PMP using DLP. One of them is that the inherent gamma nonlinearity of the DLP and CCD camera affects the output. As a result, the actual obtained fringe waveform is nonsinusoidal (Di & Naiguang 2008).

3.3.1 White light scanners by 3D3 solutions

The scanning system (see figure 6) consists of three main components: Projector (2200 Lumens to 2700 Lumens, 1024 + resolution), two 5MP high-speed HD machine vision cameras and a PC with FlexScan3D image capture software. The scanner use a projector to emit a white light pattern on to the surface of an object, two simple video cameras placed at different position scan the object and the software by triangulation of patterns renders the model in three dimensions. The first step in the scan procedure is the camera calibration using a pattern board, which the software needs to interpret the position of both cameras. When the pattern is projected the cameras provide the information to the software and render the image. The system needs a minimal 4 scans for a 360° view and is Recommended 8 scans for a full 360° view, the working range is 0.4 meters to 5 meters, and the scan speed is 1 to 6 seconds depending on scanner configuration. The common applications are: scanning faces for cosmetic surgery and burn treatments (in table 1 are presented medical applications for 3D scanners), bracing products (Knees, elbows and ankles), dental scanning replaces the need to create physical dental molds for patients.

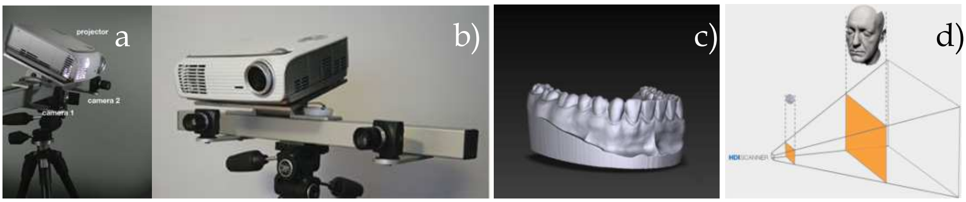

Fig. 6. a) Right view of 3D3 scanning system b) Front View of scanning system c) Dental scanning d) Field of view and face scanning

However this system only generates a 3D image and does not give as an output dimension measurements.

4. Laser scanning

Most of the contemporary non-contact 3D measurement devices are based on laser range scanning. The simplest devices, and also the least reliable, are based on the triangulation method. Laser triangulation is an active stereoscopic technique where the distance of the object is computed by means of a directional light source and a video camera. A laser beam is deflected from a mirror onto a scanning object. The object scatters the light, which is then

collected by a video camera located at a known triangulation distance from the laser (Azernikov & Fischer, 2008). Using trigonometry, the 3D spatial (XYZ) coordinates of a surface point are calculated. The charged couple device (CCD) camera's 2D array captures the surface profile image and digitizes all data points along the laser. The disadvantage of this method is that a single camera collects only a small percentage of the reflected energy. The amount of collected energy can be drastically increased by trapping the whole reflection conus. This improvement significantly increases the precision and reliability of the measurements. The measurement quality usually depends on surface reflection properties and lighting conditions. The surface reflection properties are dictated by a number of factors: a) angle of the laser ray hitting, b) surface material, and c) roughness. Owing to these factors, with some systems the measured object must be coated before scanning. More advanced systems provide automatic adaptation of the laser parameters for different surface reflection properties (Azernikov & Fischer, 2008).
There are a number of laser scanning systems on the market specifically engineered to scan manufactured parts smaller (10" L x 10" W x 16" H) than the human body. These systems are smaller than the typical laser body scanners mentioned below and employ a different scanning mechanism. The industrial units may pass a single laser stripe over the part or object multiple times at different orientations or rotate the part on a turntable. The smaller systems often have increased accuracy and resolution in their measurements when compared to their larger counterparts because of their reduced size and different scanning mechanisms. (Lerch et al., 2007)

4.1 Spatial discrimination

Given the nature of light there are discriminations to be performed in laser scanning systems, for example even in the best emitting conditions (single mode), the laser light does not maintain collimation with distance (e.g. check the beam divergence on scanner specifications sheets). In fact, the smaller the laser beam, the larger is the divergence produced by diffraction. For most laser scanning imaging device, the 3D sampling properties can be estimated using the Gaussian beam (see Figure 7) propagation formula and the Rayleigh criterion. This is computed at a particular operating distance, wavelength and desired spot size within the volume. Figure 4 illustrates that constraint (λ = 0.633 µm) (Beraldin, 2004).

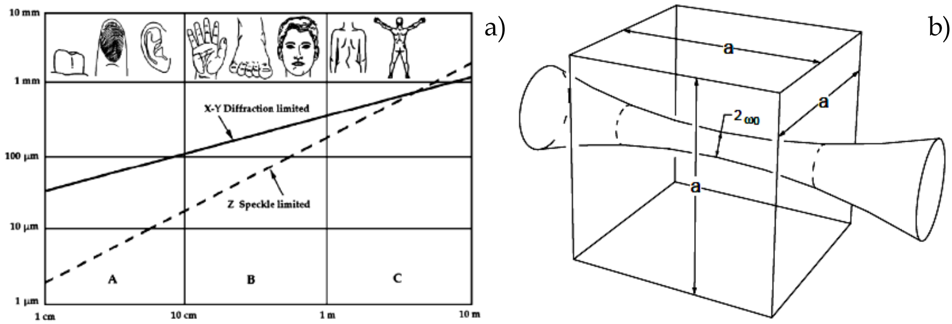

Fig. 7. a) Physical limits of 3D laser scanners as a function of volume measured. Solid line: X-Y spatial resolution limited by diffraction, Dashed line: Z uncertainty for triangulation-based systems limited by speckle. b) Gaussian Beam (Beraldin, 2004)

4.2 Body and medical 3D laser scanners

Of the diverse current methods for body scanning, laser scanners are used to graphically represent the silhouette and perform accurate measurements. The following systems are appropriate to perform the representation task but they have disadvantages which can decrease its measurement precision.

4.2.1 Vitus Smart 3D laser scanner

The scanning system developed by Human Solutions consists of two main components: the scanning assembly or booth and a PC with image reconstruction software. The scanning assembly is 4′ wide by 4′ deep by 10′ high. (See figure 8) with a structural frame to keep the device stationary; curtains are hung from the frame to minimize outside light. Located in each of the four corners is a vertical column containing the essential scanning equipment: a low energy laser, and two charge coupled device (CCD) cameras, all of which ride together in an elevator assembly that travels up and down in the vertical column. When the system is calibrated correctly, the four elevator assemblies travel down the columns in unison, sweeping the scanning zone with a horizontal plane of laser light.
The laser light illuminates the contours of an object standing within the scanning zone and the CCD cameras record discrete points on these contours at each horizontal plane. The entire scan takes approximately 12 seconds (Lerch et al., 2007).

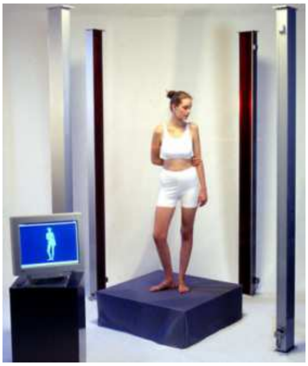

Fig. 8. Vitus 3D Laser Scanning

A computer attached to the scanner contains the user interface, data acquisition/reconstruction, and data analysis software, while interfacing with the motor controller. The computer software acquires data from the A/D converter and triangulates the discrete points for all of the horizontal planes, creating a point cloud representation of the object scanned. This process takes approximately 2 minutes to complete. After the data acquisition/reconstruction program is completed, a 3D image of the object is displayed on the computer screen. The point cloud data can be exported into proprietary and standard file formats (obj. dxf sdl. ascii) which can be imported into various computer aided design (CAD), finite element analysis (FEA). and rapid prototyping software packages (Lerch et al., 2007).
The elevated production costs of hardware components for the Vitus 3D Laser Scanning could be considered as a disadvantage. Moreover, precision electric motors should be used

for the displacement of the scanner units. Lastly, the whole scanner system must be calibrated so that the geometrical disposition of all the elements can be accurately determined. Any error in calibration will result in inaccurate measurements because there is no gap uncertainty in the calibration.

4.2.2 Konica Minolta 910

The Vivid 910 scanner (see figure 9) from Konica Minolta consists on a single camera and laser stripe, and acquires 3D data using triangulation. According to Konica the scanning process is comfortable, although subjects can see a quick flash of red when the laser stripe crosses the pupil. The laser is eye safe so the subject’s eyes can remain open during scanning. The scan takes approximately 2.5 seconds and the subject must remain motionless during that time or a poor scan will result. The Vivid 910 managed to be accurate with a repeatability of 0.003 mm. (Boehnen & Flynn, 2005). There are three different zoom lenses available and an automatic focus system that allows scanning at a wide variety of distances from the camera (there is a tradeoff between image resolution and standoff). It is somewhat sensitive to lighting conditions and is necessary to operate on indoors environments (Boehnen & Flynn, 2005).

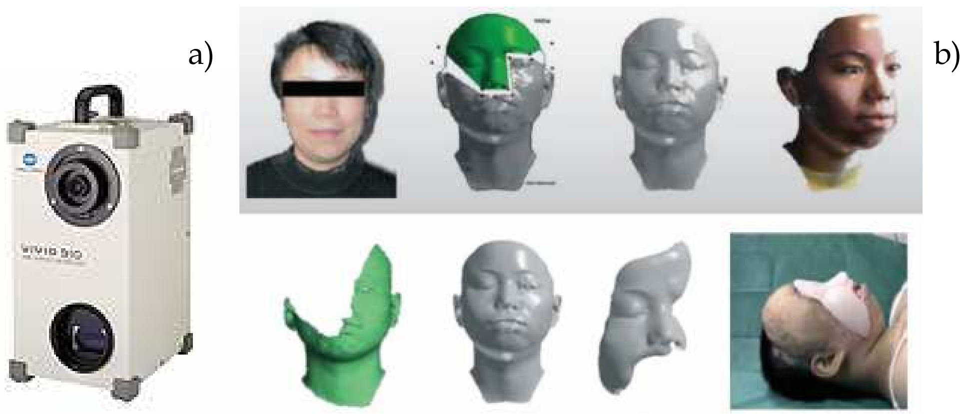

Fig. 9. a) Vivid 910 b) Rough procedures to create the missing part for visualization using Vivid scanner

4.2.3 3D Dynamic Triangulation scanner

The scanning system consists of four main components: electro-mechanical inclining angle system, laser beam projector, photodetector and software. A laser beam is projected onto the body and is detected by a photodetector which sets the angle of incidence. The system has a rotating system that allows inclining the angle for a complete scan. The system reduces measurement error because doesn’t have independent elements to coordinate like Vitus Smart. The precision is 0.04 mm and allows a radiation-free representation of the profile.
The laser and the collimator are installed in own laser positioning system (PL) see figure 10. PL has its step drive, which on a command from the onboard computer can turn PL in a horizontal plane at each for one angle pitch (Rivas et al., 2008). On the other end of the bar is

located a scanning aperture (SA) (Sergiyenko et al, 2009). Bi is the angle detected and Ci is the output angle of the laser. The system works in the next way. By the command from the computer the bar is installed so that the SA rotation axis becomes perpendicular to plane XOY of reference system. PL puts the laser with the collimator, for example, in an extreme right position. The axis of the collimator (with the help of PV-step drive) then takes extreme top position (above the horizon). The laser and the SA are switched on. SA is rotated by the electromotor EM. At each SA turn a laser ray should hit an obstacle, is reflected diffusely by it (point Sij) and returns to mirror in SA. At the moment when three objects - the point of reflection Sij, the perpendicular to mirror and the vertical axis of SA - takes their common plane, perpendicular to plane XOY while SA is rotating, an optical signal, having travelled a path "Sij - mirror M - objective O - optical channel OC - photoreceiver PR ". It makes an electrical stop signal. A start signal is previously formed by SA by means of a zero-sensor (installed on a bar b axis) (Rivas et al., 2008).

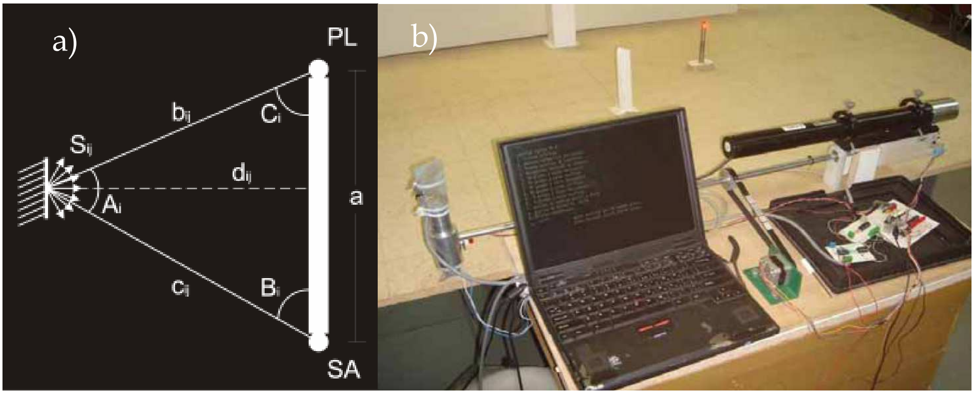

Fig. 10. a) Triangulation scheme, b) Dynamic triangulation scanner

The principle of this system is promising, although it has multiples disadvantages when the system is actually developed and running. The usage of the timing belts for the angular rotation of the system is one of them. Moreover, the system must undergo a thoroughly calibration to guarantee that the mirror rotates parallel to the system, and the receptor motor is not sufficient to guarantee constant rotational speed. Lastly, there are some components that vibrate and generate unwanted noise.

4.2.4 3D Rotational Body Scanner

The Rotational Body Scanner uses the principals of Dynamic Triangulation Scanner. (Basaca & Rodriguez, 2010). Increases its precision, decreases the mechanic noise sources and makes the addition of a stationary rotation system independent of timing belts (Rivas et al.,2008). The system receptor (see Figure 11) consist of 5 main components A) 45 degree rotational mirror, whose principal function is to direct the laser light beam towards the lenses (targets). B) Targets, whose function is to concentrate the light beam onto photodetector. C) DC Motor, which rotates the mirror. D) Photodetector, it captures the light beam located within the frequency range of the laser. E) Flat Bearing, allows the rotation in the angular axis of the system.

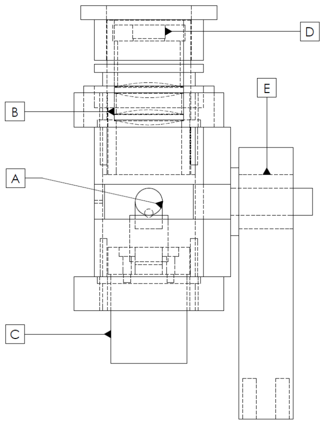

Fig. 11. System receptor

The system projector has 5 main components (see figure 12), which are the following: 1) Step Motor of angular rotation, whose main function is to control the rotation of the entire system. 2) Step motor for the mirror rotation, which controls the mirror rotation. 3) System's rotation gear, increases the precision of the system since it gives a 10:1 ratio gear-motor. 4) Mirror's rotation gear increases the precision of the system giving a 10:1 ratio gear. 5) Mirror, reflects the laser light beam towards the scanning body.

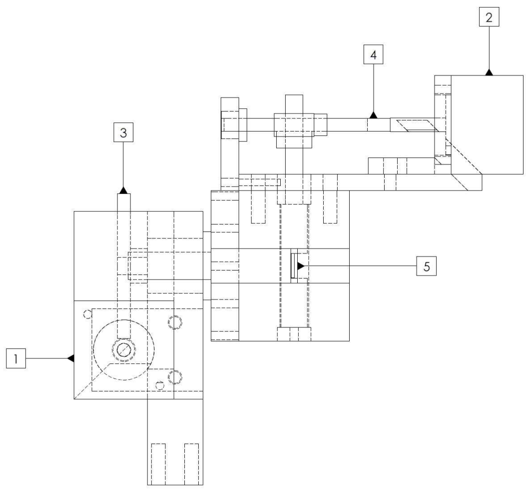

Fig. 12. System projector

The laser light projector emits the light at different angles towards the body. And at the same time the receptor rotates until it detects the light deflected by the body. When the mirror of the receptor deflects the scattered light towards the target and concentrates the light towards the photodetector, an electronic pulse is emitted which indicates the point has been detected. A relationship between the rotation time and detection time shows the angle in which the receptor detects the point. Since the projector rotation is controlled by the user, the angle of the projector is known at all times. The relationship between the 2 angles and the known distance between the projector and receptor gives each of the captured coordinates.

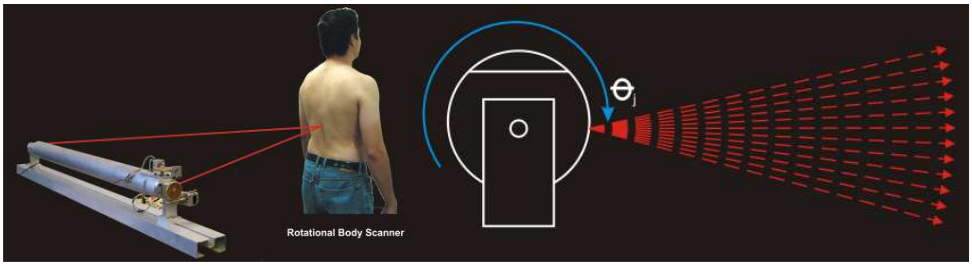

Fig. 13. 3D Rotational Body Scanner

As shown in figure 13, the projector and receptor are separated by a bar that gives the exact distance of 1 meter between them, and located in the bar is the laser light source. Within the bar the laser also gets aligned and locked avoiding measurement errors. The triangulation principle used is well known, and some of the advantages given by this system is the angular rotational mechanism (see figure 13) which allows the rotation with no chains, an increment in resolution of 10 times by using gears that gives 1 rotation for each 10 rotations that gives the step motor, inaccuracy caused by friction are decreased by using polytetraflourtethylene flat bearings which has the lowest friction coefficient of all materials, and the fabrication cost is economic.

4.3 Traceable 3D laser imaging metrology

The statement of uncertainty is based on comparisons with standards traceable to the national units (SI units) as requested by ISO 9000-9004. For example, manufacturers of theodolites and CMM manufacturers use specific standards to assess their measuring instruments. A guideline called VDI/VDE 2634 has been prepared in Germany for close range optical 3D vision systems. It contains acceptance testing and monitoring procedures useful for practical purposes for evaluating the accuracy of optical 3D measuring systems based on area scanning – bundle of rays. These systems work according to the principle of triangulation, e.g. fringe projection, Moiré techniques and photogrammetric/scanning systems based on area scanning (Beraldin et al., 2007). According to National Institute of Standards and Technology (NIST) in the Proceedings of the LADAR Calibration Facility Workshop, Gaithersburg, June 12 – 13, 2003 the steps to perform a 3D laser scanning calibration could be the following.

Calibration of the direction component: Using theodolite–type scanners, the direction affecting instrumental errors of the laser-scanner could be calibrated by procedures known from theodolites These are:

1. Vertical axis wobble, which acts as a lever effect, if the scanner does not correct this influence by inclination sensors.
2. Eccentricity of scan center.
3. Collimation axis error.
4. Horizontal axis error.

However no internationally recognized standard or certification method exists; the evaluation of the accuracy, resolution, repeatability or measurement uncertainty of a 3D imaging system still remains the responsibility of the user.

5. Conclusions

Not all scanning methods are as accurate as the diverse applications demands. None of the systems is superior in every area of applications.

The MillimeterWave based systems are sufficient for object detection but underdeveloped to be used in the medical environment where accuracy is needed. The main disadvantage of these systems is that their accuracy and contrast are sacrificed to be able to perform real time scanning.

The diverse techniques used in Photogrammety are appropriate to perform the modeling representation of the scanned objects, although not all techniques have the capability to perform measurements, such as the White Light Scanner by 3D3 Solutions mentioned above. This is one of the main reasons why the laser scanner based systems are preferred when measurements and surface areas are needed to be known, due to their attributes such as accuracy and efficiency.

If one of the system requirements to be met is that the 3D Model can be digitally rotated to offer its view in different angles, multiple laser scanner based systems can be used simultaneously. The speed of the laser scanning will be proportional to the number of systems used, since the simultaneously measurements of the multiple systems do not interfere between them. This laser scanning system attribute differs with the Photogrammetry based systems since they cannot perform the scan operation simultaneously due to the light projections interference, such as Formetric 3D/4D, which makes the speed ratio inversely proportional.

The 3D Rotational Body Scanner increases by 10 times its resolution in comparison with the former 3D Triangulation method. This is possible by using gears that gives 1 rotation per each 10 that gives the step motor. The increase in accuracy given by this improved method can be potentially used in other applications, for example, the scan of small parts of the human body, such as fingers and teeth.

Moreover, the 3D Rotational Body Scanner decreases significantly the mechanical sources of noise, and guarantee less calibration since is a more stable than the former 3D Dynamic Triangulation scanner.

The combination of the photogrammetry method and the 3D dynamic triangulation method could be an interesting area of opportunity. The image modeling phase could be obtained through the photogrammetry techniques and the accuracy and dimensional measurements could be complemented by the improved 3D Rotational Body Scanner system, although this is yet to be explored.

6. References

Azernikov, S.; Fischer, A. (2008). Emerging non-contact 3D measurement technologies for shape retrieval and processing, *Virtual and Physical Prototyping*, Vol. 3, No. 2 (June 2008) pp 85-91, ISSN: 1745-2759.

Básaca, Luis C.; Rodríguez, Julio C.; Sergiyenko, Oleg;. Tyrsa, Vera V; Hernández, Wilmar;. Nieto Hipólito, Juan I; Starostenko, Oleg. 3D Laser Scanning Vision System for

Autonomous Robot Navigation, *Proceedings of IEEE (ISIE-2010)*, Bari, Italy, July 4-7, 2010, pp.1773-1779, ISBN 978-1-4244-6390-9.

Beraldin, J.A.; Rioux, M.; Cournoyer, L.; Blais, F.; Picard, M.; Pekelsky, J (2007). Traceable 3D Imaging Metrology, *Proc. SPIE 6491*, ISBN: 9780819466044, California, USA, January 2007, SPIE, San Jose.

Beraldin, J.A. (2004) Integration of Laser Scanning and Close-range Photogrammetry the Last Decade and Beyond, *ISPRS Journal of Photogrammetry and Remote Sensing*, Volume XXXV, No. B5 (July 2004) pp. 972-983, ISSN: 1682-1750.

Bjarnason, J. E.; Chan, T. L. J.; Lee, A. W. M.; Celis, M. A.; Brown, E. R. (2004) Millimeter-wave, terahertz, and mid-infrared transmission through common clothing, *Applied Physics Letters*, Vol. 85, No. 4, (June 2004) pp. 519 -521, ISSN: 0003-6951.

Boehnen, C.; Flynn, P. (2005) Accuracy of 3D Scanning Technologies in a Face Scanning Scenario, *Proceedings of 3-D Digital Imaging and Modelling*, pp 310-317, ISBN: 0-7695-2327-7, Ontario Canada, June 2005, IEEE, Ottawa.

Calva, D.; Calva, S.; Landa, A.; Rudolph, H.; Lehman1, M. (2009). Face recognition system using fringe projection and moiré: characterization with fractal parameters, *IJCSNS*, Vol.9, No.7, (July 2009) pp 78 – 84, ISSN: 1738-7906.

Creath, K.; Wyant, J. C. (1992). Moiré and Fringe Projection Techniques*, Optical Shop Testing*, Editor: Daniel Malacara pp. 653 – 685, John Wiley & Sons, ISBN: 0-471-52232-5, New York.

Di, W.; Naiguang, L (2008). A pre-processing method for the fringe image in phase measuring profilometry, *Proc. SPIE*, Vol. 6623, No. 66231A, (March 2008) pp 1 – 8, ISSN: 0277-786X.

Emmanuel P. Baltsavias (1999). A comparison between photogrammetry and laser scanning. *ISPRS Journal of Photogrammetry and Remote Sensing*, Vol. 54, No. 2-3, (March 1999) pp. 83 – 94, ISSN: 0924-2716.

Haworth, C.D.; De Saint-Pern, Y.; Clark, D.; Trucco, E.; Petillot, Y.R. (2006). Detection and Tracking of Multiple Metallic Objects in Millimetre-Wave Images, *International Journal of Computer Vision,* Vol. 71, No. 2, (June 2006) pp 183-196, ISSN: 0920-5691

Hierholzer, E. Drerup, B. (1995). High-resolution rasterstereography. *Three-Dimensional Analysis of Spinal Deformities,* Editors: Amico, D' M. Merolli, A. Santambrogio, G.C. pp. 435 – 439, The Netherlands: IOS Press, ISBN: 90-5199-181-9, Amsterdam.

Howald, R.L.; Clark, G.; Hubert, J. Ammar, D. (2007), Millimeter Waves: The Evolving Scene, *Technologies for Homeland Security IEEE Conference on HST*, pp.234-239, ISBN: 1-4244-1053-5, Massachusetts USA, June 2007, IEEE, Woburn.

Leifer, J. (2003) A close-range photogrammetry laboratory activity for mechanical engineering undergraduates, *Frontiers in Education, 2003. FIE 2003. 33rd Annual*, Vol 2, No F2E, (November 2003) pp 7 – 12, ISSN: 0190-5848.

Lerch, T.; MacGillivary, M.; Domina, T. (2007). 3D Laser Scanning: A Model of multidisciplinary research, *Journal of Textil and Apparel, Technology and Management,* Vol. 5, No. 4 (October 2007) pp 1-21, ISSN: 1533-0915.

Lippold, C.; Danesh, G.; Hoppe, G.; Drerup, B.; Hackenberg, L. (2007). Trunk Inclination, Pelvic Tilt and Pelvic Rotation in Relation to the Craniofacial Morphology in Adults, *Angle Orthodontist*, Vol. 77, No 1, (January 2007) pp 29 – 35, ISSN: 0003-3219.

Liu, H.B.; Zhong, H.; Karpowicz, N.; Chen, Y. (2007) Terahertz Spectroscopy and Imaging for Defence and Security Applications, *Proceedings of the IEEE*, Vol. 95, No. 8, (October 2007) pp.1514-1527, ISSN: 0018-9219.

Rivas Lopez, M.; Sergiyenko, O. & Tyrsa, V. (2008). Machine vision: approaches and limitations, In: *Computer vision,* Xiong Zhihui, (Ed.), pp. 395-428. Editorial: IN-TECH, ISBN 978-953-7619-21-3, Vienna, Austria.

Rusinkiewicz, S.; Hall-Holt, O.; Levoy, M. (2002). Real-time 3D model acquisition. *ACM Transactions on Graphics (TOG)*, Vol. 21, No. 3, (July 2002) pp. 438 – 446, ISSN: 0730-0301.

Sergiyenko, O.; Hernandez, W.; Tyrsa, V.; Devia Cruz, L.; Starostenko, O. & Pena-Cabrera, M. (2009). Remote Sensor for Spatial Measurements by Using Optical Scanning, *Sensors,* 9(7), July, 2009, MDPI, Basel, Switzerland, pp. 5477-5492. ISSN 1424-8220.

Treleaven, B.; Wells, J. (2007). 3D Body Scanning and Healthcare Applications. *Computer*, Vol. 40, No. 7, (August 2007) pp. 28 – 34, ISSN : 0018-9162.

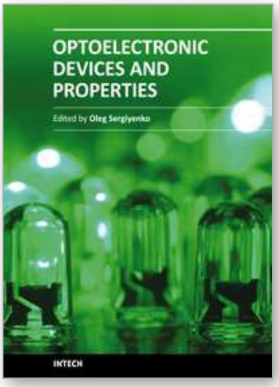

Optoelectronic Devices and Properties

Edited by Prof. Oleg Sergiyenko

ISBN 978-953-307-204-3

Hard cover, 660 pages

Publisher InTech

Published online 19, April, 2011

Published in print edition April, 2011

Optoelectronic devices impact many areas of society, from simple household appliances and multimedia systems to communications, computing, spatial scanning, optical monitoring, 3D measurements and medical instruments. This is the most complete book about optoelectromechanic systems and semiconductor optoelectronic devices; it provides an accessible, well-organized overview of optoelectronic devices and properties that emphasizes basic principles.

How to reference

In order to correctly reference this scholarly work, feel free to copy and paste the following:

Julio C. Rodríguez-Quiñonez, Oleg Sergiyenko, Vera Tyrsa, Luís C. Básaca-Preciado, Moisés Rivas-Lopez, Daniel Hernández-Balbuena and Mario Peña-Cabrera (2011). 3D Body & Medical Scanners' Technologies: Methodology and Spatial Discriminations, Optoelectronic Devices and Properties, Prof. Oleg Sergiyenko (Ed.), ISBN: 978-953-307-204-3, InTech, Available from: http://www.intechopen.com/books/optoelectronic-devices-and-properties/3d-body-medical-scanners-technologies-methodology-and-spatial-discriminations

INTECH
open science | open minds

InTech Europe
University Campus STeP Ri
Slavka Krautzeka 83/A
51000 Rijeka, Croatia
Phone: +385 (51) 770 447
Fax: +385 (51) 686 166
www.intechopen.com

InTech China
Unit 405, Office Block, Hotel Equatorial Shanghai
No.65, Yan An Road (West), Shanghai, 200040, China
中国上海市延安西路65号上海国际贵都大饭店办公楼405单元
Phone: +86-21-62489820
Fax: +86-21-62489821

Electromechanical 3D Optoelectronic Scanners: Resolution Constraints and Possible Ways of Improvement

Oleg Sergiyenko[1], Vera Tyrsa[2], Luís C. Basaca-Preciado[1], Julio C. Rodríguez-Quiñones[1], Wilmar Hernández[4], Juan I. Nieto-Hipólito[1], Moisés Rivas Lopez[1] and Oleg Starostenko[3]
[1]Autonomous University of Baja California, Mexicali-Ensenada,
[2]Polytechnic University of Baja California, Mexicali,
[3]Universidad de Las Americas, Puebla,
[4]Polytechnic University of Madrid,
[1,2,3]Mexico
[4]Spain

1. Introduction

Non-Contact optoelectronic 3D measurement is a rapidly growing field. Three-Dimensional Non-Contact Measurement Technologies are very common for research due to multiple practical applications expecting for its benefits. Many fields are using in any way 3D measurements or shape recognition, some of them there are vision assisted assembly in various branches of industry, autonomous mobile robots navigation, structural health monitoring, micro surfaces inspections, precise automated surgery, etc.

In this chapter it is expedient to mention and briefly cross-compare the following emerging technologies for 3D measurements: laser scanners, lasers based on conoscopy holography technology and 3D cameras.

Laser scanners: Most contemporary non-contact 3D measurement devices are based on laser range scanning. The simplest devices (Fischer, 2007) are based on the laser triangulation technique. This is an active stereoscopic technique in which the distance of the object is computed by means of a directional light source and a video camera. The CCD camera's 2D array captures the image of surface profile and digitizes all data points along the laser disadvantage of this method is that a single camera collects only a small percentage of the reflected energy. The amount of the collected energy can be drastically increased by trapping the entire reflection cone, thus significantly increasing the precision and reliability of the measurements.

Lasers based on Conoscopic Holography technology: Conoscopic Holography is a simple implementation of a particular type of polarized light interference process based on crystal optics. In the basic interference set-up, a point of light is projected onto a diffuse object. This point creates a light point, which diffuses light in every direction. In a conoscopic system, a complete solid angle of the diffused light is analyzed by the system. The measurement process retrieves the distance of the light point from a fixed reference plane. The problem inherent in laser scanning is its relatively low measurement speed, though it is faster than traditional contact Coordinate measurements machines (CMM's).

a) b)

Fig. 1. A scanner laser (a) and a 3D camera (b)

3D cameras: 3D photography is based on reconstructing 3D data from 2D images, taken from different points of view (stereo- graphic) the basic problem with this approach is the correspondence problem. In 3D cameras a pattern is projected on the object and the same pattern points are identified on each image. This approach is much more efficient, since it does not require marking specific points, and it can produce a very large number of measurements in one shot of camera.

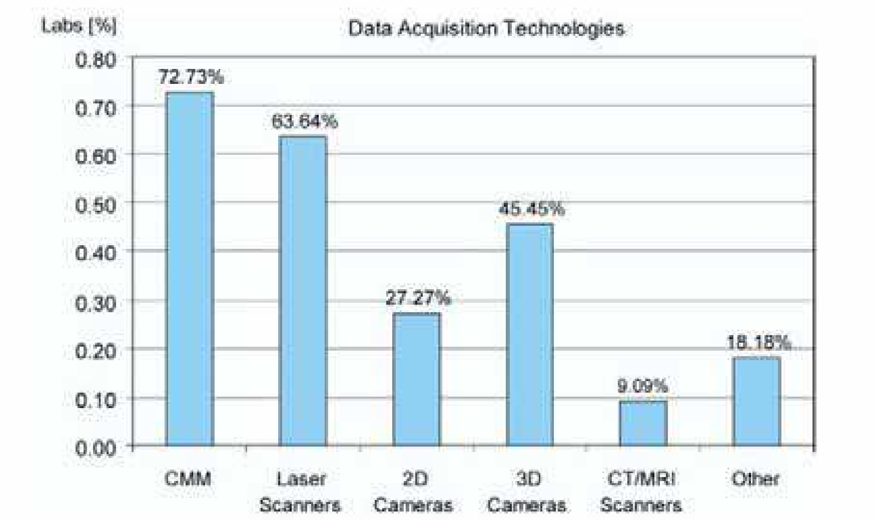

Fig. 2. Distribution of 3D scanning technologies among 23 engineering universities and research centers across Europe according to (Fischer, 2007)

The typical distribution of 3D scanning technologies research among engineering universities and research centers is given on Fig.2. CMM is still numerous due to non-innovative routines in industry with traditional investments for research. But this technology is contact and applicable for very limited area of tasks. So, the future is for laser scanning and 3D camera vision.

In fact, specialists already get a consensus regard to most evidences of these two branches. Cameras are winning in a point of less energy consuming and a relatively longer range of action. But laser scanning systems always win at resolution, accuracy and data processing time.

Basing in this, it is easy to show that for various tasks (such as: vision assisted assembly, robot navigation in densely cluttered environment, structural health monitoring, etc.) the laser scanner is an optimal way to obtain quality 3D information about objects in nearest surrounding in higher resolution.

But the majority of modern laser scanners have a certain part of rotating/moving electromechanical components, which are closely related with such negative phenomenon like mechanical vibrations, friction and wear, mechanical delays, etc.

Present paper scope is precisely to research what are the most prospective ways to increase the electromechanical laser scanners resolution and robustness. With this aim let us deeper study most typical approaches to laser scanner construction, as one of the most promising technical vision system (TVS).

2. Typical laser scanner constructions and their constraints

According to the recent literature electromechanical laser scanners have sufficiently variety in its constructions. At the same time, they have enough similarities and common components in its general structure. Let will see some of the typical constructions of electromechanical laser scanners for to have the possibility systemize such constructions and define their common advantages and lacks.

An obvious optimization of the measurement system (Wulf & Wagner, 2003) is to take the scanning method that is most suitable for the application. However, taking a 2D laser scanner with 180° scanning range and a servo drive it results in a number of possible combinations of scan planes and rotation axis to get a 3D scan. This section describes four of these combinations. We have named the scanning methods as *pitching scan*, *rolling scan*, *yawing scan* and *yawing scan top*. The *pitching scan* (Fig. 3a) has a horizontal scan plane and is pitching up and down. This method is for example used in (Surmann et al., 2001) and (Hähnel & Burgard, 2002). A method that is newly introduced here is the *rolling scan* (Fig. 3b). This scan is rotating around the center of the scanner, with the advantage of only one focus point in front of the sensor. The *yawing scan* (Fig. 3c) and the *yawing scan top* (Fig. 3d) has a vertical scan plane and is rotating around the upright z-axis. This method is used e.g. by (Wulf, O. & Wagner, B. (2003).

Let us compare constructions and advantages/disadvantages of the different laser scanner constructions according to the next literature sources: (Son et al., 2002), (Wulf & Wagner, 2003), (Nüchter, 2007), (Nüchter, 2008), (Wulf et al., 2004), (Surmann, 2003), (Surmann et al., 2001), (Hähnel & Burgard, 2002), (Blais et al., 1988), (Blais et al., 2000), (Beraldin et al., 2000), (Andersen et al., 2006), (Laurin et al., 1996), (Blais et al., 1991), (Klöör et al., 1993), (Vandapel et al., 2004), (Montemerlo & Thrun, 2004), (Pagnottelli et al., 2005), (Sergiyenko et al., 2006).

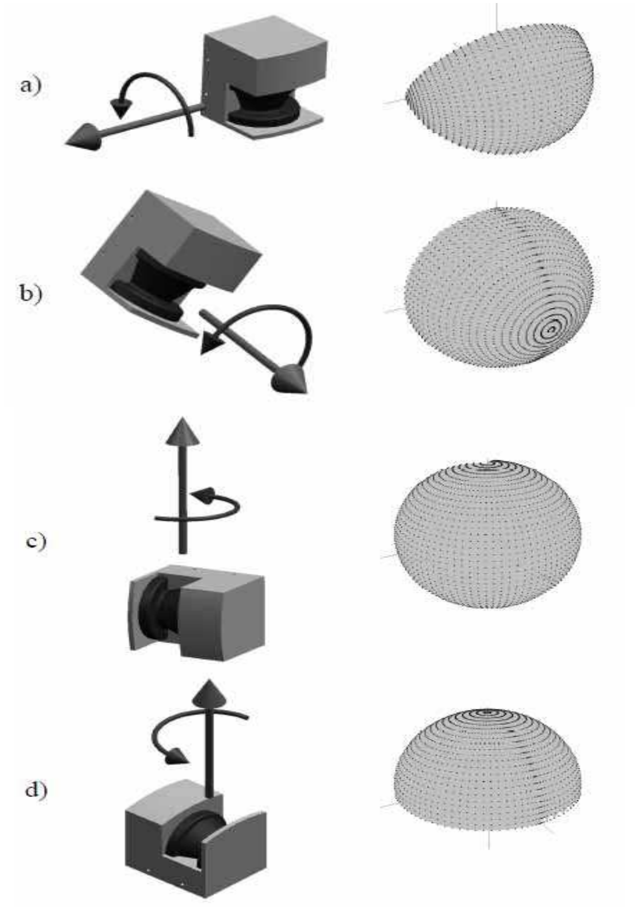

Fig. 3. The *pitching scan* (a), the *rolling scan* (b), the *yawing scan* (c) and the *yawing scan top* (d) (Wulf & Wagner, 2003)

2.1 Automated laser scanning system for reverse engineering and inspection

The mechanism of the 3D laser scanner used in this research (Son et al., 2002) is illustrated in Fig. 4. A laser stripe is projected onto a surface and the reflected beam is detected by CCD cameras. Through image processing and triangulation method, three-dimensional coordinates are acquired. The laser probe is mounted on a three-axis transport mechanism and moves along the scan path that consists of a series of predetermined line segments. It also rotates in two directions.

When the laser scanner captures an image, the system automatically finds an optical focus and keeps the standoff distance. The length of laser stripe and the stand-off distance cannot be changed by an operator. Since a laser scanner consists of optical sensors and mechanical moving parts, various constraints must be satisfied when measuring a certain point on a part (Fig. 5). The goal of this section is to generate an optimal scan plan that satisfies the following major constraints (Zussman et al., 1994):

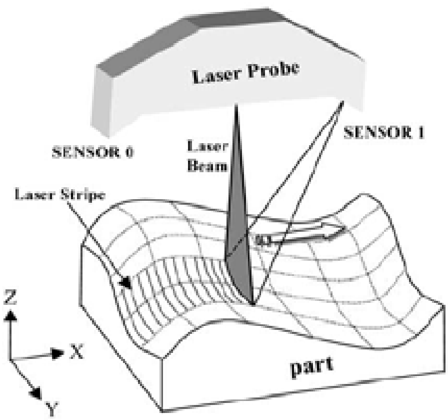

Fig. 4. Laser scanning mechanism

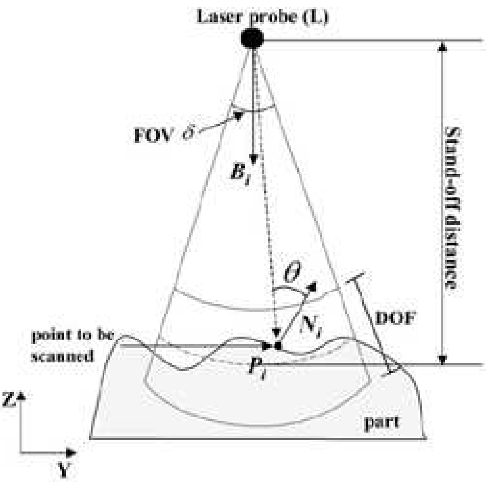

Fig. 5. Constraints for laser scanning

1. View angle: the angle between the incident laser beam and the surface normal of a point being measured should be less than the maximum view angle γ

$$d_i \bullet N_i \geq \cos(\gamma), \tag{1}$$

where

$$d_i = \frac{L - P_i}{|L - P_i|}. \tag{2}$$

2. FOV: the measured point should be located within the length of a laser stripe

$$\left(-d_i\right) \bullet B_i \geq \cos\left(\frac{\delta}{2}\right), \tag{3}$$

where δ is the FOV angle

3. DOF: the measured point should be within a specified range of distance from the laser source

$$l_{STAND} - \frac{l_{DOF}}{2} \leq \left|L - P_i\right| \leq l_{STAND} + \frac{l_{DOF}}{2}, \tag{4}$$

where l_{STAND} and l_{DOF} denotes stand-off distance and DOF length.

4. Occlusion: the incident beam as well as the reflected beam must not interfere with the part itself.
5. The laser probe should travel along a path that is collision-free.
6. If the part is shiny or transparent, preprocessing is required such as spraying.

2.2 Range error analysis of an integrated time-of-flight, triangulation and photogrammetric 3D laser scanning system

Laser scanner model (Blais et al., 2000). Models must be able to relate design parameters, laboratory measurable, and operational performance. Figure 6 illustrates the major subsystems of an active electro-optical system: projector sources and collimating optics, deflection mechanism, collecting optics, detector, signal conditioning and processing, and final output. The collecting optics images the radiation onto the detector. In the example of Figure 7, the scanner optically moves the detector's instantaneous field-of-view (IFOV) across the total field-of-view (FOV) to produce an output voltage (signal) proportional to the local scene intensity (produced by ambient light conditions) and the laser light reflected back from a reflective surface.

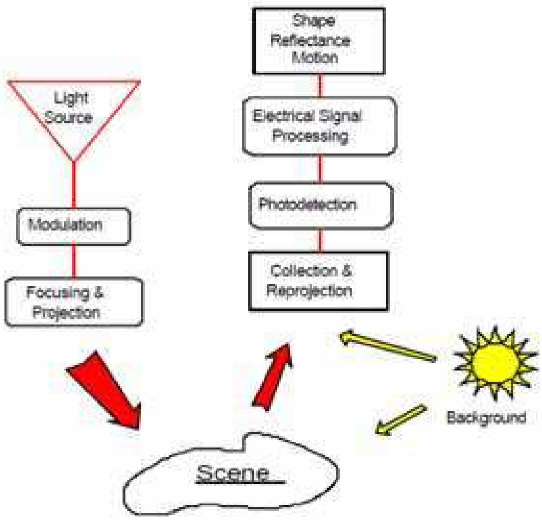

Fig. 6. Generic sensor operation applied to active electro-optical systems

The detector is at the heart of the electro-optical system because it converts the scene radiation (reflected flux) into a measurable electrical signal. Amplification and signal processing creates a signal in which voltage differences represent scene intensity differences due to various objects in the field-of-view.

The majority of electro-optical quality discussions are centered on resolution and sensitivity evaluation. System sensitivity deals with the smallest signal that can be detected. It is usually taken as the signal that produces a signal-to-noise ratio of unity at the system output. Sensitivity is dependent upon the light-gathering properties of the optical system, the responsivity of the detector, the noise of the system and, for this application, the background flux. It is independent of resolution.

In the case of metrology, resolution is not sufficient and stability and accuracy must also be considered. Resolution has been in use so long that it is thought to be something fundamental, which uniquely determines system performances and is often confused with accuracy. It is often specified by a variety of sometimes-unrelated metrics such as the Airy disk angular size, the detector subtense, or the sampling frequency. Resolution does not usually include the effect of system noise.

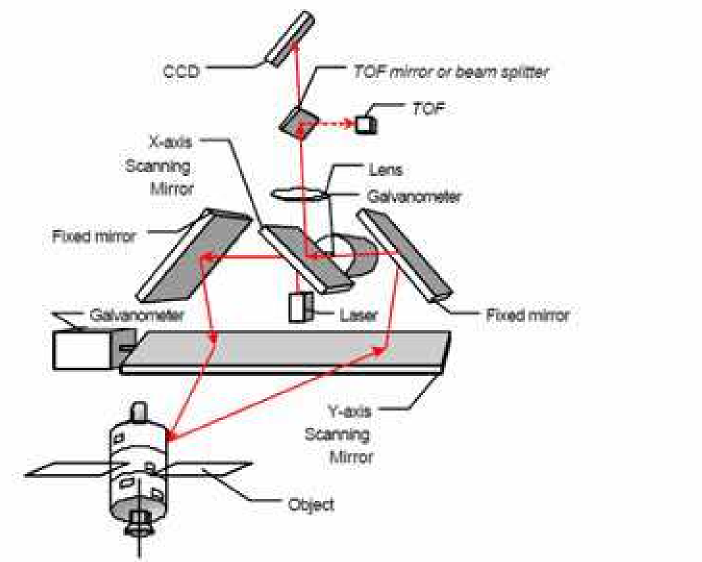

Fig. 7. Schematic representation of the auto-synchronized geometry

2.3 The auto-synchronized laser scanner

Figure 7 shows a photograph of the prototype of the auto-synchronized laser scanner developed for this demonstration. The scanner uses a variation of the auto-synchronized triangulation range sensor based on one galvanometer (Blais et al., 1988). The system comprises two orthogonally mounted scanning mirrors and a linear discrete-response photosensitive position device (e.g. linear CCD) used for short to medium range measurement as triangulation (Beraldin et al., 2000). An optional avalanche photo-diode-based Time-of-Flight (LIDAR) ranging module is used for longer-range measurement

(Laurin et al., 1996). Only resolved targets using TOF are considered for this application. Laser illumination is provided using a laser source coupled to a single-mode fiber, either pulsed (TOF mode) or CW (triangulation mode). The laser scanner operates at a relatively eye safe wavelength of 1.5 mm (compared to visible laser wavelengths).
The basic concept of auto-synchronization is that the projection of the light spot is synchronized with its detection as illustrated in Figure 7. The instantaneous field of view (IFOV) of the position sensor follows the spot as it scans the scene. Therefore, an external optical perturbation can potentially interfere with the detection only when it intersects the instantaneous field of view (IFOV) of the scanner. At this level, electronic signal processing is used to filter these false readings to obtain correct 3-D measurement (Blais et al., 1991). With synchronization, the total field of view (FOV) of the scanner is related to the scanning angles of the galvanometers and mirrors as opposed to a conventional camera-based triangulation. Here the field of view and image resolution are intimately linked (Blais et al., 1988); a large field of view produces a lower pixel resolution. In summary, the instantaneous field-of-view of the scanner plays a major role in the system sensitivity analysis.

2.4 Range measurement

Figure 7 shows the optical geometry of the auto-synchronized laser scanner. The laser scanner system can measure range information for each voxel (3-D pixel) in the scene using two modes of operation: (1) triangulation as illustrated in Figure 8, and (2) time-of-flight shown in Figure 9. It is beyond the scope of this paper to discuss the details of operation of the scanner and the exact mathematical model. This information is available from previous publications where the scanner is operated in imaging mode (Blais et al., 1988; Beraldin et al., 1993; Beraldin et al., 2000). Here, we will use the simplified models illustrated in Figure 10 to model range measurement and to associate object pose estimation obtained using video camera models shown in Figures 10 and 11 and techniques discussed in section 4.

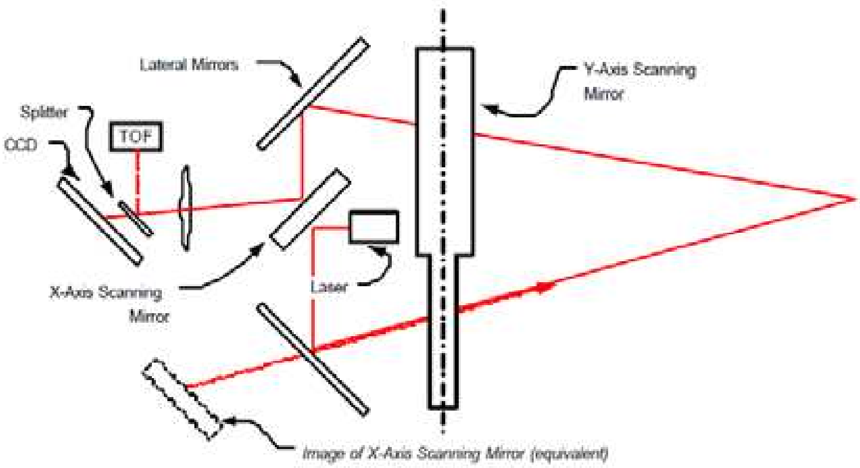

Fig. 8. Simplified geometry of the laser scanner for the triangulation mode

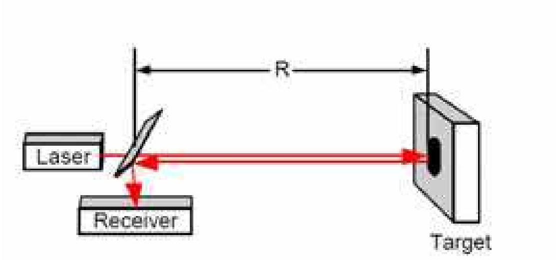

Fig. 9. Schematic of the time-of-flight principle

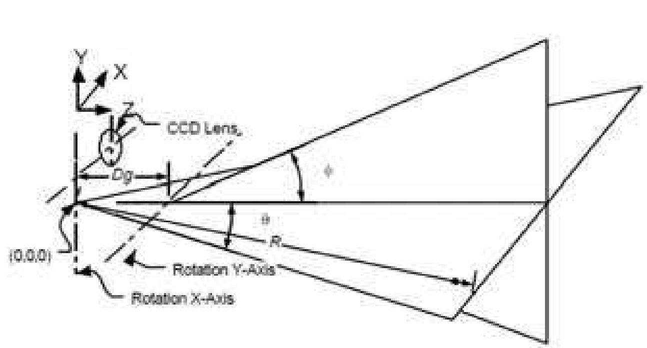

Fig. 10. Simplified geometrical model of the laser scanner showing the effect of astigmatism between the X and Y scanning axis

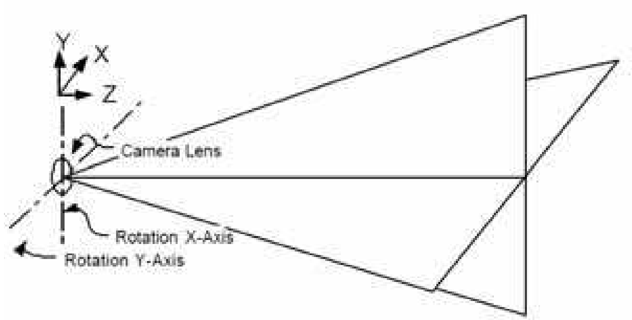

Fig. 11. Simplified geometrical model of a simple camera lens system used by conventional camera and photogrammetric methods

From (Blais et al., 1988), knowing that $R=z/\cos(\theta)$, and from Figure 10, range R can be calculated either using triangulation methods or TOF. The simplified aberrations free model is presented here. For triangulation, range is given by

$$R_{Trian} = \frac{f \cdot d}{p}\cos(\theta) + d\sin(\theta) \tag{5}$$

where f is the focal length of the lens, d is the triangulation base, θ is the deflection angle following the x-axis, and p is the position of the imaged laser spot of the position sensor (see (Blais et al., 1988) for details). For the TOF method of Figure 9, range is simply obtained based on the speed of light c and the propagation delay τ of a laser pulse:

$$R_{TOF} = c\frac{\tau}{2} \tag{6}$$

From Figure 10, the x-y-z coordinates of a point are

$$\begin{bmatrix} x \\ y \\ z \end{bmatrix} = R \cdot \begin{bmatrix} \sin(\theta) \\ (\cos(\theta) - \psi)\sin(\theta) \\ (1-\cos(\theta))\psi + \cos(\theta)\cos(\theta) \end{bmatrix} \tag{7}$$

where θ and φ are the deflection angles, and $\psi = Dg/R$ where Dg is the separation between the two scanning axis shown in Figure 10. Range R is obtained using either R_{Trian} or R_{TOF} depending on the operating mode of the scanner. Because Dg<<R, error propagation calculations (in triangulation mode) can be approximated by

$$\Delta R_{Trian} \approx \frac{R^2}{f \cdot d}\Delta p \tag{8}$$

$$\begin{aligned} \begin{bmatrix} \Delta x \\ \Delta y \\ \Delta z \end{bmatrix}^2 &= \begin{bmatrix} \sin(\theta) \\ \cos(\theta)\cdot\sin(\varphi) \\ \cos(\theta)\cos(\varphi) \end{bmatrix}^2 \left(\frac{R^2}{f \cdot d}\Delta p\right)^2 + \\ &+ \begin{bmatrix} \cos(\theta) \\ -\sin(\theta)\cdot\sin(\varphi) \\ -\sin(\theta)\cos(\varphi) \end{bmatrix}^2 R^2 \cdot \Delta\theta^2 + \begin{bmatrix} 0 \\ \cos(\varphi) \\ -\sin(\varphi) \end{bmatrix}^2 R^2\cos^2(\theta)\cdot\Delta\varphi^2 \end{aligned} \tag{9}$$

where Δp is the uncertainty associated with the laser spot measurement.

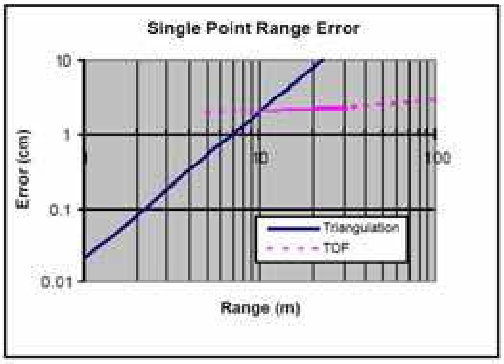

Fig. 12. Range error accuracy of the Laser Scanner System

Figure 12 shows range error measured with the scanner in triangulation (notice the R^2 dependence of the error), and from the manufacturer specifications for the TOF mode of operation (notice the almost flat error over range). Other typical system parameters for the prototype used in Figure 7 are maximum deflection angles of 0.5 rad (30 deg) and angular errors of 50-100 µrad, depending on the target array. From equation 9 and Figure 12, the total system error, for medium to long range, is mostly contributed by range error measurement ΔR, i.e., Δp the uncertainty associated with the laser spot measurement.

2.5 Traversable terrain classification for outdoor autonomous robots using single 2D laser scans

Autonomous navigation by mobile robots in unstructured or semi-structured outdoor environments presents a considerable challenge (Andersen et al., 2006). Adequately solving this challenge would allow robotic applications within industries such as agriculture, mining and logging. To achieve the level of autonomy required for such operation, a robot must be able to perceive and interpret the environment in a meaningful way. Limitations in current sensing technology coupled with a dynamically changing unknown environment, and difficulties in modeling the interaction between robot and terrain all make this task difficult.

The sensors used for this task could include vision, ultrasound, radar and laser scanner, both as combined solutions and each sensor type used individually. Multi sensor solutions would be expected to provide superior results but computational efforts and requirements of fast real-time classification make it interesting to explore what would be achievable with a single sensor.

Current work in the area tends to focus on using 3D laser scanners, vision or a combination of 3Dlaser scanners and vision. In vision solutions (Bertozzi & Broggi, 1997) argues that this problem can be divided into two sub-problems: Lane following and obstacle detection, and describes a stereo vision based solution for both. Edge detection in vision systems is one of the possibilities to identify road borders and had some success already in 1986 as described in (Wallace et al., 1986), color segmentation is used in (Fernandez & Price, 2005) for tracking of dirt roads, road types similar to the ones used in this paper. A method for road following using vision and neural network was developed by (Jochem et al., 1993). A combined stereo vision and 2D laser scanner solution for outdoor obstacle avoidance is presented in (Pagnottelli et al., 2005). Using 3D laser scanner solutions have been proposed by (Vandapel et al., 2004) by transforming point clouds into linear features, surfaces, and scatter. These were classified using a Bayesian filter based on a manually classified training set. Identification of navigable terrain using a 3D laser scanner by checking if all height measurements in the vicinity of a range reading had less than a few centimeters deviation is described in (Montemerlo & Thrun, 2004). An algorithm that distinguished compressible grass (which is traversable) from obstacles such as rocks using spatial coherence techniques with an omni-directional single line laser was developed by (Macedo et al., 2000). A method of traversing a rock field based on three metrics extracted from stereovision was likewise developed by (Wettergreen et al., 2005). A tactile and vibration-based approach to terrain classification was proposed by (Legnemma et al., 2004). A method for detection and tracking the vertical edges of the curbstones bordering the road, using a 2D laser scanner, was developed by (Wijesoma et al., 2004). Detection of borders or obstacles using laser scanners are often used both indoors and in populated outdoors environments, and is the favored method when the purpose includes map building, as in (Guivant et al., 2001; Klöör et al., 1993).

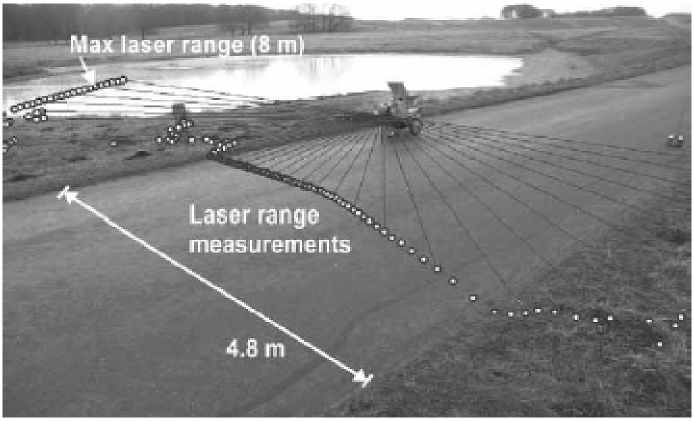

Fig. 13. The robot uses a laser scanner to detect the terrain in front of the robot

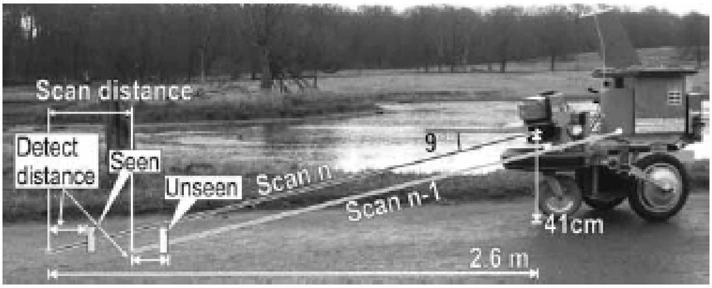

Fig. 14. The robot used in the experiments has a laser scanner at a height of 41 cm looking down in an angle of $\theta_L = 9°$. The road is therefore detected at 2.6 m. The position of the last scan (scan n − 1) is shown to illustrate the largest undetected obstacle. The unseen object is not detected in scan n − 1 and is too short to be seen by scan n

2.6 Constructing a 3D laser range finder

Now we will consider a three-dimensional laser range finder and its design.
The presented 3D laser range finder is built on the basis of a 2D range finder by extension with a mount and a servomotor. The 2D laser range finder is attached to the mount so that it can be rotated. The rotation axis is horizontal. A standard low-cost servomotor is connected on the left side (fig. 15).
It is an alternative approach if we have to rotate the range finder around the vertical axis. In (Surmann at al. 2001) it is only discussed the approach based on a horizontal rotation, but all presented algorithms can be used in the same way. The differences between both approaches are the orientation of the apex angle and the effects of dynamic objects moving through the scene, e.g. persons. Using vertical scanning, a perturbation either appears with low probability within a few scans making them useless for further data processing, or does not appear at all. The first approach on the other hand shows perturbations throughout the whole scene, but these data can still be used for robot navigation and object detection.

Fig. 15. A 3D laser range finder for autonomous mobile robots. The servo is mounted at the left side. A camera on top is used to get texture images for the realistic appearances of a 3D scene (Surmann at al. 2001)

The given setup determines an intrinsic order of the acquired data. The data coming from the 2D laser range finder is ordered anticlockwise. In addition the 2D scans (scanned planes) are ordered due to the rotation. A digital camera for texture mapping is mounted on top of the 3D laser range finder. While rotating, several photos are taken so that the texture mapping can be applied to a larger area. The 3D laser range finder uses only standard interfaces of a computer. The servomotor is directly connected to the parallel port, the 2D laser range finder to the serial port and the camera is connected to an USB port. Nowadays, every computer (esp. laptops) does have these interfaces and the built 3D laser range finder can therefore easily be used on mobile platforms. The mount and the servo are inexpensive and no special electronic devices are used, so the price of the whole system mainly depends on the used 2D laser range finder.

3. Typical constraints of laser scanners constructions

As evident from above analysis, in the different laser scanner constructions by its nature are involved the next typical constraints and limitations:

- a limited geometry of the field-of-view with non-uniformly distributed uncertainty of the sinus law application (Zussman et al., 1994), (Montemerlo & Thrun, 2004), (Sergiyenko et al. [a]; 2009), (Sergiyenko et al. [b]; 2009).
- non-uniform spatial distribution of the scanning tool – laser ray – along the variable striking distance (Guivant et al., 2001; Klöör et al., 1993) , (Surmann at al. 2001);
- not balanced torque of the rotating electromechanical system; wear process of friction surfaces and rocking of electromotor shafts (Surmann at al. 2001), (Pagnottelli et al., 2005);
- unwanted quaziperiodical noise of the complex nature in a photodetecting circuit (Básaca [a] et al., 2010);
- limited range of action due to non-lineal photodetected signal attenuation (Sergiyenko et al. a; 2009), (Sergiyenko O.Yu.; 2010).

The most prospective ways of the mentioned constraints decrease is a subject under consideration it the further sections.

4. Limitations decrease of the field-of-view geometry design

As we can observe from the several different laser scanner constructions mentioned above, they have a common point: for general compactness of device the emitter and receiver are located very closely to each other. But it is well known that for small angles a trigonometric function of sinus/tangens are approximately equal to the angle because of linearization of the trigonometric functions (truncation of their Taylor series). In our task these functions are the basic for used mathematical formalism. Hence, it causes non uniform resolution of the theoretical method inside a full field-of-view of the system. The same reason causes a problem of resolution at the angles close to 90^o.

Experimental proofs of such non-uniform uncertainty distribution are shown in (Rivas Lopez et al. [a], 2008), (Rivas Lopez et al. [b], 2008), (Rivas Lopez et al. , 2010), (Sergiyenko et al. [a]; 2009). See Fig. 16.

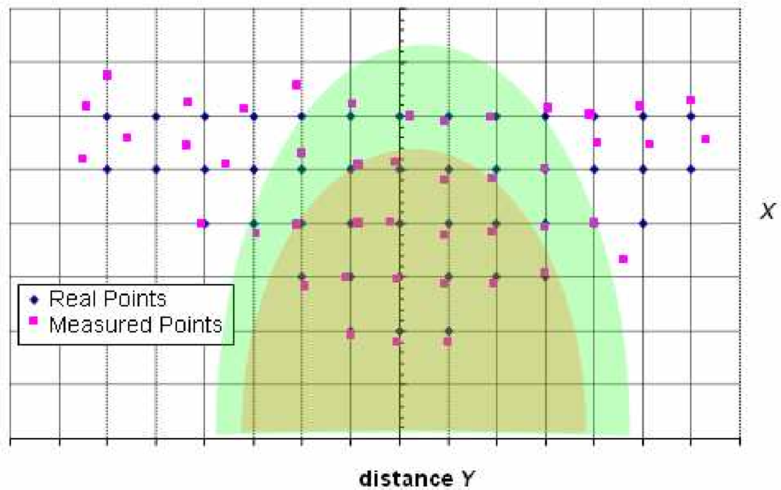

Fig. 16. Experimental graphic of point's measurement in 2D at variable obstacle positioning. TVS field-of-view and "accuracy zones", according to (Rivas Lopez et al. [a], 2008)

The accuracy of coordinates measurement is not uniform (see Fig. 16) in all TVS field-of-view, but in the olive- and green-zone correspondingly it is not more than 1% and 4% out of level of confidence (Rivas Lopez et al. [a], 2008), (Rivas Lopez et al. [b], 2008). Usually, modern regular step drives are operated with average velocity of 1 KHz. It means that we can obtain coordinates at least of 1000 points per second, each X, Y, and Z with metrological accuracy and defined uncertainties. This is a point to apply this TVS as input data sensory system.

Additionally, it is obviously that a triangulation base of 1m (used in mentioned publications) not just permits an optimal design of the optoelectronic system field-of-view, but also permits increase a computation speed for used trigonometric mathematical formalism because multiplication for 1 is an empty operation.

5. Geometrical centre search of the laser spot projection

The laser ray as the scanning tool of any laser scanner unfortunately has a non-uniform spatial distribution along the variable striking distance. This circumstance unfortunately causes that a shape and size of the laser spot projection on the scanning surface is significantly variable. It is shown in (Sergiyenko et al. [a]; 2009), (Rivas Lopez et al., 2010), and on the Fig.17.

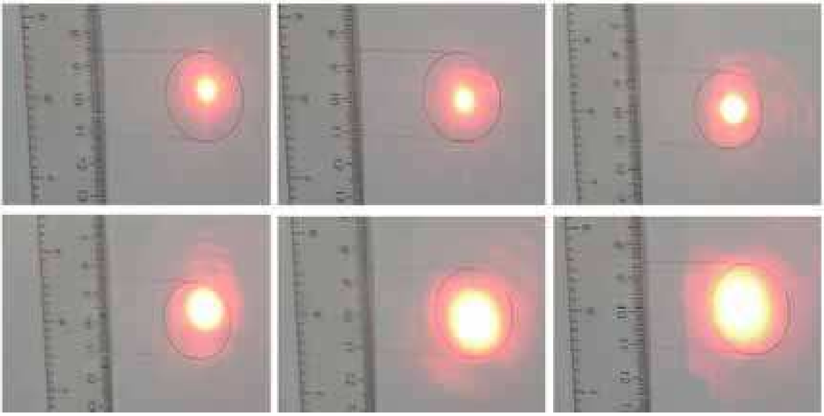

a)

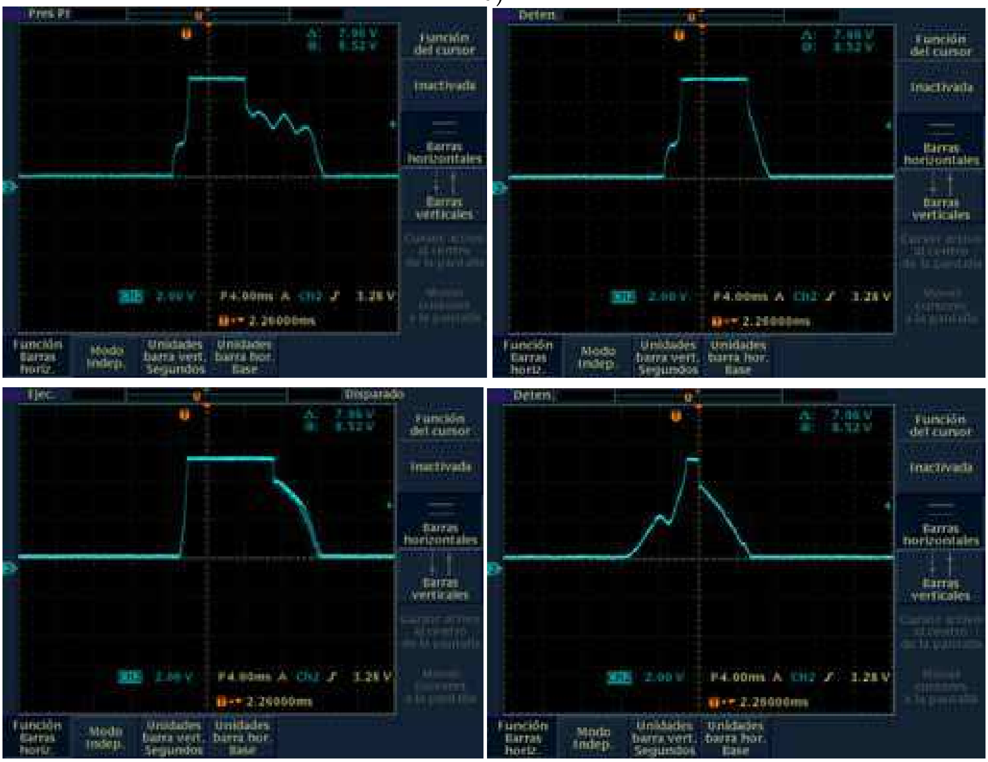

b)

Fig. 17. General view of the stop-signal at the different distances and highlighted spot sizes: a) spot sizes variation; b) stop-signal screenshot

It causes that spatial resolution of any method based on the spatial position estimation by such signals registration has a strong source of uncertainty.
The possible way for this disadvantage decrease is based on the theoretical method and special circuit of the signal energetic center search introduced in (Sergiyenko et al. [a]; 2009), (Rivas Lopez et al., 2010).

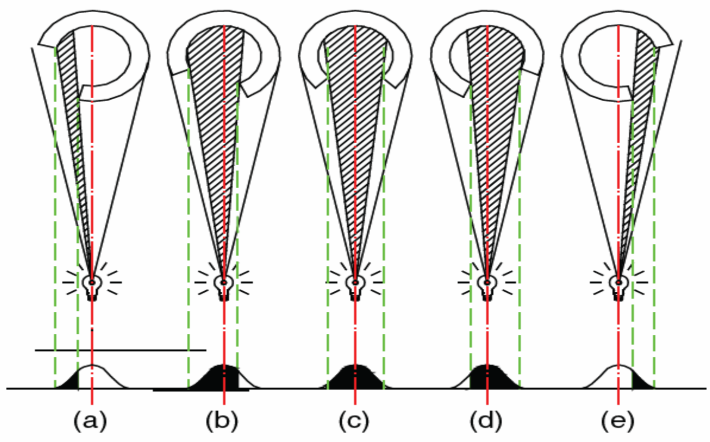

Fig. 18. The principle of noisy electrical stop-pulse formation during rotational scanning

The triangulation mathematic framework is still strongly theoretical. Because in the geometrical scheme we considering a pure geometrical objects, i.e. the straight line is precisely straight, without any curvature, have only length, all another sizes are zero; points have no any sizes and its location is characterized only by three Cartesian coordinates in the space.
Practically it is different (Rivas Lopez et al. , 2010). The optical ray it is a cone in general or even more complex shape depending on medium properties. The vertex of this cone also isn't a point, but distributed in some small spatial scope. The divergence inside this cone it is caused by many natural factors. It causes that practically the stop-pulse in photo receiver is not a short pulse of the standard form, but it is formed as shown on Fig. 18 (a-e).
It growth (Fig. 18, a) and falling down (Fig. 18, e), and fluctuating around its maximum area in figs. 18 (b-d). Taking to account the presence of some natural noise (as rule, white Gaussian noise) in this process, we can conclude that finally we need to operate the single electric signal of non-regular shape presented on Fig.19, a. Moreover, the shape and the width of this pulse are closely related to scanning velocity. But the scanning velocity in practical case is not a constant also. In this case the best problem solution is adequate signal processing. And our contribution is based on simple idea. What is it the red point on the Fig. 19, a? In the point of view of electric signals area on the graphic limited by signal curve is the energy transferred by this electric signal. So, this red point with certain small uncertainty is the signal energetic center. It is essential to note that position of the energetic center coincides for both pulses on the Fig. 19, a: ideal theoretical square pulse, and its real noisy performance. Much more essential is to note in this case, that the energetic center position uncertainty the less depends on noise, than becomes more the pulse area. In our task is the same like less scanning velocity.

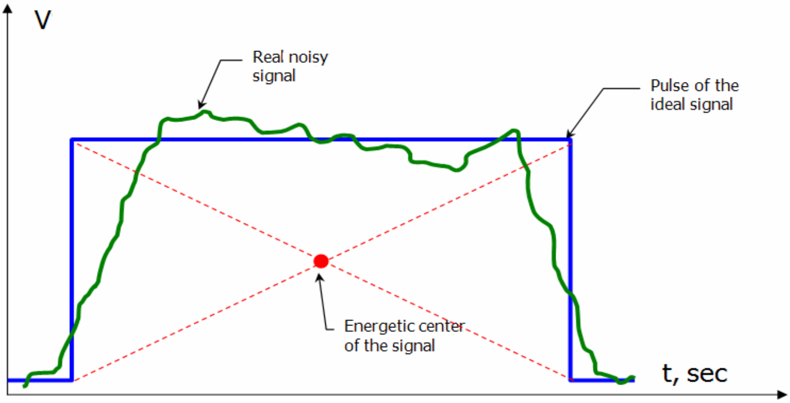

a)

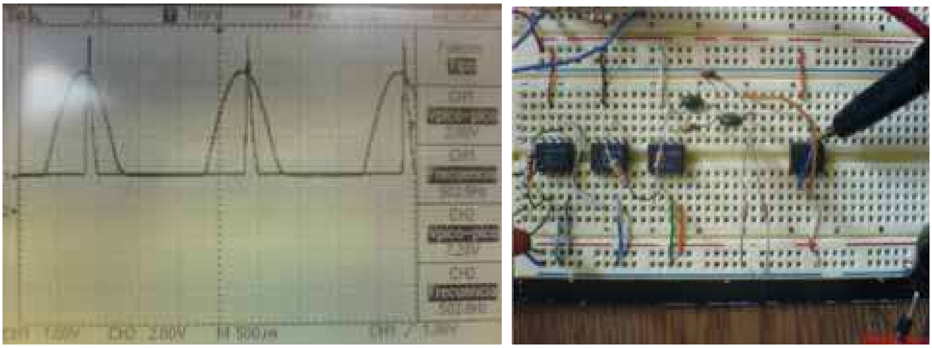

b)

Fig. 19. Method of the signal energetic center search: a) general purpose; b) differentiator circuit & functioning screenshot

From the other hand, as we consider this pulse as the optic blur equivalent registered by photosensor, it is the center of optical ray spatial cone. Such way we can detect in noisy electric signal the truth position of the unique straight line which belongs the same time the center of light source (active target) and the center of photoreceiver.
It is possible to provide practically using another strong and simple rule: the function (signal curve) maximum it is always where its derivative is zero. In another words, after finding the zero-cross position of first derivate function of the registered signal, we can find a real position of the EB in our coordinate system.
The practical realization of described operation it is possible in a several ways. However, in our primary experimentation we realize this operation using standard differentiator circuit (Fig.19, b). On the operation screenshot on Fig. 19, b it is clear evident that it is completely possible in a real time scale to obtain an electrical mark of the real light source position. Of cause it is a certain delay between real maximum position and its mark by pin-pulse (Fig. 19, b) because of differentiator circuit operating time. But it is strongly evident that it has a constant character and can be eliminated on the processing stage by simple correction factor.

6. Optimal design of laser scanner mechanical part

Serious problems of scanner normal functioning and sources of spatial resolution uncertainty are caused by not balanced torque of the rotating electromechanical system; mechanical movements delay; wear process of friction surfaces; rocking of electromotor shafts, etc.
The optimal design of the mechanical part is given in (Básaca [a,b] et al., 2010), it permits significant decrease of the most important electromechanical lacks of the previous prototype presented in (Sergiyenko et al. [a - c]; 2009), (Rivas Lopez et al. [a,b], 2008), (Rivas Lopez et al. , 2010).

(a) Prototype I system view (b) Positioning Laser (PL) (c) Scanning Aperture (SA)

Fig. 20. Prototype I

(a) Full Size Prototype II system view (b) Positioning Laser (PL) (c) Scanning Aperture (SA)

Fig. 21. Prototype II

Figure 20 shows Prototype I, this system was the first we built to demonstrate our method and although testing and experimentation were successful, we detected uncertainty points (See Fig. 17) that could be eliminated with an improved mechanical design.
Prototype II shown in Fig. 21, a, has several advantages in comparison to its predecessor; the most important is that in the new design most of the components, including the Laser are installed inside a cylindrical tube, thus placing the center of gravity in the center of the tube and providing an easier and more precise way of rotating the tube than the band used in Prototype I (see Fig. 20, a).
In other words this improvement decreases the TVS own torque which provide us with several advantages over Prototype I such as:

- The possibility of using an electric motor rated with lower torque, voltage and current per phase consumption.

- As a result, full system power consumption is reduced.
- Extended battery life which is essential for mobile applications.

Moreover, cross-comparing Fig. 20, b and Fig. 21, b and the pair Fig. 20, c - Fig. 21, c, in the constructions of PL and SA, the following improvements are presented.

The older Positioning Laser design used a fixture with a 45° mirror attached to the laser to redirect the laser beam in a 90° angle to a second 45° mirror which is attached directly to a stepper motor (Fig. 20, b). This motor is controlled to redirect the laser beam orthogonally to scan the area in front of the mobile robot.

On the other hand, the new PL design (Fig. 21, b) is based on the same general principle but has mechanical differences. E.g. the new PL has no fixture attached directly to the laser; instead of attaching the 45° mirror, part of the inside surface of the cylindrical tube is machined with mirror finish, with this, the possibility of uncertainty due to mirror displacement or improperly installed fixture is eliminated. It is the way to decrease the uncertainty deviation on Fig.17.

Another uncertainty source is that the more far away the surface marked by the laser, the greater the laser beam or spot diameter becomes. Fig 20, b shows that the laser beam travels a certain distance and is redirected by a mirror on two occasions, due to this travel, at the PL output the laser beam diameter is already greater than the originally emitted laser beam diameter.

Hence, another improvement is that the distances between the laser and the mirrors, i.e. the laser beam travel was reduced from centimeters to millimeters, by doing this the laser beam diameter in the PL output equals to the beam diameter emitted from the laser output, maintaining the lowest beam diameter possible within the TVS, therefore theoretically increasing the TVS range. Analysis of laser spot diameter variation is given in (Básaca [a,b] et al., 2010), it shows that this circumstance plays a significant role in total uncertainty distribution, and this part of general design is critical for total uncertainty decrease.

The Scanning Aperture design is maintained from Prototype I to II (Fig 20, c and Fig 21, c), the only difference is that the new SA is smaller in size and is installed within the cylindrical tube, however it's important to mention that the most critical point with the SA is to maintain it aligned in the same plane as PL in order to be able to create the dynamic triangle more solid or fixed in mechanical meaning, i.e. only this design guarantee that scanning ray and scanning plane are meeting exactly in the same plane triangle.

7. Noise filter for photoreceiver circuit

Experimental studies of electromechanical laser scanner prototype as the rule shows the presence of noise of the complex nature in a photodetecting circuit. It is caused by cross-action of two main components: mechanical vibration and, properly, optical noise.

The typical procedure of the filter design for such kind of noise, for different scanning velocities, will be introduced in full text of this paper basing on the material of publication in (Básaca [a] et al., 2010).

One of the most challenging points of normal TVS functioning is the presence of typical input noise mixed with the "stop-signal" train in the form of the screenshot on Fig. 22. This noise can be filtered by specially designed circuit (Fig. 23) with the aim of guaranteed detection of true position of the scanning ray reflected points, in other words the guaranteed localization of the real "stop-pulses".

As in every system, noise is present here too in the signal acquired from the photo receiver, after studying the signal we observed that the noise reaches maximum amplitude of 120 mV (see Fig. 22) with frequencies that vary between 400 Hz and 20 KHz. To eliminate this noise a Butterworth third order low pass filter (-60 dB per decade) was designed and implemented, see Fig. 23. The filter's output connects to a voltage level detector with a reference voltage of 120mV to reject the noise amplitude, whenever an obstacle is detected by the photo receiver a spike in the signal is detected, the voltage of this spike varies depending on the distance of the detected obstacle but is always greater than 120mV from the noise amplitude. The output of the voltage level detector is a signal of 5Vdc when an obstacle is detected and remains at 0Vdc when there is no obstacle, in other words providing us with a 0-5Vdc square signal which indicate us whether an object is present or not.

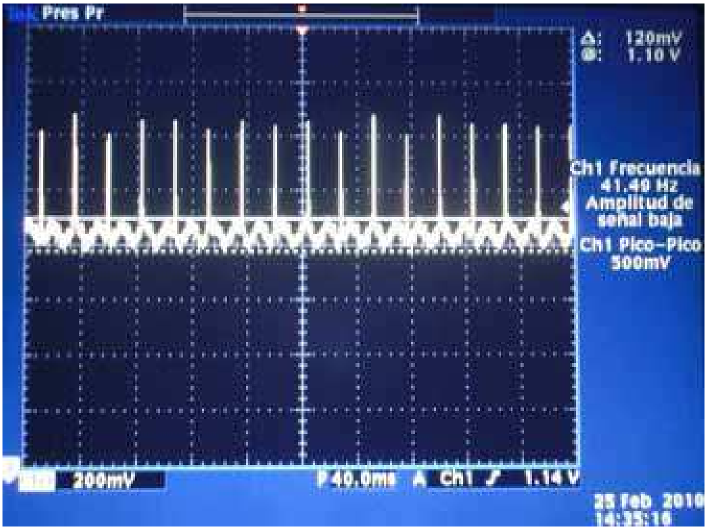

Fig. 22. Typical experimental noise voltage and frequency

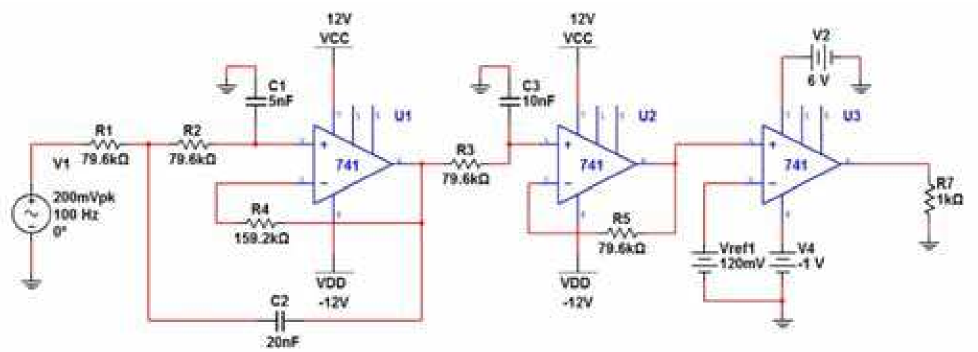

Fig. 23. Butterworth third order low pass filter (-60 dB/decade) and voltage level detector

The Butterworth type filter was chosen over other types such as Chebyshev filters due to Butterworth's more linear phase response and flat frequency response in our passband according to (Coughlin & Driscoll, 1999). Our filter was designed as follows:

$$\omega_c = 200;\ C_3 = 10nF \tag{10}$$

where ω_c is the cutoff frequency, the value assigned is 200 Hz in order to let pass the frequency band between 0 and 200 Hz, letting pass the signal of a detected obstacle and attenuating all the frequencies higher than 200 Hz.

$$C_1 = \frac{1}{2}C_3 = 5nF \tag{11}$$

$$C_2 = 2C_3 = 20nF \tag{12}$$

$$R = \frac{1}{\omega_c C_3} = \frac{1}{(6.25)(200)(5x10^{-9})} = 79.617k \tag{13}$$

$$R_1 = R_2 = R_3 = R = 79.617k\Omega \tag{14}$$

$$R_{f1} = 2R = 159.235k\Omega \tag{15}$$

$$R_{f2} = R = 79.617k\Omega \tag{16}$$

The filter with -60 dB/decade attenuation is achieved by cascading a -40 dB/decade filter and a -20 dB/decade filter. The total closed loop gain is the multiplication of each filter's gain. See Fig. 23 for the frequency response of the circuit shown on Fig. 23, (Coughlin & Driscoll, 1999).

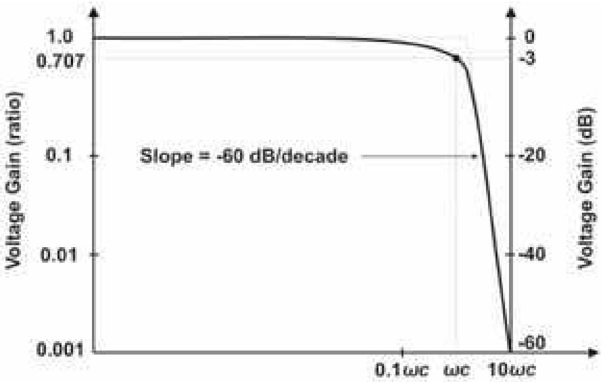

Fig. 24. Frequency response for Butterworth third order low pass filter (-60 dB/decade)

7.1 Simulation

The circuit presented on Fig. 23 was simulated with software from National Instruments, NI Multisim 10. Fig. 25, a shows a caption of a Simulated Tektronix Oscilloscope with three

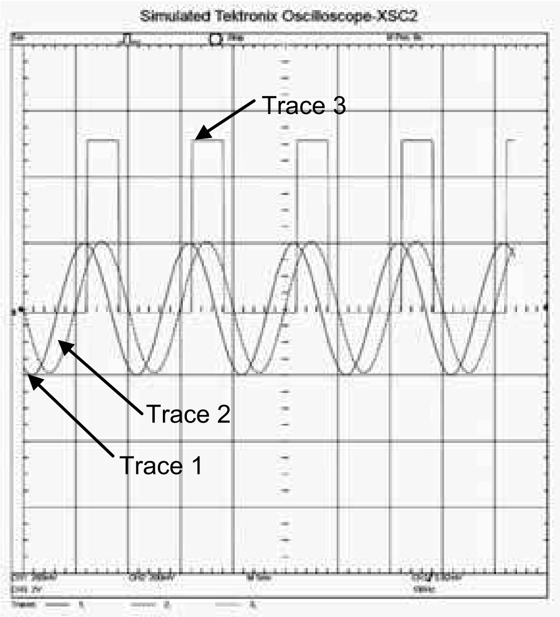

(a) Input signal is 200mV at 100 Hz; output is a 0-5Vdc square signal

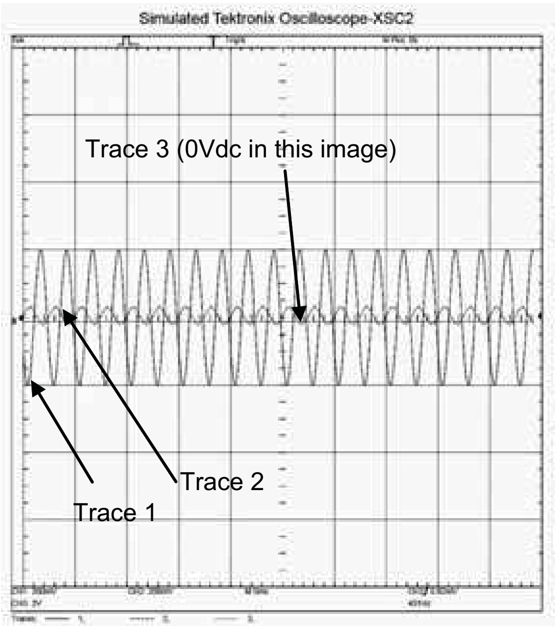

(b) Input is 200mV at 400 Hz; output is attenuated due to input frequency being higher than cutoff frequency (200 Hz), regardless of the input voltage.

Fig. 25. Low pass filter and voltage level detector output (circuit on Fig. 23)

signals, trace 1 is the circuit input signal that simulates the photo receiver output, this is the signal that is filtered and amplified, for this simulation the input signal is 200mV at 100 Hz. Trace 2 is the filter output, as shown below, the signal has the same amplitude as the original as long as its frequency is in the passband region (below 200 Hz), therefore it's not attenuated, it also has a delay of 8ms which is acceptable. And the last, trace 3, is the voltage level detector output, this signal will be 5Vdc if the signal voltage coming from the filter is greater than Vref (120mVdc), meaning an obstacle has been detected, and it remains 0Vdc if there is no obstacle in sight.

Fig. 25, b shows the case when the input signal is 200mV at 400 Hz, this frequency is in the stopband region (higher than 200 Hz), for this reason the trace 2 signal which is the filter output is attenuated to 35mV that for this purpose equals 0V. Therefore trace 3 remains at 0Vdc.

Thus, our simulation demonstrates that the designed filter can attenuate the experimentally detected undesired noise in TVS prototype above 400Hz.

7.2 Slower scanners for application in medical surgery

At the more slow scanning, which permits increase the resolution in spite of operating time, it was experimentally obtained the noise of same character, but with another typical values. Such scanning velocity decrease it is expedient, for example, for medical scanners application (Rodriguez et al., 2009).

The dead zone circuit DZC Fig. 28 cut any signal that is greater than 200mV; this eliminates any noise left over after applying the filter of -40db. The detected signal corresponding to the laser is greater than 400mV which allows the cut rise. In experimentation is carried out that useful signal is berried in noise, wish have in our case a typical form presented on Fig. 25. With the aim to delete this noise in this paper design DZC under consideration. After DZC we make a saturation of the signal and amplify to 5 Volts, thereby obtain a processable signal to detect the moment of triangulation. It should be mentioned that the period of existence of the triangle can be measured in the order of a millisecond, but this time is sufficient to calculate the necessary angles.

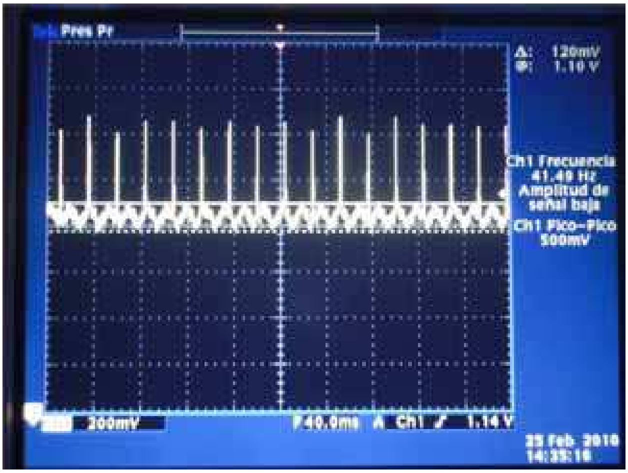

Fig. 26. 200 mv Noise, the peaks are the useful signal

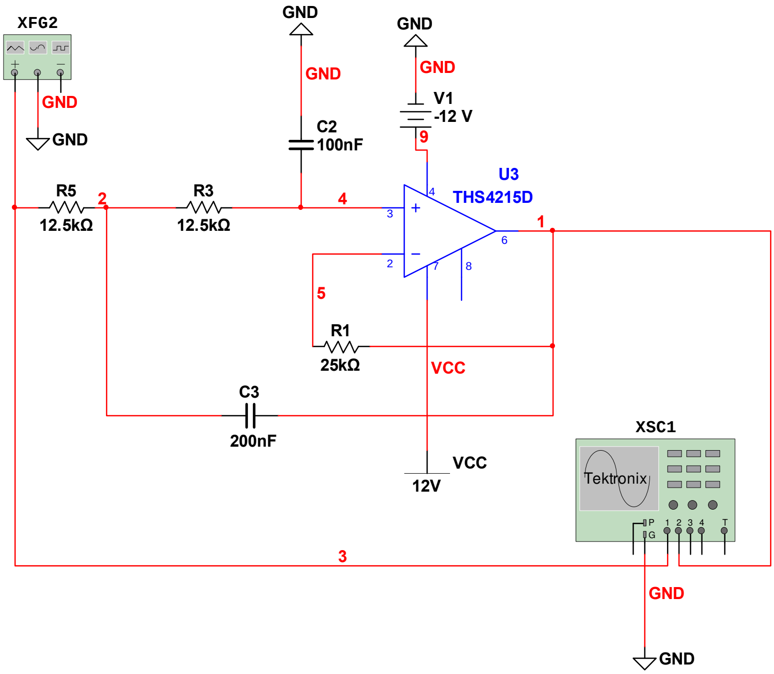

Fig. 27. Low pass Filter with -40db and fast attenuation response at 10ωc

The filter produces an attenuation of -40db/decade, after the cut-off the input magnitude decreases 40db when ω increases to a value of 10ωc Equation 18. The operational amplifier is connected so as to obtain unitary dc gain. It includes resistance R1 to the dc deviation. Since the operational amplifier circuit is a unitary gain amplifier, the voltage on C1 equals the output voltage (Coughlin & Driscoll, 1999, pp 294 – 297). The design procedure is simplified too if R3 and R5 are equal. Then follow the following equations:

Initial data

$$f_c = 90Hz \quad C_2 = 100nf \quad R_3 = R_5 = R \tag{17}$$

Cut frequency expressed in Radians/ Second

$$\omega_c = (2\pi)(f_c) \tag{18}$$

Capacitor 3 Value

$$C_3 = (2)(C_2) \tag{19}$$

Voltage Gain of the close loop

$$A_{CL} = \frac{1}{1 + j\omega RC} \quad A_{CL} = \frac{1}{1 + j1} = \frac{1}{\sqrt{2}\angle 45^{o}} \quad |A_{CL}| = \frac{1}{\sqrt{2}} = .707 \tag{20}$$

R Value using -40db as parameter

$$R = \frac{|A_{CL}|}{(\omega_c)(C_1)} \tag{21}$$

R1 Value:

$$R_1 = 2R \tag{22}$$

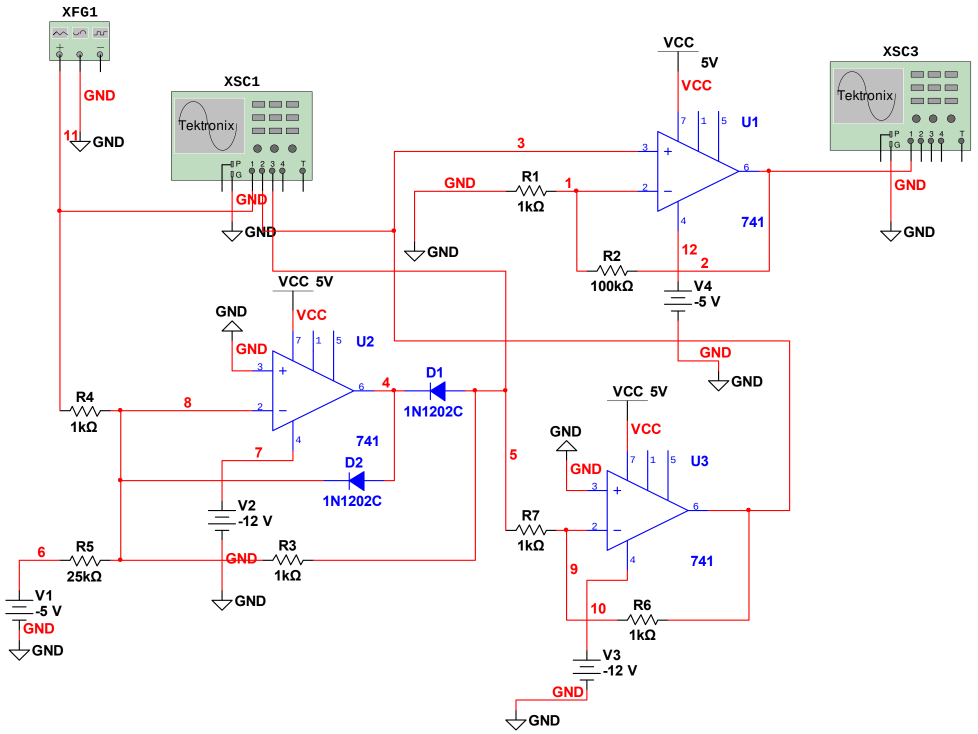

Fig. 28. Dead Zone to complement application filter circuit with saturation amplifier

Through a regulated supply voltage V1 and a resistance mR (R5) sets the reference voltage Vref. This is calculated from Equation 24. As will be shown the negative value of Vref is what defines the dead zone. The diode D2 always leads XFG1 values and set the "node 5 =-XFG1 – Vref". Whenever XFG1 exceeds the value of -Vref = 200mV, the output node 3 lets you know the amount XFG1 exceeds the value-Vref. There is a dead zone when there are values XFG1 below -Vref. (Coughlin & Driscoll, 1999, pp 200 – 204).
Initial data

$$R = R1 = R3 = R4 = R6 = R7 = 1k \tag{23}$$

Reference Voltage in the dead zone

$$V_{ref} = \frac{V_1}{m} \quad \text{(Node 6)} \tag{24}$$

Gain to be amplified and detect the signal as 0 volts or 5 volts (0 or 1 logic)

$$Gain = \frac{R2}{R1} \tag{25}$$

R5 Value

$$R5 = (m)(R) \tag{26}$$

In Fig. 30 are presented the results of simulation of the designed filter functioning. As shown Fig. 30 without a DZC the signal is not detectable (As in Fig. 26) and after DZC implementation it is eliminated undesired noise and the useful signal is clear end detectable.

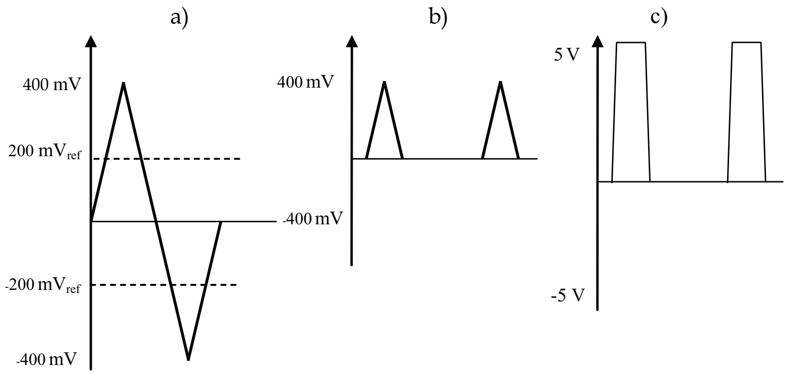

Fig. 29. a) dead zone circuit, b) Inverse Follow Circuit, c) Saturation amplifier

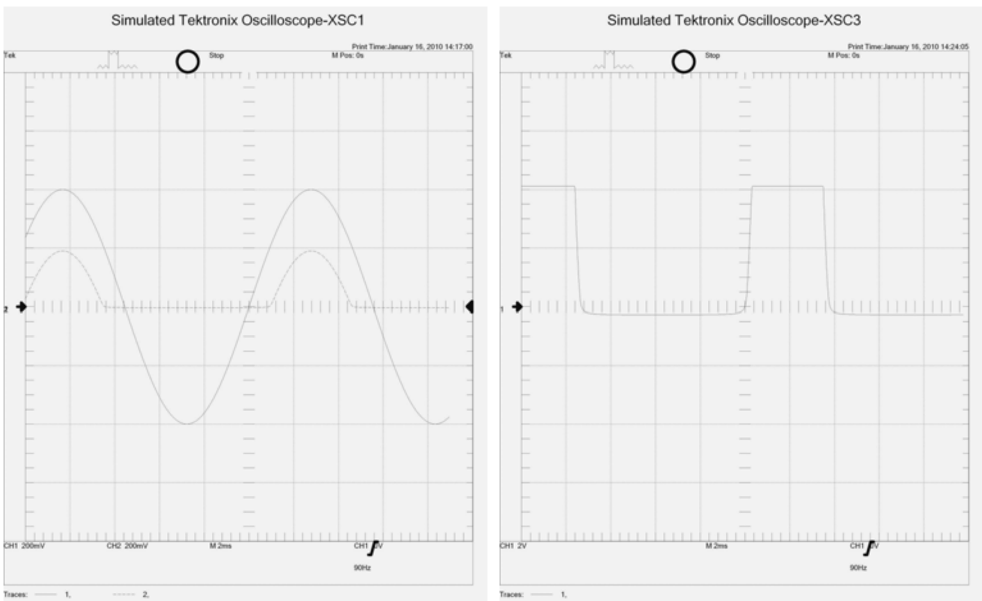

Fig. 30. Filter Output in 90 Hz Signal a) Signal as Fig. 25 without DZC b) Output Signal after DZC

8. Robust detection of the weak reflected signals

In (Sergiyenko et al. [a]; 2009), (Sergiyenko et al. [b]; 2009), (Sergiyenko et al. [c]; 2009), (Sergiyenko et al.; 2008), (Rivas Lopez et al. [a], 2008), (Rivas Lopez et al. [b], 2008), (Rivas Lopez et al. , 2010) it is shown various times that practically the most strong constraint of electromechanical laser scanner use is the signal attenuation (voltage decrease) in a photodetecting circuit. It is shown on Fig. 31:

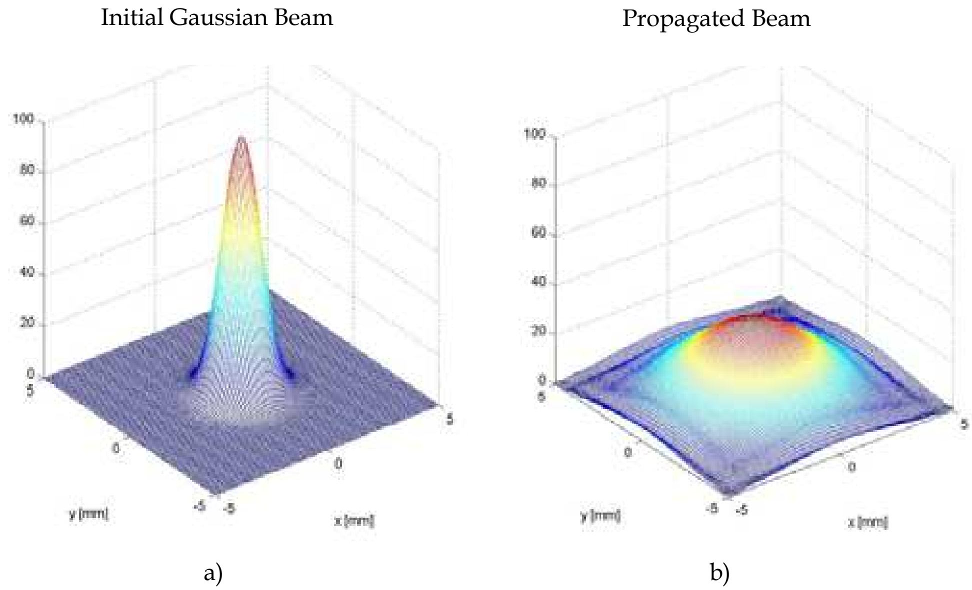

Fig. 31. a) Power distribution pattern for 0 meter from laser source. b) Power distribution pattern for 15 meters from laser source

The possible way for this disadvantage decrease is based on the theoretical method of robust photometer circuit introduced in (Hernandez, 2007), (Hernandez [a], 2008), (Sergiyenko et al. [a]; 2009), (Hernandez [b], 2008).

In the scientific literature (Hernandez [a], 2008) on photometer circuits operational amplifiers are frequently used for photodiode monitoring. Nevertheless, most of the operational amplifier connections used in this kind of application are based on basic current-to-voltage converter circuits.

Figure 32 shows the basic circuit, in which D represents the photodiode and R_f is the negative feedback resistor used to convert the photocurrent into an output voltage linearly related to the light energy.

One of the clear advantages of the circuit shown in Fig. 32 is that it is of easy implementation. Nevertheless, on the other hand, as the diode is not forming part of the feedback loop, there is no way to compensate for disturbances, variations in temperature, structure and unstructured uncertainties in the photodiode, noise, and so on.

Therefore, it is important to place the sensor in a feedback loop able to deal with the above-mentioned problems. Figure 33 shows an example of a photometer circuit with the diode placed in the feedback loop (Hernandez, 2007), (Hernandez [a], 2008), (Hernandez [b], 2008):

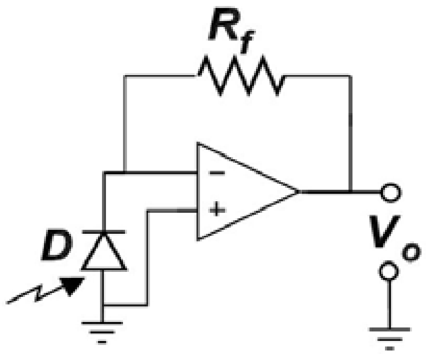

Fig. 32. Current-to-voltage converter circuit

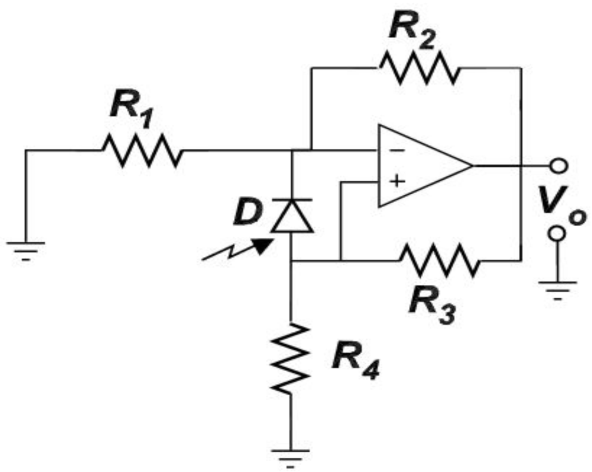

Fig. 33. Feedback photometer circuit

However, it is important to point out that in spite of the fact that the circuit shown in Fig. 33 is also of easy implementation, due to the fact that it works with positive feedback compensation it can become unstable if the values of the resistors are not chosen properly.

In (Hernandez [b], 2008), an in-depth analysis of such a circuit is carried out taking into consideration operational amplifier parameters such as the input resistance, input capacitance, open-loop gain and gain bandwidth product. Furthermore, the input-output transfer function analysis of the circuit shown in Fig.33 is carried out from the linear system theory point of view, considering that the operational amplifier is ideal.

Finally, considering the photodiode model shown in Fig. 34 (in which C_J is the junction capacitance, I_P is the light generated photocurrent, R_{SH} is the shunt resistance, R_S is the series resistance, R_L is the external load resistance and V_O is the output voltage), in (Hernandez, 2007), (Hernandez [a], 2008), (Hernandez [b], 2008) a procedure for the measurement uncertainty estimation of the circuit shown in Fig. 35 is presented.

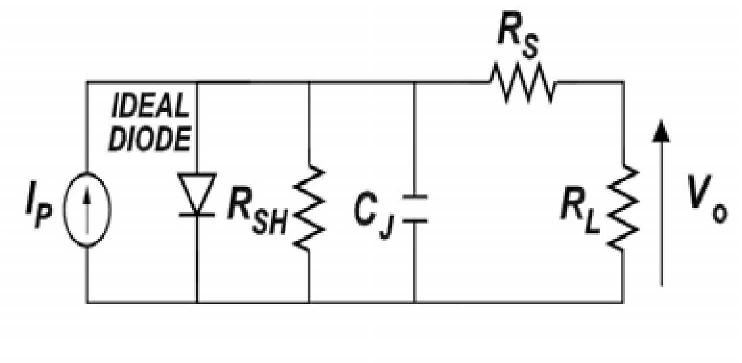

Fig. 34. Simplified version of the equivalent circuit for a photodiode

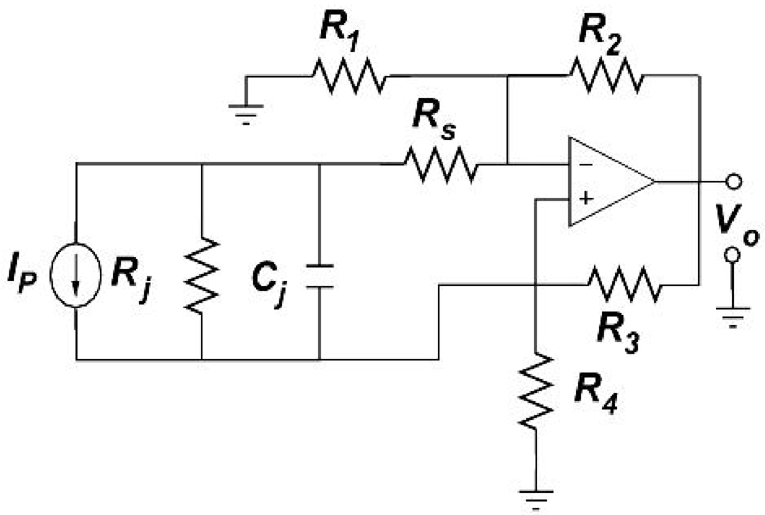

Fig. 35. Feedback photometer circuit with equivalent photodiode circuit

9. Conclusions

Finally, we can get the conclusion that possible grade of 3D scanners resolution improvements by combined application of all the mentioned actions will be efficient.

- Laser scanning systems always give a more resolution, accuracy and the better data processing time over other known Machine Vision systems. This is a reason for future research of the 3D electromechanical laser scanners for practical application matched for it in the best way. For best resolution in spatial domain it is expedient as shown above to use some additional technologies.
- Laser scanning systems always give a worse solution than other known Machine Vision systems in a part of energy consuming, medium optical conditions dependence and

range of action. So, Laser scanning systems designers always must to take in mind this fact, and to provide additional corrective measures for better system application.

- Due to non-uniform uncertainty distribution in instantaneous field-of-view (IFOV), as well in full field-of-view, it desirable the optimal geometrical design of the optoelectronic system field-of-view strictly linked to the certain practical application (i.e. static monitoring of large civil engineering structures; fast dynamic monitoring of the certain sector in indoor or outdoor autonomous robot navigation; medical scanning of the biological object with reduced movement activity; visual control of surfaces in automated assembly; etc.). In other words, the spatial sector under inspection must to be located in a smallest error sector of total TVS field-of-view. This requirement in general coincides with the basic theoretical concepts of the electro-optical system design (Fig. 5.1 on p.63 in (Wyatt, C.L., 1991)). It is expedient to note, that optimal geometrical design also permits sometimes increase a computation speed for used trigonometric mathematical formalism (for example, because multiplication or division for 1 is an empty operation).
- The use of the theoretical method and special circuit of the signal energetic center search permits us eliminate totally one of the most complex sources of uncertainty. It is uncertainty caused by irregular form and variable size of the projected light spot. It is especially important note that the variable size of the projected light spot has the non-linear relation to the distance between scanner and object surface. The uses of our theoretical method permits completely exclude this complex dependence and to establish the uncertainty rate only as a rigorous function of internal circuit parameters.
- The optimal design of the TVS mechanical part permits significant decrease of undesirable axial play, torque and wear. Mentioned above actions implementation gives a possibility to possibility of using an electric motor rated with lower torque, voltage and current per phase consumption for full system power consumption reduction and extended battery life which is essential for mobile applications.
- The typical challenging point of normal TVS functioning is the presence of input noise. As shown in the present paper, it is always necessary to realize an electronic filtration of such noise and parameters of such noise are mostly dependant on scanning velocity. Unfortunately, for this particular task only experimental test of electromechanical laser scanner prototype shows the presence of noise of the complex nature in a photodetecting circuit and its physical characteristics. It is caused by cross-action of mechanical vibration and, properly, optical noise. However, the special filter design for different scanning velocities is very similar and regular in its procedure, as it was shown in examples described in subsections 7.1 and 7.2.
- Theoretical method of robust photometer circuit introduced on photometer circuits operational amplifiers used for photodiode monitoring can permits to detect a weak signal which never been detected before in electromechanical scanners.

10. Acknowledgements

This work has been partially supported by the Autonomous University of Baja California, Mexico (projects No. 2352, in 2003-2004 and N2386, in 2005-2006) and the Ministry of Science and Innovation (MICINN) of Spain in 2009-2010 under the research project TEC2007-63121, and the Universidad Politecnica de Madrid. The authors would like to thank to various international congresses organizers, where the different aspects of the present work were presented, for fruitful discussions and valuable remarks. The authors dedicate this work to the grateful memory of Dr. Valentin Yevstaf'yevich Tyrsa; and would like to thank to Prof. Christofer Druzgalsky and Jason McDowell (Electrical Engineering Department of California State University, Long-Beach, USA) for their invaluable assistance with English language. We appreciate also Dr. Daniel Hernandez-Balbuena's invaluable assistance in a part of discussion about uncertainty of the repetitive cyclic measurements.

11. References

Andersen, J. C.; Blas, M. R.; Ravn, O.; Andersen, N. A. & Blanke, M. (2006). Traversable terrain classification for outdoor autonomous robots using single 2D laser scans. *Integrated Computer-Aided Engineering*, Vol. 13, No. 3, 2006, 223-232, ISSN 10692509.

Básaca, L.C. a; Rodríguez, J. C.; Sergiyenko, O.; Tyrsa, V.V.; Hernández, W.; Nieto Hipólito, J. I. & Starostenko, O. (2010). 3D Laser Scanning Vision System for Autonomous Robot Navigation, *Proceedings of IEEE International Symposium on Industrial Electronics (ISIE-2010)*, Bari, Italy, July 4-7, 2010, pp.1773-1779, ISBN 978-1-4244-6390-9

Básaca, L.C. b; Rodríguez, J. C.; Sergiyenko, O.; Tyrsa, V.V.; Hernandez, W.; Nieto Hipolito, J.I. & Starostenko, O. (2010). Resolution improvement of Dynamic Triangulation method for 3D Vision System in Robot Navigation task, *Proceedings of 36th Annual Conference of the IEEE Industrial Electronics Society (IECON-2010)*, Glendale, Arizona, USA, November 7-10, 2010, pp. 2880-2885. ISBN 978-1-4244-5225-5, ISSN 1553-572X

Beraldin, J.-A.; Blais, F.; Rioux, M.; Cournoyer, L.; Laurin, D. & MacLean, S.G. (2000) Eye-safe digital 3D sensing for space applications, *Optical Engineering*, Vol. 39, No, 1, January, 2000, 196-211, ISSN 0091-3286.

Beraldin, J.-A.; El-Hakim, S.F. & Cournoyer, L. (1993). Practical Range Camera Calibration, *Videometrics II Π(Proceedings Volume)*, Sabry F. El-Hakim, pp. 21-31, Proceedings of SPIE Vol. 2067, ISBN 9780819413321.

Bertozzi, M.; Broggi, A. (1997). Vision-based vehicle guidance, *Computer*, Vol. 30, No. 7, July, 1997, 49–55, ISSN 0018-9162.

Blais, F.; Beraldin, J.-A. & El-Hakim, S.F. (2000). Range Error Analysis of an Integrated Time-of-Flight, Triangulation, and Photogrammetry 3D Laser Scanning System. *Proceedings of SPIE Vol. 4035 AeroSense 2000*, pp. 236-247, ISBN 0-8194-3661-5, Orlando, FL, USA, April, 2000, SPIE, Bellingham, Washington.

Blais, F.; Rioux, M. & Beraldin, J.-A. (1988). Practical Considerations for a Design of a High Precision 3-D Laser Scanner System, *Proc. Soc. Photo-Opt. Instrum. Eng.*, Vol. 959, 1988, 225-246, ISSN 0361-0748.

Blais, F.; Rioux, M. & MacLean, S.G. (1991). Intelligent, Variable Resolution Laser Scanner for the Space Vision System, *Acquisition, Tracking, and Pointing V (Proceedings Volume)*, Michael K. Masten & Larry A. Stockum, pp. 473-479, Proceedings of SPIE Vol. 1482, ISBN 9780819405913.

Coughlin, R. F.; Driscoll, F. F. (1999). Operational Amplifier with diodes, in *Operational Amplifier and lineal integrate circuits*, Prentice Hall, Mexico DF, ISBN 970-17-0297-0, pp 294 – 297.

Fernandez, D. & Price, A. (2005). Visual detection and tracking of poorly structured dirt roads, *Proceedings of 12th International Conference on Advanced Robotics 2005. ICAR*

'05, pp. 553–560, ISBN 0-7803-9178-0, Seattle Sheraton Hotel & Towers, July, 2005, IEEE, Seattle.

Fischer, A. (2007). Digital Processing and Fusion of 3D Data from Emerging Non-Contact 3D Measurement Technologies, In: *The future of product development*, Frank-Lothar Krause, (Ed.), pp. 387-396, Springer, ISBN: 978-3-540-69819-7, Berlin, Germany.

Guivant, J. E.; Masson, F. R. & Nebot, E. M. (2001). Optimization of the simultaneous localization and map-building algorithm for real-time implementation, *IEEE Transaction on Robotics and Automation*, Vol. 17, No. 3, June 2001, 242–257, The University of Sidney, Australia, ISSN 1042-296X.

Hähnel, D; Schulz, D. & Burgard, W. Map Building with Mobile Robots in Populated Environments. *Proceedings of IEEE/RSJ International Conference on intelligent robots and systems,* pp.496-501, ISBN 0-7803-7398-7, Lausanne , SUISSE, 30 September - 4 October 2002.

Hernandez, D.; Sergiyenko, O.; Tyrsa, V.; Burtseva, L. & Rivas López, M. (2009). Signal frequency measurement by rational approximations, *Measurement*, vol.42, issue 1, Elsevier, January 2009, p. 136-144. ISSN: 0263-2241

Hernandez, W. (2007). Robustness and noise Voltage Analysis in Two Photometer Circuits, *IEEE Sensors Journal*, vol. 7, 2007, USA, pp. 1668-1674. ISSN 1530-437X

Hernandez [a], W. (2008). Linear Robust Photometer Circuit, *Sensors and Actuators A*, vol. 141, Elsevier, 2008, p.447-453, ISSN 0924-4247

Hernandez [b], W. (2008). Performance Analysis of a Robust Photometer Circuit, *IEEE Transactions on Circuits and Systems-II,* vol. 55, No.12, December, 2008, p. 106-110, ISSN: 1549-7747

Jochem, T.; Pomereau, D. & Thorpe, C. (1993). Maniac: a next generation neurally based autonomous road follower, in F. Groen, S. Hirose and C. Thorpe, eds, *Proceedings of the International Conference Intelligent Autonomous Systems IAS-3*, pp. 592–601, ISBN 90-5199-122-3, Pittsburgh, PA, USA, February 1993, IOS Press, Pittsburgh.

Klöör, P.L.; Lundquist, P.; Ohlsson, P.; Nygrds, J. & Wernersson, A. (1993) Change detection in natural scenes using laser range measurements from a mobile robot, *Proceedings of 1st IFAC International Workshop on Intelligent Autonomous Vehicles*, pp. 71–76, ISBN 0080422233, Southampton, UK, April, 1993, Pergamon Press.

Laurin, D.; Blais, F.; Beraldin, J.-A. & Cournoyer, L. (1996). An eye-safe Imaging and Tracking laser scanner system for space Applications, *Laser Radar Technology and Applications (Proceedings Volume)*, Gary W. Kamerman (Ed.), pp. 168-177, Proceedings of SPIE Vol. 2748, ISBN 9780819421296.

Legnemma, K.; Brooks, C. & Dubowsky, S. (2004). Visual, tactile, and vibration-based terrain analysis for planetary rovers, *Proceedings of IEEE Aerospace Conference 2004*, Vol. 2, March, 2004, 841–848, ISSN 1095-323X.

Macedo, J.; Matthies, L. & Manduchi, R. (2000) Ladar-based discrimination of grass from obstacles for autonomous navigation, *Proceedings of Experimental Robotics VII ISER 2000*, pp. 111–120, ISBN 3-540-42104-1, Waikiki, Hawaii, December, 2000, Springer, Waikiki.

Montemerlo, M. & Thrun, S. (2004). A multi-resolution pyramid for outdoor robot terrain perception, *Proceedings of the Nineteenth National Conference on Artificial Intelligence AAAI-04*, pp 464–469, ISBN 978-0-262-51183-4, San Jose, California, at the San Jose Convention Center, July, 2004, AAAI Press, San Jose, California.

Nüchter, A. (2007). 6D SLAM - 3D Mapping Outdoor Environments, in: Quantitative Performance Evaluation of Robotic and Intelligent Systems, *Journal of Field Robotics*, Vol. 24, No. 8-9, November, 2008, pp. 699-722, ISSN 1556-4959

Nüchter, A. (2008). Towards semantic maps for mobile robots, *Robotics and Autonomous Systems*, *Elsevier,* Vol. 56, No. 11, November, 2008, pp. 915-926, ISSN 0921-889.

Pagnottelli, S.; Taraglio, S.; Valigi, P. & Zanela, A. (2005). Visual and laser sensory data fusion for outdoor robot localisation and navigation, *Proceedings of 12th International Conference on Advanced Robotics 2005. ICAR '05*, 171–177, ISBN 0-7803-9178-0, Seattle; Washington, July 2005, IEEE, Seattle.

Rivas Lopez [a], M.; Sergiyenko, O. & Tyrsa, V. (2008). Machine vision: approaches and limitations, In: *Computer vision,* Xiong Zhihui, (Ed.), pp. 395-428. Editorial: IN-TECH, ISBN 978-953-7619-21-3, Vienna, Austria.

Rivas Lopez [b], M.; Sergiyenko, O.; Aguirre, M.; Devia, L.F.; Tyrsa, V.; & Rendón, I. (2008). Spatial data acquisition by laser scanning for robot or SHM task. *Proceedings of IEEE-IES International Symposium on Industrial Electronics (ISIE-2008)*, p.1458-1463, ISBN 978-1-4244-1666-0, Cambridge, United Kingdom, 30 June -2 July 2008, IEEEXplore, Cambridge.

Rivas Lopez, M.; Sergiyenko, O.; Tyrsa, V.; Hernández Perdomo, W.; Hernández Balbuena, D.; Devia Cruz, L.; Burtseva, L.; & Nieto Hipólito J. I. (2010). Optoelectronic method for structural health monitoring. *International Journal of Structural Health Monitoring*, Vol.9, No.2, March, 2010, SAGE Publications, pp.105-120, ISSN 1475-9217

Rodríguez, J.C., Sergiyenko, O.; Básaca, L.C. (2009). Medición de parámetros biométricos específicos en el rostro humano por medio de barrido láser dinámico (in Spanish). *Proceedings of Congreso Nacional de Estudiantes de Posgrado del Instituto de Ingeniería,* UABC Mexicali B.C, November, 25-27, 2009, 6p., ISBN: 978-607-7753-33-9.

Sergiyenko, O.; Burtseva, L.; Bravo, M.; Rendón, I. & Tyrsa V. (2006). Scanning vision System for Mobile Vehicle Navigation. *Proceedings of IEEE-LEOS Multiconference on Electronics and Photonics (MEP-2006),* p.178-181, ISBN 1-4244-0627-7, Guanajuato, Mexico, 7-10 November, 2006, IEEEXplore, Guanajuato.

Sergiyenko, O.; Tyrsa, V.; Hernandez-Balbuena, D.; Rivas López, M.; Rendón López, I. & Devia Cruz, L.F. (2008). Precise Optical Scanning for practical multiapplications. *Proceedings of IEEE-34th Annual Conference of IEEE Industrial Electronics (IECON'08)*, p.1656-1661, ISBN 978-1-4244-1766-7, Florida, USA, 10-13 November, 2008, IEEEXplore, Orlando.

Sergiyenko, O. [a]; Hernandez, W.; Tyrsa, V.; Devia Cruz, L.; Starostenko, O. & Pena-Cabrera, M. (2009). Remote Sensor for Spatial Measurements by Using Optical Scanning, *Sensors,* 9(7), July, 2009, MDPI, Basel, Switzerland, pp. 5477-5492. ISSN 1424-8220.

Sergiyenko, O. Y. [b]; Tyrsa, V. V.; Devia, L. F.; Hernandez, W.; Starostenko, O. & Rivas Lopez M. (2009). Dynamic Laser Scanning method for Mobile Robot Navigation. *Proceedings of ICROS-SICE International Joint Conference (ICCAS-SICE 2009)*, p. 4884-4889, ISBN: 978-4-907764-33-3, Fukuoka, Japan, August, 18-21, 2009, IEEEXplore, Fukuoka.

Sergiyenko, O. Yu. [c]; Hernandez, W.; Tyrsa, V. V. & Hernández-Balbuena, D. (2009). Precise Optical Scanning for multiuse. *Proceedings of IEEE-35th Annual Conference of IEEE Industrial Electronics (IECON'09)*, pp.3399-3404. ISBN 978-1-4244-4649-0/09, 3-5 November, 2009, Porto, Portugal, IEEEXplore, Porto.

Sergiyenko, O. Yu. (2010) Optoelectronic System for Mobile Robot Navigation. Springer/Allerton Press, Inc., *Journal Optoelectronics, Instrumentation and Data Processing*, Vol. 46, No. 5, October, 2010, pp.414-428 – ISSN 8756-6990

Son, S.; Park, H. & Lee, K. H. (2002). Automated laser scanning system for reverse engineering and inspection. *International Journal of machine tools and manufacture*. Pergamon Press, Great Britain, Vol. 42; No. 8, 2002, p. 889-897, ISSN 0890-6955

Surmann, H.; Lingemann, K.; Nüchter, A.; & Hertzberg, J. (2001). A 3D laser range finder for autonomous mobile robots. *Proceedings of the 32nd ISR (International Symposium on Robotics),* pp. 153 - 158, 19-21 April 2001.

Surmann, H. (2003), An autonomous mobile robot with a 3D laser range finder for 3D exploration and digitalization of indoor environments, *Journal Robotics and Autonomous Systems (JRAS), Elsevier Science*, Volume 45, No. 3-4, December, 2003, pages 181 – 198, ISSN 0921-8890.

Vandapel, N.; Huber, D.F.; Kapuria, A. & Hebert, M. (2004). Natural terrain classification using 3-d ladar data, Proceedings *of IEEE International Conference on Robotics and Automation 2004. IEEE ICRA '04*, Vol. 5, April-May, 2004, 5117–5122, ISSN 1050-4729.

Wallace, R.; Matsuzaki, K.; Goto, Y.; Crisman, J.; Webb, J. & Kanade, T. (1986). Progress in robot road-following, *Proceedings of IEEE International Conference on Robotics and Automation 1986*, Vol. 3, April, 1986, 1615–1621, ISSN 0882-4967.

Wettergreen, D.; Tompkins, P.; Urmson, C.; Wagner, M. & Whittaker, W. (2005) Sun-synchronous robotic exploration: Technical description and field experimentation, *International Journal of Robotics Research*, Vol. 24, No. 1, January, 2005, 3–30, ISSN 0278-3649.

Wijesoma, W.; Kodagoda, K. & Balasuriya, A. (2004). Road-boundary detection and tracking using ladar sensing, *IEEE Transactions on Robotics and Automation*, Vol. 20, No. 3, June, 2004, 456–464, ISSN 1042-296X.

Wulf, O.; Kai, O; Christensen, Henrik I.; Wagner, B (2004), 2D Mapping of Cluttered Indoor Environments by Means of 3D Perception, *International Conference on Robotics & Automation*, ISBN : 0-7803-8232-3, New Orleans, LA, April 2004, IEEE, New Orleans

Wulf, O. & Wagner, B. (2003), Fast 3D Scanning Methods for Laser Measurement Systems, *Proceedings of International Conference on Control Systems and Computer Science*, 2003, p. 312-317, ISBN: 973-8449-18-9 Bucharest, Romania, July 2003.

Wyatt, C.L., (1991). Electro-optical system design: For information Processing .McGraw-Hill, ISBN 0-07-072184-X, New York, 1991, 343p.

Zussman, E.; Schuler, H. & Seliger, G. (1994). Analysis of the geometrical feature detectability constraints for laser-scanner sensor planning. *The International Journal of Advanced Manufacturing Technology*, Vol. 9, No. 1, January, 1994, p. 56–64, ISSN 1433-3015.

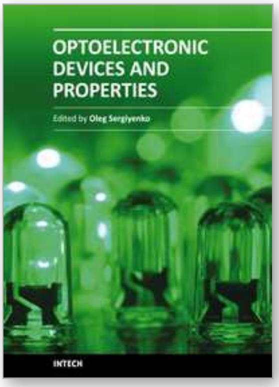

Optoelectronic Devices and Properties
Edited by Prof. Oleg Sergiyenko

ISBN 978-953-307-204-3
Hard cover, 660 pages
Publisher InTech
Published online 19, April, 2011
Published in print edition April, 2011

Optoelectronic devices impact many areas of society, from simple household appliances and multimedia systems to communications, computing, spatial scanning, optical monitoring, 3D measurements and medical instruments. This is the most complete book about optoelectromechanic systems and semiconductor optoelectronic devices; it provides an accessible, well-organized overview of optoelectronic devices and properties that emphasizes basic principles.

MÉTODO DE BARRIDO ÓPTICO PARA MEDICIÓN DE ÁNGULOS, COORDENADAS Y DESPLAZAMIENTO DE UNO O VARIOS PUNTOS EN UN PLANO BIDIMENSIONAL.

OBJETO DE LA INVENCIÓN

La presente invención propone una forma de medir las coordenadas y desplazamiento de uno o varios puntos en un plano bidimensional utilizando un nuevo método de barrido óptico.

ANTECEDENTES

La invención que se presenta se relaciona con la medición de coordenadas, y desplazamiento de puntos en un plano bidimensional, utilizando un nuevo método de barrido óptico. Existen algunos método similares, como los que se describen en las patentes de los Estados Unidos 5,455,708; 5,392,149 y 5,142,403 que aunque se asemejan en que el barrido se lleva a cabo con un espejo giratorio, su principio de operación es completamente diferente, pues los métodos de las patentes citadas arriba, utilizan un espejo poligonal configurado con varias superficies de reflexión equilaterales y equidistantes con respecto al eje de rotación, de tal forma que al girar el espejo, el haz de luz incidente es reflejado secuencialmente por cada una de las superficies para ser captado por algún elemento óptico, en tanto que la invención propuesta propone realizar el barrido con un espejo cilíndrico con una sola superficie de reflexión a 45º que a diferencia de los espejos poligonales, permite tener una medición continua y el tratamiento formal para la estimación de las coordenadas es en esencia diferente.

La invención propuesta tiene también como antecedente el sistema presentado por los inventores (Oleg Sergiyenko, Moisés Rivas y Vera Tyrsa, en el artículo titulado “Machine Vision: Approaches and Limitations”, publicado, en noviembre de 2008, como el capítulo 22 del libro Computer Vision, de editorial Intech, editor Xiong Zhihui). En esta publicación se presenta un sistema de visión 3D conformado por una apertura de barrido óptico pasivo, similar al que aquí se presenta, pero el sistema completo que se describe en la publicación citada incluye un elemento activo, es decir un elemento que emite un haz de luz por medio de un laser cuyo centro de emisión está colocado sobre una base a una distancia de 1m con respecto al centro del elemento colocado sobre la misma base, asumiendo que esta es la base de un triángulo y así, con el ángulo de emisión con respecto al punto u objeto bajo observación y el ángulo medido por la apertura de barrido determina las coordenadas del punto u objeto, la diferencia con la invención propuesta es que ésta comprende dos elementos de barrido fijados sobre una base, estos elementos de barrido son pasivos, es decir no emiten luz, solo captan la luz de una o varias fuentes emisoras colocadas en un plano bidimensional. El ángulo medido por cada uno de los elementos de barrido y la base del triángulo, con dimensión conocida, permite estimar las coordenadas 2D de la fuente emisora de luz bajo estudio y con éstas calcular el desplazamiento, en caso de existir. En el artículo

(“Optoelectronic Method for Structural Health Monitoring” publicado por los inventores en marzo de 2010, en el Vol. 9(2) del Journal Structural Health Monitoring, de editorial SAGE), se describe de manera general el funcionamiento del elemento de barrido, pero no se presenta el sistema completo con los dos elementos, ni se describe como se calcula el desplazamiento con este método en el plano 2D.

BREVE DESCRIPCIÓN DE FIGURAS.

La figura 1 es un diagrama esquemático que permite explicar el método de barrido óptico.

La figura 2 es un diagrama temporal de las señales de inicio y fin de la medición.

La figura 3 es una representación geométrica de triangulación dinámica, que auxilia para calcular las coordenadas polares de la fuente emisora de luz (1)

DESCRIPCIÓN DETALLADA DE LA INVENCIÓN

Los detalles característicos de este nuevo método de barrido óptico para medición de coordenadas y desplazamiento de uno o varios puntos en un plano bidimensional, se muestran claramente en la siguiente descripción y en los dibujos que se acompañan con carácter ilustrativo y no limitativo, así como una ilustración de aquella y siguiendo los mismos signos de referencia para indicar las partes y figuras mostradas.

La invención propuesta consiste en un método de barrido óptico para medición de coordenadas y desplazamiento de uno o varios puntos en un plano bidimensional que opera con dos dispositivos como el que se muestra en la figura 1, siendo esta ilustrativa, más no limitativa y sus fases son:

a). Se coloca la fuente emisora de luz (1), en el punto bajo estudio, a una distancia l, de dos receptores SBOP como el que se muestra en la figura 1, cada SBOP se conforma de un espejo (2) , que gira con una velocidad ω.

b). Cuando empiezan a girar en sentidos opuestos los espejos (2) contenidos en los dispositivos de barrido, y se encuentran con el haz de un emisor de luz (6), el fotodetector (5) genera un pulso eléctrico indicando el inicio de la medición del ángulo α para cada uno de los dispositivos de barrido como se ilustra en la figura 3 ; α_2 para SBOP2 y α_3 para SBOP1 este pulso es representando en la figura 2 con la marca (m1); una vez que los espejos (2) alcanzan una velocidad máxima mantienen una velocidad constante ω.

c). El haz emitido por la fuente emisora de luz(1) llega con un ángulo de incidencia β, con respecto a la perpendicular del espejo (2), por lo que es reflejado con un mismo ángulo β, de acuerdo a la ley de reflexión (C.L. Wyatt Electro-Optical System Design: For Information Processing ,NY: McGraw-Hill, p. 343, 1991), para pasar a través de un lente (3), que redirecciona el haz, quedando en paralelo con el eje central del lente, para ser captado por un fotodetector (5) o cualquier otro dispositivo que convierta la señal luminosa en una señal eléctrica, el cual genera una señal en forma de una función gaussiana (8), que posteriormente será digitalizada (9) y procesada por un computador (10) o cualquier otro dispositivo de procesamiento.

d). Detectar el máximo de la señal (8) por medios electrónicos o por medio de algoritmos, emitiendo una señal que indica el final de la medición, como se ilustra con la marca (m2) de la figura 2.

e). Se genera una frecuencia de referencia f_0, como se ilustra en la figura 2.

f). Calcular el ángulo α entre el origen y el punto bajo estudio de la siguiente manera:

El tiempo entre la señal de inicio y la señal de alto, está dado como sigue:

$$t_\alpha = \alpha / \omega \qquad (1)$$

donde α es el ángulo entre la dirección instantánea y el punto de emisión y cero de la escala angular , ω es la velocidad angular de barrido (velocidad programada del dispositivo de barrido) y t_α representa el tiempo desde que el emisor de luz(6), emite la señal de inicio, hasta que un circuito de acondicionamiento de señal emite un pulso indicando que la luz de la fuente emisora fue captada por el fotodetector(5) encontrando de esta manera el máximo valor de la amplitud de la señal(8). Por otra parte, se conoce que en una revolución completa $\alpha = 2\pi$, por lo que el periodo de tiempo en una revolución $T_{2\pi}$, está dado conforme a la siguiente expresión matemática:

$$T_{2\pi} = 2\pi / \omega \qquad (2)$$

finalmente despejando α de la fórmula (1) se obtiene lo siguiente:

$$\alpha = \omega t_\alpha \qquad (3)$$

De acuerdo con la ecuación (3) la medición del mensurando α, prácticamente se convierte en la tarea de medir el intervalo de tiempo $t_{\alpha,}$ lo cual se puede realizar por métodos conocidos (como el método descrito en: Lombardi, M. A. Legal and Technical Measurement Requirements for Time and Frequency. Measure: The journal of Measurement Science. Vol1. No. 3. 2006 y el método descrito en: Hernández Balbuena Daniel, Sergiyenko Oleg, Tyrsa Vera, Burtseva Larysa, Rivas López Moisés. Signal frequency measurement by rational approximations. Elsevier, “Measurement”, Volume 42, Issue 1, January 2009,). Sin embargo, la medición de intervalos cortos de tiempo (ω =10r/s, $T_{2\pi}$ = 100 μs), se convierte en una tarea complicada. Por esta razón es conveniente excluir de la ecuación (3) la variable tiempo. La manera de hacerlo se presenta en la figura 2, donde se puede observar que el intervalo $T_{2\pi}$ es igual a la distancia entre las marcas m1 y m2, el cual está expresado por el código $N_{2\pi}$ definido en la ecuación (4).

$$N_{2\pi} = T_{2\pi} \cdot f_0 \qquad (4)$$

Por otro lado, el intervalo de tiempo t_α que es igual a la distancia entre las marcas m1 y m2, puede ser expresado por el código $N\alpha$ que se define como sigue:

$$N_\alpha = t_\alpha \cdot f_0 \qquad (5)$$

donde f_0 es una frecuencia de referencia estándar. De esta manera se puede excluir la variable tiempo de la ecuación (3) para expresarla en la forma siguiente (Rivas López Moisés, Sergiyenko Oleg, Tyrsa Vera, Hernández Perdomo Wilmar, Hernández Balbuena Daniel, Devia Cruz Luis, Burtseva Larisa, Nieto Hipólito Juan Iván. Optoelectronic Method for Structural Health Monitoring. SAGE Publications, “International Journal of Structural Health Monitoring”, Vol. 9,No.2, Marzo de 2010):

$$\alpha = 2\pi \cdot N_\alpha / N_{2\pi} \qquad (6)$$

donde α es el valor de la coordenada angular del emisor de luz, colocado en un punto de interés . Esta ecuación se puede generalizar como se expresa en la ecuación (7), debido a que el punto de interés puede ser colocado en diferentes posiciones o bien, pueden existir diferentes puntos de interés ubicados sobre el eje vertical (subíndice *j*) u horizontal (subíndice *i*) .

$$\alpha_{ij}=2\pi\cdot N_{\alpha_{ij}} \big/ N_{2\pi_{ij}} \quad (7)$$

Al excluir la variable tiempo en la estimación de α, se obtiene un resultado teórico muy significativo. Todas las fuentes de incertidumbre asociadas con la medición de tiempo mencionadas en (Daniel Hernández Balbuena, Oleg Sergiyenko, Vera Tyrsa, Larysa Burtseva, Moisés Rivas López. Signal frequency measurement by rational approximations. Elsevier, “Measurement”, Volume 42, Issue 1, January 2009, Pages 136-144), (Lombardi, M. A. Legal and Technical Measurement Requirements for Time and Frequency. Measure: The journal of Measurement Science. Vol1. No. 3. 2006. pp.60-69) son iguales para ambos intervalos N_α y $N_{2\pi}$, por lo que todos los errores instrumentales se eliminan en la operación de división en las fórmulas (6) y (7). Para la tarea técnica bajo consideración, eso establece una incertidumbre a nivel prácticamente despreciable por ejemplo: para una f_0 igual a 1MHz tenemos una graduación distinguible angular igual a 360°/ 1000000= 0.00036°, esta resolución es aceptada para cualquier aplicación técnica moderna de monitoreo de integridad de estructuras y en medición de desplazamiento para diferentes aplicaciones industriales.

g). Las coordenadas de los puntos de interés en el plano bidimensional se miden utilizando dos dispositivos de barrido colocados a una distancia conocida y aplicando triangulación dinámica, que consiste en lo siguiente: Si colocamos dos dispositivos de barrido SBOP1 y SBO2 a una distancia conocida (a), se forma un triángulo como se ilustra en la figura 3, y partiendo de la ley de los senos:

$$\frac{a}{sen(\alpha_1)}=\frac{b}{sen(\alpha_2)}=\frac{c}{sen(\alpha_3)} \quad (8)$$

Se puede concluir que la distancia entre los dispositivos de barrido y la fuente emisora está dada por la formula (9).

$$\mathrm{d}(\mathrm{a},\alpha_2,\alpha_3)=\frac{a.sen(\alpha_2).sen(\alpha_3)}{sen(180-(\alpha_2+\alpha_3))} \qquad (9)$$

Esta distancia ***d*(*a, α_2, α_3*)**, es el valor de distancia entre la base del triángulo y la fuente emisora, que depende de las variables ***α_2, α_3*** y de la distancia conocida **a**, esta distancia puede variarse para reducir la dimensión del sistema de barrido.

Si se tienen varios puntos de interés en el plano bidimensional se necesita en el caso general (X_{ij}, Y_{jj}) *punt*os, donde *i* corresponde a desplazamiento en el eje x, mientras que *j* corresponde al desplazamiento en el eje y.

Para obtener las coordenadas cartesianas de los resultados de mediciones angulares del sistema en cada fuente ubicada en ij, (Rivas López Moisés, Sergiyenko Oleg, Aguirre Mario, Devia Luis, Tyrsa Vera, and Rendón Ismael, Spatial data acquisition by laser scanning for robot or SHM task. IEEE-IES Proceedings “International Symposium on Industrial Electronics”ISIE-2008, Cambridge, United Kingdom, 30 de junio -2 de julio de 2008), se utilizarán las siguientes expresiones matemáticas que pueden ser deducidas del parámetro básico d_{ij} y del triángulo básico de la Figura 3, utilizando la relación entre lados y ángulos de un triángulo (Barchett, Raymond A., College Algebra with Trigonometry. ISBN: 0-07-003864-3. Mc graw hill . USA 1984), donde d_{ij} se puede expresar como sigue:

$$\mathrm{d}_{\mathrm{ij}}=a\frac{Sen\,\alpha_{2ij}\cdot Sen\,\alpha_{3ij}}{Sen\left[180^\circ-\left(\alpha_{2ij}+\alpha_{3ij}\right)\right]} \qquad (10)$$

En la Figura 3, el centro la base del triángulo coincide con el centro de la longitud de la línea imaginaria que une los dos dispositivos de barrido SBOP1 y

SBOP2. De igual manera las coordenadas en el punto P_{ij} (x_{ij},y_{ij}) se pueden determinar con las fórmulas (11),(12), como se muestra a continuación:

$$x_{ij} = a \cdot \frac{Sen\alpha_{2ij} \cdot Sen\alpha_{3ij}}{Sen\left[180^\circ - \left(\alpha_{2ij} + \alpha_{3ij}\right)\right]} \qquad (11)$$

$$y_{ij} = -a \cdot \left(\frac{1}{2} + \frac{Sen\alpha_{2ij} \cdot Cos\alpha_{3ij}}{Sen\left[180^\circ - \left(\alpha_{2ij} + \alpha 3_{ij}\right)\right]} \right) \qquad (12)$$

El eje y de las coordenadas cartesianas coincide con el eje central de la línea imaginaria entre SBOP1 y SBOP2 y el eje x es ortogonal al eje y.

h). En caso de existir desplazamiento, éste se calcula definiendo el vector de posición inicial $P_{ij}(x_{ij},y_{ij})$ y el vector de posición final $R_{ij}(X_{ij},Y_{ij},)$, entonces el desplazamiento se obtiene con el vector $U_{ij} = P_{ij} - R_{ij}$..

REIVINDICACIONES

Habiendo descrito suficiente nuestra invención, la consideramos como una novedad y por lo tanto reclamamos como de nuestra exclusiva propiedad, lo contenido en las siguientes reivindicaciones:

1. Un método de barrido óptico para medición de ángulos, coordenadas y desplazamiento de uno o varios puntos en un plano bidimensional, que se caracteriza por las siguientes etapas:
    a. Se coloca una fuente emisora de luz (1) en el punto bajo estudio a una distancia l de los dispositivos de barrido SBOP1 y SBOP2 separados a una distancia *a*.
    b. Cuando empiezan a girar los espejos (2) contenidos en los dispositivos de barrido, y se encuentran con el haz de un emisor de luz (6), el fotodetector (5) genera un pulso eléctrico indicando el inicio de la medición del ángulo α para cada uno de los dispositivos de barrido; α_2 para SBOP2 y para α_3 SBOP1 representando de esta manera la marca (m1); una vez que los espejos (2) alcanzan una velocidad máxima mantienen una velocidad constante ω.
    c. Se detecta el haz de luz emitido por la fuente emisora de luz (1) que tiene un ángulo de incidencia β con respecto a la perpendicular de los espejos (2), por lo tanto es reflejada por un

mismo ángulo β, posteriormente pasa a través de un lente (3) para ser captado por el fotodetector (5) que convierte la señal luminosa en una señal eléctrica generando de esta manera una función gaussiana (8)

d. Se detecta el máximo de la señal (8) por medios electrónicos o por medio de algoritmos, emitiendo una señal que indica el final de la medición, representado de esta forma la marca (m2).

e. Se genera un tren de pulsos a una frecuencia f_0 para determinar el número de pulsos contados cuando se detectó el máximo de la función (8) N_α ; se determina también el número de pulsos contados en un periodo de giro de los espejos (2) $N_{2\pi}$.

f. Se calculan los ángulos α_2 y α_3 por medio de la siguiente relación

$$\alpha = 2\pi \cdot N_\alpha / N_{2\pi}$$

g. Se calculan las coordenadas cartesianas la fuente emisora de luz (1) de las siguientes relaciones:

$$x = a \cdot \frac{Sen\alpha_2 \cdot Sen\alpha_3}{Sen\left[180^\circ - (\alpha_2 + \alpha_3)\right]}$$

$$y = -a \cdot \left(\frac{1}{2} + \frac{Sen\alpha_2 \cdot Cos\alpha_3}{Sen\left[180^\circ - (\alpha_2 + \alpha 3)\right]} \right)$$

2. El método de barrido óptico según la reivindicación 1, que se caracteriza además porque los espejos de los dispositivos de barrido

SBOP1 y SBOP2 giran a la misma velocidad ω pero en sentidos opuestos, y también dichos espejos tienen una superficie de reflexión a 45°.

3. El método de barrido óptico según la reivindicación 1, que se caracteriza porque en vez de espejos se puede utilizar cualquier superficie reflectiva cilíndrica, con un corte a 45°.

4. El método de barrido óptico según la reivindicación 1, que se caracteriza porque cuando se cuenta con más de una fuente emisora de luz las coordenadas cartesianas se calculan con las siguientes expresiones:

$$\mathrm{x}_{\mathrm{ij}} = a \cdot \frac{Sen\alpha_{2ij} \cdot Sen\alpha_{3ij}}{Sen\left[180^{\circ} - \left(\alpha_{2ij} + \alpha_{3ij}\right)\right]}$$

$$\mathrm{y}_{\mathrm{ij}} = -a \cdot \left(\frac{1}{2} + \frac{Sen\alpha_{2ij} \cdot Cos\alpha_{3ij}}{Sen\left[180^{\circ} - \left(\alpha_{2ij} + \alpha 3_{ij}\right)\right]} \right)$$

RESUMEN

La invención consiste en un método de barrido óptico para medición de ángulos, coordenadas y desplazamiento de uno o varios puntos en un plano bidimensional. A diferencia de otros sistemas que utilizan para el barrido óptico un espejo giratorio poligonal, la invención propuesta es un método que comprende una forma de realizar el barrido utilizando un espejo cilíndrico giratorio con una superficie de reflexión a 45º, permitiendo tener una medición continua del ángulo requerido para calcular las coordenadas y el desplazamiento del punto de interés.

Para medir el ángulo α , un pulso eléctrico que indica el inicio de la medición es generado al detectarse la luz de un emisor sincronizado con el origen y otro pulso es generado al final de la medición al detectarse una fuente de luz ubicada en el punto de interés. Un tren de pulsos con frecuencia de referencia f_0, permite calcular el ángulo α con la siguiente fórmula:

$$\alpha = 2\pi \cdot N_\alpha / N_{2\pi}$$

donde N_α es la cantidad de pulsos, contados desde el inicio hasta el final de la medición y $N_{2\pi}$ es la cantidad de pulsos en un periodo.

Una vez obtenido el ángulo α, se obtienen las coordenas y el desplazamiento mediante un tratamiento matemático.

ANEXOS

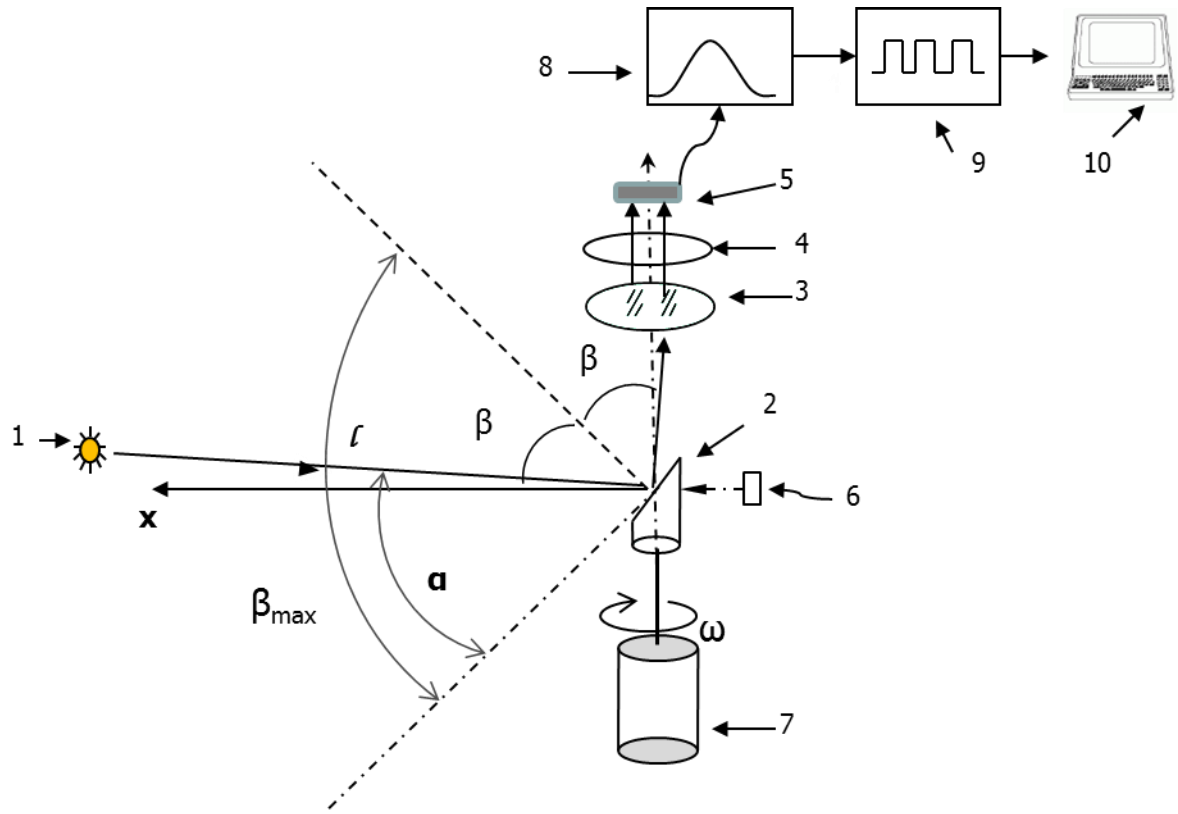

RECEPTOR SBOP

Figura 1

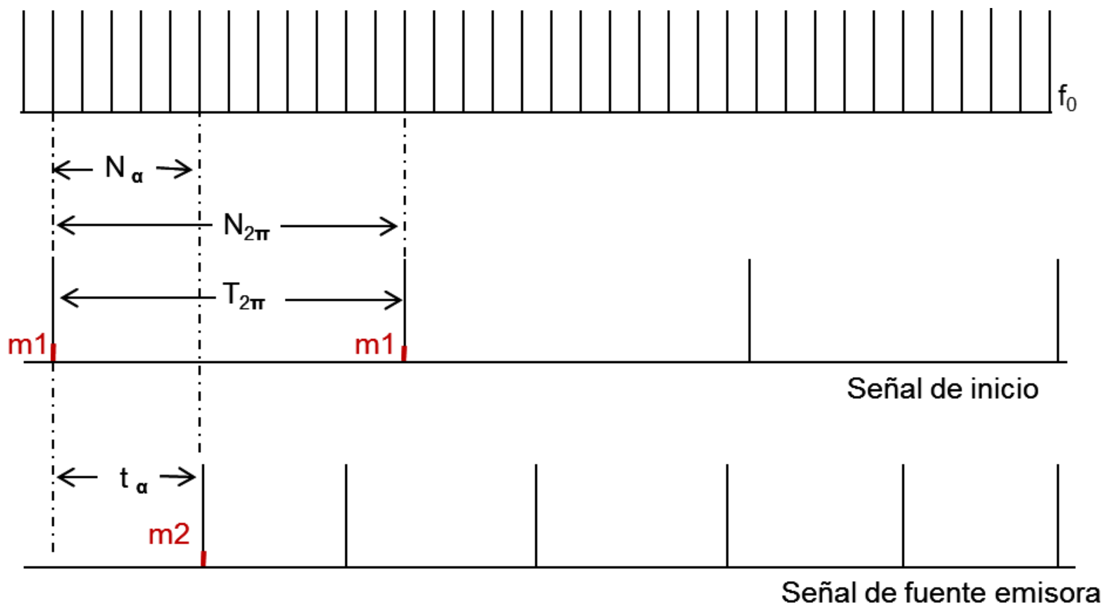

Figura 2

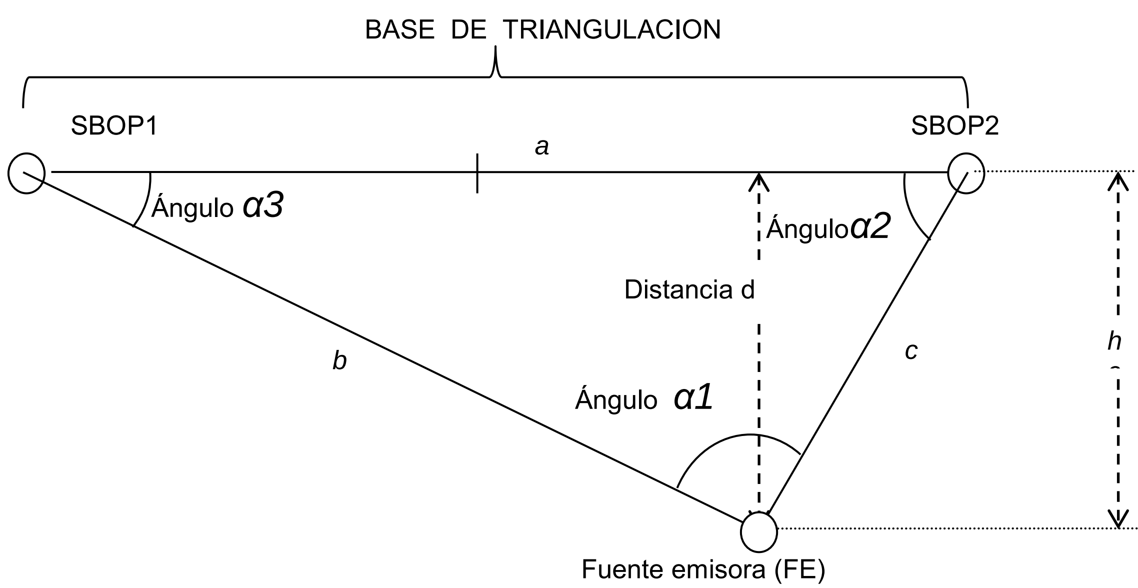

Figura 3

SISTEMA DE BARRIDO ÓPTICO PARA MEDICIÓN DE ÁNGULOS, COORDENADAS Y DESPLAZAMIENTO DE OBJETOS EN UN PLANO BIDIMENSIONAL.

OBJETO DE LA INVENCIÓN

La presente invención propone un sistema para medir las coordenadas, ángulos y desplazamiento de grandes objetos en un plano bidimensional utilizando un sistema de barrido óptico.

ANTECEDENTES

La invención que se presenta consta de un sistema de barrido óptico que implementa el método desarrollado por el mismo inventor, también presentado en otra solicitud de patente mexicana, y se relaciona con la medición de ángulos, coordenadas, y desplazamiento de objetos, utilizando un sistema de barrido óptico. Existen otros sistemas de barrido similares, como los que se describen en las patentes de Estados Unidos 5,455,708; 5,392,149 y 5,142,403 que aunque se asemejan en que utilizan para el barrido un espejo rotatorio, su principio de operación es completamente diferente, pues los sistemas de las patentes citadas arriba, utilizan un espejo poligonal configurado con varias caras de reflexión equilaterales y equidistantes con respecto al eje de rotación, de tal forma que al girar el espejo, el haz de luz incidente es reflejado secuencialmente por cada una de las caras para ser captado por algún elemento óptico, en tanto que la invención propuesta comprende un espejo cilíndrico con una sola superficie de reflexión a 45º que a diferencia de los espejos poligonales, permite tener una medición continua y el tratamiento formal para la estimación de las coordenadas es en esencia diferente.

La invención propuesta tiene también como antecedente el sistema presentado por los inventores Oleg Sergiyenko, Moisés Rivas y Vera Tyrsa, en el artículo titulado "Machine Vision: Approaches and Limitations", publicado, en noviembre de 2008, como el capítulo 22 del libro Computer Vision, de editorial Intech, editor Xiong Zhihui .En esta publicación se presenta un sistema de visión 3D conformado por una apertura de barrido óptico pasivo, similar al que aquí se presenta, pero el sistema completo que se describe en la publicación citada incluye un elemento activo, es decir un elemento que emite un haz de luz por medio de un laser cuyo centro de emisión está colocado sobre una base a una distancia de 1m con respecto al centro del elemento colocado sobre la misma base, asumiendo que esta es la base de un triángulo y así, con el ángulo de emisión con respecto al punto u objeto bajo observación y el ángulo medido por la apertura de barrido determina las coordenadas del punto u objeto, la diferencia con la invención propuesta es que ésta se comprende dos elementos de barrido óptico fijados sobre una base, estos elementos de barrido son pasivos, es decir, no emiten luz, solo captan la luz de una o varias fuentes emisoras colocadas en un plano bidimensional. El ángulo medido por cada uno de los elementos de barrido y la base del triángulo con dimensión conocida, permite estimar las coordenadas 2D del punto u objeto bajo estudio y con estas calcular el desplazamiento, en caso de existir. En el artículo "Optoelectronic

Method for Structural Health Monitoring” publicado por los inventores en marzo de 2010, en el Vol. 9(2) del Journal Structural Health Monitoring, de editorial SAGE, se describe de manera general el funcionamiento del elemento de barrido, pero no se presenta el sistema completo con los dos elementos, ni se describe como se calcula el desplazamiento con este sistema en el plano 2D, adicionalmente en la invención propuesta existe una diferencia en la forma de detectar el inicio de la medición, pues en la publicación citada el sensor de inicio está colocado sobre el volante de balanceo, en tanto que en la presente propuesta el sensor de inicio está colocado frente al espejo.

BREVE DESCRIPCIÓN DE FIGURAS.

Las figuras 1 y 2 muestran una vista frontal del sistema de barrido completo.

La figura 3 es una vista en detalle del dispositivo de barrido.

La figura 4 es un diagrama esquemático que ilustra el funcionamiento del dispositivo de barrido óptico.

La figura 5 es un diagrama temporal de las señales de inicio y fin de la medición y la figura 6 es una representación geométrica de triangulación dinámica.

DESCRIPCIÓN DETALLADA DE LA INVENCIÓN

Los detalles característicos de este novedoso sistema de barrido óptico para medición de ángulos, coordenadas y desplazamiento de un objeto en un plano bidimensional se muestran claramente en la siguiente descripción y en los dibujos que se acompañan con carácter ilustrativo y no limitativo, así como una ilustración de aquella y siguiendo los mismos signos de referencia para indicar las partes y figuras mostradas.

La invención propuesta consiste en un sistema para medición de ángulos, coordenadas y desplazamiento de grandes objetos. Como se ilustra en las figuras 1 y 2, el sistema comprende dos dispositivos de barrido (1),(2), unidos por una barra (3), que forma parte de un dispositivo de nivelación tridimensional (4), el cual está sostenido en una base (5), esta base puede girar para que el sistema pueda fijarse sobre el piso, como se observa en la figura 1, o pueda quedar suspendido en la parte inferior de un techo, al costado de una pared o en cualquier otra estructura, figura 2. El dispositivo de nivelación (4), que puede ser por ejemplo: un dispositivo de burbuja, con ajuste manual o un sistema electromecánico manual o automático, permite ajustar la posición de referencia del sistema girándolo, ajustándolo y nivelándolo sobre los tres ejes. Cada dispositivo de barrido (1),(2) como se muestra en las figuras 1 y 2, comprenden todos los elementos ilustrados en la figura 3, en esta se identifica un emisor de luz (6), que está sincronizado con el origen y genera un pulso al iniciar la medición, un dispositivo cilíndrico con una superficie reflectiva a 45º (7), por ejemplo un espejo cilíndrico con un corte a 45º, está sujetado a un dispositivo (11) que le permite girar a una velocidad angular predefinida, este dispositivo puede ser un motor de corriente continua o cualquier otro elemento que le permita girar. Un lente biconvexo (8) que permite concentrar la luz en el área de captación de un sensor (10), en caso necesario se puede agregar un filtro de interferencia (9). Estos tres últimos elementos (8, 9, 10) integran el canal óptico del dispositivo de barrido y se encuentran dentro de unas cápsulas cilíndricas (14), construidas con metal ligero, por ejemplo aluminio o cualquier otro material similar. El espejo cilíndrico (7) también se encuentra dentro de una cápsula (15), pero esta contiene una apertura que le permite captar la luz de una fuente emisora externa. Dos volantes (12) y (13), permiten balancear el movimiento angular del espejo (7). Los espejos cilíndricos (7) de los dispositivos de barrido (1 y 2) giran a la misma velocidad, pero en sentidos opuestos. En la figura 4 se presenta un diagrama esquemático de cada dispositivo de barrido (1 y 2), para ilustrar su operación conforme al método desarrollado por los mismos autores, presentado en otra solicitud de patente mexicana, conforme a este método los dispositivos de barrido operan de la manera siguiente: una fuente emisora de luz (19) es colocada en el punto bajo estudio a una distancia l, del centro del espejo (7) del receptor, el espejo gira con una velocidad predefinida ω. El haz de luz emitido por la fuente emisora de luz ubicada en un punto de interés (19), llega con un ángulo de incidencia β, con respecto a la perpendicular del espejo (7), por lo que es reflejado con un mismo ángulo β, de acuerdo a la ley de reflexión (C.L. Wyatt Electro-Optical System Design: For Information Processing ,NY: McGraw-Hill, p. 343, 1991), para pasar a través de un lente (8), que redirecciona el haz, quedando en paralelo con el eje central del lente, para ser captado por el fotodetector (10), el cual genera una señal analógica (18), que posteriormente será digitalizada por un circuito electrónico diseñado para ello (17) y procesada por un computador (18) o cualquier otro sistema de procesamiento. El sensor también puede ser tal que emita una señal digital por ejemplo un CCD, para ser procesada directamente por el computador (18). Cuando el espejo (7) empieza a girar y se encuentra la luz del emisor (6), el fotodetector (10) genera un pulso eléctrico indicando el inicio de la medición del angulo α, posteriormente al seguir girando el espejo (7) y al reflejar la luz de la fuente emisora ubicada en un punto de interés (19) hacia el fotodector (10), éste manda un pulso eléctrico indicando el final de la medición del angulo α; este pulso se ilustra en la figura 5, con las marcas m1 y la medición termina cuando el fotodetector (10), emite la señal de alto para finalizar (marcas m2 en la figura 5); el intervalo $T_{2\pi}$ es igual a la distancia entre las marcas m1 y m1, el cual está expresado por el código $N_{2\pi}$ definido en la ecuación (1) donde f_0 es una frecuencia de referencia, conocida.

$$N_{2\pi} = T2\pi \cdot f_0 \qquad (1)$$

Por otro lado, el intervalo de tiempo t_{α} que es igual a la distancia entre las marcas m1 y m2, puede ser expresado por el código Nα que se define como sigue:

$$N\alpha = t_{\alpha} \cdot f_0 \qquad (2)$$

donde f_0 es una frecuencia de referencia conocida, de esta manera se puede calcular α en la forma siguiente (Rivas López Moisés, Sergiyenko Oleg, Tyrsa Vera, Hernandez Perdomo Wilmar, Hernández Balbuena Daniel, Devia Cruz Luis, Burtseva Larisa, Nieto Hipólito Juan Iván. Optoelectronic Method for Structural Health Monitoring. SAGE Publications, “International Journal of Structural Health Monitoring”, Vol. 9,No.2, Marzo de 2010):

$$\alpha = 2\pi \cdot N_{\alpha} / N_{2\pi} \qquad (3)$$

siendo α el valor de la coordenada angular de la fuente emisora de luz, colocada en un punto de interés con referencia a cada sistema de barrido. Esta ecuación se puede generalizar como se expresa en la ecuación (4), debido a que el punto de interés puede ser colocado en diferentes posiciones o bien, pueden existir al mismo tiempo diferentes puntos de interés ubicados en diferentes lugares en la superficie de un objeto sobre el eje vertical (subíndice j) u horizontal (subíndice *i*) .

$$\alpha_{ij} = 2\pi \cdot N_{\alpha_{ij}} / N_{2\pi_{ij}} \qquad (4)$$

Al excluir la variable tiempo en la estimación de α, se obtiene un resultado teórico muy significativo. Todas las fuentes de incertidumbre asociadas con medición de tiempo mencionados en (Daniel Hernández Balbuena, Oleg Sergiyenko, Vera Tyrsa, Larysa Burtseva, Moisés Rivas López. Signal frequency measurement by rational approximations. Elsevier, “Measurement”, Volume 42, Issue 1, January 2009, Pages 136-144), (Lombardi, M. A. Legal and Technical Measurement Requirements for Time and Frequency. Measure: The journal of Measurement Science. Vol1. No. 3. 2006. pp.60-69) son iguales para ambos intervalos N_{α} y $N_{2\pi}$, por lo que todos los errores instrumentales se eliminan en la operación de división en las fórmulas (3) y (4). Para la tarea técnica bajo consideración, eso establece una incertidumbre a nivel prácticamente despreciable por ejemplo: para una f_0 igual a 1MHz tenemos una graduación distinguible angular igual a 360°/ 1000000= 0.00036°, este resultado para cualquier aplicación técnica moderna de monitoreo de integridad de estructuras y en medición de desplazamiento para diferentes aplicaciones industriales.

Nuestra invención también permite medir coordenadas de un punto en un objeto en un plano bidimensional, utilizando dos dispositivos de barrido colocados a una distancia conocida y utilizando un método de triangulación dinámica, que consiste en lo siguiente: si dos dispositivos de barrido óptico DBO1 y DBO2 se colocan a una distancia conocida a, se forma un triángulo como se muestra en la figura 6 y partiendo de la ley de los senos:

$$\frac{a}{sen(\alpha_1)} = \frac{b}{sen(\alpha_2)} = \frac{c}{sen(\alpha_3)} \qquad (5)$$

Se puede concluir que la distancia entre los dispositivos de barrido y la fuente emisora está dada por la formula (6).

$$\mathrm{d}(\mathrm{a}, \alpha_2, \alpha_3) = \frac{a.sen(\alpha_2).sen(\alpha_3)}{sen(180 - (\alpha_2 + \alpha_3))} \qquad (6)$$

Esta distancia ***d*(*a*, *α*$_2$, *α*$_3$)**, es el valor de distancia entre la base de trinagulación, y la fuente emisora que está en el ángulo sólido del campo de visión θ de nuestro sistema.

Para poder cubrir la superficie completa de un objeto bajo observación, por ejemplo la estructura de un puente, se necesita en el caso general (A_i,B_j)

puntos, donde *i* corresponde a desplazamiento en un eje, por ejemplo el eje horizontal y *j* al desplazamiento en un segundo eje, por ejemplo el eje vertical. Para obtener las coordenadas cartesianas de los resultados de mediciones angulares del sistema en cada paso de barrido *i,j*, (Rivas López Moisés, Sergiyenko Oleg, Aguirre Mario, Devia Luis, Tyrsa Vera, and Rendón Ismael, Spatial data acquisition by laser scanning for robot or SHM task. IEEE-IES Proceedings “International Symposium on Industrial Electronics”ISIE-2008, Cambridge, United Kingdom, 30 de junio -2 de julio de 20089), se utilizarán las siguientes expresiones matemáticas que pueden ser deducidas del parámetro básico d_{ij} y del triángulo básico de la Figura 6, utilizando la relación entre lados y ángulos de un triángulo (Barchett, Raymond A., College Algebra with Trigonometry. ISBN: 0-07-003864-3. Mc graw hill . USA 1984), donde d_{ij} se puede expresar como sigue:

$$\mathrm{d}_{\mathrm{ij}} = a\frac{Sen\alpha_{2ij} \cdot Sen\alpha_{3ij}}{Sen\left[180^{\circ} - \left(\alpha_{2ij} + \alpha_{3ij}\right)\right]} \qquad (7)$$

En la Figura 6, el centro de la base del triángulo coincide con el centro de la longitud de la barra (3) como se aprecia en las Figuras 1 y 2. De igual manera las coordenadas en el punto ij (x_{ij},y_{ij}) se pueden determinar con las fórmulas (8) y (9), como se muestra a continuación:

$$\mathrm{x}_{\mathrm{ij}} = a \cdot \frac{Sen\alpha_{2ij} \cdot Sen\alpha_{3ij}}{Sen\left[180^{\circ} - \left(\alpha_{2ij} + \alpha_{3ij}\right)\right]} \qquad (8)$$

$$\mathrm{y}_{\mathrm{ij}} = -a \cdot \left(\frac{1}{2} + \frac{Sen\alpha_{2ij} \cdot Cos\alpha_{3ij}}{Sen\left[180^{\circ} - \left(\alpha_{2ij} + \alpha_{3ij}\right)\right]}\right) \qquad (9)$$

El eje y de las coordenadas cartesianas coincide con el eje central de la barra y el eje x es ortogonal al eje y. Para la medición del desplazamiento, se define el vector de posición inicial $P_{ij}(x_{ij},y_{ij})$ y el vector de posición final e inicial $R_{ij}(X_{ij},Y_{ij},)$, entonces el desplazamiento se obtiene con el vector $U_{ij} = P_{ij} - R_{ij}$.

EJEMPLOS DE APLICACIÓN

Este sistema se puede aplicar, para detectar deformaciones de puentes, presas, inclinación y movimiento de edificios y desplazamiento de fallas geológicas, sin que estas aplicaciones sean limitativas.

REIVINDICACIONES

Habiendo descrito suficiente nuestra invención, la consideramos como una novedad y por lo tanto reclamamos como de nuestra exclusiva propiedad, lo contenido en las siguientes reivindicaciones:

1.- Un sistema de barrido óptico para medición de ángulos, coordenadas y desplazamiento de objetos en un plano bidimensional que se caracteriza porque comprende de dos dispositivos de barrido (1,2) unidos mediante una barra (3), dicha barra sostiene un dispositivo de nivelación tridimensional (4), ésta a su vez esta sostenida por una base (5)

2.- El sistema de barrido según la reivindicación 1, que se caracteriza además porque el dispositivo de nivelación (4) se selecciona de un grupo de un dispositivo de burbuja con ajuste manual, un sistema electromecánico manual o automático.

3.- El sistema de barrido según la reivindicación 1, que se caracteriza además porque cada dispositivo de barrido (1 y 2) está compuesto de un emisor de luz para indicar inicio de la medición (6); un dispositivo cilíndrico con una superficie reflexiva a 45° (7), dicho dispositivo está montado sobre el volante (12) y éste a la vez sobre otro volante (13), estos volantes van sujetos a un dispositivo que los hace girar (11); el dispositivo (7) junto con los volantes (12 y 13) van alojados dentro de una capsula (15); además el emisor de luz (6) se encuentra unido a un costado de la capsula (15), la capsula (15) cuenta con una abertura tal que permite captar la luz de la fuente emisora de luz ubicada en un punto de interés (19); además en la parte superior de la capsula (15) se encuentra unida una capsula cilíndrica (14), la cual aloja en su parte inferior un lente biconvexo (8) , un filtro de interferencia (9) y un sensor (10) en la parte superior del cilindro (14).

4.- El sistema de barrido según la reivindicación 1 que se caracteriza además porque la base (5) es giratoria logrando que el sistema pueda fijarse en el piso, techo o cualquier superficie útil para fijar el sistema.

5.- El sistema de barrido según la reivindicación 1 que se caracteriza además porque la base porque las superficies reflectivas (7) de los dispositivos de barrido (1) y (2) giran a la misma velocidad pero sentidos opuestos.

RESUMEN

La invención comprende un sistema de barrido óptico para medición de ángulos, coordenadas y desplazamiento de un objeto en un plano bidimensional. El sistema se caracteriza porque comprende dos dispositivos de barrido, que a diferencia de otros dispositivos que utilizan para el barrido óptico un espejo giratorio poligonal, la invención propuesta utiliza en cada dispositivo de barrido un espejo cilíndrico con una superficie de reflexión a 45º, estos espejos giran a la misma velocidad pero en sentidos opuestos. Cuando el espejo (7) empieza a girar a una velocidad predefinida ω y se encuentra la luz de un emisor (6) sincronizado con el origen, un fotodetector (10) genera un pulso eléctrico indicando el inicio de la medición del ángulo α. Posteriormente al seguir girando el espejo y al reflejar la luz de la fuente emisora ubicada en un punto de interés (19) hacia el fotodetector , éste manda un pulso eléctrico indicando el final de la medición. Una vez obtenido el ángulo α, mediante triangulación se calculan las coordenadas cartesianas de la fuente de luz ubicada en el punto de interés, con estas coordenadas se calcula el desplazamiento en caso de existir.

FIGURAS (Anexo)

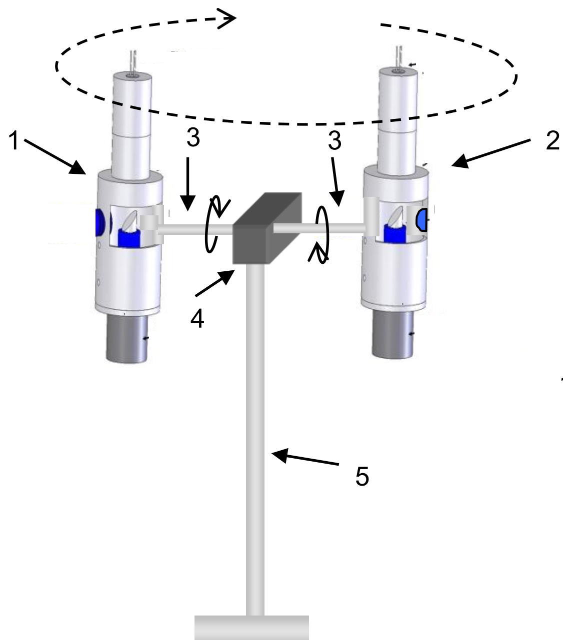

Figura 1

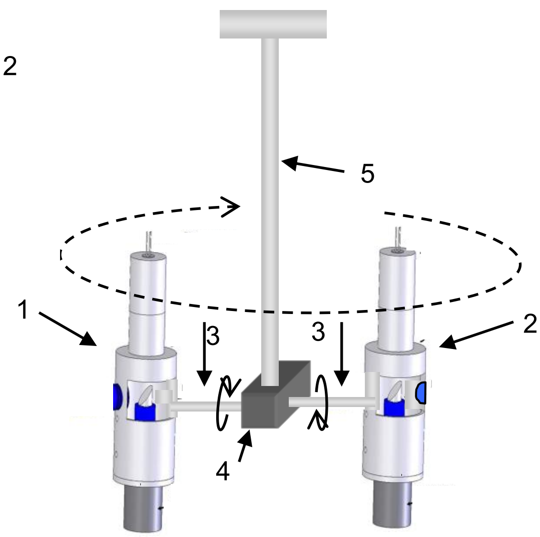

Figura 2

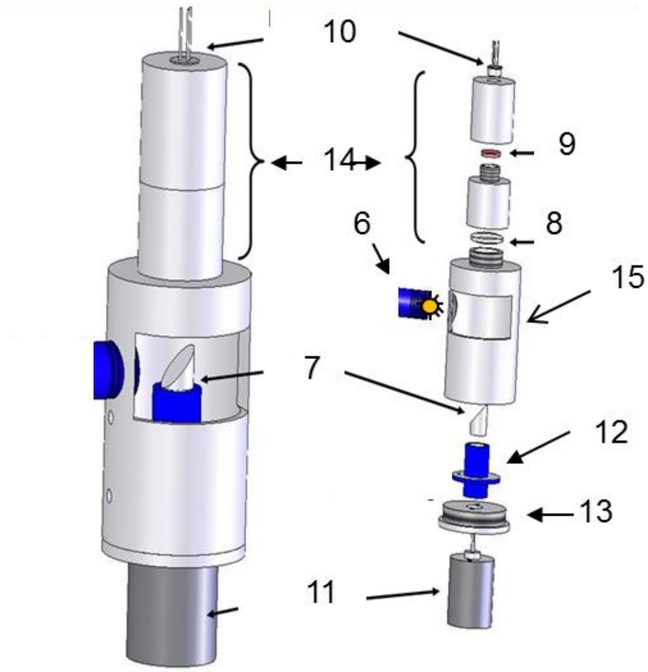

Figura 3

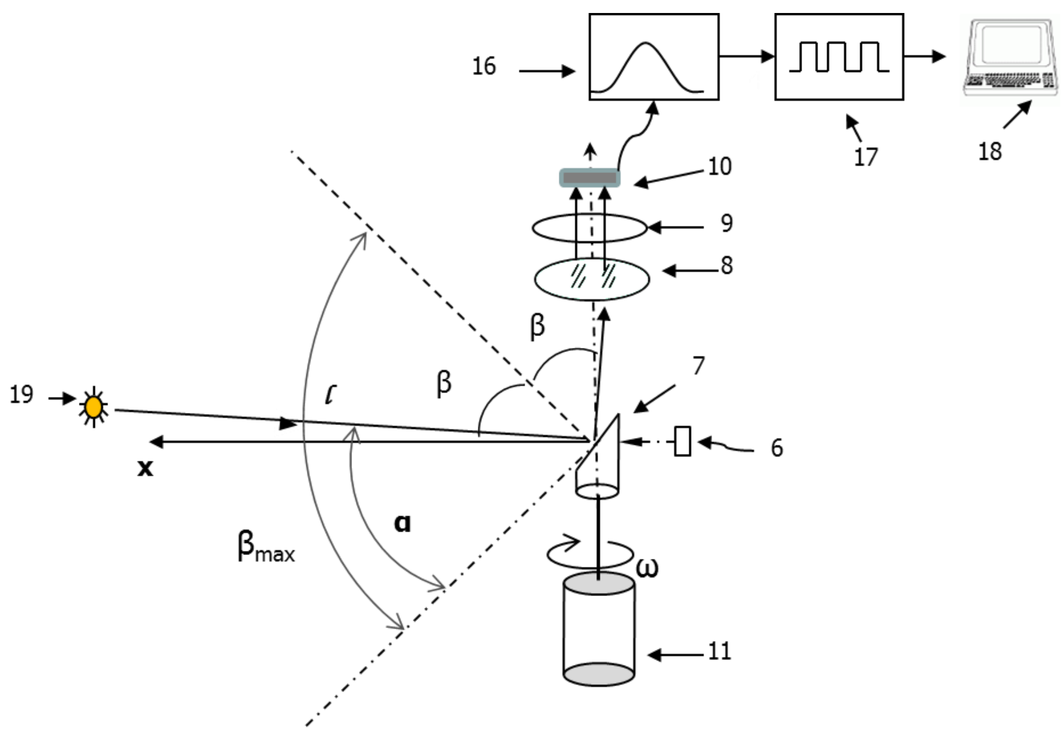

Figura 4

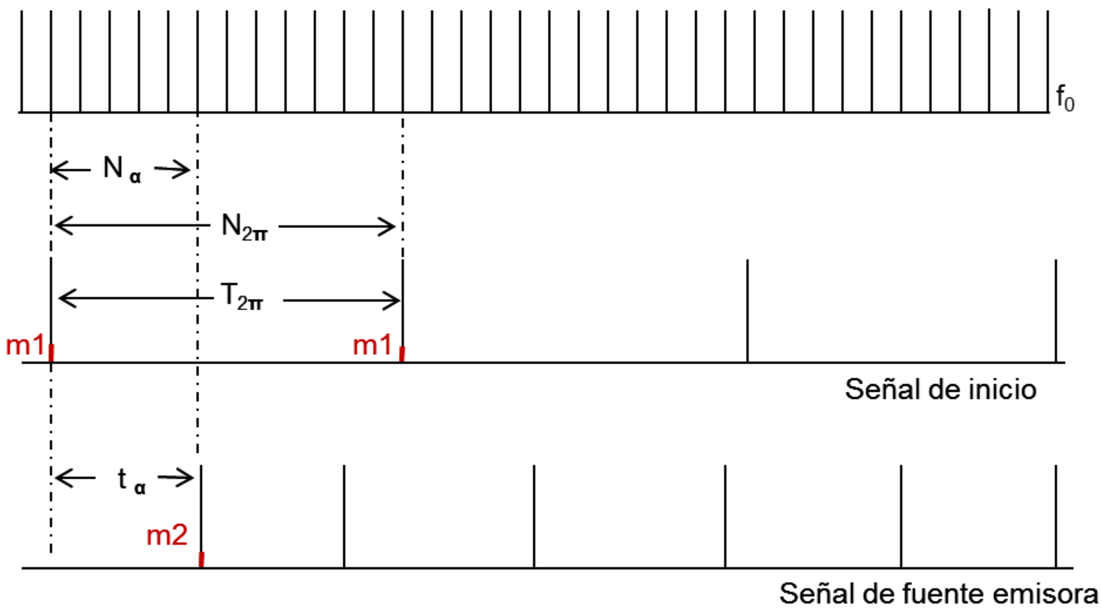

Figura 5

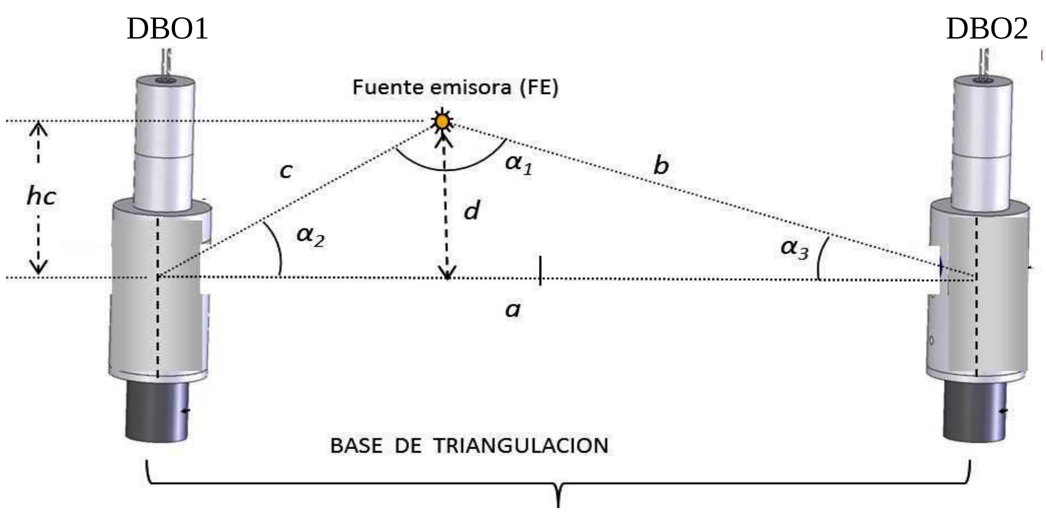

Figura 6